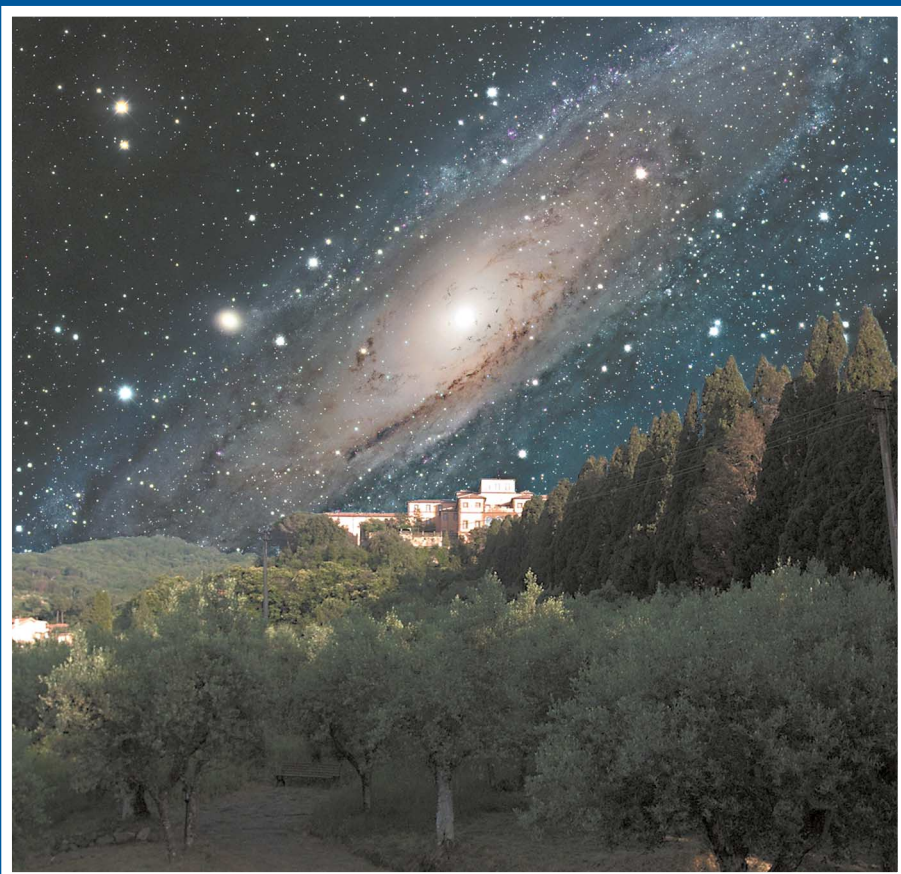ISTITUTO NAZIONALE DI FISICA NUCLEARE
Laboratori Nazionali di Frascati
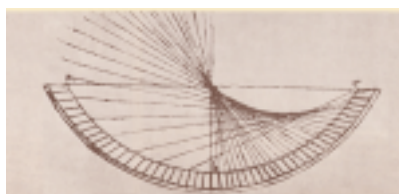
FRASCATI PHYSICS SERIES

Proceedings of the Third International Workshop on

FRONTIER SCIENCE 2004
PHYSICS AND ASTROPHYSICS IN SPACE

Editors
A. Morselli, P. Picozza, M. Ricci

Proceedings of the Third International Workshop on
FRONTIER SCIENCE 2004
PHYSICS AND ASTROPHYSICS IN SPACE

FRASCATI PHYSICS SERIES

Series Editor
Stefano Bianco

Technical Editor
Luigina Invidia

Cover:
Foreground: Villa Mondragone, picture by Aldo Morselli, background: Andromeda galaxy, Astronomy Picture of the Day, http://antwrp.gsfc.nasa.gov/apod/, photo composition by C. Federici (LNF, INFN).

Logo (pag.V):
M.C. Escher, Sphere Spirals (1958).

Volume XXXVII

White page

FRASCATI PHYSICS SERIES

Proceedings of the Third International Workshop on
FRONTIER SCIENCE 2004
PHYSICS AND ASTROPHYSICS IN SPACE

IV

FRASCATI PHYSICS SERIES

Volume XXXVII

Proceedings of the Third International Workshop on
FRONTIER SCIENCE 2004
PHYSICS AND ASTROPHYSICS IN SPACE

Editors
A. Morselli, P. Picozza, M. Ricci

Villa Mondragone, Monteporzio
and
Laboratori Nazionali INFN, Frascati
June 14 –19, 2004

VI

PREFACE

This Conference is the third of a series of Conferences after the first edition held in Frascati in October 2002 and the second one in Pavia, September 2003. Each conference focuses on one topic, selected from among the most lively subjects in nuclear and sub-nuclear physics, astrophysics, mathematics, theoretical physics, earth science, instrumentation, electronics, computing, and others. The conference consists of plenary sessions devoted in part to invited talks by senior scientists and in part to selected presentations by young researchers, and a poster session. Each year special awards and credits are given to relevant contributions presented by young researchers.

This year the Conference – with an attendance of more than 150 people from 10 countries - was dedicated to the most recent developments in Astroparticle and Cosmic-ray Physics, Observational Cosmology, Gamma-ray, Dark Matter and Gravitational Waves with a special focus on the status and perspectives of Space programs.

This field concerns the study of the fundamental laws of the Nature through the observation of the most energetic events in our Universe by the detection of cosmic rays, gamma rays and gravitational waves from space. It involves the knowledge of the cosmic rays composition, their origin, acceleration and propagation and the possibility to explore New Physics that could manifest itself through systematic investigation of the different experimental data.

The field is now emerging as a very stimulating and active one and it is complementary to the particle physics experiments performed at accelerators, underground, and at mountain laboratories. The vitality of the field is witnessed by the large number of experiments in progress and planned, like – just to mention some - the balloon experiments BESS and BOOMERanG, the space experiments PAMELA and AMS for antimatter cosmic rays detection, AGILE and GLAST for gamma rays, EUSO for the extreme high energy cosmic rays, LISA for gravitational waves.

Moreover, the need of advanced technologies both on Earth and in Space requires a close interaction with technological industries and aerospace companies, providing a very fruitful exchange of expertise and know-how. The involvement of small and medium high-tech enterprises in a joint discussion on the interplay between space research and space industries was an opportunity that the Conference provided during its works.

An additional mission of the series of these Conferences is to convey the importance of the field identified as a frontier in modern science to the general public. An open public lecture in Italian was given by Franco Pacini on the most recent advances in Observative Astronomy and Astrophysics.

We warmly thank the session chairpersons and all the speakers for their contribution to the scientific success of the Conference.

The Conference was sponsored and supported by the Department of Physics of the University of Roma "Tor Vergata", the Italian Istituto Nazionale di Fisica Nucleare (INFN) and the LABEN, CAEN and HAMAMATSU Companies.

We wish to thank the International Advisory Committee members for their valuable scientific advice and support all along the course of the conference organization.

Special thanks go to all the people involved in the Conference organization: We are particularly grateful to Liù Catena, Marta Solinas and Cristina D'Amato for their valuable help in preparing and dealing with all the logistics and for the day-by-day assistance both at Villa Mondragone and Frascati Laboratories and Roberta Antolini for the organization of the visit to Gran Sasso Laboratories.

We would also like to thank the Rector of the University of Roma "Tor Vergata", Alessandro Finazzi Agrò for hosting the first three days of the Conference at Villa Mondragone, the Director of the INFN Frascati National Laboratories, Sergio Bertolucci, for hosting the last two days of the Conference and the Director of INFN Gran Sasso National Laboratories, Eugenio Coccia, for making possible the visit to the experimental halls on the last day.

We acknowledge the support and assistance of the Comune di Frascati for the organization of the Public Lecture.

Finally, our special thank goes to Luigina Invidia, of the Servizio Informazione Scientifica of the Frascati Laboratories, for the technical editing of these Proceedings.

The book is available in electronic format at http://www.lnf.infn.it/sis/frascatiseries
http://www.roma2.infn.it/iwfs04/iwfs.html

February 2005   Franco Luigi Fabbri, Piergiorgio Picozza

VIII

FrontierScience Awards

The Frontier Science Organizing Committee, to encourage and promote the participation of young researchers to the event, has presented a number of selected young physicists with a FrontierScience Award for the best oral contributions and posters.

An international jury of senior physicists participating at the conference has evaluated the young physicist oral contributions on the basis of the scientific relevance, clearness and originality, while the best posters have been selected based on the votes cast by all the attendees during the poster session.

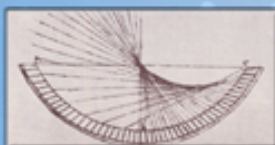The awarded researchers of the two categories are:

Best Oral Presentation by a Young Physicist
  Michela Chiosso *(Torino University, Italy)*

Best Poster by a Young Physicist
  Sabina Chita *(Max-Planck-Insitut fur Radioatronomie, Bonn, Germany)*

Third International Conference on Frontier Science
Villa Mondragone, Monteporzio Catone (Roma) Italy
June 14-19, 2004

Frontier Science 2004
Physics and Astrophysics in Space

The Conference is dedicated to the most recent developments in Astroparticle and Cosmic-ray Physics, Observational Cosmology, Gamma-rays and Dark Matter with a special emphasis on the status and perspectives of Space Programs. Invited speakers will review key topics while young researchers will present recent scientific achievements.

Organized by:
Università di Roma "Tor Vergata" and Roma II, INFN
Laboratori Nazionali di Frascati, INFN

International Advisory Committee

Since 2002
J. J. Aubert - IN2P3
J. Butler - Fermilab
J. Dorfan - SLAC
E. Iarocci - INFN
L. Maiani - CERN
A. N. Skrinsky - Novosibirsk
H. Sugawara - KEK
A. Wagner - DESY
M. Witherell - Fermilab

Since 2003
A. Bialas - Krakow Univ.
P. Cvitanovic - Atlanta Univ.
M. Gell-Mann - Santa Fe Univ.
L. Kadanoff - Chicago Univ.
S. Kauffman - Santa Fe Univ.
S. Lovejoy - Montreal Univ.
G. Nicolis - Bruxelles Univ.
G. Parisi - Roma "La Sapienza"
I. Procaccia - Rehovot Univ.

Since 2004
S. Bertolucci - INFN
P. Carlson - Stockholm Univ.
P. Fleury - Ecole Polytechnique
N. Gehrels - NASA GSFC
J. Ormes - NASA GSFC
M. Panasyuk - Moscow Univ.
G. Setti - INAF
S. Ting - MIT Boston
A. Wolfendale - Durham Univ.

Steering Committee

Permanent Members:
G. Casati - Como Univ.
F.L. Fabbri - INFN Frascati
G. Pancheri - INFN Frascati
S. Ratti - INFN Pavia

Scientific Secretary:
M. Ricci - INFN Frascati

Organizing Committee

L. Benussi - INFN Frascati
M. Bertani - INFN Frascati
S. Bianco - INFN Frascati
L. Bongiorno - INFN Frascati
V. Buttaro - Roma "Tor Vergata"
R. de Sangro - INFN Frascati
F.L. Fabbri - INFN Frascati (Co-Chair)
A. Lionetto - INFN Roma II
A. Morselli - INFN Roma II
P. Picozza - Roma "Tor Vergata" (Co-Chair)
C. Pittori - Roma "Tor Vergata"
M. Ricci - INFN Frascati
R. Sparvoli - INFN Roma II

Secretariat:
M.C. D'Amato - INFN Frascati
M. Legramante - INFN Frascati
M. Solinas - INFN Roma II

E_mail: FrontierScience@roma2.infn.it - http://frontierscience.lnf.infn.it

XI

Poster Session's award ceremony.
From left to right: A. Jacholkowska, A. Morselli, S. Chita, M. Ricci, F.L. Fabbri.

Young Physicist's award ceremony.
From left to right: P. Spillantini, A. Jacholkowska, M. Chiosso, A. Morselli,
M. Ricci, F.L. Fabbri.

Social Dinner: from left to right: D. Currie, I. Moskalenko, P. Michelson,
D. Kniffen and wife, A. Paolozzi.

Social Dinner: from left to right: A. Watson, S. Bertolucci, F. L. Fabbri.

Social Dinner.
Some members of the Organizing Committee
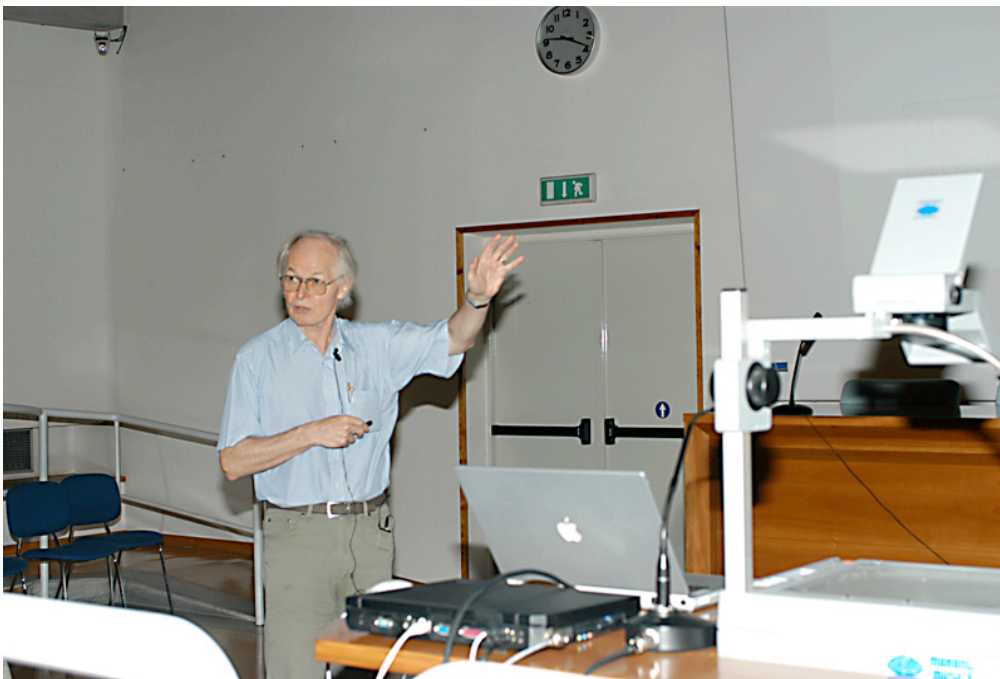
A. Watson's talk

TABLE OF CONTENTS

V   GAMMA RAYS IN SPACE **229**

VII VHE/UHE COSMIC RAYS 395

VIII GRAVITATIONAL WAVES AND FUNDAMENTAL PHYSICS IN SPACE   483

Part I

OBSERVATIONAL COSMOLOGY

A NEW ERA OF PRECISION COSMOLOGY: COBE, WMAP, PLANCK AND BEYOND

AMEDEO BALBI [a,b]

[a] *Dipartimento di Fisica, Università di Roma "Tor Vergata",
via della Ricerca Scientifica, Roma, Italy*

[b] *INFN, Sezione di Roma II, via della Ricerca Scientifica, Roma, Italy*

Abstract

In the past few years, cosmology has experienced an enormous progress. Our understanding of the physics of the early Universe, of its evolution and current large-scale structure, lies now on firmer grounds than in the past. This was due, on one side, to breakthroughs in theoretical research and, on the other side, to the impressive advancements made by observational techniques, which allowed to collect a large quantity of high-quality data. A fundamental role in entering what has been dubbed "the era of precision cosmology" has been played by the study of the cosmic microwave background (CMB). This review highlights the progress made in CMB investigation in the last decade, emphasizing the results from space missions, such as the COBE satellite, that opened a new era in the investigation of the cosmos, and the recent WMAP satellite, ending up with some future prospects from the forthcoming Planck Surveyor.

1   Introduction

The cosmic microwave background (CMB) is a powerful tool to investigate the physics of the early Universe and to constrain the parameters of the standard cosmological model. It provides a picture of the Universe when it was only a few hundred thousand years old, at the time when neutral atoms formed and photons decoupled from the matter. The fact that the COBE satellite (see Section 2) found the CMB to have a black body spectrum to an astonishing precision [8] is a clear signature of an early period of matter-radiation equilibrium and a major triumph for the big bang model.

Since the distribution of the CMB photons reflects that of matter at the time of decoupling, any inhomogeneities in the matter density (needed to seed structure formation in the Universe by gravitational instability) must leave an imprint as fluctuations of the CMB temperature. CMB temperature anisotropy was first detected by COBE in the early 90's [26] (see Section 2). The fact that the level of anisotropy is very small (about a part in one thousand, corresponding to temperature fluctuations of some tens of μK) simplifies the task of making theoretical prediction of the anisotropy pattern, since linear perturbation theory can be applied.

Most cosmological information encoded in the anisotropy pattern is concentrated at angular scales smaller than about 1 degree on the sky, corresponding to perturbations that were inside the horizon (i.e. in causal contact) before decoupling. On these scales, physical processes in the early Universe were able to leave their imprint on the CMB. The main CMB observable is the angular power spectrum of temperature anisotropy, C_l (see Figure 1). Since each l is related to an angular scale θ on the sky given approximately by $l \sim 180°/\theta$, the power spectrum at high l's probes sub-horizon angular scales at the time of decoupling and carries the imprint of physical processes which occurred in the early Universe. Conversely, low l's basically probe initial conditions in the early Universe (although secondary processes may alter the CMB photon distribution after decoupling).

The detailed shape of the CMB power spectrum is strongly dependent on cosmological parameters. For example, given an initial distribution of density perturbations in the early Universe, the relative height of the peaks in C_l represents a good indicator of the density of baryonic matter in the Universe. On the other hand, the position of the peaks depends on the way the physical scale of sound horizon at decoupling is mapped into an angular dimension on the sky. This mainly depends on the geometry of the Universe: for example, in an open Universe, a certain physical scale at decoupling is seen today under a smaller angle than in a flat Universe. The position of the peaks in the CMB angular power spectrum is the best indicator of the total density of the Universe available to cosmologists.

2 The COBE satellite

NASA launched the COBE (COsmic Background Explorer) satellite in 1989, with the purpose of performing full sky observations of the CMB from space. The COBE results were first announced in 1992, causing a revolution in observational and theoretical cosmology. The FIRAS (Far Infra-Red Absolute Spectrometer) instrument aboard COBE measured the energy spectrum of the CMB with stunning precision. The black body nature of the CMB was proved conclusively, signing a huge success of the big bang model [8]. The CMB temperature measured by FIRAS is 2.725 ± 0.001 K [17].

The DMR (Differential Microwave Radiometer) instrument detected for the first time tiny temperature fluctuations in the CMB, of order 10^{-5}, at angular scales of about $7°$ [26]. The importance of this result cannot be overemphasized. The CMB anisotropy measured by COBE was interpreted as having cosmological origin, reflecting inhomogeneities in the distribution of matter in the universe at the time of decoupling. This is crucial for understanding the initial conditions that seeded the formation of the large-scale structure we observe in the present Universe. The microwave sky observed by COBE is shown in the upper map of Figure 2 [2]. This map does not include the dipole anisotropy (corresponding to temperature differences in directions making an angle of $180°$) of order 10^{-3} of the average temperature, which is due to our motion with respect to the background photons.

In the decade following the release of the COBE results, the experimental efforts focused on measuring the CMB anisotropy at intermediate and small angular scales, that were not accessible to COBE because of its low angular resolution. Several experiments, conducted from 1992 to 1998, either from the ground or from balloon-borne payloads, explored the CMB angular power spectrum in the region between few arcminutes to about one degree. Although each single experiment could only probe a narrow band in l-space, the combined measurements seemed to indicate a rise in the power spectrum at $l \sim 200$.

Thanks to the progress in detector technology, between 1998 and 2000 the experiments TOCO [18], BOOMERanG [5] and MAXIMA [12] were able independently, for the first time, to clearly resolve the first acoustic peak in the angular power spectrum. BOOMERanG and MAXIMA also produced the first high-resolution (about 10 arcminutes) maps of the CMB, although on small patches of the sky. The detection of the first peak served to support the inflationary scenario, and allowed to measure the total energy density of the universe with unprecedented accuracy. This turned out to be very close to the critical value, $\Omega \simeq 1$, corresponding to a flat universe [1, 5].

Later, in 2001, the DASI [11], BOOMERanG [6] and VSA [10] experiments detected hints of a second acoustic peak in the CMB power spectrum, further strengthening the case for the adiabatic nature of primordial fluctuations. Then, in 2002, the Archeops [4] experiments secured the measurement of the

Table 1: Some cosmological parameters estimated by WMAP (from [3])

Parameter	Symbol	Value
Total density	Ω	1.02 ± 0.02
Baryon density	Ω_b	0.044 ± 0.004
Dark matter density	Ω_m	0.27 ± 0.04
Dark energy density	Ω_Λ	0.73 ± 0.04
Equation of state of dark energy	w	< -0.78 (95% C.L.)
Hubble constant (km s^{-1} Mpc^{-1})	H_0	71^{+4}_{-3}
Age of the Universe (Gy)	t_0	13.7 ± 0.2
Optical depth of the Universe	τ	0.17 ± 0.04
Spectral index of primordial density perturbations	n_s	0.93 ± 0.03

first acoustic peak, and the CBI [20] and ACBAR [16] experiments explored the spectrum at smaller angular scales, measuring the expected damping of primary anisotropy.

3   The WMAP satellite

The WMAP (Wilkinson Microwave Anisotropy Probe) satellite[1], launched by NASA aboard a Delta rocket on June 30, 2001, represents the state of the art of CMB experiments. In many ways, WMAP is a follow-up to COBE. It was designed to make full-sky map of CMB anisotropy by looking at temperature differences in the sky, using differential radiometers in five frequency bands. WMAP scans large regions of the sky in relatively short times, with a strong cross-linking among observations performed at different times: this is very useful to control systematic effects and correlated instrumental noise. WMAP operates from the L2 Lagrangian point, completing a full sky coverage in a six month period. WMAP detector technology is based on HEMT (High Electron Mobility Transistor) radiometers, passively cooled at about 90 K.

Results of the first year of observations by WMAP (August 2001-August 2002), corresponding to two full-sky surveys, were announced at the beginning of 2003 (see [3] and companion papers cited therein). Data collected later are currently being analyzed. The pattern of anisotropy seen in the WMAP maps is consistent with that observed by COBE after four years of observation. WMAP has 30 times better resolution than COBE. When the WMAP map is degraded at COBE resolution, the difference map is below the instrumental

[1]http://map.gsfc.nasa.gov
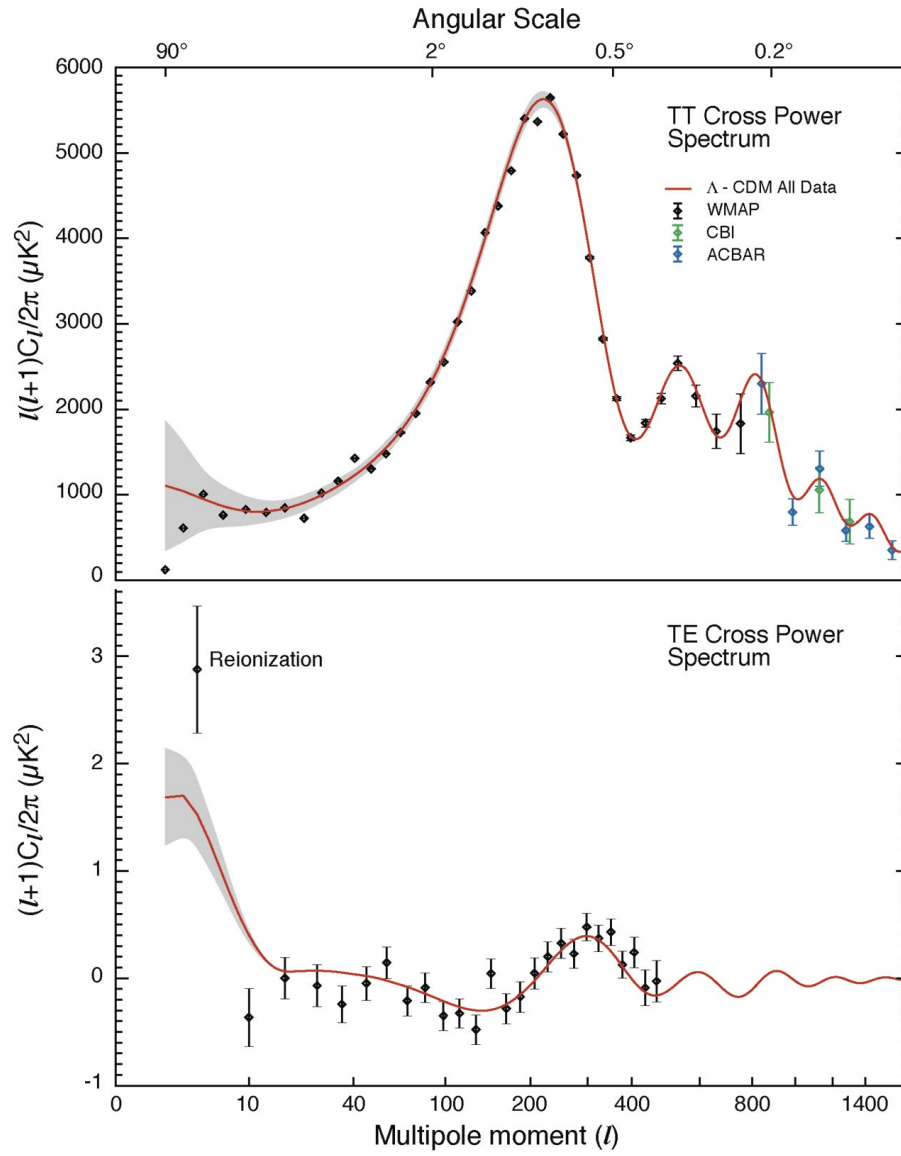
Figure 1: The CMB angular power spectrum. *(Top)*: the temperature power spectrum. The dots are the measurements from the WMAP [3], ACBAR [16] and CBI [20] experiments. The continuous line is the theoretical model which best fits the data. The grey region represents the cosmic variance uncertainty for this theoretical model. *(Bottom)*: the temperature-polarization correlation power spectrum. Note that this is not multiplied by the usual factor of l. (From [3])
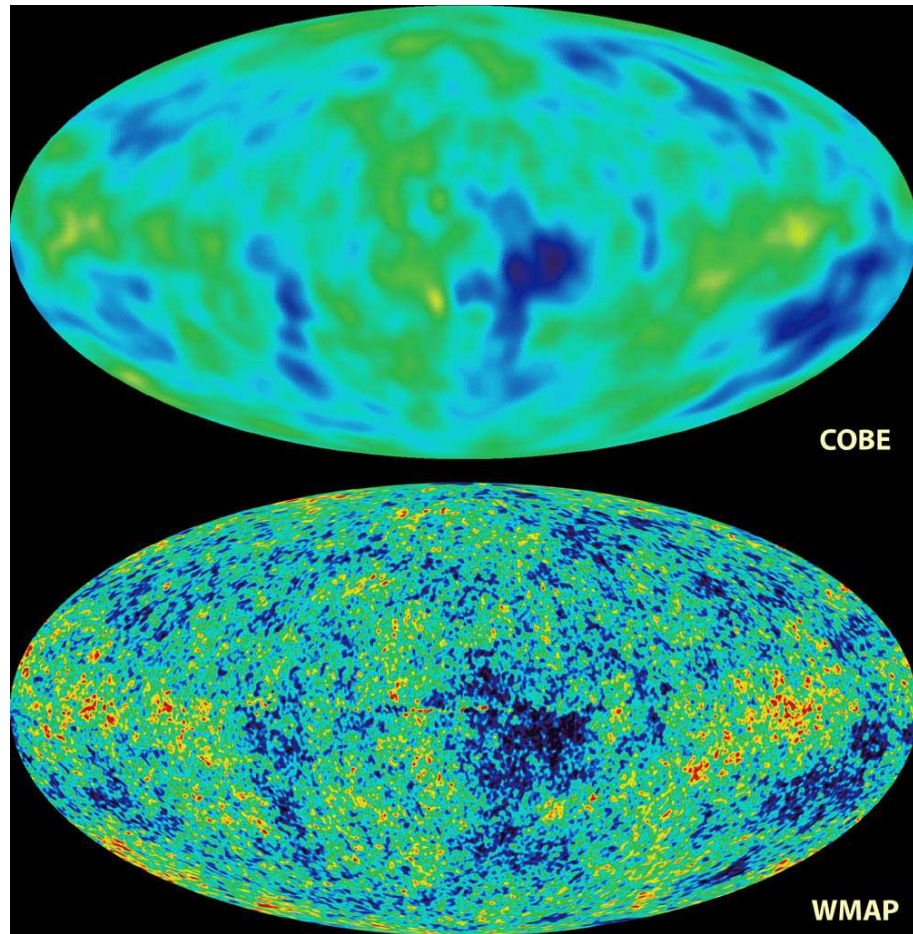
Figure 2: Maps of CMB temperature anisotropy. The sky, in galactic coordinates, is represented in Mollweide projection. Red spots are hotter the average, blue spots colder. Temperature scale is about $\pm 100\mu$K. In the upper panel, the map produced by COBE/DMR after 4 years of observation [2]. In the lower panel, the map produced by WMAP after 1 year of observation [3]. WMAP has 30 times better resolution than COBE. The contribution from galactic emission and the dipole anisotropy have been subtracted from the maps. (Courtesy NASA/WMAP science team)

noise level.

Figure 1 shows the CMB temperature anisotropy power spectrum measured by WMAP. This is the best currently available measurement of the power spectrum and is limited by cosmic variance up to $l \simeq 350$. WMAP results provide an extraordinary confirmation of the theoretical predictions. The presence of at least two acoustic peaks in the power spectrum is evident. The cosmological interpretation of these results lends further support to the standard cosmological model based on big bang plus inflation. A flat universe, with adiabatic, gaussian, scale-invariant primordial density fluctuations is perfectly consistent with the WMAP data. The values of the main cosmological parameters, estimated using the WMAP data, are summarized in Table 1. These values are generally more precise than those obtained with other kinds of observations, and are consistent with them. For example, the baryon density at recombination measured by WMAP is in agreement with big bang nucleosynthesis predictions and measurements of the primordial abundance of light elements [19, 23, 7]; the Hubble constant value agrees with the measurement by the Hubble Space Telescope [9]; the age of the Universe is consistent with the value from stellar observables [24, 13]; finally, the dark matter content of the Universe is in agreement with the one derived by the large-scale matter distribution [27]. The low value of the matter density, combined with the fact that $\Omega \simeq 1$, confirms that most of the energy density in the Universe is provided by dark energy, as recently indicated by high-redshift type Ia supernovae observations [22, 25]. When combined with other astronomical data (high-redshift type Ia supernovae and the matter distribution inferred from redshift surveys) WMAP observations are able to constrain the equation of state of the dark energy component (see Table 1). The outstanding concordance among completely different kinds of observations testifies the level of maturity reached by cosmology in recent times.

A fraction of the CMB signal is predicted to be linearly polarized. Although the polarized component is expected to be small (about 10% of the total signal) it carries valuable cosmological information. A first detection of CMB polarization, in agreement with theoretical predictions, has been announced by the interferometric experiment DASI [15]. WMAP detected a correlation between CMB temperature anisotropy and polarization, as expected theoretically [14]. This allowed to set limits on the reionization history of the Universe. The integrated optical depth to reionization measured by WMAP is $\tau = 0.17 \pm 0.04$. For a range of plausible models, this corresponds to a reionization at redshift $z_r = 20^{+10}_{-9}$ (95% C.L.) or an epoch $t_r = 180^{+220}_{-80}$ Myr (95% C.L.) after the big bang. Two features of the temperature-polarization correlation measured by WMAP gave further support to the inflationary scenario and to adiabatic primordial density perturbations: the presence of an antipeak at $l \simeq 130$, corresponding to scales that were outside the horizon

at decoupling, and the presence of a peak at $l \simeq 300$ that is out of phase with the first peak in the temperature power spectrum (see Fig. 1).

WMAP mission has been approved for 4 years of operation in L2. In the next few years, further data and analysis will provide more and more detailed cosmological information.

4   The Planck Surveyor

Despite its extraordinary achievements, the WMAP mission does not represent the end of the story. Much remains to be told about the CMB temperature anisotropy. On one hand, WMAP angular resolution does not allow to investigate the damping tail of the CMB power spectrum: although the first two acoustic peaks in the spectrum are now accurately resolved, higher l's are affected by large uncertainties. Other experiments, especially interferometers, are starting to unveil the small angular scale details of the anisotropy pattern, but much work needs to be done. On the other hand, WMAP maps are still affected by a non negligible instrumental noise, which strongly reduces the possibility of direct pixel space analyses.

ESA's Planck Surveyor[2], planned for launch in 2007, will represent the third-generation CMB space mission. The main product of the Planck mission will be full-sky maps in 9 frequency bands between 30 and 900 GHz. Planck frequency coverage will be the widest ever for a single microwave experiment. This is crucial to separate the various components that constitute the observed signal, and will allow the investigation of a large variety of poorly known astrophysical processes, both galactic and extragalactic. Planck will carry on board two different instruments: the HFI (High Frequency Instrument), based on bolometric detectors, and the LFI (Low Frequency Instrument), which uses HEMT radiometers. Exploiting this redundancy and comparison among measurements will be extremely important for the detection and removal of systematics.

Planck's instrumental sensitivity will be several times better than WMAP's. The design of Planck's detectors and optics (a 1.5 m primary mirror and a off-axis secondary, coupled to an array of corrugated horns in the focal plane) will allow to obtain the best possible resolution at each frequency, making it possible to resolve details of a few arcminutes in the sky.

The accuracy of the CMB angular power spectrum measurement by Planck will be limited by cosmic variance and by unavoidable foreground contamination, over the entire range of angular scales relevant to the primary CMB anisotropy, i.e. from $l = 2$ up to $l \sim 1000$, well below the damping scale.

---

[2]http://astro.estec.esa.nl/Planck

This will allow to fully extract the vast amount of cosmological information encoded in the CMB. Planck will be able to measure the cosmological parameters to unprecedented accuracy, minimizing the need of external input from other observations.

The full-sky maps produced by Planck will have a signal-to-noise ratio much larger than 1: this means that Planck's maps will be real pictures of the Universe at recombination. This will allow to accurately investigate physical processes which affect the CMB statistics beyond the angular power spectrum, such as small deviations from gaussianity of the primordial fluctuations, predicted in some theoretical scenarios.

Planck will be the definitive mission for the investigation of CMB temperature anisotropy. On the other hand, Planck detectors were also designed to be sensitive to the polarized component of the CMB signal, although not explicitly optimized for this measurement. This will allow Planck to say something relevant on the new frontier of CMB investigation.

5   Conclusions

Cosmology has developed into a fully mature science. The parameters of the big bang model are now known with great accuracy, and the constraints are expected to get tighter in the future. Inflation has not been falsified, and its main predictions are strikingly consistent with observations. The results obtained using completely different cosmological probes are in remarkable agreement among themselves, as well as with theoretical predictions. Nonetheless, many fundamental questions are still open (see, e.g., [21]). The pace of experimental and theoretical progress, however, does not seem to be close to a halt.

References

[1] Balbi A. et al. 2000, ApJ, 545, L1

[2] Bennett C. L. et al., 1996, ApJ, 464, L1

[3] Bennett C. L. et al., 2003, ApJS, 148, 1

[4] Benoît A. et al., 2003, A&A, 399, L19

[5] de Bernardis P. et al., 2000, Nature, 404, 955

[6] de Bernardis P. et al., 2002, ApJ, 564, 559

[7] D'Odorico S. et al., 2001, A&A, 368, L21

[8] Fixsen D. J., Cheng E. S., Gales J. M., Mather J. C., Shafer R. A., Wright E. L., 1996, ApJ, 473, 576

[9] Freedman W. L. et al., 2001, ApJ, 553, 47

[10] Grainge K. et al., 2003, MNRAS, 341, L23

[11] Halverson N. W. et al., 2002, ApJ, 568, 38

[12] Hanany S. et al., 2000, ApJ, 545, L5

[13] Hansen B. M. S. et al., 2002, ApJ, 574, L155

[14] Kogut A. et al., 2003, ApJS, 148, 161

[15] Kovac J. M., Leitch E. M., Pryke C., Carlstrom J. E., Halverson N. W., Holzapfel W. L., 2002, Nature, 420, 772

[16] Kuo C.-L. et al., 2002, ApJ, astro-ph/0212289

[17] Mather J. C., Fixsen D. J., Shafer R. A., Mosier C., Wilkinson D. T., 1999, ApJ, 512, 511

[18] Miller A. D. et al., 1999, ApJ, 524, L1

[19] O'Meara J. M. et al., 2001, ApJ, 552, 718

[20] Pearson T. J. et al., 2003, ApJ, 591, 556

[21] Peebles P. J. E., 2003, astro-ph/0311435

[22] Perlmutter S. et al., 1999, ApJ, 517, 565

[23] Pettini M. & Bowen D. V., 2001, ApJ, 560, 41

[24] Reid I. N., 1997, AJ, 114, 161

[25] Riess A. G. et al., 2001, ApJ, 560, 49

[26] Smoot G. F. et al., 1992, ApJ, 396, L1

[27] Verde L. et al., 2002, MNRAS, 335, 432

EXTRAGALACTIC RESULTS FROM THE SLOAN DIGITAL SKY SURVEY

Richard G. Kron [a,b]

[a] *Fermi National Accelerator Laboratory, P.O. Box 500,*
Batavia, IL 60510, USA

[b] *Department of Astronomy and Astrophysics, The University of Chicago,*
5640 S. Ellis Avenue, Chicago, IL 60637, USA

Abstract

A brief review of the status of and data from the Sloan Digital Sky Survey
is presented, followed by references to the papers on extragalactic topics
that were reviewed in the talk.

1   The Survey

The Sloan Digital Sky Survey (SDSS) is about to begin its last year of
operations. By mid-2005, we expect to have imaged at least 7000 square
degrees in the North Galactic Cap in five filters. These imaging data enable
spectroscopic targets to be selected, specifically galaxies to a surface density of
100 per square degree and quasars to a surface density of 13 per square degree.
The galaxy selection includes a category called Luminous Red Galaxies that are
selected by both magnitude and color criteria to be essentially volume-limited

to z $\approx$ 0.4 (see Figure 1). By mid-2005 we expect to have obtained at least 5000 square degrees of spectroscopic coverage in the North Galactic Cap.

The SDSS data (photometric and spectroscopic) are characterized by the high uniformity and the high precision with which the calibrations have been made, attributes that are required for sensitive measures of structure across wide angles in the sky. The project is described in [1], and the details of the spectroscopic target selection are given in [2, 3, 4]. The data are being released via a web interface (www.sdss.org/dr2 - see [5]).

The project itself, and the nature of the selection of spectroscopic targets, was designed to address extragalactic problems, specifically the properties of galaxies, large-scale structure as a function of galaxy properties, cluster identification, and quasar statistics (luminosity function, evolution, and redshift distribution to high redshifts). The SDSS has made significant contributions to all of these fields, and we expect much more to come from the analysis of the completed catalogs. Other results have also been achieved, including notably weak-lensing of background galaxies, the discovery of strongly lensed quasar images, and the detection of supernovae in the spectroscopic survey.

2   Extragalactic Results

In this talk I present a sampling of some extragalactic results from SDSS. The papers from which results are reviewed include the following:

Schneider, D.P. et al. 2003 AJ 126, 2579 (quasar catalog)

Fan, X. et al. 2001 AJ 121, 54 (evolution of the quasar luminosity function for 3.6 < z < 5)

White, R.L. et al. 2003 AJ 126, 1 (ionization of the IGM at z > 6 from quasar spectra)

Tegmark, M. et al. 2004 ApJ 606, 702 (3-D galaxy power spectrum)

Tegmark, M. et al. 2004 Phys Rev D 69, 103501 (cosmology from large-scale structure combined with CMB)

Scranton, R. et al. astro-ph 0307335 (Integrated Sachs-Wolfe Effect and dark energy)

Bahcall, N.A. et al. 2003 ApJ 585, 182 (constraint on sigma_8 and Omega_m from the cluster mass function)

Sheldon, E.S. et al. 2004 AJ 127, 2544 (galaxy-mass correlation function from weak lensing)

Oguri, M. et al. 2004 ApJ 605, 78 (widest-separation image lensed by a cluster)
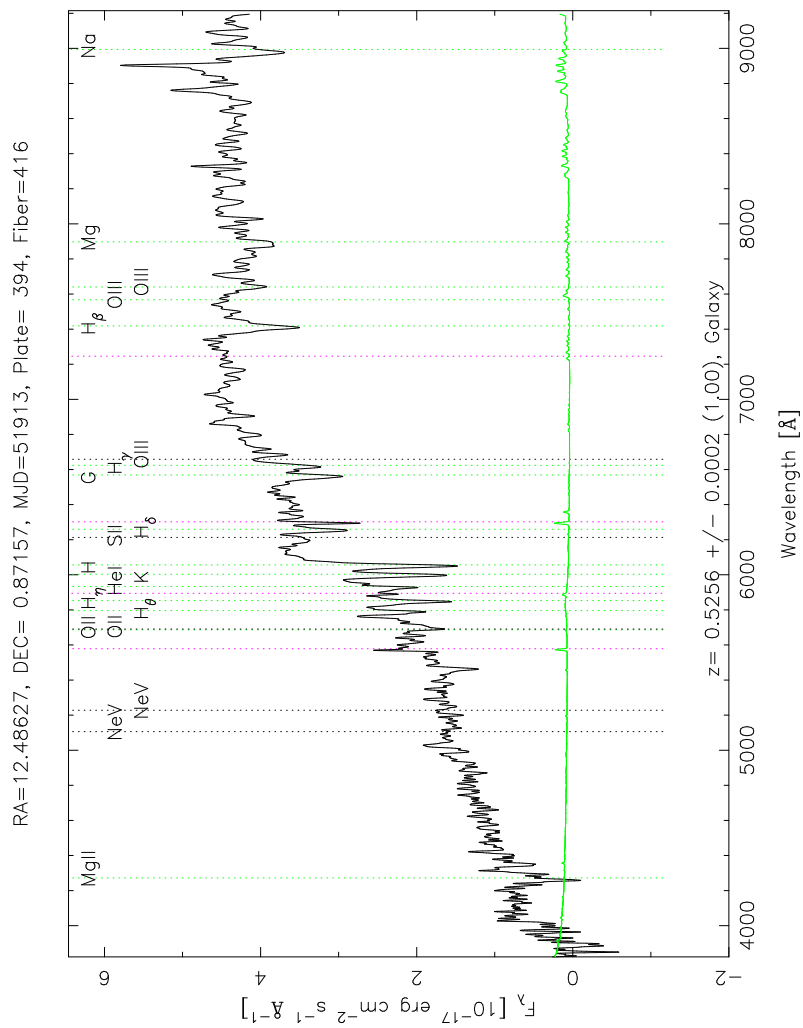
Figure 1: An example of a luminous red galaxy at z = 0.526, chosen to have relatively high signal-to-noise ratio. This plot illustrates some of the features of the SDSS spectroscopic data base, namely the flux calibration and the automated line identification, redshift, and spectral type.

3   Acknowledgments

References

[1] D.G. York et al., *Astron. J.*, **120**, 1579 (2000).

[2] D.J. Eisenstein et al., *Astron. J.*, **122**, 2267 (2001).

[3] G.T. Richards et al., *Astron. J.*, **123**, 294 (2002).

[4] M.A. Strauss et al., *Astron. J.*, **124**, 1810 (2002).

[5] K. Abazajian et al., *Astron. J.*, **128**, 502 (2004).

THE HEATING OF CLUSTERS OF GALAXIES BY BUYOANT BUBBLES

Sabina-Mădălina Chiţă[a],[b] Peter L. Biermann[b]

[a] *University of Bucharest, România*

[b] *MPIfR, Uni-Bonn, Germany*

Abstract

Recently X-ray observations of clusters of galaxies confirmed that radio galaxiess, their jets and hot spots do provide a substantial energy input into the intracluster medium, as had been suggested a long time ago based on cosmic ray arguments. We wish to note that such an energy input is highly intermittent, and should have been much stronger in the early universe, when active galactic nuclei were more than an order of magnitude more active per comoving volume.

1 Introduction

Regular clusters of galaxies are one of the largest organized structures in the universe. They typically contain hundreds of galaxies, spread over a region whose size is roughly 10^{25} cm. Their total masses exceed 10^{48} g. They were first studied in detail by Wolf (1906), although the tendency for galaxies to cluster on the sky had been noted long before this.

2   Review

After Ginzburg suggested more than forty years ago, that the radio galaxy M87 might be the source of the highest energy cosmic rays, a very specific physical model based on the emission spectra in the infrared/ optical/ ultraviolet by Biermann & Strittmatter (ApJ 1987) found that in fact 10^{21} eV protons were implied to exist in the jet of M87 and its knots. This then leds to the development of detailed models for the cosmic ray production of jets and radio hot spots (Rachen & Biermann 1993 AA, and Rachen et al. 1993 AA), and to the development of the jet-disk symbiosis picture that connected jet power to disk power (Falcke et al. 1994, 1995, 1996 up to 2004). This suggested that the energy input from radio galaxies is substantial. There are suggestions that the mass estimates from lensing and X-rays were somewhat discrepant, and one solution was to argue that cosmic rays and magnetic fields indeed make up an extra pressure in the intracluster medium (Enßlin et al. 1997 ApJ). Again in a parallel development relativistic bubbles had been found first in the Perseus cluster and now in many clusters, were radio galaxies clearly produce bubbles of radio emitting relativistic gas which holds it own against the outside pressure of the hot thermal gas (Böhringer et al.). Yet another problem had been that the cooling flows implied by X-ray observations often led to inconsistent mass accretion rates for the central black holes. And then recently the X-ray spectra of the Virgo cluster (Böhringer et al.) clearly demonstrate that there is distributed heating emanating from the jet of M87, once and for all demonstrating that the jet carries a lot of energy, thus confirming all the earlier arguments. Churazov et al. then discussed the details and showed that this heating is really required. The search is now on for the exact mechanism of this distributed heating and the debate has an interesting analogy in the many years when the heating and driving of the Solar wind was discussed, a question which has only recently found a tentative solution involving magnetic fields (Parker). We wish to note that the energy input from radio galaxies involves intermittency, and so involves multiple shock waves in a highly magnetic medium. It is maybe no surprise to note that cooling flow clusters with radio galaxies are just those that show the evidence for the strongest magnetic fields (see Enßlin et al. 1997).

3   Long term effects upon a cluster structure (work in progress)

Inconsistency of hydrostatic models and observations leads us to consider another model. This model is inherently nonstationary; hydrostatic models are probably inedequate. Clusters consist mostly of early Hubble type galaxies, almost all of which have a massive central black hole, and this black hole grew to its present mass through accretion, implying that there has been an active galactic nucleus in the past, for elliptical galaxies quite likely a radio galaxy.

Therefore we need a hydrodynamic model which consists of an initial temporary equilibrium with a low density region in the center. Then a bubble will form which is continously(intermitentelly) injected with radio plasma from the jet at the center of the grid. Bubbles rise and break up, convecting, heating and mixing with the cluster medium. We are trying to see what happens if the jet is continous and if the jet is intermittent. We are using spherical symmetry in 2D with grid resolution of several hundred.

$$\frac{\partial f}{\partial t} + v_r \frac{\partial f}{\partial r} - \frac{\partial \Phi_G}{\partial r} \frac{\partial f}{\partial v_r} = 0 \tag{1}$$

$$v_\varphi = v_\theta = 0$$

$$f = f(r, v_r, t)$$

$$\frac{\partial \rho}{\partial t} + \frac{1}{r^2} \frac{\partial}{\partial r}(r^2 \rho v_r) = 0 \tag{2}$$

$$\rho \frac{\partial \overrightarrow{v}}{\partial t} + \rho(v\nabla)\overrightarrow{v} = -\rho\nabla\Phi_G - \nabla P_{int} \tag{3}$$

$$\rho \frac{\partial v_r}{\partial t} + \rho \left(v_r \frac{\partial v_r}{\partial r} \right) = -\rho \frac{\partial \Phi_G}{\partial r} - \frac{\partial P}{\partial r} \tag{4}$$

$$\frac{\partial}{\partial t}\left(\frac{\rho v_r^2}{2} + \rho\varepsilon \right) = -\frac{1}{r^2}\frac{\partial}{\partial r}\left[r^2 \rho v_r \left(\frac{v_r^2}{2} + \omega \right) \right] \tag{5}$$

By using the numerical simulation code VH-1[Collela & Woodward (J. Comp. Phys., 54, 174)] we are trying a test simulation for few hundred to few thousand grid cells.

4   Summary

Intermittent redistribution and super sonic of buoyant radio plasma from AGN activities has an important influence on the heating and mass exchange between central and outer regions of galaxies clusters.

5   References

- Brüggen,M., Kaiser ,C.R., Churazov,E., &Enßlin T.E. 2002,MN-RAS,331,545

- Collela & Woodward (J. Comp. Phys., 54, 174)

- Churazov, E., Brüggen, M., Kaiser,C.R.,Böhringer,H.,&Forman,B.2001,ApJ,554,261

- Cox,D.P.,Apj,178,:159-168,1972 November 15

- Ettori, S.,,MNRAS,000,000

- Fabian,A.C. 1994 et al.2003a,b,,MNRAS,344,43

- Falcke H.et al A& A 383,854-863(2002)

- Forman,W. et al.2004 ,ApJ,submitted,astro-ph/0312576

- Landau,L.D & Lifshitz,E.M.1975, Fluid Mechanics,Pergamon Press

- Parker E.N. AJ 536:331–334,2000 June 10

- Rachen J.P.& Biermann P.L. 1993 AA,272,161R

- Sarazin,C.L.,X-ray emission from clusters of galaxies ,1988

- Sutherland, R. S. & Dopita, M. A., 1993, ApJS, 88, 253

- Wolf,M. 1906,Astr.Nach.,170,No.4069,211

CCD CAMERA FOR SPACE-BASED SOLAR CORONA OBSERVATIONS

A. Gherardi[a], E. Pace[a], L. Gori[a], M. Focardi[a], M. Sozzi[b],
G. Rossi[a], F. Tosetti[a]

[a] *XUVLab, Dipartimento di Astronomia e Scienza dello Spazio,
Università di Firenze (Italy)*

[b] *CAISMI-CNR Firenze*

Abstract

Starting from a ground testing CCD camera prototype (with innovative features like a full remote control and a high level of versatility combined to an intuitive user interface), the XUVLab working group is designing the rocket version of the CCD camera for the HERSCHEL (Helium Resonant Scattering in the Corona and HELiosphere)/SCORE (Solar CORona Experiment) suborbital mission; the requirements are very low readout noise, low power consumption, low mass budget, a very small package and a good level of versatility. Four CCD cameras will be the detectors of UVCI (Ultraviolet and Visible Light Coronagraph), an innovative instrument to be tested during the SCORE mission.

27

1 The HERSCHEL/SCORE suborbital mission

HERSCHEL/SCORE is conceived as a NASA Sounding Rocket Program providing new EUV/UV and visible-light coronal observations to directly measure and to characterize in detail the properties of the two most abundant elements, Hydrogen and Helium, acquiring images of solar corona and disc for $\sim$ 300 seconds. In particular, HERSCHEL will be able to provide:

- The first global images of the *HeII* corona
- The first global EUV images of the corona for the two most abundant elements, *H* and *He*
- The first maps of *He* abundance in the corona
- The first global maps of the solar wind outflow (H^0 and He^+ outflow)
- Polarimetric measurement in the visible of the solar extended corona
- A proof-of-principle for the UVCI (Ultra violet and Visible-light Coronal Imager), one of the remote sensing instruments payload of the Solar Orbiter.

The HERSCHEL payload consists of the EUV Imaging Telescope (EIT), similar to the SOHO/EIT instrument, and two UVCIs. The latter is a reflecting coronagraph designed to get images of the full corona from 1.4 to 4 $R_\odot$ in the *HI Lyα* line at 121.6 nm (first UVC) and in the *HeII Lyα* line at 30.4 nm (second UVC) and to make polarimetric measurements in the visible spectral region.

The coronagraph is externally occulted and its optical design is based on novel solutions to improve the stray light rejection and to use the same optical components to focus the radiation in the selected wavelength bands. Furthermore the UVC coronagraph is equipped with a novel polarimetric group in order to measure the coronal polarized radiation in the visible band: this polarimeter implements a LCVR (Liquid Crystal Variable Retarder) plate by Meadowlark.

The detectors for the visible-light channels and for *HeII* channel of the UVC are three CCD cameras provided by the XUVLab experimental team of the Dept. of Astronomy and Space Science of the University of Florence. The cameras will be developed starting from the laboratory prototype that will be used for ground applications, following the rocket specifications, and optimized to operate the selected sensor. Each camera will operate at a high pixel rate (nominally 500 kHz) and will satisfy requirements, such as very low readout noise, high quantum efficiency, wide dynamic range, good linearity and uniformity.

2 CCD camera laboratory prototype

Some features of the CCD camera laboratory prototype are: tunable pixel rate up to 2 Mpx/s; temperature control (-75^oC to $+10^o$C); automatic acquisition

procedures with varying pixel rate and exposure time; remote (TCP/IP) debugging and testing available; tunable clocks and bias to allow easy interface with any CCD; external peripheral control (motors, shutters, auxiliary sensors, etc); high dynamic range (16 bits 2 Msample/s); portable version available with laptop connections, battery power supply and closed-cycle cooling system included; 8 e$^-$ readout noise.

A feature that is not included in the rocket version, but that is desirable for tests and optimization, is a full versatility that allows:

- an arbitrary pattern generation of the digital clock waveforms, to operate our camera with a variety of CCDs and to fine-tune the selected sensor
- fully programmable biases and clock levels, signal gain and pixel rate
- satisfying the HERSCHEL requirements like the data transfer protocols between the detector and the main computer, as well as limitations on weight, power, size: a customizable camera can be modified while a commercial camera is usually not
- generating an additional synchronous trigger to drive the polarimeter during the image acquisition.

The most important feature of the cameras is a novel Sequencer which provides an excellent versatility and a reliable clock generation even at high frequencies (up to 2 MHz).

The laboratory prototype consists of two main parts: the controller and the camera head.

The controller includes all circuits needed to manage the image readout and the signal processing; the camera head hosts the sensor and the proximity electronics.

The main aim of the laboratory prototype is the characterization of the electronics and the tests of the image acquisition system performances.

3   CCD camera rocket prototype

Like most of space instrumentations, the CCD camera for HER-SCHEL/SCORE must satisfy some requirements:

- Low power consumption
- Low mass budget
- Compactness
- Mechanical hardness

For the suborbital application ($\sim$ 300 km altitude), is not needed radiation hardness. Further requirements are very low readout noise and high efficiency, due to the scarce flux of photons in the *HeII* channel and the low polarimetric signal; the field of view is required up to 4 solar radii. The short acquisition time requires a frame transfer architecture CCD, in order to acquire an image

during the readout of the previous one; the pixel-rate is 500 kpix/s. The CCD camera design foresees 7 PCB board of which six inside the CCD camera case and one fixed on the optical bench:

- Sequencer and Clock Driver board
- CCD, Preamplifier and Peltier cell cooler
- Correlated Double Sampler (CDS) and ADC converter
- Power Supplies and Bias Generator
- Peltier Supply and temperature control
- SpaceWire interface
- LCVR Controller

The CCD which fits the requirements of the CCD camera for HER-SCHEL/SCORE experiment, is the CCD47-20 by E2V. It is a back illuminated, 1024 X 1024 image format CCD, with 13μm pixel size and a frame transfer architecture, midband coated for polarimetric images and UV coated for *HeII*.

4   Conclusions

The HERSCEL/SCORE experiment (planned for may 2006) is the first of three test launches to evaluate the performances and the functionality of UVCI (one innovative instrument of the Solar Orbiter payload), and its capability to accomplish the mission scientific goals. The PCB boards and the aluminium case for the first CCD camera rocket prototype are already made and the electrical, mechanical and functionality tests are started. Some tests to measure the readout noise level, to characterize the CCD cameras performances and to calibrate the LCVR are scheduled by the 2004 end.

References

[1] E. Antonucci et al., *Ultraviolet and Visibile-light Coronagraph for the Solar Orbiter Mission* (2001).

[2] J. Daniel Moses et al., *Simultaneous Measurement of Electron, Hydrogen, and Helium Density in the Solar Corona: The HERSCHEL Investigation (Helium Resonant Scattering in the Corona and Heliosphere)*, NASA Proposal (2002).

[3] A. Gherardi et al., *CCD camera for ground- and space-based solar corona observations*, Proceedings SPIE (2003).

[4] A. Gherardi, *Elettronica di controllo per la camera CCD del canale polarimetrico di HERSCHEL*, Degree Thesis, Florence University (December 2002).

Part II

PARTICLE PHYSICS AND ASTROPHYSICS

OLD IDEAS AND NEW TWISTS IN STRING COSMOLOGY

Massimo Giovannini[a]

[a] *Department of Physics, Theory Division, CERN, 1211 Geneva 23, Switzerland*

Abstract

Some of the phenomenological implications of string cosmological models are reviewed with particular attention to the spectra of the tensor, scalar and vector modes of the geometry. A class of self-dual string cosmological models is presented. These solutions provide an effective description of cold bounces where a phase of accelerated contraction smoothly evolves into an epoch of decelerated Friedmann-Robertson-Walker expansion dominated by the dilaton. Some of the general problems of the scenario (continuity of the perturbations, reheating, dilaton stabilization...) can be successfully discussed in this framework.

1   Introduction

Heeding observations, the large-scale temperature fluctuations detected in the microwave sky are compatible with a quasi-flat spectrum of curvature inhomogeneities. Quasi-flat means that the Fourier transform of the two-point function of scalar fluctuations depends on the comoving momentum k as k^{n_s-1} with $n_s \simeq 1$. Taking only the WMAP determination of n_s [1], the scalar

33

spectral index lies in a rather narrow range $0.95 \leq n_s \leq 1.03$. For later convenience, if $n_s \geq 1$ the spectra are said to be blue, if $n_s \leq 1$ the spectra are said to be red, and, finally, if $n_s \gg 1$ the power spectra are called violet.

From the observations at smaller angular scales, it is by now established that the temperature fluctuations exhibit oscillations (the so-called Sakharov or Doppler oscillations) as a function of the sound horizon at decoupling. From the typical structure of these oscillations it is possible to argue that the curvature fluctuations present outside the horizon after equality (but before decoupling) were also constant. If the curvature fluctuations are constant, the solutions of the evolution of the density contrasts and of the peculiar velocities for the various species present in the plasma imply that the fluctuations in the total entropy density vanish at large distance scales. These initial conditions for the evolution of the CMB anisotropies are often named *adiabatic*.

In the context of conventional inflationary models based on a single field the scalar fluctuations of the geometry have naturally a quasi-flat spectrum and are also constant at large scales after matter-radiation equality. The quasi-flatness of the spectrum is related to the quasi-constancy of the Hubble expansion rate and of the Ricci scalar during the inflationary phase. More precisely, in the context of single-field inflationary models, the curvature scale has a monotonic behaviour versus the (cosmic or conformal) time coordinate and it is always (slowly) decreasing. Since the curvature scale decreases, it can be argued, on a general ground, that a true physical singularity is present in the far past [2]. However, the dynamics of the initial singularity is screened by the long period of inflation during which the possible gradients arising in the matter fields are diluted and eventually erased if the duration of inflation exceeds 65-efolds (see for instance [3]).

In the context of string cosmological models the conventional inflationary scenario seems quite difficult to obtain and, therefore, in the past fifteen years various cosmological models inspired by string theory have been explored. One of the features of these models is that the curvature scale is far from being constant but it is rather steeply increasing at least during a sizable portion of the early history of the Universe. In these models *a* singularity is often encountered just after the phase of growing curvature and gauge coupling. This problem is not an easy one to address both technically and conceptually. Owing to the mentioned phase of growing curvature, the perturbation spectra obtained in string cosmological models are far from being quasi-flat. They are, indeed, rather violet and, hence, at least in their most simplistic realization, incompatible with standard CMB physics.

There are by now several variations on this pre-big bang theme. Besides the original pre-big bang (PBB) scenario [4, 5], based on the duality symmetries of string cosmology, new models incorporating brane and M-theory ideas have been proposed under the generic name of ekpyrotic (EKP) scenarios [6, 7]. The

various proposals differ in the way the scale factor behaves during the growing-curvature phase. However, they all share the feature of describing a bounce in the space-time curvature. A common theoretical challenge to all these models is that of being able to describe the transition between the two regimes.

2   Tensor, Scalar and Vector modes in string cosmological models

String cosmological models are naturally formulated in more than four dimensions. This occurrence implies that the fluctuations of a higher dimensional geometry may be more complicated than a simple four-dimensional space-time. However, in order to simplify the discussion let us consider, as it was done in the past, the dimensionally reduced low-energy string effective action which can be written as

$$
S_{\text{eff}} - \int d^4 x \sqrt{-G} e^{-\varphi} \Big[\frac{1}{2\lambda_s^2} \Big(R + G^{\alpha\beta} \partial_\alpha \varphi \partial_\beta \varphi + V(\varphi) - \frac{1}{12} H_{\mu\nu\alpha} H^{\mu\nu\alpha} \Big)
$$
$$
+ \frac{1}{4} F_{\mu\nu} F^{\mu\nu} + ... \Big]. \tag{1}
$$

Eq. (1) is the typical outcome of the compactification of ten-dimensional superstrings on a six-dimensional torus. Concerning the above expression few specifications are in order:

- λ_s is the string length scale, related to the Planck length scale as $\ell_{\text{P}} = e^{\varphi/2} \lambda_s$;

- $\varphi = \Phi_{10} - \ln V_6$ is the four-dimensional dilaton field which can be expressed in terms of the ten-dimensional dilaton Φ_{10} and in terms of the volume of the six-dimensional torus;

- $V(\varphi)$ is the four-dimensional dilaton potential;

- $H^{\mu\nu\alpha}$ is the antisymmetric tensor field which related, in four dimensions, to a pseudo-scalar field σ as $H^{\mu\nu\alpha} = e^\varphi \epsilon^{\mu\nu\alpha\rho} / \sqrt{-G} \partial_\rho \sigma$;

- $F_{\mu\nu}$ is a generic Abelian gauge field;

- the ellipses stand for other fields (other Abelian fields, fermions...) and for the corrections which can be both of higher order in $\lambda_s^2 \partial^2$ (higher derivatives expansion producing quadratic corrections to the Einstein-Hilbert action) and of higher order in e^φ (loop expansion).

Equation (1) is written in the so-called string frame metric where the Ricci scalar R is coupled to the four-dimensional dilaton. Other frames can be defined by redefining appropriately the metric and the dilaton. A particularly useful frame is the Einstein frame where the Ricci scalar is not directly coupled to φ.
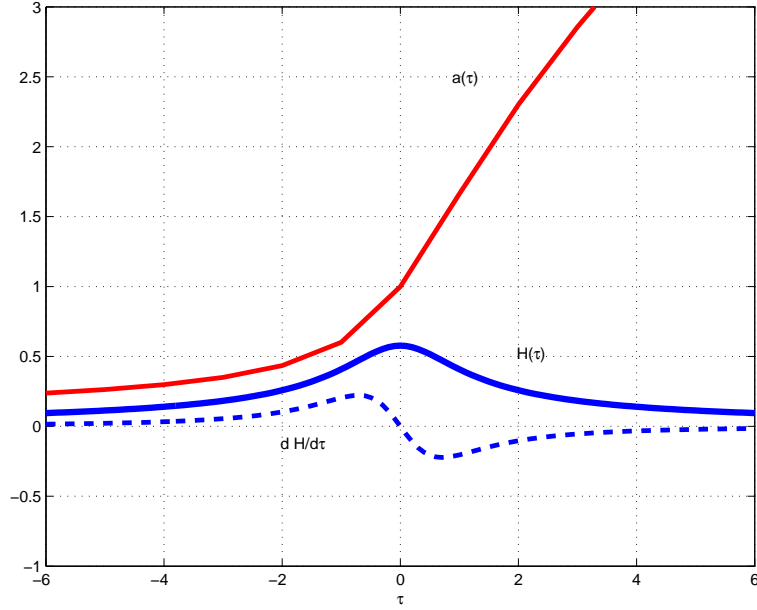
Figure 1: The evolution of the Hubble expansion rate H, its derivative, and of the scale factor $a(\tau)$ in the cold bounce models. The variable $\tau = t/t_0$ is the cosmic time coordinate (in the string frame) rescaled by the typical time scale of the bounce, t_0.

As already mentioned the evolution equations for the metric and the dilaton can lead to singular solutions. This situation is, however, not generic since also non-singular solutions can be found [8, 9, 10] and an example is reported Fig. 1. The solutions illustrated in Fig. 1 can be derived in the presence of a dilaton potential depending directly not on φ but on $\overline{\varphi} = \varphi - \log\sqrt{-G}$, i.e. the shifted dilaton usually defined in the context of the $O(d,d)$-covariant description of the low-energy string effective action [11]. Viewed from the point of view of the Einstein frame dynamics, these solutions describe a phase of accelerated contraction evolving smoothly into an epoch of decelerated expansion [10]. The two regimes of the solution are connected, by scale-factor-duality [4].

2.1 Tensors

The spectrum of the tensor modes in models where the Hubble expansion rate is increasing has been computed in various steps [12]. The amplified tensor modes of the geometry lead to a stochastic background of gravitational waves
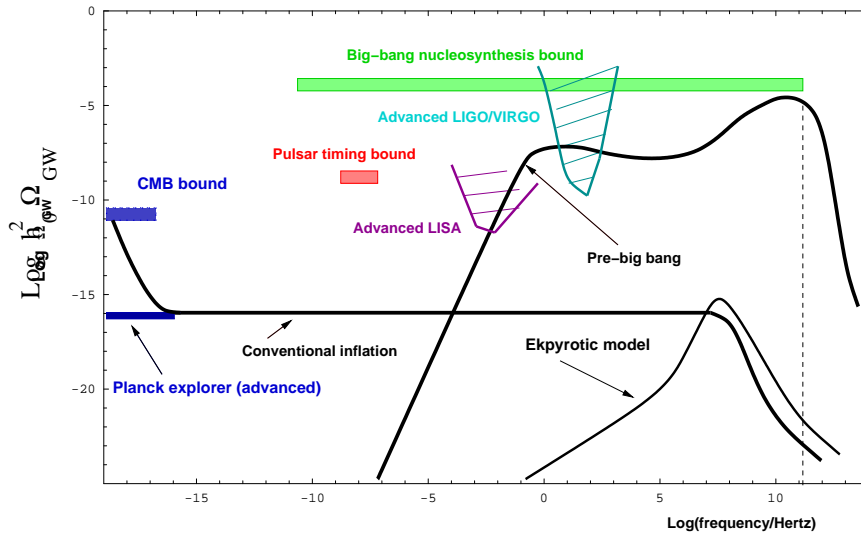
Figure 2: The spectrum of relic gravitons from various cosmological models expressed in terms of Ω_{GW} (h_0 is the experimental indetermination on present value of the Hubble expansion rate).

(GW) with violet spectrum both in the GW amplitude and energy density. This expectation is confirmed also in the context of the models illustrated in Fig. 1 as well as in the context of other non-singular models. In Fig. 2 the GW signal is parametrized in terms of the logarithm of $\Omega_{GW} = \rho_{GW}/\rho_c$, i.e. the fraction of critical energy density present (today) in GW. On the horizontal axis of Fig. 1 the logarithm of the present (physical) frequency is reported. In terms of Ω_{GW} the GW spectrum of conventional inflationary models is flat (or, more precisely, slightly decreasing) as a function of the present frequency. In the case of string cosmological models $\Omega_{GW} \propto \nu^3 \ln \nu$, which also implies a steeply increasing power spectrum. This possibility spurred various experimental efforts both for resonant mass detectors [14] and for microwave cavities [15, 16] since the signal may be rather strong at high frequencies and, anyway, much stronger than the conventional inflationary prediction

The sensitivity of a pair of VIRGO detectors to string cosmological gravitons has been specifically analyzed [13] with the conclusion that a VIRGO pair, in its upgraded stage, can certainly be able to probe wide regions of the parameter space of these models. If we maximize the overlap between the two detectors [13] or if we reduce (selectively) the pendulum and pendulum's internal modes contribution to the thermal noise of the instruments, the visible region (after
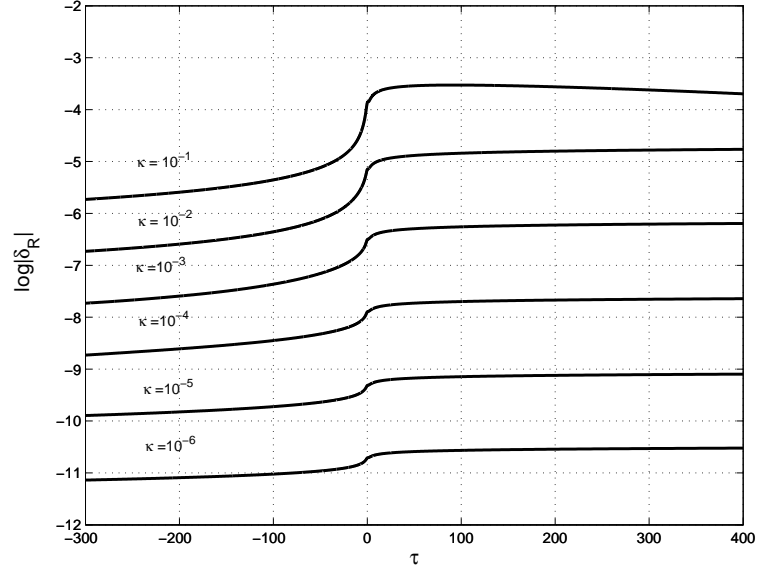
Figure 3: The Fourier transform of the two-point function of $\mathcal{R}$ computed for different comoving momenta as a function of the cosmic time coordinate.

one year of observation and with SNR equal to one) of the parameter space will get even larger. Unfortunately, as in the case of the advanced LIGO detectors, also in the case of the advanced VIRGO detector the sensitivity to a flat spectrum will be irrelevant for ordinary inflationary models. It is worth mentioning that blue energy spectra of relic gravitons can also arise in the context of quintessential inflationary models [17, 18]. In this case $\Omega_{\mathrm{GW}} \propto \nu \ln \nu$ (see [18] for a full discussion).

2.2 Scalars

The spectrum of the tensor modes of the geometry is not controversial because the tensor fluctuations of the geometry are defined as a rank-two (divergenceless and traceless) tensor in three dimensions. Consequently they are invariant under infinitesimal coordinate transformations. Scalar perturbations, in contrast, do depend on the specific coordinate system and are described, in four dimensions by a single propagating degree of freedom. This problem is only partially alleviated by the possibility of defining variables which are invariant under coordinate transformations. In fact, different choices are equally allowed like:

- Bardeen potentials (curvature perturbations on shear free hypersurfaces) usually denoted by Ψ;

- curvature perturbations on comoving hypersurfaces, usually denoted by $\mathcal{R}$;

- curvature perturbations on constant density hypersurfaces, usually denoted by ζ;

and as well as other choices. The variables listed above are related by specific differential relations, once one of them is reliably computed, all the other follow.

Using various descriptions (both gauge-invariant and gauge-dependent), in [19] it was argued that the spectra of scalar fluctuations are also violet with a scalar spectral index $n_s = 4$. The same analysis, applied to the case of ekpyrotic models, would lead to $n_s = 3$. The pre-big bang estimates [19] have been questioned on various grounds. The bottom line of these arguments would be that in single field pre-big bang or ekpyrotic models the spectrum of the tensor modes is violet but the spectrum of the scalar modes may be flat or even red, i.e. increasing at large distance scales. The analysis of the models illustrated in Fig. 1 seems to give unambiguous answer: while the evolution of the Bardeen potential is rather complicated around the bounce the time dependence of both $\mathcal{R}$ and ζ is rather smooth. Furthermore, not only the spectrum of $\mathcal{R}$ and ζ is, as expected, blue but it is also in agreement with the analytical estimate. The results for the evolution of $\mathcal{R}$ is illustrated in Fig. 3. The value of the comoving momentum increases from bottom to top. Hence, the spectrum is increasing as a function of k, as expected. An accurate numerical determination discussed in [9] also shows that $\delta_{\mathcal{R}} \sim k^{3/2}$ with specific logarithmic corrections. The spectrum of the Bardeen potential has been also computed accurately in [9] with the result that $\delta_{\Psi} \sim k^{-1/2}$ as expected from the analytical estimates.

2.3 Vectors

Vector modes of the metric are not excited in the context of conventional inflationary models. If the background geometry has more than four dimensions, vector modes are, on the other hand expected [20]. It is also possible to envisage the situation where rotational modes of the geometry are excited by the fluctuations of the velocity field [21]. The cold-bounce solutions illustrated in Fig. 1 can be generalized to include fluid sources [10] as well as internal (contracting) dimensions [22]. It was recently argued that vector modes of the geometry can be produced in pre-big bang and ekpyrotic/cyclic scenarios [21]. In particular, it was argued that the vector modes of the geometry may lead to a growing mode prior to the occurrence of the bounce. In [22] this expectation has been verified but it has also been shown that, in four dimensions, the growing vector mode present before the bounce turns into a

decaying mode after the bounce. Going beyond four dimensions, the vector modes of the geometry are copiously produced [22]. The higher-dimensional examples provided in [22] support the evidence that, in realistic semi-realistic models these spectra may be red.

2.4   Heating up the cold bounce

The cold bounce solutions discussed in [8] and ([9] have certainly realistic features. However there are two less realistic aspects

- after the bounce the Universe is cold and dominated by the dilaton field;

- the dilaton field is not stabilized in the sense that it does not reach constant value.

These two problems may be solved if the back-reaction of the various massless fields (i.e. massless gauge bosons, for instance) is included. In [10] the back-reaction effects of high-frequency photons has been included. The numerical results show indeed that the cold bounce solution may be consistently heated up. When the radiation starts dominating the dilaton field also freezes.

3   Summary

In the PBB case it was admitted early on that the tensor [12] and adiabatic-curvature perturbations [19] had too large a spectral index to be of any relevance at cosmologically interesting scales (while being possibly important for gravitational waves searches [13]). Isocurvature perturbations (related to the Kalb–Ramond two-form) can instead be produced with an interestingly flat spectrum [23], but have to be converted into adiabatic-curvature perturbations through the so-called curvaton mechanism [24] (see also [25, 26]) before they can provide a viable scenario for large scale-anisotropies [27]. Proponents of the ekpyrotic scenario, while agreeing with the PBB result of a steep spectrum of tensor perturbations, have also repeatedly claimed [28] to obtain "naturally" an almost scale-invariant spectrum of adiabatic-curvature perturbations, very much as in ordinary models of slow-roll inflation. These claims have generated a debate (see for instance [29]), with many arguments given in favour or against the phenomenological viability of EKP scenarios in the absence of a curvaton's help. The reasons for the disagreement can be ultimately traced back to the fact that the curvature bounce is put in by hand, rather than being derived from an underlying action. This leaves different authors to make different assumptions on how to smoothly connect perturbations across the bounce itself, and this often results in completely different physical predictions.

A specific class of models has been illustrated [8, 9]. In these models the evolution of the background geometry and of the dilaton coupling is regular

and specific testable predictions are possible. On the basis of these semi-analytical models it can be argued that in single field pre-big bang models the spectrum of the scalar and tensor modes of the geometry is, as expected from previous estimates, violet. The situation changes when the evolution of the fluctuations of the Kalb-Ramond field is consistently included. In this case a flat spectrum of curvature fluctuations can be obtained and compared to the observed anisotropies in the CMB (see [27] for a complete discussion).

References

[1] H. V. Peiris *et al.*, Astrophys.J.Suppl. **148**, 213 (2003); D. Spergel *et al.*, Astrophys.J.Suppl. **148**, 175 (2003).

[2] A. Borde and A. Vilenkin, Phys. Rev. Lett. **72**, 3305 (1994); A. Borde, A. H. Guth and A. Vilenkin, Phys. Rev. Lett. **90**, 151301 (2003).

[3] R. Brandenberger, Lect.Notes Phys. **646**, 127 (2004).

[4] G. Veneziano, Phys. Lett. **B265**, 287 (1991).

[5] M. Gasperini and G. Veneziano, Phys. Rep. **373**, 1 (2003).

[6] J. Khouri, B. A. Ovrut, P. J. Steinhardt and N. Turok, Phys. Rev. **D64**, 123522 (2001).

[7] J. Khouri, B. A. Ovrut, N. Seiberg, P. J. Steinhardt, and N. Turok, Phys. Rev. **D65**, 086007 (2002).

[8] M. Gasperini, M. Giovannini and G. Veneziano, Phys. Lett. B **569**, 113 (2003).

[9] M. Gasperini, M. Giovannini and G. Veneziano, arXiv:hep-th/0401112 (Nucl. Phys. B, in press)

[10] M. Giovannini, Class. Quant. Grav. **21**, 4209 (2004).

[11] K. A. Meissner and G. Venziano, Mod. Phys. Lett. A **6** 3396 (1991).

[12] M. Gasperini and M. Giovannini, Phys. Lett. B **282**, 36 (1992); Phys. Rev. D **47**, 1519 (1993);R. Brustein, M. Gasperini, M. Giovannini and G. Veneziano, Phys. Lett. B **361**, 45 (1995).

[13] D. Babusci and M. Giovannini, Int.J.Mod.Phys.D **10** 477 (2001); Class.Quant.Grav.**17**, 2621 (2000).

[14] P. Astone *et al.* Astron. Astrophys. **351**, 811 (1999).

[15] Ph. Bernard, G. Gemme, R. Parodi and E. Picasso, Rev. Sci. Instrum **72**, 2428 (2001).

[16] A. M. Cruise, Class. Quantum Grav. **17**, 2525 (2000); Mon. Not. R. Astron. Soc **204**, 485 (1983).

[17] P. J. E. Peebles and A. Vilenkin, Phys. Rev. D **59**, 063505 (1999).

[18] M. Giovannini, Class. Quant. Grav. **16**, 2905 (1999); M. Giovannini, Phys. Rev. D **60**, 123511 (1999); D. Babusci and M. Giovannini, Phys. Rev. D **60**, 083511 (1999);M. Giovannini, Phys.Rev. D **58**, 083504 (1998).

[19] R. Brustein, M. Gasperini, M. Giovannini, V. F. Mukhanov and G. Veneziano, Phys. Rev. D **51**, 6744 (1995).

[20] M. Giovannini, Phys. Rev. D **55**, 595 (1997).

[21] T. J. Battefeld and R. Brandenberger, arXiv:hep-th/0406180.

[22] M. Giovannini, Vector fluctuations from multidimensional curvature bounces, arXiv:hep-th/0407124.

[23] E. J. Copeland, R. Easther and D. Wands, Phys. Rev. **D56**, 874 (1997).

[24] K. Enqvist and M. S. Sloth, Nucl. Phys. **B626**, 395 (2002); D. H. Lyth and D. Wands, Phys. Lett. **B524**, 5 (2002); T. Moroi and T. Takahashi, Phys. Lett. **B522**, 215 (2001).

[25] D. Lyth, Phys. Lett. **B579**, 239 (2004).

[26] M. Giovannini, Phys. Rev. D **69**, 083509 (2004); Phys.Rev. D **67** 123512 (2003).

[27] V. Bozza, M. Gasperini, M. Giovannini and G. Veneziano, Phys. Lett. B **543**, 14 (2002); Phys. Rev. D **67**, 063514 (2003).

[28] J. Khouri, B. A. Ovrut, P. J. Steinhardt and N. Turok, Phys. Rev. **D66**, 046005 (2002); S. Gratton, J. Khoury, P. J. Steinhardt, and N. Turok, Phys.Rev.D **69**, 103505 (2004).

[29] D. H. Lyth, Phys. Lett. B **526**, 173 (2002); Phys.Lett. B **524**, 1 (2002); R. Brandenberger and F. Finelli, JHEP **11**, 056 (2001).

AMS: A PARTICLE DETECTOR IN SPACE

Bilge M. Demirköz[a], *for the AMS collaboration*

[a] *Massachusetts Institute of Technology, Cambridge, MA 02139, U.S.A*

Abstract

Alpha Magnetic Spectrometer(AMS) is an particle physics experiment
that will be on the International Space Station for three years. It will
look for anti-matter and dark matter with good discrimination against
backgrounds and measure the cosmic ray spectrum up to 3 TeV/nucleon
with high statistics.

1 Introduction

AMS is a magnetic spectrometer which measures the momentum, the charge,
the velocity and the energy of a particle using a super-conducting magnet
and complementary detectors, shown in Fig. 1. Reconstructing the particle's
curvature in the magnetic field of AMS allows for the measurement of
momentum and charge of the particle. AMS has been designed to allow
for cross-checks between measurements from different detectors. High energy
gamma rays which convert to e^+e^- in the detector can also be identified and
their energy determined.

The core of AMS is a super-conducting magnet. Inside this magnet are 8
planes of silicon strip detectors. Above and below the silicon tracker are two
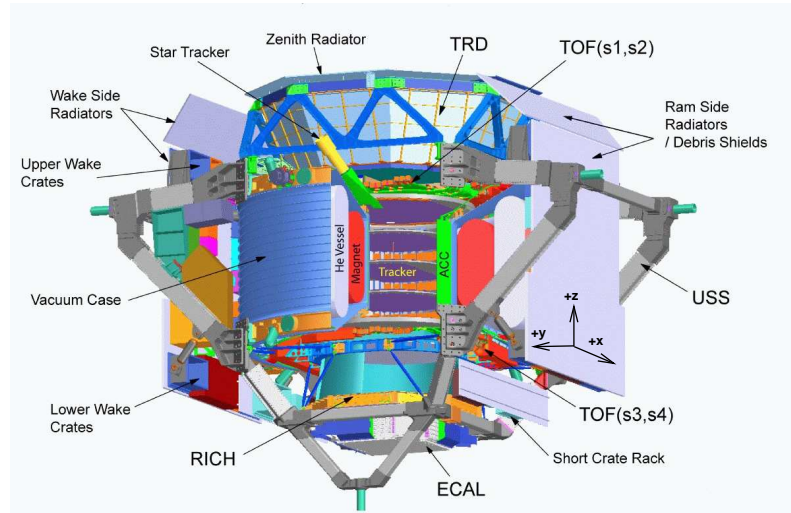
Figure 1: The AMS detector

orthogonal planes of time of flight (TOF) scintillator detectors. Complementing the spectrometer is a Transition Radiation Detector, a Ring Imaging Čerenkov (RICH) detector and an Electromagnetic Calorimeter (Ecal). The detectors are supported mechanically by the USS (Unique Support Structure) which also provides the connection to the Space Shuttle or the International Space Station (ISS). Two star trackers allow AMS to know the orientation better than $1'$, much better than the ISS instruments. The geometric acceptance is about $0.5m^2sr$ for the full detector.

The high precision detectors described above will enable AMS to exceed the sensitivities reached by previous experiments. AMS will measure charged cosmic ray spectra of individual elements up to $Z \approx 26$ into the TeV region and high energy gamma rays up to hundreds of GeV, [1]. AMS will accumulate high statistics and improve on the results of other experiments. It will directly search for antimatter in space, such as anti-He and anti-C and also for dark matter, [2]. Dark matter annihilation in the galactic halo could produce slight excesses in gamma-ray, positron and anti-proton spectra and simultaneous measurement of these different channels will strongly constrain dark matter models [3]. In addition, the search will achieve a high statistics study of light nuclei and isotopes, such as deuterium, tritium, ^{3}He and ^{4}He. Unstable isotope ions with long lifetime like ^{10}Be and ^{26}Al are of particular interest because they provide a measurement of the confinement time of charged particles in galaxies, [4]. The cosmic ray fluxes of these cosmic ray components have never been measured

before over such a large momentum range.

The AMS experiment must survive and function under a harsh space environment of temperature variances, vacuum, radiation and vibration. For example, the day to night variation in temperature can be as high as 100^oC on some orbits. Special attention has been paid to each of these space conditions by the collaboration and measures have been taken in order to avoid problems during the launch as well as the flight. In the case of temperature variations, thermal coating and radiators have been designed to reduce these variations. AMS components have been vibration tested to 6.8 Grms and also shock-tested to 17G. Some critical components have been placed in wake side of AMS due to an unlikely but possible collision with orbital debris or micrometeorites. Other components have been tested to withstand such a collision. Electronic components have been chosen according to extensive ion-beam tests and can withstand the ionizing flux of ≈ 1000 cm^{-2}s^{-1}. These components also have been conformally coated to avoid sparking which can happen as the pressure in the cargo bay of the shuttle drops from atmospheric pressure to the vacuum of $< 10^{-10}$ Torr of space. Also, all components have to function under the fringe field of the 0.86 T AMS magnet and have been tested under such conditions. To ensure that AMS will function safely and reliably during its full life time of 3 years or more, several components are redundant and the design is at least two-fault tolerant wherever possible. All this has been done under a tight weight and power budget; the detector in total weighs 14809 lbs and consumes only 2 kW of power.

The AMS experiment must operate without services and human intervention for the full duration of this flight. To test the operations and control of such a particle detector in space, the AMS collaboration designed an engineering version. This pre-cursor experiment, AMS-01, flew on board of the Space Shuttle Discovery (STS-91) for ten days in June 1998 at an altitude of 320-390 km. AMS-01 had a 0.14 T permanent magnet, and no TRD or Ecal. It collected data on primary cosmic rays in low earth orbit in the rigidity interval from 0.1 GeV to 200 GeV. Although it was an engineering flight, several physics results were published, [5]. The collaboration gained invaluable experience in dealing with space hardware and operations. AMS-02 will improve on the results of this mission mainly by the introduction of a super-conducting magnet and larger acceptance and exposure time leading to higher statistics and e^+ and e^- identification.

2 AMS Subdetectors

AMS measures the rigidity of a particle, its charge and the sign of the charge independently. Finding the rigidity, R, of a particle which is defined as p/Z, is also equivalent to making a measurement of Br, where r is the
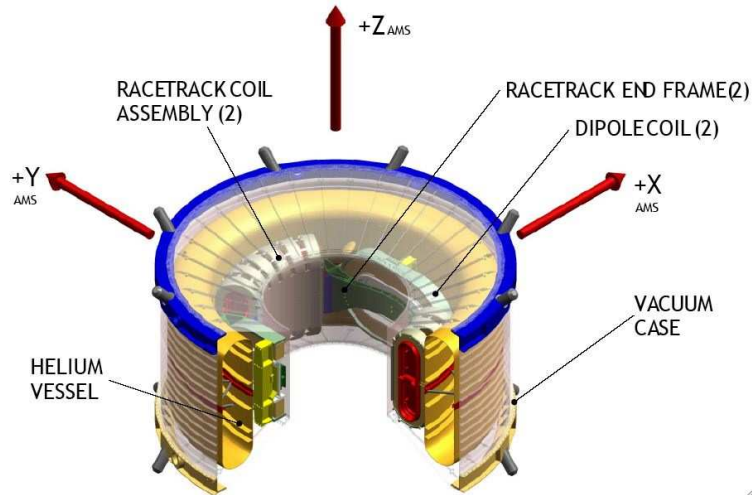
Figure 2: The AMS magnet, [6].

radius of curvature. The rigidity is measured mainly by the tracker. The energy deposition in the silicon tracker, the TOF, the Ecal and the TRD also provides independent measurements of the charge of the particle as well as the measurement in the RICH. The sign of the charge is determined from the bending by the magnetic field by the tracking system. The velocity is measured by the TOF, the TRD and the RICH sub-detectors. The multiple measurement of the same physical quantity using different techniques allows for cross-checks. The reconstruction of an event is done using a track fitting algorithm using position and momentum information from all sub-detectors. Here we briefly discuss the magnet and each sub-detector.

2.1   AMS-02 Magnet

The magnetic dipole field is achieved by an arrangement of 14 superconducting coils. The two large "dipole" coils will provide most of the transverse field while the smaller 12 "racetrack" coils contain the return flux, as seen in Fig. 2. This arrangement minimizes the stray field outside of the magnet, which would be hazardous to the system that provides air to the astronauts during EVAs (extra-vehicular activities) also known as space-walks. The total dipole moment has been minimized in the design because a non-zero dipole moment would exert a torque on the ISS, towards aligning itself with the earth's magnetic field. The coils are all electrically connected carrying a current of 459 A and the total inductance is 48.9 H. The total stored energy is 5.15 MJ. The whole magnet

will be cooled to a temperature of 1.8 K by 2500 liters of pressurized super-fluid helium. The system is being constructed by Space Cryomagnets Ltd in England. The magnet will be cylindrical in shape with an inner diameter 1.2 m and length 0.8 m. It will provide the 0.86 T at the center of AMS and 0.78 Tm^2 Bending power, [6]. The magnet bends particles in the Y-plane of the AMS-coordinates.

2.2   Transition Radiation Detector

In a TRD, transition radiation (TR) is emitted when a relativistic particle moves across an interface of two media with different dielectric constants, [7]. The media in this case are a TR "radiator" and vacuum. Due to properties of the radiator and the other materials in the detector, the emitted radiation becomes appreciable when the Lorentz factor of the particle is greater than 1000. The radiation that is detected is in the X-ray region of the spectrum (1-30 keV). The total energy loss includes the ionization losses of the charged particle. The TRD is the only detector identifying ultra-relativistic particles. Though the probability of a photon being released at each interface is low, one uses multiple layered radiators to increase this effect. This radiation is detected using proportional high-Z gas drift tubes. The radiation ionizes the gas mixture in the straw drift tube and the pulse of electrons is amplified. This pulse is proportional to the energy deposited in the tube by the particles.

The AMS TRD consists of 20mm thick layers of fleece radiator material (LRP-375) and 6mm proportional straw tubes filled with $Xe:CO_2$=80:20 gas. The TRD consists of 20 layers of such radiator and proportional tube detectors, stacked in a conically shaped octagon support structure. The 6mm proportional tubes are arranged into modules of 16. There are 328 modules in total with lengths up to 2m. The upper and lower four TRD layers run parallel to the magnetic field whereas the middle 12 are orthogonal to the field. This provides tracking information for all charged particles.

With 20 layers of the AMS TRD, a rejection factor of 10^{-2}-10^{-3} of protons from positrons can be expected. The rejection achieved is highly dependent on a constant signal height of the proportional tubes. The AMS TRD proportional tubes will be operated at a gain of 3000 with the $Xe:CO_2$ gas in the tubes at 1.2atm. This pressure will prevent collapse of straws of the TRD before launch at Kennedy Space Center. The total gaseous volume is 230 liters and it will slowly be leaking into space. As gas tightness is a critical design issue, each TRD module is tested for leaks and only modules which leak less than $10^{-4}lmbar/s/m$ are accepted as flight modules, [8]. To replenish the system and keep the pressure in the active volume of the TRD constant in space, a gas system has been designed. The avalanche gain is a strong function of the high voltage, which is foreseen to be kept at 1500V, the gas mixing accuracy and of the temperature, which varies up to 100° in space. Diffusion through the

straw foils is different for Xenon and CO_2 and must be balanced. Therefore the rejection critically depends on the accuracy of the TRD gas supply system, keeping the ratio constant.

The gas supply system comprises of a module for supply, one for circulation, and manifolds for distribution, [9]. These subsystems will each be under the control of dedicated and redundant electronics cards. An automated mixing program will premix Xenon and CO_2 gases to the necessary proportion using the law of partial pressures. A series of high pressure valves and pressure sensors in the supply unit will mix the gas into a buffer volume. 109 lbs of Xenon and 11 lbs of CO_2 are needed for the full mission. A maximum of 7 liters will be transfered from the buffer through the circulation box to the TRD every day, in a mixture compensating for the different losses of Xe and CO_2. The circulation box circulates the full TRD volume three times a day increasing uniformity and monitoring gas parameters. The manifolds distribute the gas to the TRD module, detect leaks and isolates them if needed. The gas system has been designed to provide a signal stability of the TRD to 3%.

The AMS TRD is essential for the dark matter signal in the positron spectrum and can cleanly separate positrons from the background protons with 10^{-2}-10^{-3} accuracy in the energy regime between 10-300 GeV.

2.3   Time of Flight(TOF) system

The time of flight system consists of four layers of plastic scintillator paddles. The scintillation light is collected by two light guides on each side and the two photo-multiplier signals are added together. The light guides have been designed to accommodate for the high magnetic fields present at the photo-multiplier locations. There are two orthogonal layers of counters above the silicon tracker, consisting of eight counters each. Also, below the tracker, there are two orthogonal layers consisting of ten and eight counters respectively. The TOF system provides the trigger for the AMS detector and measures the transit time of singly charged particles with 140psec accuracy, [10]. It also gives information about the energy loss, which is related to the charge of a particle, and coordinates of the particle. Another set of scintillation counters called anti-coincidence counter (ACC) surrounds the full perimeter of the silicon tracker and avoids triggering on particles which traverse the detector sideways.

2.4   Silicon Tracker

The silicon tracker is composed of $41.360 \times 72.045 \times 0.300 mm^3$ double-sided silicon microstrip sensors, [11]. The silicon sensors are then grouped together, for readout and biasing, in ladders of different lengths to match the cylindrical geometry of the AMS magnet. There are 8 silicon planes and the distance between planes 1 and 8 is one meter. The total area of this double sided

silicon detector will be $7m^2$. The space resolution in the bending y-plane is 10μm. The ladders have to be aligned accurately to maintain this high space resolution. The silicon tracker provides the tracking and bending information of the particle essential for the rigidity reconstruction as well as energy loss information, for a charge measurement. The AMS-01 tracker although smaller, proved this concept and the tracker alignment scheme. The AMS-02 tracker will provide a momentum resolution of 2% at 1 GeV and of 4% at 100 GeV.

2.5   Electromagnetic Calorimeter (ECAL)

The Electromagnetic calorimeter is a 3-dimensional fine-granularity sampling calorimeter with a total of 17 radiation lengths. It consists of 1mm diameter scintillating fibers glued by epoxy between grooves of lead plates. Each super-layer contains 10 layers of scintillator and is 18.5mm thick. The full detector is 9 super-layers alternatively oriented along the X and Y axis with 5 super-layers viewing the bending plane (Y view). Imaging of the shower development in 3D allows for the discrimination between hadronic and electromagnetic cascades. The Ecal will complement the TRD in the rejection of protons from the positron sample and will provide 10^{-3} rejection. With the final design, the energy resolution of the Ecal is $12\%/\sqrt{E} + 2\%$, [12]. The Ecal can also be operated in single trigger mode and can make measurements of cosmic gamma rays.

2.6   Ring Imaging Čerenkov Detector (RICH)

The AMS RICH detector has a low refractive index radiator, Silica aerogel with an index of $n = 1.03$. The Čerenkov photons are collected by a pixelized photo-multiplier matrix with pixel size, 8.5 mm^2. Between the radiator on the top and the photo-multipliers on the bottom, is an empty space of 45.8cm surrounded by a conical shaped mirror, increasing the reconstruction efficiency, [13]. Since the Čerenkov angle, $\theta_c = 1/n\beta$, the β measurement follows straightforwardly from the Čerenkov angle reconstruction. The velocity measurement from RICH is a very different technique from the detectors that provide velocity information and hence complements them. For singly charged particles, it will provide a $\Delta\beta/\beta$ resolution 0.1% and also help extend the electric charge separation up to iron.

3   Conclusions

The cosmic ray spectrum will be explored, in space for the first time, by high statistics at large energies in pursuit of dark matter and antimatter.

References

[1] R. Battiston, *astro-ph/9911241*.

[2] B. Alpat, *astro-ph/0308487*;
A. Barrau, *astro-ph/0103493*;
V. Shoutko *et al*, *Int. J. Mod. Phys.* A17:1817-1828, 2002.

[3] A. Jacholkowska, these proceedings.

[4] A. Bouchet, *Nucl. Phys. A* 688:417-420, 2001.

[5] J. Alcaraz *et al*, *Phys. Lett.* B490:27-35, 2000;
J. Alcaraz *et al*, *Phys. Lett.* B461:387-396, 1999;
J. Alcaraz *et al*, *Phys. Lett.* B484:10-22, 2000;
J. Alcaraz *et al*, *Phys. Lett.* B472:215-226, 2000.

[6] B. Blau *et al*, *Nucl. Phys. Proc. Suppl.* 113:125-132, 2002;
S. Harrison *et al*, *IEEE Trans. on Appl. Supercond.* 13:1381-1384.

[7] B. Dolgoshein, *Nucl. Instrum. Meth.* A326:434-469, 1993.

[8] T. Siedenburg *et al*, *Nucl. Phys. Proc. Suppl.* 113:154-158, 2002.

[9] U. Becker *et al*, http://ams.cern.ch/AMS/TRDGas/TRDGasSummary 4April2003.ps.

[10] V. Bindi *et al*, *hep-ex/0305074*;
D. Casadei *et al*, *Nucl. Phys. Proc. Suppl.* 113:133-138, 2002;
C. Sbarra, these proceedings.

[11] W. J. Burger, *Nucl. Phys. Proc. Suppl.* 113:139-146, 2002;
M. Paniccia, these proceedings;
P. Zuccon, these proceedings.

[12] P. Maestro, *PhD Thesis, University of Siena*, 2003;
F. Cadoux *et al*, *Nucl. Phys. Proc. Suppl.* 113:159-165, 2002;

[13] F. Barao *et al*, *Nucl. Instrum. Meth.* A502:310-314, 2003;
M. Buenerd, *Nucl. Instrum. Meth.* A502:158-162, 2003;
T. Thuillier *et al*, *Nucl. Instrum. Meth.* A491:83-97, 2002.

THE PAMELA SPACE MISSION

Mark Pearce[a]
Representing the PAMELA Collaboration

[a] *KTH Physics Department, AlbaNova University Centre, Stockholm, Sweden*

Abstract

The PAMELA experiment will be launched on-board a Resurs DK1 earth observation satellite in 2005. During the three year mission, the primary objective of PAMELA is to measure the flux of antiprotons (80 MeV - 190 GeV) and positrons (50 MeV - 270 GeV) in the cosmic radiation. The wide energy range and large statistics, $O(10^4)$ antiprotons and $O(10^5)$ positrons, will allow sensitive tests of cosmic ray propagation models and searches for exotic sources of antiparticles. Antinuclei searches with a sensitivity of $O(10^{-8})$ in the antihelium/helium ratio will also be conducted and the light isotope component of cosmic rays and solar phenomena studied. PAMELA consists of a time-of-flight system, a transition radiation detector, a magnetic spectrometer, an anticoincidence shield, an electromagnetic imaging calorimeter with shower-tail catcher and a neutron detector.

51

1 Introduction

The PAMELA[1] experiment [1] will be mounted inside a pressurised vessel attached to a Resurs DK1 earth-observation satellite which will be launched into orbit by a Soyuz TM2 rocket in 2005. The satellite will execute a semi-polar (70.4° inclination) elliptical orbit with an altitude varying between 300 km and 600 km. Three years of data-taking are expected. PAMELA is built around a 0.4 T permanent magnet spectrometer ('tracker') equipped with double-sided silicon detectors which will be used to measure the sign, absolute value of charge and momentum of particles. The tracker is surrounded by a scintillator veto shield ('anticounters') which is used to reject particles which do not pass cleanly through the acceptance of the tracker. Above the tracker is a transition radiation detector based around proportional straw tubes and carbon fibre radiators. This allows electron-hadron separation through threshold velocity measurements. Mounted below the tracker is a silicon-tungsten calorimeter. This measures the energies of incident electrons and allows topological discrimination between electromagnetic and hadronic showers (or non-interacting particles). A scintillator is mounted beneath the calorimeter to provide an additional trigger for high energy electrons and is followed by a neutron detection system (^{3}He-filled tubes within a polyethylene moderator) for the selection of very high energy electrons and positrons (up to 3 TeV) which shower in the calorimeter but do not necessarily pass through the spectrometer. A scintillator telescope system provides the primary experimental trigger and time-of-flight particle identification. The principle of operation is shown schematically in figure 1. PAMELA stands approximately 1.3 m high, has an overall mass of approximately 470 kg and a power consumption of approximately 360 W. PAMELA is being constructed by the WiZard collaboration, which was originally formed around Robert Golden who first observed antiprotons in space. There are now 12 institutions involved in building PAMELA. There are 6 INFN groups in Italy (Bari, Florence, Frascati Laboratories, Naples, Rome (Tor Vergata) and Trieste) and an additional Italian group from CNR/IROE (Florence). Outside of Italy, groups from The Royal Institute of Technology, KTH (Sweden); Siegen University (Germany) and three Russian groups from the Moscow Engineering and Physics Institute, MEPHI, the Lebedev Institute of Russian Academy of Sciences (Moscow) and the Ioffe Institute of Russian Academy of Sciences (St Petersburg) participate.

---

[1]Payload for Antimatter Matter Exploration and Light-nuclei Astrophysics.
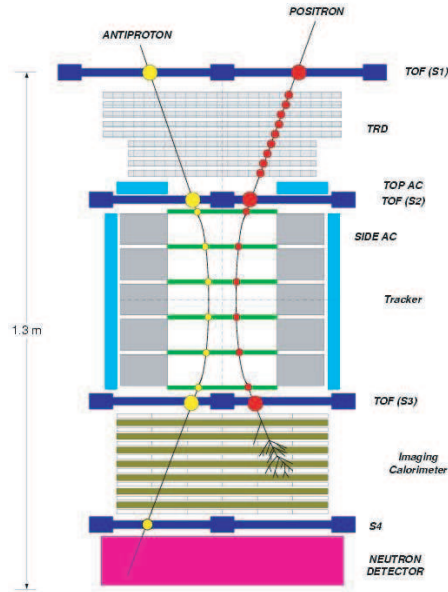
Figure 1: A schematic view of the PAMELA experiment. An antiproton and positron event are shown to illustrate the particle identification technique.

2 Scientific goals

The primary objective of PAMELA is to measure the energy spectrum of antiprotons and positrons in the cosmic radiation. All contemporary measurements (except those from the AMS test flight on the Space Shuttle in 1998) originate from balloon-borne experiments operating at altitudes around 40 km for approximately 24 hours. There is still a residual amount of the earth's atmosphere above the detecting apparatus at this altitude ($\sim$5 g/cm^2) with which cosmic rays can interact and this complicates the interpretation of data. A satellite-borne experiment benefits from a lack of atmospheric overburden and a longer data-taking time. Per year, at least 10^5 positrons and 10^4 antiprotons are expected. These data sets exceed what is available today by several orders of magnitude and will allow significant comparisons between competing models of antimatter production. Distortions to the energy spectra are very interesting because of possible contributions from exotic sources, such as the annihilation of supersymmetric neutralino particles - candidates for the dark matter in the universe [2]. Sensitivity to the low energy part of the spectrum is a unique capability of PAMELA and arises because the semi-

Particle	Number (3 years)	Energy Range
p	3×10^8	80 MeV - 700 GeV
$\bar{p}$	$> 3 \times 10^4$	80 MeV - 190 GeV
e^-	6×10^6	50 MeV - 2 TeV
e^+	$> 3 \times 10^5$	50 MeV - 270 GeV
He	4×10^7	80 MeV/n - 700 GeV/n
Be	4×10^4	80 MeV/n - 700 GeV/n
C	5×10^5	80 MeV/n - 700 GeV/n
$\bar{H}e$ limit (90% C.L.)	7×10^{-8}	80 MeV/n - 30 GeV/n

Table 1: Expected particle samples after a three year PAMELA mission.

polar Resurs orbit overcomes the earth's geomagnetic cut-off. Measurements at low energies will allow solar modulation effects and exotic processes such as primordial black hole evaporation to be studied [3]. Another PAMELA goal is to measure the antihelium/helium ratio with a sensitivity of at least 10^{-7}, i.e.: a factor of 50 improvement on the current limits [4]. An observation of antihelium would be a significant discovery as it would be the first sign of primordial antimatter left over from the Big Bang. Although optimised for the detection of antimatter, PAMELA will also study protons, electrons and light nuclei up to Z=6. The expected particle samples after three years of operation are summarised in table 1. Other concurrent physics goals are discussed elsewhere in these proceedings [5].

3   Detector performance

Only the tracking system and calorimeter are discussed in this section. Further details of the other parts of the PAMELA apparatus can be found elsewhere [6].

3.1   Magnetic spectrometer

The magnetic spectrometer or 'tracker' [7] consists of 5 modules of Nd-B-Fe alloy interleaved with 6 planes of 300 μm thick doubled-sided silicon detectors. The tracking cavity is 445 mm tall and has a cross-section of 132×162 mm^2, defining the overall acceptance of PAMELA to be 20.5 cm^{2}sr. The mean bending field inside the tracking cavity (0.43 T) is almost uniform. In the bending view, the silicon detectors have an implantation pitch of 25 μm and a read-out pitch of 50 μm. Capacitive coupling between adjacent strips is used to improve the spatial resolution. Figure 2 shows how the momentum resolution of the tracker evolves with momentum. From this data a maximum detectable
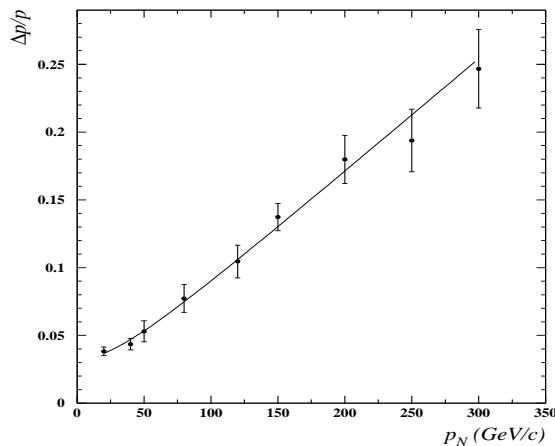
Figure 2: The momentum evolution of the tracker momentum resolution, compiled using test beam electron data.

rigidity[2] (where the error on the rigidity is 100%) of (1183±54) GV/c can be extracted. In practice, simulations have shown that 'spillover' effects will limit the maximum detectable antiproton (positron) momentum to ~200 GeV/c (~300 GeV/c).

3.2   Electromagnetic Calorimeter

The sampling electromagnetic calorimeter [8] is made from 44 planes (24×24 cm^2) of single-sided silicon sensors interleaved with 22 layers of tungsten absorbers. Each tungsten absorber is 0.26 cm (0.74 X_0) thick. The total depth of the calorimeter is therefore 16.3 X_0 (0.6 λ). The silicon strips are arranged in a Si-x/W/Si-y fashion to allow topological shower reconstruction. The performance of the calorimeter has been extensively studied with simulations tuned using data from earlier balloon flights of a similar calorimeter and more recent testbeam studies at CERN. Figure 3 shows that a combined measurement of the shower topology and deposited energy can be used to distinguish between electromagnetic and hadronic showers. This is particularly important when trying to identify positrons from a large background of cosmic ray protons in space, for example. This concept is further illustrated in figure 4, which shows testbeam data recorded at a momentum of 200 GeV/c for protons and electrons. By simply considering the number of 'hit' silicon

---

[2]The rigidity of a particle is defined as momentum / charge.
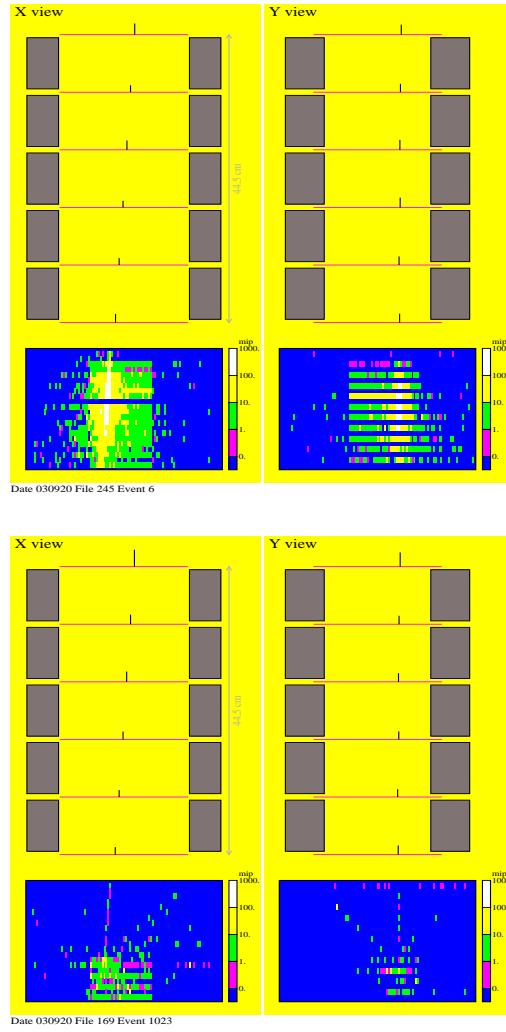
Figure 3: An event display of a 100 GeV/c electron (upper) and proton (lower) from test beam data. The tracking system and calorimeter are shown. In the Y-view only the odd calorimeter planes have been read out. Note the difference in the deposited calorimeter energy between the two cases.
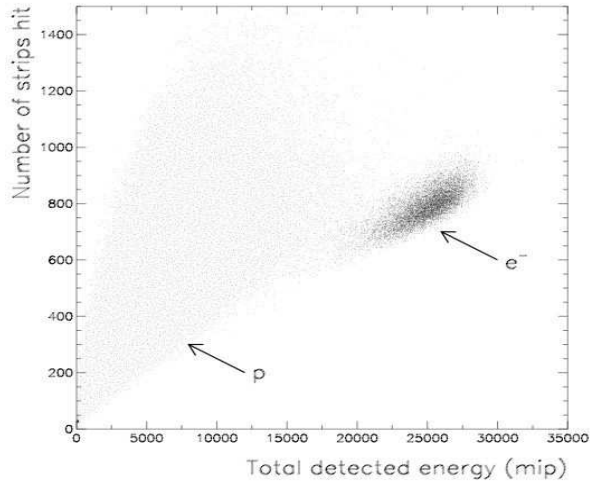
Figure 4: The total number of 'hit' silicon strips plotted against the total energy detected in the calorimeter. The data comes from a test beam conducted at an momentum of 200 GeV/c.
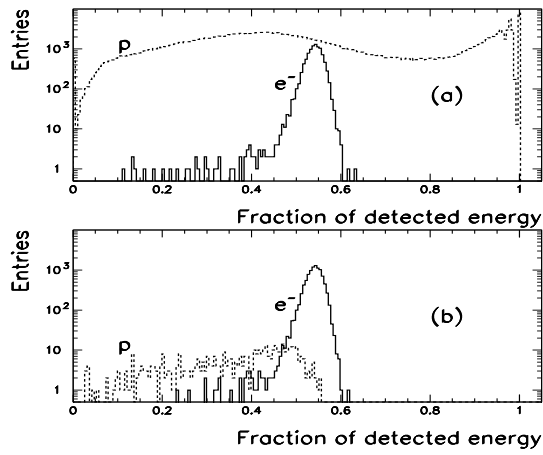
Figure 5: The fraction of the total detected calorimeter energy deposited into a cylinder of radius 1.5 silicon strips and centred on the track of the incident particle. (a) The complete data set. (b) Those events surviving a restriction on the total detected energy, see figure 4.

strips and the total energy deposited in the calorimeter, a clear separation can be drawn between the two particle samples. In the upper part of figure 5, the fraction of energy deposited in a cylinder with a radius of 1.5 silicon strips and centred on the particle track is shown for the two particle types. The electron-induced shower is clearly more localised in the calorimeter than the hadronic counterpart. With the addition of a constraint on the total energy deposited in the calorimeter (lower part of figure 5), a rejection factor exceeding 10^4 for protons and electrons at 95% selection efficiency in positron and antiproton measurements, respectively, can be obtained. The energy resolution of the calorimeter is constant at 5.5% in the range 20 GeV - 200 GeV. The self-trigger mode of the calorimeter allows the stand-alone registration of electrons up to an energy of approximately 2 TeV - a region where there are currently very few measurements. In this mode, the instrumental acceptance is increased to 470 cm^{2}sr. An energy resolution of approximately 12% is possible between 200 GeV and 700 GeV. At 1 TeV, the energy resolution climbs to approximately 16%, due to incomplete shower containment.

4   Summary and outlook

PAMELA is a general purpose instrument for cosmic ray physics in space which will open a new chapter in the subject after its launch in 2005. The performance of the detectors has been rigorously checked with simulations and particle beams and the design performance confirmed. After many years of qualification and performance studies, the launch of PAMELA from the Baikonur cosmodrome in 2005 is eagerly awaited by the collaboration!

References

[1] http://wizard.roma2.infn.it/pamela.

[2] L. Bergström et al., Phys. Rev. D 59 (1999) 43506.

[3] K. Maki et al., Phys. Rev. Lett. 76 (1996) 3474.

[4] J. Alcarez et al., Phys. Lett. B 461 (1999) 387.

[5] M. Casolino, these proceedings.

[6] M. Boezio et al., Proc. SpacePart 2003. To appear Nucl. Phys. B (and references therewithin).

[7] O. Adriani et al., Nucl. Instr. and Meth. A 511 (2003) 72.

[8] M. Boezio et al., Nucl. Instr. and Meth. A 487 (2002) 407.

HELIOSPHERIC COSMIC RAY OBSERVATIONS WITH PAMELA EXPERIMENT

M. Casolino[b,a], L. Marcelli[b,a], V. Mikhailov[c], P. Picozza[b,a],
S. Russo[b,a]

[b] *INFN, Sezione di Roma II, via della Ricerca Scientifica, Roma, Italy*

[a] *Dipartimento di Fisica, Università di Roma "Tor Vergata", via della Ricerca Scientifica, Roma, Italy*

[c] *MEPHI, Moscow Engineering and Physics institute, Moscow, Russia*

Abstract

PAMELA is a satellite borne experiment to be placed in low Earth orbit on board of the ResursDK1 Russian satellite in the year 2005. It consists of a permanent magnet core with a silicon microstrip detector, a Transition Radiation Detector, a Time of Flight system and a Silicon Tungsten tracking calorimeter. Its main aim is the investigation of the cosmic radiation: origin and evolution of matter in the galaxy, search for antimatter and dark matter of cosmological significance, understanding of origin and acceleration of relativistic particles in the galaxy. The detector can however be used also to address issues relative to the solar - terrestrial environment (above 50 MeV) such as Solar particle events (isotopic composition of H and He, e^- and e^+ spectrum) and composition and temporal dependence of the trapped and albedo particles component. In this work the observational capabilities of Pamela in these contexts will be addressed.

1   Introduction

The Pamela spectrometer [1] will be launched in a semi-polar orbit (70.4^o inclination and altitude between 300 and 600 km) in the year 2005. Its expected lifetime will be 3 years. The primary scientific objectives of Pamela are: 1) Measurement of the energy spectrum of antiprotons (80 MeV - 190 GeV) and positrons (50 MeV - 270 GeV); 2) Measurement of the proton (80 MeV - 700 GeV), electron (50 GeV - 2 TeV) and light nuclei (up to several hundred of GeV/n); 3) Measurement of the antihelium/helium ratio with sensitivity of at least 10^{-7}.

To achieve these goals, the instrument uses a permanent magnet (0.4 T) with six layers of double-sided silicon microstrip detectors to measure particle rigidity and sign. Lepton/Hadron identification is ensured by a Transition Radiation Detector (TRD) located on top of the magnet and a Silicon-Tungsten Immaging Calorimeter (44 planes; 16.3 Radiation Lenghts). Trigger and albedo particle rejection are given by a series of scintillator counters placed on top of the detector, above the magnet and below it. A neutron detector on bottom ensures lepton/hadron identification at high energies. In this work we focus mainly on the observational capabilities of Pamela in respect to solar and heliospheric cosmic rays.

2   Solar Particle Events

The launch of Pamela is expected in the first half of 2005, about 5 years from the last solar maximum (Sept. 2000). The number of solar proton events in the three years of operations can be estimated from [2]: taking into account our minimum energy acceptance of 80 MeV we expect about 10 significant events during Pamela lifetime. The background particle rate on the topmost scintillator could be very high for intense events, therefore a dedicated trigger for Solar active days is currently under study. The observation of solar particle events with a magnet spectrometer will allow for the first time to perform:

- Measurement of the positron component. Positrons are produced mainly in the decay of π^+ coming from nuclear reactions occurring at the flare site and they have up to now only been measured indirectly by remote sensing of the 511 keV gamma ray annihilation line. Using the magnetic spectrometer it will be possible to separately analyze the high energy tail of electron and positron spectra at 1 AU obtaining information both on the production and propagation in the heliosphere.

- Measurement of the proton component. Pamela can measure the energy spectrum of solar protons in a very wide energy range (from 80 MeV to some GeV). These measurements will be correlated with

other instruments placed in different points of the magnetosphere to give information on the acceleration and propagation mechanisms of SEP events. Up to now there has been no direct measurement [3] of the high energy ($> 1 GeV$) proton component of SEPs. The importance of a direct measurement of this spectrum is related to the fact [4] that there are many events where the energy of protons is above the highest ($\simeq 100 MeV$) detectable energy range of current spacecrafts but is below the detection threshold of ground Neutron Monitors[5]. However, at these energies, is possible to examine the turnover of the spectrum, where we find the limit acceleration processes at the Sun. Pamela has a maximum trigger rate of 100 Hz and a geometrical factor of 20.5 cm^2 sr. This implies that we will be able to read all events with a integral flux ($E > 80 MeV$) up to $4p/cm^2$ s sr. For such events we expect about 2×10^6 events/day (assuming a spectral index of $\gamma = 3$ we have 2×10^3 events/day above 1 GeV). Larger events saturate the trigger, so in this case the number of protons will be of the order mentioned or lower due to dead time.

- Measurement of the nuclear component. The same arguments of the proton component can be applied to the study of the heavy nuclei component of SEP events. We expect $\simeq 10^4$ ^4He nuclei and $\simeq 10^2$ ^3He nuclei for gradual events and more for impulsive ones. This statistics will allow to examine in detail the amount of the ^3He component and understand selective nuclear enhancement processes in the high energy range of impulsive [6] events to gather information on the selective acceleration processes.

- Neutron component. Neutrons are produced in nuclear reactions at the flare site and can reach the Earth before decaying. Although there is no devoted trigger for neutrons, the background counting of the detector will measure in great detail the temporal profile and distribution of solar neutrons.

- Lowering of the geomagnetic cutoff. The high inclination orbit of the satellite Resource will allow to study [7, 8] the variations of cosmic ray geomagnetic cutoff due to the interaction of the solar particle event with the geomagnetic field.

3   Jovian electrons

Pioneer 10 discovered Jovian electrons at $1 - 25 MeV$ at a distance of $\simeq 1$ AU from Jupiter [10, 11]. Since then Jovian electrons have been measured in several interplanetary missions. It is known that Jupiter is the strongest electron source at low energies (< 25 MeV) in the heliosphere within an 11 AU radius. Its spectrum has a power law [9] of $\gamma = 1.65$ increasing above
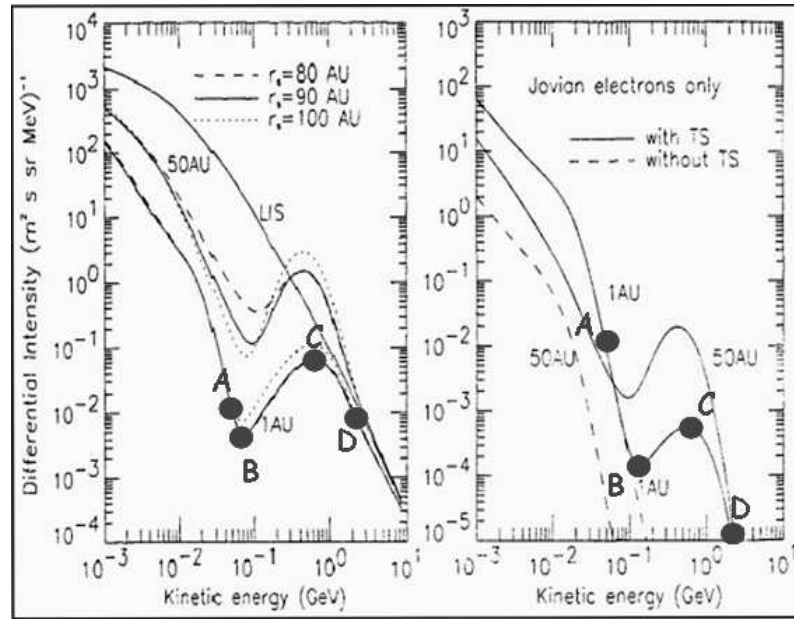
Figure 1: Left: All electron differential spectra at various distances from the Sun. Right: Jovian component. The dots represent Pamela observations: AB = Primary component; BC - CD = Reaccelerated component[13].

25 MeV, where the galactic component becomes dominant. At 1 AU IMP-8 could detect Jovian electrons in the range (0.6 - 16 MeV) and measure its modulation by the passage of Coronal Interaction Regions (CIR) with 27 days periodicity [11, 12]. There are also long term modulation effects related to the Earth-Jupiter synodic year of 13 months duration: Jovian electrons follow the interplanetary magnetic field lines so, when the two planets are on the same solar wind spiral line, their transit from Jupiter to the Earth is eased and the flux increases, whereas when the two planets lie on different spiral lines the electron flux decreases.

Pamela is able to detect electrons from a minimum energy of 50 MeV. At this energy, however, geomagnetic shielding will reduce the active observation time reducing total counts. It will be however possible to study for the first time the high energy Jovian electron component and test the hypothesis of reacceleration at the Solar Wind Termination Shock (TS). It is known that cosmic rays originating outside the heliosphere can be accelerated at the solar wind termination shock. Also Jovian electrons, transported outward by the solar wind, reach the termination shock and can undergo shock acceleration

Interval	Galactic and Jovian e^- (N/3days) At 1 AU	Galactic and Jovian e^- (N/3days) With Cut-off
AB $(50 - 70MeV)$	70±8	5±2
BC $(70 - 600MeV)$	10200±100	2030±40
CD $(600MeV - 2GeV)$	12300±100	4570±70
Total	22570±208	6605±112

Interval	Jovian e^- (N/3days) At 1 AU	Jovian e^- (N/3days) With cut-off
AB $(50 - 130MeV)$	100±10	10±3
BC $(130 - 600MeV)$	95±10	20±5
CD $(600MeV - 2GeV)$	90±9	35±6
Total	285±29	65±14

Table 1: Top: Expected galactic and Jovian electron counts with Pamela detector in the various energy ranges. Bottom: Only Jovian contribution. Energy ranges: AB = Primary component; BC -CD = Reaccelerated component; The right column represents Pamela expectations taking into account the geomagnetic cutoff.

increasing their energy; part of these electrons are scattered back in the heliosphere. The position of the shock (still unknown and placed at about 80 - 100 AU) can affect the reaccelerated electron spectrum [13]. In Table 3 are shown the expected electron counts with Pamela detector (TS=90 AU, Heliospheric boundary=120 AU) using the spectrum calculated in [13]. The first column contains the fluxes outside the magnetosphere, whereas the second takes into account the geomagnetic cutoff along Pamela orbit. If counts are grouped in three day bins it is possible to accumulate enough statistics to extract the signal and monitor short term (CIR) variations. It will be therefore possible to detect electrons in the three energy ranges: 50-70 MeV, at the lower limit of Pamela detection, these electrons represent the primary non-reaccelerated component; 70-600 MeV, in this energy range the main reaccelerated component will be clearly observable; above 600 MeV, where electrons of mostly galactic origin will be detected. On the overall the Jovian component amounts to about 1% of the total galactic flux. This effect will therefore be measurable with our instrument, which will be able to extract the long and short term modulation effects. In addition it is possible that the reacceleration of electrons at the solar wind termination shock is modulated by the solar cycle: with three years of observations toward the solar minimum

it will be possible to detect also this effect. In addition to these phenomena, charge dependent modulation effects will be studied by comparing the temporal dependence of electron and positron spectra.

4 Conclusions

We have discussed some observational capabilities of Pamela in respect of Solar particle events and other heliospheric processes. In addition also Solar modulation at 1 AU and secondary particle production in the atmosphere will be studied in parallel to the main physics objectives of this experiment.

References

[1] Simon, M., Proc. XXVIII ICRC.

[2] Shea, M., 2001, Proc. XXVII ICRC, Sh1.07, 3401.

[3] Miroshnichenko, L., Solar Cosmic Rays, Kluwer, 2001.

[4] Ryan, J. et al., Sp. Sci. Rew., **93**, 35, 2000.

[5] Bazilevskaya, G. A., Svirzevskaya, A. K., 1998, Spa. Sci. Rev. **85**, 431.

[6] Reames, D.V., 1999, Spa. Sci. Rev. **90**, 413.

[7] Ogliore,R. C., 2001, Proc. XXVII ICRC, Sh3.06-234, 4112.

[8] Leske, R.A., et al, 2001, Jour. Geoph. Res. **106**, A12, 30011.

[9] M. D. Rodriguez - Frias, R. Gomez-Herrero, L. del Peral, J. Sequeiros, R. Muller-Mellin, H. Kunow, Proc 1st Solar and Space Weather Euroconference, 'The Solar Cycle and Terrestrial Climate', Santa Cruz de Tenerife, Spain, 25-29 September 2000 (ESA SP-463, December 2000)

[10] Simpson J. A., Trans. Am. Geophys. Union, 55, 556 (1974).

[11] Eraker J. H., The Astrophysical Journal, 257, 862 (1982).

[12] Chenette D. L., Journal of Geophys. Research, 83, 2243 (1980).

[13] Poitgieter M. S. and Ferreira E. S., Journal of Geophys. Research, 107, A7 SSH 1-1 (2002).

TECHNIQUES FOR SHOWERS IDENTIFICATION IN PAMELA CALORIMETER

F. VOLPE[a,b]

[a] *Dipartimento di Fisica, Università degli Studi di Bari,*
via Amendola 173, 70126 Bari, Italy

[b] *INFN, Sezione di Bari, via Amendola 173, 70126 Bari, Italy*

Abstract

In this paper we propose a particle classification system for the imaging calorimeter of the PAMELA satellite-borne experiment. The system is based on a first step in which an elaborated pre-processing is performed and discriminating and descriptive variables are selected. In the second step the selected features are used as input for supervised algorithms which classify the data. The algorithms tested in this work are Artificial Neural Network and Support Vector Machines.

The system was tested with a large simulated data set, composed by 40 GeV/c momentum electrons and protons. Moreover, in order to study the classification power of the calorimeter for experimental data, we have also used biased simulated data. A proton contamination in the range $10^{-4} \div 10^{-5}$ at an electron efficiency greater than 95% was obtained. The results are adequate for the PAMELA imaging calorimeter and show that the approach to the classification based on soft computing techniques is complementary to the traditional analysis performed using optimized cascade cuts on different variables.

1 Introduction

Payload for Antimatter Matter Exploration and Light-nuclei Astrophysics (PAMELA) is a satellite-borne experiment devoted to investigate the matter antimatter symmetry of the Universe and other cosmological subjects through precise cosmic ray measurements [1]. The primary aims of the experiment include measurements of the energy spectra of $\bar{p}$, e^+ and light nuclei in cosmic radiation. The experiment will be performed on-board of the Russian Resurs-DK1 satellite, which will be launched into space in 2004. Three years of data collecting are expected.

  The calorimeter of this experiment will allow the discrimination between electromagnetic, hadronic showers and non-interacting particles. This means that the problem of extraction of signal from background strongly regards the PAMELA calorimeter. In this work a particle classification system based on soft computing techniques is proposed for PAMELA calorimeter.

2 The PAMELA calorimeter

The PAMELA calorimeter is a sampling detector composed by 11 modules, each formed by two series of: single-sided silicon plane (X view), tungsten absorber, single-sided silicon plane (Y view) for a total number of 44 silicon layers and 22 absorber layers. The calorimeter has a high granularity both in the longitudinal (Z) and in the transversal (X and Y) directions. In the Z direction the granularity is determined by the thickness of the absorber layers; each tungsten layer is 0.26 cm thick, which corresponds to 0.74 X_0(radiation lengths). The transverse granularity is due to the segmentation of each silicon layers into 96 strips with a pitch of 2.4 mm.

  These technical characteristics make the calorimeter a very powerful particle identifier detector: due to its high granularity the calorimeter is particularly suitable for reconstructing the spatial development of a shower-event. Indeed, it has been designed to extract the antiproton/positrons signal from the large background generated by the electron/proton flux. The expected background contamination of this detector is of the order of 10^{-4} for p/e^+ and $\bar{p}/e^-$ measurements at a signal efficiency of 95% [2].

3 Classification by supervised methods

Here we propose an alternative approach to perform the classification between electromagnetic and hadronic showers in the PAMELA calorimeter. Instead of using traditional methods based on cascade cuts on discriminating variables, in this work we show how the classification can be performed for this detector using supervised algorithms.

Each classification based on soft computing techniques requires to be preceded by a pre-processing phase in which the variables to be used as input for the classifier are chosen. The pre-processing is necessary because the complex information coming from the calorimeter has to be reduced; this is the so called dimensionality reduction. For each event in the calorimeter a RoI (Region of Interest) is determined: by means of a longitudinal segmentation of the detector, a block of ten consecutive silicon planes containing the relevant features for each event is selected. The 9 discriminating variables chosen for this work are the following: 1) total energy released in the RoI, 2) total energy released outside the RoI, 3) total number of hit strips in the RoI, 4) total number of hit strips outside the RoI, 5) total energy released in a cylinder of 1 Moliere radius around the track direction in the RoI, 6) total energy released in a cylinder of 1 Moliere radius around the track direction outside the RoI, 7) total number of hit strips in a cylinder of 1 Moliere radius around the track direction in the RoI, 8) total number of hit strips in a cylinder of 1 Moliere radius around the track direction outside the RoI, 9) total energy released in the plane of maximum interaction, i.e. having the higher energy deposit. In this way each event in the calorimeter is represented by a point in a 9-dimensional feature space and can be submitted in this form as input to the classifier.

Two supervised methods have been tested in this work for a fine discrimination between electromagnetic and hadronic showers: Artificial Neural Networks (ANN) and Support Vector Machines (SVMs).

3.1 Artificial neural networks

As neural network we have used a standard two layered feed-forward network [3]. The input layer has 9 neurons according to the dimension of the feature space; the hidden layer has a number of neurons varying from 2 to 10 and the output layer has only one neuron which, in the training phase, is set to 1 when signals are submitted to the network and to 0 otherwise.

As transfer function a sigmoid has been used and in the training phase the weights on the network have been iteratively updated by the gradient descent rule. At each iteration the error function reduces until a minimum is attained, which may be a local or a global one. In our case the network is trained using an overtraining procedure, which assumes the network trained when the error function has reached the global minimum.

3.2 Support vector machines

SVMs [4] are sophisticated and powerful non-parametric classifiers. In the case of two linearly separable classes SVMs search among the infinite number of linear classifiers that separate the data, for the one that has the smallest generalization error. Intuitively, a good choice is the hyperplane that leaves

the maximum margin between the two classes, where the margin is defined as the sum of the distances of the hyperplane from the closest point of the two classes. The data points which lie at the border between the two classes are called *support vectors*. Their number is usually small and Vapnik showed that it is proportional to the generalization error of the classifier. In the case of two not separable classes we can still look for the hyperplane that maximizes the margin and minimizes a quantity proportional to the number of misclassification errors, but this search has to be performed in high (possibly infinite) dimensional space. The original training data are mapped into this new space where the decision boundary is determined. Many functions, called Kernel functions, can be used for the mapping of the original training data, so that SVMs can operate in different configuration.

SVMs minimize *structural risk* [4], i.e. instead of constructing a decision function by minimizing the training error on a representative data set (as ANN do), it is chosen in a way to minimize an upper bound on the test error. The minimization of the *structural risk* allow an increment of the confidence level with which the classifier classifies unseen data set and consequently its generalization power.

4   Application to data and results

This study has been performed using a data set obtained by means of CERN-GEANT 3.21 official collaboration simulation code GPAMELA release 4.01 [5]. The data set used for this study is composed by 10^5 electron and 10^5 interacting protons of 40 GeV/c of momentum, with the PAMELA electromagnetic calorimeter reproduced in the simulation as in the final flight version.

The experimental data can be different from the data used for the learning phase of the classification system. For this reason it is particularly useful to consider classification systems with a very high generalization power. Besides testing two different supervised algorithms, we used validation data, which simulate experimental data with different behavior respect to the training data (biased data). The selected learning data set is composed by the same amount of electrons and protons (8×10^3) and used for the training of the classification systems. A validation set of about 10^5 electrons and 10^5 protons is used for the performance estimate. Moreover three further different data set, obtained by the validation data set, have been used. They have been generated introducing a random bias in the original data set up to the 10%, 20% and 30% of the original value.

The results obtained are shown in Figure 1. In the unbiased case the electromagnetic and hadronic showers detected by the calorimeter can be distinguished, using the particle classification system here proposed, with a signal efficiency greater than 95% and a background contamination in the range
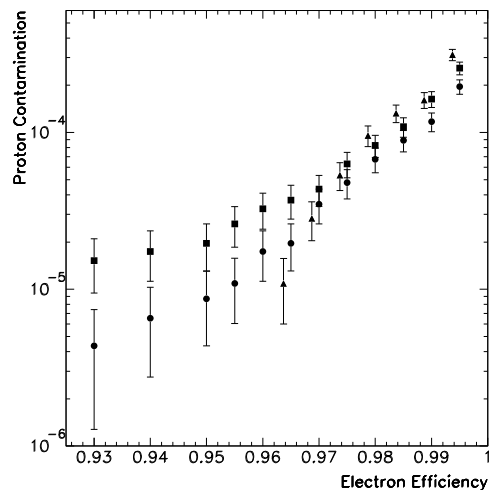
Figure 1: Proton contamination *vs* electron efficiency on unbiased data: SVMs (circle), ANN (square) and FLD(triangle).

$10^{-5} \div 10^{-4}$; as comparison we show also the results obtained using the Fisher linear discriminant (FLD) [6]. ANN and FLD show similar results, but SVMs have the best performance. In the hypothesis of experimental data different from the data used for the learning phase of the classification system, Support Vector Machines and FLD appear less adequate than ANN for different values of the bias. We show in Figure 2 only the case with a bias up to 30%, but the same is for the other bias. It's interesting to point out that ANN show a very stable classification power also with 30% biased data. In all cases the performances obtained by classifying the data of imaging calorimeter with the particle classification system here proposed, are appropriate for the specific requirement of the PAMELA experiment.

5   Conclusions

The classification system here proposed can provide an accurate and efficient selection of electromagnetic and hadronic showers. Different classification algorithms have been tested on unbiased and biased data set. Artificial neural networks gives the best performances and seem to be more stable than support vector machines. The results appear significantly good for the application to the particle classification task of the PAMELA calorimeter and suggest a
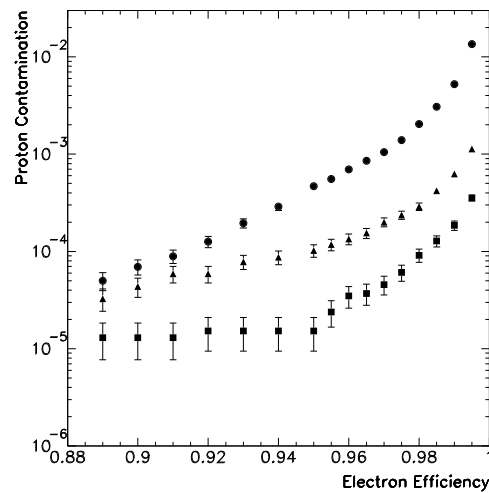
Figure 2: Proton contamination *vs* electron efficiency on biased data up to 30%: SVMs (circle), ANN (square) and FLD(triangle).

complementary use of these strategies together with the traditional cascade cuts analysis, which require a more complicate elaboration step for the choice and the tuning of cut combinations. Methods like SVMs and ANN have the great advantage, once trained, to give an immediate classification and this aspect can be exploited for a fast event identification.

References

[1] M. Circella et al., *Nuclear Instrument and Methods A* **518** (2004) 153-157.

[2] M. Boezio et al., *Nuclear Instrument and Methods A* **487** (2002) 407.

[3] J. Hertz, A. Krogh, R.G. Palmer, *Introduction to the theory of neural computation*, Addison-Wesley (1991).

[4] V. Vapnik, *Statistical Learning Theory*, John Wiley & Sons, New York (1998)

[5] http://www.ba.infn.it/~ambriola/gpamela.

[6] R.A. Fisher, *Contributions to Mathematical Statistics*, John Wiley & Sons, New York (1950).

THE SCINTILLATOR COUNTERS OF THE TOF OF THE AMS-02 EXPERIMENT

Cristina Sbarra[a]

for the AMS-TOF Bologna Group

[a] *INFN Sezione di Bologna, Viale B.Pichat 6/2 40127 Bologna, Italy*

Abstract

The Time Of Flight system of the AMS-02 detector is beeing built in the INFN laboratories of Bologna. The high magnetic field produced by the AMS-02 superconducting magnet imposes the utilization of special PMTs and light guides for the TOF counters. The TOF detector must give the fast trigger to the whole AMS experiment and must measure the absolute charge by particle energy loss, at least up to z=20. To control the TOF-02 performances, a series of thermal-vacuum tests together with a beam test have been made, and the results are quite encouraging.

1 Introduction

The TOF apparatus of the AMS-02 experiment [1] is being built at the INFN laboratories of Bologna. The operation in space imposes several requirements on the mechanical design and on the servicing electronics for the TOF system. The modules have to be housed in a light-tight and robust cover and the support structure of the modules has to conform the NASA specification, so vibrational and thermal-vacuum tests on the structure components have to be done.

2 The requirements for the TOF of the AMS-02 experiment

The Time Of Flight system of AMS-02 will provide:

1. the fast trigger to the experiment;

2. the measurement of the time of flight of the particles traversing the detector with a resolution sufficient to distinguish upward from downward going particles at a level of at least 10^{-9}, and electrons from anti-protons at $E < 1.5$ GeV;

3. the measurement of the absolute charge of the particle in addition to the measurements done by the silicon tracker and by the RICH.

Thus the TOF scintillators must give a very fast and reliable response to the energy lost by the particle traversing the detector. The system will also provide a measurement of the particles charge with a resolution to distinguish nuclei up to $Z \leq 20$: a dynamic range of more than 10000 in the measurement of the pulse height is thus required (taking into account the attenuation along the counter and the need to have a good measurement of singly charged particles).

3 The TOF-02 design and mechanics

The geometrical acceptance of the TOF has been fixed at $0.4 \, \mathrm{m}^2$sr to maximize the sensitivity of the spectrometer for antimatter search. To match the acceptance of the magnet, each plane of the TOF system covers roughly a circular area of about $1.2 \, \mathrm{m}^2$, with $12 \, \mathrm{cm}$ wide scintillator pads of different length, overlapped by $0.5 \, \mathrm{cm}$ to avoid geometrical inefficiencies.

The high absolute value of the field ($1.5 \div 2 \mathrm{kG}$) forced the adoption of a special kind of PMT (fine mesh Hamamatsu R5946). Even though the fine mesh can operate inside intense magnetic fields, their response depends strongly on the angle between the field and their longitudinal axis (see section 3.1). Thus, tilted light guides were designed in order to minimize this angle for each PMT.

3.1 The fine mesh PMTs

To study the behaviour of the fine mesh photomultiplier Hamamatsu R5946 in the magnetic field, they were performed significant tests in the Bologna laboratory: it was measured the PMT response to a red light emitting diode (LED) inside the poles of an electro-magnet (maximum field 4 kG) on a movable stand which could be be rotated at a maximum angle of 90°. The photomultiplier response was measured for different values of the magnetic field $\vec{B}$ and of the angle between the tube axis and the field direction [2].

A complete simulation of the fine mesh phototubes has also been developed [3] and the results of the simulation are in good agreement with the

Fine mesh transit time difference vs angle

Fine mesh gain vs angle
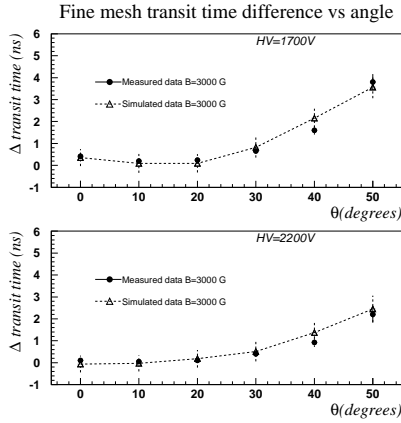
Figure 1: Measured and simulated transit time difference ($t_{B>0} - t_{B=0}$) for fine mesh photomultipliers in a magnetic field B=3000 G, as a function of the angle θ between $\vec{B}$ and the PM axis [3].
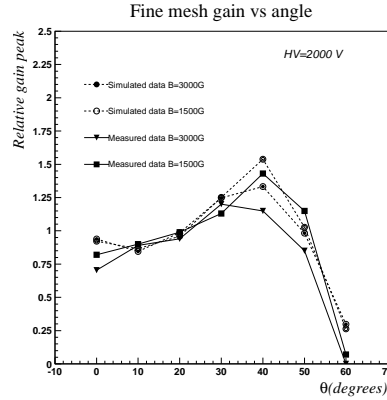
Figure 2: Measured and simulated PM gain versus the angle between the magnetic field and the PM axis [3]: the fine mesh response drops down above $\sim$ 30°, both in the data and in the simulation.

data taken, both for the fine mesh response in time and for the gain response, for various inclination of the PM inside the magnetic field. Figures 1 and 2 show the data taken together with the simulation made. The results of both measured data and simulation show that the fine mesh cannot work for $\theta > 30°$, because of their time response degradation and since their gain has an abrubpth fall [2].

3.2   Counters

The plastic scintillator of the TOF counters is by Eljen-Technology (Texas-USA), 12 cm wide, 1 cm thick. They are of variable widht and variable lenght ($117 \div 134$ cm). Figure 3 shows a view of the TOF couple of upper planes with the scintillators and the light guides.

   The first prototypes were characterized in the laboratory and tested in a heavy ions beam in 2002 and 2003. On each side, up to 15 cm long clear plastic guides collect the scintillator light on the photocathodes of two (or three) R5946 Hamamatsu photomultipliers. The bialkali photocathode sensitivity matches the scintillator light spectrum. In 2004 the TOF counters have been characterized in the Bologna laboratory with a proper cosmic ray telescope. The results of the TOF counters caracterization can be consulted on line [5].
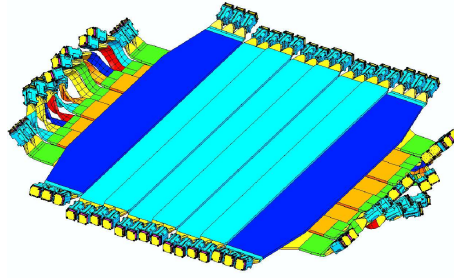
Figure 3: Upper TOF couple of planes (the edge counters are of trapezoidal shape).

4 Space qualification tests

The TOF detector will undergo variations of temperatures from $-20°C$ to $+50°C$ and it will survive the strong acceleration produced by the shuttle launch, and its measurements should not be affected by this vibration. Hence, thermal-vacuum and mechanical tests must be carried on with the TOF structure, before the flight.

A group of 10 photomultipliers was tested in the Bologna thermal-vacuum simulator at a pressure of $10^{-7} \div 10^{-6}$ mbar with temperature varying between $-30°C$ and $+55°C$. They were re-calibrated after each cycle of temperature and their characteristics remained the same [4]. Other six PMTs were also monitored for the dark current.

Figure 4 shows the variation of the dark current versus temperature for a couple of phototubes. Even if an increase is clearly measured at high temperature, the dark current is always negligible [6].

5 Beam test results

In 2003, four scintillators (named C1,C2,C3 and C4) were used with a 158 GeV/c/A ion beam obtained from the primary In SPS beam and tuned with the H8 selection line. Data analysis is still in progress for this beam test run.

Two of the scintillators used (C2,C3) represented the worst situations, with twisted and bended light guides. The charge peaks of the most problematic counter (C2) are clearly seen in figure 6. The charge resolution was also computed, both for the anode signal and for the dynode signal (passive sums of the two PMTs), as it can be noticed in fig. 5.

From the time of flight measurements between the different counters (for example C2-C3 is shown in figure 7) it is possible to infer the TOF resolution,
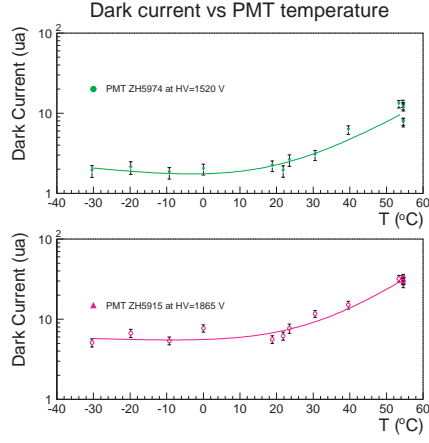
Figure 4: Fine mesh dark current as a function of the temperature [6] for a couple of phototubes. High gain PM on top, low gain PM on bottom.
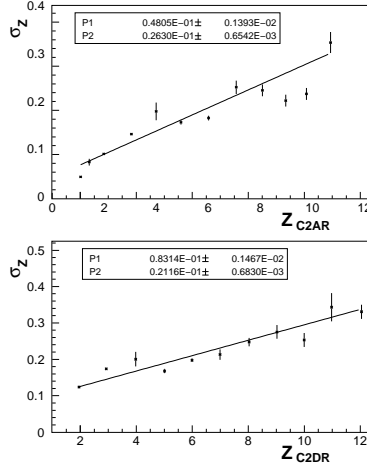
Figure 5: C2 charge resolution as a function of the particle charge for anode (above) and dynode (below) signals.
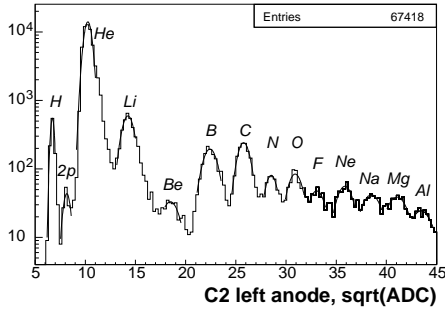
Figure 6: Square root of the integrated charge measured with left anode of a TOF counter (peak "2p" is due to singly charged particles crossing in time).
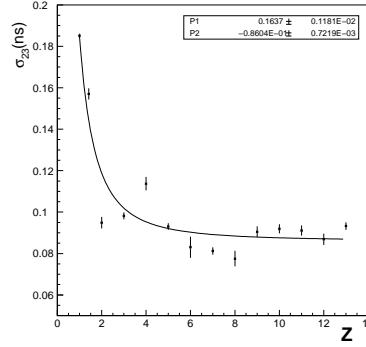
Figure 7: Resolution on the time of flight between two TOF counters (named C2 and C3 respectevely) as a function of the particle charge.

that turns out to be of the order of 130 ps for singly charged particles [1].

---

[1] for the four planes $\sigma_{tof} \simeq \frac{\sigma_{23}}{\sqrt{2}}$

References

[1] AMS collaboration, *The Alpha Magnetic Spectrometer (AMS) on the International Space Station*, Published on Physics Reports, vol. 366/6, pp.331-404 (2002).

[2] L.Brocco *et Al..*,*Behavior in strong magnetic field of the photomultipliers for the TOF system of the AMS-02 space experiment*, Proc. 27th ICRC (2001).

[3] G.Levi, R.Martelli, C.Sbarra, *The Mesh PM for the AMS Time of Flight, comparison between simulation and measurements*, NIMA 530/3, pp. 419-425 (2004).

[4] L.Amati *et Al.* , *Space Qualification and Beam Test Results for the TOF of AMS-02* Proc. of the 9th Topical Seminar on Innovative Particle and Radiation Detectors (2004) Siena. To be published on Nuclear Physics B

[5] http://ams.bo.infn.it/database/Counters

[6] F. Giovacchini, G. Levi, R. Martelli, L. Quadrani, C.Sbarra, *Fine Mesh Thermovacuum Tests*, AMS-BO Internal Note (2004).

AMS-02: HIGH PRECISION TRACKING AND ION SELECTION WITH A SILICON TRACKER IN SPACE

Paolo Zuccon[a]

on behalf of

the AMS Tracker Collaboration

[a] *INFN, Sezione di Perugia, via Pascoli, Perugia, Italy*

Abstract

AMS-02 is a magnetic spectrometer foreseen to be installed on the ISS. The goal of AMS is to search for antimatter in the cosmic rays, to search for signals of dark matter and to do accurate measurements of cosmic rays fluxes. The core of the spectrometer is a silicon tracker which provides the measurements of the traversing particle rigidity and charge. Six ladders of the AMS02 tracker have been exposed to a test beam to evaluate the spatial resolution and the charge measurement capability.

1 Introduction

The Alpha Magnetic Spectrometer (AMS) is a particle physics experiment that will be installed on the International Space Station in 2007 for a mission of minimum three years. AMS is a magnetic spectrometer realized with a 0.8 T superconducting magnet, a microstrip silicon tracker and a plastic scintillator time of flight (TOF) system. A transition radiator detector (TRD), a ring

image cerenkov detector (RICH) and an electromagnetic calorimeter (ECAL), complete the instrument allowing for a better particle identification.

The goals of the AMS mission are: to search for antimatter nuclei in the cosmic rays, to look for dark matter annihilation signals and to do accurate measurements of the cosmic rays fluxes up to rigidities of some TV.

The AMS microstrip silicon detector, composed of 8 planes placed in the magnet bore covering a lever arm of about one meter, accurately measures the trajectory of the particles. The measurement of the energy deposited in the silicon wafers allows also to determine the charge of the traversing particle.

The AMS silicon wafers are high resistivity double sided microstrip detectors. The strips on the two sides run in orthogonal directions allowing the measurement of two coordinates. On the junction side (p-side), which measures the bending coordinate, there are 2560 strips with an implantation (readout) pitch of 27.5(110) μm for an expected resolution of ~ 8 μm (*He* nuclei). On the ohmic side (n-side) there are 1536 strips with an implantation(readout) pitch of 52(208) μm for an expected resolution of ~ 20 μm (*He* nuclei).

The double silicon wafers are arranged in ladders of variable length from 9 up to 15 wafers, for a total of 192 ladders, ~ 2800 wafers and ~ 8 m^2 of instrumented area.
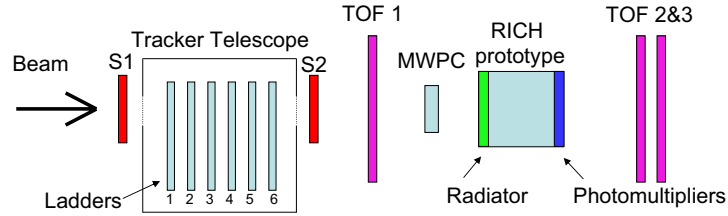
Figure 1: Setup of the CERN test beam.

Detailed information on AMS and on the silicon tracker can be found in [1, 2] and references there in.

2   The test beam

To evaluate the performances of the AMS tracker 6 flight ladders have been exposed to a test beam together with a prototype of the RICH detector and three TOF scintillator slabs. The setup of test beam is sketched in fig.1.

The detectors were installed in the T9 PS experimental hall at CERN and they have been exposed to proton and ions beams. The ions, produced in the interaction between high energy *In* with a *Be* target, have been magnetically selected to obtain A/Z=2 and A/Z=2.25 beams. The average momentum per nucleon was ~ 10 GeV/n for all the beams.

3   Cluster selection and charge determination

The energy deposited in the silicon by a relativistic particle of charge Z is proportional to Z^2 and follows a Landau distribution.

The readout system of the AMS tracker has been designed to cover a large dynamic range, to have the capability to separate heavy ions. The front end electronics is a custom designed hybrid board based on the VA-hdr9a readout chip, a high dynamic range chip based on the VA and on the Viking chips [3].

Non linear effect on the signal collection in the microstrips on the silicon, and the details of the implementation of the read out chains, introduce some deviation from the linear behavior.

The major observed effects are: 1. a dependence of the mean collected signal on the particle impact position in the gap between two readout strips; 2. a non linear behavior of the signal as the charge increases. Both these effects appear with different features on p and n sides.
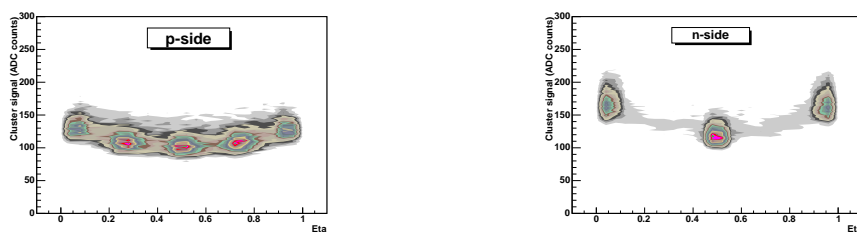
Figure 2: Total signal versus eta for *He* nuclei. Left p-side, right n-side.

To better determine the charge of a traversing particle a set of correction factors have been calculated using clean samples of the different ion species. These samples have been obtained imposing tight cuts on the signal of the first ladder and studying the behavior of the signals in the remaining five. Fig.2 shows the dependence of the signal as function of our estimation of the impact position in between two readout strips (Eta). Our definition of Eta is:

$$Eta = \frac{S_R}{S_L + S_R} \tag{1}$$

where S_R and S_L are the signals of the left and the right readout strips with respect the reconstructed impact point.

Different behaviors as a function of Eta have been observed with the increase of the particle charge and with respect the wafer side considered. As an example, fig.3 shows the observed Eta dependence for different charges.

Fig.4 shows the relation between the total signal (Eta corrected) and the particle charge. A linear behavior is observed on the n-side up to Z=13, above
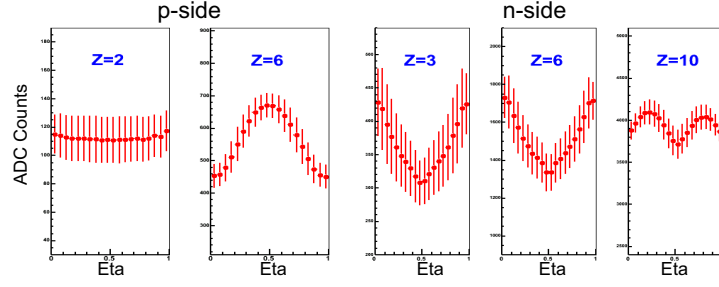
Figure 3: Average signal versus Eta for the two silicon sides and for different charges.

this threshold the slope becomes steeper and the resolution worsens. On the p-side instead a linear behavior is observed below Z=5 and above Z=10, in between a non-linear transition zone is present.
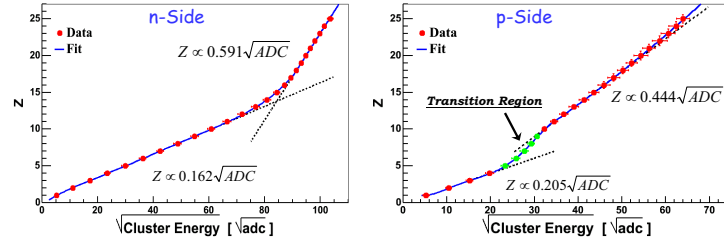
Figure 4: Charge of the sample versus the square root of the mean Eta corrected signal. Left n-side, right p-side.

The Eta dependence of cluster signal varies smoothly with the deposited energy. A set of correction factors depending on the Eta and on the cluster signal have been calculated to linearize the detector response.

Fig.5 (left) shows the truncated mean of the signals on the 6 ladders with all the corrections applied. A clear correlation between the measurements on the two sides is observed. The spots corresponding to the different ions can be recognized almost up to Iron. A comparison with the charge measurements from the RICH detector is shown in fig.5 (right). A very good correlation between the two detectors is observed.

4   Spatial resolution

To study the spatial resolution of the AMS ladders for different ions we selected the events which have signals compatible with the desired charge both on p and
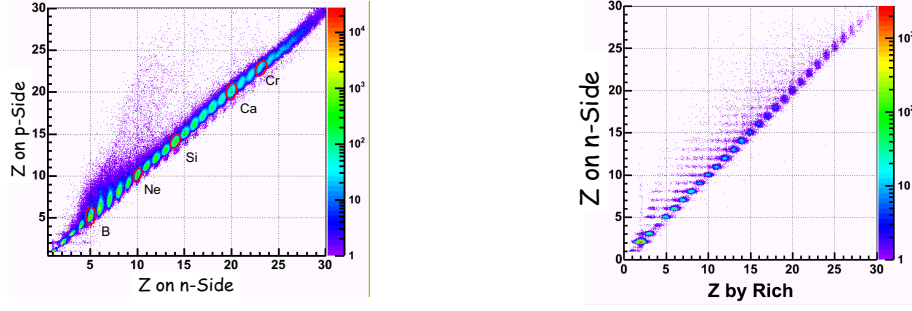
Figure 5: Left: p-side vs n-side charge measurement with 6 ladders. Right: n-side tracker charge versus the RICH charge.

n sides and on all the six ladders.
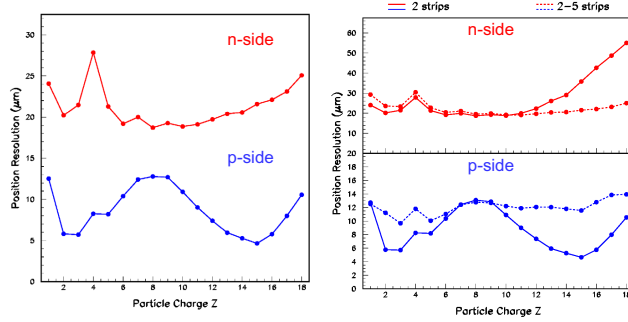
Figure 6: AMS tracker spatial resolution versus charge. Left: best resolution. Right: CoG calculated using two strips(solid line) and up to 5 strips(dashed line).

For each event a linear fit of the cluster positions on the ladders excluding the 4th ladder has been made. The distribution of the distance δ between the cluster on the 4th ladder and the position predicted by the fit, has been considered.

A double gaussian distribution well describes the distribution of δ, with the broader gaussian accounting for less than 20% of the events. The sigma of the narrower gaussian (σ_δ) represents the spatial resolution of our detector (σ_{det}) convoluted with the error of the prediction from the linear fit(σ_{Fit}). The resolution is then defined as:

$$\sigma_{det} = \sqrt{\sigma_{delta}^2 - \sigma_{Fit}^2} \tag{2}$$

A preliminary estimation of the tracker resolution is shown in fig. 6(left).

The influence on the resolution of the number of strips used in the definition of the cluster position (Center of Gravity) has been studied as shown in fig.6 (right). For the p-side the best resolution is obtained using a CoG calculated with only two strips, for the n-side a wider definition of the cluster improves the resolution for $Z > 11$.

5   Conclusions

Preliminary results on the AMS-02 silicon ladders performances have been presented in terms of spatial resolution and absolute charge measurement. The analysis of beam test data has shown that a single point resolution better than $10(20)$ μ can be obtained in the measurement of the bending (non bending) coordinate for He ions, while keeping this figure better than $20(30)$ μ for a wide range of the particle charge. The low noise level of the detector results in a good efficiency for low Z ion detection and the wide dynamic range of the readout system allows the charge determination for an extent range of ion species. The combined charge measurement of the six ladders under beam test has shown a charge discrimination capability up to Z=24, confirmed by the independent measurement of the RICH module. In the full AMS-02 tracker, where a combined measurement from eight ladders will be available, ion identification up to Fe will be reached.

References

[1] B. Demirkoz *AMS: A particle Physics experiment in the space* These Proceedings.

[2] M. Paniccia *The AMS02 Silicon Tracker* These Proceedings.

[3] E. Nygard et al. Nucl. Instrum. Meth. A301 (1991) 506.

THE AMS-02 TRACKER

Mercedes Paniccia[a]

[a] *Département de Physique Nucléaire et Corpusculaire, Université de Genève,
24 quai Ernest-Ansermet, CH-1211 Genève, Suisse*

Abstract

The Silicon Tracker is the central detector of the AMS-02 magnetic
spectrometer. Eight layers of double sided silicon microstrip sensors
embedded in a magnetic field of $\sim 0.8\ T$ allow for an accurate 3D
reconstruction of particle trajectories. The tracker is made of $\sim 6.4\ m^2$
of silicon with a single point resolution of 10 (30) μm in the bending (not
bending) coordinate. In this paper, a detailed description of the tracker
system is presented.

1 Introduction

After the successful test flight in 1998 [1], the AMS detector has been redesigned
to improve its performances for future operation on the International Space
Station. The AMS-02 detector is a large acceptance ($\sim 0.5\ m^2 sr$) and high
sensitivity spectrometer. Its main components are a superconducting magnet
and a silicon tracking device (Figure 1).

The superconducting magnet is cooled by evaporating liquid helium and
has a reservoir for about three years operation without refill. Its dipolar field,
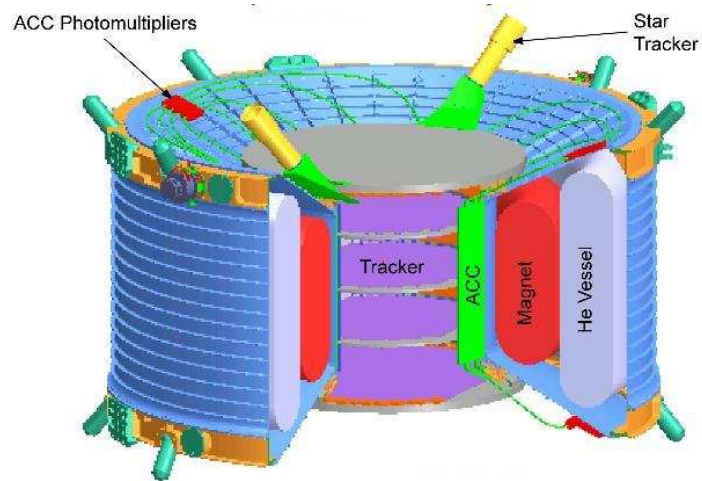
Figure 1: Layout of the AMS-02 Tracker inserted into the magnet system. Also visible are the magnet cooling system, the Anti-Coincidence Counter (ACC) and the Star Tracker.

normal to the aperture of the magnet, is based on a magic ring configuration of race track coils around a pair of Helmholtz coils. It amounts to $\sim 0.8\ T$ close to the center, six times the field strength of the AMS-01 permanent magnet, thus extending the rigidity range for charged particles up to few TV.

In order to remove the heat dissipation generated inside the magnet by the Tracker front-end electronics a dedicated thermal control system has been developed. It is based on a mechanically pumped two-phase loop with carbon dioxide as working fluid.

An Anti-Coincidence Counter (ACC) placed inside the inner bore of the magnet allows to reject particles entering the tracker laterally, outside the main acceptance.

A Star Tracker has been added to the AMS-02 set-up to ensure accurate knowledge about the instrument orientation, since the ISS attitude is rather variable.

2   The Silicon Tracker

The AMS-01 tracker was the first application in space of the high precision silicon technology developed for position measurements in accelerator experiments [2]. The high modularity, low voltage levels ($< 100\ V$), and gas-free operation of the device is well suited to operation in space. The 1998 shuttle
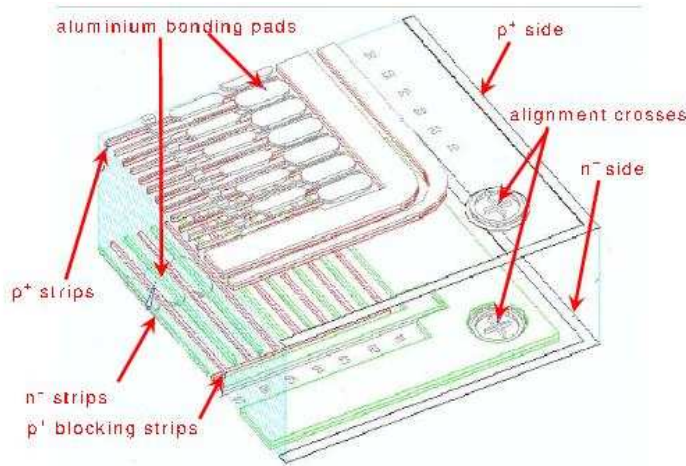
Figure 2: Layout of the AMS-02 double-sided silicon microstrip sensor.

test flight demonstrated both the successful adaptation of the technology to the space environment and the feasibility of large area detectors.

Silicon microstrip sensors were originally developed for vertex detectors in colliding beam experiments in order to provide a few high precision position measurements near the interaction point. The AMS application differs considerably. The tracking information is provided uniquely by the silicon sensors, which implies a large surface area and higher inter-strip capacitances. The major challenges were to maintain the required mechanical precision and low-noise performance in the large scale application, and to do so in outer space.

2.1   The AMS-02 silicon sensors

The AMS-02 Tracker is built with double-sided silicon microstrip sensors. The n-type, high resistivity (> 6 $k\Omega$) sensors are biased with the punch-through technique and p^+ blocking strips, implanted on the n-side, are used to minimize the influence of surface charge on the position measurement obtained from the ohmic side [3]. The sensor design uses capacitive charge coupling [4] with implantation (readout) strip pitches of 27.5 (110) μm for the p-side and 52 (208) μm for the n-side. The finer pitch p-side strips are used to measure the bending coordinate and the orthogonal n-side strips measure the not bending coordinate. Furthermore the measurement of the specific energy loss, $dE/dx \propto Z^2$, in the silicon allows nuclei identification. Figure 2 shows
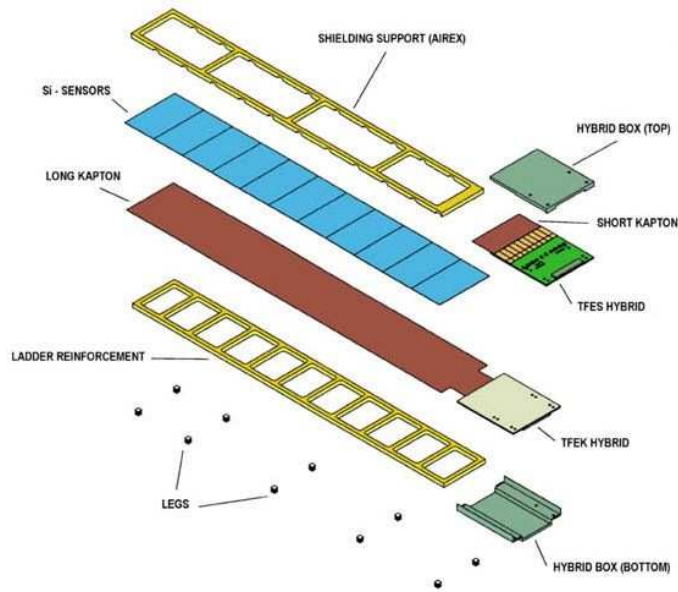
Figure 3: Exploded view of the silicon ladder.

the AMS-02 sensor layout.

The ionization loss of singly charged particles traversing the fully depleted, reverse-biased 300 ± 10 μm thick sensor is described by a Landau distribution [5]. The peak energy loss of a singly charged, minimum ionizing particle at normal incidence produces $22,000$ electron-hole pairs [6]. The opposite sign charge carriers drift rapidly $(10 - 25$ $ns)$ in the electric field to the two surfaces (p/n) where the accumulated charge on metallized strips is fed to the front-end electronics. The position of the particle is determined by the relative signal levels observed at the readout strip positions. At the single sensor level, the position resolution depends on the sampling pitch and the signal-to-noise performance.

2.2   The construction of the Silicon Tracker

The silicon sensors are arranged in 192 ladders, made of variable number of sensors (from 7 to 15) with daisy chained strips. Figure 3 shows the principal elements of the silicon ladder and the main components of the readout hybrids. A thin film, 50 μm, metalized upilex, glued directly to the silicon sensors, serves as routing cable to bring the n-side signals to the n-side front-end hybrid, which is located at the ladder end closest to the magnet wall. The flexible upilex film
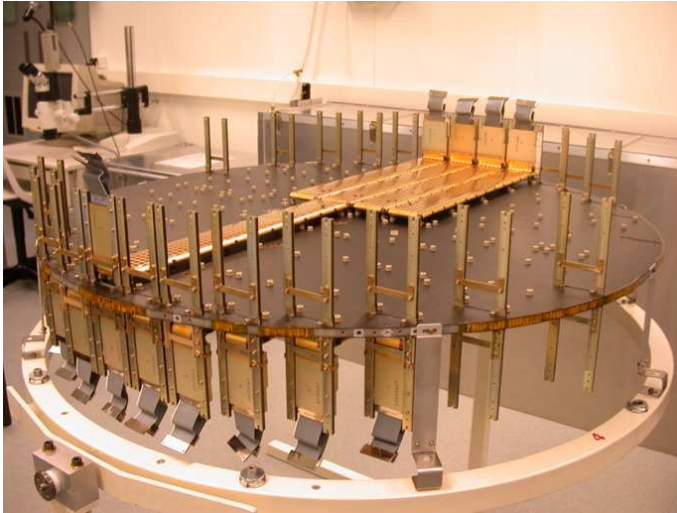
Figure 4: Plane number 3 being assembled.

and a second short upilex film joining the p-side strips to the p-side front-end hybrid allow the two hybrids to be placed back-to-back, perpendicular to the detection plane, thus minimizing the material in the sensitive region of the Tracker. Finally an electromagnetic shield, in the form of a doubly-metalized upilex film, surrounds each ladder.

The silicon sensors of each ladder are supported by a 5 mm thick foam that is glued to the n-side upilex film. The exposed surface of the foam is covered with a 100 μm thick layer of carbon fiber. Small 5 mm^3 aluminum frames are glued to the carbon fiber surface (the exact number depends on the ladder length). The aluminum frames contain a screw fixation hole which is used to attach the ladder to the tracker plane.

During the production phase each ladder undergoes an extensive series of quality control tests (mechanical and electrical). Furthermore several tests with particles beams have been performed on selected ladders and other tests are foreseen to be performed before the end of the assembly of the tracker. Very good performances of the silicon ladders have been found both in spatial resolution and in nuclei identification [7, 8, 9].

The ladders are installed in 8 layers, on 5 planes of an ultra-light support structure composing the whole tracker. The tracker planes located inside (outside) the magnet are a composite structure with two 220 (700) μm thick layers of carbon fiber surrounding a 12 (40) mm thick, low density aluminum honeycomb interior, $\rho = 16.02$ (32.0) kg/m^2. The diameter of the inner (outer)

planes is 1.0 (1.4) m. The three inner planes are equipped with ladders on both sides, while the outer planes are equipped with ladders only on one side.

3 Conclusions

The ladder production has been organized between University of Geneva, INFN-Perugia, ETH-Zurich, University of Bucarest, University of Turku, Skobeltsyen INP, Southeast University and an industrial firm in Italy (G&A Engineering). Until now 80% of ladders have been produced and three out of eight layers have been fully equipped with ladders at University of Geneva. Figure 4 shows the innermost plane of the Tracker during the assembly. The Tracker assembly will be completed by June 2005 and it will be integrated inside the magnet in June 2006.

References

[1] M. Aguilar et al., *Physics Reports*, **366/6** (2002) 331.

[2] M. Acciarri et al., *Nucl. Instr. and Methods*, A **351** (1994) 300.

[3] G. Batignani et al., *Nucl. Instr. and Methods*, A **277** (1989) 147.

[4] J.B.A. England et al., *Nucl. Instr. and Methods*, A **185** (1981) 43.

[5] J.B. Birk, *Proc. Phys. Soc.*, A **64** (1951) 874.

[6] D.E. Groom et al., *Eur. Phys. J.*, C **15** (2000) 180.

[7] P. Zuccon, *These Proceedings*.

[8] C.H. Chung, *The construction of the Alpha Magnetic Spectrometer for the International Space Station*, Submitted to *Nucl. Instr. and Methods*.

[9] B. Alpat, *Charge determination of nuclei with the AMS-02 Silicon Tracker*, Submitted to *Nucl. Instr. and Methods*.

ANTARES STATUS & MILESTONES: NEWS FROM DEEP-SEA

Thierry Pradier[a], for the Antares Collaboration[1]

[a] *Université Louis-Pasteur & Institut de Recherches Subatomiques - IReS,
23 rue du Loess BP 28 - F67037 Strasbourg, France*

Abstract

The Antares project aims to build a deep-sea Cerenkov Telescope for High Energy Neutrino Astronomy located in the Mediterranean Sea. The experiment, currently in the construction phase, has recently achieved an important milestone: the operation of a prototype line and of a line with monitoring instruments. These deployments allowed a thorough understanding of environmental parameters.

1 High Energy Neutrinos and AstroParticle Physics

The advantage of using neutrinos as new messengers lies on their weak interaction cross-section: unlike protons or gammas, they provide a cosmological-range, unaltered information from the very heart of their sources. The

---

[1] *http://antares.in2p3.fr*

drawback is that their detection requires a huge detection volume. In all those aspects, neutrinos are comparable to gravitational waves (GW). This comparison applies also to the sources of high energy neutrinos themselves.

Such sources, either galactic or extra-galactic, are compact objects, involving relativistic movements of masses and particles, all necessary ingredients to have an efficient gravitational wave emission (see section 2.3). Most of those sources have already been extensively observed in γ: supernovae and their remnants, pulsars, microquasars and AGNs, gamma-ray bursters. The main question is to know whether or not those photons are produced by electrons *via* inverse compton/synchrotron emission or by protons/nuclei *via* production of neutral and charged pions, which decay to produce photons and neutrinos.

2   The ANTARES Neutrino Telescope

ANTARES is a sort of a fixed target experiment: a cosmic neutrino interacts in the Earth and produces a muon that propagates in sea water. The Cerenkov light emitted by the muon is detected by an array of photomultipliers arranged in strings, able to reconstruct the energy and direction of the incident muon/neutrino.

The main physical backgrounds are twoflod. Atmospheric muons, produced in the upper atmosphere by the interaction of cosmic rays, can be discarded because of their downward direction. Atmospheric neutrinos on the other hand are more delicate to identify: produced on the other side of the Earth, they have exactly the same signature as the cosmic signal ANTARES awaits for. They also represent a powerful calibration tool.

2.1   The ANTARES Collaboration and the detector

The goal of the European collaboration ANTARES [1] is thus to build an underwater telescope dedicated to high energy neutrinos. Around 20 particle physics laboratories, astrophysics and oceanography institutes are taking part in the project. The selected site is in the Mediterranean Sea, 40 km from Toulon (Southern France), at a depth of 2500m.

The detector consists in twelve lines, each one being composed of 25 storeys. On each storey, 3 photomultipliers are looking downward, to be sensitive to upward-going muons only. The layout of the detector is described in Figure 1.

2.2   Physics Performance

The performances of ANTARES as a Neutrino Telescope are mainly estimated studying the effective are, as defined below (which convolved with a neutrino
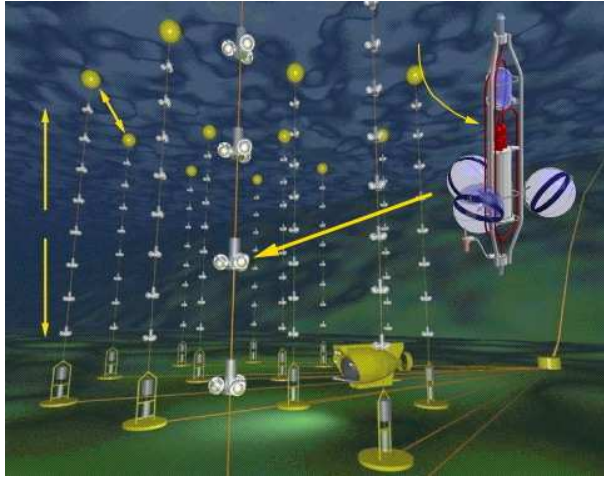
Figure 1: Artist's view of the final ANTARES Neutrino Telescope.

flux determines the event rate) and background rejection capabilities, mostly based on the angular resolution and energy reconstruction.

The *effective area* is defined as the ratio of detected neutrinos per unit of time over the incident neutrino flux. For angles around the vertical, as can be seen in Figure 2, it reaches its maximum for an energy $E_{max} \simeq 10^5 eV$, and then decreases because of the shadowing of the earth.

The *angular resolution* is constant and equal to 0.2° (48 arcsec) for energies higher than 10 TeV as shown in Figure 2; below this energy, the resolution is dominated by kinematics. Above 10 TeV ANTARES will really be able to pinpoint a source in the sky, with the same resolution as the actual satellites dedicated to one of the most promising sources for high energy neutrinos, namely Gamma-Ray Bursters.

Due to its location, ANTARES will cover a 3.5π *sr* fraction of the sky. AMANDA, the largest currently operational experiment, and soon ICECUBE, located at the South Pole, will only cover 2π *sr*, but with the same exposition during the day. Furthermore, ANTARES will be able to observe the Galactic Centre, where INTEGRAL has recently observed a great deal of new point-like gamma sources. The two detectors will nevertheless be complementary with an instantaneous overlap of 0.5π *sr*.
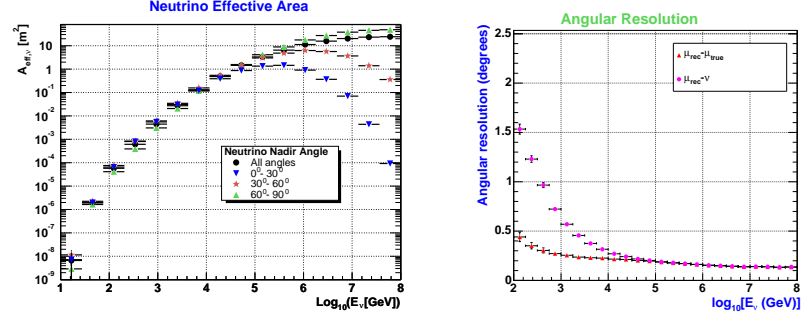
Figure 2: Effective area vs neutrino energy for various zenith angles (left) and expected angular resolution both for muons and neutrinos (right).

2.3   A step forward in Multi-Messenger Astronomy

With the forthcoming operation of HESS or GLAST for γ, AUGER for UHE cosmics rays, VIRGO for GW and ANTARES for high energy ν, the years to come will bring a harvest of new information related to the most energetic and powerful phenomena in the universe.

Good candidates for such a multi-messenger approach are microquasars, the galactic equivalents of quasars. More than 10 of these objects have been observed in our galaxy in all electromagnetic domains, and some models show that ANTARES could detect up to tens of events per year from some of them [2]. Furthermore, if the ultra-relativistic plasma "blob" ejected by microquasars is compact enough, efficient GW emission could take place [3], thus making the coincident neutrino emission easier to detect by ANTARES.

3   Deployments and Prototype Lines

Before launching the mass production of the lines, two prototypes of the final lines were built and deployed. Figure 3 illustrates the structure of the prototypes, together with the dates of previous deployments.

The deployments, connections and recovery of the lines were successful, and most of the components worked properly. One major problem showed up, though. Because of a broken optical fibre in the cable of the Prototype Sector Line (PSL), the clock signal only reached the bottom of the String Control Module, thus preventing any coincidence measurements between storeys. The accuray in time calibration thus only reached $\sim 1ms$.

In about 100 days of running time, a large amount of data has nonetheless been recorded, and background light counting rates were extracted.
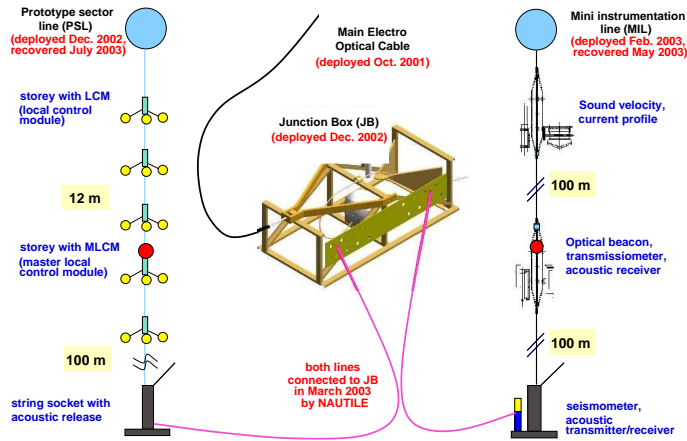
Figure 3: Description of the prototype lines connected in 2003.

Background Light & Flow-induced Bioluminescence

The counting rates as recorded by the PMTs shows large and short-lived peaks, due to bioluminescent organisms (plankton), over a continuous base-line coming both from β-decay of ^{40}K and bacteria, as previously observed [4]. Both the fraction of bursts and the continuous level are subject to great variations (see Figure 4, left plot, for an example).

Correlations with sea currents for the mean counting rates showed behaviours which could be the signature of flow-induced bioluminescence in the turbulences/boundary layers around the detector itself (see [5] and references therein). Figure 4 (right plot) shows the mean intensity (in kHz) as a function of sea current velocity.

4 Milestones for ANTARES and KM3NET

The past years have seen the installation/operation of some of the key components in ANTARES. Next year, the PSL will be redeployed with a new electro-mechanical cable, together with an improved instrumentation line, and the mass production for all the lines will be launched. The ANTARES neutrino telescope is now scheduled to be operational by 2007, but physics studies will begin before its completion.

ANTARES must be seen as the first stage toward a km^3-scale telescope, for which European institutes involved in current neutrino astronomy pro-jects (ANTARES, NEMO and NESTOR) are already collaborating. This network,
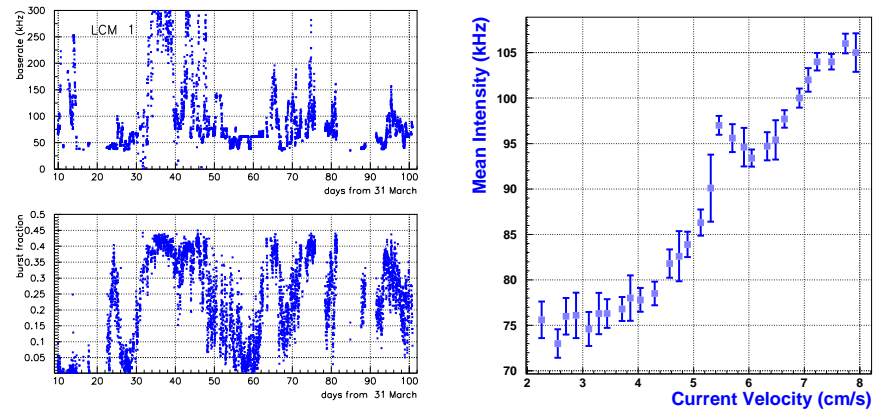
Figure 4: Variations of background light burst/continuous components (PSL data, left). Correlation between mean counting rate and sea current (right).

KM3NeT [6], will give birth to a telescope with which neutrinos will be as common a messenger as gamma-rays are now.

References

[1] ANTARES Collaboration, *astro-ph/9707136* & *astro-ph/9907432*.

[2] G. F. Burgio, *Detecting High-Energy ν from microquasars with* ANTARES, proceedings of the Vth microquasars workshop, Beijing (2004), *astro-ph/0407339*.

[3] E. B. Segalis *et al.*, *Emission of gravitational radiation from ultra-relativistic sources*, Phys. Rev. **D64**, 064018 (2001).

[4] ANTARES Collaboration, *Background light in potential sites for the* ANTARES *undersea neutrino telescope*, Astropart. Phys. **13** 127-136 (2000).

[5] A.-S. Cussatlegras & P. Le Gal, *Bioluminescence of the dinoflagellate Pyrocystis noctiluca induced by laminar and turbulent Couette flow*, Journal of Experimental Marine Biology and Ecology, in Press (2004) (available online at *http://www.sciencedirect.com*).

[6] *http://www.km3net.org*

YODA++: A PROPOSAL FOR A SEMIAUTOMATIC SPACE MISSION CONTROL

M. Casolino[a], M. P. De Pascale[a], M. Nagni[a,b], P. Picozza[a]

[a] INFN, Sezione di Roma II - Dipartimento di Fisica, Università di Roma "Tor Vergata", Via della Ricerca Scientifica, Roma, Italy

[b] corresponding author, nagni@roma2.infn.it

Abstract

YODA++ is a proposal for a semi-automated data handling and analysis system for PAMELA (PA) space experiment. The core of the routines have been developed to process raw data downlinked from the Resurs DK1 satellite (housing PAMELA) to the ground station in Moscow. Raw data consist of the scientific data and are complemented by housekeeping and orbital information. Housekeeping information will be analyzed in short time (1hour) from download to monitor the status of the experiment and to assist in mission planning and acquisition configuration. A prototype for the visualization of the data will run on a TOMCAT web application server, allowing an off-line analysis tool using just a browser and taking advantage of part of already written code for the maintenance system. Development of data retrieving is in production phase, while a GUI interface for human monitoring, is on preliminary phase as well as a JSP/JSF web application facility. On a longer timescale (1-3 hours from download) scientific data are analyzed, indexed and stored in ROOT files for further calibration and processing. YODA++ is currently being used in the integration and testing on ground of Pamela data.

1   Introduction

The main objectives of PAMELA are the accurate measurements of the antiproton and positron fluxes, with a sensitivity and statistics out of the reach of balloon-borne experiments. The energy range goes from below 100 MeV to above 100 GeV and the search of antihelium with a sensitivity better than 10^{-7} in antihelium to helium ratio[1]. The PAMELA telescope will be installed on board of the Russian Resurs DK-1 satellite and will be launched in the year 2005. The expected data flow of the experiment will be 20 GByte/day, divided in four different downlink sessions over two stations. Data quality and housekeeping information will need to be analyzed in short time for the mission planning of the experiment. The software running on the on-board CPU, has been developed using a realtime operative system software [2, 3]. The acquisition of housekeeping data was designed in order to have an efficient control system on ground too, to recognize and correct anomalies. After the quicklook phase, another requirement to be met is to share data through the collaboration as soon as are available in a file/data format widely used and as much flexible as possible. In this spirit we used the CERN's ROOT framework[4] either to develop a custom analysis tool and to store data in a worldwide used file format.

2   Yoda evironment: General scheme

YODA in an acronym for Your Own Data Analysis. It is a system designed to store and retrieve data allowing users to perform analysis at different levels with different tools. At the first step it handles data processing for the Ground Segment, namely:

- Statistics on raw data to determine quality of transmission;

- Statistics on inner instrument packet data to determine instrument status;

- High flexibility to minimize reprocessing caused by unforeseen situations;

- Storage of preanalyzed data in such a way to allow an easy successive access either to telemetry and physical data;

- Ground infrastructure as simple as possible to minimize maintenance costs;

- Data have to be available worldwide through internet with the smallest delay possible;
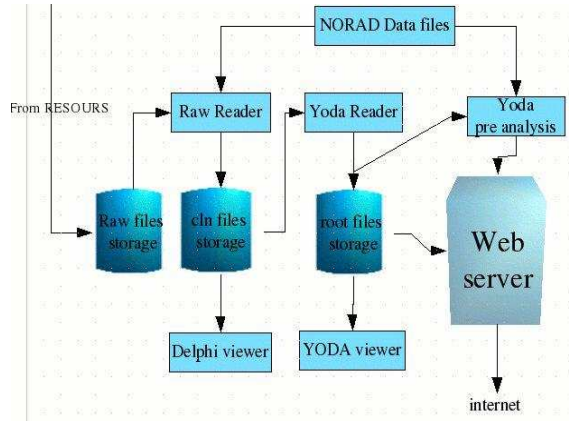
Figure 1: Left: The data flow from downlink to distribution. It is possible to see the three main processing steps and their dependencies.

   The data have to pass a three-step process (see Figure 1) before the physics data can be considered qualified for analysis. Each of these steps is governed by a specific tool; in the first step the RawReader (RR) collects the data from the receiving station and process it in order to estimate the quality of transmission and to remove the headers introduced by the inner satellite transmission protocol. The first step produces intermediate files used the second step by the YodaReader (YR) which has to check if the stream satisfies the Pamela protocol in order to extract the several types of packets defined in the Pamela transmission protocol. The third step represents the physics data analysis.
The first two steps of data processing are used to recognize peculiar situations not managed by PA onboard software or to check response to earth previously transmitted commands.

3   Satellite data colection: from satellite to ground

The mean expected amount of particle data information from Pamela is about 2 Gbyte per a day; the expected background from false triggers coming from secondary particles produced in the main body of the satellite is about 18 Gbyte. The information is stored in memory device of the satellite Resurs-DK1 and can be transmitted to ground by portions in several downlink sessions.
The receiving antenna system TNA-7D has a parabolic reflector of 7 m in diameter and azimuth-elevation fulcrum-rotating mechanism and has two frequency diverged radio channels. Pamela data reception is performed at

Digital Processing Data System (DPDS), which is the component of Moscow Ground station at NTSOMZ institute with high-rate disk recording and transmission system. The information from DPDS enters to operational data set archive server. This server provides security connection with the ground segment of Pamela where first analysis takes place.
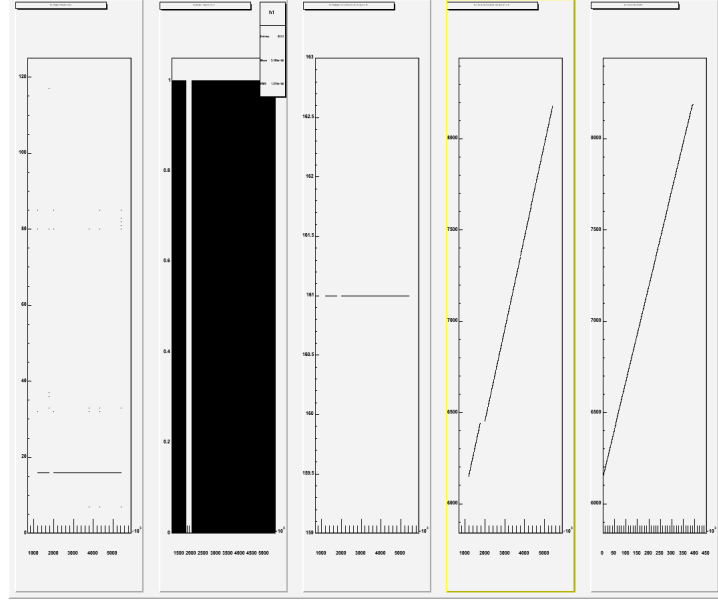
Figure 2: From left to right: 1) A typical time distribution for packet type vs. time (ms). Note the line along the Y=16 representing Physics Data Packet and the pause around t=2000ms due to end of data taking. 2) PhysicalEvent packet rate (Hz). In this case the acquisition was fixed at one event/second with an forced trigger 3) PhysicalEvent packet lenght (bytes). In this readout only some detectors are read, giving a total packet length of 161 bytes. 4) PhysicalEvent packet counter. Note the pause in the counter when the acquisition is stopped. 5) Packet Counter vs position in the downlinked file.

4 The YODA reader

For our specific needs the objects composing the YR tool have been modelled over the ROOT libraries to generate a corresponding file structure. C++ was used as the main programming language.
In general we have four types of objects:

- **packet types objects**: these objects wrap both, the specific data produced by the single devices (TrackerPacket, CalorimeterPacket, etc...) or by the CPU controlled procedures (several telemetry packets);

- **algorithms type objects**: meanwhile the packets could be considered as a static structure, that is just like wrappers, these classes (TrackerReader, CalorimeterReader, several telemetries reader) are the dynamical conterpart which knows the rules about how to read and check the data of each specific packet from the raw data (that is the files generated from the Raw Reader);

- **a class containing utility methods**: this class (PamelaRun) and the derived ones (SpecificModelPamelaRun) represents an interface between YODA and the ROOT objects and structures (TFiles and TTrees);

- **an additional facade class**: inside it, is defined an user interface command line and in the end is where the main reside.

The packet types are structured around a protocol wrapper, called *Header* which is meant to define general characteristic of the specific data inside it. Each packet uses its own specific reader; each reader is a derivation of a common parent for all the various readers: the *Algorithm* object. We want to stress how the flexibility of this approach have made possible to insert in the reader classes some FORTRAN routines; at the same time specific interfaces are in a developing phase to allow the same group to be able to read ROOT files inside their FORTRAN programs. The facade class is nothing more than an interface needed to organize the interaction with the user command line or the graphical user interface (GUI) whatever it should be available. In conclusion our code can be represented as a the action of the EventReader searching in the stream of data for the Header packet signature. The stream is then passed to the HeaderReader which will check if the various parameter defined inside the actual stream are coherent with the header parameters (PacketLength, Counter, OBT, CRC,etc....); if several constrains are verified, the EventReader will call the specific Reader according to the PacketId in the header as mapped previously and in the end, through the PamelaRun class, the EventReader will store the read packet and the relative header. Once the data are extracted the files can be managed using the ROOT framework either by direct interaction with the root files or using specific scripts taking advantage of the CINTerpreter (CINT). The collection of all these scripts constitutes the so called *YODA Viewer*, which can be either a stand-alone GUI (a prototype has already been implemented using the Signal-Slot features of the ROOT GUI libraries on a Model-View-Controller architecture) but it can be a web application too, extracting the graphs from the same application serving

the internet users; the main reason for this is because to minimize the code to write; the YODA viewer shows the most meaningful information about the downlinked data and in the end about anomalies; this can be done using some ROOT batch scripts activated by files modification; also if in a preliminary phase is being developed an on-demand web application (WA) running on a TOMCAT server (wrote using JSP/JSF specifications).

References

[1] Simon, M., XXVIII ICRC, OG 1.5, 2117 Tsukuba, Japan, 2003.

[2] Straumann, T. Open Source Real-Time Operating Systems Overview, "8th International Conference on Accelerator and Large Experimental Physics Control Systems", San Jose, USA, 2001.

[3] F. Altamura, M. Casolino, et al., "The Pamela CPU", these proceedings.

[4] ROOT - An Object Oriented Data Analysis Framework, Proceedings AIHENP'96 Workshop, Lausanne, Sep. 1996, Nucl. Inst. and Meth. in Phys. Res. A 389 (1997) 81-86. See also http://root.cern.ch/.

THE CENTRAL PROCESSING UNIT OF PAMELA EXPERIMENT

F. Altamura[a], A. Basili[a], M. Casolino[a], M.P. De Pascale[a],
M. Minori[a], M. Nagni[a], P. Picozza[a], O. Adriani[b], G. Castellini[b,c],
P. Papini[b], P. Spillantini[b], M. Boezio[d], F. Sebastiani[e],
G. Alfarano[e], S. Tassa[e]

[a] INFN, Sezione di Roma II - Dipartimento di Fisica, Università di Roma "Tor
Vergata", Via della Ricerca Scientifica, Roma, Italy

[b] INFN sez. Firenze-University of Firenze, Firenze.

[c] IFAC-CNR, Firenze.

[d] INFN sez. Trieste-University of Trieste, Trieste.

[e] Nergal s.r.l., Roma

Abstract

The Pamela experiment aims to measure with great precision the
antimatter present in our galaxy in the form of high energy particles; also
galactic, solar and trapped components of cosmic rays will be studied.
The experiment will be placed on a Russian Resurs-DK1 satellite and
launched into a 350 * 600 km orbit with and inclination of 70.4 degrees
in the year 2005. The processing unit of the experiment is based on
a ERC-32 architecture (a SPARC v7 implementation) running a real
time operating system (RTEMS). The main purpose of the unit is to
handle slow control, acquisition and store data on a 2 GB Mass Memory.

Communications between Pamela and the main satellite are done via a 1553B bus. Data acquisition from the detectors (TRD, Time of Flight, Magnetic Spectrometer, Electromagnetic Calorimeter, Anticoincidence system, Neutron detector, Bottom scintillator) is performed via a 2Mbyte/s interface. Download from the Pamela memory to satellite main storage is handled by a 16Mbyte/s bus. The daily amount of data transmitted to ground will be up to 20 GB/day. In this work we describe the CPU of the experiment and the general software scheme.

1   Introduction

The main objectives of PAMELA are the accurate measurements of the antiproton and positron fluxes with a sensitivity and statistics out of the reach of balloon-borne experiments. The energy range goes from below 100 MeV to above 100 GeV and the search of antihelium with a sensitivity better than 10^{-7} in antihelium to helium ratio[1]. The PAMELA telescope will be installed on board of the Russian Resurs DK-1 satellite and will be launched in the year 2005. The experiment is designed in an hierarchical - modular structure where the subdetectors handle all fast acquisition and data suppression before sending data to the acquisition board which interfaces them to the CPU. Data are then stored in the mass memory before transfer to the satellite. The intermediate boards have all their redundancy; all detectors are divided in section designed to continue working - even though with degraded performances - even in case of partial failures.

2   The Central Processing Unit

The Central Processing Unit of Pamela, is manufactured by Laben S.P.A. and handles all slow control, interaction with the satellite, data acquisition, storage and downlink. The CPU box is a space qualified system composed by:

- a central processor (CPU) ERC32 SPARC V7 with a clock of 24 MHz using a PROM of 128 KB for the boot, 4 MB of RAM, two banks x 512 KB of EEPROM.

- an avionics standard 1553B BUS interface board from/to the Resurs satellite. The CPU executes all the commands received from the Resurs satellite through this bus; these commands can be used to set the acquisition modes, reprogram the detectors or the CPU itself. This interface also acts as monitor for the Resurs to asynchronously control that the PAMELA experiment is properly running.

- a Pamela InterFace (PIF) board: a high speed board which transfers data from the detectors to the Mass Memory. Furthermore it contains two fast bus for Data Command communication with the detectors;

- a multipurpose Telemetry and Control board (TMTC) containing various digital, ADC/DAC interfaces to interact with the detectors and the subsystems of the experiment.

3   Software

The SPARC/ERC32 CPU is running RTEMS 4.0[2], a hard real time operative system, with microkernel model, that provides all primitives for multitasking, interrupt manager, timers, events, mailboxes, semaphores, signals, clock handling. The PAMELA Software Application is running on the top of the RTEMS Executive. RTEMS doesn't require system reserved tasks to run for itself. The Software handles communication from and to peripherals Front-Ends (FE) plugged to the IDAQ for the physical data event acquisition: format and send FE commands, wait for the answers, write them to the mass memory and, if needed, perform some check; this is what is typically done during the Initialization (include the program loading for the DSPs), Calibration and Acquisitions. The Software also manages changing of operative modes of peripherals according to the orbit position (proper macrocommands are provided by the satellite). Beside, the CPU software handles the programming of all subsystems and peripheral boards via a dedicated Housekeeping Board: Relay Board, Gas System Board and all acquisition boards: IDAQ, AC, Tracker sensor, Calorimeter, S4. The software also check and handles the power management: turn on and off power supplies of all boards and FE, manage main/spare switching and check for anomalies.

Telemetries (temperature, power, contact closure) coming from Telemetry interface are also periodically sampled and stored in the Mass Memory (MM) for post analysis on ground and in the telemetries format region of the 1553B interface. Beside, CPU also checks telemetry values in order to point out anomalies to perform certain actions. The Gas System software has to perform some main task: periodic container purge, periodic TRD purge , check for pressure and temperatures values to be in some ranges and beside handle all safety and recovery procedures. In the software eight tasks are running for low-level purpose (i.e. History Area, Macrocommand Dispatcher, File Manager (mass memory), House Keeping Manager, PIF Manager) running at high priority. In the application level we have four tasks at lower priority: Run Manager (acquisition and all interaction with IDAQ-PIF-MM), Pamela Manager (general control), Slow Control Manager (housekeeping and alarms) and Gas System Manager. The message exchange programming paradigm is used: tasks wait for a message from its own mailbox that other tasks or
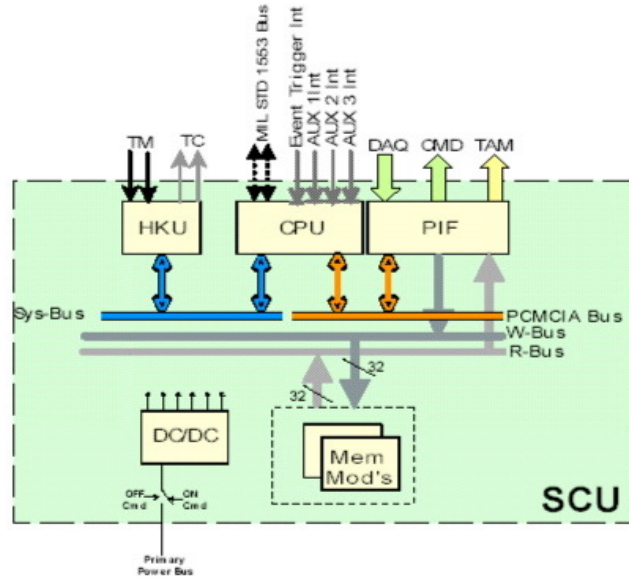
Figure 1: Scheme of the Pamela CPU and its block scheme with the Housekeeping board (HKU), the fast acquisition board (PIF), the memory module.

interrupts send. All the software, including the OS, is written in C, cross-compiled under an ordinary Linux/Intel PC using the "sparc-rtems" porting of the GNU compiler and GNU tools (gdb,ld,mn,...). Remote debugging, loading and firmwaring could be made using gdb. Many other utilities and languages have been used in the development: UNIX programming, Perl, C++, CVS.

The PAMELA software is based on a multitask architecture. It largely uses the communication and synchronization features provided by the operating system. Data transfer and synchronization between cooperating tasks and/or ISRs is made using RTEMS tools like semaphores, events and message queues. The PAMELA Application is divided in three logical layers:

1. Drivers and Modules: this layer is in charge of managing the protocol of boards, the interrupt, communication bus 1553B, MM drivers, File System, etc..

2. Low Level Tasks layer: those tasks handle the high priority process like dispatching of the macrocommand and the accessing to shared resources like TMTC board.

3. High Level (or Application) layer: those task are in charge to
   handle the main flow of the application: manage the acquisition and
   FE's configuration, handle error and alarm condition, power supplies
   management, Gas System handles.

3.1   Tasks

PAMELA software uses a typical paradigm for multitasking[3]: operating
system objects are all created at the software initialization (as soon as after
bootstrap) and never destroyed. For each task the system creates the task
objects with its own priority and its entry point (a function pointer) and
the corresponding mailbox for this task that implements a message queue. A
message queue (FIFO) allows the passing of messages among tasks and ISRs.
It can contain a variable number of messages.

Low Level Tasks

Low level tasks in PAMELA interact with some resource providing a
transparent functionality.

1. HKManager: provides interface to the TMTC and through it provides a
   high level interface to the Housekeeping Board.

2. ReportGenerator: reporting status of the software for the 1553B chip.

3. HistoryArea: provides logging functionalities to store datas in 1553B
   shared memory read by Resurs and while in debugging mode used for
   logging output to serial ports.

4. DiagSupervisor: the lowest priority tasks that make a scrubbing of the
   RAM in order to detect parity error and active the EDAC mechanism of
   the CPU.

5. MCMDDispatcher: the 1553B interrupt receives a macrocommand
   and sends it to this task that analyze the data structure of the
   macrocommand, dispatching it to the proper task.

6. PatchDumpManager: used for patching the software on the EEPROM
   and dumping arbitrary RAM or EEPROM data from ground.

7. MMSUManager: manage access to the MM registers in particular to
   program the WRITE DMA between PIF and MM.

High Level Tasks

Four high level task manages the main application process.

- PamManager: it is a task that receives most of the macrommands from the MCMDDispatcher and manages them. Beside it holds the main state machine of the PAMELA software and controls the behavior of the other two tasks: Run Manager and SCManager. As soon as one of these task has completed the requested operation it notifies to the PamManager the end of the operations with a return code and an optional error code.

- RunManager: it is the task for the acquisition process. Its goal is to assemble command queues for different FEs, store them into the PIF, send them to the Intermediate Board, wait for the answer, store results into the MM, detect some FE error condition and locally manage some of them.

- SlowControlManager: this task manages all monitoring signal, power supply, checks temperature, voltage, via TMTC and Housekeeping Board. Besides it checks and sets the correct power supply configuration after the boot process of PAMELA, handles the power on and power off of PAMELA and of FEs and manages recovery and error handling in case of anomaly.

- GasSystemManager: The Gas system is an electromechanical system whose operative modes are controlled by a driver board which is programmed and handled by the PSCU through the software gas task. This separate task is necessary because of the long duration of operations ($\simeq$hours) which involves filling or purging a container with gas, opening and closing electromechanical valves, measuring pressures and temperatures related to the various system components.

References

[1] Simon, M., XXVIII ICRC, OG 1.5, 2117 Tsukuba, Japan, 2003.

[2] RTEMS official documentation: http://www.rtems.com/onlinedocs/releases/4.0.0/doc

[3] Straumann, T. Open Source Real-Time Operating Systems Overview, "8th International Conference on Accelerator and Large Experimental Physics Control Systems", San Jose, USA, 2001.

THE TOF AND TRIGGER ELECTRONICS OF THE **PAMELA** EXPERIMENT FOR THE SEARCH OF PRIMORDIAL ANTIMATTER IN SPACE

S. Russo [a], G.C. Barbarino [a], M. Boscherini [b], D. Campana [a],
W. Menn [b], G. Osteria [a], M. Simon [b]

[a] *Dipartimento di Scienze Fisiche, Università di Napoli "Federico II", and INFN,*
Sezione di Napoli, via Cintia, Napoli, Italy

[b] *FB Physik, Universität Siegen, Walter-Flex-Straße, Siegen, Germany*

Abstract

The **PAMELA** experiment (a Payload for Antimatter Matter Exploration and Light-nuclei Astrophysics) is a space borne apparatus (which will be launched at the end of 2005 on board a Soyuz rocket) devoted to the study of the antiparticle component of cosmic rays. Its scintillator telescope system will provide the primary experimental trigger and time-of-flight particle identification.

1 Introduction

The **PAMELA** apparatus [1], following the general requirements to obtain particle identification, comprises essentially of a Transition Radiation Detector (TRD) as a β selector, a magnetic spectrometer (characterized by a MDR of

800 GV/c) to measure particle's charge and momentum, an imaging calorimeter to discriminate at the level of $10^4 \div 10^5$ between electromagnetic and hadronic showers, and a Time-of-Flight (ToF) system with a time resolution of about 110 ps.

The Time-of-Flight system [2] of PAMELA is composed of several layers of plastic scintillators read out by photo-multiplier tubes. The ToF must provide a fast signal for triggering data acquisition in the whole instrument, measure the flight time of particles crossing its planes in order to derive their velocity β and eventually reject *albedo* particles, and determine the absolute value of charge z of incident particles through the multiple measurement of the specific energy loss dE/dx in the scintillator counters. Additionally, segmentation of each detector layer in strips can provide a rough tracking of particles, thus helping the magnetic spectrometer to reconstruct their trajectory outside the magnet volume.

2   ToF electronics and trigger
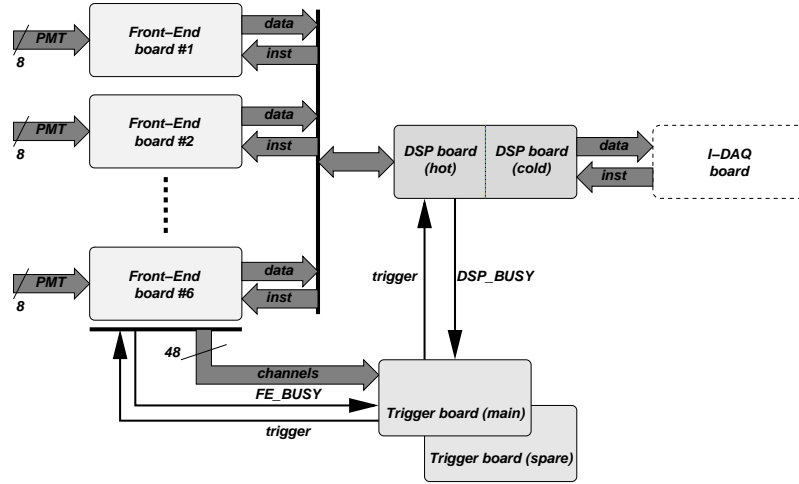
Figure 1: General ToF electronics layout.

The ToF and trigger electronics for PAMELA is a complex system made of nine boards in the 6U VME format. These are the six Front-End (FE) boards, the DSP board and the two identical trigger boards (one "hot", the other "cold"). The purpose of this system is to collect the signals coming from the 48 PMTs of the ToF, measure their arrival time with respect to the trigger pulse and their charge, generate the signals for the trigger, handle the busy

logic for all subsystems, and interfacing the ToF system with the general data acquisition system of the PAMELA apparatus.

The ToF electronics has to comply to the following requirements:

- guarantee a wide dynamic range in the charge measurement to allow the measurement of the energy release of $z > 1$ particles (up to carbon);

- add a negligible contribution to the overall ToF time resolution. This implies a contribution from time digitization which has to be less or equal than 50 ps.

In the mean time, the electronics must ensure a low power consumption, a high reliability and good radiation hardness. Generally speaking, the space environment is highly hazardous for our apparatus, both for the wide temperature ranges and the high doses of ionizing radiations, and since no replacement for defective components is possible once the satellite is in orbit, the issue of reliability of all the electronic devices is crucial for the survival of the instrument during the three years of expected mission lifetime. Therefore a great effort has been paid in implementing both hardware and software redundancy, that is to mean the replication of at least all critical components. An overall scheme of the ToF and trigger electronics is shown in Fig. 1.

2.1   Front End board

Each FE board receives the analog signals coming from 8 PMTs. For each channel the input is split in two branches, which are fed into the time and charge sections, respectively. The first section measures the arrival time of the signal with respect to the trigger pulse, and generates the signal for trigger formation. The other section measures the charge of the PMT signal.

Time section

For each PMT, the anode line is coupled to a fast discriminator. To minimize the time-walk effect, a double threshold discriminator has been chosen, mod. AD8611 manufactured by Analog Devices, which has a maximum propagation delay of 4 ns. Its two thresholds can be set by remote, each through a DAC. The discriminated signals are shaped, translated in the LVDS standard and sent to the trigger board. The discriminator is part of a more complex logic that controls a double-ramp Time-to-Amplitude-to-Time (TAT) converter. A low-loss, low-thermal drift, storage capacitor is charged with a high-stability constant current source during the time between the pulse edges of the FE discriminator signal and the trigger signal. The arrival time of the latter starts the discharging of the capacitor with a constant current which is about 200 times smaller than the previous. Hence, measuring the discharging time, a

time expansion factor of 200 is obtained. A fast discharge is produced if the trigger is not generated within 150 ns from the signal edge. The logic needed to control the TAT converter is fully implemented in a low-power, rad-tolerant FPGA, mod. 54SX08A manufactured by Actel [3]. Since each of these devices serves two channels, four of these FPGAs are mounted on the FE board.

Charge section

The amplitude of each PMT pulse is measured with a Charge-to-Time (CT) Converter. A charge amplifier collects the anode current from the PMT and provides an output signal which is proportional to the total current. A pulse stretcher operates by charging-up a capacitor at the peak value of the input waveform and then discharges it linearly. This signal has a length proportional to the maximum voltage reached on the capacitor and hence to the PMT charge. The last stage of the CT converter is a discriminator that generates the digital pulse with a length equal to discharging time of the pulse stretcher.

Digital section

The output digital signals coming either from the time of charge sections, are sent to a 100 MHz multichannel, common start, Time-to-Digital Converter (TDC), fully implemented in a FPGA, mod. 54SX32A manufactured by Actel. The circuit (realized with a 12 bits Gray counter and 8 registers) has a 10 ns resolution over a time window of 40.95 μs, which means (taking into account the time expansion factor) a 50 ps resolution on a 200 ns range. The first edge of the trigger signal starts the counter: when a new signal edge arrives at one of the channel inputs, the hit control logic writes the current value of the free running counter in its own register. The registers are 12+4 bits long to encode the channel number. Since each TDC receives a signal for measuring the time and one for the charge from each channel, the board houses two converters. The readout and the initialization of the TDCs is performed by a dedicated 54SX32A FPGA which acts as an interface between the FE and the DSP boards. Upon request from the DSP board it acquires data from the two TDC and writes them in a 16 hits-deep FIFO. Data are then serialized and transmitted according the Data-Strobe protocol at 16 Mbit/s.

2.2 DSP board

The readout of all PAMELA data is performed through a Data-Strobe serial link, with a dedicated link for each subsystem. To readout the six FE boards of the ToF subsystem an interface DSP board has been developed which collects the data from all the boards and transmit it, through the serial link, to the main
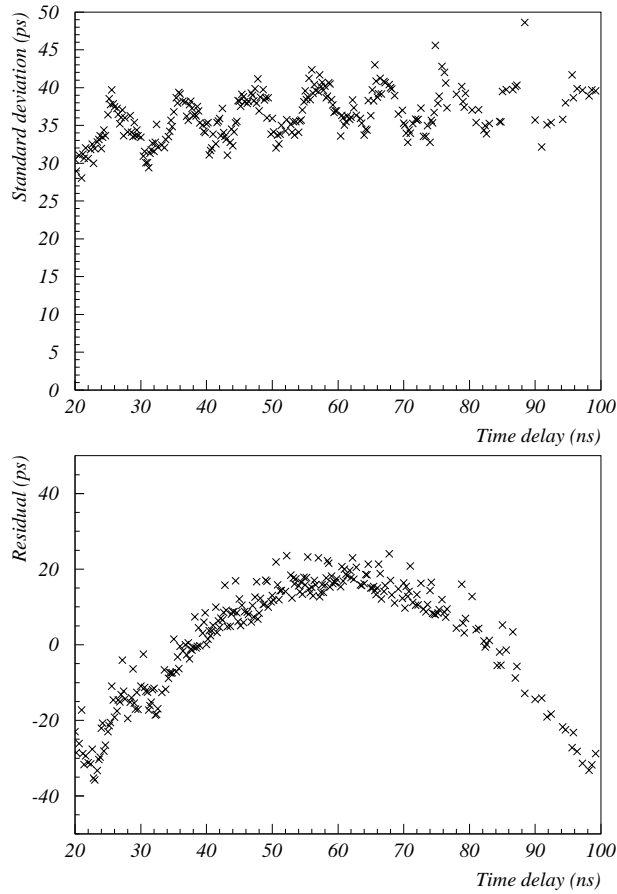
Figure 2: Results from the measurement of the integral nonlinearity.

DAQ. On this board is mounted a Digital Signal Processor (DSP), mod. ADSP-2187L manufactured by Analog Devices. The DSP collects the data and builds the data packet for the main DAQ. All the state machines needed to decode the macrocommands from the CPU of PAMELA and to control the interface with the DSP, are implemented on a 54SX32A FPGA. Another FPGA of the same kind controls the data flow with the FE boards. In order to increase the reliability of the system, two copies of this circuit are implemented on the same VME board: the "cold" version can be turned on if there is a failure of the "hot" one, thus preserving the full functionality of the board.

2.3   Trigger board

The trigger board is a complex digital board that generates the first level trigger for the apparatus and performs several more tasks. It receives the 48 signals from the ToF system for the main trigger and 8 signals from the other subsystems capable to generate self-trigger for particular events. To guarantee synchronization of the data acquisition the trigger board manages the 20 busy lines coming from each of the PAMELA subsystems. All the input and output lines are in the LVDS standard. About 60 rate counters, dead/live-time counters and the logic to generate calibration pulses sequence for different subsystem of the apparatus are also implemented on the board. The logic is distributed on 9 54SX32A FPGAs. Control masks select trigger types and allows the selection of failed (noisy or dead) ToF channels. The pattern of the channels fired for each trigger is generated for each event. A DSP (ADSP-2187L) is used to manage the data structure organization and to monitor the rate counters of the ToF channels and other subsystems.

3   Performance of the ToF electronics

Many tests of the performances of the ToF electronics has been made on the flight model of FE boards. Time resolution and integral nonlinearty have been mesured with a pulse generator, mod. 81132 manufactured by Agilent [4]. In Fig. 2 the results of two measurements are shown.

References

[1] M. Pearce, *The PAMELA Space Mission*, these proceedings

[2] D. Campana, *The Time-of-Flight System of the PAMELA Experiment*, Proc. 28th ICRC, Tsukuba, Japan (2003)

[3] *Actel SX-A family, V4.0, April 2003 - www.actel.com*

[4] Agilent Technologies, *81130 A 400/660 MHz Pulse data generator reference guide*

Part III

COSMIC RAYS

113

PROPAGATION OF COSMIC RAYS AND DIFFUSE GALACTIC GAMMA RAYS

Igor V. Moskalenko

NASA Goddard Space Flight Center, Code 661, Greenbelt, MD 20771, U.S.A.

Joint Center for Astrophysics/University of Maryland, Baltimore County Baltimore, MD 21250, U.S.A.

Abstract

This paper presents an introduction to the astrophysics of cosmic rays and diffuse γ-rays and discusses some of the puzzles that have emerged recently due to more precise data and improved propagation models: the excesses in Galactic diffuse γ-ray emission, secondary antiprotons and positrons, and the flatter than expected gradient of cosmic rays in the Galaxy. These also involve the dark matter, a challenge to modern physics, through its indirect searches in cosmic rays. Though the final solutions are yet to be found, I discuss some ideas and results obtained mostly with the numerical propagation model GALPROP. A fleet of spacecraft and balloon experiments targeting these specific issues is set to lift off in a few years, imparting a feeling of optimism that a new era of exciting discoveries is just around the corner. A complete and comprehensive discussion of all the recent results is not attempted here due to the space limitations.

1 Introduction

Research in astrophysics of cosmic rays (CR) and γ-rays provides a fertile ground for studies and discoveries in many areas of particle physics and cosmology. Examples are the search for dark matter (DM), antimatter, new particles, and exotic physics; studies of the nucleosynthesis, acceleration of nuclei and their transport through CR spectra and composition analysis; the effects of heliospheric modulation; the origin of Galactic and extragalactic diffuse γ-ray emission; formation of the large scale structure of the universe as traced by γ-rays.

In its turn, the astrophysics of CR and γ-rays depends very much on the quality of the data and their proper interpretation. The accuracy of data from current CR experiments on interplanetary spacecraft such as Ulysses, Advanced Composition Explorer (ACE), and the two Voyagers, specialized balloon-borne experiments such as Super-TIGER, BESS-Polar, CREAM, and the new space-based missions such as Pamela and AMS far exceeds the accuracy of the current propagation models, of which the "leaky-box" model has remained one of the main research tools for the last 50 years. The new major γ-ray observatory GLAST will improve the sensitivity for the diffuse high-energy γ-rays produced in CR interactions in the interstellar medium (ISM) by a factor of 30. These near-future missions are specifically designed to search for the signatures of DM, search for antimatter, study the diffuse Galactic and extragalactic γ-rays, and provide outstanding quality data on γ-ray sources and CR species in a wide energy range. This presents a great opportunity for new discoveries that requires accurate, testable and readily accessible modeling to exploit.

On the other hand, the whole of our knowledge is based on measurements done only at one point on the outskirts of the Galaxy, the solar system, and the assumption that particle spectra and composition are (almost) the same at every point of the Galaxy. The latter may not necessarily be correct. γ-rays and radio-waves (synchrotron) are able to deliver the information directly from distant Galactic regions thus complementing that obtained from CR measurements. Some part of the diffuse γ-rays is produced in energetic nucleon interactions with gas via π^0 production, another is produced by electrons via inverse Compton scattering and bremsstrahlung. These processes are dominant in different parts of the spectra of γ-rays, therefore, if deciphered the γ-ray spectrum can provide information about the large-scale spectra of nucleonic and leptonic components of CR. Combining all the data collected by different experiments into a realistic interpretive model of the Galaxy, we have a better chance to understand the mechanisms of particle acceleration and the role of energetic particles in the dynamics and evolution of the Galaxy and make essential progress in related areas.

2 Cosmic Rays and Diffuse γ-rays

CR are energetic particles which come to us from outer space and are measured through satellites, balloon-, and ground-based instruments. The energy density of CR particles is about 1 eV cm^{-3} and is comparable to the energy density of interstellar radiation field (ISRF), magnetic field, and turbulent motions of the interstellar gas. This makes CR one of the essential factors determining the dynamics and processes in the ISM. The spectrum of CR can be approximately described by a single power law with index –3 from 10 GeV to the highest energies ever observed $\sim 10^{21}$ eV. The only feature confirmed by observations of many groups is a "knee" at $\sim 3 \times 10^{15}$ eV. Meanwhile, the origin of the CR spectrum is not yet understood.

The sources of CR are believed to be supernovae (SNe) and supernova remnants (SNRs), pulsars, compact objects in close binary systems, and stellar winds. Observations of X-ray and γ-ray emission from these objects reveal the presence of energetic particles thus testifying to efficient acceleration processes in their neighborhood [1]. Particles accelerated near the sources propagate tens of millions years in the ISM before escaping into the intergalactic space. In the course of CR propagation, secondary particles and γ-rays are produced, and the initial spectra of CR species and composition change. The destruction of primary nuclei via spallation gives rise to secondary nuclei and isotopes which are rare in nature, antiprotons, and pions ($\pi^{\pm}$, π^0) that decay producing secondary $e^{\pm}$'s and γ-rays.

Measurements of CR isotopic abundances are able to provide detailed information about the acceleration mechanisms, source composition, and processes in the ISM. However, the energy range below 20 GeV/nucleon is strongly affected by the heliospheric modulation, which is a combination of effects of convection by the solar wind, diffusion, adiabatic cooling, different kinds of drifts, and diffusive acceleration. The Pioneer, the two Voyagers, and Ulysses missions contributed significantly to understanding the global aspects of modulation and limiting the number of modulation models' free parameters, yet the relative importance of various terms in the Parker equation is not established and appears to vary significantly over 22 year period [2]. The most widely used are the spherically symmetric force-field and Fisk approximations [3].

The diffuse γ-ray continuum emission is the dominant feature of the γ-ray sky. It is an evidence of energetic CR proton and electron interactions with gas and the ISRF, and is created via π^0-decay, inverse Compton, and bremsstrahlung. This emission in the range 50 keV – 50 GeV has been systematically studied in the experiments OSSE, COMPTEL, and EGRET on the Compton Gamma-Ray Observatory as well as in earlier experiments, SAS 2 and COS B [4]. The observation of diffuse γ-rays provides the most direct test of the proton and electron spectra on the large Galactic scale.

3   Models of Cosmic-Ray Propagation

The analytical methods include the so-called leaky-box model and diffusion models (e.g., disk-halo diffusion model, the dynamical halo wind model, the turbulent diffusion model, reacceleration model). The leaky-box model treats a galaxy as a box with reflecting boundaries and small leakage, so that a particle travels across it many times before escaping. In this model the principal parameter is an effective escape length or grammage and particles, gas, and sources are distributed homogeneously. The leaky-box model has no predictive power or can even be wrong in cases when the distribution of gas or/and radiation field is important, such as radioactive isotopes (including K-capture isotopes), diffuse Galactic γ-rays, electrons, positrons (because of their large energy losses) etc. It also can not account for spatial variations of CR intensity. Diffusion models [5] are more realistic, distinguishing between the thin Galactic disk and extensive halo, often with different diffusion coefficient. The technique used, e.g., the weighted slab technique, which splits the problem into astrophysical and nuclear parts, may, however, give significant errors in some cases. The alternative way is the direct numerical solution of the diffusion transport equations for the entire Galaxy and for all CR species.

The modeling of CR diffusion in the Galaxy includes the solution of the transport equation with a given source distribution and boundary conditions for all CR species. The transport equation describes diffusion and energy losses and may also include [6] the convection by a hypothetical Galactic wind, distributed acceleration in the ISM due to the Fermi second-order mechanism, and non-linear wave-particle interactions. The boundary conditions assume free particle escape into the intergalactic space.

The study of stable secondary nuclei (Li, Be, B, Sc, Ti, V) allows one to determine the ratio (halo size)/(diffusion coefficient) and the incorporation of radioactive secondaries ($^{10}_{4}$Be, $^{26}_{13}$Al, $^{36}_{17}$Cl, $^{54}_{25}$Mn) is used to find the diffusion coefficient and the halo size [7, 8]. The derived source abundances of CR may provide some clues to mechanisms and sites of CR acceleration. However, the interpretation of CR data, e.g., the sharp peak in the secondary/primary nuclei ratio (e.g., B/C), depends on the adapted physical model. The leaky-box model fits the secondary/primary ratio by allowing the path-length distribution vs. rigidity to vary. The diffusion models are more physical and explain the shape of the secondary/primary ratio in terms of diffusive reacceleration in the ISM, convection by the Galactic wind, or by the damping of the interstellar turbulence by CR on a small scale.

K-capture isotopes in CR (e.g., $^{49}_{23}$V, $^{51}_{24}$Cr) can serve as important energy markers and can be used to study the energy-dependent effects. Such nuclei usually decay via electron-capture and have a short lifetime in the medium. In CR they are stable or live essentially longer as they are created bare by fragmentation of heavier nuclei while their β^{+}-decay mode is suppressed. At

low energies, their lifetime depends on the balance between the processes of the electron attachment from the interstellar gas and stripping thus making their abundances in CR energy-dependent. This opens a possibility to probe the diffusive reacceleration in the ISM and heliospheric modulation [9].

The study of transport of the CR nuclear component requires the consideration of nuclear spallation, radioactive decay, and ionization energy losses. Calculation of isotopic abundances involves hundreds of stable and radioactive isotopes produced in the course of CR interactions with interstellar gas. A thorough data base of isotopic production and fragmentation cross sections and particle data is thus a critical element of models of particle propagation that are constrained by the abundance measurements of isotopes, antiprotons, and positrons in CR. Meanwhile, the accuracy of many of the nuclear cross sections used in astrophysics is far behind the accuracy of the current CR experiments, such as Ulysses, ACE, and Voyager, and clearly becomes a factor restricting further progress. The widely used semi-phenomenological systematics have typical uncertainties more than $\sim 30\%$, and can sometimes be wrong by an order of magnitude [10]; this is reflected in the value of propagation parameters.

Increasingly accurate balloon-borne and spacecraft experiments justify the development of sophisticated and detailed propagation models with improved predictive capability. Ideally, such a model has to incorporate all recent developments in astrophysics, such as detailed 3-dimensional maps of the Galactic gas derived from radio and IR surveys, the Local Bubble structure and local SNRs, the spectrum and intensity of the ISRF, Galactic magnetic fields, details of composition of interstellar dust, grains, as well as theoretical work on particle acceleration and transport in Galactic environments. A detailed gas distribution is important for accurate calculations of the spectra of $e^{\pm}$'s, radioactive species, and for calculation of γ-ray flux and skymaps from electron bremsstrahlung and from the decay of π^0's produced by CR interactions. The ISRF is essential for electron and positron propagation (energy losses) and γ-ray production by inverse Compton scattering. The magnetic field provides useful constraints on the electron spectrum via synchrotron emission, and may establish preferential directions of propagation of CR particles. Inclusion of the Local Bubble and SNRs enables us to study CR intensity and spectral variations in the local ISM.

A well-developed and sophisticated propagation model, in return, provides a basis for many studies in astrophysics, particle physics, and cosmology. The indirect DM search is a good example. A clear feature found in the spectra of CR antiprotons, positrons, or diffuse γ-rays would be a "smoking gun" for DM [11]; but nature is unlikely to be so cooperative. A more reasonable expectation is that the DM signature, if any at all, will be a weak broad signal on top of a background requiring a reliable propagation model to be able to discriminate

the signal.

Modern computer codes incorporating recent developments in astrophysics and nuclear physics do exist. One example is GALPROP [8, 12, 13], a numerical model and a computer code (written in C++) of CR propagation in the Galaxy; this is the most advanced 3-dimensional model to date. The model is designed to perform CR propagation calculations for nuclei ($^1_1$H to $^{64}_{28}$Ni), antiprotons, electrons, positrons, and computes γ-rays and synchrotron emission in the same framework; it includes all relevant processes and reactions. The GALPROP model has been proven to be a useful and powerful tool to study the CR propagation and related phenomena. Its results (and the code) are widely used as a basis for many studies, such as search for DM signatures, origin of the elements, the spectrum and origin of Galactic and extragalactic diffuse γ-ray emission, heliospheric modulation etc. The GALPROP code, or components of it, are being used by the members of experimental teams, such as GLAST, AMS, Pamela, HEAT, ACE, TIGER, and requested by many other researchers world-wide.

4 Science Frontiers in Astrophysics of Cosmic Rays

4.1 Diffuse γ-rays and Cosmic-Ray Gradient

The puzzling excess in the EGRET data above 1 GeV relative to that expected [4] has shown up in all models that are tuned to be consistent with local nucleon and electron spectra [12, 14]. Is it a key to the problems of CR physics, an evidence of the Local Bubble, a signature of exotic physics (e.g., WIMP annihilation, primordial black hole evaporation), or just a flaw in the current models? This also has an immediate impact on the extragalactic background radiation studies since its spectrum and interpretation are model dependent. An apparent discrepancy between the radial gradient in the diffuse Galactic γ-ray emissivity and the distribution of CR sources (SNRs) has worsened the problem [12].

The puzzle of the "GeV excess" has lead to an attempt to re-evaluate the reaction of π^0-production in pp-interactions. A calculation made using Monte Carlo event generators to simulate high-energy pp-collisions confirmed previous results [15]. A parametrization [16] gives larger number of π^0's produced at high energies compared to a standard formalism [17] while consistent with pion data; its effect on diffuse γ-rays is not studied yet.

Another leading reason for the discrepancy discussed is that the local CR particle spectra (nucleons and/or electrons) may be not representative of the Galactic average. The local source(s) and propagation effects (e.g., energy losses) can change the spectrum of accelerated particles. A flatter Galactic nucleon spectrum has been suggested as a possible solution to the "GeV excess" problem [15, 18]. This requires the power-law index of proton spectrum of about

–2.4–2.5, however, it is inconsistent with measurements of CR $\bar{p}$ and e^+ fluxes [19]. Besides, the GeV excess appears in all directions [14] implying that this is not a feature restricted to the gas-related emission. A flatter (hard) electron spectrum, justified by the random nature of CR sources and large energy losses, may explain the GeV excess in terms of inverse Compton emission [20]. However, the required fluctuations are too large and the calculated spectrum of diffuse γ-rays is inconsistent with EGRET data above 10 GeV [14].

In the new analysis of the Galactic diffuse γ-ray emission [14], CR $\bar{p}$ data were used to fix the Galactic average proton spectrum, while the electron spectrum is adjusted using the spectrum of diffuse γ-rays themselves. The derived electron and proton spectra are found to be *compatible* with those measured locally considering fluctuations due to energy losses, propagation, or possibly details of Galactic structure. The effect of anisotropic inverse Compton scattering in the halo can increase the high-latitude Galactic γ-ray flux up to 40% [21]. The model shows a good agreement with EGRET spectra of diffuse γ-ray emission from different sky regions (<100 GeV). Some part of the excess can be associated with SNRs where freshly accelerated particles strike gas particles nearby producing harder γ-ray spectra [22]. The increased Galactic contribution to the diffuse emission reduces an estimate of the extragalactic γ-ray background [14]. The new extragalactic background shows a positive curvature, which is expected if the sources are unresolved blazars or annihilations of the neutralino DM [23].

The discrepancy between the radial gradient in the diffuse Galactic γ-ray emissivity and the distribution of SNRs [24], believed to be the CR sources, can be plausibly solved [25] if the X_{CO}-factor ($\equiv N_{H_2}/W_{CO}$) increases by a factor of 5–10 from the inner to the outer Galaxy. The latter is expected from the Galactic metallicity gradient.

4.2   Secondary Antiprotons in CR

Secondary antiprotons are produced in the same interactions of CR particles with interstellar gas as positrons and diffuse γ-rays. Their unique spectral shape is seen as a key link between physics of CR and diffuse γ-rays and could provide important clues to such problems as Galactic CR propagation, possible imprints of our local environment, heliospheric modulation, DM etc.

New $\bar{p}$ data with larger statistics [26] triggered a series of calculations of the secondary $\bar{p}$ flux in CR. The diffusive reacceleration models have certain advantages compared to other propagation models: they naturally reproduce secondary/primary nuclei ratios in CR, have only three free parameters (normalization and index of the diffusion coefficient, and the Alfvèn speed), and agree better with K-capture parent/daughter nuclei ratio. The detailed analysis shows, however, that the reacceleration models produce too few $\bar{p}$'s [13] because matching the B/C ratio at all energies requires the diffusion coefficient

to be too large. The discrepancy in $\bar{p}$ flux is $\sim 40\%$ at 2 GeV.

The difficulty associated with antiprotons may indicate new effects. It may indicate [13] that propagation of low-energy particles is aligned to the magnetic field lines instead of isotropic diffusion. If our local environment (the Local Bubble) influences the spectrum of CR, then the problem can be solved by invoking a fresh "unprocessed" nuclei component at low energy [27]; the evidence for SN activity in the solar vicinity in the last few Myr supports this idea. More intensive CR flux in distant regions will also produce more antiprotons and diffuse γ-rays [14].

The computed interstellar flux of secondary antiprotons can be used to test the models of solar modulation. Using a steady-state drift model of propagation in the heliosphere, the predictions are made for p's and $\bar{p}$'s fluxes near the Earth for the whole 22 year solar cycle [13, 28]; this includes different modulation levels and magnetic field polarities.

4.3   Indirect Searches for Dark Matter

The nature of the non-baryonic DM is a mystery. One of the preferred candidates for non-baryonic DM is a weakly interacting massive particle (WIMP). In most models the WIMP is the lightest neutralino χ^0 [29], which arises naturally in supersymmetric extensions of the Standard Model of particle physics. Another candidate is a Kaluza-Klein particle [30], a hypercharge B^1 gauge boson, whose thermal relic density is consistent with the WMAP measurements. Annihilations of DM particles produce leptons, quarks, gluons, and bosons, which eventually decay to ordinary particles. The DM particles in the Galactic halo or at the Galactic center [31] may thus be detectable via their annihilation products (e^+, $\bar{p}$, $\bar{d}$, γ-rays) in CR [32]. The approach is to scan the SUSY parameter space to find a suitable candidate particle to fill the excesses in diffuse γ-rays, $\bar{p}$'s, and e^+'s over the predictions of a conventional model. A preliminary results of the "global fit" to the e^+'s, $\bar{p}$'s, and diffuse γ-ray data simultaneously look promising [33].

5   Conclusion

The choice of topics discussed in this paper is personal and by no means complete. More complete list would include the origin of 511 keV line from the inner Galaxy, γ-ray bursts, ultra-high energy CR, as well as a more comprehensive discussion of the DM, SUSY, and dark energy. Other contributions to the Conference will fill these gaps.

References

[1] Koyama, K., et al., Nature **378**, 255 (1995)
Allen, G. E., et al., ApJ **558**, 739 (2001)

[2] Potgieter, M. S., Spa.Sci.Rev. **83**, 147 (1998)

[3] Gleeson, L. J., & Axford, W. I., ApJ **154**, 1011 (1968)
Fisk, L. A., J.Geoph.Res. **76**, 221 (1971)

[4] Hunter, S. D., et al., ApJ **481**, 205 (1997)
Moskalenko, I. V., et al., in *The Multiwavelength Approach to Unidentified Gamma-Ray Sources,* eds. K. S. Cheng & G. E. Romero, Kluwer, Dordrecht, in press (2004) (astro-ph/0402243)

[5] Jones, F. C., et al., ApJ **547**, 264 (2001)

[6] Seo, E. S., & Ptuskin, V. S., ApJ **431**, 705 (1994)
Zirakashvili, V. N., et al., A&A **311**, 113 (1996)
Ptuskin, V. S., et al., 28th ICRC, p.1929 (2003)

[7] Ptuskin, V. S., & Soutoul, A., A&A **337**, 859 (1998)
Webber, W. R., & Soutoul, A., ApJ **506**, 335 (1998)

[8] Strong, A. W., & Moskalenko, I. V., ApJ **509**, 212 (1998)

[9] Soutoul, A., et al., A&A **336**, L61 (1998)
Jones, F. C., et al., Adv.Spa.Res. **27**, 737 (2001)
Niebur, S. M., et al., J.Geoph.Res. **108**, A10, 8033 (2003)

[10] Yanasak, N. E., et al., ApJ **563**, 768 (2001)
Moskalenko, I. V., et al., 27th ICRC, p.1836 (2001)
Moskalenko, I. V., & Mashnik, S. G., 28th ICRC, p.1969 (2003)

[11] Bergström, L., et al., Phys.Rev.Lett. **87**, 251301 (2001)

[12] Strong, A. W., et al., ApJ **537**, 763 (2000)

[13] Moskalenko, I. V., et al., ApJ **565**, 280 (2002)

[14] Strong, A. W., et al., ApJ **613**, in press (2004) (astro-ph/0406254)
Strong, A. W., et al., ApJ **613**, in press (2004) (astro-ph/0405441)

[15] Mori, M., ApJ **478**, 225 (1997)

[16] Blattnig, S. R., et al., Phys.Rev. D **62**, 094030 (2000)

[17] Stephens, S. A., & Badhwar, G. D., Astrophys.Spa.Sci. **76**, 213 (1981)

[18] Gralewicz, P., et al., A&A **318**, 925 (1997)

[19] Moskalenko, I. V., et al., A&A **338**, L75 (1998)

[20] Porter, T. A., & Protheroe, R. J., J.Phys. G **23**, 1765 (1997)
Pohl, M., & Esposito, J. A., ApJ **507**, 327 (1998)
Aharonian, F. A., & Atoyan, A. M., A&A **362**, 937 (2000)

[21] Moskalenko, I. V., & Strong, A. W., ApJ **528**, 357 (2000)

[22] Berezhko, E. G., & Völk, H. J., ApJ **611**, 12 (2004)

[23] Salamon, M. H., & Stecker, F. W., ApJ **493**, 547 (1998)
Elsässer, D., & Mannheim, K., Astropart.Phys., in press (2004)

[24] Case, G. L., & Bhattacharya, D., ApJ **504**, 761 (1998)
Lorimer, D. R., in *Young Neutron Stars and Their Environments*, eds. F.
Camilo & B. M. Gaensler, IAU Symp. **218**, 105 (2004)

[25] Strong, A. W., et al., A&A **422**, L47 (2004)

[26] Orito, S., et al., Phys.Rev.Lett. **84**, 1078 (2000)
Beach, A. S., et al., Phys.Rev.Lett. **87**, 271101 (2001)
Boezio, M., et al., ApJ **561**, 787 (2001)

[27] Moskalenko, I. V., et al., ApJ **586**, 1050 (2003)

[28] Langner, U. W., & Potgieter, M. S., J.Geoph.Res. **109**, A01103 (2004)

[29] Jungman, G., et al., Phys.Rep. **267**, 195 (1996)
Bergström, L., Rep.Progr.Phys. **63**, 793 (2000)

[30] Cheng, H.-C., et al., Phys.Rev.Lett. **89**, 211301 (2002)

[31] Gunn, J. E., et al., ApJ **223**, 1015 (1978)
Stecker, F. W., ApJ **223**, 1032 (1978)
Silk, J., & Srednicki, M., Phys.Rev.Lett. **53**, 624 (1984)
Gondolo, P., & Silk, J., Phys.Rev.Lett. **83**, 1719 (1999)
Gondolo, P., Phys.Lett. B **494**, 181 (2000)

[32] Baltz, E. A., & Edsjö, J., Phys.Rev. D **59**, 023511 (1998)
Bergström, L., et al., ApJ **526**, 215 (1999)
Baltz, E. A., & Bergström, L., Phys.Rev. D **67**, 043516 (2003)
Gondolo, P., et al., J.Cosmol.Astropart.Phys. **7**, 8 (2004)

[33] de Boer, W., et al., hep-ph/0312037; astro-ph/0408272

COSMIC RAY ORIGIN AND SUPERNOVA REMNANTS

G. PÜHLHOFER

Landessternwarte Heidelberg Königstuhl 12, 69117 Heidelberg, Germany

Abstract

I will review the current status of the investigation of Supernova remnants (SNRs) with respect to their high energy emission, which should elucidate whether they are the main sources of Cosmic rays up to the knee in the Cosmic ray particle spectrum. The theoretical picture has made considerable progress in the last years, namely the non-linear kinetic acceleration theory and its application to actual astrophysical sources. Observationally, ground based imaging atmospheric Cherenkov telescopes (IACTs) and X-ray satellites provide currently the most valuable results to test the theories: IACTs because they are directly imaging the high energy particles in the source, and X-ray detectors because of their high sensitivity and excellent spatial resolution. I will describe the current reserch status of two young SNRs, Cassiopeia A and SN 1006.

1 Introduction

Supernova remnants (SNRs) are since a long time believed to be the main accelerators of Cosmic Rays (CR), up to energies of the so called knee in the

CR spectrum at $\sim 10^{15}$ eV. Supernovae (SN) are the only known sources in our Galaxy that release sufficient energy in order to sustain the steady production of Cosmic rays within our Galaxy, and there exists an established theoretial picture of the ongoing acceleration processes.

Particles are thought to be diffusively accelerated in SN shocks, with an expected source particle spectrum having a E^{-2} power law. This is consistent with the CR energy spectrum at Earth ($\propto E^{-2.7}$), in combination with the measured energy dependence of the secondary to primary ratio in high energy CRs [1], caused by an energy dependent particle escape which leads to a steepening of the initial source spectrum. Regarding the astrophysical acceleration sites, SN certainly lead to the development of accelerating shocks in their remnants, and can confine particles up to the required energies. That particles can be accelerated in SN shocks indeed up to 10^{15}eV has been recently confirmed in the theory of magnetic field amplification [2, 3].

The recent application of the non-linear kinetic acceleration theory to a number of representative SNRs [4, 5, 6] provided valuable insights into the problem how well we are actually able to verify the picture with observations. Generally speaking, direct evidence for acceleration up to the highest involved energies can only be obtained via the direct observation of the particles at the acceleration sites, by detecting their photon emission and obtaining astronomical pictures of the objects. Detections or flux limits at TeV energies as obtained with Imaging Atmospheric Cherenkov Telescopes (IACT) are therefore crucial for testing the models.

However, the interpretation is somewhat complicated: protons release π^0-decay induced photons, while electrons can emit TeV photons via the Inverse Compton (IC) process or nonthermal Bremsstrahlung (NB). One is primarily interested though in the accelerated protons, since they constitute the majority (>99%) of the CR, and only for hadrons a comprehensive theoretical description exists, including the injection of suprathermal particles into the acceleration process. The discrimination between hadronically and leptonically induced TeV emission is not straight forward: depending on source parameters, it is possible that the modeled IC spectrum resembles a hard E^{-2} spectrum as expected for hadrons, and is not cooled to a much steeper spectrum at TeV energies. And although hadrons are overall much mode abundant, electrons can radiate under certain circumstances much more efficiently than hadrons. Hence the sole detection of TeV γ-rays is not sufficient, more detailed information is required to show that indeed the sought-after hadrons were found.

Energetic electrons are visible across a large fraction of the electromagnetic spectrum: synchrotron emission from non-thermal electrons is detected from radio up to X-rays, while hadrons are only accessible in the MeV to TeV band. The excellent angular resolution of the detectors in the radio to X-ray frequency range is extremely valuable to study the morphology of the acceleration sites.

In the next two sections, I will sketch the observational progress of the search for the Cosmic ray acceleration sites over the last years. Then follows a short review of the non-linear kinetic acceleration theory. I will then describe the current status of the high energy observations of two young SNRs, Cassiopeia A and the remnant of SN 1006, and discuss the impacts on CR research.

2   The search for the Cosmic ray accelerators

With the EGRET detector onboard the Compton Gamma Ray Observatory, a handful of SNRs were detected to show γ-ray emission. However, these data faced the problem that possible contributions from pulsars could not be excluded; the CR acceleration is expected to take place primarily in SNR bow shocks. The contribution from pulsars to the γ-ray emission is expected to cut off at GeV energies, making TeV observations more meaningful than GeV observations.

At energies above several GeV, ground based instruments which detect the particle showers induced by the high energy photons in the atmosphere become feasible, and have much larger collection areas than satellite based instruments. Particle detector arrays have a large field of view (FoV) and are therefore capable to provide all sky maps, however their limited sensitivity rendered them unusable so far for SNR investigations. Until now, only IACTs have sufficient sensitivity to detect γ-rays from SNRs. Due to their limited FoV ($\leq 5°$), only a limited fraction of the sky could be investigated so far.

With the HEGRA IACT system, a broader section of the Galactic plane accessible in the Northern hemisphere was investigated [7]. The sensitivity of this scan was unfortunately insufficient to detect individual SNRs, and an ensemble limit of 19 SNRs (with distance <10 kpc) rendered a flux limit which was close but still a factor two above what was expected from basic theory [8]. Hence, although the examination of a representative sample of the SNR population is desireable to test the models and the overall energy budget, so far the research has focused on the investigation of individual SNRs to obtain signals or meaningful upper limits.

The initial observations of SNRs with IACT instruments were conducted on shell type SNRs which are believed to be well in the Sedov phase, and are ideally interacting with molecular clouds (leading to an enhanced π^0-decay signal). The Whipple and HEGRA experiments reported upper limits on a couple of SNRs [9, 10], which were in some cases (IC 443, G 78.2+2.1) below an extrapolation of the EGRET data, under the assumption of a simple power law $F(>E) \propto E^{-1.0..-1.2}$. However, given the possible leptonic contribution from pulsars to the EGRET fluxes, the results could not be interpreted as cutoffs of the hadron spectra above GeV energies.

3   The X-ray view of Supernova remnants

ASCA observations revealed continuum emission from the rims of SN 1006 [11], which was interpreted as synchrotron emission from high energy electrons accelerated at the bow shock of this SNR. Later, RXTE measurements of several young SNRs (Cas A, Tycho's SNR, RCW 86, Kepler's SNR, and SN 1006) revealed power-law spectra at and above 10 keV [12], which suggested that this class of SNRs can accelerate electrons up to $\sim$100 TeV. However, one must note that the synchrotron interpretation of the X-ray spectra is not entirely unambiguous, also non-thermal Bremsstrahlung from electrons with much lower energies can lead to powerlaw-like spectra at these energies [13].

The Chandra satellite provides extremely good spatial resolution, but is limited in its energy range to below $\sim$10 keV. Nevertheless, the images derived from the continuum-dominated parts of the spectrum can be used for important morphological mapping of the synchrotron emission from high energy electrons. The very narrow, rim-like structures found in several young SNRs [14] have been used by different authors to derive magnetic field estimates at the bow-shock positions (e.g. [13, 15]). The narrow structures are explained by rapid synchrotron cooling of high energy (TeV) electrons. This leads to narrow X-ray continuum filaments, which can be morphologically different from the thermal X-ray images, and from the radio images which are due to lower energy electrons not suffering from synchrotron cooling. The derived magnetic fields are of the order of $100\,\mu$G and above, much higher than what one would expect from shock compression of the interstellar magnetic field alone. This is considered as strong evidence for efficient hadronic CR acceleration, since magnetic field amplification in strong shocks is naturally expected in the framework of acceleration theory [2].

4   The nonlinear kinetic acceleration theory

The application of the Fermi acceleration process to astrophysical shocks was pioneered by [16, 17, 18, 19]. Ellison and Baring (e.g. [20]) used Monte Carlo codes to simulate particle acceleration in Supernova remnants (with the simplification of plane-parallel shocks), including the injection of supra-thermal electrons and hadrons into the acceleration process, which is a decisive ingredient for the understanding of the overall efficiency of the process.

The most detailed description of the particle acceleration process in SNRs became available with the works of Berezhko and Völk, who developed and elaborated a kinetic acceleration theory, in which the Fokker-Planck equations for the particle distributions are solved semi-analytically. In this model, the hydrodynamics of the gas as well as the backreaction of the energetic particles to the acceleration process is considered. The inclusion of the backreaction refines the theory from a test particle to a non-linear description of the process, which

leads to a modification of the particle and the resulting γ-ray emission spectra. The time evolution of the high energy particle content and the corresponding γ-ray emission was elaborated in [21], by solving the spherically symmetric transport equation semi-analytically. The theory was extended for the case of the expansion of a SNR into an inhomogeneous environment in [22].

The theory resulted in a typical efficiency of the transfer of kinetic energy into accelerated CRs of about 50%, higher than the average value of 10% which is needed to replenish the CR particles escaping the Galaxy by SNRs. However, the spherically symmetric solution does not take into account that the surrounding magnetic field structure in which the SNR is evolving cannot be spherically symmetric itself. Injection of particles into the acceleration process can only take place in regions where the shock normal is nearly parallel to the magnetic field lines. Only in these regions, strong production of Alfen waves can occur, which is essential for the efficient acceleration process. In [23], an overall reduction factor of the acceleration efficiency of 20% to 15% was estimated for a homogeneous and Parker-spiral magnetic field configurations.

The injection of suprathermal particles into the acceleration process is not inherently described in the theoretical description. This issue was addressed in [4], using the fact that electrons are inevitably accelerated together with hadrons, without strongly influencing the shock. They can be considered as test particles in a given shock structure and a given magnetic field. The measured broad-band synchrotron emission of individual sources can be used to estimate the injection efficiency, the effective magnetic field, and the ratio of electrons to protons. The post-shock magnetic field, which is expected to be strongly amplified due to the strong acceleration process, can independently be estimated from the synchrotron losses of the electrons, as determined from small scale X-ray structures measured by the Chandra satellite. Both methods yield acceptable agreement in considered cases like Cas A, Tycho's SNR or SN 1006.

5 The high energy view of Cassiopeia A

Cas A is a favourable target for the investigation of CR (and subsequent γ-ray) production in young SNRs in the northern hemisphere, given (among others) its brightness and non-thermal emission in X-rays. Only morphological studies in γ-rays are yet out of reach for current instruments, since the source size is only 5'. The morphology in the radio and X-ray bands is dominated by an overall spherical appearence, with a bright radio and X-ray rim. The remnant also exhibits knot-like structures with varying radio spectral index, which are not considered in detail in the present modeling.

Cas A is believed to be a remnant of a type Ib supernova. The progenitor star was presumably a massive Wolf Rayet star, which has emitted strong stellar
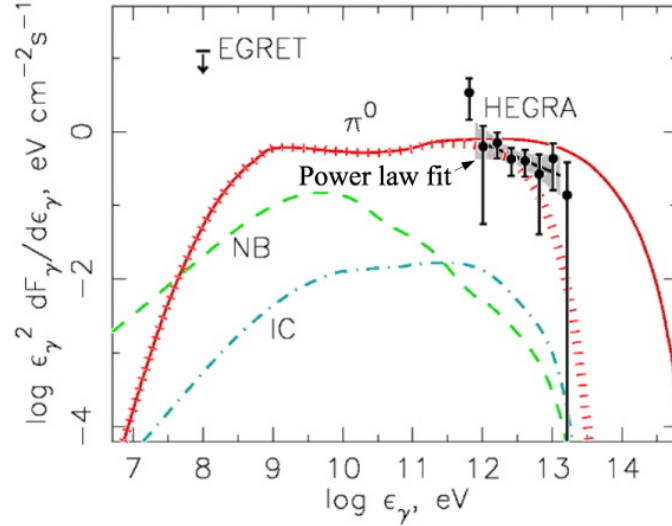
Figure 1: High energy emission from Cassiopeia A. The model curves are from the kinetic acceleration theory applied to the remnant [5].

winds in which the supernova remnant is evolving. Adopting the description of the surrounding medium by [24], the bright radio rim of Cas A is a result of the interaction of the wind of the last blue supergiant phase of the progenitor star with the red supergiant wind of the preceding phase, with a ring density of $\sim 10\,\mathrm{cm}^{-3}$. The blast wave has already left this region and is located in the unperturbed red supergiant wind region. This idea has been confirmed by the Chandra satellite that impressively imaged the location of the blast wave. Also from Chandra data, the high post-shock magnetic fields of $500\,\mu\mathrm{G}$ [5] have been confirmed [25, 13].

Besides the inhomogeneous gas density, equally important for particle acceleration is the magnetic field configuration around Cas A. It is assumed that a Parker spiral configuration has been produced by the progenitor wind. Due to turbulences, sufficent portions of the shock "see" a parallel magnetic field, the fraction of the shock in which efficient particle acceleration can take place was estimated to be $\sim 15\%$. At high energies, HEGRA detected a weak TeV γ-ray signal from Cas A at the level of $\sim 3\%$ of the Crab flux [26]. The HEGRA data points can be described by a power law with differential spectral index of $\Gamma = -2.45 \pm 0.45$, as indicated by the shaded area in Fig.1.

The full description of the time dependent modeling of the high energy acceleration processes can be found in [5]. Fig. 1 shows the resulting expected high energy emission from electrons (through IC and NB) and from hadronically

induced π^0-decay. The measured flux level measured by HEGRA is well reproduced by the π^0-decay emission, while the leptonically induced channels fall short of the measured flux by nearly two orders of magnitude. The IC channel was computed considering the Cosmic Microwave Background as well as stellar IR photons, the difference between hadronically and leptonically induced emission at 1 TeV is considered a robust result. A similar result was derived by [13], albeit with a somewhat reduced margin between modeled IC and measured TeV flux, which similarly was interpreted to be due to hadronic origin.

As shown in Fig. 1, the HEGRA spectrum marginally differs from the predicted hard spectrum at 1 TeV. The dotted curve shows that possible increased escape of protons from the remnant can lead to a lower cutoff energy for protons, which would result in a better fit to the data, but would also mean that Cas A is already in a decreasing stage concerning high energy particle production.

6   SN 1006: The perfect object to study Cosmic ray acceleration?

The remnant of SN 1006 is believed to be an ideal source to study particle acceleration in SNRs. SN 1006 is the remnant of a type Ia SN explosion, and is extended for both X-ray and γ-ray instruments. Nonthermal X-rays were detected by several satellites. The X-ray image shows a clear bipolar structure, which is expected for a shock expanding into a homogeneous medium, since efficient acceleration can only take place in the poles where shock normal and magnetic field are quasi-parallel. This interpretetion was recently confirmed by an analysis of the XMM image of SN 1006 [27]. From the broadband synchrotron spectrum and from the small scale structure, an effective downstream magnetic field of $150\,\mu$G was estimated [30]. The small scales were again interpreted as a proof for efficient CR acceleration, which makes hadronic γ-ray emission from this remnant a more likely explanation than a leptonic interpretation, which is also discussed frequently in the literature (e.g. [28]).

However, the TeV signal reported by CANGAROO from the northeastern rim of SN 1006 [28] could not be verified by the H.E.S.S. telescopes (see Fig. 2, [29]). Neither from the northeastern rim nor from the entire remnant, a TeV signal was detected. Since the modeled hadronic TeV emission strongly depends on the gas density around SN 1006, which has considerable uncertainty (0.05 - $0.3\,\mathrm{cm}^{-3}$), the data are still compatible with the expected hadronic emission level, if a low density is adopted [30]. Only a by a factor of a few improved upper limit could constrain the hadronic emission channel. At the same time, no IC emission is detected, which is consistent with the estimated high magnetic field in the shell.
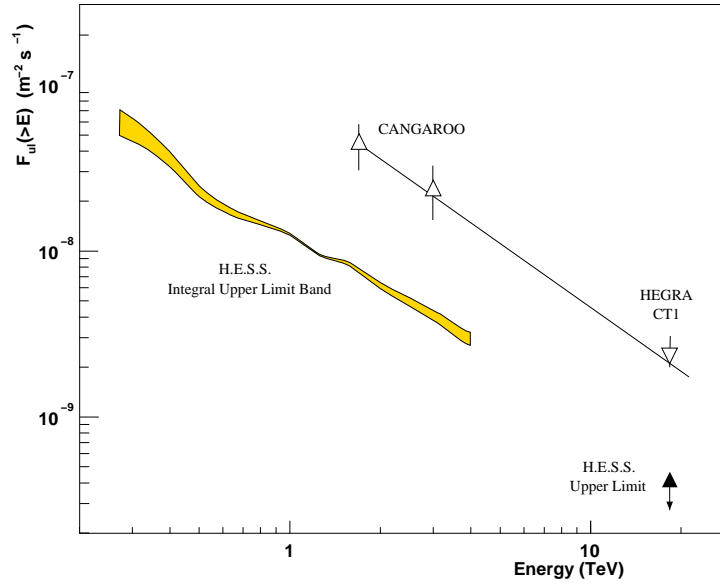
Figure 2: The high energy emission from SN 1006 measured by CANGAROO and the upper limits derived by H.E.S.S. for the same region.

7   Conclusions

The non-detection of γ-ray emission from the remnant of SN 1006 with H.E.S.S. may look as a drawback for the efforts to establish SNRs as the sources of Galactic CRs. The search for explanations of the difference between the CANGAROO and H.E.S.S. results is beyond the scope of this paper. But one should consider that, from a theoretical point of view, the high γ-ray flux measured by CANGAROO was initially quite unexpected [10]. The hadronic modeling was able to describe the data provided by CANGAROO, but can also easily accomodate for the upper limit provided by H.E.S.S., given the possible range of ambient matter density in SN 1006 [30]. And, the new limits now allow consistent IC modeling using the high, amplified magnetic field which is thought to exist in the remnant shell.

Cassiopeia A is a likely source of CR hadrons, given the TeV signal and the current status of modeling. A confirmation of the weak TeV signal by new instruments is yet desireable. In the meantime, the H.E.S.S. collaboration has published the first resolved γ-ray image of a SNR, from RX J1713-3946 [31], a SNR which was already claimed by the CANGAROO experiment to emit TeV radiation [32]. The image provided by H.E.S.S. clearly shows a shell-type γ-ray morphology, and the hard spectrum makes this source a prime candidate for

hadronic CR acceleration. Detailed modeling of the high energy emission from RX J1713-3946 as measured by H.E.S.S. is yet to be done.

TeV astronomy has so far detected serendipitously two sources without counterpart in other wavebands, which are presumably of Galactic origin. The lack of X-ray emission from TeV J2032+4130 detected by HEGRA [33] makes hadronic acceleration the likely cause for the TeV emission. For HESS J1303-631 [34], a detailed investigation is pending. Whether sources of this kind contribute significantly to the Galactic CR energy budget is an open question.

At present, the SNR acceleration theory is in good agreement with current high energy detections and upper limits. The idea that SNRs are responsible for the bulk of Cosmic Rays is supported by the energy budget argument as well as from current observations. With the high sensitivity in TeV γ-rays which is now available (H.E.S.S., CANGAROO III) or will soon be available (MAGIC, VERITAS), a census of the SNR population through a survey of a representative subset is feasible. Surveys of the Galactic plane might reveal whether unforeseen competitors will join the population of Galactic cosmic ray sources.

References

[1] E. Juliusson, P. Meyer, D. Müller, **Phys. Rev. L.**, 1972, 29, 445.

[2] A.R. Bell, **MNRAS**, 2004, 353, 550.

[3] E.G. Berezhko, H.J. Völk, **A&A**, 2004, 427, 525.

[4] E.G. Berezhko, L.T. Ksenofontov, H.J. Völk, **A&A**, 2002, 395, 943.

[5] E.G. Berezhko, G. Pühlhofer, H.J. Völk, **A&A**, 2003, 400, 971.

[6] H.J. Völk et al., **A&A**, 2002, 396, 649.

[7] F.A. Aharonian et al. (HEGRA Collaboration), **A&A** 2002, 395, 803.

[8] L.O'C. Drury, F.A. Aharonian, H.J. Völk, **A&A**, 1994, 287, 959.

[9] J.H. Buckley et al. (Whipple collaboration), **A&A**, 1998, 329, 639.

[10] H.J. Völk, 1997, In: de Jager O.C. (ed.), Proc. Krüger Park Work. on TeV Gamma Ray Astrophysics, p.87, astro-ph/9711204.

[11] K. Koyama et al., **Nature**, 1995, 378, 255.

[12] R. Petre et al., **A. N.**, 1999, 320, 199.

[13] J. Vink and J.M. Laming, **ApJ**, 2003, 584, 758.

[14] A. Bamba et al., **Advances in Space Research**, 2004, 33, 376.

[15] E.G. Berezhko, L.T. Ksenofontov, H.J. Völk, **A&A**, 2003, 412, L11.

[16] G.F. Krymsky, **Soviet Phys. Dokl.**, 1977, 23, 327.

[17] R.D. Blandford and J.P. Ostriker, **ApJ**, 1998, 221, L29.

[18] A.R. Bell, **MNRAS**, 1978, 182, 147 and 443.

[19] W.I. Axford, E. Leer, G. Skadron, in: Proc. of the 15th ICRC, Plovdiv, Bulgaria, 1978, 11, 132.

[20] D.C. Ellison et al, **ApJ**, 2000, 540, 292.

[21] E.G. Berezhko and H.J. Völk, **Astropart. Phys.**, 1997, 7, 183.

[22] E.G. Berezhko and H.J. Völk, **A&A**, 2000, 357, 283.

[23] H.J. Völk, E.G. Berezhko, L.T. Ksenofontov, **A&A**, 2003, 409, 563.

[24] K.J. Borkowski et al., **ApJ**, 1996, 466, 866.

[25] E.G. Berezhko and H.J. Völk, **A&A**, 2004, 419, L27.

[26] F.A. Aharonian et al. (HEGRA Collaboration), **A&A**, 2001, 370, 112.

[27] R. Rothenflug et al., **A&A**, 2004, 425, 121.

[28] T. Tanimori et al., **ApJ** 1998, 497, L25.

[29] G.P. Rowell et al. (H.E.S.S. Coll.), in: Proc. Int. Symp. on High Energy Gamma-Ray Astronomy, Heidelberg, to be published by AIP, New York.

[30] L.T. Ksenofontov et al., in: Proc. Int. Symp. on High Energy Gamma-Ray Astronomy, Heidelberg, to be published by AIP, New York.

[31] F.A. Aharonian et al. (H.E.S.S. Collaboration), **Nature** 2004, 432, 75.

[32] H. Muraishi et al., **A&A**, 2000, 354, L57.

[33] F.A. Aharonian et al. (HEGRA Collaboration), **A&A** 2002, 393, L37.

[34] M. Beilicke et al. (H.E.S.S. Coll.), in: Proc. Int. Symp. on High Energy Gamma-Ray Astronomy, Heidelberg, to be published by AIP, New York.

ANTIPROTONS AND COSMIC RAYS PROPAGATION

Fiorenza Donato[a,b]

[a] *Max-Planck Institut für Physik, Föhringer Ring 6, Munich, Germany*

[b] *INFN, Sezione di Torino, via Giuria 1, Torino, Italy*

Abstract

We present the results obtained in the framework of a 2-zones diffusion model for galactic cosmic rays. We analyse the boron-to-carbon ratio (B/C), and discuss how the available data can constrain the parameter space. The selected parameters are then used to calculate the secondary antiproton spectrum. Theoretical predictions and measurements agree very well. The astrophysical uncertainties for this species are modest, but they are enormously amplified when considering antiprotons of supersymmetric origin. However, we demonstrate that antiprotons are the best indirect detection means for very light relic neutralinos.

1   The Diffusion Model

The propagation of cosmic rays in the Galaxy has been considered in the framework of a two-zone diffusion model, which has been described at length in Refs. [1, 2, 3].
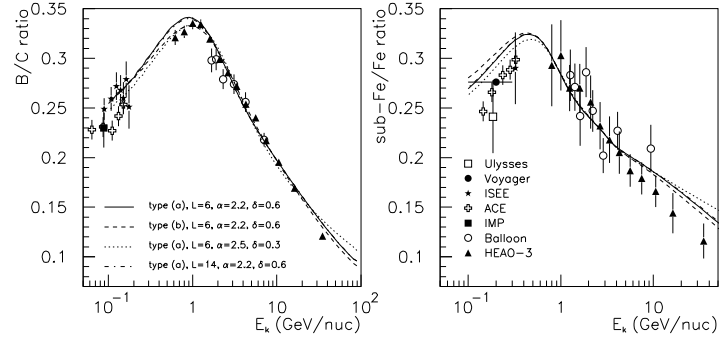
Figure 1: The B/C and sub-Fe/Fe spectra for several sets of propagation parameters giving the best fit to B/C (see [2]).

The spatial diffusion of cosmic rays is assumed to occur uniformly in the whole (disk and halo) diffusion volume, with the same strength. The corresponding diffusion coefficient has been defined as $K(E) = K_0 \beta (\mathcal{R}/1\,\mathrm{GV})^\delta$, where $\mathcal{R}$ stands for the particle rigidity and K_0 and δ are free parameters of the model. We consider the possibility that a Galactic wind blows the particles away from the disk in the z vertical direction, with a constant speed V_c. It induces an adiabatic dilution of the energy. We also take into account the presence of minimal reacceleration on random hydrodynamic waves, *i.e.* diffusion in momentum space, described by a coefficient K_{pp}. This process is assumed to occur only in the disk and is related to the velocity of disturbances in the hydrodynamical plasma V_A, called Alfvén velocity. In summary, our diffusion model has five free parameters K_0, δ, L, V_c, V_A, with the option to fix or not the power α and the shape of the injection spectrum.

The sets of diffusion parameters were constrained in [1, 2] by analysing stable nuclei, mainly by fitting the boron to carbon ratio B/C. Due to large experimental errors, the sub-Fe/Fe data do not constrain further the parameter space. Typical spectra (modulated at $\Phi = 500$ MV) are shown in Fig. 1, for different values of the parameters α and δ, along with the data points. All the models displayed give similar spectra, which would be difficult to sort by eye. This may explain why some of these models (*e.g.* those with $\delta = 0.3$) are retained in other studies.

We studied the compatibility of our diffusion model with current data on β-radioactive isotopes ^{10}Be, ^{26}Al and ^{36}Cl [4]. These species diffuse on a typical distance $l_{\mathrm{rad}} \equiv \sqrt{K \gamma \tau_0}$ before decaying: not only the diffusion coefficient

K, but also the lifetime $\gamma\tau_0$, depends on energy, due to the relativistic time stretch. These species are therefore *very* sensitive to the characteristics of the local interstellar medium (LISM), much more than stable species. The Solar System is embedded in an underdense region, usually called the Local Bubble. The bubble leads substantially to a decrease in the spallation source term of the radioactive species. We modeled the bubble as a hole in the thin disc approximation and the radius of this hole is considered as an unknown parameter in the analysis. In [4] we provided the theoretical tools to treat the presence of the hole in the galactic disc in our two-zone diffusion model. The major result we found is that at the center of the bubble, the radioactive fluxes are decreased as $N^{r_{\text{hole}}}/N^{r_{\text{hole}}=0} \propto \exp(-r_{\text{hole}}/l_{\text{rad}})$. Using the diffusion parameters allowed by the B/C data [1, 2] to compute the ^{10}Be/^{9}Be and ^{36}Cl/Cl ratios, we find that data are consistent only with models with a bubble of radius $r_{\text{hole}} \sim 60 - 100$ pc, in relatively good agreement with direct observations, and the case for $r_{\text{hole}} = 0$ pc is disfavored.

2   Secondary antiprotons

Proton and helium cosmic rays interact with the interstellar hydrogen and helium nuclei, producing quarks and gluons that subsequently can hadronize into antiprotons. A calculation of this secondary antiproton flux has been done in Ref. [5], to which we refer for details. Fig. 2 displays - along with experimental data - the computed antiproton flux with the contributions to the total flux coming from the various nuclear reactions: from top to bottom are represented the contribution of p–p, p–He, He–p and He–He. First of all, we notice that the calculated spectrum agrees very well with the data points. This strong result gives confidence in our consistent treatment of nuclei and antiproton propagation. Second, even if the main production channel is the spallation of cosmic ray protons over interstellar hydrogen, we see that the contribution of protons over helium is very important, particularly at low energies (where a hypothetical primary signature would be expected). It emphasizes the necessity of having a good parameterization of the p–He reaction.

Fig.3 shows the uncertainties deriving from the propagation parameters and from the scarce knowledge of some nuclear cross sections, and have been calculated according to [5]. The resulting scatter is 9% from 100 MeV to 1 GeV, reaches a maximum of 24% at 10 GeV and decreases to 10% at 100 GeV. This estimate of the uncertainties related to diffusion may be considered as quite conservative. The uncertainties related to nuclear physics obtain a shift of the upper and the lower curve with respect to the central one of the order of 22–25 % over the energy range 0.1–100 GeV. The major uncertainties come then from nuclear physics and are already comparable to experimental error
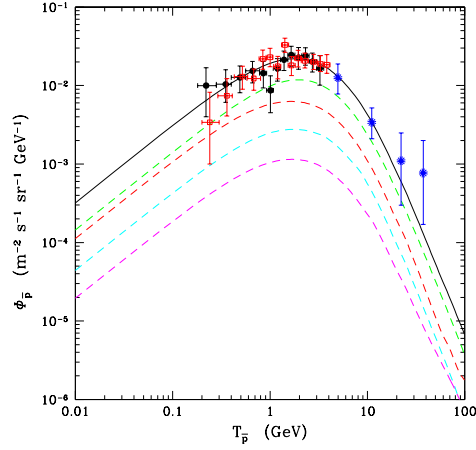
Figure 2: Solid line shows the total top-of-atmosphere (TOA) secondary antiproton spectrum for the set of diffusion parameters giving the best χ^2 for B/C. Dashed lines are the contributions to this total flux from various nuclear reactions (from top to bottom: p–p, p–He, He–p and He–He). Data points are taken from BESS 95+97 (filled circles), BESS 98 (empty squares) and Caprice (starred).
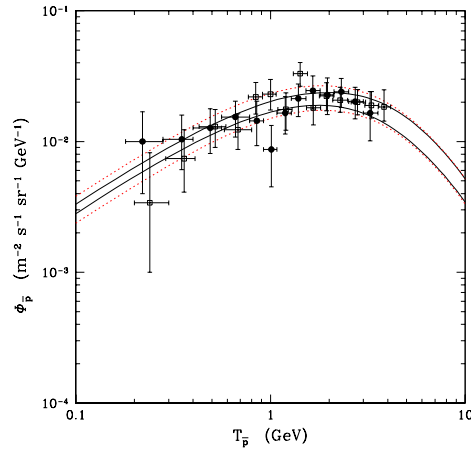
Figure 3: Uncertainty on the evaluation of the (TOA) secondary antiproton spectrum. Solid band: uncertainty on the propagation parameters, dotted band: uncertainty due to nuclear physics.

bars. As antiproton spectrum measurements should better in the near future, antiproton studies could be limited by nuclear indeterminacies.

3   Antiprotons from dark matter annihilation

If the dark matter is under the form of neutral, massive supersymmetric particles, we may expect that they annihilate in pair producing quarks and gluons. These elementary particles can then hadronize and give birth to antiproton nuclei. In principle, an excess of low–energy antiprotons is the signature of an unconventional production. Antiproton production from primary cosmic–ray spallations is the natural background to any unconventional excess that would signal for instance the presence of the putative neutralinos. The calculation of this primary component has been performed in [6], to which we refer for further details. The solutions of the spatial diffusion equations are now very different than for the secondary counterpart, due to the fact that in the present case the antiproton sources (neutralinos) pervade the all diffusive volume. This characteristic breaks the degeneracy on the propagation parameters that we can observe for B/C and for secondary antiprotons, whose sources are located only in the thin disc.

We have implemented a supersymmetric scheme, which we call eMSSM (effective Minimal Supersymmetric Standard Model, see [6] and refs. therein) directly at the electroweak scale, which is where the phenomenology of neutralino dark matter is actually studied. The large number of free parameters is reduced by a set of assumptions which are sufficient to shape the properties of the model at the electroweak scale. We have calculated the primary antiproton fluxes deriving from neutralino annihilations and considering different possibilities for the propagation parameters. Our reference configuration is the one which provides the best fit to B/C [1, 6]. In Fig.4 we have plotted the secondary flux (as from [5]) and our predictions for primary fluxes at different neutralino masses in the eMSSM: $m_\chi = 60, 100, 300, 500$. We notice that the primary flux from neutralino annihilation is at most of the same order of magnitude as the secondary flux, and this occurs for neutralino masses close to their current lower bound in the eMSSM, which is around $m_\chi \simeq 50$ GeV. The representative supersymmetric configurations refer to a large antiproton production for each mass. This indicates that the antiproton signal for neutralino dark matter will hardly produce an excess over the secondary flux, for the median (and best) choice of the astrophysical parameters which govern the diffusion and propagation of antiprotons in the Galaxy.

However, the same primary antiproton fluxes calculated with propagation parameters providing a 4-sigma deviation from the best fit on B/C, differ by almost an order of magnitude - at least at low energy - from the reference (best fit) configuration. This means that the scarce knowledge of the astrophysical
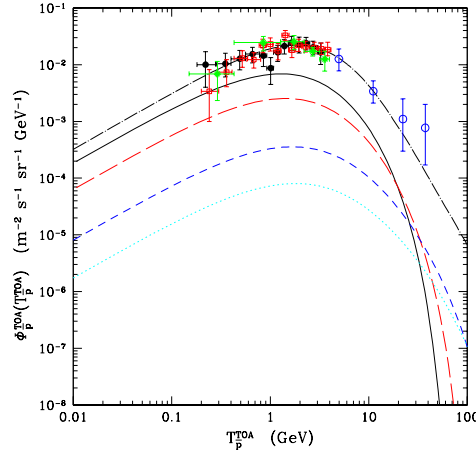
Figure 4: TOA antiproton fluxes for a few representative supersymmetric case: solid line refers to $m_\chi = 60$ GeV, long–dashed to $m_\chi = 100$ GeV, short–dashed to $m_\chi = 300$ GeV and dotted to $m_\chi = 500$ GeV. The upper dot–dashed curve corresponds to the antiproton secondary flux. Full circles: BESS 1995-97 data; open squares: BESS 1998; stars: AMS and empty circles: CAPRICE.

parameters induces an uncertainty of about 2 orders of magnitude on the calculation of primary antiproton fluxes This is almost independent on the specific supersymmetric configuration. The large variation in the primary signal is due to the fact that the exotic signal is more sensitive to astrophysical parameters than the standard, as already underlined. Second, this has to be weighted by the fact that the secondary flux has in its source term an additional $K(E)$. Fig. 5 shows the TOA antiproton fluxes for the $m_\chi = 100$ GeV reference configuration and for the maximal and minimal sets of astrophysical parameters. The figure shows that solar modulation has the effect of depleting the low–energy tail of the antiproton flux. It is evident how huge the astrophysical uncertainty band is.

As shown in [7], in Supersymmetric models without gaugino-mass unification at the grand unification scale, neutralinos can be lighter than the current lower bound of 50 GeV, which instead occurs in the case of gaugino–universal models. In [7] (see also refs. therein) we discussed the properties of these light neutralinos as relic particles and showed that an absolute lower limit of 7 GeV on the neutralino mass m_χ can be placed by applying the most recent determinations of the upper bound on the Cold Dark Matter (CDM) content in the Universe. Being the supersymmetric antiproton flux inversely dependent on the neutralino squared mass, it is easy to expect that for these light neutralinos the antiproton flux could provide interesting information. To show
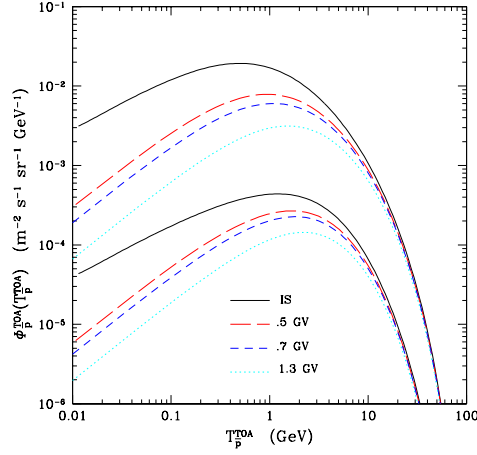
Figure 5: Top–of–atmosphere antiproton fluxes as a function of the antiproton kinetic energy for the m_χ=100 GeV reference case. The upper (lower) set of curves refers to the maximal (minimal) set of of astrophysical parameters. Solid curves show the interstellar fluxes. Broken curves show the effect of solar modulation at different periods of solar activity: $\phi = 500$ MV (long dashed), $\phi = 700$ MV (short dashed), $\phi = 1300$ MV (dotted).
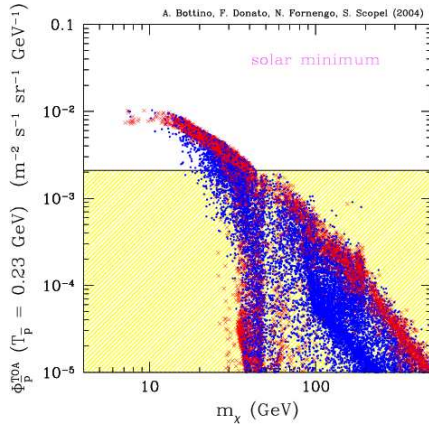
Figure 6: Antiproton flux at $T_{\bar{p}} = 0.23$ GeV as a function of the neutralino mass, calculated at solar minimum. See text for details

quantitatively how the experimental data could constrain the supersymmetric parameters, in Fig. 6 we display the antiproton flux evaluated at $T_{\bar{p}} = 0.23$ GeV for a full scan of our supersymmetric model described in [7]. As expected, the scatter plot is prominent at small masses. It is remarkable that for $m_{\chi} \approx 25$ GeV the scatter plot is funnel-shaped. The reason is explained in [7]. The set of propagation parameters is the one giving the best fit to the B/C ratio. The shaded region denotes the amount of primary antiprotons which can be accommodated at $T_{\bar{p}} = 0.23$ GeV without entering in conflict with the BESS experimental data and secondary antiproton calculations [7]. Due to the astrophysical uncertainties, the primary antiproton flux can be lowered by an order of magnitude. This prevents us from deriving any constraint on the supersymmetric parameters, if one assumes a very conservative attitude in the selection of the propagation parameters. We wish to stress that any further breakthrough in the knowledge of the astrophysical parameters would allow a significant exploration of small mass configurations, in case the conservative set of parameters is excluded. Should the effect of antiproton propagation turn out to be equivalent to the one obtained with the best fit set, the analysis of cosmic antiprotons would prove quite important for exploring very light neutralinos. This is particularly true for neutralino masses below ≈ 15 GeV, in view of the typical funnel shape displayed in the scatter plots.

References

[1] D. Maurin, F. Donato, R. Taillet, and P. Salati, Ap. J. **555**, 585 (2001).

[2] D. Maurin, R. Taillet, F. Donato, Astron. & Astrophys. **394**, 1039 (2002).

[3] D. Maurin et al., in Research Signposts, "Recent Developments in Astrophysics", astro-ph/0212111.

[4] F. Donato, D. Maurin, and R. Taillet, Astron. & Astrophys. **381**, 539 (2002).

[5] F. Donato et al., Ap. J. **563**, 172 (2001).

[6] F. Donato et al., Phys. Rev. D **69**, 063501 (2004).

[7] A. Bottino, F. Donato, N. Fornengo, S. Scopel, Phys. Rev. D **70**, 015005 (2004).

UNCERTAINTIES OF ANTIPROTON AND POSITRON SPECTRA FROM B/C DATA

Vladimir Zdravković and Aldo Morselli

[a] *INFN, Sezione di Roma II, and Dipartimento di Fisica, Università di Roma "Tor Vergata", via della Ricerca Scientifica, Roma, Italy*

Abstract

We have studied the total variation of e^+ and $\bar{p}$ top of the atmosphere spectra due to the parameters uncertainties of the Milky Way geometry, models of propagation and cross sections. As input we used the B/C data and Galprop code for propagation analysis. We have derived also the uncertainty bands for subFe/Fe ratio, H and He.

1 Production and Propagation of Cosmic Rays in the Milky Way

We have chosen Galprop [1] as a public code for the treatment of propagation of all cosmic rays (CR) together. Our scope has been to determine the total uncertainties in the calculation of e^+ and $\bar{p}$ top of the atmosphere spectra due to the uncertainties of geometrical and propagation parameters and cross sections. Here we give very short description of processes included in propagation equation:

Table 1: Allowed values for DR model propagation parameters.

par./val.	$z[kpc]$	$D_0[cm^2 s^{-1}]$	δ	γ	$V_A[km s^{-1}]$
minimal	3.0	$5.2\ 10^{28}$	0.25	2.35	22
best fit	4.0	$5.8\ 10^{28}$	0.29	2.47	26
maximal	5.0	$6.7\ 10^{28}$	0.36	2.52	35

Table 2: Allowed values for the propagation parameters for DC model.

par./val.	$z[kpc]$	$D_0[\frac{cm^2}{s}]$	δ_2	$\frac{dV_C}{dz}[\frac{km}{s\,kpc}]$	γ_1	γ_2
minimal	3.0	$2.3\ 10^{28}$	0.48	5.0	2.42	2.14
best fit	4.0	$2.5\ 10^{28}$	0.55	6.0	2.48	2.20
maximal	5.0	$2.7\ 10^{28}$	0.62	7.0	2.50	2.22

$$
\begin{aligned}
\frac{\partial \psi(\mathbf{r},p,t)}{\partial t} &= q(\mathbf{r},p) + \nabla \cdot (D_{xx}\nabla\psi - \mathbf{V}_c\psi) + \frac{d}{dp}p^2 D_{pp}\frac{d}{dp}\frac{1}{p^2}\,\psi \\
&- \frac{\partial}{\partial p}\left[\dot{p}\psi - \frac{p}{3}(\nabla\cdot\mathbf{V}_c)\psi\right] - \frac{1}{\tau_f}\psi - \frac{1}{\tau_r}\psi\,,
\end{aligned}
\tag{1}
$$

where $\psi(\mathbf{r},p,t)$ is total phase space density. This equation is valid for all the types of particles. Isotropic diffusion is defined by the coefficient that depends from rigidity (momentum per unit of charge, $\rho = \frac{p}{Z}$) $D_{xx} = \beta D_0(\rho/\rho_0)^\delta$. The convection velocity field $\mathbf{V}_c$, that corresponds to the Galactic wind, has a cylindrical symmetry and its z-component is the only one different from zero. It increases linearly with the distance z from the galactic plane , in agreement with magnetohydrodynamical models [3]. Reacceleration is determined by the diffusion coefficient for the impulse space D_{pp} that is a function of the corresponding configuration space diffusion coefficient and of the Alfven velocity V_A in the framework of quasi-linear MHD theory [2]. Of course, Alfven velocity and convection velocity gradient in Milky Way for reacceleration and convection terms are unknown parameters of propagation (there are no other sources of information from which we could extract them, except the spectra of cosmic rays) and their possible range will be constrained by the analysis of fits of suitable data.

The same procedure is valid for constraining the height of the galactic halo and the other unknown parameters. This will be analyzed further in order to obtain all the possible spectra of antiprotons and positrons using the
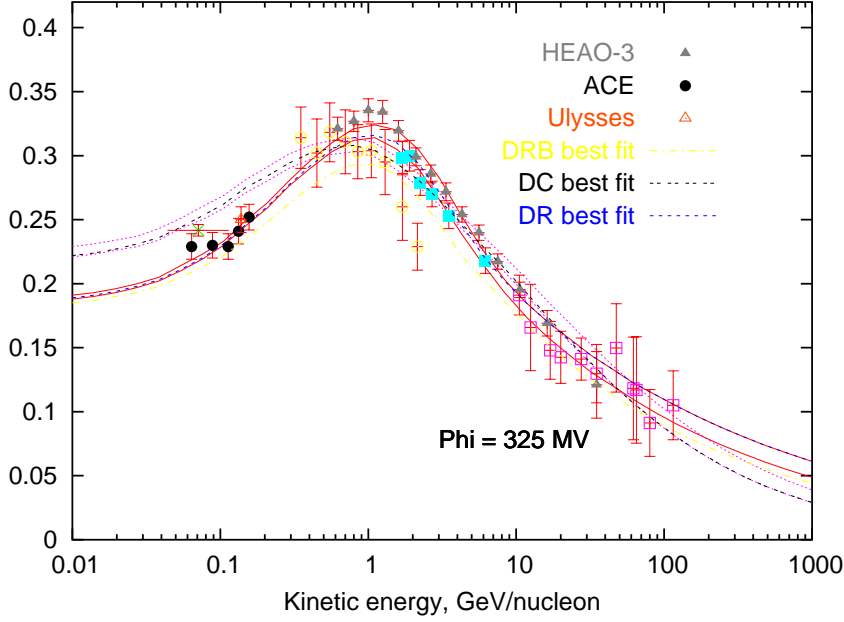
Figure 1: Enveloping curves of all the good fits of B/C data [11] for DR and DC model with their best fits inside and the best fit for DRB model.

sets of the constrained parameters. Injected spectra of all primary nuclei are power law in impulse $dq(p)/dp \propto p^{-\gamma}$. This power law approximation has been shown to be allowed in the framework of diffusive shock acceleration models, as well as in model with a small break in the injection indexes γ [4, 6]. Source term $q(\mathbf{r}, p)$ for secondaries contains cross sections for their production from progenitors on H and He targets. The last two terms in equation 1 are loss terms with characteristic times for fragmentation and radioactive decay. Propagation equation is solved numerically, using the Crank-Nicholson algorithm.

The heliospheric modulation in the vicinity of the Earth has to be taken in account. We have used a model in which transport equation (that describes diffusion processes in the heliosphere and includes effects of heliospheric magnetic field and solar wind) is solved in the force field approximation [7]. In this case solar modulation is a function of just a single parameter that describes the strength of the modulation. All the dynamical processes are simulated with relatively simple changing of the interstellar spectra during the propagation inside the heliosphere, described by the formula
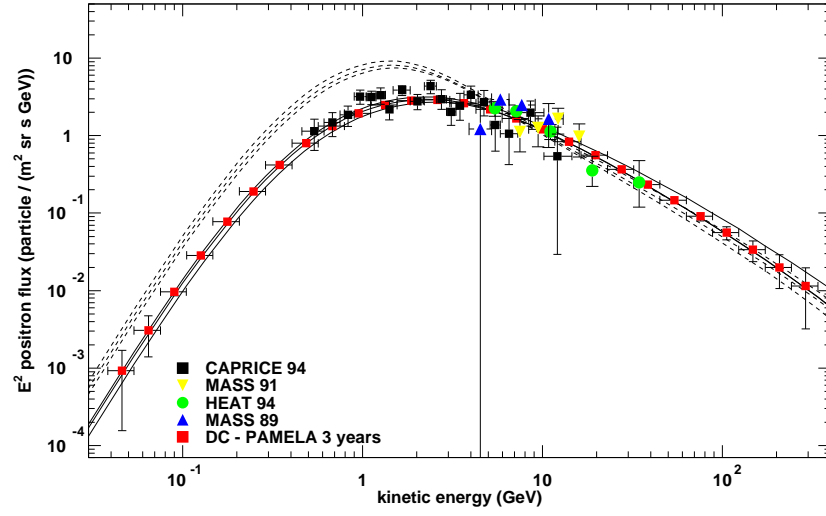
Figure 2: Total uncertainties of e^+ fluxes and spectra that correspond to the parameters of the best B/C fit for DC, DR and DRB model. Experimental data (from [8]) vs. PAMELA expectations for DC model.

$$\frac{\Phi^{toa}(E^{toa})}{\Phi^{is}(E^{is})} = (\frac{p^{toa}}{p^{is}})^2, \tag{2}$$

$$E^{is} - E^{toa} = |Ze|\phi \tag{3}$$

where E and p are energies and impulses of the interstellar and top of the atmosphere fluxes and ϕ is the unique parameter that determines the solar modulation.

2 Uncertainties of CR Spectra

We were treating the two extreme cases of propagation models: the first that uses diffusion and reacceleration (DR) and the second that contains diffusion and convection (DC) [5]. Many parameters in the propagation equation are free and must be constrained by experimental data. Secondary to primary CR ratios are the most sensitive quantities on variation of the propagation

parameters. The most accurately measured parameter is boron to carbon ratio (B/C). We have used a standard χ^2 test:

$$\chi^2 = \sum_n \frac{1}{(\sigma_n^{B/C_{exp}})^2} (\Phi_n^{B/C_{exp}} - \Phi_n^{B/C_{teo}})^2 \qquad (4)$$

For DR model we have required reduced χ^2 less than 2 for the fit of the experimental data [11] (fig. 1). We take the data with relatively small solar modulation between 325 MV and 600 MV where the force field approximation is better justified than for high modulation parameters. The allowed ranges of all parameters are given in table 1. Using them we have found the enveloping curves of all the e^+ and $\bar{p}$ spectra that present upper and lower bounds of uncertainty band. For e^+ relative uncertainty is varying from 30% under 1 GeV to 15% around 10 GeV while for $\bar{p}$ is from about 10% up to 15%.

For DC model (fig. 1) we have taken all the reduced χ^2 values less than 2.8 for the variation of D_0, diffusion indexes δ_1, below, and δ_2, above the reference rigidity $\rho_0 = 4$ GV, z, V_c and injection index for primary nuclei γ_1 below the reference rigidity $\rho_0^\gamma = 20$ GV and γ_2 above it. Positive variations around $\delta_1 = 0$ gave unsatisfactory fit. In order to take the smallest possible break of this index we have decided not to take negative δ_1 values. Allowed values for the propagation parameters can be found in table 2. The same analysis as for DR model gives relative e^+ error between 20% above the maximum and 30% below it while for $\bar{p}$ is about 20% around 20 MeV, 17% around the maximum and 25% around 20 GeV. We calculated PAMELA expectations for e^+ (fig. 2) and $\bar{p}$ (fig. 3) (parameters of the best B/C fit) using its geometrical factor and detector characteristics [8] during the three years mission in which it will measure with high statistics various cosmic rays spectra. We have found also spectra that correspond to the parameters of the best fit of B/C data for subFe/Fe ratio (another important ratio for testing the parameters of the propagation models, protons, He and e^- as well as corresponding uncertainties. For DC model fits are good, while DR overestimates p, He and e^-.

We have also seen how the obtained antiproton spectra change on variation of the most important antiproton production cross sections. Those are reactions that include all the types of hydrogen and helium. Antiprotons are created in the interactions of primary cosmic rays (protons and other nuclei) of sufficiently high energies with interstellar gas. Dominant processes are interactions of high energy primary protons with hydrogen, for example $p + p \rightarrow p + p + p + \bar{p}$. Parameterization of this cross sections used in our version of Galprop code is given by Tan and Ng [9]. Other used cross sections, those of primary protons with other nuclei, are studied in reference [10]. From these, the most important are those that involve helium and they contribute less than 20% of the total production of all the antiprotons. All the heavier nuclei together give just a few percents of the total production. Simultaneous settings of all the production
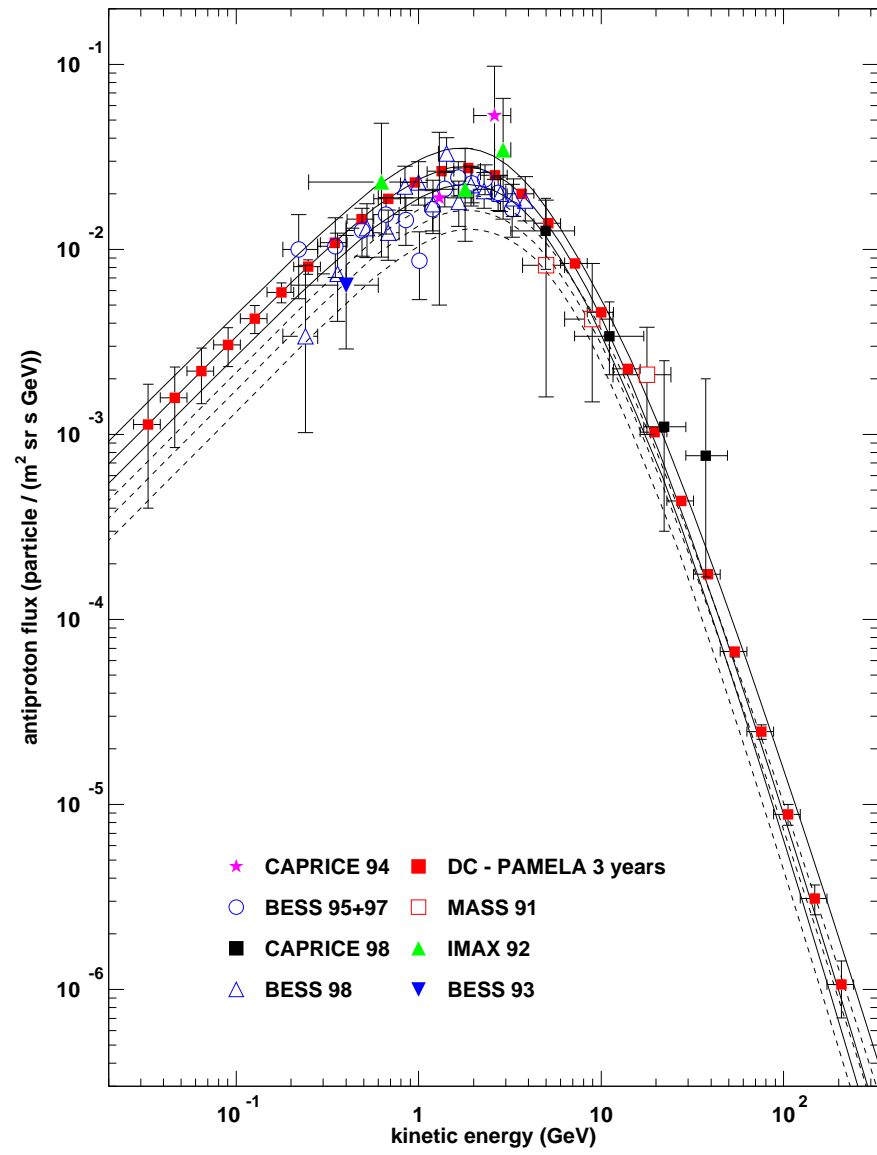
Figure 3: Total uncertainty of $\bar{p}$ fluxes and spectra that correspond to the parameters of the best B/C fit for DC and DRB model. Experimental data (from [8]) vs. PAMELA expectations for DC and DRB model.

cross sections to the maximum/minimum rise/lower the upper/lower parameter uncertainty bounds. Errors obtained in this way give contributions to the total uncertainties varying from 20% up to 25% in the case of DR model and, almost the same, from 20% up to 24% for DC model, depending of the energy range of the spectra. Non production cross sections, the so called tertiary component, correspond to inelastically scattered secondaries $\bar{p} + X \rightarrow \bar{p} + \tilde{X}$. Those processes tend to bring down the energies of the antiprotons of relatively high energies, flattening like that the spectra. But, even if their uncertainty is relatively big, this does not give relevant change of the spectra because tertiary contribution is very small.

Changing of another exactly unknown quantity, He/H ratio, in a reasonable range from 0.08 to 0.11 gives a relatively small contribution, that vary from 3% - 7% depending of the energy, for both e^+ and $\bar{p}$ uncertainty, and for both of the models. Total uncertainties of e^+ and $\bar{p}$ are presented at fig. 2 and fig. 3 respectively. They vary from 35% up to 55% for antiprotons and from 20% up to 40% for positrons roughly for both of the models in the current experimental data energy range.

3   Conclusions

For e^+ in DR model even when the uncertainties are included the curve of the minimal e^+ production still remains above the experimental results. Breaking the primary spectra gently improves just the low energy part of the spectra below the maximum, but even the minimal predictions still remain bigger than the experimental results around the maximum as well as below it. On the other side, this disturbs a little the best B/C fit (fig. 1), it is not sufficient to match protons and helium, that are still overestimated and, in the end, e^- remain largely overproduced at low energies, even more than without the break. Uncertainty bands of $\bar{p}$ in DR models touch the experimental data from below, which can be improved easily with any primary component that is coming from eventual neutralino annihilation or some other exotic contribution. For DC model all the results are good, with some problems with B/C data only. In this framework exotic contributions remain possible at high energies (E > 20 GeV), and at lower energies due to the relatively large uncertainties.

References

[1] Strong, A. W., Moskalenko, I. V., 1998, ApJ, 509, 212.

[2] Fermi, E., 1949, Phys. Rev., 75, 1169; Seo, E. S., Ptuskin, V. S., 1994, ApJ, 431, 705; Berezinskii, V. S., Bulanov, S. V., Dogiel, V. A., Ginzburg, V. L., Ptuskin, V. S. 1990, Astrophysics of Cosmic Rays (North Holland, Amsterdam).

[3] Zirakashvili, V. N., Breitschwerdt, D., Ptuskin, V. S., Volk, H. J., 1996, A&A, 311, 113

[4] Blandford, R. D. & Ostriker, J. P. (1980) ApJ, 237, 793; Strong, A. W., Mattox, J. R., 1996, 308, L21.

[5] Moskalenko, I. V., Strong, A. W., Ormes, J. F., Potgieter, M. S., 2002, ApJ, 565, 280.

[6] Ellison, D. C., Slane, P., Gaensler, B. M., astro-ph/0106257.

[7] Gleeson, L. J., Axford, W. I., 1996, ApJ, 154, 1011; Perko, J. S., 1987, A&A, 184, 119.

[8] Picozza, P., Morselli A., 2003. J. Phys. G: Nucl. Part. Phys., 29, 903-911.

[9] Tan, L. C., Ng, L. K., 1983, J. Phys. G, 9, 227 and 1289.

[10] Gaisser, T. K., Schaefer, R. K., 1992, ApJ, 394, 174.

[11] ACE: A. J. Davis at al., 2000, AIP Conf. Proc. 528, ed. R. A. Mewaldtet al. (AIP, New York); Ulysses: Du Vernois, M. A. at al., 1996, A&A, 316, 555; Voyager: A. Lukasiak et al., 1999, Proc. 26th Int. Cosmic-Ray Conf. (Salt Lake City), 3, 41; HEAO 3: Engelmann, J. J. et al., 1990, A&A, 233, 96; Caldwell, J. H., Meyer, P., 1977, Proc. 15th Int. Cosmic-Ray Conf. (Plovdiv), 1, 243; Dwyer, R. 1978, ApJ, 224, 691; Juliusson, E. 1974, ApJ, 191, 331; Simon, M., et al. 1980, ApJ, 239, 712.

PRODUCTION OF SECONDARY LIGHT ANTIMATTER NUCLEI IN THE GALAXY AND IN THE ATMOSPHERE

B. Baret[a], R. Duperray[a], L. Derome[a], D. Maurin[b], K. Protasov[a],
M. Buénerd[a]

[a] *Laboratoire de Physique Subatomique et Cosmologie, CNRS/IN2P3,*
53 Av. des Martyrs, 38026 Grenoble cedex, France

[b] *Service d'Astrophysique, SAp CEA-Saclay,*
F-91191 Gif-sur-Yvette CEDEX, France

Abstract

The flux of light antinuclei A$\leq$ 4 induced near earth by Cosmic Ray interactions with the interstellar matter in the Galaxy and with the earth atmosphere is calculated in a proven phenomenological framework and with parameters fitted on experimental data. The hadronic production of antinucleons is based on a recent parametrization of a wide set of accelerator data. The production of light anti-nuclei is calculated using coalescence models tested on the available experimental data. The non annihilating inelastic scattering process for the $\bar{d}$ and $\bar{p}$ is taken into account as well as the contribution of the $\bar{p}A$ interaction for the production of antimatter.

1   Introduction

The search for primordial antimatter is one of the most challenging current prospects for Cosmic Ray physics. Antiprotons and antideutons also constitute a probe for revealing the nature of dark matter. New satellite experiments will undertake these in the forthcoming years complementing existing balloon borne experiments. It is thus of great importance to get the best possible knowledge of the flux of locally produced antimatter. After having presented the necessary nuclear interaction models, the results of the calculus of the galactic secondary production within the Leaky Box Model and of the corresponding atmospheric production thanks to a Monte Carlo simulation will be presented.

2   Nuclear processes

The $\bar{p}$ production differential cross section from interactions on nuclei and nucleon used here is an improved analytical form fitted on a large amount of data [1] already used in a previous work of estimation of atmospheric $\bar{p}$ fluxes [2].

The production of light antimatter, namely $\bar{d}$, $\bar{t}$, $^3\bar{He}$ and $^4\bar{He}$, has been considered in the framework of the simple coalescence model. This model is based on the idea that two particles in hot nuclear matter will coalesce if they are found within a certain range - the coalescence radius - in the configuration space, or equivalently a certain relative momentum in the center-of-mass - the coalescence momentum - in the phase space [3]. The momentum spectrum for a nucleus of mass A produced by coalescence can then be expressed as the Ath power of the antinucleon spectrum from the same reaction, times a coalescence coefficient.

This model has been applied to a set of antideuteron cross section production data available. The results obtained from a fit of a selected sample of data leads to a coalescence momentum parameter value p_0=79 MeV/c [4]. This value is 30% higher than the value previouly used in [5], which is quite important since it goes withe the $3(A-1)^{th}$ power in the expression of the coalescence coefficient.

Antiparticle can suffer non annihilating inelastic rescattering (NAR) with matter particles. This is equivalent to an energy loss and thus will populate the low energy region. Since signal like dark matter annihilation are searched in this range, the phenomenon has to be taken into account carefully. This has been done for galactic and atmospheric $\bar{p}$ and $\bar{d}$ in a more realistic way than the previous works, based on the few data available [4][6].

Besides the classical pA interactions, the antimatter production from $\bar{p}A$ has been included. This phenomenon accounts for the production of a $\bar{d}$ for example from an incident $\bar{p}$ which will undergo a NAR in the target and produce an antineutron in it. These two antinucleons will then coalesce to form a $\bar{d}$.
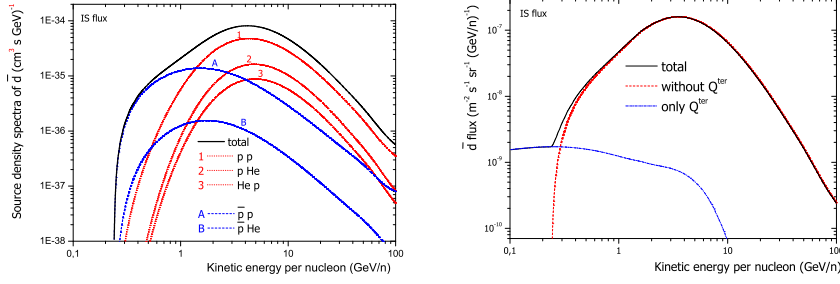
Figure 1: Left panel: contributions of the different channels in the $\bar{d}$ secondary source term. Right panel: $\bar{d}$ secondary source term with and without NAR contribution

The fact that the $\bar{p}$ flux is five order of magnitude smaller than the proton flux is counterbalanced by the fact that only one antinucleon has to be created [1]. As we will see in the study of the galactic source term, the contribution of this phenomenon is non negligible.

3   Galactic production

The galactic propagated fluxes resulting from the interactions presented above are now presented in the framework of the leaky box model. The model is simple, widely successful and highly useful. It relies on a single effective phenomenological parameter - the escape length λ_{esc} [7] - incorporating the physics (diffusion and convection) of the transport process. It is an economical direct way to provide results on secondary fluxes. Therefore, it is very well suited to address the impact of the cross sections used here on the $\bar{p}$ and $\bar{d}$ fluxes. $\lambda_{esc}(T_{\bar{A}})$ is taken from [8] and the composition and density of the ISM are from [9]. Since these numbers are not perfectly known, the results have been checked to fit the experimental $\bar{p}$ spectrum.

The importance of the new ingredients with respect to the previous works for $\bar{d}$ production can be seen on the figure 1 on the source terms. On the left panel one can see that the $\bar{p}p$ channel populates significantly the low energy range, where DM signals will be searched. On the right panel one can see the contribution of the NAR component. It is significant only at very low energies, *i.e.* below 200 MeV per nucleon. Consequently it will be washed out by the solar modulation which is equivalent to a shift of the spectrum toward low energies.

The spectral distributions of the calculated galactic fluxes for mass 1 to 4
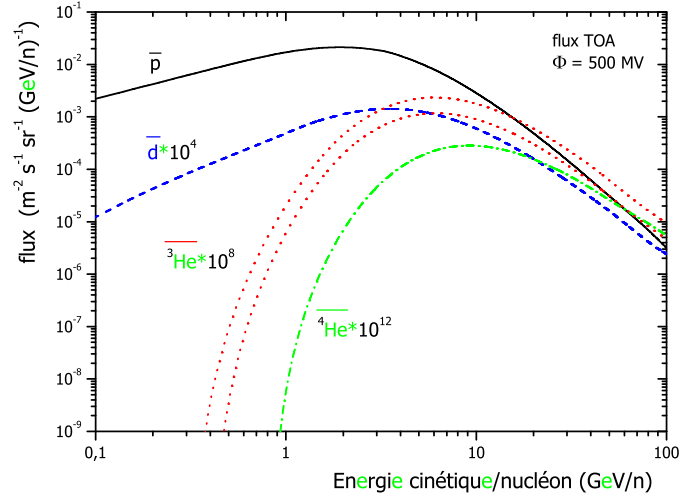
Figure 2: Galactic modulated secondary fluxes of $\bar{p}$, $\bar{d}$, $^3\bar{H}e$ and $^4\bar{H}e$ multiplied by the indicated factors for convenience (see text).

antinuclei are displayed on Fig. 2 . The calculated $\bar{d}$, $^3\bar{H}e$ and $^4\bar{H}e$ flux have been multiplied by 10^4, 10^8, 10^{12} respectively for presentation purpose. These fluxes are significantly higher than those derived in [10], the difference being mainly due to the larger value of the coalescence momentum used in this work. The upper of the two dashed lines for $^3\bar{H}e$ includes the addition of the $\bar{t}$ flux, this latter nucleus decaying into $^3\bar{H}e$ in about 12 years.

4   Atmospheric production

The estimation of the secondary antinuclei fluxes of atmospheric origin has been calculated thanks to a three dimensional Monte Carlo simulation of the propagation and interaction of particles in the Earth's atmoshere and magnetic field. This simulation has succesfully accounted for the secondary fluxes of protons and light nuclei and is discribed in [11].

Recent $\bar{p}$ data at balloon and mountain altitudes have been compared with the simulation result. At 2770 m and 38 km the amount of matter above the detector are respectively 930 g/cm^2 and 5 g/cm^2 which represent approximately 10 and 1/10 interaction length. The results have been found to be in fair agreement with the data at 2770 m and the previous calculations [12] based on
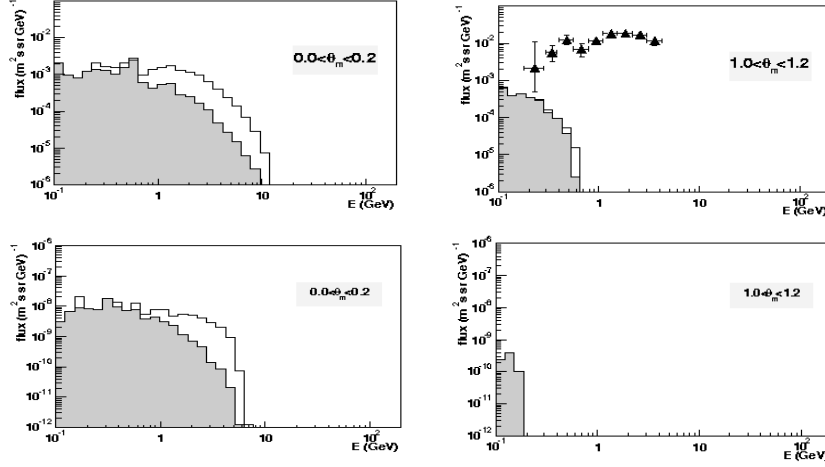
Figure 3: Calculated downward $\bar{p}$ (top) and $\bar{d}$ (down) fluxes at 400km for equatorial (left) and polar (right) geomagnetic latitude θ_m. The grey histogram represents the NAR contribution and the full circle the $\bar{p}$ BESS99 data [12]

Particles number	$\bar{p}$	$\bar{d}$	^3He	^4He
Galactic	10^6	15	10^{-3}	10^{-7}
Atmospheric	5×10^5	3-4	10^{-4}	10^{-9}

Table 1: Approximate expected number of secondary particles for 3 years of data taking of the AMS02 experiment.

tranportation equation resolution at 38 km.

The spectra at satellite altitude (400 km) present radically different features since particles have been geomagnetically trapped as can be seen on figure 3. This has two important consequences for $\bar{p}$ and $\bar{d}$. First, their dynamics in the Earth magnetic field is such that their fluxes is significant only under the geomagnetic cut-off. This means that it will be possible to separate them from the galactic fluxes. Secondly the mechanism of magnetic trapping favours low energy particles. This explains why the NAR component is so important and even dominant at this altitude since this phenomenon decreases the particle's energy and makes them hence more easely trapped.

5 Conclusion

The number of antinuclei for three year of data taking with the AMS experiment is presented in the table 1. The much smaller amount of particles of atmospheric origin compared to the galactic fluxes comes from the magnetic trapping. Indeed these particles are produced at high energy and the trapping favours low energy particles. The large amount of atmospheric $\bar{p}$ will provide a good test for nuclear models and the spectral shape will allow a separation between galactic and atmospheric secondaries. AMS02 may detect some $\bar{d}$ from galactic and even atmospheric origin, but no $\bar{H}e$ which therefore remains a good candidate for primordial antimatter search.

References

[1] R. Duperray et al., Phys.Rev. D68:094017(2003).

[2] C.Y.Huang et al., Phys.Rev. D68:53008(2003).

[3] S.T. Butler and C.A. Pearson, Phys. Rev. 129,836(1963).

[4] R. Duperray et al.Eur. Phys. J. A16,27(2003).

[5] F. Donato, N. Fornengo, and P. Salati, Phys.Rev. D62:043003(2000).

[6] B. Baret, PhD Thesis, Université Joseph Fourier, Grenoble, France, October 2004.

[7] F.C. Jones, A. Lukasiak, V. Ptuskin and W. Webber, Astroph. J. 547,264(2001).

[8] W.R. Webber et al., Astroph. J. 457,435(1996).

[9] M. Simon, A. Molnar, and S. Roesler, ApJ499(1998)250.

[10] P. Chardonnet, J. Orloff, and P. Salati, Phys. Lett. B409,313(1997). A. Shwarzshild and C. Zupančic Phys. Rev. 129,854(1963).

[11] L. Derome et al., Phys. Lett. B489,1(2000); L. Derome and M. Buénerd Phys. Lett. B529,139(2001).

[12] Y. Asoaka et al., Phys. Rev. Lett. 88,051101(2002).

[13] S.T. Maeno et al., Astro. Part. Phys. 16,121(2001).

Part IV

DARK MATTER

SUPERSYMMETRIC MODELS: SUSY CANDIDATES FOR DARK MATTER

A. Bottino[a]

[a] *Università di Torino, Dipartimento di Fisica Teorica and Istituto Nazionale di Fisica Nucleare, Sezione di Torino Via P. Giuria 1, 10125, Torino, Italia,*
E-mail: bottino@to.infn.it

Abstract

Cosmological observations point to the existence of a considerable amount of dark matter in the Universe. To find particles suitable to describe this matter one has to resort to extensions of the Standard Model. Here we discuss how supersymmetry, which is one of the best motivated among these extensions, offers quite interesting candidates for cold dark matter. Relic neutralino is discussed in detail.

1 Dark Matter in the Universe

As discussed in a number of talks at this conference, new data on Cosmic Microwave Background (CMB) and Large Scale Structure (LSS) are providing determinations of the matter/energy contents of the Cosmos with remarkable precision. These results refine previous determinations of the matter/energy budget in our Universe, which may be summarised as follows: i) a host of

independent observational data on galactic halos, clusters of galaxies, and large scale structures point to the following range for the matter density: $0.2 \lesssim \Omega_m \lesssim 0.4$ (notice that for any constituent i we define, as usual, $\Omega_i \equiv \rho_i/\rho_{crit}$, where ρ_i is the density of that constituent and $\rho_{crit} \equiv 3H_0^2/(8\,\pi\,G) = 1.88 \times 10^{-29}\ h^2\ g \cdot cm^{-3}$; h is the Hubble parameter, defined as $h = H_0/(100\ km \cdot s^{-1} \cdot Mpc^{-1})$); ii) CMB measurements (see, for instance, Refs.[1, 2, 3]) give that the total density in the Universe is close to the critical one: $\Omega \simeq 1$; iii) high-redshift SNIa measurements (High-z SN Search [4], SN Cosmology Project [5]) give $0.8\ \Omega_m - 0.6\ \Omega_\Lambda \simeq -0.2 \pm 0.1$. Using $\Omega = \Omega_m + \Omega_\Lambda$ and any pair of the previous three points, one obtains $\Omega_m \sim 0.3$, $\Omega_\Lambda \sim 0.7$.

What is the nature of the matter density? As far as visible matter is concerned, observationally we have $\Omega_{vis} \lesssim 0.01$. Furthermore, from primordial nucleosynthesis it turns out that the baryonic abundance is $0.019 \lesssim \Omega_b h^2 \lesssim 0.021$ or $0.03 \lesssim \Omega_b \lesssim 0.05$ (in very good agreement with measurements of CMB acoustic peaks). Thus, combining this data with the previously quoted range $0.2 \lesssim \Omega_m \lesssim 0.4$, one concludes that: i) some dark matter is baryonic, but ii) most of it is non-baryonic.

Thus, it turns out that to find particles suitable to constitute the big bulk of dark matter we have to resort to extensions of the Standard Model. One trivial extension of the SM is provided by light neutrinos ($m_\nu < 1\ MeV$). However, these particles fall into the category of hot relics (that is, particles which decouple from the primordial plasma, when they are relativistic).

The theory of formation of cosmological structures implies that small-scale structures are erased by hot relics, because of free-streaming. The suppression of power spectrum on small scales induced by light neutrinos can be quantified as follows [6]

$$\frac{\Delta P_m}{P_m} \simeq -8\frac{\Omega_\nu}{\Omega_m}. \tag{1}$$

Using the data of the 2dF Galaxy Redshift Survey [7] one puts a bound on the density contribution due to light neutrinos as compared to the total matter contribution:

$$\frac{\Omega_\nu}{\Omega_m} < 0.13. \tag{2}$$

This means that the big bulk of dark matter has to be made up of cold relics, that is, particles which decouple from the primordial plasma, when they are non-relativistic. These particles have to be massive, stable (or their lifetime must be at least of the order of the age of the Universe), and have to be only weakly interacting. Hence their generic name: WIMPs.

Before we move to some physical candidate for these cold relics, let us mention how recently combined analyses of LSS properties and CMB data

have provided new, accurate determinations of various cosmological parameters (though dependent on the assumption of some priors). By combining WMAP results with the 2dF Galaxy Survey and Lyman α forest data, in Ref. [8] one derives the following range for the CDM relic abundance: $\Omega_{CDM}h^2 = 0.1126 \pm 0.009$. Based on these results, in the following we will assume that the cold dark matter is bounded at 2σ level by the values: $(\Omega_{CDM}h^2)_{\min} = 0.095$ and $(\Omega_{CDM}h^2)_{\max} = 0.131$. An independent determination (Ω_{CDM} is provided by the Sloan Digital Sky Survey Collaboration [9]; this new data agrees with the results of Ref. [8].

Many various extensions of the Standard Model provide good candidates for WIMPs. No doubt that one of the most interesting extensions of the SM is represented by supersymmetric theories, for a number of basic reasons related to particle physics. As an extra bonus, supersymmetric theories can naturally offer very appealing candidates for cold dark matter.

2 Supersymmetric models

Though theoretically well motivated, Susy theories still miss experimental validation. Thus, there exist a large variety of schemes; this situation prevent the theory from being really predictive.

One of the major unknowns is due to the supersymmetry-breaking mechanism. Three main schemes are usually investigated: the gravity-mediated mechanism, the gauge-mediated, and the anomaly-mediated one. The nature of the LSP depends on the susy-breaking mechanism and on the region of the parameter space. In what follows we discuss some phenomenological implications of the Minimal Supersymmetric extension of the Standard Model (MSSM) in the gravity-mediated scheme and in regions of the parameter space where the LSP is the neutralino [10].

The model we employ here is an effective MSSM scheme at the electroweak scale, defined in terms of a minimal number of parameters, only those necessary to shape the essentials of the theoretical structure of MSSM and of its particle content. In our model no gaugino-mass unification at a Gut scale is assumed. The assumptions that we impose at the electroweak scale are: a) all squark soft–mass parameters are degenerate: $m_{\tilde{q}_i} \equiv m_{\tilde{q}}$; b) all slepton soft–mass parameters are degenerate: $m_{\tilde{l}_i} \equiv m_{\tilde{l}}$; c) all trilinear parameters vanish except those of the third family, which are defined in terms of a common dimensionless parameter A: $A_{\tilde{b}} = A_{\tilde{t}} \equiv A m_{\tilde{q}}$ and $A_{\tilde{\tau}} \equiv A m_{\tilde{l}}$. As a consequence, the supersymmetric parameter space consists of the following independent parameters: $M_2, \mu, \tan\beta, m_A, m_{\tilde{q}}, m_{\tilde{l}}, A$ and R. In the previous list of parameters we have denoted by μ the Higgs mixing mass parameter, by $\tan\beta$ the ratio of the two Higgs v.e.v.'s, by m_A the mass of the CP-odd neutral Higgs boson and by R the ratio of the U(1) gaugino mass to the SU(2) one,

i.e.: $R \equiv M_1/M_2$.

This model has been discussed in Refs. [11, 12, 13, 14]. In this series of papers it has been derived that, in models where gaugino-mass unification is not assumed, the present lower limit on neutralino mass is provided by the cosmological upper bound on the cold dark matter abundance (one finds $m_\chi \gtrsim$ 7 GeV. In Refs. [12, 13, 14] theoretical expectations for direct and indirect searches of relic neutralinos are discussed, with particular emphasis for the light ones (*i.e.* those with $m_\chi \lesssim 50$ GeV). Notice that in models with gaugino mass unification the lower bound $m_\chi \gtrsim 50$ GeV follows from the LEP lower bound on the chargino mass.

We report now some results derived in [12, 13, 14] for the expected rates for direct and indirect detection. In the numerical random scanning of the supersymmetric parameter space the following ranges are used: $1 \leq \tan\beta \leq 50$, 100 GeV $\leq |\mu|$, $M_2 \leq 1000$ GeV, 100 GeV $\leq m_{\tilde{q}}, m_{\tilde{l}} \leq 1000$ GeV, sign(μ) = $-1, 1$, 90 GeV $\leq m_A \leq 1000$ GeV, $-3 \leq A \leq 3$, $0.01 \leq R \leq 0.5$. The following experimental constraints are imposed: accelerators data on supersymmetric and Higgs boson searches, measurements of the $b \rightarrow s + \gamma$ decay and of the muon anomalous magnetic moment $a_\mu \equiv (g_\mu - 2)/2$. The range used here for the $b \rightarrow s + \gamma$ branching ratio is $2.18 \times 10^{-4} \leq BR(b \rightarrow s + \gamma) \leq 4.28 \times 10^{-4}$. For the deviation of the current experimental world average of a_μ from the theoretical evaluation within the Standard Model we use the 2σ range: $-142 \leq \Delta a_\mu \cdot 10^{11} \leq 474$; this interval takes into account the recent evaluations of Refs. [15, 16]. Also the current upper limit of the branching ratio of $B_s \rightarrow \mu^+ + \mu^-$ is included [14].

3   Direct detection

For neutralino-matter interactions, coherent effects systematically dominate over spin-dependent ones, thus the rates for direct detection are conveniently expressed in terms of the quantity $\xi\sigma_{\text{scalar}}^{(\text{nucleon})}$ [17], where $\sigma_{\text{scalar}}^{(\text{nucleon})}$ is the neutralino–nucleon scalar cross–section and ξ is a rescaling factor between the neutralino local matter density ρ_χ and the total local dark matter density ρ_0: $\xi \equiv \rho_\chi/\rho_0$. Following a standard assumption, ξ is taken as $\xi = \min(1, \Omega_\chi h^2/(\Omega_{CDM} h^2)_{\min})$.

In Fig. 1 we display the scatter plot of the quantity $\xi\sigma_{\text{scalar}}^{(\text{nucleon})}$ as a function of m_χ. This scatter plot shows that, in the mass range 6 GeV $\lesssim m_\chi \lesssim 25$ GeV, the quantity $\xi\sigma_{\text{scalar}}^{(\text{nucleon})}$ falls in a narrow funnel ; this funnel is delimited from below by configurations with $\Omega_\chi h^2 \sim (\Omega_{CDM} h^2)_{\max} = 0.131$, and delimited from above by supersymmetric configurations with a very light Higgs boson (close to its lower experimental bound of 90 GeV) and with an $\Omega_\chi h^2$ below $(\Omega_{CDM} h^2)_{\min}$. For $m_\chi \lesssim 10$ GeV only values of $30 \lesssim \tan\beta \leq 50$ and 100 GeV $\leq |\mu| \lesssim 300$ GeV contribute, while in the interval 10 GeV $\lesssim m_\chi \lesssim 25$
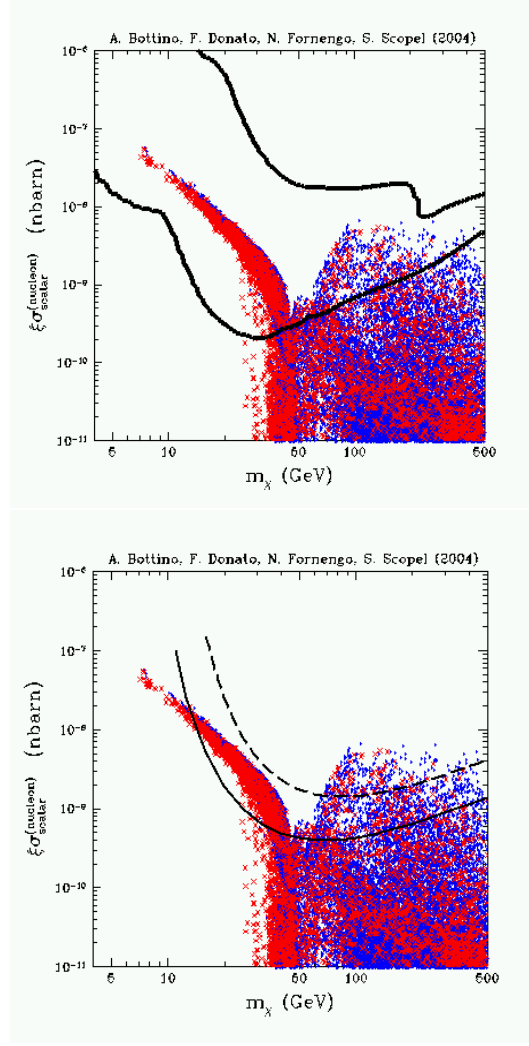
Figure 1: Scatter plot of $\xi\sigma_{\text{scalar}}^{(\text{nucleon})}$ versus m_χ. Crosses (red) and dots (blue) denote neutralino configurations with $\Omega_\chi h^2 \geq (\Omega_{CDM} h^2)_{\min}$ and $\Omega_\chi h^2 < (\Omega_{CDM} h^2)_{\min}$, respectively $((\Omega_{CDM} h^2)_{\min} = 0.095)$ (a) The curves delimit the DAMA region where the likelihood-function values are distant more than 4σ from the null (absence of modulation) hypothesis [18]; this region is the union of the regions obtained by varying the WIMP DF over the set considered in Ref. [21]. (b) The solid and the dashed lines are the experimental upper bounds given by the CDMS [19] and the EDELWEISS [20] Collaborations, respectively, under the hypothesis that the WIMP DF is given by an isothermal distribution with a standard set of astrophysical parameters.

GeV $\tan\beta$ extends also to lower values around 8 and $|\mu|$ is not significantly constrained. Moreover, for $m_\chi \lesssim 20$ GeV, m_A is strongly bounded from above by $(\Omega_{CDM}h^2)_{\max}$. Notice that the dip at $\simeq 45$ GeV is due to the Z–pole in the annihilation cross–section.

It is also remarkable that, within the funnel, the size of $\xi\sigma_{\text{scalar}}^{(\text{nucleon})}$ is large enough to make light relic neutralinos explorable by WIMP direct experiments with the current sensitivities. To illustrate this point, in Fig. 1 the theoretical predictions of Refs. [12, 13, 14] are compared with the experimental data of Refs. [18, 19, 20]. In panel (a) the contour line of the annual modulation of Ref.[18] is shown, in panel (b) the upper bounds of Refs. [19, 20] are displayed.

In deriving its contour line, the DAMA Collaboration has taken into account a rather large class of possible phase–space distribution functions (DF) for WIMPs in the galactic halo. The categories of DFs considered in Ref. [18] are those analyzed in Ref. [21]; the annual–modulation region displayed in Fig. 1, panel (a), is the union of the regions obtained by varying over the set of the DFs considered in Ref. [21]. From Fig. 1(a) it is derived that the entire population of relic neutralinos with $m_\chi \lesssim 25$ GeV as well as a significant portion of those with a mass up to about 50 GeV are within the annual–modulation region of the DAMA Collaboration. Thus, this yearly effect could be due to relic neutralinos of light masses, in alternative to the other possibility already discussed in Refs. [17] on neutralinos with masses above 50 GeV.

The experimental upper bounds of Refs.[19, 20], displayed in panel (b) of Figure 1, are derived under the assumption of an isothermal distribution and for a single set of the astrophysical parameters: $\rho_0 = 0.3$ GeV $\cdot$ cm^{-3}, $v_0 = 220$ km $\cdot$ s^{-1} (v_0 is the local rotational velocity). For the case of light neutralinos the EDELWEISS bound (dashed line) is marginal, the one from CDMS (solid line) can potentially put constraints on neutralino masses in the 10 GeV $\lesssim m_\chi \lesssim$ 20 GeV. However, to set a solid constraint on the theoretical predictions, it is necessary to derive from the experimental data the upper bounds on $\xi\sigma_{\text{scalar}}^{(\text{nucleon})}$ for a large variety of DFs and of the corresponding astrophysical parameters (with their own uncertainties); the intersection of these bounds would provide an absolute limit to be used to possibly exclude a subset of supersymmetric population. An investigation by the CDMS Collaboration along these lines would be very interesting. It is worth noticing that a more effective comparison of theoretical results with experimental data will be feasible, only when the analysis of different experimental results in terms of $m_\chi - \xi\sigma_{\text{scalar}}^{(\text{nucleon})}$ is presented for each analytic form of the DF, separately. This is also the unique way of comparing results of different experiments among themselves.

4 Indirect detection

Indirect signals can be produced by neutralino self–annihilations in the galactic halo or inside celestial bodies. In Ref. [14] theoretical predictions of indirect rates for relic neutralinos are compared with current experimental data on measurements of gamma–rays and antiprotons in space and of up-going muons at neutrino telescopes; results are presented for a wide range of the neutralino mass, from the established lower bound of 7 GeV up to 500 GeV. The main conclusions can be summarised as follows (for details we refer to [14]): 1) Present data on gamma-rays do not put any constraints on the supersymmetric flux, unless very steep density profiles, disfavored by current simulations, are employed; however, it is shown that, in case of a significant enhancement effect as compared to the Navarro-Frank-White distribution, the EGRET excess could be explained by a neutralino of a mass around 30-40 GeV. 2) The present measurements of up-going muons from the center of the Earth put some constraints on neutralino configurations for masses above 50 GeV. For lighter neutralinos, explorations by neutrino telescopes require a substantial increase in sensitivity with an energy threshold close to 1 GeV. Investigations of light neutralinos by up-going muons from the Sun are very disfavored. 3) In the case of cosmic antiprotons, no constraint on the supersymmetric parameters can be derived, if one assumes a very conservative attitude in the selection of the propagation parameters. However, it is remarkable that indeed the signal at very small masses is close to the level of detectability. Some breakthrough in the knowledge of the astrophysical parameters could allow a significant exploration of small mass configurations. This is particularly true for neutralino masses below about 15 GeV.

The case of antiprotons is particularly worth of some details. The secondary antiproton flux already provides a satisfactory agreement with current experimental data, and then no much room is left to primary contributions. This situation suggests that antiproton data could be used to place significant constraints on supersymmetric parameters. However, one has to notice that, as shown in [22], the supersymmetric primary flux is affected by uncertainties much larger than those related to the secondary flux. This is due to the fact that the sources of the latter are located in the galactic disk. On the contrary, the relic neutralinos are expected to be distributed in the whole galactic halo and then produce an antiproton flux much more sensitive to the astrophysical parameters.

To show quantitatively how the experimental data could constrain the supersymmetric parameters, in Fig. 2 we display the antiproton flux evaluated at $T_{\bar{p}} = 0.23$ GeV for a full scan of our supersymmetric model above. As expected, the scatter plot is prominent at small masses. Furthermore, it is remarkable that for $m_\chi \lesssim 25$ GeV the scatter plot is funnel-shaped. The two panels of Fig. 2 correspond to two different sets of the propagation parameters.
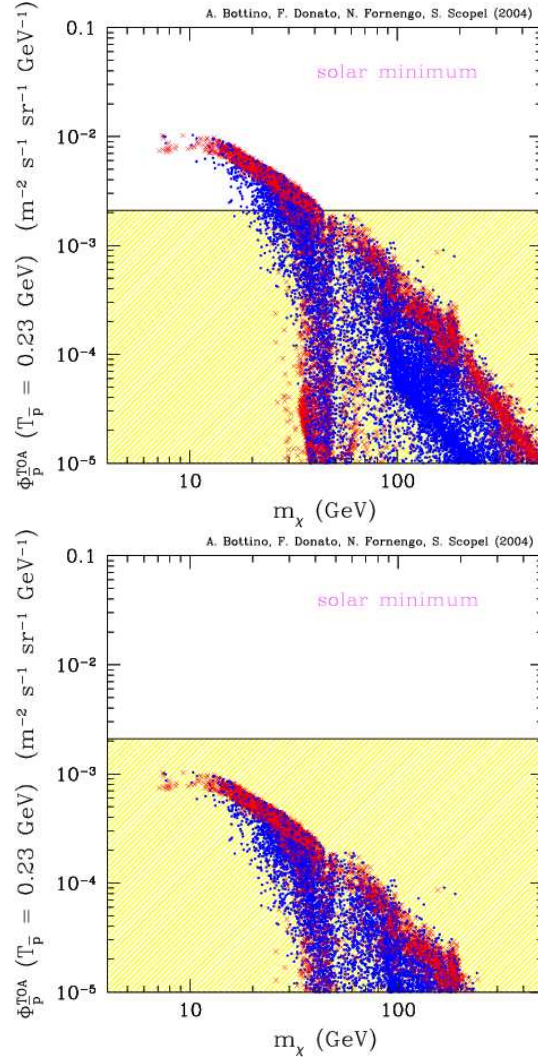
Figure 2: Antiproton flux at $T_{\bar{p}} = 0.23$ GeV as a function of the neutralino mass, calculated at solar minimum. The scatter plots are derived by a full scan of the parameter space of the supersymmetric model described in the text. A spherical isothermal dark matter density profile has been used. The solar modulation is calculated at the phase of solar minimum. Crosses (red) and dots (blue) denote neutralino configurations with $0.095 \leq \Omega_\chi h^2 \leq 0.131$ and $\Omega_\chi h^2 < 0.095$, respectively. The shaded region denotes the amount of primary antiprotons which can be accommodated at $T_{\bar{p}} = 0.23$ GeV without entering in conflict with the experimental BESS data [23] and secondary antiproton calculations [24]. LEFT PANEL: the best fit set for the astrophysical parameters is used. RIGHT PANEL: the astrophysical parameters which provide the most conservative antiproton fluxes are used.

One, used in the left panel, is the set giving the best fit to the B/C ratio, while the other, hereby denoted as the conservative set and used in the right panel provides the lowest (secondary and primary) antiproton fluxes. A spherical cored isothermal distribution for dark matter has been used. However, as mentioned before, a different choice does not significantly modifies the scatter plots. The shaded region denotes the amount of primary antiprotons which can be accommodated at $T_{\bar{p}} = 0.23$ GeV without entering in conflict with the BESS experimental data [23] and secondary antiproton calculations [24].

From the right panel of Fig. 2 we conclude that, within the current astrophysical uncertainties, one cannot derive any constraint on the supersymmetric parameters, if one assumes a very conservative attitude in the selection of the propagation parameters. It is worth noticing that even within this choice, some supersymmetric configurations at very small masses are close to the level of detectability.

We can conclude that indeed relic neutralinos represent a very stimulating field of theoretical and experimental investigations. Measurements at accelerators will have to tell us if supersymmetry is really an ingredient of our physical world.

References

[1] R. Stompor et al., Astrophys.J. **561**, L7 (2001).

[2] J. E. Ruhl et al., Astrophys.J. **599**, 786 (2003).

[3] D.N. Spergel et al., Astrophys. J. Suppl. **148**, 175 (2003).

[4] A. Riess et al., Astron. J. **116**, 1009 (1998).

[5] S. Perlmutter et al., Astrophys. J. **517**, 565 (1999).

[6] W. Hu, D.J. Eisenstein and M. Tegmark, Phys. Rev. Lett. **80**, 5255 (1998).

[7] O. Elgaroy et al., Phys.Rev.Lett. **89**, 061301 (2002).

[8] D.N. Spergel *et al.*, Astrophys. J. Suppl. **148**, 175 (2003).

[9] M. Tegmark et al., in press on Phys. Rev. D, astro-ph/0310723.

[10] The literature concerning theoretical analyses of the neutralino as the LSP, in various supersymmetric models, is extremely vast. Among these papers: L. Bergström and P. Gondolo, Astroparticle Phys. **5**, 263 (1996); E. Gabrielli, S. Khalil, C. Munoz, E. Torrente-Lujan, Phys. Rev. **D63** (2001) 025008; V.A. Bednyakov and H.V. Klapdor-Kleingrothaus, Phys. Rev. **D63**, 095005 (2001); J.L. Feng, K.T. Matchev and F. Wilczek, Phys. Lett. **B482**, 388 (2000); A.Corsetti and P.Nath, Phys.Rev. **D64**,

125010 (2001); J.R. Ellis, Keith A. Olive, Y.Santoso, V.C. Spanos, Phys. Lett.**B565**, 176 (2003); R. Arnowitt and B. Dutta, hep-ph/0204187; A.B. Lahanas, D.V. Nanopoulos and V.C. Spanos, Nucl. Phys. Proc. Suppl. **124**, 159 (2003).

[11] A. Bottino, N. Fornengo and S. Scopel, Phys. Rev. D **67**, 063519 (2003) [hep-ph/0212379].

[12] A. Bottino, F. Donato, N. Fornengo and S. Scopel, Phys. Rev. D **68**, 043506 (2003) [hep-ph/0304080]

[13] A. Bottino, F. Donato, N. Fornengo and S. Scopel, Phys. Rev. D **69**, 0307303 (2004) [hep-ph/0307303]

[14] A. Bottino, F. Donato, N. Fornengo and S. Scopel, Phys. Rev. D **70**, 015005 (2004) [hep-ph/0401186]

[15] M. Davier et al., Eur.Phys.J. C **31**, 503 (2003).

[16] K. Hagiwara et al., hep-ph/0312250.

[17] A. Bottino, F. Donato, N. Fornengo, S. Scopel, Phys. Lett. B **423**, 109 (1998); Phys. Rev. D **62**, 056006 (2000); Phys. Rev. D **63**, 125003 (2001).

[18] R. Bernabei *et al.*, Riv. N. Cim. 26 n. 1, 1 (2003).

[19] D.S. Akerib *et al.*, arXiv:hep-ex/0405033.

[20] A. Benoit *et al.*, Phys. Lett. B **545**, 43 (2002).

[21] P. Belli, R. Cerulli, N. Fornengo and S. Scopel, Phys. Rev. D **66**, 043503 (2002).

[22] F. Donato, N. Fornengo, D. Maurin, P. Salati, R. Taillet, Phys. Rev. D **69**, 063501 (2004) [astro-ph/0306207].

[23] S. Orito, *et al.* (BESS Collaboration), Phys. Rev. Lett. **84**, 1078 (2000); T. Maeno, *et al.* (BESS Collaboration), Astropart. Phys. **16**, 121 (2001).

[24] F. Donato *et al.*, Astrophys. J. **563**, 172 (2001).

DIRECT SEARCH FOR DARK MATTER

R. BERNABEI [a], P. BELLI [a], F. CAPPELLA [a], F. MONTECCHIA [a,1],
F. NOZZOLI [a], A. INCICCHITTI [b], D. PROSPERI [b], R. CERULLI [c],
C. J. DAI [d], H. H. KUANG [d], J. M. MA [d], Z. P. YE [d,2]

[a] *Dipartimento di Fisica, Università di Roma "Tor Vergata",*
INFN, Sezione di Roma II, I-00133, Roma, Italy

[b] *Dipartimento di Fisica, Università di Roma "La Sapienza",*
INFN, Sezione di Roma, I-00185, Roma, Italy

[c] *INFN - Laboratori Nazionali del Gran Sasso, I-67010 Assergi (Aq), Italy*

[d] *IHEP, Chinese Academy, P.O. Box 918/3, Beijing 100039, China*

Abstract

DAMA is an observatory for rare processes based on the development
and use of various kinds of radiopure scintillators; it is operative deep
underground at the Gran Sasso National Laboratory of I.N.F.N.. Several
low background set-ups have been realized with time passing and many
rare processes have been investigated. In particular, the DAMA/NaI
set-up ($\simeq$ 100 kg highly radiopure NaI(Tl)) has effectively investigated
the model independent annual modulation signature for Dark Matter
particles in the galactic halo. With the total exposure of 107731 kg ×
day it has pointed out a model independent evidence for the presence of

[1]also: Università Campus Bio-Medico" di Roma, 00155, Rome, Italy
[2]also: University of Zhao Qing, Guang Dong, China

a Dark Matter particle component in the galactic halo at 6.3 σ C.L.; some of the many possible corollary model dependent quests for the candidate particle have also been investigated. At present the second generation DAMA/LIBRA set-up ($\simeq$ 250 kg highly radiopure NaI(Tl)) is in operation deep underground.

1 Introduction

DAMA is an observatory for rare processes based on the development and use of various kinds of radiopure scintillators. Several low background set-ups have been realized; the main ones are: i) DAMA/NaI ($\simeq$ 100 kg of highly radiopure NaI(Tl)), which took data underground over seven annual cycles and was put out of operation in July 2002 [1, 2, 3, 4, 5, 6, 7, 8, 9, 10, 11, 12, 13]; ii) DAMA/LXe ($\simeq$ 6.5 kg liquid Xenon) [14]; iii) DAMA/R&D, which is devoted to tests on prototypes and small scale experiments [15]; iv) the new second generation DAMA/LIBRA set-up ($\simeq$ 250 kg highly radiopure NaI(Tl)) in operation since March 2003. These set-ups have investigated many rare processes. Moreover, in the framework of devoted R&D for radiopure detectors and PMTs, sample measurements are regularly carried out by means of the low background DAMA/Ge detector, installed deep underground since $\gtrsim$ 10 years and, in some cases, by means of Ispra facilities.

In the following we will focus the presentation only on the $\simeq$ 100 kg radiopure NaI(Tl) set-up, DAMA/NaI, and on its results on the annual modulation signature.
The DAMA/NaI set-up and its performances have been described in ref.[1] and further information on its performances and upgrading can be found in refs.[2, 10]. Two PMTs were coupled to each NaI(Tl) crystal through 10 cm long Tetrasil-B light guides (acting also as optical windows) and worked in coincidence with hardware thresholds at single photoelectron level in order to assure high efficiency for the coincidence at few keV level [1]. The energy threshold of the experiment, 2 keV, was determined by means of X ray sources and of keV range Compton electrons on the basis also of the features of the noise rejection procedure and of the efficiencies when lowering the number of available photoelectrons [1].

The model independent annual modulation signature (originally suggested in [16]) is very distinctive since it requires the simultaneous satisfaction of all the following requirements: the rate must contain a component modulated according to a cosine function (1) with one year period, T, (2) and a phase, t_0, that peaks around $\simeq 2^{nd}$ June (3); this modulation must only be found in a well-defined low energy range, where WIMP induced recoils can be present (4); it must apply to those events in which just one detector of many actually "fires" (*single-hit* events), since the WIMP multi-scattering probability is negligible

(5); the modulation amplitude in the region of maximal sensitivity is expected to be $\lesssim 7\%$ (6). This latter rough limit would be larger in case of other possible scenarios such as e.g. those in refs. [17, 18]. To mimic such a signature spurious effects or side reactions should be able both to account for the whole observed modulation amplitude and to contemporaneously satisfy all the requirements.

2   The final model independent result over 7 annual cycles

A model independent approach on the data of the seven annual cycles offers an immediate evidence of the presence of an annual modulation of the rate of the *single-hit* events in the lowest energy region as shown in Fig. 1 – *left*, where the time behaviour of the measured (2-6) keV residual rate of the *single-hit* events is reported. The data favour the presence of a modulated
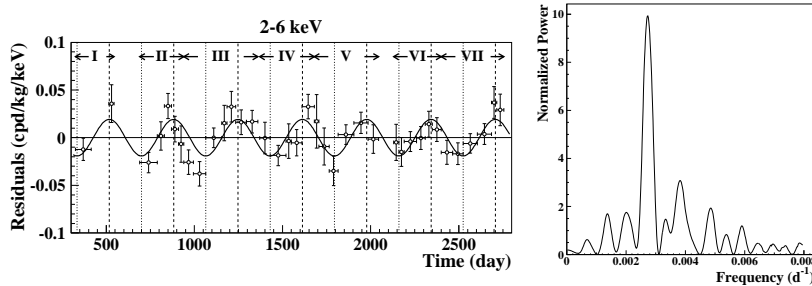
Figure 1: *On the left*: model independent experimental residual rate for *single-hit* events in the (2–6) keV energy interval as a function of the time over 7 annual cycles (total exposure 107731 kg × day); end of data taking July 2002. The experimental points present the errors as vertical bars and the associated time bin width as horizontal bars. The superimposed curve represents the cosinusoidal function behaviour expected for a WIMP signal with a period equal to 1 year and phase exactly at 2nd June; the modulation amplitude has been obtained by best fit. See ref. [2]. *On the right*: power spectrum of the measured (2–6) keV *single-hit* residuals calculated including also the treatment of the experimental errors and of the time binning. As it can be seen, the principal mode corresponds to a frequency of $2.737 \cdot 10^{-3}$ d^{-1}, that is to a period of $\simeq 1$ year.

cosine-like behaviour ($A \cdot \cos\omega(t - t_0)$) at 6.3 σ C.L. and their fit for the (2–6) keV cumulative energy interval offers modulation amplitude equal to (0.0200 ± 0.0032) cpd/kg/keV, $t_0 = (140 \pm 22)$ days and $T = \frac{2\pi}{\omega} = (1.00 \pm 0.01)$ year, all parameters kept free in the fit. The period and phase agree with those expected in the case of a WIMP induced effect ($T = 1$ year and t_0 roughly at $\simeq 152.5^{th}$ day of the year). The χ^2 test on the (2–6) keV residual rate disfavours the hypothesis of unmodulated behaviour giving a probability of

$7 \cdot 10^{-4}$ ($\chi^2/d.o.f. = 71/37$). The same data have also been investigated by a Fourier analysis as shown in Fig. 1 – *right*. Modulation is not observed above 6 keV [2]. Finally, a suitable statistical analysis has shown that the modulation amplitudes are statistically well distributed in all the crystals, in all the data taking periods and considered energy bins. More arguments can be found in ref. [2]. A careful investigation of all the known possible sources of systematic
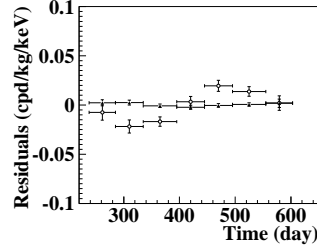
Figure 2: Experimental residual rates over seven annual cycles for *single-hit* events (open circles) – class of events to which WIMP events belong – and over the last two annual cycles for *multiple-hits* events (filled triangles) – class of events to which WIMP events do not belong – in the (2–6) keV cumulative energy interval. They have been obtained by considering for each class of events the data as collected in a single annual cycle and using in both cases the same identical hardware and the same identical software procedures. The initial time is taken on August 7th. See text.

and side reactions has been regularly carried out and published at time of each data release while detailed quantitative discussions can be found in refs. [2, 10]. No systematic effect or side reaction able to account for the observed modulation amplitude and to mimic a WIMP induced effect has been found. As a further relevant investigation, the *multiple-hits* events collected during the DAMA/NaI-6 and 7 running periods (when each detector was equipped with its own Transient Digitizer with a dedicated renewed electronics) have been studied and analysed by using the same identical hardware and the same identical software procedures as for the case of the *single-hit* events (see Fig. 2). The *multiple-hits* events class – on the contrary of the *single-hit* one – does not include events induced by WIMPs since the probability that a WIMP scatters off more than one detector is negligible. The fitted modulation amplitudes are: $A = (0.0195 \pm 0.0031)$ cpd/kg/keV and $A = -(3.9 \pm 7.9) \cdot 10^{-4}$ cpd/kg/keV for *single-hit* and *multiple-hits* residual rates, respectively. Thus, evidence of annual modulation is present in the *single-hit* residuals (events class to which the WIMP-induced recoils belong), while it is absent in the *multiple-hits* residual rate (event class to which only background events belong). Since the same identical hardware and the same identical software procedures have been used to analyse the two classes of events, the obtained result offers an

additional strong support for the presence of Dark Matter particles in the galactic halo further excluding any side effect either from hardware or from software procedures or from background.

In conclusion, the presence of an annual modulation in the residual rate of the *single-hit* events in the lowest energy interval (2 – 6) keV, satisfying all the features expected for a WIMP component in the galactic halo is supported by the data of the seven annual cycles at 6.3 σ C.L.. This is the experimental result of DAMA/NaI. It is model independent; no other experiment whose result can be directly compared with this one is available so far in the field of Dark Matter investigation.

3 Some corollary model dependent quests for a candidate

On the basis of the obtained model independent result, corollary investigations can also be pursued on the nature and coupling of the WIMP candidate. This latter investigation is instead model dependent and – considering the large uncertainties which exist on the astrophysical, nuclear and particle physics assumptions and on the parameters needed in the calculations – has no general meaning (as it is also the case of exclusion plots, of expected recoil energy behaviours and of the WIMP parameters evaluated in indirect search experiments). Thus, it should be handled in the most general way as we have pointed out with time passing [6, 7, 8, 9, 10, 11, 12, 13, 2].

Candidates, kinds of WIMP couplings with ordinary matter and implications, cross sections, nuclear form factors, spin factors, scaling laws, halo models, priors, etc. are discussed in ref. [2] and we invite the reader to this reference since these arguments are necessary to correctly understand the results obtained in corollary quests and the real validity of any claimed model dependent comparison in the field.

In the following some of the results obtained in ref. [2] for some of the many possible model dependent quests for a WIMP candidate are shown; obviously, they are not exhaustive of the many scenarios possible at present level of knowledge, including those depicted in some more recent works such as e.g. refs. [18, 19].

DAMA/NaI is intrinsically sensitive both to low and high WIMP mass having both a light (the ^{23}Na) and a heavy (the ^{127}I) target-nucleus; in previous corollary quests WIMP masses above 30 GeV (25 GeV in ref. [6]) have been presented [7, 9, 11, 12, 13] for few (of the many possible) model frameworks. However, that bound holds only for neutralino when supersymmetric schemes based on GUT assumptions are adopted to analyse the LEP data [20]. Thus, since other candidates are possible and also other scenarios can be considered for the neutralino itself as recently pointed out (in fact, when the assumption on the gaugino-mass unification at GUT scale is released neutralino masses down to $\simeq$ 6 GeV are allowed [21, 22]), the present model dependent lower

bound quoted by LEP for the neutralino in the supersymmetric schemes based on GUT assumptions (37 GeV [23]) is simply marked in the following figures.

For simplicity, here the results of these corollary quests for a candidate particle are presented in terms of allowed regions obtained as superposition of the configurations corresponding to likelihood function values *distant* more than 4σ from the null hypothesis (absence of modulation) in each of the several (but still a limited number) of the possible model frameworks considered in ref. [2]. These allowed regions take into account the time and energy behaviours of the single-hit experimental data and have been obtained by a maximum likelihood procedure (for a formal description see e.g. refs. [6, 7, 9]) which requires the agreement: i) of the expectations for the modulated part of the signal with the measured modulated behaviour for each detector and for each energy bin; ii) of the expectations for the unmodulated component of the signal with the respect to the measured differential energy distribution and - since ref. [9] - also with the bound on recoils obtained by pulse shape discrimination from the devoted DAMA/NaI-0 data [3]. The latter one acts in the likelihood procedure as an experimental upper bound on the unmodulated component of the signal and – as a matter of fact – as an experimental lower bound on the estimate of the background levels. Thus, the C.L.'s, we quote for the allowed regions, already account for compatibility with the measured differential energy spectrum and with the measured upper bound on recoils.

Fig. 3, 4, 6 show some of the obtained allowed regions; details and
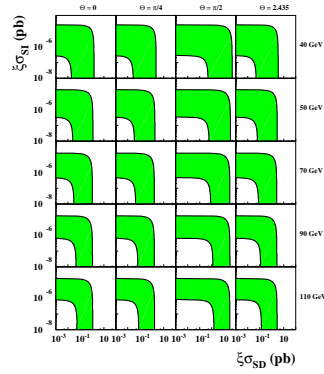
Figure 3: *Case of a WIMP with mixed SI&SD interaction for the model frameworks given in ref. [2].* Coloured areas: example of slices (of the 4-dimensional allowed volume) in the plane $\xi\sigma_{SI}$ vs $\xi\sigma_{SD}$ for some of the possible m_W and θ values. Inclusion of other existing uncertainties on parameters and models would further extend the regions; for example, the use of more favourable form factors and/or of more favourable spin factors than the ones considered here would move them towards lower cross sections. For details see ref. [2].
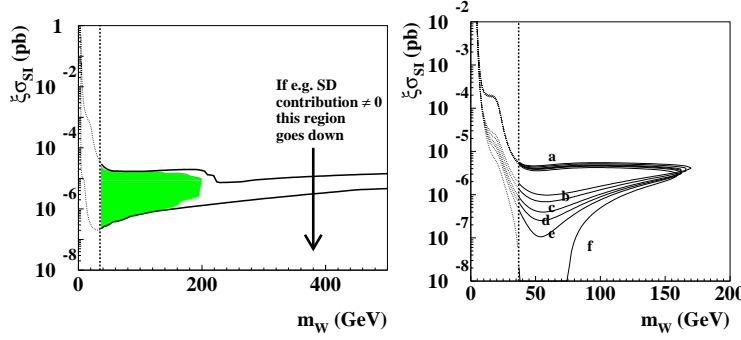
Figure 4: *On the left : Case of a WIMP with dominant SI interaction for the model frameworks given in ref. [2].* Region allowed in the plane $(m_W, \xi\sigma_{SI})$. The vertical dotted line represents a bound in case of a neutralino candidate when supersymmetric schemes based on GUT assumptions are adopted to analyse the LEP data; the low mass region is allowed for neutralino when other schemes are considered (see e.g. refs. [21,22]) and for every other WIMP candidate. While the area at WIMP masses above 200 GeV is allowed only for few configurations, the lower one is allowed by most configurations (the colored region gathers only those above the vertical line). The inclusion of other existing uncertainties on parameters and models would further extend the region; for example, the use of more favourable SI form factor for Iodine alone would move it towards lower cross sections. *On the right: Example of the effect induced by the inclusion of a SD component different from zero on allowed regions given in the plane $\xi\sigma_{SI}$ vs m_W.* In this example the Evans' logarithmic axisymmetric $C2$ halo model with $v_0 = 170$ km/s, ρ_0 equal to the maximum value for this model and a given set of the parameters' values (see ref. [2]) have been considered. The different regions refer to different SD contributions for the particular case of $\theta = 0$: $\sigma_{SD} = 0$ pb (a), 0.02 pb (b), 0.04 pb (c), 0.05 pb (d), 0.06 pb (e), 0.08 pb (f). Analogous situation is found for the other model frameworks. For details see ref. [2].

descriptions of the symbols are given in ref. [2]. Here we only remind that $tg\theta$ is the ratio between the WIMP-neutron and the WIMP-proton effective spin-dependent coupling strengths and that θ is defined in the $[0,\pi)$ interval. Obviously, larger sensitivities than those reported in the following figures would be reached when including the effect of other existing uncertainties on the astrophysical, nuclear and particle Physics assumptions and related parameters; similarly, the set of the best fit values would also be enlarged as well.

The theoretical expectations in the purely SI coupling for the particular case of a neutralino candidate in MSSM with gaugino mass unification at GUT scale released [22] are also shown in Fig. 5.
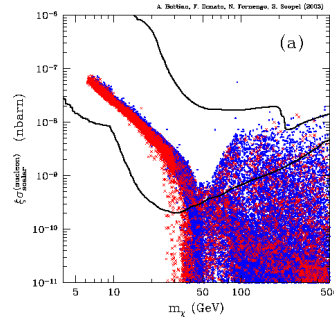
Figure 5: Figure taken from ref. [21]: theoretical expectations of $\xi\sigma_{SI}$ versus m_W in the purely SI coupling for the particular case of a neutralino candidate in MSSM with gaugino mass unification at GUT scale released; the curve is the same as in Fig. 4-*left*.

Specific arguments on some claimed model dependent comparisons can be found in ref. [2]. They already account, as a matter of fact, also e.g. for the more recent model dependent CDMS(-II) claim [24] (based on a statistics of 19.4 kg · day, on data selection and discrimination procedures), where DAMA/NaI is not correctly and completely quoted and the more recent result of the 7 annual cycles [2] is quoted but not accounted for (as also done in some talks at this Conference). In addition, in the particular scenario of [24], uncertainties from the model (from astrophysics, nuclear and particle physics assumptions) as well as some experimental ones (e.g. quenching factor assumed 1, etc.), are not accounted at all and the existing interactions and scenarios to which CDMS is largely insensitive – on the contrary of DAMA/NaI – are ignored. Similar arguments also hold for the EDELWEISS case discussed in this conference.

4   Conclusions and perspectives

DAMA/NaI has been a pioneer experiment investigating as first the WIMP annual modulation signature with suitable sensitivity and control of the running parameters. During seven independent experiments of one year each one, it has pointed out the presence of a modulation satisfying the many peculiarities of an effect induced by Dark Matter particles, reaching a significant evidence. As a corollary result, it has also pointed out the complexity of the quest for a candidate particle mainly because of the present poor knowledge on the many astrophysical, nuclear and particle physics aspects. At present after a devoted R&D effort, the second generation DAMA/LIBRA (a $\simeq$250 kg more radiopure NaI(Tl) set-up) has been realised and put in operation since March 2003. Moreover, a third generation R&D toward a possible ton NaI(Tl) set-up, we proposed in 1996 [25], is in progress.
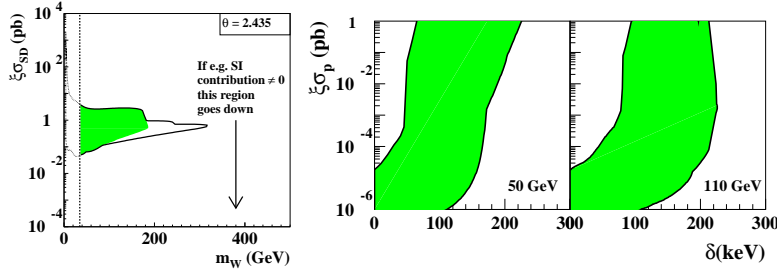
Figure 6: *On the left: Case of a WIMP with dominant SD interaction in the model frameworks given in ref. [2].* Example of a slice (of the 3-dimensional allowed volume) in the plane $(m_W, \xi\sigma_{SD})$ at a given θ value (θ is defined in the $[0, \pi)$ range); here $\theta = 2.435$ (Z_0 coupling). For the definition of the vertical line and of the coloured area see the caption of Fig. 4. Inclusion of other existing uncertainties on parameters and models (as discussed in ref. [2]) would further extend the SD allowed regions. For example, the use of more favourable SD form factors and/or more favourable spin factors would move them towards lower cross sections. Values of $\xi\sigma_{SD}$ lower than those corresponding to this allowed region are possible also e.g. in case of an even small SI contribution (see ref. [2]). *On the right: Case of a WIMP with* preferred inelastic *interaction in the model frameworks given in ref. [2].* Examples of slices (coloured areas) of the 3-dimensional allowed volume ($\xi\sigma_p$, δ, m_W) for some m_W values. Inclusion of other existing uncertainties on parameters and models would further extend the regions; for example, the use of more favourable form factors and of different escape velocity would move them towards lower cross sections. For details see ref. [2].

References

[1] R. Bernabei et al., *Nuovo Cimento* A **112**, 545 (1999).

[2] R. Bernabei et al., *La Rivista del Nuovo Cimento* **26** (2003) 1-73 (*astro-ph/0307403*).

[3] R. Bernabei et al., *Phys. Lett.* B **389**, 757 (1996).

[4] R. Bernabei et al., *Nuovo Cimento* A **112**, 1541 (1999).

[5] R. Bernabei et al., *Phys. Lett.* B **408**, 439 (1997); P. Belli et al., *Phys. Lett.* B **460**, 236 (1999); R. Bernabei et al., *Phys. Rev. Lett.* **83**, 4918 (1999); P. Belli et al., *Phys. Rev.* C **60**, 065501 (1999); R. Bernabei et al., *Phys. Lett.* B **515**, 6 (2001); F. Cappella et al., *Eur. Phys. J. direct* C **14**, 1 (2002).

[6] R. Bernabei et al., *Phys. Lett.* B **424**, 195 (1998).

[7] R. Bernabei et al., *Phys. Lett.* B **450**, 448 (1999).

[8] P. Belli et al., *Phys. Rev.* D **61**, 023512 (2000).

[9] R. Bernabei et al., *Phys. Lett.* B **480**, 23 (2000).

[10] R. Bernabei et al., *Eur. Phys. J.* C **18**, 283 (2000).

[11] R. Bernabei et al., *Phys. Lett.* B **509**, 197 (2001).

[12] R. Bernabei el al., *Eur. Phys. J.* C **23**, 61 (2002).

[13] P. Belli et al., *Phys. Rev.* D **66**, 043503 (2002).

[14] R. Bernabei et al., *Nuovo Cimento* A **103**, 767 (1990); *Nuovo Cimento* C **19**, 537 (1996); *Astrop. Phys.* **5**, 217 (1996); *Phys. Lett.* B **387**, 222 (1996) and *Phys. Lett.* B **389**, 783 (1996) (err.); *Phys. Lett.* B **436**, 379 (1998); *Phys. Lett.* B **465**, 315 (1999); *Phys. Lett.* B **493**, 12 (2000); *New Journal of Physics* **2**, 15.1 (2000); *Phys. Rev.* D **61**, 117301 (2000); *Eur. Phys. J. direct* C **11**, 1 (2001); *Nucl. Instrum. Methods* A **482**, 728 (2002); *Phys. Lett.* B **527**, 182 (2002); *Phys. Lett.* B **546**, 23 (2002); in "Beyond the Desert 03", Springer (2004) 541.

[15] R. Bernabei et al., *Astrop. Phys.* **7**, 73 (1997); R. Bernabei et al., *Nuovo Cimento* A **110**, 189 (1997); P. Belli et al., *Nucl. Phys.* B **563**, 97 (1999); P. Belli et al., *Astrop. Phys.* **10**, 115 (1999); R. Bernabei et al., *Nucl. Phys.* A **705**, 29 (2002); P. Belli et al., *Nucl. Instrum. Methods* A **498**, 352 (2003); R. Cerulli et al., *Nucl. Instrum. Methods* A **525**, 535 (2004).

[16] K.A. Drukier et al., *Phys. Rev.* D **33**, 3495 (1986). K. Freese et al., *Phys. Rev.* D **37**, 3388 (1988).

[17] D. Smith and N. Weiner, *Phys. Rev.* D **64**, 043502 (2001).

[18] K. Freese et al. *astro-ph/0309279*.

[19] G. Prezeau et al., *Phys. Rev. Lett.* **91**, 231301 (2003).

[20] D.E. Groom et al., Eur. Phys. J. C15 (2000) 1

[21] A. Bottino et al., Phys. Rev. D67 (2003) 063519; A. Bottino et al, hep-ph/0304080; D. Hooper and T. Plehn, MADPH-02-1308, CERN-TH/2002-29, [hep-ph/0212226]; G. Bélanger, F. Boudjema, A. Pukhov and S. Rosier-Lees, hep-ph/0212227

[22] A. Bottino et al., *Phys. Rev.* D **69**, 037302 (2004).

[23] K. Hagiwara et al., Phys. Rev. D66 (2002) 010001

[24] CDMS coll., *astro-ph/0405033*.

[25] R. Bernabei et al.,*Astrop. Phys.* **4**, 45 (1995); R. Bernabei, "Competitiveness of a very low radioactive ton scintillator for particle Dark Matter search", in the volume *The identification of Dark Matter*, World Sc. pub. 574(1997).

PROSPECTS FOR THE DARK MATTER
DETECTION IN AMS02 DETECTOR

AGNIESZKA JACHOLKOWSKA FOR AMS COLLABORATION [a]

[a] *IN2P3/CNRS, UMR 5139, Université de Montpellier II, place Eugène Bataillon,*
34095 Montpellier, France

Abstract

The prospects for the Dark Matter detection in AMS02 detector are presented. The uncertainties for measured fluxes of e^+, $\bar{p}$ and γ. are discussed. The complementarity of different searches in various channels is underlined.

1   Introduction

The astrophysical measurements of the star rotation velocities in the galaxies, of the large structure populations, of the gravitationnal arc phenomena and the independent results on the $\Omega_b h^2$ from the WMAP mission, suggest that the dominating matter content of the Universe is dark, cold and not baryonic [1] . Following hypotheses contribute to the construction of the Cold Dark Matter (CDM) pardigm [1] : the dark matter is composed of Weakly Interacting Massive Particles (WIMPs) which are neutral and stable and originate from the Big Bang era. The Supersymmetric theories (SUSY) offer an excellent

WIMP candidate, the neutralino which is a mixture of the superpartners of the neutral Higgs and of the Electro-Weak gauge bosons. The neutralino may have elastic interactions with nucleons or annihilate in the halo of the Dark Matter and produce stable particles: gamma, leptons and hadrons. These interactions provide two ways of probing the dark matter nature: directly, in the underground detectors (Direct searches) and indirectly, by the astrophysical observations via ground based or spatial telescopes (Indirect searches). The Direct and Indirect searches are complementary: the theoretical description of the spin-independant and spin-dependant cross-sections is related to the annihilation cross-section via the cross-symmetry. Also the experimental effects coming from nuclear physics and astrophysics as from the halo nature, which can be local, diffuse, clumpy or related to a source will affect differently the measurements.

Concerning the hypothesis for the WIMP being the lightest neutralino, the real breakthrough will come from the LHC experiments. In case of discovery, the future results will provide the search windows in SUSY parameter space for the Direct and Indirect searches.. At present, the indirect limits in MSSM model on the neutralino mass of about 50 GeV from LEP and constraints from the relic density $\Omega_{DM} h^2 = 0.111 \pm 0.009$ from WMAP [2] allow to discard a multitude of models. It should be stressed that apart a conventional neutralino candidate, there are few less orthodox candidates proposed by the particle physics. In the extra-dimension models the lightest Kaluza-Klein particle [3] provides an alternative predictive paradigm to the mSUGRA/MSSM neutralino. The Q-balls [4], composed of baryons and s-particles can be stable and linked to the Supersymmetry, unfortunately with no possible cross-checks with direct particle physics observations. The gravitino which could be a LSP in case of the Anomaly-Mediated SUSY breaking scenario [5] , is a well motivated and interesting candidate but because of being very light, it offers few possibilities of detection. All these possible candidates will be searched for by the Direct and Indirect detection experiments, in particular by the AMS experiment, which will allow the detection in various WIMP annihilation channels.

2   Indirect searches: flux measurement

The studies of the elementary interactions of various types of particles in the galactic and extra-galactic medium allows to combine our knowledge in astrophysics and in the elementary particle physics domain. The input from these domains is used for the Cosmic Ray flux predictions and measurement interpretations. The measured flux for the WIMP annihilations [6] can be parametrized as being proportional mainly to themean cross-section times velocity product divided and proportional to the neutralino mass squared

(reflecting the particle physics choice of candidate), and by the astrophysical element composed of the square of the dark matter halo density and of the Cosmic Ray propagation factors. In case of the SUSY neutralino candidate [6] the flux depends on couplings and mass spectrum and in weaker way on many other SUSY parameters. Various predictions were published [7] for the MSSM and mSUGRA models all showing lower predicted sensitivity of experiments for larger neutralino masses. The present evaluated uncertainty on flux in these models cover range up to 10^3 and these uncertainties propagate also to the alternatif scenarios discussed in the previous section.

The astrophysical dependences decompose into two main astrophysical factors which are the dark matter halo profile of the observed source and the propagation parameters for different types Cosmic Rays. Many parametrizations for the halo profile were proposed last years for the Galaxy or other sources like Navarro-Frenk-White, Klypin, Moore, SWT profiles, as can be found in [8] . The most important feature of the halo behaviour is its steepness in the source central region. The mostly studied source at present is the Galactic Centre but predictions for other sources like M31 and M87 galaxies or Dwarf Spheroidals (e.g. DRACO, Sagittarius) or Globular Clusters exist [9] . Moreover, the Super Massive Black Hole (SMBH) can strongly enhance or reduce the expected fluxes [10] . Most of the charged Cosmic Rays originate from the secondary interactions in the local, few kpc halo. Only exotic WIMP annihilations can provide primary charged Cosmic Rays which rates will also depend on the propagation parameters. The fluxes of the charged Cosmic Rays measured in the Earth vicinity will depend on the propagation parameters like diffusion length, solar modulation, galactic wind, presence of the SNRs (local bubble). The primary fluxes from the WIMP annihilations may be also enhanced by factors of few due to the presence of clumps in the dark matter halo as discussed in [11] . The studies of primary and secondary charged Cosmic Ray production will strongly interfere with dark matter detection and will be discussed below for the AMS experiment.

In summary, the astrophysical uncertainties on flux range between 10^2 and 10^6 depending on the WIMP annihilation channel [12] and are much larger comparing to the Direct searches astrophysical uncertainties where mainly the local halo modification or large WIMP velocity dispersion may introduce a factor of 10 in rates.

3   Dark Matter detection by AMS

The AMS02 experiment offers the possibility of probing the Cosmic Ray composition, Antimatter search, the Dark Matter composition and Gamma-ray sources. It will provide high precision data, which escape from the atmospheric effects that obscure the measurements performed by the balloon experiments.
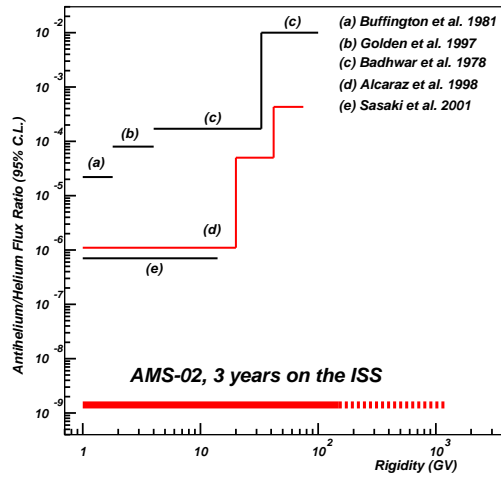
Figure 1: AMS02 expectation vs results from AMS01 and other experiments for the $\overline{He}/He$ ratio.

The AMS02 detector will allow the detection and identification of almost all types of particles composing the cosmic rays such as protons, nuclei, electrons and gamma or their CP symmetric partners for charged particles. The detailed description of the AMS02 detector elements and performances, as well as those related to the trigger and electronics systems, can be found in [13]. As a figure of merit, we show in Figure 1 the gain in sensitivity to the anti-helium search in AMS compared to the present values after a 3-year mission on ISS.

3.1 AMS strategy

The AMS experimental strategy relies on a long term of 3 to 5 year measurements on ISS as the expected fluxes are low compared to the present experimental sensitivities. The scan of point-like sources and diffuse sources may decrease the effects coming from the astrophysical uncertainties. The detection of various decay channels from WIMP annihilations is possible due to the completness of the AMS02 detector which will measure energy and angular spectra of hadrons, leptons and gamma. Moreover, AMS will focus on the anti-particle or gamma detection with large energy lever arm. The background contributions in these channels have lower expected values as they originate from the secondary interactions of the charged Cosmic Rays [14] . The interpretation of the measured yields and spectra will rely on the knowledge of the backgrounds which estimations have been presented in recent publications
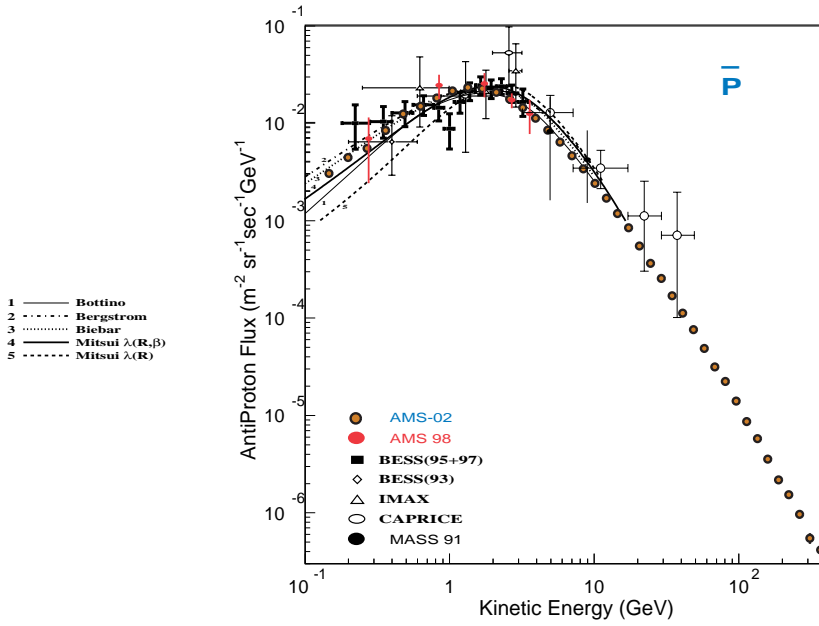
Figure 2: AMS-02 3 years secondary $\bar{p}$ flux

[14] . AMS will not only measure precisely the proton, electron and nuclei spectra but also the main parameters of the Cosmic Ray models such as B/C ratio (or any secondary/primary ratio) which fixes the diffusion coefficients or the $^{10}Be/^{9}Be$ ratio which is related to the e^+ production and propagation processes [14] . Finally, a procedure of common fit to the multi-channel data is being developed in AMS following to a recent example of such a fit published in [15] . It has to be underlined here that the knowledge of the systematic effects is ensured by a possibility of a simultaneous study of various channels by one experiment. The observed deviations from the standard Cosmic Ray spectra should then provide coherent results on masses and parameters of WIMP candidates.

3.2 Antiproton, positron and gamma channels

Antiproton flux: measurements of CR $\bar{p}$ flux are few and, at high energy, not very precise. Several attempts of interpreting these measurements have shown the difficulty of deducing $\bar{p}$ propagation properties since an exotic origin such as neutralino annihilation cannot be excluded [16] . For high m_χ a high-energy excess of $\bar{p}$ is measurable. AMS-02 will measure accurately the $\bar{p}$ spectrum up
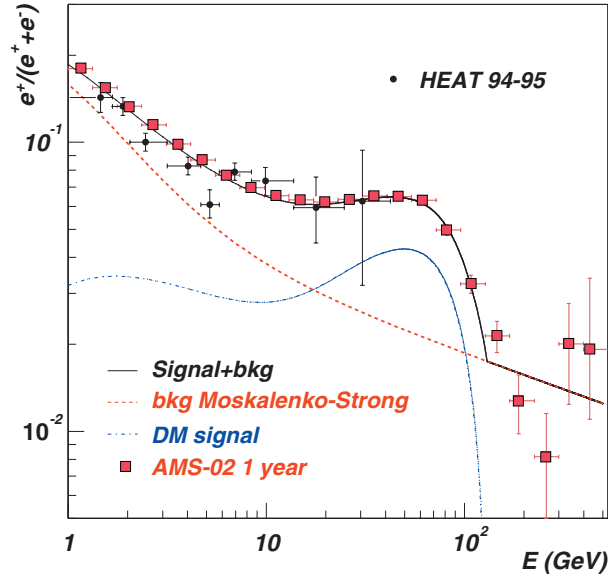
Figure 3: AMS-02 e^+ fraction in the case of a primary e^+ from annihilating χ [18] .

to hundreds GeV with a few percent energy resolution[4] as shown in Figure 2. The anti-deuterium channel can also be considered as promising for long term exposure [17].

Positron flux: recently [18] , the e^+ production from the neutralino annihilitaion in the galactic halo has been simulated according to several models in the MSSM frame.The standard e^+ flux from the secondary inteactions has been also calculated by means of a diffusion model proposed by [14] . Figure 3 displays the positron fraction as measured in one year compared to the HEAT data showing a statistically not very significant bump around 7 GeV. The results from neutralino with mass of 130.3 GeV signal simulation boosted by a factor of 50 are also presented as an example of a hypothesis fitting the HEAT data.

Gamma flux: the AMS potential for the dark matter detection in the channels with a γ in the final state was performed in mSUGRA models [20] with DARKSUSY and SUSPECT [19] packages described in [9] . The Navarro-Frenk-White halo parametrization was chosen following [8] . In Figure 4, the mSUGRA scan of the γ flux as a function of the m_χ is shown. Both the particle physics model (large m_0) and astrophysical paremeters, can be qualified as optimistic scenario. The 95% CL was obtained by a 3σ fluctuation of the
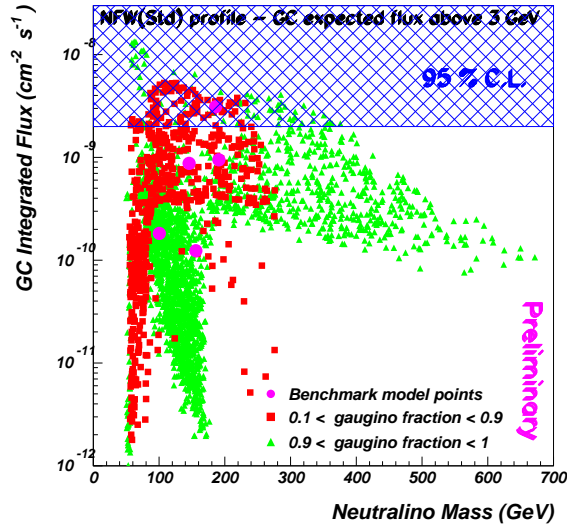
Figure 4: The integrated γ flux from GC as a function of m_χ for mSUGRA, large m_0 scan as expected for a standard NFW halo profile [8] .

diffuse gamma background spectrum as measured by EGRET. With 3 GeV energy threshold, AMS will reach the sensitivity of $(2.0 \pm 0.2)10^{-9} cm^{-2}s^{-1}$ in a 3 years exposure.

4 Summary

The AMS02 experiment will provide high precision Cosmic Ray data starting with 2008 and at least during three years on. The completeness of the AMS02 detector will allow to measure simultaneously the possible Dark Matter annihilation signals and standard Cosmic Ray backgrounds. This will be done by anti-particle measurement with a common fit procedure applied to at least three measured channel data.

References

[1] L. Bergstrom, Rept.Prog.Phys. 63 (2000) 793

[2] A. Heister, et al., Phys.Lett.B 583 (2004) 247-263,
    D.N. Spergel, et al., astro-ph/0302209

[3] G. Bertone, G. Servant, G. Sigl, Phys.Rev.D68 (2003) 004008

[4] S. Kasuya, M. Kawasaki, Phys.Rev.Lett.B 85 (2000) 2677

[5] T. Moroi, L. Randall, Nucl.Phys.B 570 (2000) 455-472

[6] L. Bergstrom et al., Astropart. Phys. 9 (1998) 137-162,
    E.A. Baltz, J. Edsjo, K. Freese, P. Gondolo, Phys.Rev.D65 (2002)

[7] R. Barbieri, S. Ferrara, C.A. Savoy, Phys.Lett.B 119 (1982)

[8] J.F. Navarro, C.S. Frenk, S.D.M. White, ApJ 490 (1997) 493,
    F. Stoehr, et.al, asto-ph/0307026

[9] A. Falvard, E. Giraud, A. Jacholkowska et al.,Astropart.Phys.vol20 (2004)
    467-484,
    E.A. Baltz, et al.,Phys.Rev.D 61 (2000) 023514,
    E. Giraud, et al., astro-ph/0209230

[10] D. Merritt, Phys.Rev.Lett.92 (2004) 201304

[11] F. Stoehr, et.al, asto-ph/0203342

[12] P. Salati, Complementarity between Direct and Indirect searches
     Workshop, Montpellier (2003)

[13] B. Demirkoz, proceedings in "Physics and Astrophysics in Space"
     (2004),Frascati, Italy

[14] I.V. Moskalenko, A. Strong, Phys.Rev.D 60 (1999) 063003

[15] W. de. Boer, et al., astro-ph/0309029

[16] L. Bergstrom, J. Edsjo, P. Ullio, Astrop.Jour. 526,(1999) 215,
     F. Donato, et al.,astro-ph/0306312,
     I.V. Moskalenko, et al., ApJ 565 (2002) 280,
     I.V. Moskalenko, et al., ApJ 586 (2003) 1050

[17] F. Donato, N. Fornengo, P. Salati, Phys.Rev.D 62 (2000) 043003

[18] P. Maestro, Ph.D. Thesis, University of Siena, AMS-Note 2003-01-01

[19] DARKSUSY, http://www.physto.se/ edsjo/darksusy,
     SUSPECT, http://www.lpm.univ-montp2.fr:7082/ kneur/suspect.html

[20] A. Jacholkowska, G. Lamanna, E. Nuss, M. Sapinski AMS-Note 2003-05-
     01

ANTIMATTER SEARCHES AS PROBES OF SUSY DARK MATTER

Stefano Profumo [a,b], Piero Ullio [a,b]

[a] *SISSA/ISAS, via Beirut 2-4, 34013 Trieste, Italy*

[b] *INFN, Sez. di Trieste, 34014 Trieste, Italy*

Abstract

We investigate the discrimination perspectives for neutralino dark matter at future antimatter search experiments. Theoretically well motivated benchmark scenarios are introduced, with the purpose of comparing projected experimental search strategies, and in order to show in which cases antimatter searches could be of particular relevance. We resort to *visibility ratios* (*i.e.* signal-to-sensitivity ratios) which allow a comparison among different neutralino dark matter detection techniques. We also introduce a novel quantity, I_ϕ, defined as an integral of the squared expected exotic signal over the background, which allows to estimate the future reach of antimatter search experiments independently of the experimental apparatus. We point out that antiprotons, positrons and antideuterons searches constitute a primary neutralino dark matter search strategy for a class of large annihilation rates models, which will be largely probed at upcoming experiments, like PAMELA and AMS-02.

1   Introduction

The Dark Matter (DM) problem, *i.e.* the observation that the majority of the matter content of the Universe is made of some kind of non-luminous and non-baryonic gravitationally interacting substance, stands as one of the greatest challenge in astroparticle physics. As now, many particle candidates have been proposed to solve the DM puzzle, and an extensive experimental program has been deployed with the purpose of detecting and understanding this elusive not less than seemingly inevasible component of the Universe. One of the best theoretically motivated candidates is the *lightest supersymmetric particle*, LSP, of the minimal supersymmetric extension of the Standard Model (MSSM), which turns out to be an ideal DM claimant, provided it is the lightest neutralino (as it is the case in large parameter space regions of many SUSY breaking scenarios).

Complementarity between direct detection and indirect detection methods has been repeatedly stressed [1]. However, the question regarding how competitive a given detection technique is compared to the others, can be addressed only resorting to particular particle physics frameworks, and making definite assumptions about the features of the Milky Way DM Halo.

In the present paper we address the issue of confronting a set of leading DM search strategies, focusing in particular on antimatter searches [2]. Pair annihilation is the mechanism which sets the thermal relic abundance of neutralinos; although the density of neutralinos in DM halos today is much smaller than in the early Universe environment, there is still a finite probability for WIMPs in the Galactic halo to annihilate in pairs. In these annihilations the same amount of matter and antimatter is produced; while the matter component is likely to be very subdominant compared to standard astrophysical sources, there seems to be no standard primary source of antimatter, with the bulk of the (scarce) antimatter component in cosmic rays which is likely to be of secondary origin, i.e. generated in the interaction of primary cosmic rays (mainly protons) with the interstellar medium (mainly hydrogen and helium). The goal is then to identify, through their peculiar spectral features, the WIMP-induced antimatter fluxes, or at least to exclude those DM candidates which would overproduce antimatter compared to the relatively low background term.

We will first outline our particle physics setup, in sec. 2, defining a set of benchmark neutralino models which we claim to be of particular relevance at antimatter searches; then, in sec. 3, we provide the details of our calculation of the antimatter fluxes. Finally, sec. 4 is devoted to the question of the future discrimination sensitivity at antimatter search facilities, and summarizes the comparison of the latter with different direct and indirect detection techniques. We draw our conclusions in sec. 5.

Model	$M_{1/2}, m_{3/2}, M_3$	$\tan\beta$	$\mathrm{sgn}(\mu)$	Defining Condition
Funnel	$700 \div 1450$	55	> 0	$2\,m_\chi \simeq m_A$
AMSB	$23 \div 231$	50	> 0	$m_0 = 1500$ GeV
NUGM	$879 \div 1096$	50	> 0	$M_1/M_3 = 10,\ M_2/M_3 = 2,\ \widetilde{H} = 99.8\%$

Table 1: The defining parameters for three SUSY models under consideration (see [2] for details).

2   Large Annihilation Rates Benchmark Models

From the point of view of indirect detection experiments, the most favorable situation in the particle physics setup occurs when neutralinos feature large pair annihilation rate $\langle\sigma_{\mathrm{ann}}v\rangle$. Since the thermal relic abundance of neutralinos in a standard cosmological setup forces $\langle\sigma_{\mathrm{ann}}v\rangle \simeq 3\cdot 10^{-27}\mathrm{cm}^3\mathrm{s}^{-1}/\Omega_{\mathrm{CDM}}h^2$, resorting to models with a large annihilation rate translates into assuming that either non-thermal mechanisms of neutralino production, or cosmological enhancement processes are operative [3]. We focus here on three benchmark neutralino scenarios, respectively featuring bino, wino and higgsino like LSP's (see Tab. 1). The models present remarkable purity in their dominant gauge-eigenstate component, in all cases larger than 98%, and the values for $\langle\sigma_{\mathrm{ann}}v\rangle$ lie, at a sample neutralino mass of 300 GeV, between 10^{-24} and 10^{-25} cm^{3}s^{-1}.

3   Computing Antimatter Yields

We discuss here the case of neutralino-induced antiproton, positron and antideuteron cosmic ray fluxes. The stable antimatter species generated by neutralino annihilations are simulated using the Monte Carlo code `Pythia` [4] 6.154, and we take the conservative cored Burkert profile as the reference DM halo model [5]. Concerning the propagation of charged cosmic rays through the Galactic magnetic fields, we consider an effective two-dimensional diffusion model in the steady state approximation where the diffusion coefficient D takes the form of a broken power law in rigidity, R,

$$
\begin{aligned}
D &= D_0\,(R/R_0)^{0.6} & \text{if} \quad R \geq R_0 \\
D &= D_0 & \text{if} \quad R < R_0\,.
\end{aligned}
\tag{1}
$$

We take eq. (1) with $D_0 = 2.5 \times 10^{28}$ cm^2 s^{-1} and $R_0 = 4$ GV, in a cylindrical diffusion region of radius equal to 30 kpc and half height equal to 4 kpc, plus a galactic wind term (see [2] for details). Finally, to sketch solar modulation effects we implement the one parameter model based on the analytical force-field approximation [7] taking for simplicity the parameter `smod` to be charge-independent.
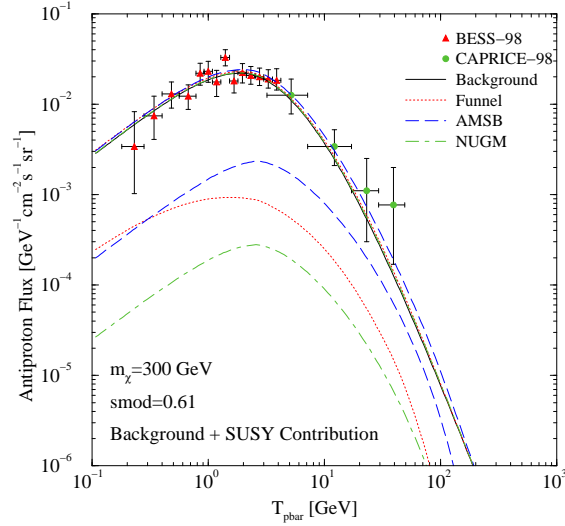
Figure 1: The solar modulated antiproton flux, as a function of the antiprotons kinetic energy T_{pbar} [2].

Fig. 1 shows the spectral features, after solar modulation for a given step along the solar activity cycle, of primary antiprotons and of the background, comparing the total expected signals to the data taken during the corresponding modulation phase. The figure refers to a common neutralino mass of 300 GeV. As regards the secondary antimatter fluxes, which play here the role of backgrounds, our estimates are produced running the `Galprop` [6] code in the configuration for propagation parameters we have adopted for the signals. We remark that we find, for both antiprotons and positrons, that the computed backgrounds provide by themselves excellent fits of the data: we obtain, for background only, a reduced χ^2 equal to 0.82 for antiprotons and to 0.95 for positrons. Excessive exotic signals may be therefore statistically ruled out [2].

4   Discrimination of SUSY DM Through Antimatter

New generation space-based experiments for antimatter searches PAMELA and AMS [8] will tremendously enhance the resolution and accuracy of positron and antiproton spectra measurements, as compared to existing balloon borne results. With the purpose of assessing discrimination capabilities of future experimental facilities, we will sketch here the possibility of disentangling an exotic component out of a standard secondary background. To this extent, we introduce a novel quantity, I_ϕ, to compare the case of a pure background
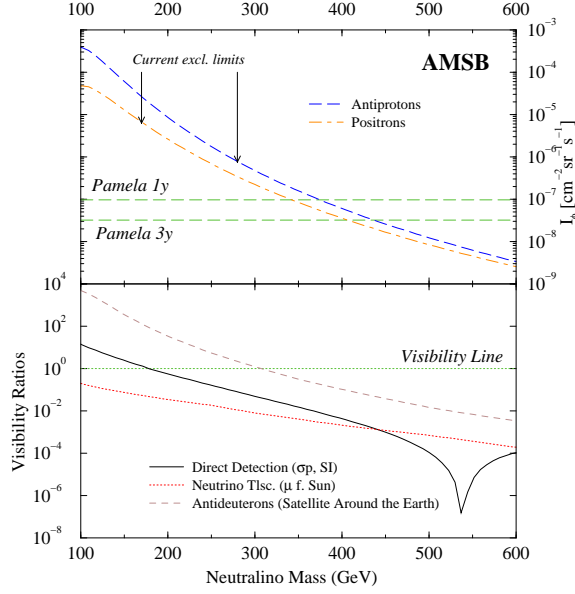
Figure 2: The comparison of future sensitivities for various detection techniques in the **AMSB** model.

measurement to that of the occurrence of a signal. It can be shown [2] that a signal with flux ϕ_s can be discriminated from a background flux ϕ_b at a payload with geometrical factor A and time of data acquisition T, at 95% C.L., if

$$I_\phi \equiv \int_{E_{\min}}^{E_{\max}} \frac{\phi_s^2}{\phi_b} \mathrm{d}E > \frac{(\chi^2)_{n_\mathrm{b}}^{95\%}}{A \cdot T}, \tag{2}$$

where $(\chi^2)_{n_\mathrm{b}}^{95\%}$ corresponds to n_b degrees of freedom, namely the number of energy bins of the data. We focus, for definiteness, on the case of the PAMELA detector, with an effective area of 24.5 cm^{2}sr, an exposure time of 3 years, and resorting to a trial energy binning as sketched in ref. [8]. This corresponds to a critical $I_\phi \simeq 3.2 \cdot 10^{-8}$cm^{-2}sr^{-1}s^{-1}.

As regards antideuterons, the background is expected to be totally negligible in the low energy regime, and we refer here to the proposed gaseous antiparticle spectrometer (GAPS) [9], looking for antideuterons in the energy interval 0.1-0.4 GeV per nucleon, with an estimated sensitivity level of 2.6×10^{-9}m^{-2}sr^{-1}GeV^{-1}s^{-1}.

Fig. 2 compares future detection perspectives in the **AMSB** benchmark model [2]. Direct and indirect detection techniques rates are given in terms of signal to sensitivity ratios (*Visibility Ratios*). Remarkably, the most promising

detection strategies, as emerging from the upper panel of the figure, reside in antiproton searches, but both positron and antideuteron searches look more promising than direct detection. We point out that our conclusions could have been even stronger had we resorted to a cuspy halo profile [2].

5 Conclusions

We considered antimatter yields in three benchmark scenarios with large annihilation rates, respectively featuring a bino, wino and a higgsino-like lightest neutralino. We introduced a new parameter I_ϕ which allows, given a SUSY model, to reliably assess its visibility at given future experiments. The comparison of future experimental DM search strategies shows that antimatter searches may be highly competitive with respect to both direct detection and neutrino telescopes. In some cases, such as for antiprotons in a wino DM scenario, antimatter searches may be *the only viable DM detection technique.* In the context of SUSY models with large annihilation cross sections, and in view of the imminent launch of space-based dedicated experiments, antimatter searches are therefore to be considered as a highly promising path towards the detection of DM.

References

[1] G. Jungman, M. Kamionkowski and K. Griest, Phys. Rep. **267** (1996) 195; L. Bergström, Rept. Prog. Phys. **63** (2000) 793.

[2] S. Profumo and P. Ullio, JCAP **0407** (2004) 006 [arXiv:hep-ph/0406018].

[3] S. Profumo and P. Ullio, JCAP **0311** (2003) 006 [arXiv:hep-ph/0309220]; S. Profumo and P. Ullio, arXiv:astro-ph/0404390.

[4] T. Sjöstrand, arXiv:hep-ph/9508391.

[5] A. Burkert, Astrophys. J. **447** (1995) L25.

[6] Galprop numerical package, http://www.mpe.mpg.de/~aws/propagate.html

[7] L.J. Gleeson and W.I. Axford, Astrophys. J. **149** (1967) L115; L.A. Fisk, J. Geophys. Res. 76 (1971) 221.

[8] O. Adriani et al. (Pamela Collaboration), Proc. of the 26th ICRC, Salt Lake City, 1999, OG.4.2.04; P. Picozza and A. Morselli, J. Phys. **G29** (2003) 903; S. Ahlen et al. (Ams Collaboration), Nucl. Instrum. Methods **A350** (1994) 351;

[9] K. Mori et al., Astrophys. J. **566** (2002) 604.

NEW CONSTRAINTS ON DARK ENERGY

Carolina J. Ödman [a], Alessandro Melchiorri [a]

[a] *Dipartimento di Fisica, Università di Roma "La Sapienza",
Ple Aldo Moro 2 - 5, 00185 Roma, Italy*

Abstract

We present the cosmological observations that provide evidence for a dark
energy component in the make-up of the universe. We review different
types of models and their properties. We then show constraints on the
value of the dark energy equation of state obtained from observations
of the cosmic microwave background, large-scale structure, supernovae
of type 1a and other observations. We obtain that observations are
consistent with a cosmological constant and that the preferred value of
the equation of state of dark energy is smaller than -1.

1 The Dark Energy problem

In order to understand why Dark Energy (DE) is keeping so many cosmologists
busy, one must first go back to the energy density budget of the universe

$$\Omega_{\mathrm{b}} + \Omega_{\mathrm{DM}} + \Omega_{\mathrm{K}} + \Omega_{\mathrm{DE}} = 1 \tag{1}$$

where Ω_{X} is ratio of the energy density of component X to the critical density
corresponding to a flat geometry of the universe. We are considering baryons

b, cold dark matter DM and dark energy DE. Ω_K is the spatial curvature of the universe expressed in units of energy density.

The second ingredient to the DE problem lies in observations of distant supernovae of type 1a (SNe). They appear dimmer than expected in a universe dynamically dominated by gravitation: SNe data show that the expansion of the universe is accelerating. In Friedman's equation

$$\ddot{a} = -\frac{4\pi G}{3}(\rho + p)a, \tag{2}$$

where a is the scale factor of the universe, ρ the total energy density and p the pressure, this translates into the condition that the dominant component in the universe has *negative* pressure: $\rho + 3p < 0$.

Finally, large-scale structure (LSS) measurements from galaxy redshift surveys [1, 2] show evidence for a low matter density Ω_m and the temperature fluctuations of the cosmic microwave background (CMB) points towards a flat cosmic geometry. This suggests the presence of a dominant DE component which provides the drive to the observed acceleration of the cosmic expansion.

$$\left.\begin{array}{rcl} \Omega_b + \Omega_{DM} & \cong & 0.3 \\ \Omega_K & = & 0 \end{array}\right\} \rightarrow \Omega_{DE} \cong 0.7 \tag{3}$$

2 Models of DE

DE is parametrised by its equation of state defined as

$$w_{DE} = \frac{p_{DE}}{\rho_{DE}}. \tag{4}$$

In order to achieve acceleration in equation 2 the DE equation of state must obey $w_{DE} < -\frac{1}{3}$. The evolution of the energy density of each component can be expressed in terms of redshift z and its equation of state w.

$$\Omega_X(z) = \Omega_{X,0}(1 + z)^{3(1 + w_X)} \tag{5}$$

where $\Omega_{X,0}$ is the present relative desnity of component X. In [4], Bean & al. show that DE cannot be a significant contributor to the total energy density in the early universe as it would change the primordial abundances from Big Bang Nucleosynthesis (BBN).

Historically, the first DE candidate is Einstein's cosmological constant

$$\Omega_\Lambda = \frac{\Lambda c^2}{3 H_0^2} \quad , \quad w_\Lambda = -1 \tag{6}$$

where H_0 is the present value of the Hubble paramter and c is the speed of light. Λ represents a vacuum energy with negative pressure. The problem with

a cosmological constant is that it suffers from fine-tuning and its value in the very early universe is 120 orders of magnitude smaller than any other energy scale.

Quintessence models [5] are a class of DE candidates described by a scalar field Φ rolling down a potential $V(\Phi)$ such that

$$
\begin{aligned}
\text{energy density:} \quad \rho_\Phi &= K(\Phi) + V(\Phi) \quad \text{and} \\
\text{pressure:} \quad p_\Phi &= K(\Phi) - V(\Phi)
\end{aligned}
\tag{7}
$$

where $K(\Phi)$ is the kinetic energy of the field. In order to achieve negative pressure, the quintessence field must obey the slow-roll condition $V(\Phi) > K(\Phi)$. The equation of state can take values $-2/3 \leq w_\Phi \leq -1$. Such models suffer from fine-tuning problems unless they display *tracker* behaviour [6]. For a large range of initial conditions tracker models evolve quickly towards an attractor solution which tracks the dominant component (radiation, matter, etc.). Such models provide an explanation for the fact that the DE energy density is comparable to the matter energy density today but their energy scale in the early universe is still too small.

Another DE candidate is the Chaplygin gas [7]. In this case, the DE equation of state evolves in time $w_{DE} = w_{DE}(z)$. Chaplygin gas models unify dark matter and dark enery. In the distant past, the gas acts like matter and at present times it acts like DE:

$$
\begin{aligned}
w_{DE} &\sim 0 \quad \text{in the early universe} \\
w_{DE} &\leq -1 \quad \text{in the late universe.}
\end{aligned}
\tag{8}
$$

The problem with this class of models is the calculation of the evolution of perturbations and the formation of structures. The speed of sound of the Chaplygin gas $c_s^2 = \partial p_{DE}/\partial \rho_{DE}$ takes non-trivial values.

The value of the equation of state of phantom DE [8] models lies below -1. From equation 4, it appears that this violates the weak energy condition: $p + \rho \geq 0$. The fate of a universe dominated by phantom DE is catastrophic. It ends in a "big rip" at a finite time. Phantom DE models fit the observations well but involve exotic physics.

3   Constraints on the DE equation of state

The value $w_\Lambda = -1$ is often considered to be the limiting case for DE models. As mentioned above any value below that requires strange physics. Because of the nature of the observations, comparaison of data to DE models is made through the luminosity and angular diameter distances. Observations are only able to constrain a function of an effective value of the equation of state or w
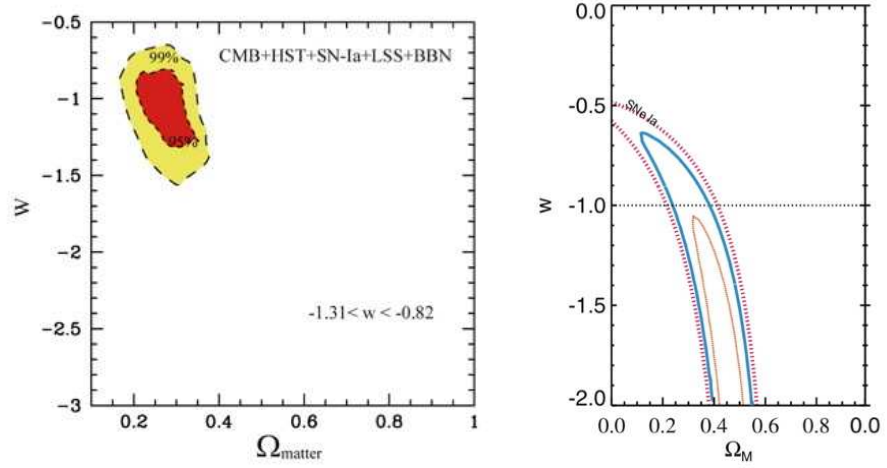
Figure 1: Constraints on the equation of state of DE.

integrated over the history of the universe:

$$w_{\mathrm{DE}}^{\mathrm{eff}} \sim \frac{\int w_{\mathrm{DE}}(a)\Omega_{\mathrm{DE}}(a)da}{\int \Omega_{\mathrm{DE}}(a)da} \tag{9}$$

In [9] Maor & al. show that DE models exist whose equation of state never takes values below -1 but appear to have an effective value of the equation of state below -1. Moreover, the exclusion of $w_{\mathrm{DE}} < -1$ results in a biased estimation of w_{DE} from observations.

A Bayesian approach is used to examine observational data of the CMB, LSS, SNe and other cosmological probes. The likelihood of a model of DE corresponds to the probability of observing what is seen if that model were the correct description of the universe. The value of the DE equation of state is thereby constrained.

In February of 2003, the first year of observations of the CMB from the WMAP satellite [3] were made public. In [10] Melchiorri & al. obtain constraints on the DE equation of state and the matter density before and after the WMAP results. They find that a cosmological constant is not ruled out but most of the 1σ confidence region in the $w_{\mathrm{DE}} - \Omega_{\mathrm{m}}$ plane lies below $w_{\mathrm{DE}} = -1$.

Since, more SNe observations have become available. In [11] Tonry & al. also include data from the 2dF galaxy redshift survey and obtain $-1.48 < w_{\mathrm{DE}} < -0.72$ at the 95% confindence level for a flat universe. Riess & al. [12]

obtain $-1.21 < w_{\mathrm{DE}} < -0.89$ at the 68% confidence level for a flat universe using observations from 186 SNe reaching a redshift of 1.55. The breakthrough in the Riess & al. observations lie in their detection of the turn-over time when the expansion of the universe changed from decelerating to accelerating. This transition is detected to be at a redshift of $z = 0.46 \pm 0.13$.

Figure 1 shows the results obtained from our latest analysis using the new SNe data. We obtain from SNe alone that $w_{\mathrm{DE}} < -0.6$ at the 95% confidence level. A cosmological constant is consistent with the data but lower values of w_{DE} are preferred. We obtain $-1.31 < w_{\mathrm{DE}} < -0.82$ at the 95% level with CMB and LSS data as well as BBN constraints and the HST constraint on the value of the Hubble parameter [13].

4   Conclusion

An increasing number of observations of the CMB, SNe and LSS show that some form of DE must be present. The detection of the transition from deceleration to acceleration of the expansion of the universe confirms that SNe detect DE and do not suffer from some other astrophysical effect. A satisfying theoretical model has still to be found even if the constraints on DE models shrink with the increasing amount of data. At present the data cannot eliminate any particular class of models.

In the future, more data from the second year of observations from the WMAP satellite will tighten the constraints further. The SNAP and Planck missions are being developed [15] and other observations providing indirect constraints on DE are bcoming available [14].

References

[1] http://www.mso.anu.edu.au/2dFGRS
Efstathiou & al. *Evidence for a non-zero Λ and a low matter density from a combined analysis of the 2dFGRS and CMB Anisotropies*, Mon.Not.Roy.Astron.Soc. 330 (2002) L29

[2] http://www.sdss.org/
A. C. Pope & al. *Cosmological Parameters from Eigenmode Analysis of SDSS Galaxy Redshifts*, Astrophys.J. 607 (2004) 655-660

[3] http://map.gsfc.nasa.gov/
D. N. Spergel & al. *First Year WMAP Observations: Determination of Cosmological Parameters*, Astrophys.J.Suppl. 148 (2003) 175

[4] R. Bean & al. *Early-universe constraints on a Primordial Scaling Field*, Phys.Rev. D64 (2001) 103508

[5] B. Ratra & P. J. E. Peebles *Cosmological consequences of a rolling homogeneous scalar field*, Phys.Rev. D37 (1988) 3406
I. Zlatev, L. Wang & P. J. Steinhardt *Quintessence, Cosmic Coincidence, and the Cosmological Constant* Phys.Rev.Lett. 82 (1999) 896-899

[6] L. Wang & al. *Cosmic Concordance and Quintessence*, Astrophys.J. 530 (2000) 17-35

[7] L. Amendola & al. *WMAP and the Generalized Chaplygin Gas*, JCAP 0307 (2003) 005
R. Bean & O. Dore *Are Chaplygin gases serious contenders to the dark energy throne?*, Phys.Rev. D68 (2003) 023515

[8] R. R. Caldwell *A Phantom Menace? Cosmological consequences of a dark energy component with super-negative equation of state*, Phys.Lett. B545 (2002) 23-29
A. Melchiorri *New Constraints on Dark Energy*, Proc. Rencontres de Moriond 2004, astro-ph/0406652.

[9] Maor & al. *Measuring the Equation-of-state of the Universe: Pitfalls and Prospects*, Phys.Rev. D65 (2002) 123003

[10] A. Melchirri & al. *The State of the Dark Energy Equation of State*, Phys.Rev. D68 (2003) 043509

[11] J. L. Tonry & al. *Cosmological Results from High-z Supernovae*, Astrophys.J. 594 (2003) 1-24

[12] A. Riess & al. *Type Ia Supernova Discoveries at z¿1 From the Hubble Space Telescope: Evidence for Past Deceleration and Constraints on Dark Energy Evolution*, Astrophys.J. 607 (2004) 665-687

[13] W. L. Freedman & al. *Final Results from the Hubble Space Telescope Key Project to Measure the Hubble Constant*, Astrophys.J. 553 (2001) 47-72

[14] S. P. Boughn & R. G. Crittenden *Cross Correlation of the Cosmic Microwave Background with Radio Sources: Constraints on an Accelerating Universe*, Phys.Rev.Lett. 82 (2002) 021302

[15] http://snap.lbl.gov/ & http://www.rssd.esa.int/index.php?project=Planck

LATEST RESULTS AND FUTURE OF THE EDELWEISS EXPERIMENT

B. CENSIER[a], FOR THE EDELWEISS COLLABORATION

[a] *Centre de Spectrométrie Nucléaire et Spectrométrie de Masse,*
Bât. 108, F-91405 Orsay Cedex (France)

Abstract

The latest results of the EDELWEISS-I WIMPs direct detection experiment are presented, including the simultaneous use of 3 heat and ionisation 320g germanium bolometers with improved energy threshold. EDELWEISS-I is already sensitive to the most optimistic SUSY models. Testing more favored models will require a higher target mass, but also an improved background rejection, as will be done in EDELWEISS-II. This second phase and R&D work on detector improvements are presented.

1 Dark matter and the WIMPs hypothesis

Since Zwicky's observations of the Coma cluster [1], we know there is a huge discrepancy between densities evaluated by mass-luminosity relationships, and by methods based on kinematical arguments. This discrepancy has been confirmed on every scale, from galaxies to large scale structures. Several methods involving gravitational lensing[2], CMB measurements[3]or big-bang nucleosynthesis[4], converge toward one conclusion: unless our understanding of gravity is to be reconsidered, about 25% of the universe's energy budget is made of an unknown, non-radiating and non-baryonic type of matter. Given these constraints, today's most favored dark matter candidates are Weakly Interactive Massive Particles (WIMPs), with a mass between a few tens and a few hundreds of GeV/c^2. Our galaxy is believed to bathe in a WIMPs halo, and EDELWEISS is aiming at the detection of these galactic WIMPs.

2   Direct detection with EDELWEISS-I

WIMPs trapped in our galaxy would have relative velocities of a few hundred km/s. Elastic recoils on target nuclei then lead to a typical energy deposit of a few tens of keV, most of the events being expected at low energies, with a very low detection rate (<1 event/kg/day). The main experimental constraints are thus a low energy threshold, a good energy resolution, and a severe control of the background interactions.

Passive shielding for a low background environment: EDELWEISS is located in Modane underground laboratory, in the Fréjus tunnel, where most of the cosmic-ray induced muons are absorbed through 1700m of rock overburden. The typical muon flux is 4 muons/m^2/day, while the neutron flux is about 1.6×10^{-6}neutrons/cm2/day. To further ensure a low background environment, a passive shielding made of 30cm thick paraffin moderates the fast neutron flux, whereas copper and lead shields minimize the gamma-ray background.

Active rejection with Heat-and-Ionisation bolometers: One of the main EDELWEISS features is an additional active background rejection technique. It allows event by event discrimination between two types of populations, namely 'electron recoils' (γ's and β's) and 'nuclear recoils'(neutrons or WIMPs). This is based on the simultaneous measurement of charge and phonon signals, in an ultra-pure germanium absorber cooled down to $\approx$17mK. Electron recoils, the main source of radioactive background, are indeed producing a higher ionisation-over-recoil ratio than nuclear recoils (Fig.1). The rejection factor for electron recoils is better than 99.9% for a recoil energy threshold of 15keV, as shown by gamma-ray source calibrations. The Ge crystal is fitted with Al electrodes for charge collection. A typical event generates a few thousand of electron-hole pairs, which drift in a collecting field of the order of 1V/cm. Typical collection times are a few hundred ns. Phonon measurements are made by a Neutron Transmutation Doped Ge thermistor (NTD) glued on the absorber. It measures temperature rise of some tens of μK, with typical time constant of several tens of ms.

3   Final results of EDELWEISS-I

Three 320g detectors are operated. The acquisition was previously triggered on the ionisation channel, with a recoil energy threshold of 30keV at 100% efficiency (20 keV for one detector). For the last data sample, acquisition was triggered on the phonon channel, resulting in a lowering of the energy threshold down to 15keV recoil energy. In this additional 22.66 kg.day exposure, there are 33 events compatible with nuclear recoils above 15 keV, most of them being under 30keV, with one neutron coincidence in two detectors. Attributing all these events to WIMPs interaction, a conservative limit on WIMPs scaterring
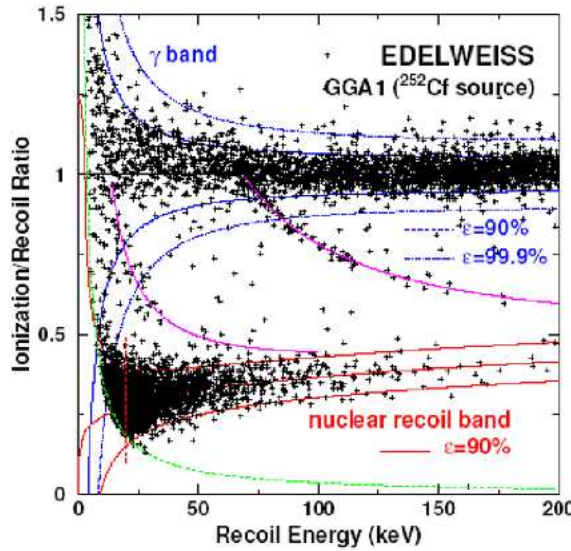
Figure 1: Ionisation over recoil ratio vs. recoil energy for a neutron source calibration.[5]

cross-section is calculated with the optimum interval method[7](Fig.2). It confirms our detection sensitivity with a total 60kg.day fiducial exposure. Fig.2 also presents the first results of CDMS-II in the Soudan underground laboratory using an additional cut on the time delay and rise time of the athermal phonons signal for miscollected surface events identification.

4   EDELWEISS-II

Once EDELWEISS-I was dismounted, the installation of EDELWEISS-II has started in April 2004. The goal is an increase of a factor ≈100 in detection sensitivity (down to 10^{-8}pb cross sections). The target mass will be increased, with up to 120 detectors (≈36kg). These will be cooled down to $\approx 20mK$ in a 100L cryostat which has been developed and tested in CRTBT (Grenoble). In the first phase (expected for 2005), 21 Ge bolometers with NTD sensors and Al electrodes will be operated, together with 7 new type detectors fitted with NbSi thin films (see next section). Nevertheless, increasing the mass is not sufficient. As showed by EDELWEISS-I, two main limitations must be overcome. First, the neutron background, originating from the radioactivity of the rock (low energy neutrons) and from the interaction of high energy muons in the surrounding rock and inside the experiment must be reduced. With this respect, a muon veto made of about 140m^2 of plastic scintillators (developped
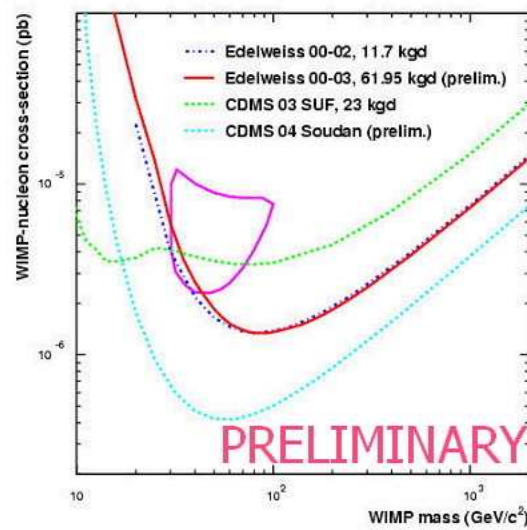
Figure 2: Exclusion curves of CDMS and EDELWEISS, under the assumption of spin-independent interaction of neutralino, assuming a standard spherical and isothermal halo[6]. The 3σ zone of the DAMA candidate is also shown [9].

at FZ-Karlsruhe) will surround the cryostat, in addition to an improved passive shielding of 50cm polyethylen and 20cm of lead. Second, the existence of a so-called 'dead layer' with poor charge collection has been demonstrated[10]. As a consequence, electron recoil events occuring closer than a few 10s of μm from an electrode may mimic a nuclear recoil. The use of amorphous Ge or Si layers between the metallic electrodes and the Ge crystal has been shown to greatly improve this point[11]. At such a sensitivity level, however, the identification of near-electrode events is of great concern.

5   R&D for near-electrodes events identification

Two possibilities, that may be complementary and give a useful redundancy, are explored:

Measurement of out-of-equilibrium phonons: At low temperatures, the mean free path of these high energy phonons is large enough for considering their detection in a massive bolometer. With NTD sensors, however, they tend to be absorbed by the glue used to fix the thermistor. A new type of heat

and ionisation bolometer are thus developed at CSNSM(Orsay). Thermometry as well as charge collection, are performed using evaporated thin NbSi films (typically 100nm thick). The good coupling between NbSi films and the Ge crystal allows non-thermal phonons detection. In particular, they have been shown to exhibit an enhanced transient part in the case of near electrodes events[12]. NbSi bolometers of mass 200g have been tested in Modane. The first encouraging results show a rejection of 90% of miscollected events, by cutting 50% of the total number of events. The next step will be to improve charge collection efficiency by means of an amorphous Ge layer and a more efficient electrode geometry.

Time-resolved measurement of the ionisation signal: Low noise charge amplifiers have been developped for this purpose, cryogenic setup being a handicap due to large wire capacitance. The second challenge is the modelisation of charge transport. At such low temperatures, the drift velocity versus field relationship is non-linear, and due to low collection fields, the space charge effects may become important [13](coulombian interaction between carriers, trapped charge). A simulation code involving all these aspects has been developed. On small test detectors, a 1mm resolution on the distance of the event from the electrodes has been achieved at 122keV [14], proving the potential of the method. At lower energies, of great significance for dark matter detection, it is however limited by a too high signal-over-noise ratio. With this respect, a collaboration between CSNSM, CEA and LPN has been settled, for the development of new charge amplifiers, with high electron mobility GaAs transistors as front-end components.

6   Conclusion

The analysis of the whole data sample of EDELWEISS-I, involving a better energy threshold, are confirming the sensitivity initially achieved on a smaller data sample. EDELWEISS-II will push the detection limits further thanks to a higher target mass and an improved shielding. The low sensitivity levels achieved will require a deeper understanding of the background, especially rare neutrons events, but also of the physical processes taking place in cryogenic detectors.

References

[1] F. Zwicky, Helv. Phys. Acta **6**, 110 (1933)

[2] L. Van Waerbeke et al., A&A **393**, 369 (2002)

[3] D.N. Spergel et al., Astrophys. J. Suppl. **148**, 175 (2003)

[4] S. Burles et al., Phys. Rev. D **63**, 063512, (2001)

[5] O. Martineau et al., Nucl. instr. meth. A, **530**, 426 (2004)

[6] J.D. Lewin and P.F. Smith, Astropart. Phys., **6**, 87 (1996)

[7] S. Yellin, Phys. Rev. D, **66**, 032005 (2002)

[8] A. Benoit et al., Phys. Lett. B, **43**, (2002)

[9] R. Bernabei et al., Riv. N. Cim., **26**, 1 (2003)

[10] A. Benoit et al., Phys.Lett. B **479**, 8 (2000)

[11] T. Shutt et al., Proceedings of LTD-8(1999)

[12] S. Marnieros et al., Nucl. Instr. Meth. A, **520**, 185 (2004)

[13] B. Censier et al., Nucl. Instr. Meth. A **520**, 156 (2004)

[14] A. Broniatowski et al., AIP conference proceedings, **605**, 521 (2001)

ANISOTROPIC SCINTILLATORS FOR PARTICLE DARK MATTER DIRECT DETECTION

F. NOZZOLI [a], R. BERNABEI [a], P. BELLI [a], A. INCICCHITTI [b]

[a] *Dipartimento di Fisica, Università di Roma "Tor Vergata",*
INFN, Sezione di Roma II, via della Ricerca Scientifica, Roma, Italy

[b] *Dipartimento di Fisica, Università di Roma "La Sapienza",*
INFN, Sezione di Roma, I-00185, Roma, Italy

Abstract

Some aspects on the possibility to exploit the WIMP directionality signature by using anisotropic scintillators are discussed.

1 Introduction

Among the possible signatures that could be exploited to investigate the dark matter particle component in the galactic halo, the directionality (based on the correlation between the direction of the nuclear recoils from WIMP-nucleus elastic scatterings and the Earth's galactic motion) is particularly attracting [1]. An experimental approach to exploit it by means of anisotropic scintillators was firstly pointed out by some of us in ref. [2] and revisited more recently in ref. [3]; on this basis some preliminary activities have also recently been carried out by various authors [4, 5]. In the following we will underline the peculiarities of the signature and an evaluation, obtained by using a modeling, of the sensitivity achieved with an hypothetical anthracene set-up.

2   Some general considerations on WIMP arrival direction

As the detector is considered fixed to the Earth surface, the expected mean WIMP arrival direction is opposite to the Earth velocity direction $\vec{v}_d(t)$ in the galactic halo. Considering the crucial role played by $\vec{v}_d(t)$ in the *directionality signature*, let us preliminarily devote this short section to its suitable evaluation. The detector velocity in the galactic rest frame can be expressed as: $\vec{v}_d(t) = \vec{v}_{rot} + \vec{v}_{LSR} + \vec{v}_E(t)$, where $\vec{v}_{rot}$ is the rotational velocity of the Milky Way around its polar axis, $\vec{v}_{LSR}$ is the solar system's velocity with respect to the Local Standard of Rest and $\vec{v}_E(t)$ is the Earth velocity around the Sun. The direction of $\vec{v}_d(t)$ identifies a point, P, where the WIMPs preferentially come from, in the celestial sphere. The galactic equatorial coordinates of P are near to $315.8^o R.A.$ and $49.6^o decl.$ [1]. When instead a laboratory rest frame such as e.g. the azimuth-zenith horizontal frame is considered, the direction of $\vec{v}_d(t)$ roughly describes in the sky a circular trajectory centered in the Earth polar axis because of the Earth diurnal rotation, implying a large diurnal time dependence of the $\vec{v}_d(t)$ direction. As an example, Fig. 1.a shows the directions in the sky (identified by the polar and azimuthal angles $\phi_a(t)$ and $\theta_z(t)$) of $\vec{v}_d(t)$ calculated for the next three years as they would be observed at the Gran Sasso National Laboratory (LNGS) of I.N.F.N. ($42^o27'N$ *latitude* and $13^o10'50"E$ *longitude*).

However, it is much more convenient for our purposes to consider instead an horizontal coordinate frame located at the North pole (described by the "polar-zenith", $\theta_{pz}(t)$, and by the "polar-azimuth", $\phi_{pa}(t)$); in fact, in this case the area in the sky of interest for the calculation of the signal rate is only a strip, see Fig. 1.b. In the following discussion we will consider this latter more convenient reference frame.

3   The anthracene as a *directional* detector

The peculiarity of an anisotropic scintillator, such as anthracene $C_{14}H_{10}$ and stilbene $C_{14}H_{12}$, is that its light response, and obviously the quenching factors, to heavy particles (p, α, recoil nuclei, ...) depends on their impinging direction with the respect to the crystal axes. In particular, measurements performed in the past and also confirmed recently by [4, 5] have shown that the light response of an anthracene scintillator to α particles impinging in the direction of the b-axis (a-axis) is 66% (80%) of the light response obtained when the same particles impinge in the direction of c'-axis (where the light yield reaches its maximum value) [7]; see left side of Fig. 2. Thus, in principle, the features

---

[1] The NOVAS routines [6] allow to calculate the contribution of Earth motion around the Sun and the little annual variation with respect to P.
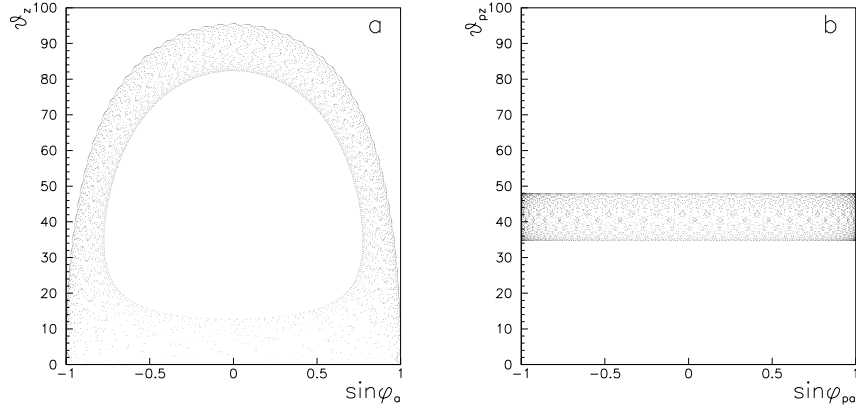
Figure 1: The various directions, in the sky, of the detector galactic velocity $\vec{v}_d(t)$ calculated for the next three years as viewed from LNGS ($42^o27'N$ *latitude* and $13^o10'50"E$ *longitude*) in the local horizontal coordinate frame (a) and in the coordinate frame located to the North pole (b). See text.

of the anisotropic scintillators could be exploited in further investigations on the WIMP component in the galactic halo. In fact, heavy ionizing particles with a preferred direction (like recoil nuclei induced by WIMP-nucleus elastic scatterings) could be discriminated from the electromagnetic background (for which no scintillation light anisotropy is observed in those scintillators) by comparing the low energy distributions measured by using different orientations of the crystal axes; for details see [3] and references therein.

As shown in Fig. 1.b, the "polar-zenith" angle, θ_{pz}, is always near 40°; therefore, if at a certain time of the day the WIMPs come mainly from the top, 12 hours later they come near the horizon and from North; see the right side of Fig. 2. Thus, if a scintillator with an anisotropic light yield is considered, a suitable arrangement for such an experiment is to install the set-up with the detectors' axis having the largest *quenching factor* value (the c' axis in anthracene) in the vertical direction, and with the axis having the smallest *quenching factor* value (the b axis in anthracene) towards the North. In this way, the behaviour of the energy spectrum of the WIMP induced nuclear recoils diurnally varies and, therefore, also the counting rate. In practice, the investigation can be performed as a function of $\vec{v}_d(t)$. In the following, to offer a simple example on corollary model dependent implications of such a signature, the results of some calculations obtained for the case of a possible anthracene set-up are shown. In particular, we use the *quenching factor* values
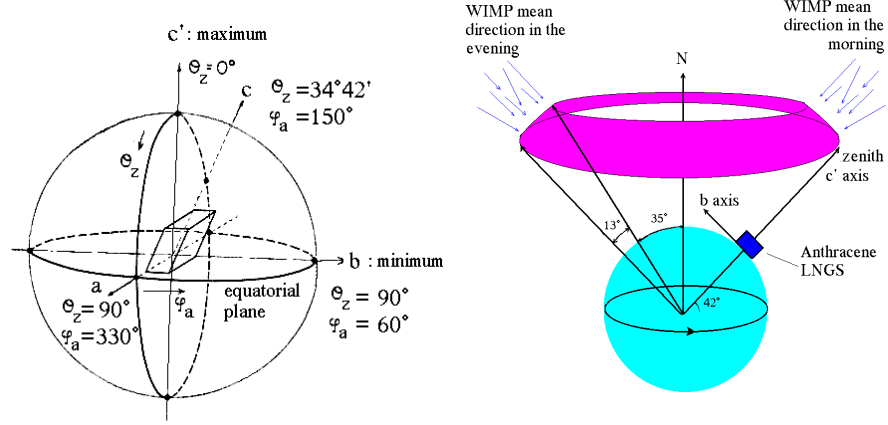
Figure 2: *Left*: a schematic representation of the crystal axes of anthracene. The *quenching factor* is maximum in the direction of c' axis, which is perpendicular to the *ab* plane [8]. *Right*: a schematic representation of the experimental approach mentioned in the text. The anthracene detector is placed ideally at LNGS with c' axis in the vertical direction and b axis pointing to the North. The area in the sky from which the WIMPs are preferentially expected is highlighted.

for the c' axis: $q_{H,c'} = 0.2$ and $q_{C,c'} = 0.1$ and for the ratios $\frac{q_{c'}}{q_a} = 1.23$ and $\frac{q_{c'}}{q_b} = 1.52$ (these latter ones have been assumed equal for the two atomic species) [7]. Moreover, a simplified single model framework has also been fixed [2]: i) purely spin-independent (SI) coupling, ii) a simple exponential form factor, iii) a simple spherical isothermal WIMP halo model. For this given model framework the signal counting rate expected in an anthracene detector has been calculated considering as an example a WIMP with $m_W = 50$ GeV and $\sigma_p = 3 \cdot 10^{-6}$ pb.

On the left side of Fig. 3 it is shown the counting rate expected for the assumed model scenario as a function of the WIMP arrival direction with the respect to the crystal axes, using the schematic configuration of Fig. 2. A clear dependence on ϕ_{pa} (which gives the observed rate diurnal variation because of the Earth daily rotation) is expected.

---

[2]for some discussions on models see e.g. [1] and references therein.
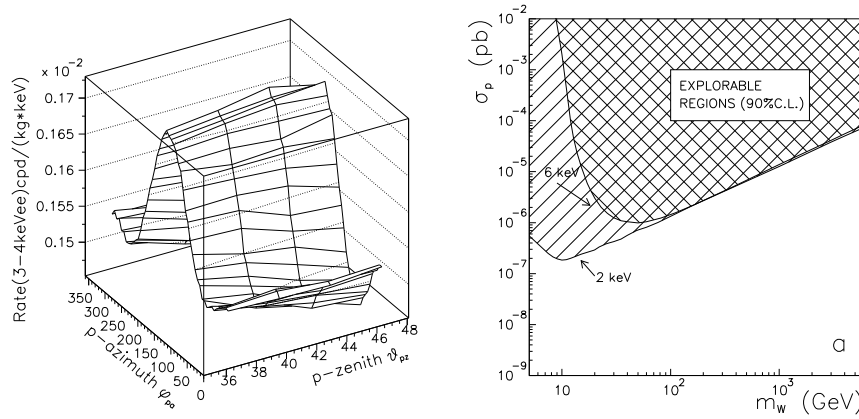
Figure 3: *Left*: example of the expected rate, in the 3-4 keV energy windows, versus the detector's (or Earth's) possible velocity directions for the particular choice of parameters and model summarized in the text (see also ref. [3]). *Right*: sensitivity (90% C.L.) reachable in the corollary model dependent interpretations with the *directionality signature* for a 500 kg anthracene detector, in 10 y of running – provided a time-independent background $b = 10^{-4}$ cpd/kg/keV and a SI coupled WIMP – for 2 and 6 keV energy thresholds in the simplified model framework given in the text and in ref. [3].

4 Reachable sensitivities

An evaluation of the sensitivity achievable with an hypothetical anthracene set-up with statistics of 5000 kg × y and a background level of $b = 10^{-4}$ cpd/kg/keV is given in ref. [3]. On the right side of Fig. 3 the explorable region (at 90% C.L.) in the plane σ_p and m_W is given for the considered model. However, although the relatively good sensitivities reported in Fig. 3, the feasibility of such an experiment would present several practical difficulties requiring the use of a very large number of small anthracene detectors as well as the necessity of a new special development to create efficient, small size, high gain, highly radiopure scintillation light collector devices. In particular, organics scintillators are expected to have low WIMP-nucleus cross section because the low atomic weight of H and C. Ref. [3] shows that an hypothetical anisotropic scintillator with the same characteristics of the anthracene described above, but with an atomic weight of A=140, will have nominal sensitivity more than one order of magnitude better. Thus, it appears suitable to pursue R&D's toward the realization of anisotropic scintillators

having significantly larger size, higher light response, higher atomic weight and anisotropy features similar or better than those of the anthracene scintillator.

References

[1] R. Bernabei et al., *Riv. Nuovo Cimento* 26 n1 (2003) 1; astro-ph/0307403.

[2] P. Belli, R. Bernabei, A. Incicchitti and D. Prosperi, *Il Nuovo Cim.* C15 (1992) 475.

[3] R. Bernabei, P. Belli, F. Nozzoli, A. Incicchitti, *Eur. Phys. J.* C 28 (2003) 203.

[4] N.J.C. Spooner et al., *Int. Workshop on Identification of Dark Matter*, World Scientific (1997) 481.

[5] Y. Shimizu, M. Minowa, H. Sekiya, Y. Inoue, *Nucl. Instr. & Meth.* A496 (2003) 347.

[6] http://aa.usno.navy.mil/software/novas/

[7] J. B. Birks: *The Theory and Practice of Scintillation Counting* (Pergamon Press Ltd., London,1976); P. H. Heckmann, *Z. Phys.* 157 (1959) 10; P. H. Heckmann, H. Hansen and A. Flammersfeld, *Z. Phys.* 162 (1961) 84; W. F. Kienzle and A. Flammersfeld, *Z.Phys.* 165 (1961) 1; K. Tsukada, S. Kikuchi, *Nucl. Inst. & Meth.* 17 (1962) 286; K. Tsukada, S. Kikuchi and Y. Miygawa, *Nucl. Inst. & Meth.* 37 (1965) 69; F. J. Kratochwill, *Z. Phys.* 234 (1970) 74; F. D. Brooks and D. T. Jones, *Nucl. Inst. & Meth.* 121 (1974) 69.

[8] K. Tsukada, S. Kikuchi, *Nucl. Inst. & Meth.* 17 (1962) 286.

SEARCH FOR SOLAR AXIONS BY PRIMAKOFF EFFECT IN NAI CRYSTALS

R. Bernabei [a], P. Belli [a], F. Montecchia [a,b], F. Nozzoli [a],
A. Incicchitti [c], D. Prosperi [c], R. Cerulli [d], C.J. Dai [e], H.L. He [e],
H.H. Kuang [e], J.M. Ma [e], S. Scopel [f]

[a] Dipartimento di Fisica, Università di Roma "Tor Vergata", and INFN, Sezione di
Roma II, I-00133, Roma, Italy

[b] Università Campus Bio-Medico di Roma, I-00155, Rome, Italy

[c] Dipartimento di Fisica, Università di Roma "La Sapienza" and INFN, sezione di
Roma, I-00185, Roma, Italy

[d] INFN - Laboratori Nazionali del Gran Sasso, I67010, Assergi (Aq), Italy

[e] IHEP, Chinese Academy, P.O. Box 918/3, Beijing 100039, China

[f] Dip. di Fisica Teorica, Università di Torino and INFN, sez. Torino, I-10125
Torino, Italy

Abstract

A search for solar axions exploiting the Primakoff coherent converion of
these particles into photons in the NaI(Tl) crystals of DAMA/NaI set-up
is presented.

211

1   Introduction

The axion was introduced in 1977 as the Nambu–Goldstone boson of the Peccei–Quinn (PQ) symmetry proposed to explain CP conservation in QCD [1]. The theory does not provide restrictions on axion mass, therefore in the past a certain number of experiments was realised to search for these particles in a large extent, without success.

Various experimental and theoretical considerations have restricted at present the axion mass to the range 10^{-6}eV $\lesssim m_a \lesssim 10^{-2}$eV and $m_a \sim$ eV. It has also been noted that axions with a similar mass could be candidate as a possible component of the Dark Matter in the Universe.

Axions can efficiently be produced in the interior of the Sun by Primakoff conversion of the blackbody photons in the fluctuating electric field of the plasma. The outgoing axion flux has an average energy, E_a, of about 4 keV since the temperature in the Sun core is $T \sim 10^7 K$. In the hypothesis of no direct coupling between axion and leptons (*hadronic axion*) and including in the solar model helium and metal diffusion, the flux of solar axions depends on the squared root of the dimensionless coupling constant $\lambda = (g_{a\gamma\gamma} \times 10^8/\text{GeV}^{-1})^4$ [2, 3], where $g_{a\gamma\gamma}$ is the coupling constant of the conversion of the axion into a photon; its value depends on the considered axion model [4, 5].

When solar axions interact with the electric field of the crystal's atoms detectable X–rays can be produced via a coherent effect, and, if the Bragg condition is fulfilled, a strong enhancement of the possible signal can be expected. Thus, a distinctive signature for solar axion can be searched for by comparing the experimental counting rate with the expected one by taking into account the position of the Sun in the sky during the data taking [6, 7, 8]. We note that positive results or bounds on $g_{a\gamma\gamma}$ obtained by this approach are independent on m_a and, therefore, overcome the limitations of some other techniques which are instead restricted to a limited mass range [9, 10].

DAMA experiment has searched for solar axions exploiting this approach [11] by means of the $\simeq$ 100 kg NaI(Tl) DAMA set-up [12] running deep underground in the Gran Sasso National Laboratory of I.N.F.N.. The Laboratory is located at $42^o27'N$ latitude, $13^o11'E$ longitude and 940 m level with respect to the mean Earth ellipsoid.

2   Experimental set-up

DAMA/NaI set-up – consisting in $\simeq$ 100 kg of highly radiopure NaI(Tl) – and its performances have been described in detail elsewhere [12]. Here we only remind that the data of this analysis have been collected with nine 9.70 kg NaI(Tl) crystal scintillators – $(10.2 \times 10.2 \times 25.4)$ cm^3 each one – enclosed in suitably radiopure Cu housings and coupled through two 10 cm long tetrasil-B light guides to two photomultipliers EMI9265-B53/FL work in coincidence at

single photoelectron level. The detectors are enclosed in a low radioactive copper box inside a low radioactive shield made by 10 cm copper and 15 cm lead. The lead is surrounded by 1.5 mm Cd foils and about 10 cm of polyethylene. A high purity (HP) Nitrogen atmosphere is maintained inside the copper. The whole shield is enclosed in a sealed plexiglas box also maintained in HP Nitrogen atmosphere as well as the glove-box which is located on the top of the shield to allow the detectors calibration in the same running conditions without any contact with external environment. The installation is subjected to air conditioning. The typical energy resolution is $\sigma/E = 7.5\%$ at 59.5 keV.

As of interest here, the energy, the identification of the fired crystal and the absolute time occurrence are acquired for each event.

3 Results

For a detailed discussion about the data analysis one can refer to [11]; here we only recall that expected rate for solar axion in a crystalline detector is directly proportional to the adimensional constant λ and depends on the particular features of the NaI lattice and on the position of the Sun respect to the detector. In particular, it is possible to introduce the coordinates θ_z, angle between the vector pointing to the Sun and one crystallographic axis of the NaI crystal (here the growth symmetry axis, gsa), and ϕ_{az}, angle between the horizontal plane of the crystal and the plane containing both the Sun and gsa. They are related to the versor $\hat{k}$ of the axion momentum, which identifies the Sun position in the sky, by the expression: $\hat{k} = -\hat{x}sin(\theta_z)cos(\phi_{az}) - \hat{y}sin(\theta_z)sin(\phi_{az}) - \hat{z}cos(\theta_z)$. In this analysis in order to be the most conservative on the used crystals features, only a symmetry around gsa has been condsidered, and the expected counting rate was calculated by averaging over the ϕ_{az} coordinate. This average reduces the sensitivity achievable here with respect to the case when three crystalline axes orientations are taken into account.

The expected counting rate in the NaI detector – averaged over ϕ_{az} – is reported in Figure 1 as a function of θ_z considering 2 keV energy bin from 0 to 8 keV. Other energy intervals up to 16 keV are shown in ref. [11].

Since the mean value of the expected counting rate in energy intervals above 10 keV is significantly lower than at low energy, in the present analysis the energy range 2 keV (software energy threshold of our experiment) to 10 keV has been considered [11]. The data analysed here refer to a statistics of 53437 $kg \cdot day$.

To investigate with high sensitivity either the possible presence of a solar axion signal or to achieve upper limit on λ (and, consequently, on $g_{a\gamma\gamma}$), we exploit the time dependence of the solar axion signal. For this purpose the distribution of the experimental data as a function of θ_z is investigated. A code using the NOVAS (*Naval Observatory Vector Astrometry Subroutines*)
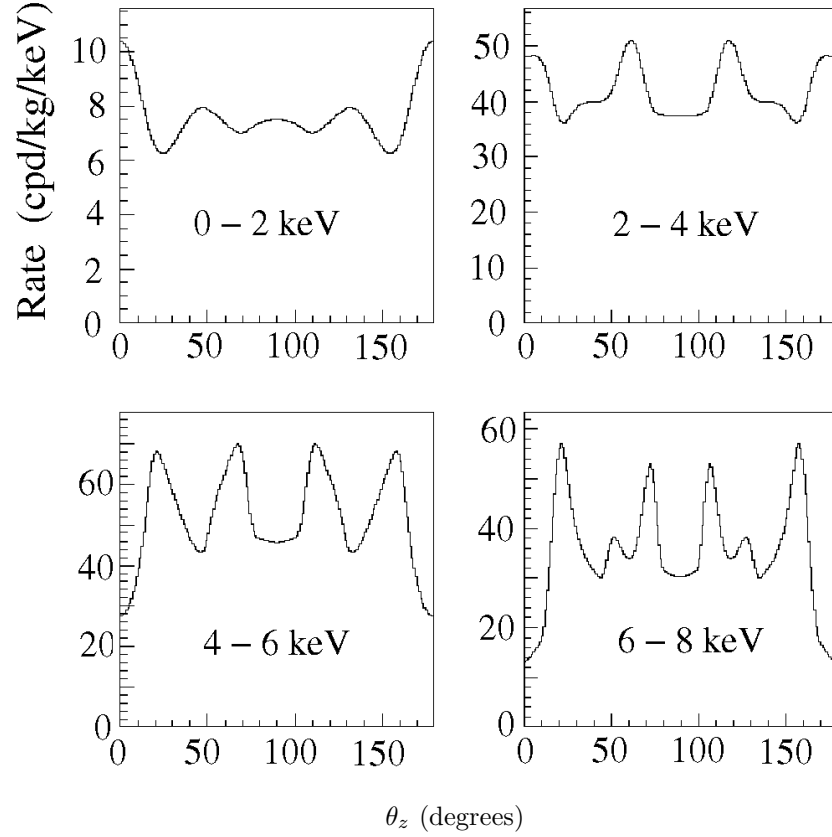
Figure 1: Expected counting rate for solar axions in NaI(Tl) evaluated for $\lambda = 1$ as a function of θ_z in the energy intervals: 0-2 keV, 2-4 keV, 4-6 keV, 6-8 keV. The rate is averaged over ϕ_{az}. Other energy intervals up to 16 keV are shown in ref. [11].

routines [13] has been developed to evaluate the distribution of the experimental data as a function of θ_z. Then, a standard maximum likelihood analysis has been carried out by accounting for the fired crystal, using 1 keV bins for the energy and 1° bins for θ_z [11]. Since the orientations of the *gsa*'s of the nine crystals, used in this experiment, were not known (for detailed discussion see [11]), the calculation of λ has been repeated for every possible configuration of the nine *gsa*'s in the set-up. It can be inferred that all the obtained λ values are compatible with absence of signal. Therefore, the most conservative upper limit obtained for λ has been cautiously considered in the evaluation of the bound on $g_{a\gamma\gamma}$. The obtained conservative value for λ from the maximum likelihood analysis has been $(4.3 \pm 3.1) \times 10^{-4}$. According to the standard
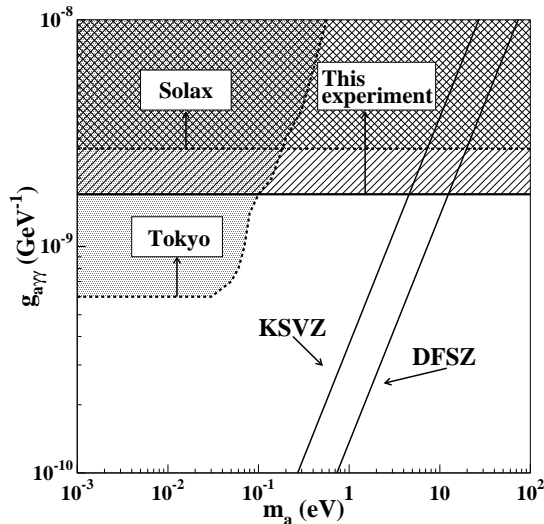
Figure 2: Exclusion plot for $g_{a\gamma\gamma}$ versus m_a. The limit achieved by the present experiment ($g_{a\gamma\gamma} \leq 1.7 \times 10^{-9} GeV^{-1}$ at 90% C.L.) is shown together with the expectations of the KSVZ and DFSZ models. The results of other – previous to our experiment – direct searches for solar axions by Solax [8] (exploiting the same technique as our experiment) and by the Tokyo helioscope [10] are also shown for comparison. For the sake of completeness, we note that recently the new result from CAST collaboration excludes $g_{a\gamma\gamma}$ down to 10^{-10} GeV^{-1} for $m_a < 10^{-2}$ eV.

procedure [14], this result gives an upper limit on the coupling of axions to photons: $\lambda \leq 8.4 \times 10^{-4}$ (90% C.L.), which corresponds to the limit: $g_{a\gamma\gamma} \leq 1.7 \times 10^{-9} GeV^{-1}$ (90% C.L.).

In fig. 2 the region in the plane $g_{a\gamma\gamma}$ versus m_a excluded at 90% C. L. by this experiment is shown.

4 Conclusions

The obtained limit on λ is about one order of magnitude more stringent than the one set by the COSME and SOLAX collaborations [7, 8], while the limit on the coupling constant $g_{a\gamma\gamma}$ has been improved by a factor 1.6 with respect to these experiments. The obtained result is at present the best direct limit on solar axions conversion in crystals and for axion masses larger than $\simeq 0.1$ eV is better also than the limit set by the helioscopes.

In conclusion, this experiment has explored the axion mass window $m_a \sim$ eV still open in the KSVZ model (where $g_{a\gamma\gamma} = 3.7 \times 10^{-10} \ GeV^{-1} \frac{m_a}{eV}$) and has allowed to exclude KSVZ axions for $m_a > 4.6$ eV at 90% C.L.

References

[1] R. D. Peccei and H. R. Quinn, *Phys. Rev. Lett.* **38** (1977) 1440.

[2] K. van Bibber, P.M. McIntyre, D.E. Morris and G.G. Raffelt, *Phys. Rev.* **D39** (1989) 2089.

[3] A.O. Gattone et al., *Nucl. Phys.* **B** (Proc. Suppl.) 70 (1999) 59.

[4] M. Dine, W. Fishler and M. Srednicki, *Phys. Lett.* **B104** (1981) 199; A.P. Zhitnitskii, *Sov. J. Nucl.* **31** (1980) 260.

[5] J.E. Kim, *Phys. Rev. Lett.* **43** (1979) 103; M.A. Shifman, A.I. Vainshtein and V.I. Zakharov, *Nucl. Phys.* **B166** (1980) 493.

[6] E.A. Pascos and K. Zioutas, *Phys. Lett.* **B323** (1994) 367.

[7] A. Morales et al., *hep-ex/0101037.*

[8] S. Cebrián et al., *Astropart. Phys.* **10** (1999) 397.

[9] C. Hagmann et al., *Phys. Rev. Lett.* **80** (1998) 2043; S. Matsuki, talk given at the II International Workshop on the Identification of Dark Matter (IDM98), Buxton, England, 7–11 September 1998.

[10] S. Moriyama et al., *Phys. Lett.* **B434** (1998) 147.

[11] R. Bernabei et al., *Phys. Lett.* **B515** (2001), 6.

[12] R. Bernabei et al., *Phys. Lett.* **B389** (1996) 757, R. Bernabei et al., *Phys. Lett.* **B408** (1997) 439. R. Bernabei et al., *Phys. Lett.* **B424** (1998) 195. R. Bernabei et al., *Il Nuovo Cim.* **A112** (1999) 545. R. Bernabei et al., *Phys. Lett.* **B450** (1999) 448. P. Belli et al., *Phys. Lett.* **B460** (1999) 236. R. Bernabei et al., *Phys. Rev. Lett.* **83** (1999) 4918. P. Belli et al., *Phys. Rev.* **C60** (1999) 065501. R. Bernabei et al., *Il Nuovo Cimento* **A112** (1999) 1541. R. Bernabei et al., *Phys. Lett.* **B480** (2000) 23. P. Belli et al., *Phys. Rev.* **D61** (2000) 023512. R. Bernabei et al., *Eur. Phys. J.* **C18** (2000) 283. R. Bernabei et al., *Phys. Lett.* **B509** (2001) 197. F. Cappella et al., *Eur. Phys. J.-direct* **C14** (2002) 1. P. Belli et al., *Phys. Rev.* **D66** (2002) 043503. R. Bernabei et al., *La Rivista del Nuovo Cimento* **26** (2003) 1-73 (*astro-ph/0307403*).

[13] http://aa.usno.navy.mil/software/novas/

[14] Particle Data Group, R.M. Barnett et al., *Phys. Rev.* **D54** (1996) 1.

SEARCHES FOR Q-BALLS, FOR NEUTRAL STRONGLY INTERACTING MASSIVE PARTICLES AND FOR NEUTRAL NUCLEARITES WITH DAMA/NAI

F. Cappella[a], R. Bernabei[a], P. Belli[a], F. Montecchia[a], M. Amato[b],
G. Ignesti[b], A. Incicchitti[b], D. Prosperi[b], R. Cerulli[c], C.J. Dai[d],
H.L. He[d], H.H. Kuang[d], J.M. Ma[d], G.X. Sun[d], Z. Ye[d]

[a] *Dipartimento di Fisica, Università di Roma "Tor Vergata" and INFN, Sezione di Roma2, I-00133 Rome, Italy*

[b] *Dipartimento di Fisica, Università di Roma "La Sapienza" and INFN, Sezione di Roma, I-00185 Rome, Italy*

[c] *INFN - Laboratori Nazionali del Gran Sasso, I-67010 Assergi (Aq), Italy*

[d] *IHEP, Chinese Academy, P.O. Box 918/3, Beijing 100039, China*

Abstract

Q-balls, neutral Strongly Interacting Massive Particles (SIMPs) and neutral nuclearites have been searched for at the Gran Sasso National Laboratory by using two "planes" of detectors in the $\simeq$ 100 kg highly radiopure NaI(Tl) DAMA set-up.

1   Introduction

In this paper we present results on a search for neutral SIMPs, for neutral nuclearites and for Q-balls. These results have been obtained by searching for delayed coincidences between two "planes" of detectors in the $\simeq$ 100 kg highly radiopure NaI(Tl) DAMA set-up [1, 2] during 350.05 days (exposure of 1.1 $\cdot 10^6$ cm^2 sr day). The set-up is placed deep underground in the Gran Sasso National Laboratory of INFN [3] and it is shielded from cosmic rays by a rock depth of about 3400 m.w.e. Each considered "plane" is made up of three 9.70 kg (10.2 cm $\times$ 10.2 cm $\times$ 25.4 cm) NaI(Tl) detectors. The two "planes" – 23.2 cm center-to-center distance – are separated by another one not considered in the trigger (see fig. 1). A description of the DAMA/NaI set-up and its performances are given in Ref. [1, 2].
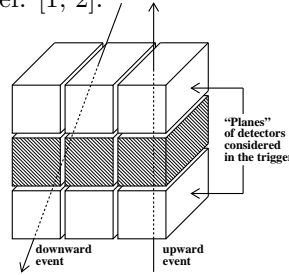
Figure 1: Schematic front view of the detectors (see text).

Delayed coincidences corresponding both to "downward" and "upward" patterns have been acquired, that is coincidences in which a scintillation pulse in one detector of a "plane" is followed – within 350 to 3000 ns time window – by another scintillation pulse in one detector of the other "plane" (particles velocity, β, ranging roughly from 10^{-4} to $5 \cdot 10^{-3}$).

We have considered here two energy regions: 4 to 60 keV electron equivalent for mainly single scattering events and above 60 keV electron equivalent for multiple scatterings inside the crystals giving pulses with multi-bumps/long-time structure.

For the mainly single scattering events, we have obtained the limit < 5.12 downward + upward delayed coincidences at 90% C.L. (considering a Poissonian distribution with background [4], having two delayed coincidences observed and 0.2 random coincidences expected during the given running time). Furthermore, since no delayed coincidence with multi-bump/long-time structure has been detected above 60 keV, the upper limit in this case is < 2.3 events at 90% C.L.. Moreover, the results presented in the following for neutral SIMPs and neutral nuclearites include also the data collected with a previous set-up, named "F" in the following, (zero delayed coincidences observed in both energy regions for an exposure of 132980 cm^2 sr day) [5]. A Montecarlo

calculation has been performed in order to estimate the main effect of the matter crossed by the particles before reaching the underground set-up. In the calculation we have accounted for the chemical composition of the overlaying mountain (downward events) and for the mean composition of the different regions inside the Earth (upward events) [6, 7]. On this basis results have been achieved on neutral SIMPs, neutral nuclearites and Q-balls as summarized in the following.

2 Exclusion plots for neutral SIMPs

Neutral SIMPs are particles with masses (M_S) between few GeV and the GUT scale and cross sections on protons (σ_p) up to $\simeq 10^{-22}$ cm^2, embedded in the galactic halo (therefore, with $\beta \simeq 10^{-3}$). Possible candidates of this kind have been suggested in several model scenarios [8, 6]. The SIMPs are considered here to be trapped in the gravitational field of the Galaxy with a quasi-maxwellian velocity distribution having $v_{rms} = 270$ km/s and an escape cut-off velocity of 650 km/s. The local galactic halo density is assumed to be $\rho_S = 0.3$ GeV/cm^3.

Both interactions with Sodium and Iodine nuclei have been taken into account in the calculations. The expected counting rates for upward and downward delayed coincidences in the two considered energy region depend on the SIMP mass, M_S and on the SIMP elastic cross section, σ_{A_i}, on the scattered nucleus A_i (^{23}Na or ^{127}I); for details see ref. [6] and references therein. According to ref. [9] the SIMP-proton cross section, σ_p, has been considered to allow some model dependent comparison with results obtained by different experiments. It is related to σ_{A_i} by the formulas given in ref. [6] for the spin-independent (SI) and spin-dependent (SD) cases. Moreover, the quenching factors we measured [10] for Na and I nuclei in NaI(Tl) are used to determine the energy scale for recoils.

The exclusion plots at 90% C.L. in the σ_p versus M_S plane both for SI and SD interactions have been determined by comparing the experimental upper limits on the downward + upward delayed coincidences with their expectations. The results are shown in Fig. 2.

The present analysis confirms and extends the previously excluded regions for the considered scenario (dashed lines contours [11, 12, 5]); in particular, the maximum reachable M_S is increased here up to $M_S \simeq 4 \cdot 10^{16}$ GeV.

3 Exclusion plots for neutral nuclearites

The nuclearites may constitute a new form of matter, which would contain roughly equal number of up, down and strange quarks; they have been already searched for by using several different techniques [5, 13]. The limit obtained in the multiple scattering region (< 2.3 events at 90% C.L.) can also be used to calculate a model independent upper limit on slow moving neutral nuclearites. In this case the rate of neutral nuclearites depends only on geometrical factors
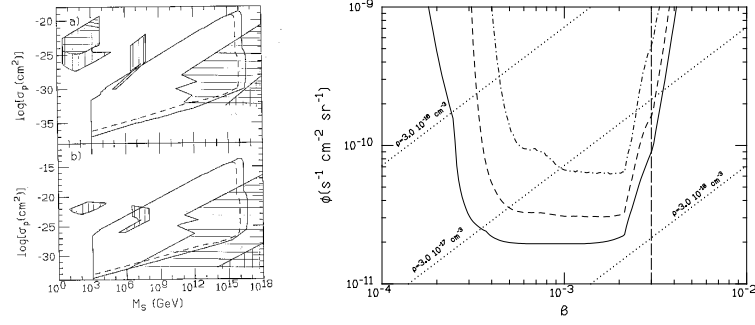
Figure 2: *Left:* the solid contours represent the obtained 90% C.L. exclusion plots in the plane (σ_p, M_S): for SI (a) and SD (b) interactions. *Right:* Model independent 90% C.L. limit contour on the flux of neutral nuclearites. Moreover, for comparison, the regions allowed by the global analysis of G. D. Starkman et al. [9] for various cases are also shown. See ref. [6].

being the cross section large enough to induce always a total detected energy above 60 keV. The obtained model independent 90% C.L. limit contour on the flux of neutral nuclearites as a function of β is shown in Fig. 2-right (if $\beta \simeq 10^{-3}$ then $\Phi < 1.9 \cdot 10^{-11}$ s^{-1}cm^{-2}sr^{-1}, 90%C.L.). The poorer limits on Φ at $\beta \gtrsim 2 \cdot 10^{-3}$ and $\beta \lesssim 4 \cdot 10^{-4}$ are due to the decreasing of detection efficiency. The solid line is the "geometrical limit", which corresponds to $\sigma_p \gtrsim 10^{-28}$ cm^2 for SI interactions with $M_S > 10^6$ GeV and to $\sigma_p \gtrsim 10^{-24}$ cm^2 for SD interactions with $M_S > 10^5$ GeV. The dependence on σ_p is also shown for the SI case by the dashed line ($\sigma_p = 1.5 \cdot 10^{-30}$ cm^2) and by the dotted-dashed one ($\sigma_p = 1.0 \cdot 10^{-30}$ cm^2).

4   Exclusion plots for Q-balls

Theories with low-energy supersymmetry predict the existence of stable non-topological solitons, named Q-balls, with mass greater than about 10^8 GeV. The Q-balls (see Ref. [14] and references therein) may be considered in supersymmetric theories as coherent states of squarks, sleptons and Higgs fields; the condition for stable Q-balls is satisfied when the energy scale, M_S, of the SUSY breaking is low (from 100 GeV and 100 TeV).

The energy losses of charged and neutral Q-balls versus β in the crossed matter have been calculated according to the modelling of ref. [15]. The limit obtained in the multiple scattering region for upward and downward delayed coincidences has been used to calculate a limit on Q-balls flux.

In Fig. 3 the 90% C.L. exclusion limits on Q-ball flux, ϕ, as a function of β for charged Q-balls having Z=1 (a) and Z=8 (b) are reported for $M_Q = 10^{13}$ GeV (dotted curves), $M_Q = 10^{16}$ GeV (dashed curves) and $M_Q = 10^{20}$ GeV (solid contour and "geometrical limit"). Intermediate contours in the (ϕ, β)
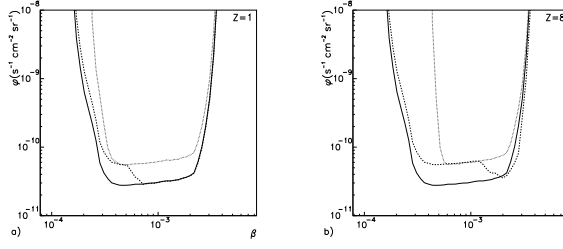
Figure 3: Exclusion plots at 90% C.L. in the plane (ϕ,β) for charged Q-balls with Z=1 (a) and Z=8 (b). See text and ref. [7].

plane with respect to the (a) and (b) cases would be obtained for Q-balls with intermediate Z values (for details see Ref. [7]).

Fig. 4 shows the 90% C.L. exclusion plots in the plane (ϕ,β) for neutral Q-balls with the given M_Q and M_S values; the solid contour is again the "geometrical limit". It can be noted that, for a given M_Q, larger M_S values imply smaller cross section for a neutral Q-ball [15]. This gives rise to larger mean free path in the detector and, therefore, the detection efficiency sharply drops down and the limit on ϕ is poorer.
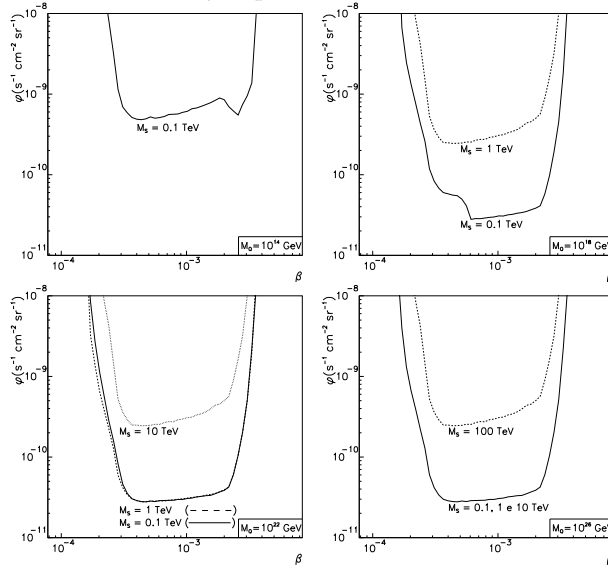
Figure 4: Exclusion plots at 90% C.L. in the plane (ϕ,β) for neutral Q-balls with $M_Q = 10^{14}$ GeV, 10^{18} GeV, 10^{22} GeV and 10^{26} GeV. See ref. [7].

In particular, the 90% C.L. "geometrical limit" for the flux of charged Q-balls e.g. when Z=1 and $M_Q = 10^{20}$ GeV is: $\phi < 2.8 \cdot 10^{-11}$ s^{-1}cm^{-2}sr^{-1} ($\beta \simeq 10^{-3}$). The same value also holds for the "geometrical limit" of the neutral Q-balls flux when $M_Q = 10^{26}$ GeV and $0.1 < M_S < 10$ TeV. In

this latter case it is above that published e.g. by the lake Baikal underwater Ghyrlyanda array [16], while for charged Q-balls better limits could be reached by analysing the MACRO data as mentioned also in ref. [15].

5   Conclusion

Searches for neutral SIMPs, neutral nuclearites and Q-balls have been performed looking for peculiar delayed coincidences. No positive hints have been found; thus, exclusion plots in various scenarios have been obtained in the σ_p versus M_S plane for the SIMPs and in the ϕ versus β plane for neutral nuclearites and Q-balls.

References

[1] R. Bernabei et al., Il Nuovo Cim. A112 (1999) 545.

[2] R.Bernabei et al., Riv. Nuovo Cim. 26 n.1 (2003) 1-74 (astro-ph/0307403) and references therein.

[3] E. Bellotti, Nucl. Instr. & Meth. A264 (1988) 1.

[4] K. Hikasa et al., Phys. Rev. D45 (1992) III.40.

[5] C. Bacci et al., Astroparticle Phys. 4 (1996) 195.

[6] R. Bernabei et al., Phys. Rev. Lett. 83 (1999) 4918.

[7] F. Cappella et al., Eur. Phys. J.-direct C14 (2002) 1.

[8] J. Rich et al., Phys. Lett. B 194 (1987) 173; T.K. Hemmick et al., Phys. Rev. D41 (1990) 2074; D. Chung et al., Phys. Rev. D57 (1997) 4606; C. Albuquerque et al., Phys. Rev. D59 (1999) 015021; V. Berezinsky et al., Phys. Lett. B422 (1998) 163; R. N. Mohapatra and S. Nandi, Phys. Rev. Lett. 79 (1997) 181; S. Raby, Phys. Rev. D56 (1997) 2852.

[9] G. D. Starkman et al., Phys. Rev. D41 (1990) 3594.

[10] R. Bernabei et al., Phys. Lett. B389 (1996) 757.

[11] D. O. Caldwell, Nucl. Phys. B (Proc. Supp.) 28A (1992) 273.

[12] C. Bacci et al., Astroparticle Phys. 2 (1994) 13.

[13] A. De Rujula and S.L. Glashow, Nature (London) 312 (1984) 734; MACRO coll., Phys. Rev. Lett. 69 (1992) 1860.

[14] A. Kusenko et al., Phys. Rev. Lett. 80 (1998) 3185.

[15] D. Bakari et al., Astropart. Phys. 15 (2001) 137; J. Derkaoui et al., Astrop. Phys. 9 (1998) 173; G. Giacomelli, Riv. Nuovo Cim. 7 (1984).

[16] I.A. Belolaptikov et al., astro-ph/9802223.

STRUCTURE FORMATION, CMB AND LSS IN A MIRROR DARK MATTER SCENARIO

Paolo Ciarcelluti [a,b]

[a] *Dipartimento di Fisica, Università di L'Aquila,*
67010 Coppito AQ, Italy

[b] *INFN, Laboratori Nazionali del Gran Sasso, 67010 Assergi AQ, Italy*

Abstract

Here we show the behaviour of the mirror dark matter and the differences from the more familiar CDM candidate for structure formation.

1 Introduction

The idea that there may exist a hidden mirror sector was suggested long time ago by Lee and Yang [1], and the model with exact parity symmetry interchanging corresponding fields of two sectors was proposed many years later by Foot at al. [1].

If the mirror (M) sector exists, then the Universe along with the ordinary (O) particles should contain their mirror partners, but their densities are not the same in both sectors. Instead, Berezhiani et al. [3] showed that the BBN bound on the effective number of extra light neutrinos implies that the M sector has a temperature lower than the O one.

All the differences with respect to the ordinary world can be described in terms of only two free parameters in the model, $x \equiv T'/T$ and $\beta \equiv \Omega'_{\rm b}/\Omega_{\rm b}$, where T (T') and Ω_b (Ω'_b) are respectively the ordinary (mirror) photon temperature and the ordinary (mirror) baryon density.

If $\Omega'_b \geq \Omega_b$, mirror baryons emerge as a possible dark matter candidate (MBDM) [2]; the peculiar properties of mirror dark matter were discussed in ref. [3].

2 Relevant length scales

The important moments for the structure formation are related to the matter-radiation equality (MRE) and to the matter-radiation decoupling (MRD) epochs. The MRE occurs at the redshift

$$1 + z_{\rm eq} = \frac{\Omega_m}{\Omega_r} \approx 2.4 \cdot 10^4 \frac{\Omega_m h^2}{1 + x^4} \ . \tag{1}$$

The MRD temperature in the M sector $T'_{\rm dec}$ can be calculated following the same lines as in the O one [3], and hence

$$1 + z'_{\rm dec} \simeq x^{-1}(1 + z_{\rm dec}) \simeq 1100 \, x^{-1} \ , \tag{2}$$

so that the MRD in the M sector occurs earlier than in the O one. Moreover, for a value $x < x_{\rm eq} \simeq 0.046 \left(\Omega_m h^2\right)^{-1}$, the mirror photons would decouple yet during the radiation dominated period.

The relevant scale for gravitational instabilities is M Jeans mass (defined as the minimum scale at which, in the matter dominated epoch, sub-horizon sized perturbations start to grow); its maximum value is expressed in terms of the O one as

$$M'_{\rm J,max} \approx \beta^{-1/2} \left(\frac{x^4}{1 + x^4}\right)^{3/2} \cdot M_{\rm J,max} \ , \tag{3}$$

which, for $\beta \geq 1$ and $x < 1$, means that the Jeans mass for the M baryons is lower than for the O ones. If, e.g., $x = 0.6$ and $\beta = 2$, then $M'_{\rm J} \sim 0.03 \, M_{\rm J}$.

Density perturbations in MBDM on scales $M \geq M'_{\rm J,max}$ which enter the horizon at $z \sim z_{\rm eq}$ undergo uninterrupted linear growth after $z_{\rm eq}$. Perturbations on scales $M \leq M'_{\rm J,max}$ start instead to oscillate after they enter the horizon, thus delaying their growth till the epoch of M photon decoupling.

As occurs for perturbations in the O baryonic sector, also the M baryon density fluctuations should undergo the strong collisional Silk damping around the time of M recombination, so that the smallest perturbations that survive the dissipation will have the mass

$$M'_S \sim [f(x)/2]^3 (\beta \, \Omega_b h^2)^{-5/4} 10^{12} \, M_\odot \ , \tag{4}$$

where $f(x) = x^{5/4}$ for $x > x_{\text{eq}}$, and $f(x) = (x/x_{\text{eq}})^{3/2} x_{\text{eq}}^{5/4}$ for $x < x_{\text{eq}}$. For $x \sim x_{\text{eq}}$ we obtain $M'_S \sim 10^{10} \ M_{\odot}$, a typical galaxy mass.

3   CMB and LSS spectra

In order to make quantitative predictions we computed numerically the evolution of scalar adiabatic perturbations in a flat Universe in which is present a significant fraction of mirror dark matter at the expenses of diminishing the CDM contribution and maintaining constant Ω_m. We have chosen a "reference
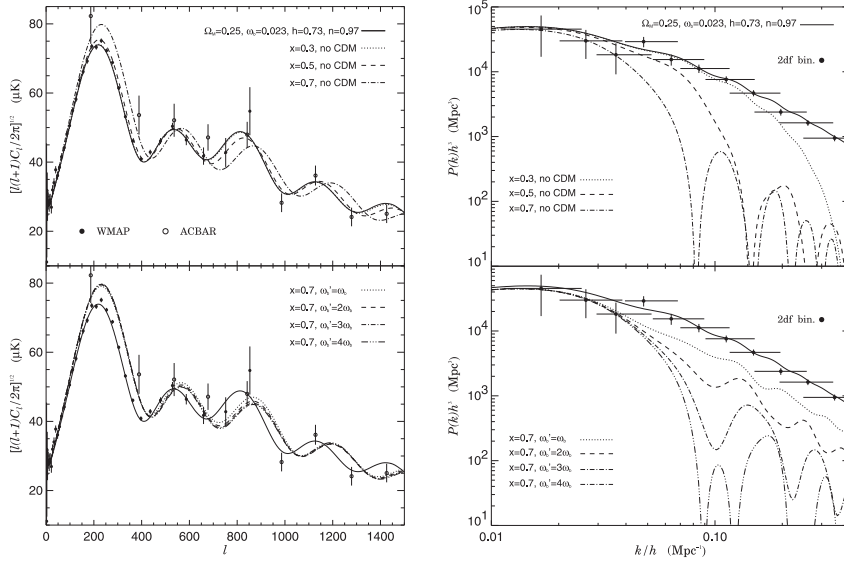
Figure 1: CMB (*left*) and LSS (*right*) power spectra for different values of x and ω'_{b}, as compared with a reference standard model (solid line) and with observations (WMAP, ACBAR and 2dF binned data [5]). Models where dark matter is entirely due to MBDM (no CDM) are plotted in *top panels* for $x = 0.3, 0.5, 0.7$, while models with mixed CDM+MBDM ($\beta = 1, 2, 3, 4 \ ; \ x = 0.7$) in *bottom panels*.

cosmological model" with the following set of parameters: $\omega_b = 0.023$, $\Omega_m = 0.25$, $\Omega_\Lambda = 0.75$, $n_{\text{s}} = 0.97$, $h = 0.73$.

The dependence of the CMB and LSS power spectra on the parameters x and β is shown in fig. 1. The predicted CMB spectrum is quite strongly dependent on the value of x, and it becomes practically indistinguishable from the CDM case for $x < x_{\text{eq}} \simeq 0.3$. However, the effects on the CMB spectrum rather weakly depend on the fraction of mirror baryons. As a result of the

oscillations in MBDM perturbation evolution, one observes oscillations in the LSS power spectrum; their position clearly depends on x. Superimposed to oscillations one can see the cut-off in the power spectrum due to the Silk damping.

Our predictions can be compared with the observational data in order to obtain some general bound on the mirror parameters space.

(i) The assumption that DM is entirely due to mirror baryons is not compatible with present LSS data unless x is small enough: $x < x_{eq} \approx 0.35$.

(ii) High values $x > 0.5$ are excluded even for a relatively small amount of mirror baryons. On the other hand, intermediate values $x = 0.3 - 0.5$ can be still allowed if the MBDM is a subdominant component of dark matter.

(iii) For small values of x, say $x < 0.3$, neither the linear LSS power spectrum nor the CMB angular power spectrum can distinguish the MBDM from the CDM.

References

[1] T.D. Lee and C.N. Yang, Phys. Rev. **104**, 254 (1956); Y. Kobzarev, L. Okun, I. Pomeranchuk, Yad. Fiz. **3**, 1154 (1966); R. Foot, H. Lew, R. Volkas, Phys. Lett. **B272**, 67 (1991); Z. Berezhiani, A. Dolgov, R.N. Mohapatra, Phys. Lett. **B375**, 26 (1996).
For a review: R. Foot, astro-ph/0309330; astro-ph/0407623; Z. Berezhiani, hep-ph/0312335.

[2] L. Bento, Z. Berezhiani, Phys. Rev. Lett. **87**, 231304 (2001); R. Foot, R. Volkas, hep-ph/0402267.

[3] Z. Berezhiani, D. Comelli, F. Villante, Phys. Lett. **B503**, 362 (2001); A.Y. Ignatiev, R.R. Volkas, Phys. Rev. **D68**, 023518 (2003); Z. Berezhiani, P. Ciarcelluti, D. Comelli, F. Villante, astro-ph/0312605; P. Ciarcelluti, astro-ph/0312607.

[4] R. Foot, hep-ph/0308254; astro-ph/0403043; astro-ph/0405362.

[5] M. Tegmark, A.J.S. Hamilton, Y. Xu, MNRAS **335**, 887 (2002); C.L. Bennett et al., Astrophys. J. Suppl. **148**, 1 (2003); C.L. Kuo et al., Astrophys. J. **600**, 32 (2004).

Part V

GAMMA RAYS IN SPACE

PAST, PRESENT AND FUTURE IN GAMMA RAYS

Donald A. Kniffen [a,b]

[a] *School of Computational Sciences George Mason University,*
Fairfax, Virginia 22030, USA

[b] *Science Missions Directorate, NASA Headquarters, Washington, DC 20546, USA*

Abstract

The history of high-energy gamma-ray astronomy has now stretched over five decades. With an early history of balloon flights and satellites, the great promise of the rich return from observations from this window to the Universe is just now at its threshold. From the pioneering results from the EGRET on the Compton Gamma Ray Observatory, to the great expectations for AGILE and GLAST in the next few years, the richness of the content contained in these most energetic photons will finally be realized. Motivated by the ability to probe the cosmic rays throughout the Milky Way, EGRET has demonstrated that high-energy gamma-ray astronomy is more than a galactic probe. These high-energy photons extend to the most powerful emitters at very great distances in the early Universe. The next decade will be a true golden age of high-energy gamma-ray astronomy with leaps in observing capability that promise great new discoveries beyond the exciting expectations.

1   Motivation

The foundation for high-energy gamma-ray astronomy rests on theoretical, experiment, and observational progress throughout the last half of the 20th century. To understand the promise of the future, it is important to review how we reached our current view of the high-energy cosmos.

Beginning in the late 1950s, theoretical progress began to show that the penetrating power of gamma-rays and their origin in the highest energy physical processes would lead to a valuable probe of the dynamic processes that shape structures on many scales outside the solar cavity and hence unavailable to in-situ measurement. The penetrating nature would make it possible to reach throughout the Milky Way, and, perhaps eventually, beyond.

The first prediction involved the probe of energetic electrons by observing the photons from their Compton scattering interactions with the interstellar photon fields of many origins [1], boosting the photons to gamma-ray energies.

The seminal work generally considered to be the motivation for the search for the illusive cosmic gamma rays was that of P. Morrison [2] in which the author made an assessment of the fluxes expected from a variety of gamma-ray sources. Subsequently this assessment was shown to be overly optimistic, but it served the impetuous for encouraging instrumentalists to develop modest instruments to begin the search.

Subsequently, several other authors [3, 4, 5, 6, 7] refined the expectations and spurred the observers.

The motivations included the use of gamma rays as a probe of various energetic process occurring in a variety of astrophysical settings within the Milky Way and beyond. The processes included hadronic particle interactions with interstellar gas and dust, bremsstrahlung interactions on interstellar material by energetic cosmic-ray electrons, Compton scattering by the electrons with interstellar photon fields boosting the photons to gamma-ray energies, nucleosynthesis products produced in supernovae, and particle anti-particle annihilation. Armed with these motivations, many experimentalists began the search, first with very modest instruments flown on scientific balloons and small satellites and then ever more sophisticated searches with larger satellite missions. In the next section we will recap this exciting venture.

2   The Past

The first searches for gamma rays were by cosmic-ray physicists seeking the origin of cosmic rays by studying their distribution throughout the Milky Way Galaxy. The OSO-3 satellite experiment of Clark, Garmire and Kraushaar [8] was the first to give an unambiguous indication of the galactic gamma rays from the cosmic-ray induced component. This observation was confirmed by

observations from a balloon-borne telescope by Fichtel, Kniffen Hartman and Sommer [9]. However it was not until the first satellite results from SAS-2 [10]and COS-B [11] that the details of the galactic diffuse emission with its signature of the galactic structure became apparent.
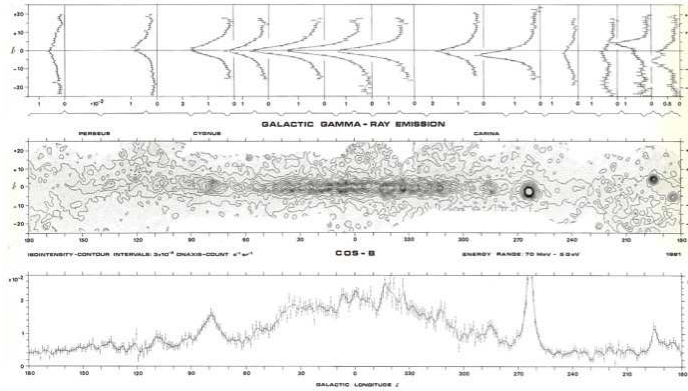
Figure 1: The COS-B map of ≥100 MeV gamma-rays from the galactic plane showing the irregularity in the longitude distribution due to galactic structure.

Though many discrete sources were reported by balloon-borne missions, the first catalog of high-energy gamma-ray sources was obtained with the COS-B satellite [12]. While some of these sources may have been localized excesses in the diffuse emission, this result was nevertheless the basis for many counterpart searches.
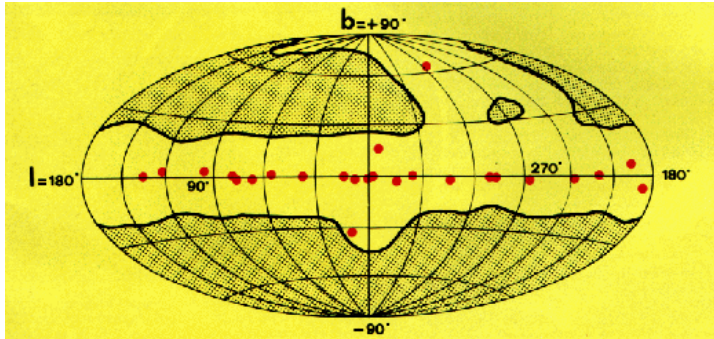
Figure 2: The second COS-B catalog of high-energy gamma-ray sources.

While there were many other early balloon and satellite missions, The next major advance in the field of high-energy gamma-ray astronomy came with the launch of the Compton Gamma Ray Observatory (CGRO) [13] in 1991. This mission contained four instruments covering over six orders of magnitude in energy, and provided the first comprehensive survey of the full sky.

Figure 3: The Compton Gamma Ray Observatory just following release from the Shuttle.

The Energetic Gamma-Ray Experiment (EGRET) [14] on CGRO covered the energy range above about 30 MeV to several GeV. This experiment produced the first full-sky map of the high-energy sky and a catalog of 271 discrete sources, less than half identified with objects known at other wavelengths.

3   The Present

There have been no other high-energy gamma-ray experiments flown since EGRET. Activity has been centered on gamma-ray bursts, including the
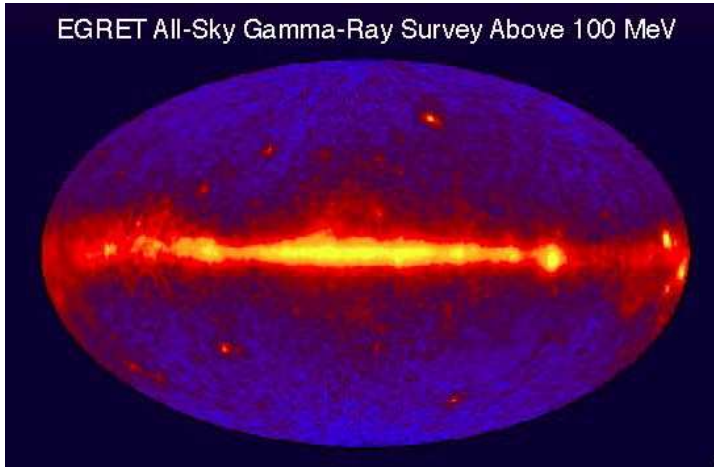
Figure 4: The EGRET composite view of the entire gamma-ray sky ≥100 MeV.
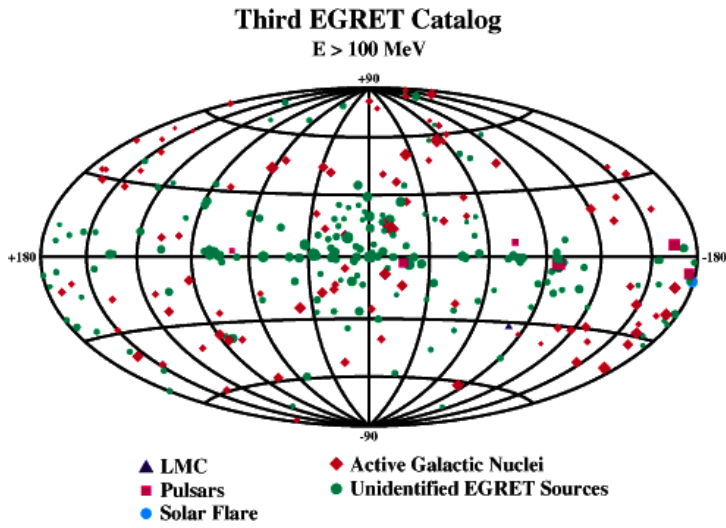
Figure 5: The Third EGRET Catalog of high-energy gamma-ray sources.

excellent results from CGRO/BATSE that provided a paradigm shift in our understanding of these objects. Prior to the BATSE results the consensus was that these events originated in a galactic population of neutron stars. BATSE found an isotropic distribution that was inconsistent with this interpretation

[15].

2704 BATSE Gamma-Ray Bursts
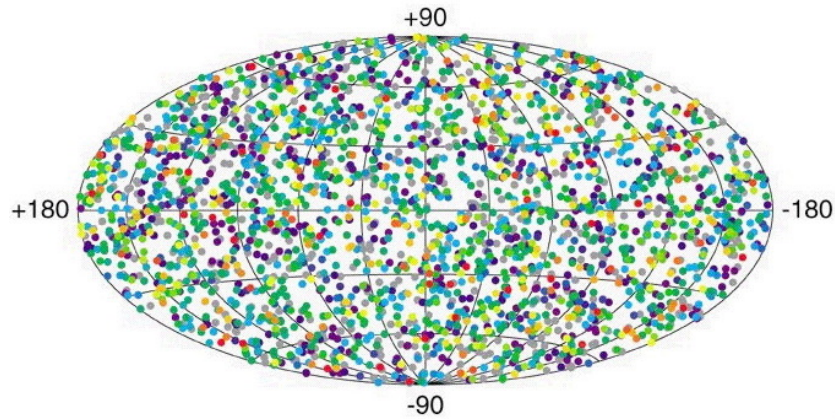
Figure 6: The BATSE catalog of 2704 gamma-ray bursts showing an isotropic distribution.

The next major advance in the field of gamma-ray bursts has been the ability provided first by The Italian-Dutch BeppoSAX mission [16] and subsequently by NASA's High Energy Transient Explorer (HETE)[17] to pinpoint the locations of the burst to enable counterpart searches. More recently ESA's INTEGRAL Mission [18] has also provided good burst positions. The combination of these missions and the follow-up observations they make possible has brought us much closer to understanding these powerful events.

4   The Future

High-energy gamma-ray astronomy is on the verge of a true golden era in the field. With the AGILE [19]and GLAST [20] missions, which are the subject of papers in these proceedings, both scheduled to launch within the next three years. The Large Area Telescope (LAT) on GLAST will provide a factor of nearly 40 increase in sensitivity and a much finer angular resolution over any previous detector and an energy range overlapping with ground-based Cherenkov telescopes. Our knowledge of the high energy Universe will extend to the most energetic and exotic processes imaginable.

References

[1] E. Feenberg and H. Primakoff, *Interactions of Cosmic-Ray Primaries with Sunlight and Starlight*, Phys. Rev. *73*, 449-469, (1948)

[2] P. Morrison, *On Gamma-Ray Astronomy*, Il Nuovo Cimento *7*, 858-864, (1958)

[3] S. Hayakawa, H. Okuda, Y. Tanaka, Y. Yammamoto, *Cosmic Electron and Gamma Rays*, Suppl. Prog. in Theo. Phys. *30*, 153-203, (1964)

[4] R.J. Gould, G.R. Burbidge, *High Energy Cosmic Photons and Neutrinos*, Annales d'Astrophys. *28*, 171-201, (1965)

[5] V.L. Ginsburg, S.J. Syrovatskii, *Some Problems of Gamma- and X-Ray Astronomy*, Soviet Phys. Uspekhi *7*, 696-720, (1965)

[6] K. Greisen, *Experimental Gamma-Ray Astronomy*,Perspec. in Mod. Phys. Interscience, 355-382, (1966)

[7] G.G. Fazio, *Gamma Radition from Celestial Objects*, Ann. Rev. Astron. Astrophys. *5*, 481-524, (1967)

[8] G.W. Clark, G.P. Garmire, W.L. Kraushaar, *Observations of High-Energy Cosmic Gamma Rays*, Astrophys. J. Lett. *53*, L203-L207, (1968)

[9] C.E. Fichtel, R.C. Hartman, D.A. Kniffen, M. Sommer, *Gamma-Ray Observations of the Galactic Center and some Possible Point Sources*, Astrophys. J. *171*, 31-40, (1972)

[10] D.A. Kniffen, R.C. Hartman, D.J. Thompson, C.E. Fichtel, *Galactic Plane Gamma-Radiation*, Astrophys. J. *186*, L105-L109, (1973)

[11] H.A. Mayer-Hasselwander, K. Bennett K., G.F. Bignami, R. Buccheri, P.A. Caraveo, W. Hermsen, G. Kanbach, F. Lebrun, G.G. Lichti, J.L. Masnou, J.A. Paul, K. Pinkau, B. Sacco, L. Scarsi, B.N. Swanenburg, R.D. Wills, *Large scale distribution of galactic gamma radiation observed by COS-B*, Astron. Astrophys. *105*, 164-175, (1982)

[12] B.N. Swanenburg,K. Bennett, G.F. Bignami, R. Buccheri, P. Caraveo, W. Hermsen, G. Kanbach, G.G. Lichti, J.L. Masnou, H.A. Mayer-Hasselwander, J.A. Paul, S. Sacco, L. Scarsi, R.D. Wills, *Second Cos B Catalog of High-Energy Gamma-Ray Sources*, Astrophys. J. *243*, L69-73, (1981)

[13] D.A. Kniffen, *The Gamma-Ray Observatory*, Annals of the New Academy of Sciences *571*, 482-496, (1989)

[14] G. Kanbach, D.L. Bertsch, A. Favale, C.E. Fichtel, R.C. Hartman, R. Hofstader, E.B. Hughes, S.D. Hunter, B.W. Hughlock, D.A. Kniffen, Y.C. Lin, H.A. Mayer-Hasselwander, P.L. Nolan, K. Pinkau, H. Rothermel, E. Schneid, M. Sommer, D.J. Thompson, *The Project EGRET (Energetic Gamma-Ray Experiment Telescope) on NASA's Gamma-Ray Observatory GRO*, Space Science Reviews *49*, 69-84, (1988)

[15] W.S. Paciesas, C.A. Meegan, G.N. Pendleton, M.S. Briggs, C. Kouve-liotou, T.M. Koshut, J.P. Lestrade, M.L. McCollough, J.J. Brainerd, J. Hakkila, W. Henze, R.D. Preece, V. Connaughton, R.M. Kippen, R.S. Mallozzi, G.J. Fishman, G.A. Richardson, M. Sahi, *The Fourth BATSE Gamma-Ray Burst Catalog (Revised)*, Astrophys. J. Suppl. *122*, 465-495, (1999)

[16] L. Scarsi, *SAX Overview*, Astron. and Astrophys. Suppl. *97*, 371-383, (1993)

[17] G.R. Ricker, J.-L. Atteia, G.B. Crew, J.P. Doty, E.E. Fenimore, M. Gassi, C. Graziani, K. Hurley, J.G. Jernigan, N. Kawai, D.Q. Lamb, M. Matsouka, G. Pizzichini, Y. Shirasaki, T. Tamagawa, R. Vanderspeck, G. Vedrenne, J. Villasenor, S.E. Woosley, A.Yoshida, *The High-Energy Transient Explorer (HETE): Mission and Science Overview*, AIP Conf. Proc. *662*, 3-16, (2003).

[18] C. Winkler, T.J.-L Courvoisier, G. Di Cocco, H. Gehrels, A. Giménez, S. Grebebev, W. Hermsen, J.M. Mas-Hesse, F. Lebrun, N. Lund, G.G.C. Palumbo, J. Paul, J.-P. Roques, H. Schnopper, V. Schönfelder, R. Sunyaev, B. Teegarden, P. Ubertini, G. Vedrenne, A.J. Dean, *The INTEGRAL Mission*, Astron.and Astrophys. *411*, L1-L6, (2003)

[19] Tavani, M., *The AGILE Mission*, these proceedings, (2004)

[20] Michelson, P., *The GLAST Mission*, these proceedings, (2004)

THE AGILE GAMMA-RAY MISSION

M. Tavani [a,b,c]

[a] *IASF-CNR, via Fosso del Cavaliere 100, I-00133 Roma, Italy*

[b] *Dipartimento di Fisica, Universitá Tor Vergata, Roma, Italy*

[c] *Consorzio Interuniversitario Fisica Spaziale (CIFS)*

Abstract

The AGILE Mission is dedicated to gamma-ray astrophysics above 30 MeV during the period 2005-2007 and beyond. The main features of AGILE are: (1) excellent imaging and monitoring capabilities simultaneously in the γ-ray (30 MeV – 30 GeV) and hard X-ray (15-45 keV) energy ranges (reaching 1-3 arcminute source positioning for intense sources); (2) large fields of view for the gamma-ray imager (2.5 sr) and hard X-ray imager (0.8 sr); (3) very good timing (improving by almost three orders of magnitude the instrumental deadtime for γ-ray detection compared to EGRET); and (4) optimal imaging and triggering capability for GRBs and other high-energy transients. The AGILE scientific program is being developed emphasizing a quick response to gamma-ray/hard X-ray variable sources and multiwavelength studies of Galactic snf extragalactic objects.

1   Introduction

Gamma-ray astrophysics is in an exciting discovery phase. Detection of gamma-rays above 30 MeV from space is made possible by the development and operation of particle detectors under extreme conditions. The current knowledge of the gamma-ray sky above 30 MeV is based on the scientific results of important missions: SAS-2, COS-B, and EGRET on board of the Compton Gamma-Ray Observatory. More than 300 gamma-ray sources are known today, with many surprises, puzzles, and open questions.

Making further progress require a substantial improvement in detecting performance of gamma-ray instruments. Three are the areas of improvement that need to be addressed by future gamma-ray missions:

- **optimal angular resolution and a large field of view (FOV)** for gamma-ray detection above 30 MeV (apparently contradictory requests !), improving EGRET error boxes and FOV at least by a factor of 4;

- **microsecond-level timing** for photon tagging, and deadtimes for gamma-ray detection substantially below 1 ms;

- **simultaneous X-ray and gamma-ray detection, and on-board triggering and alert capability for fast X-ray transients**.

The space missions AGILE [1, 2, 3] and GLAST [4] are the next space projects to meet the challenge. It turns out that AGILE and GLAST instrument configurations are very differently optimized. The large area of the GLAST gamma-ray imaging detector (LAT) with a full-size calorimeter, and the operations foreseen for a decade will lead to a large exposures of the whole sky and the detection of very faint and persistent sources with good spectroscopic data. The science goals of a Small Mission such as AGILE are differently focussed as discussed here. It is important to note that the gamma-ray imagers of AGILE and GLAST (both based on solid state technology of Silicon microstrip detectors) are expected to produce equivalent Point-Spread Functions between 100 MeV and 1 GeV, with similar capabilities for the positioning of *γ-ray transients lasting a few days* during phases of the GLAST sky-scanning mode Both missions can then be considered *complementary for the detection of transient sources* and aimed at reaching an **"arcminute gamma-ray astrophysics"** with different methods: by the combined X-gamma-ray imaging in case of AGILE, and by a large effective area at gamma-ray energies in case of GLAST. It will be exciting to see both missions developing and reaching their scientific goals during the next years.
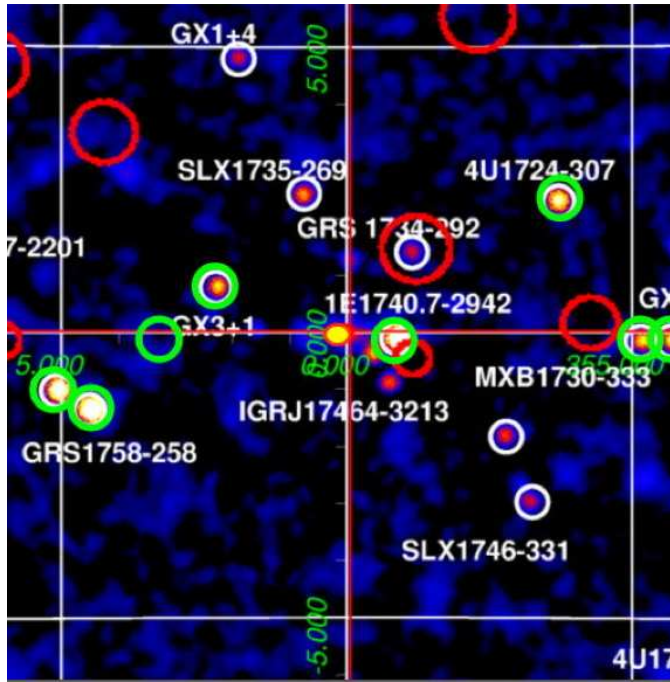
Figure 1: Example of simultaneous hard X-ray and gamma-ray detection and monitoring of high-energy sources to be performed by AGILE. The image shows the *Integral* source map (18-60 keV) of the Galactic Center ($\sim 10^o \times 10^o$) [5, 6] superimposed with the positions of known gamma-ray sources (red ellipses representing their error boxes) of the 3rd EGRET Catalog [7]. The position of the EGRET gamma-ray source near the Sgr A* position is marked in filled yellow color. Hard X-ray sources detectable by Super-AGILE above 20 mCrab at 20 keV are marked in green.

2   The AGILE Mission

AGILE is currently in Phase D. The mission space and ground segments are being developed and are in the final construction stage. Launch is planned by the PSLV rocket during the fourth quarter of 2005.

The AGILE scientific instrument is mostly based on the state-of-the-art and reliably developed technology of solid-state silicon detectors developed by the Italian INFN laboratories. The instrument is light (~ 130 kg) and effective in detecting and monitoring gamma-ray sources within a large field of view ($\sim 1/5$ of the whole sky). The philosophy we adopted is to develop one integrated instrument made of three detectors with broad-band detection and imaging capabilities.
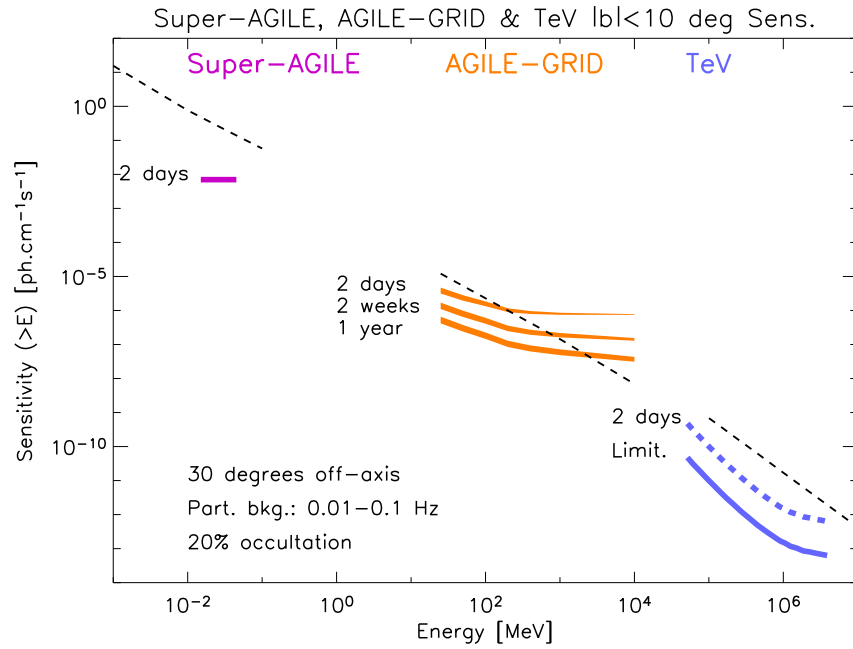
Figure 2: Source integral sensitivity of the AGILE imaging detectors in the hard X-ray energy band (15-45 keV, Super-AGILE) and in the gamma-ray band (30 MeV - 30 GeV, GRID) for different observation timescales (from [8]). The short time-scale (thick dashed curve) and limiting sensitivity of the new generation of TeV telescopes (e.g., H.E.S.S., [9]) is also shown. The light black dashed curve is the integral flux of the Crab Nebula.

The AGILE **Gamma-Ray Imaging Detector (GRID)** is sensitive in the energy range $\sim$ 30 MeV–50 GeV. It is characterized by an optimal spatial resolution and by the smallest ever obtained deadtime for gamma-ray detection ($\lesssim$200 μs). GRID consists of a Silicon-Tungsten Tracker, a Cesium Iodide Mini-Calorimeter, an Anticoincidence system made of segmented plastic scintillators, and fast readout electronics and processing units. The GRID is designed to achieve an optimal angular resolution (source location accuracy $\sim 5' - 20'$ for intense sources), an unprecedently large field-of-view ($\sim$ 3 sr), and a sensitivity comparable to that of EGRET for on-axis (and substantially better for off-axis) point sources.

AGILE will be greatly enhanced by its detection and imaging capabilities in the hard X-ray range (15-45 keV). The **Super-AGILE** detector consists of an additional plane of four Silicon square units positioned on top of the GRID Tracker plus an ultra-light coded mask structure with a top absorbing

mask at the distance of 14 cm from the Silicon detectors. The main goals of Super-AGILE are the simultaneous gamma-ray and hard X-ray detection of astrophysical sources (unprecedented for gamma-ray instruments), optimal source positioning (1-3 arcmins, depending on intensity), fast gamma-ray burst and transient alert and on-board trigger capability.

The CsI **Mini-Calorimeter** (MC) will also detect and collect events independently of the GRID. The energy range for this non-imaging detector is 0.3–200 MeV, and it can be very useful to provide spectral and accurate timing information of transient events. The content of a cyclic MC event buffer will be transmitted to the ground for impulsive events (solar flares, GRBs, other transients).

AGILE with its combination of GRID, MC, and Super-AGILE is an innovative instrument, with an optimal expected performance for transients (gamma-ray bursts, solar flares, unidentified gamma-ray sources, AGNs) and steady sources (e.g., pulsars). The fast AGILE electronic readout and data processing (resulting in very small detectors' deadtimes) allow for the first time the systematic search for sub-millisecond gamma-ray transients [2].

The AGILE Team currently includes scientists from the CNR Istituto di Astrofisica Spaziale and Fisica Cosmica (IASF), INFN laboratories, and the Universities of Trieste, Roma-Tor Vergata, and Roma-La Sapienza. The instrument development and scientific operations will take advantage of the work of the **AGILE Multiwavelength Group** composed of scientists from the international community interested in correlated observations and theoretical investigations related with AGILE results.

Despite its simplicity, moderate weight and cost, AGILE is ideal to perform a large number of scientific investigations:

- detecting and monitoring Active Galactic Nuclei (AGNs),

- detecting and imaging gamma-ray bursts (GRBs) with high efficiency in the energy ranges 15 keV - 30 GeV,

- mapping the diffuse Galactic emission with a substantial improvement of the model,

- studying pulsed gamma-ray emission from radiopulsars;

- identifying many of the currently mysterious EGRET unidentified gamma-ray sources;

- carrying out high-precision timing and Quantum Gravity tests.

The new twist of AGILE is certainly the combination of simultaneous hard X-ray and gamma-ray imaging together with very accurate timing.

It is clear today that successful investigations of gamma-ray sources rely on coordinated space and ground-based observations. The AGILE Science Program will be focused on a prompt response to gamma-ray transients and alert for follow-up multiwavelength observations. AGILE will provide crucial information complementary to the many space missions that will be simultaneously operational (INTEGRAL, NEWTON, CHANDRA, SWIFT, ASTRO-E2). Furthermore, it can support ground-based investigations in the radio, optical, and TeV bands (H.E.S.S, MAGIC, VERITAS). Part of the AGILE Science Program will be open for Guest Investigations on a competitive basis. Quicklook data analysis and fast communication of new transients will be implemented as an essential part of the AGILE Science Program.

References

[1] Tavani M., et al., *Science with AGILE*, AP-26, http://agile.mi.iasf.cnr.it.

[2] Tavani M., Proceedings of the XXI Texas Symposium on Relativistic Astrophysics, Florence 10-14 December 2002, eds. R. Bandiera, F. Salvati, F. Pacini (2003).

[3] Tavani M., Proceedings of the 4-th AGILE Workshop, *X-Ray and Gamma-Ray Astrophysics of Galactic Sources*, Rome, 11-13 June 2003, eds. M. Tavani, A. Pellizzoni, S. Vercellone (2004).

[4] Michelson, P., Proceedings of the XXI Texas Symposium on Relativistic Astrophysics, Florence 10-14 December 2002, eds. R. Bandiera, F. Salvati, F. Pacini (2003).

[5] Bird A.J. et al., Ap.J. Letters, 607, 33. (2004).

[6] Revnivtsev C. et al., *Astron. Letters*, in press, astro-ph/0402027 (2004).

[7] Hartman R. et al., Ap. J. Supp. Series, 123, 79 (1999).

[8] Tavani M., Pellizzoni A., Vercellone S., et al., in preparation (2005).

[9] Aharonian, F., private communication (2004).

THE SWIFT GRB MIDEX MISSION

Paolo Giommi[a],
On behalf of the Swift Team

[a] *Agenzia Spaziale Italiana, Viale Liegi 26, 00198 Roma, Italy*

Abstract

Swift is a multi-frequency, rapid-response space observatory dedicated to gamma-ray burst astrophysics. Swift is a NASA MIDEX mission in collaboration with Italy and UK, and it is scheduled for launch on November 17th, 2004. The Swift observatory is composed by three instruments: the Burst Alert Telescope (BAT), which is a wide-field coded-mask gamma-ray camera, a X-ray telescope (XRT) and a UV-Optical telescope (UVOT), providing wide and narrow field-of-view capability. The BAT gamma-ray camera is expected to detect and image more than 100 GRBs per year with a few arcminutes position accuracy. Following a GRB detection, the Swift spacecraft will autonomously re-point its narrow-field telescopes towards the source within 20-75 seconds. This will allow to determine the burst position with arcsec and subarcsec accuracy, together with detailed spectral and timing information. Rapid GRB notifications with accurate position information will be quickly transmitted to the ground and distributed worldwide. In addition to the fast downlink capability, the Swift satellite has also the upload capability to slew to GRB and transients detected by other observatories.

1 INTRODUCTION

Gamma Ray Bursts (GRBs) are very luminous gamma ray events, lasting from 0.01 to 1000 s, during which they shine as the brightest gamma rays source in the sky. They have been discovered over thirty years ago (Klebesadel et al. 1973) and their origin remained for a long time one of the most puzzling and elusive astronomical questions. BATSE, aboard the Compton Gamma-Ray Observatory, detected roughly one GRB per day and discovered that their sky distribution is isotropic (Meegan et al. 1992), strongly suggesting an extragalactic origin of these sources. However, at that time no information on the distance or the precise location was available. The GRBs duration is known to be bimodal with most of the short bursts ($\sim 25\%$ of all GRBs) lying roughly in the range 0.1–1 s, while most of the long bursts are in the range 2–100 s; short GRBs have a γ-ray spectrum harder than long GRBs (e.g. Fishman & Meegan 1995). The real breakthrough came from the *Beppo*SAX satellite with the discover in 1997 of the existence of X-ray and optical afterglow emission from GRBs (Costa et al. 1997, Van Paradijs et al. 1997). The *Beppo*SAX mission had highly innovative properties such as a wide energy bandpass from γ to soft X-rays, a good positional accuracy (~ 1 arcmin) and a relatively fast re-pointing capability, down to 6–8 hours. These unique properties allowed the *Beppo*SAX and optical follow up teams to detect the X-ray and optical afterglow emission, thus firmly establishing that these explosive events are associated to distant galaxies, and settling a controversy on their galactic or extragalactic origin that lasted over 25 years. HETE II (e.g. Ricker et al. 2003) and INTEGRAL (e.g. Mereghetti et al. 2003) are now providing several new valuable arcmin positions of GRBs. From all these new data we have learned that more than 90% of GRBs have an X-ray afterglow, about half of them also show an optical afterglow and approximately one third show a radio afterglow. The light curves of the X-ray and optical afterglows follow a power-law temporal decay, with a power-law index in the range 1–2 and breaks that are often detected during the evolution of the light curve that can be followed for months (see figure 1). The energy spectra of the afterglows are also characterized by a power law spectral distribution; however, emission lines have been detected in some cases in the X-ray band. These were either interpreted as lines from iron (e.g. Piro et al. 2000), or lines from lighter elements (Reeves et al. 2002). However, the theoretical interpretation of these features is not straightforward and many issues remain open (e.g. Lazzati 2003). The most accepted model for GRBs is the so-called fireball scenario (Mészáros & Rees 1993; Rees & Mészáros 1992), while for the progenitors there are two hypothesis: a) the merging of two neutron stars (or a neutron star and a black hole or a black hole and a white dwarf) (Narayan et al. 1992), in this case the site of the explosion should not be associated with the site where the stars formed, b) the explosion of a very massive, rapidly spinning star (Woosley 1993; Vietri & Stella 1998), in this case
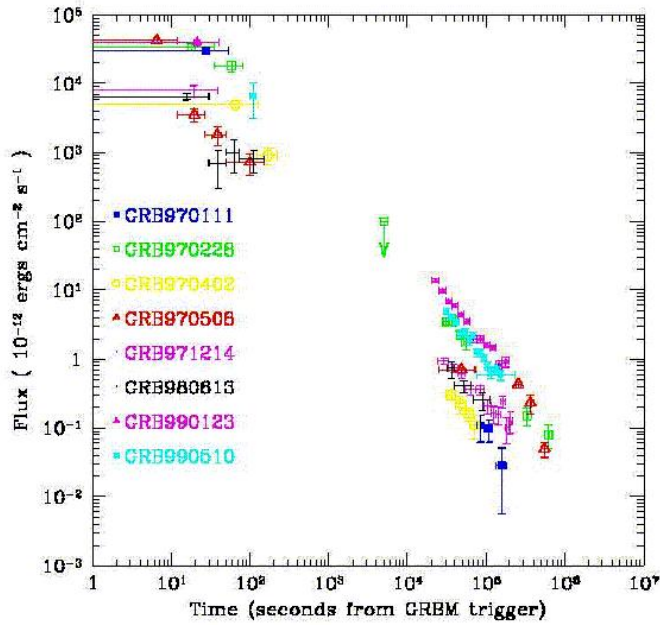
Figure 1: The fast decay of the afterglow X-ray flux, following a power law decay, with some breaks interpreted as due to beaming affects.

the GRB should be associated with star forming regions. So far three GRBs have been definitely associated with a supernova explosion (Galama et al. 1998, Stanek et al. 2003, Della Valle et al. 2003). GRBs and their afterglows during the early phases are so bright that they could be detected up to extremely large distances and used to study the IGM in a much more efficient way than even the brightest QSOs. Moreover, if it turns out that they can be used as standard candles, we will be able to probe the geometry of the Universe at very large distances. If GRBs indeed already existed during the very early stages of the evolution of the Universe, they could be associated to the end phase of the massive Pop. III stars, which are foreseen by some models for the re-ionisation of the Universe (e.g. Lamb & Reichart 2001).

2 Swift Designed to Answer GRB Key Questions

Despite fundamental progress over the past few years, many intriguing and deep questions about the origin of GRBs still remain open such as what is

the relation of GRBs to galaxies, stellar populations and to the history of star formation in the Universe? By identifying accurate positions of bursts with respect to their host galaxies, and their redshift distribution, we can tackle the problem of whether bursts are indeed related to the death of compact stars such as neutron stars and/or black holes, or to unusual star formation paths, or yet again to unknown and unidentified objects. The burst redshift distribution will provide crucial information about the star formation in the Universe which is known to strongly evolve up to redshifts of 1.5 - 2.0. Finally, GRBs will allow us to determine the dust material in distant galaxies, deducing the extinction curve, and to determine the structure and ionisation of intergalactic medium at very high redshifts. To improve our understanding in this field it is necessary to
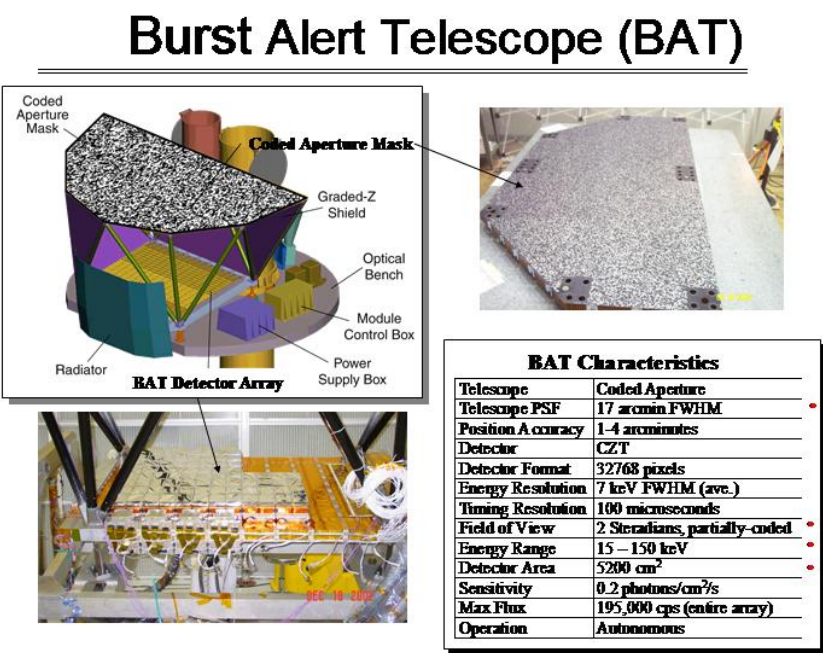
Figure 2: An artist view of the BAT experiment, together with the real coded mask and the CdZnTe detector array. The table provides the relevant BAT parameter.

build a large database including high quality data taken on different timescales and at various frequencies that can be used to constrain current and future theories. It is clear that this requires a new satellite fully dedicated to the study of GRBs and their afterglows. The requirements for the capabilities of this satellite are dictated by what we already know, mostly thanks to the

*Beppo*SAX experience. This new mission must be able to study the afterglows immediately following the GRB explosion, when the emission is brightest; it must be able to perform multiwavelength afterglow observations for at least a few hundred events; it must have arcsec position capability and be able to transmit the information immediately to the ground to trigger spectroscopy follow-up observations with the largest optical telescopes; it should also be able to determine the sub-arcsec position for hundreds of GRBs for host galaxy identification and GRB origin determination; it should provide the redshifts for hundreds of GRBs.

XRT: the Swift X-ray Telescope
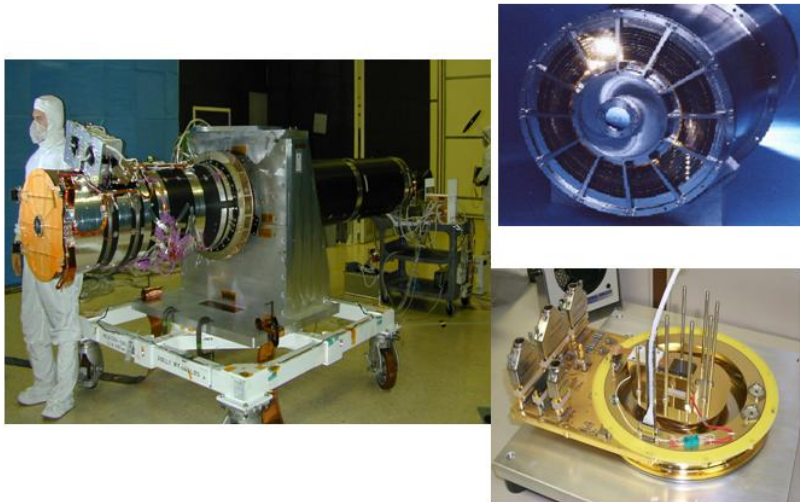
Figure 3: This figure show the XRT telescope fully assembled. The Mirror Module (upper right) and the inside of the focal plane camera (lower right) are also shown.

All these chracteristics were included in a proposal for a new satellite, called Swift, which was submitted to NASA in response to a MIDEX call in 1998, as a US-led mission (PI: Neil Gehrels) with significant contributions from Italy and UK. Swift was selected for flight in 1999 and will be launched on November 17th, 2004 from the Kennedy Space Center with a Delta launcher. The satellite will conduct a survey of the sky to detect and observe gamma-ray bursts, soft gamma-ray repeaters and other high energy transients. As a by-product Swift will also conduct the first sensitive hard X-ray all sky survey, 50 times deeper

UVOT Hardware
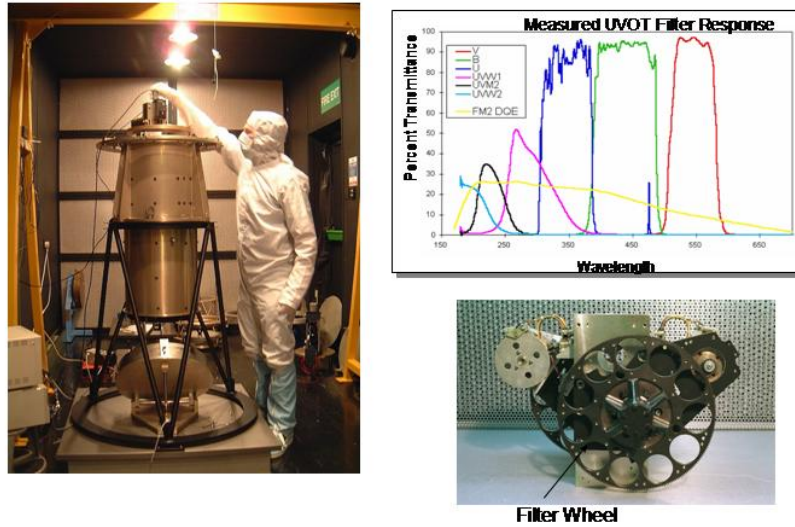
Figure 4: The UVOT telescope during a test (left), together with the measured transmission of the six filters (upper right). The filter wheel is shown on the lower right.

than that of the HEAO1/A-4 experiment. Swift is a multiwavelength satellite sensitive from the hard X-ray, 15-150 keV, to the soft X-ray, 0.3-10 keV, down to the UV and optical bands. Swift is also the fastest space observatory ever built, capable of re-pointing a GRB afterglow in 20 to 75 seconds, depending on how far off-axis the event has been detected in the wide field instrument (see below). If the afterglow power law decay observed by the *Beppo*SAX and other satellites, can be extrapolated back to the first few moments after the explosion, then the Swift X-ray and UV-optical telescopes will see a very bright source, even brighter than the Crab in the X-ray band. For this reason we will be able to perform detailed X-ray CCD spectroscopy, search for the presence of X-ray spectral lines and, if present, use them to determine the redshift of GRB. We can also search for the presence of absorbing material and study its characteristics, both locally around the GRB and at cosmological distances along the line of sight.

Swift will carry on board three different instruments: BAT, XRT and UVOT. The Burst Alert Telescope (BAT) covers the 10-150 keV energy band

and uses a coded aperture mask (see figure 2) to provide the detection and localization of the GRB with 1-4 arcmin position accuracy, depending on the burst brightness. This detector will be 5 times more sensitive than BATSE and covers $\sim 2\,sr$ (partially-coded) of the sky. BAT will detect $\sim 100-150$ GRBs per year, depending on the model assumed for the GRB evolution and luminosity function. BAT has a large array of CdZnTe detectors for a total of $5200\,cm^2$ and it has been developed at the Goddard Space Flight Center.

The X-ray Telescope (XRT) has been developed by a consortium led by the Penn State University (PSU - USA), together with the Osservatorio Astronomico di Brera (OAB - Italy) and the Leicester University (UL - UK). OAB provided the mirror module, while UL provided the CCD camera (see figure 3). XRT has an Half Energy Width (HEW) of 18 arcsec at 1.5 keV and 22 at 8.1 keV, and a field of view of 24x24 arcmin^2 in the energy range of 0.3–10 keV. The total effective area is $\sim 130\,cm^2$ at 1.5 keV and $\sim 55\,cm^2$ at 6.4 keV. XRT will give the position of the X-ray afterglows with an accuracy of < 5 arcsec in less than 100 s since the GRB explosion. XRT will make fast CCD spectroscopy from the initial acquisition, up to few hours after the burst, with spectrophotometry for up to 4 days and broad-band light curves for months.

The UV-Optical Telescope (UVOT) is a 30 cm Ritchey-Chrétien with an image-intensified CCD covering the range 170 to 650 nm. It is a copy of the XMM Optical Monitor (figure 4, right panel) and is capable of reaching a sensitivity of $m_B = 24$ in 1000 s. The FOV will be of 17x17 arcmin^2. The optical point spread function is of 0.3 arcsec, allowing for a sub-arcsec location of the GRB optical-UV afterglow against foreground stars. A filter wheel provides 6 colors and two grisms (see figure 4, left panel). With these filters it will be possible to determine the photometric Lyman cutoff redshift of an optical afterglow in the range $1 < z < 4$. The UVOT telescope is built by PSU (USA) and MSSL (UK). The three instruments are all coaligned and the typical observation scenario will be as follows. As soon as a new GRB is detected by BAT, the satellite will autonomously slew the XRT and UVOT to the BAT-determined GRB location in an interval of time between 20 and 75 seconds, depending on where in the BAT FOV the GRB is detected. A satellite downlink (TDRSS) makes the BAT positions and burst characteristics available in $< 10\,s$, the XRT position available in $< 100\,s$, a UVOT finding chart available in $< 300\,s$. The UVOT filter sequence will be completed in 7200 s. All this early GRB information, likewise any urgent command will be trasmitted from or to the satellite via the TDRSS link. The Swift data, either related to the burst or to other objects, will normally be sent down via the Malindi ground station which is the main link between Swift and the Mission Operation Center (MOC). The Malindi ground Station is provided and operated by the Italian Space Agency (ASI), while the MOC is located at PSU, in State College, Pennsylvania. Swift will typically monitor 2-3 GRB

afterglows at the same time. In addition there will be an uplink capability through TDRSS to re-point the satellite within a few minutes following an external alert triggered by a GRB or other transient phenomenon detected by other missions. Besides the GRBs and afterglow locations, that are immediately distributed world-wide, the Swift data will be rapidly acquired, processed and distributed to the science teams and to the general astronomical community through three data centers located in the USA, Italy and UK.

References

[1] Costa E., et al., 1997, Nature 387 783

[2] Della Valle M., et al., 2003, A&A 406, L33

[3] Fishman G.I., Meegan C.A., 1995, ARAA 33, 415

[4] Galama T.J., et al., 1998, Nature 395, 670

[5] Klebesadel R.W., et al. 1973, ApJ 182, L85

[6] Lamb D., Reichart D., 2001, in *Gamma-Ray Burst in the Afterglow Era: 2nd Workshop*, eds E.Costa et al., ESO Astr. Symp., Berlin: Springer Verlag, 236

[7] Lazzati D., 2003,in *Beaming and Jets in Gamma Ray Bursts*, AstroPh/0211174

[8] Meegan C., et al., 1992, Nature 355, 143

[9] Mereghetti S., et al., 2003, ApJ 590, L73

[10] Mészáros P. & Rees M.J., 1993, ApJ 405, 278

[11] Narayan R., Paczyński B., Piran T., 1992, ApJ 395, L83

[12] Piro L., et al., 2000, Science 290, 955

[13] Reeves J.N., et al., 2002, Nature 416, 512

[14] Rees M.J. & Mészáros P., 1992, MNRAS 258, P41

[15] Ricker G.R., et al., 2003, AAS 202, 5401

[16] Stanek K.Z., et al., 2003, ApJ 591, L17

[17] Van Paradijs J., et al., 1997, Nature 368, 686

[18] Vietri M., Stella L., 1998, ApJ 507, L45

[19] Woosley S.E., 1993, ApJ 405, 273

THE GRB/SN CONNECTION

Zeljka Bosnjak [a], Annalisa Celotti [a], Giancarlo Ghirlanda [b]

[a] *SISSA/ISAS, via Beirut 2-4, I-34014 Trieste, Italy*

[b] *INAF, Observatory of Brera, via Bianchi 46, I-23807 Merate (LC), Italy*

Abstract

We considered a sample of BATSE gamma-ray bursts that have an indication to be associated with supernovae. The detailed temporal and spectral analysis of the sample is presented. The GRB redshifts were estimated by using the empirical laws that correlate various properties of GRBs with their intrinsic energy release. We found that the GRBs spatially coincident with SNe are predominantly single-peaked events, having low energy spectra softer than the average control sample of BATSE GRBs.

1 Introduction

Growing evidence has been gathered that links the origin of gamma-ray bursts with supernova explosion. The first observation of a GRB/SN association came with GRB 980425 that was found to be coincident with SN 1998bw [1]; however both events had peculiar properties with respect to their classes. The newest case of association, GRB 030329/SN 2003dh [2] involved a 'classical'

GRB event and a supernova resembling SN 1998bw. Various models for the progenitor of the (long) gamma-ray bursts were proposed in order to explain the association of the GRB/SN events. The present observations favour the scenarios in which the launch of a GRB jet follows the core collapse of a massive star, i.e. 'collapsar' and 'supranova' models [3],[4].

Those observations also raised the issue of the possible existence of a sub-category of GRBs originating from supernovae. We investigated the fundamental properties of gamma-ray bursts for which there is an indication of being associated with a supernova (e.g. temporal and directional coincidence, a bump in the late-time light curve) in order to find out whether they have characteristic properties different from the bulk of BATSE GRBs. Particular properties of the GRB/SN sample might indicate whether there is a different underlying physical mechanism at work and whether the observations may be interpreted within a single scenario (Bosnjak et al, in prep.).

2   Sample selection

We selected the sample of GRBs by cross-correlating the BATSE current catalog[1] and the SN catalog of IAUC[2], associating the events on the basis of temporal and positional coincidence. The basis of the sample consisted of previous GRB/SN pairs reported by [5] and [6]. We extended these works considering approximately the dates not included in their selection (after Nov. 20, 1997 up to May 26, 2000). We searched for SNe in the BATSE GRB error box with the SN discovery date in the time interval 10 days before and 30 days after the GRB onset (i.e. we considered time delays comparable to the time for SNe to reach the optical maximum, $\sim$20 days). The cross-corelation of the GRB-SN catalogs yielded 16 new GRB/SN coincident events. Coordinates from the IPN were available for 2 gamma-ray bursts and both associations were excluded. By including the GRB/SN pairs from the previous searches and the 7 GRBs with an indication for being associated with a supernova (i.e. a bump in the late-time optical afterglow or an indication of a line feature in X-ray, [7], [8]), the sample consists of 36 gamma-ray bursts possibly associated with supernovae.

3   Temporal analysis

We developed an algorithm performing the least-squares fit to the GRB pulse profiles superimposed to the background, adopting the lognormal model as a

---

[1]http://cossc.gsfc.nasa.gov/batse/BATSE_Ctlg/index.html
[2]http://cfa-www.harvard.edu/iau/lists/Supernovae.html
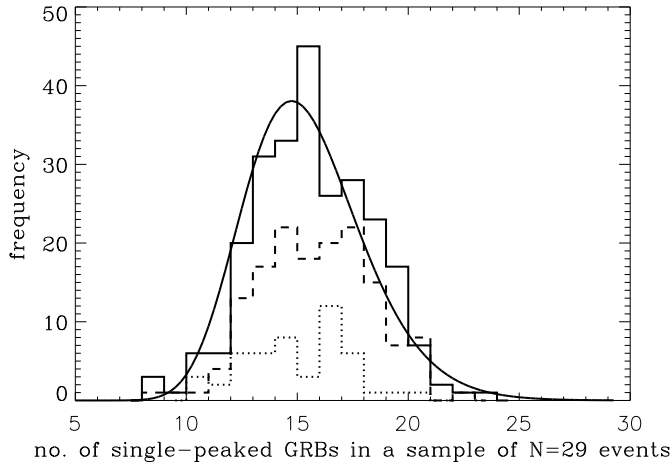
Figure 1: The distributions of the number of single-peaked gamma-ray bursts in a random sample of N=29 GRBs. The dotted line represents the distribution when n=50 samples were extracted from the total sample of 1445 bursts; dashed and solid line represent the distributions for n=150 and n=250 samples, respectively. The fit of the lognormal distribution for n=250 extracted samples is also shown.

description of the pulse profile [9], i.e.

$$I(t) = \begin{cases} A_{\max} \ e^{-\frac{1}{2}\left(\frac{\log(t-t_0)-\mu}{\sigma}\right)^2}, & t > t_0 \\ 0 & \text{otherwise} \end{cases}$$

where μ and σ refer to the mean and standard deviation respectively of the log time after the pulse onset at t_0. The analysis was performed on the time scale of 64 ms for long bursts and of 2 ms for short bursts.

The resulting distribution of FWHMs is consistent with that obtained for a sample of single-peaked GRBs [9] at a significance level P_{KS}=0.63. We examined in detail the possibility that GRBs associated with SNe are single-peaked. We therefore considered as a control sample 1455 BATSE bursts. Each GRB was analyzed and characterized by the number of pulses in the time history. By applying the same procedure to the subset of 29 GRBs from the GRB/SN sample, we obtain 23 single-peaked events. Via n random extractions of N=29 GRBs from the whole sample we then determined the probability of obtaining 23/29 single-peaked GRBs by chance, which results to be 0.004
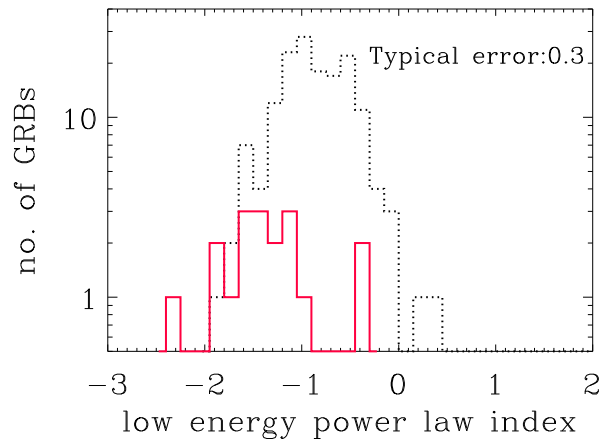
Figure 2: Low energy power law index distribution for gamma-ray bursts of the GRB/SN subsample; the dotted histogram represents the result obtained by [12].

(Fig.1).

4   Spectral analysis

Gamma-ray burst spectra in the BATSE energy range (25-1800 keV) are usually described with the phenomenological model [10], presented by two smoothly connected power laws. The value of the low energy power law index α varies for different emission models and therefore may be used to distinguish between the various scenarios that can give rise to the observed spectrum. For example [11], optically thin synchrotron emission from relativistic electrons (in its simplest version) predicts a limiting value of $\alpha = -\frac{2}{3}$.

We performed the analysis of the time integrated spectra; for most of the bursts (16) we used the High Energy Resolution (HER) data with 128-energy channel resolution; in 5 cases (short bursts) we used the Medium Energy Resolution (MER) data that consist of 16-energy channel spectra. The methodology follows that applied by [12] to the large sample of bright BATSE GRBs. We compared the spectral parameters obtained for bursts from the GRB/SN sample with the results reported in [12]. A K-S test performed on the distributions of the low energy power law index α (Fig.2) yields that the two distributions are significantly different ($P_{KS}=3.7\times10^{-5}$). That is, bursts
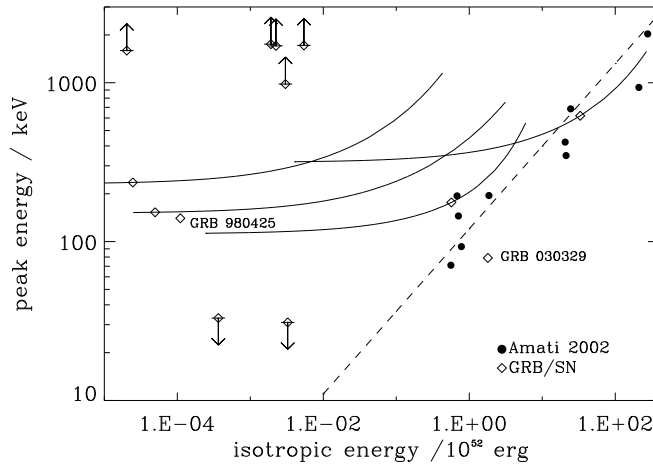
Figure 3: The relation proposed by [13] (best fit as dashed line). The GRBs from the GRB/SN sample are shown at the position corresponding to the redshift of the 'coincident' supernova (diamonds) while the solid curves represent their position were they located at different redshifts (between 0.1 and 4). GRBs whose spectra only allowed to determine upper/lower limits to E_p are shown as arrows (at the redshift of their 'associated' SN). Also the position of GRB 980425 is marked on the diagram.

from the GRB/SN sample have low energy spectra softer than those analyzed by [12], with an average $\alpha \sim$ -1.5. We do not find statistically significant differences in the value of high energy power law index when comparing the two distributions.

5   Redshift estimate

Several empirical correlations have been put forward which allow to estimate the GRB redshift and intrinsic energy release using their temporal and spectral characteristics. We adopted some of these to investigate the reality of the GRB/SN association. [13] by investigating the spectral and energetics properties of 12 GRBs with known redshifts, suggested the existence of a correlation between the intrinsic peak energy E_p and isotropic total radiated energy E_{rad}: $E_p \propto E_{rad}^{0.52}$. We thus calculated the peak energy E_p and total intrinsic energy under the same assumptions as [13] (Fig.3). Some bursts could follow the relation only if they were located at high redshifts (z>1.5). More

interestingly, some of the GRB/SN events do not approach it at all (for any redshift), opening the possibility that they form a separate class of the bursts characterized by low energetics. Strong support to this argument comes from GRB 980425 which has indeed properties clearly peculiar with respect to the GRBs with known redshift used for calibration.

6   Conclusions

We presented the detailed temporal and spectral analysis of the sample of GRBs that are found to be coincident in time and position with supernovae, or have indications of an underlying supernova in the late time afterglow light curve. We find that these GRBs are statistically different from the bulk of events in two important properties:(1)their light curves (with 64 ms time resolution) are mostly single-peaked events and (2)their low energy spectral component is softer ($\alpha \sim$ -1.5) than what commonly observed for BATSE GRB.

References

[1] T. Galama et al, 1998, Nature, 396, 670

[2] J. Hjorth et al, 2003, Nature, 423,847

[3] S.E. Woosley et al, 1999, ApJ,516,788

[4] M. Vietri & L. Stella, 1998, ApJ, 507, L45

[5] L. Wang & J. Wheeler, 1998, ApJ, 504, L87

[6] R. Hudec et al, 1999, A&AS. 138, 475

[7] J. Bloom et al, 1999, Nature, 401, 453

[8] L. Piro et al., 1999, A&AS, 138, 431

[9] J. Norris et al, 1999, ApJ, 518, 901

[10] D. Band, 1993, ApJ, 413, 281

[11] M. Tavani, 1996, ApJ, 466, 768

[12] R.D. Preece et al, 2000, ApJS,126,19

[13] L. Amati, 2002, A&A, 390, 81

PULSAR BOW-SHOCKS: A PROBE FOR THE INTERACTION BETWEEN RELATIVISTIC PARTICLE WINDS AND THE INTERSTELLAR MEDIUM

A. Pellizzoni [a], F. Mattana [a], S. Mereghetti [a], A. De Luca [a],
P. Caraveo [a], M. Tavani [b], M. Conti [a]

[a] *Istituto di Astrofisica Spaziale e Fisica Cosmica,*
Sezione di Milano "G. Occhialini" - CNR,
via Bassini 15, I-20133 Milano, Italy

[b] *Istituto di Astrofisica Spaziale e Fisica Cosmica,*
Sezione di Roma - CNR,
via Fosso del Cavaliere, 100 I-00133 Roma, Italy

Abstract

The study of pulsar bow-shocks is one of the most promising ways towards the understanding of the interactions between neutron stars relativistic winds and their environment. These objects are best resolved as Hα nebulae but velocity-driven features are seen also in the radio and X–ray bands and represent interesting targets for future gamma-rays telescopes. We present a preliminary multiwavelength catalogue of pulsar bow-shocks.
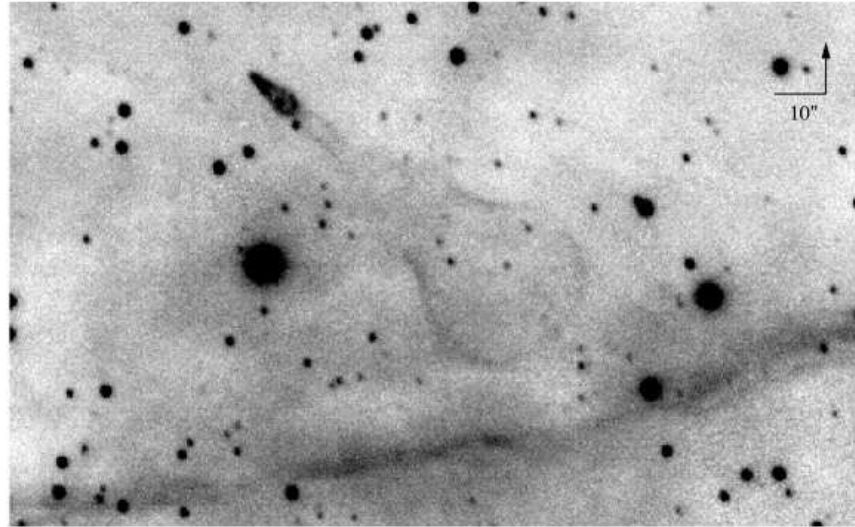
Figure 1: The Guitar Nebula: an example of Hα bow-shock with "cometary" shape due to the supersonic motion (>1000 km/s) of the radio pulsar B2224+65 with direction close to the plane of sky [6].

1   Pulsar Wind Nebulae

Most of the spin-down energy of a pulsar ($\dot{E}_{rot}$ =10^{35}-10^{39} erg/s for youngest sources) is expelled in its surrounding in the form of a relativistic ($\gamma \sim 10^6$) magnetized wind. When the pulsar wind is confined by an external pressure (M), a shock might occur at the equilibrium distance (R_{SO}) between the wind pressure and M:

$$\frac{\dot{E}_{\text{rot}}}{4\pi R_{SO}^{2}c} = M$$

At this termination shock, particles are accelerated and synchrotron radiation is emitted up to X-ray and gamma-ray energies. A Pulsar Wind Nebula (PWN) becomes then observable, representing a sort of calorimeter for the energy emitted by the neutron star. There are different types of PWNe depending mainly on the origin and strength of the external pressure M. Static PWNe or plerions (e.g. Crab nebula) could originate from supernova cold ejecta inside the SNR shell interacting with the overpressurized pulsar wind; "binary" PWNe (e.g. PSR J0737-3039) could result from the interaction between the winds of two orbiting stars; "bow-shock" PWNe (e.g. Black Widow) for which M is the ram pressure originating from the supersonic motion of the pulsar interacting with the interstellar medium (ISM). In this case, $M=\rho V^2$ where ρ is the ISM
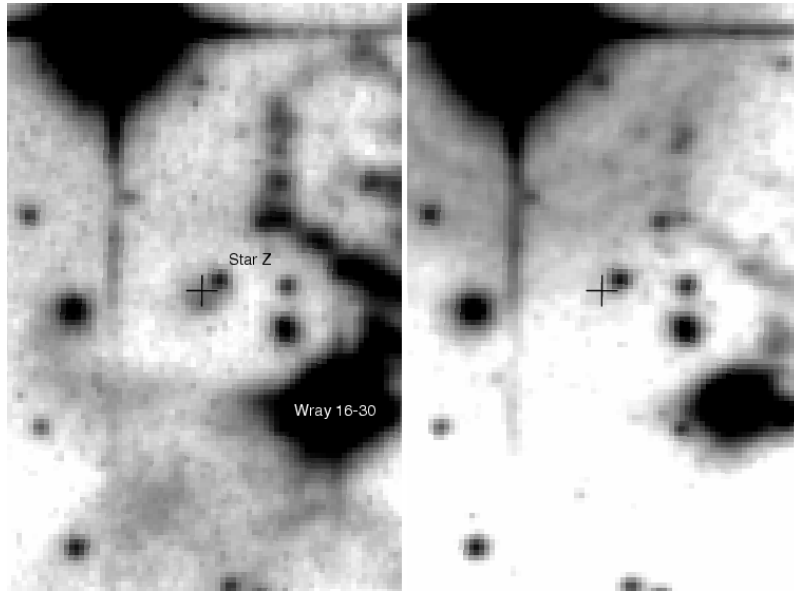
Figure 2: Hα (left) and R band (right) images of the central region of SNR G266.2-1.2. The cross indicates the position of the neutron star AX J0851.9-4617.4. The roughly circular nebula of 6" only visible in the Hα filter is coincident with the position of the X-ray source. It represents an example of "bullet" bow-shock (NS motion close to the line of sight and/or low velocity) [16]

density and V is the pulsar velocity. For typical pulsar velocities of $\sim$100 km/s and ISM density of $\sim$1 cm^{-3}, the resulting ram pressure is $M \sim 10^{-10} g/(s^2 cm)$ and the stand-off distance is R$_{SO}$$\sim$10^{16}-10^{17}cm, that means structures resolved at few arcsec (for d$\sim$1 kpc) from the NS [25] [3]. Pulsar bow-shocks can be observed through excitation lines of ISM atomic hydrogen (Hα line) or by synchrotron emission by wind particles in the magnetic field compressed by the shock that is typically of the order of 10^{-4}-10^{-5} Gauss. Pulsar Bow-Shocks are faint (L=10^{-5}-10$^{-3}\dot{E}_{rot}$), but in principle they are common phenomena (they require PSR velocities of only a few 10 km/s for their formation) and therefore represent an interesting challenge for future high-energy telescopes aimed to detect their synchrotron emission. The study of pulsar bow-shocks is of paramount importance to obtain information on the structure of the external regions of the pulsar magnetosphere (geometry and particle energies) and properties of the interstellar medium (density, ionisation).

2   Classification of Pulsar Bow-shocks

A clear classification of pulsar bow-shocks is still not well defined owing to the poor sample of available objects, their weakness and the difficulty to distinguish them from other kinds of PWNe (not all bow-shaped PWNe are bow-shocks). As a first step in order to better assess their properties as a population we have built a catalogue (Table 1) based on the identification criteria described in the previous chapter. Only 10 bow-shocks are firmly detected in $H\alpha$ and/or in radio and X–rays. Another set of 10 candidates needs confirmation. Known bow-shocks are tipically associated to energetic and nearby pulsars (including few millisecond pulsars) with "normal" characteristics apart from their high $\dot{E}_{rot} \times V^2/d^2$ values. About 50% of the sources are observed in the X–ray and radio bands and another $\sim$50% is visibile only in $H\alpha$. Only one case ("The Black Widow") is firmly detected in both energy bands. According to their morphologies, two general classes of bow-shocks can be identified; (1) "comet shaped" bow-shocks, as the Guitar nebula (Figure 1), characterized by high speed (>1000 km/s) and proper motion in the plane of the sky; (2) "bullet" bow-shocks (Figure 2) characterized by low pulsar velocity and/or motion along the line of sight. The first class allows to study wind asymmetries and gradient density in the ISM. The latter class includes objects more difficult to identify due to the absence of peculiar geometrical strucures, but it includes a potentially wider sample of bow-shocks useful for population studies.

The search for new pulsar bow-shocks could improve luminosity models poorly constrained by the existing observations. The expected $H\alpha$ luminosity (see e.g. [16], and references therein) is roughly proportional to the neutron star velocity V, its rotational energy loss $\dot{E}_{\rm rot}$, and the fraction X of neutral hydrogen in the interstellar medium: $L_{\rm H\alpha} \propto V \dot{E}_{\rm rot} X$. This relation fits known sources quite well, but its dependence on the neutral hydrogen fraction, a very uncertain parameter, implies rather uncertain $H\alpha$ flux predictions even in case of nearby pulsars clearly showing bow-shocks at other wavelengths. For example, Geminga shows a striking bow-shock in X–rays but it is undetected in $H\alpha$ [5] implying a remarkably low neutral hydrogen fraction <0.01. A possible explanation of this could be that the synchrotron emission from the shock or from the neutron star could pre-ionize the ISM inhibiting $H\alpha$ emission. Exahustive broad-band emission models for pulsar bow-shocks should then properly account for synchrotron losses and adiabatic expansion of the PWN which depend on many input parameters reflecting the evolutionary state of the system and the ambient conditions. Thus, such models are clearly speculative without new valuable multiwalength observations and an in-depth analysis of existing X–rays and $H\alpha$ surveys improving the current sample of pulsar bow-shocks. Interesting observations could be also provided by future gamma-ray missions as AGILE and GLAST. Some of the unidentified gamma-rays sources on the Galactic Plane could be bow-shocks associated to energetic

Table 1: Preliminary catalogue of firmly identified (upper panel) and candidate (lower panel) pulsar bow-shocks. New multiwavelength observations ranging from radio to gamma-ray bands are expected to improve this poor sample in the near future

Name	$H\alpha$, X, radio	d kpc	$log(\dot{E}_{rot})$ erg/s	V km/s	$ref.$
PSR J0437-4715	H - -	0.14	34.1	180	1,23
CXOU J061705.3+222127 (IC443)	- X R	1.5	-	250	15
PSR B1757-24 ("Duck")	- X R	5.0	36.4	<590	14
PSR B1853+01 (W44)	- X R	2.6	35.6	370	17
PSR J1747-2958 ("Mouse")	- X R	5.0	36.4	180	9
J1856.5-3754	H - -	0.14	-	240	13,22
PSR B1957+20 ("Black Widow")	H X -	1.5	35.0	220	20
PSR B0740-28	H - -	1.9	35.2	220	12
PSR J2124-3358	H - -	0.27	33.6	100	8
PSR B2224+65 ("Guitar Nebula")	H X? -	2.0	33.1	2500	7,26
PSR B1951+32 (CTB80)	H X R	2.5	36.6	300	19
PSR J0633+1746 (Geminga)	- X -	0.16	34.5	120	5
PSR J0537-6910 (N157B)	- X R	50	38.7	600	21
PSR B1929+10	- X? -	0.33	33.6	160	18
PSR B1643-43 (G341.2+0.9)	- - R	6.9	35.6	470	11
AXJ0851.9-4617.4 ("Bullet")	H - -	<2	-	-	16
PSR J1016-5857	- X R	3?	36.4	-	4
GeVJ1809-2327	- X ?	1.8	-	-	2
PSR B1823-13	- X? -	4.1	36.5	-	10
G0.13-0.11	- X R	-	-	-	24

pulsars with beaming emission not intersecting the line of sight, then difficult to identify because of the lack of pulsed emission.

References

[1] Bell, J.F., et al.,1995, ApJ, 440, L81

[2] Braje, T.M., et al., 2002, ApJ, 565, L91

[3] Bucciantini, N., 2002, A&A, 387, 1066

[4] Camilo, F., et al., 2001, ApJ, 557, L51

[5] Caraveo, P.A, et al., 2003, Sci, 301, 1345

[6] Chatterjee, S., & Cordes, J.M., 2002, ApJ, 575, 407

[7] Chatterjee, S., & Cordes, J.M., 2004, ApJ, 600, L51

[8] Gaensler, B.M., et al., 2002, ApJ, 580, L137

[9] Gaensler, B.M., et al., 2003a, aph0312362

[10] Gaensler, B.M., et al., 2003b, ApJ, 588, 441

[11] Giacani, E.B., et al., 2001, AJ, 121, 3133

[12] Jones, D.H., et al., 2002, A&A, 389, L1

[13] Kaplan, D.L., et al., 2002, ApJ, 571, 447

[14] Kaspi, V.M., et al., 2001, ApJ, 562, L163

[15] Olbert, C.M., et al., 2001, ApJ, 554, L205

[16] Pellizzoni, A., et al., 2002, A&A, 393, L65

[17] Petre, R., Kuntz, K.D., Shelton, R.L., 2002, ApJ, 579, 404

[18] Pivovaroff, M.J., 2003, priv. comm.

[19] Safi-Harb, S., et al., 1995, ApJ, 439, 722

[20] Stappers, B.W., et al., 2003, Science, 299, 1372

[21] van der Swaluw, E., et al. 2004, aph0311388

[22] van Kerkwijk, M.H., & Kulkarni, S.R., 2001, A&A, 380, 221

[23] van Straten, W., et al., 2001, Nature, 412, 158

[24] Wang, Q.D., et al., 2002, ApJ, 581, 1148

[25] Wilkin, F.P., 1996, 459, L31

[26] Wong, S., et al., 2002, AAS HEAD, N17.120

NEW INSIGHTS ON BLAZAR DUTY-CYCLE AND GAMMA-RAY ACTIVITY

Stefano Vercellone [a], Simona Soldi [a,c], Andrew Chen [a,b],
Marco Tavani [e,b]

[a] IASF-CNR, via Bassini 15, Milano, Italy

[b] CIFS, Viale Settimio Severo 63, Torino, Italy

[c] ISDC, Chemin d'Ècogia 16, 1290 Versoix, Switzerland

[e] IASF-CNR, Via del Fosso del Cavaliere 101, Roma, Italy

Abstract

Active Galactic Nuclei (AGNs) detected in the gamma-ray energy band
30MeV - 50GeV show high variabilty on all observable time scales.
Unfortunately, the sparse coverage of *EGRET* makes it difficult to firmly
characterize blazar transient behaviour, for example their duty cycle.

In the context of a preliminary study of candidate sources potentially
observable by the forthcoming gamma-ray missions *AGILE* and *GLAST*,
we report on a recent estimate of the gamma-ray blazar duty-cycle
obtained by means of a statistical analysis of *EGRET* data compared
with bootstrap simulations of a simplified gamma-ray activity model.

1   Introduction

Among Active Galactic Nuclei (AGN), *blazars* show strong flux variability at almost all frequencies of the spectral energy distribution (SED). The *EGRET* instrument on-board of CGRO detected, above 30 MeV, blazars as a *class* of γ-ray sources [1], identifying 67 objects, and detecting 27 candidates. Gamma-ray blazars are characterised by high variability on different time–scales, from one day (e.g. PKS 1622-297) to one month (e.g. PKS 0208-512). This large spread in time variability and the sparse coverage obtained by *EGRET* make it difficult to quantify parameters such as the *duty–cycle* (i.e. the fraction of time spent in a flaring state) and/or the characteristic time–scale of γ-ray activity for this class of sources.

A preliminary result was obtained by [2], based on the Second *EGRET* Catalogue assuming that the link between the radio and the γ-ray emission can be used to derive the γ-ray luminosity function. Under these assumptions, they found that a duty–cycle $\zeta = 0.03$ is consistent with the data. One weakness of this analysis is that the radio-gamma relationship is highly uncertain.

The aim of this Paper is to summarize a recent result on the estimate of the blazar duty–cycle and γ-ray variability [3].

2   The Blazar γ-ray variability

In order to investigate the blazar γ-ray duty–cycle, we analysed the 3EG AGN sample, looking for recurrent activity. For each source we considered the number of viewing periods (VPs) during which it was close enough to the pointing direction ($< 40°$, the FOV radius) that its exposure for that VP was greater than zero. For each source we calculated the *Exposure* (EXP), defined as the sum of the exposures during each single viewing period.

In order to estimate the γ-ray activity level, we computed the number of times that a source was in a *high-state* (HSN) i.e. when the flux of the i-th VP was greater than a given threshold. We establish that a source is in a high-state when 1) the flux of the i-th VP is in excess of 1.5 times the mean flux of the source, and 2) the 1-σ uncertainty of the measurement at the high state is less than the deviation of the measurement from the mean. The mean flux is defined as the weighted mean of all the detections and upper limits, assuming the weight $w(\sigma) = 1/\sigma$, where σ is the uncertainty of the measurement for detections, while $\sigma = UL$ for the upper limits. If two high-states were less than 2 weeks apart (the typical duration of an *EGRET* pointing), we gathered them into a single high-state coincident with the first one.

Given EXP and HSN, we computed an *activity index* (ψ) of each AGN as follows:

$$\psi_{\mathrm{src}} = HSN_{\mathrm{src}} \times [EXP_{\mathrm{src}}]^{-1} \ [\mathrm{cm}^{-2}\mathrm{s}^{-1}] . \tag{1}$$

Figure 1: Four different examples of blazar γ-ray activity as a function of exposure. *Top-left panel:* 3EG J0845+7049 with $HSN = 1$ despite its high exposure; *Top-right panel:* 3EG J1733−1313 which, for a similar exposure, has $HSN = 5$; *Bottom-left panel:* 3EG J0530+1323 which showed a possible periodicity in its high-state status, and *Top-right panel:* 3EG J0340−0201 which has a very low exposure ($\sim 64 \times 10^7$ cm^{2}s), but showed 2 high-states in a few observations. Crosses show the value of the discrete ψ for each VP containing the source. The inset displays the discrete ψ curve on a smaller scale to show the finer details.

This index provides an estimate of blazar γ-ray activity, weighted by the exposure. Sources with high ψ have a γ-ray activity which is highly variable. Sources with $\psi = 0$ do not show significant flux variability. We analysed the behaviour of each single source having $\psi \neq 0$ during its time history. Fig. 1 shows the discrete ψ for some *EGRET* sources as a function of *EXP*. We show four different examples of activity behaviour: 1) 3EG J0845+7049, with a single $HSN = 1$ despite its large exposure; 2) 3EG J1733−1313, which, for a similar exposure, has $HSN = 5$; 3) 3EG J0530+1323, showing a possible periodicity in its high-state status, and 4) 3EG J0340−0201, which has a very low exposure ($\sim 64 \times 10^7$ cm^{2}s), but showed 2 high-states in a few observations.

Sources that have $HSN = 1$ (e.g., 3EG J0845+7049) show a rise of ψ^k_{src} followed by a decay after reaching a single high state, while sources that have high HSN (e.g. 3EG J0530+1323) show a saw-tooth pattern, corresponding to alternately increasing/decreasing of ψ^k_{src}.

We distinguish sources for which the activity level $\psi = 0$ (population A, 36 per cent), and the ones having $\psi \neq 0$ (population B, 64 per cent). A remarkable difference appears in the two populations when we compare the ratio between flat-spectrum radio quasars (FSRQs) and BL-Lac objects (BLs). Population A is almost equally divided between FSRQs and BLs ($\sim$60 and $\sim$40 per cent, respectively), while Population B is dominated by FSRQs (~ 80 per cent). FSRQs are generally more variable and more luminous in the γ-ray energy band than BLs, which could explain the higher fraction of these sources in Population B. A possible correlation is found between the activity level and the black hole mass, with a probability P_{rand} of a randomly distributed sample of objects on the order of $\sim 10^{-2}$. We suggest that the use of the ψ statistic is more robust than the use of the HSN, since the latter is not weighted by the *EGRET* coverage.

3   The blazar gamma-ray duty–cycle

We develop a simplified model of *EGRET* blazar activity that yields rough, but quantifiable, estimate of physical parameters of interest. In this simplified model, we make several assumptions:

1. that all of the *EGRET* blazars exhibit the same basic behaviour. While observationally unjustified, this assumption is necessary to model the average behaviour.

2. that only those blazars detected by *EGRET* are part of the population of interest.

3. that the behaviour of all *EGRET* blazars can be characterised by a simple model with only two free parameters, the duty–cycle, χ, and the characteristic time–scale, T. Each blazar will spend a period of time whose average length is T at a low flux level (*off*) before emitting a γ-ray flare of duration τ at a high flux level (*on*), then returning to a low level. The duty–cycle is then defined as the fraction of time spent in the *on* state:

$$\chi = \frac{\tau}{\tau + T} \ . \tag{2}$$

Note that all blazars have the same characteristic time–scale T, but the duration of each individual quiescent periods is drawn from a Poisson distribution with mean T.

We explored the parameter space of (χ, T). For each pair of χ and T under consideration, we generated 100 sets of 67 simulated light curves covering the entire time interval of *EGRET* Cycle 1 to 4 (1620 days), one for each blazar. The time sequence of *on-off* states was determined by drawing the durations of the *off* states from a Poisson distribution with mean T. The durations of the *on* states were fixed at τ. To obtain the observed fluxes, we used a bootstrap procedure. Each light curve was compared with the observation history of the corresponding AGN. If a given viewing period (VP) coincided with an *on* state, the observed flux was randomly drawn from the distribution of all fluxes *detected* from all *EGRET* blazars during a single VP. Otherwise, the observed flux was randomly drawn from the distribution of all *upper limits* (i.e. non-detections) at *EGRET* blazar positions during a single VP. For each AGN the flux values assigned to each VP were used to calculate its HSN (and therefore its categorisation as Population A or B) in the same manner as the actual *EGRET* blazar HSN. The result is 100 sets of simulated blazar light curves, each with a ratio $R_{AB} = \#\text{Pop.A}/(\#\text{Pop.A} + \#\text{Pop.B})$. Thus for each pair of values of (χ, T), we have obtained a distribution of 100 simulated values of R_{AB}, each with a mean and variance. Therefore, we are able to define a confidence region of (χ, T) pairs whose mean values of R_{AB} are within one standard deviation of the observed value $R_{AB} = 24/67 = 0.36$. For values of R_{AB} close to the observed value, the simulations give a standard deviation of 0.05. We ran 100 simulations each for 390 (χ, T) pairs, ranging from $0 < T < 450$ days and from $0 < \chi < 1$. Fig. 2 shows the results.

Points in Fig. 2 represent the mean value of R_{AB} for each value of T and χ. The filled squares represent those ratio values between $0.31 \leq R_{AB} \leq 0.41$, small filled circles represent $0.0 \leq R_{AB} < 0.31$, while crosses represent $0.41 < R_{AB} \leq 1.0$. Taking into account our simplifying assumptions, including the restriction that the observed *EGRET* blazars form the entire population of γ-ray emitting blazars, the only region consistent with the observations is the region where $0.31 \leq R_{AB} \leq 0.41$. The region with high R_{AB} produces too few flaring sources, while the region with low R_{AB} produces too many. This implies that the true characteristic time–scale T lies between 50 and 400 days, the duty–cycle χ becoming more extreme for lower values of T. Note that for the Stecker & Salamon duty–cycle of 0.03 the characteristic time–scale T would be on the order of 50 days.

If we should take into account a wider sample of γ-ray blazar, by including radio blazars emitting at a level of 250 mJy, we would obtain that the low R_{AB} region to remain excluded, because adding more sources is unlikely to reduce the absolute number of Population B sources predicted, which is higher than the number observed. On the other hand, the (χ, T) pairs in the high R_{AB} region may now be consistent with the *EGRET* data. Therefore, the region in (χ, T) space where formerly the R_{AB} was consistent with the observed value

Figure 2: Mean ratio $R_{AB} = \#Pop.A/(\#Pop.A + \#Pop.B)$ from simulations of *EGRET* -detected blazars only.

now forms a lower bound to the possible values of T for a given value of χ.

4   Conclusions

The results presented here summarize a more detailed analysis presented in [3] where we discuss the implications on the duty–cycle estimate of a sample of candidate γ-ray AGNs extracted from recently published radio catalogues. A firm estimate of the duty–cycle will be a scientific goal of future γ-ray missions such as *AGILE* and *GLAST* . Their wide FOV ($\sim 60°$) will allow monitoring of a large number of AGNs for each pointing on long time–scales.

References

[1] Hartman R. C. et al., 1999, ApJS, 123, 79

[2] Stecker F. W., Salamon M. H., 1996, ApJ, 464, 600

[3] Vercellone S., Soldi S., Chen A.W., Tavani M., 2004 MNRAS, 353, 890

GAMMA-RAY EMISSION FROM THE GALAXY

ANDREA GIULIANI [a,b], ANDREW CHEN [a,b], SANDRO MEREGHETTI [a],
ALBERTO PELLIZZONI [a], MARCO TAVANI [c] , STEFANO VERCELLONE [a]

[a] *Istituto di Astrofisica Spaziale e Fisica Cosmica, Sezione di Milano*
via Bassini 15, Milano, Italy

[b] *Consorzio Interuniversitario per la Fisica Spaziale,*
via Settimio Severo 63, Torino, Italy

[c] *Istituto di Astrofisica Spaziale e Fisica Cosmica, Sezione di Roma*
via Fosso del Cavaliere 100, Roma, Italy

Abstract

The interaction between cosmic rays and the Galactic interstellar medium
produces the diffuse gamma-ray emission observed from past space
missions. The study of this emission can provide information on the
distribution of cosmic rays, diffuse gas and interstellar radiation. A
detailed modelization of this component is necessary also for the analysis
of the point sources embedded within it. Here we present the model of
galactic diffuse emission developed for the AGILE mission.

1 Introduction

The study of Galactic diffuse gamma emission will be one of the main scientific objectives of AGILE, the ASI satellite for gamma-ray astronomy that will be launched in 2005. The AGILE solid-state tracker (the GRID instrument) will be able to cover π sr of the sky with one single pointing with an on-axis effective area about one half of that of EGRET and considerably better above $30°$ off axis. This means that AGILE will collect, for the same observing time, a number of diffuse photons larger by a factor of two. AGILE will also have an angular resolution about a factor two better than the EGRET one for photons with energy larger than 400 MeV, with a point spread function depending weakly on off-axis angle. In order to better exploit these capabilities, a very accurate model of the interstellar gamma-ray emission is required for the analysis of AGILE data.

2 The AGILE interstellar emission model

The AGILE diffuse emission model is a 3D grid with bins of $0.25°$ in galactic longitude and latitude (l,b) and 0.2 kpc in distance along the line of sight (r). The gamma emissivity is supposed to be produced by the interaction of cosmic rays with the interstellar medium through three physical process: protons interact with the interstellar-medium nuclei (pp scattering), producing π^0, which in turn decay in a gamma pair. Electrons, instead, interact with the diffuse matter by bremsstrahlung and with the interstellar radiation field (ISRF) by inverse Compton. It is convenient to express the interstellar-medium gamma emissivity $g(l, b, r, E)$ by separating the terms depending on the cosmic rays from those related to their target density.

$$g(l, b, r, E) = [q_{pp}(l, b, r, E) + q_{br}(l, b, r, E)][n_{H_2}(l, b, r) + n_{HI}(l, b, r)] + \quad (1)$$
$$+ q_{iC}(l, b, r, E)n_{ph}(l, b, r)$$

where q_{pp} and q_{br} are the gamma luminosity per cm^3 per hydrogen atom due to either pp scattering or bremsstrahlung, while q_{iC} is the gamma luminosity per cm^3 per photon due to inverse Compton. n_{HI}, n_{H_2} and n_{ph} are, respectively, the density of molecular hydrogen, the density of atomic hydrogen and the density of ISRF photons. In order to model the galaxy matter distribution we use the HI and CO radio surveys recently completed which are more accurate than the previous ones. For the HI hydrogen distribution we used the Leiden-Dwingeloo 21 cm survey [3]. This survey covers the sky above declination –30°. The Leiden-Dwingeloo survey improves the previous results especially in terms of sensitivity (an order of magnitude better), velocity range and resolution. For the region around the south celestial pole, which is not covered by this survey,

Figure 1: The AGILE emission model for the first Galactic quadrant. Full resolution images are available at the web site:
$http : //www.mi.iasf.cnr.it/ \sim giuliani/galaxy$

we used other observations, such as those from the Maryland-Parkes survey [5]. In order to obtain the distribution of molecular hydrogen we use the CO observations described in Dame et al. 2001 [2]. Cosmic rays produce gamma rays through the inverse Compton interaction with photons of the cosmological background and of the interstellar radiation field (ISRF). In order to account for this component we use the analytical model proposed by Chi & Wolfendale [1]. It describes the ISRF as the result of three main contributions: far infrared (due to dust emission), near infrared and optical/UV (due to stars emission). One of the objectives of gamma ray diffuse emission studies is to discriminate between cosmic ray models. For this reason our gamma ray emissivity model can include different analytical and numerical cosmic ray models which have been developed in the last years. The results presented in these proceedings are obtained by using the cosmic ray model given by the numerical code GALPROP [6] which derives the cosmic ray distribution accounting for physical processes like diffusion and energy losses.

3   Cosmic-Ray Studies

The observed features of the galactic gamma-ray diffuse emission depend both on the interstellar medium distribution and on the cosmic ray distribution. In order to test theoretical models it is convenient to decouple cosmic-ray information from matter distribution. The spectrum $S(E, l, b)$ of the diffuse emission observed by EGRET from the Galactic plane consist of two main components, namely proton-proton and bremsstrahlung emissivities convolved with matter distribution. For the plane region, $|b| < 5°$, in fact, the inverse Compton contribution can be neglected.

$$S(E, l, b) = S_{pp}(E, l, b) + S_{br}(E, l, b) \tag{2}$$

where

$$S_{pp}(E, l, b) = \frac{1}{4\pi} \int q_{pp}(E, l, b, r) n_H(l, b, r) dr \tag{3}$$

$$S_{br}(E, l, b) = \frac{1}{4\pi} \int q_{br}(E, l, b, r) n_H(l, b, r) dr \tag{4}$$

where n_H is the total Hydrogen density ($n_H = n_{HI} + n_{H_2}$). To separate the contributions due to the matter distribution and that due to cosmic rays, we define a function $\overline{q}_{pp}(E, l, b)$:

$$\overline{q}_{pp}(E, l, b) = \frac{\int_0^\infty q_{pp}(E, l, b, r) n_H(l, b, r) dr}{\int_0^\infty n_H(l, b, r) dr} \tag{5}$$

which is the average value of q_{pp}, weighted on the matter distribution along the line of sight. $\overline{q}_{br}(E, l, b)$ can be obtained in an analogous way. In order to fit the observed spectrum we have built two "reference components" obtained by multiplying the local emissivity for the hydrogen column:

$$S_{pp}^0(E, l, b) = \frac{1}{4\pi} q_{pp}^{model}(E) \int n_H(l, b, r) dr \tag{6}$$

$$S_{br}^0(E, l, b) = \frac{1}{4\pi} q_{br}^{model}(E) \int n_H(l, b, r) dr \tag{7}$$

where q_{pp}^{model} and q_{br}^{model} are the local emissivities expected from the comic ray model we have assumed. This evaluation makes sense under the assumption that the spectra of q_{pp} and q_{br} are not very different along the plane of the Galaxy. This is a good approximation because the proton spectrum is not expected to vary in the Galaxy. The electrons distribution, instead, is probably inhomogeneous for electrons of energy larger than some GeV, but the gamma ray emission for bremsstrahlung around 100 MeV is mainly due to electrons of

Figure 2: Average value of gamma-ray emissivity due to pp scattering, weighted on the matter distribution, versus galactic longitude, derived from EGRET observations.

Figure 3: Average value of gamma-ray emissivity due to bremsstrahlung, weighted on the matter distribution, versus galactic longitude, derived from EGRET observations.

some hundreds of MeV. We have then fitted the EGRET observations of cycles from 1 to 9 for the galactic plane, in which the set of gamma-ray photons is binned in ten energy ranges. The fit consists in finding two set of coefficients k_{pp} and k_{br} such as

$$S(E, l, b) \sim k_{pp}(l, b)S_{pp}^0(E, l, b) + k_{br}(l, b)S_{br}^0(E, l, b) \tag{8}$$

The value of k_{pp} and k_{br} is, in general, different for every sky direction; these coefficients are hence functions of l and b. From equations 2 and 8 we can obtain:

$$S_{pp}(E, l, b) = k_{pp}(l, b)S_{pp}^0(E, l, b) \tag{9}$$

then:

$$k_{pp}(l, b) = \frac{S_{pp}(E, l, b)}{S_{pp}^0(E, l, b)} = \frac{\frac{1}{4\pi}\overline{q_{pp}}(E, l, b) \int n_H(l, b, r)dr}{\frac{1}{4\pi}q_{pp}^{model}(E) \int n_H(l, b, r)dr} = \frac{\overline{q_{pp}}(E, l, b)}{q_{pp}^{model}(E)} \tag{10}$$

hence k_{pp} represents the average value of q_{pp}, weighted on the matter distribution, and normalized to $q_{pp}^{model}(E)$. k_{br} can be obtained in an analogous way. k_{pp} and k_{br} are proportional to the gamma-ray emissivities q that are, in turn, proportional to the average value of proton and electron density respectively. In figures 2 and 3 the distributions of k_{pp} and k_{br}, respectively, are represented as a function of galactic longitude.

References

[1] X. Chi & A.W. Wolfendale, J.Phys.G 17, 987 (1991)

[2] T.M. Dame T.M. et al., ApJ 547, 792 (2001)

[3] D. Hartmann & Burton W.B., Atlas of Galactic Neutral Hydrogen, Cambridge Univ. Press. (1997)

[4] S.D. Hunter et al., ApJ, 481, 205 (1997)

[5] Kerr F.J. et al, AAS 66, 373 (1986)

[6] Strong A.W., Moskalenko I.V. , Reimer O., ApJ 537, 763 (2000)

PRELIMINARY STUDY FOR USING THE GLAST LAT CALORIMETER AS GRB DETECTOR

Francesco Longo [a], Monica Brigida [b], Giancarlo Ghirlanda[c]

[a] *Dipartimento di Fisica, Università di Trieste and INFN, Sezione di Trieste via Valerio 2, Trieste, Italy*

[b] *Dipartimento Interateneo di Fisica "M.Merlin", Università di Bari, and INFN, Sezione di Bari, via E. Orabona 4, Bari, Italy*

[c] *INAF, Osservatorio Astronomica di Brera, via Bianchi 46, Merate, Italy*

Abstract

The GLAST high energy gamma ray telescope is an international space mission designed to detect gamma-rays in the energy band 20 MeV - 300 GeV. It has two complementary instruments: the LAT telescope made of a silicon tungsten tracker and a CsI calorimeter; and the GBM a gamma-ray burst monitor for triggering and studying GRB in the energy range (5 keV - 30 MeV). In this study we present a possible use of the GLAST LAT CsI calorimeter as a separate GRB detector.

1   Introduction

The Gamma-ray Large Area Space Telescope (GLAST) is an international mission that will study the high-energy phenomena in gamma-ray universe[1]. GLAST is scheduled for launch in May 2007. GLAST is instrumented with a hodoscope of 18 Silicon planes with 12 slabs of 0.03 X_0 thick tungsten converter and 4 with a 0.21 X_0 thick tungsten layer, followed by a 8.5 X_0 thick calorimeter made of 4 pairs of orthogonal layers of 24 CsI bars; the hodoscope is surrounded by a segmented plastic anticoincidence shield. This instrument (see Figure 1), called the Large Area Telescope (LAT), is sensitive to gamma rays in the energy range between 30 MeV and 300 GeV. The energy range, the field of view and the angular resolution of the GLAST LAT are highly optimized so that the LAT is expected to have a factor $\sim$30 larger sensitivity than its predecessor EGRET (operated in the years 1991-2000). This improvement should enable the detection of several thousands of new high-energy sources, the study of gamma-ray bursts and other transients, the resolution of different contributions to the the gamma-ray diffuse emission, the search for evidence of dark matter and the detection of AGNs, pulsars and SNRs. A detailed description of the scientific goals of GLAST mission and an introduction to the experiment can be found elsewhere[2].

2   The GLAST Burst Monitor

Aside from the main instrument LAT, a secondary instrument, the GLAST burst monitor (GBM), is foreseen. With this monitor one of scientific objectives of the mission, the determination of the high-energy behaviour of gamma-ray bursts can be can be ensured. Its task is to increase the detection rate of gamma-ray bursts for the LAT and to extend energy coverage (from $\sim$ 10 keV to $\sim$ 30 MeV). It will provide real-time burst locations over a wide FoV to allow repointing the GLAST spacecraft. Time-resolved spectra of many bursts will allow the investigation of the relation between the keV and the emission from GRBs over unprecedented seven decades of energy. This is crucial for unveiling the emission mechanism of GRBs [3]. In fact, the simultaneous monitoring of the emission over a large energy range will help to investigate the nature of its possible different components, i.e. whether the GeV emission is produced by the same GRB event or its due to its interaction with the ambient medium.

The GLAST Burst Monitor (GBM) energy range extends down to 10 keV and is partially overlapped to the LAT band and for its capabilities is expected to augment the LAT capabilities in studying GRBs[3].

Figure 1: Picture of the GLAST LAT instrument structure.

3   GLAST LAT Simulation Software

GLAST LAT is a complex system, and detailed computer simulations are required to design the instrument, to construct the response functions and to estimate the residual background in orbit. To accomplish these tasks an object-oriented C++ application called *Gleam* (GLAST LAT Event Analysis Machine) was implemented by the GLAST LAT collaboration. The structure of the GLAST LAT off-line software is described in Figure 2. An important characteristic is the separation of the packages according to their responsibilities. Many packages have been developed explicitly by the GLAST LAT collaboration for the specific items required by the simulation of a high energy gamma-ray telescope.

Among them, the Source Generation is the first algorithm called within the particle loop. Its task is to generate particles according to physical characteristics. This algorithm must store the information on the temporal and spectral behaviour of the source, as well as on the orbital characteristics of GLAST. It provides the description of incoming particles and is responsible for setting the current time, the particle energy, direction, and type. The

Figure 2: General scheme for simulation and reconstruction within the GLAST LAT off-line software framework.

package takes into account also the satellite orbit. Within this package a series of default sources is implemented: they include sources for testing purposes as well as the description of astrophysical spectra and the expected particle and albedo gamma backgrounds. An extension of this algorithm has been implemented for simulating transient sources such as Gamma-Ray Bursts (GRB). It can be used for studying the capability of GLAST for the observation of rapid transient fluxes in general. The algorithm which is responsible for generating the interactions of particles with the detector is based on the Geant4 MonteCarlo toolkit[4], an Object Oriented (OO) simulator of the passage of particles through matter. Its application areas include high energy physics and nuclear experiments, medical science, accelerator and space physics. A series of classes have been implemented to retrieve the geometry hierarchy of the full GLAST LAT detector for different purposes as graphical outputs, the Montecarlo geometry construction and reconstruction-digitization tasks. Figure 3 shows the external appearance of the calorimeter of one of the GLAST LAT towers visualized with FRED, a new event display being adopted by the LAT collaboration[5].

Figure 3: Calorimeter module of one of the GLAST LAT towers visualized with FRED.

4   LAT Calorimeter as GRB detector

Using the GLAST LAT full simulation[6], in this study we present preliminary results on the possible use of the LAT CsI calorimeter as an independent GRB detector. Its main role might be to confirm the GBM primary triggers and to possibly detect independently particular classes of GRBs, similarly to the AGILE minicalorimeter operated as a GRB detector[7].

In this study we used a similar approach to that used by Ghirlanda et al. (2004) in deriving the AGILE sensibility to GRB. An important cautionary note is that the GLAST LAT data acquisition and electronics system as not been presently designed to allow GRBs detection. In this preliminary study we adopt a typical GRB detection logic as those already implemented for past GRB monitors, while using the real geometrical (e.g. FOV) and structural (e.g. energy range) parameters of the LAT calorimeter.

Following the recipe adopted by Ghirlanda et al. 2004 [7] we investigated how the LAT calorimeter might response to GRBs simulated with typical spectral and temporal characteristics as those observed in the present largest Batse population of bursts. To this aim we simulated the response of GLAST LAT calorimeter to monochromatic photons at different energies and different angles, simply counting the ACD vetoed rate of detected events in three different energy bands. We studied also the mean rate of events in the same bands (E< 1 MeV, 1 MeV< E < 10 MeV, E>10 MeV) due to the average background expecte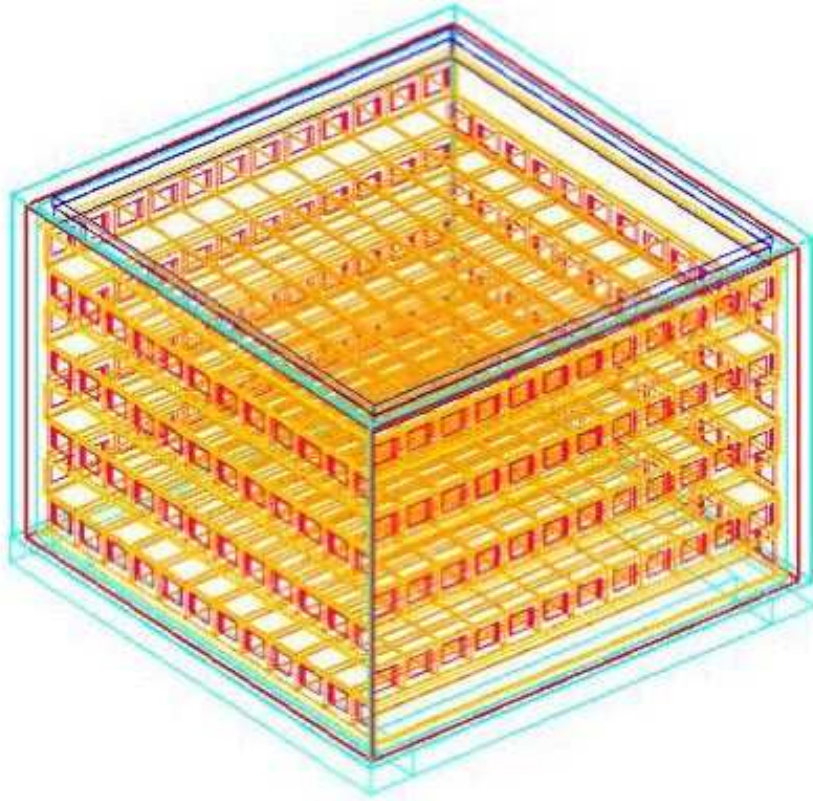d for the GLAST orbit. These events should mimic the on–flight typical background rate detected by the LAT calorimeter. This is a fundamental ingredient for GRB detection as these events characterize themselves as fast transient emission episodes at some significant (n*σ) level above the average instrumental background. For the GRB source emission we assumed the typical GRB spectrum[8] composed by a low and a high energy powerlaw (with photon spectral index -1.25 and -2.5, respectively) and allowed the peak spectral energy to vary within the energy band of the LAT calorimeter. The final output of this simulation is the minimum flux (integrated over the range 50-300 keV to be compared with typical bursts fluxes) necessary to trigger the LAT calorimeter. The dependence of the trigger sensitivity on the burst peak energy is reported in fig.4. In this figure we also show the sample of the brightest GRBs detected by Batse ([8], [9]). It is clear that with these simple assumptions we should expect that typical GRBs with a relatively large flux (i.e. above 50 phot/cm^2 sec) could be detected by the LAT calorimeter in almost the three bands. The energy dependence of the sensitivity shows anyway that particularly hard events (with peak energy above 1 MeV) might be detected down to somewhat lower fluxes. This represent an opportunity to study the possible sub-population of bursts with extremely high peak energies. The lower energy range (i.e. < 1 MeV) has a batter sensitivity compared to the other two channels and in this range in principle it might be possible to

Figure 4: Sensitivity of GLAST LAT calorimeter for GRB as function of GRB peak energy for the assumed spectral form (see text). The different lines correspond to three reference bands(dot-dashed E> 10 MeV, dotted 1 < E < 10 MeV, solid E< 1 MeV). Dotted line at the bottom is the Batse sensitivity, for comparison. The sensitivity is represented as the minimum flux (in the energy range 50 -300 keV) a burst should have to exceed of at least at 4σ the average background. Also reported are two samples of bright Batse bursts: open circles[8] and filled circles[9].

have $\sim 15\%$ of the Batse bright sample above threshold.

References

[1] http://glast.gsfc.nasa.gov/

[2] GLAST Science Brochure (March 2001),
    `http://glast.gsfc.nasa.gov/science/resources/`

[3] A. von Kienlin et al. (2004), `astro/ph 0407144`, to appear in SPIE
    conference proceedings vol 5488, "UV-Gamma Ray Space Telescope
    Systems," Glasgow UK, 21-24 June 2004.

[4] S. Agostinelli *et al.*, (2003), Nucl.Instrum.Methods A506, 250.

[5] M. Frailis and R. Giannitrapani, Talk given at 2003 Conference for
    Computing in High-Energy and Nuclear Physics (CHEP 03), Published
    in eConf C0303241:MOLT010,2003 e-Print Archive cs.gr/0306031.

[6] W. Atwood *et al.*, (2004) to appear in Calor2004 proceedings, Perugia
    Italy, March 29 - April 2, 2004.

[7] G. Ghirlanda *et al.*, (2004), to appear in GRB2003 proceedings, SantaFe
    New Mexico USA, September 8 - 12, 2003.

[8] D.L. Band et al., (1993), ApJ 413, 281

[9] R.D. Preece et al., (2000), ApJS 126, 19

WAVELET METHOD FOR SOURCE DETECTION IN GLAST PHOTON-COUNTING IMAGES

Francesca Marcucci [a], Claudia Cecchi [a], Gino Tosti [a]

[a] INFN and Dipartimento di Fisica, Università degli Studi di Perugia

Abstract

The wavelet technique applied to the EGRET data and to the simulated GLAST events has shown that this non-parametric method can be used, together with the maximum likelihood analysis for the identification of point sources in high energy photon counting images. We will present the study of an algorithm for source detection and its application to GLAST and EGRET data.

1 Introduction

Analysis of γ-ray data is carried out in the photon counting regime, where the information for most sources has to be extracted from a handful of photons. Classical analysis methods (i.e. Likelihood) need of intensive computing and *a priori* assumptions about the model underlying data. With the advent of the new generation of space-telescopes, in particular GLAST, a large amount of data will be available since the first days of operation, then fast as well as reliable analysis methods are needed. This is why non parametric algorithms

(i.e. Wavelet) have been already introduced as an alternative to the standard ones.

In this paper a new detection algorithm based on the wavelet transform will be described. Results from the application on 6-days all sky simulated GLAST data and EGRET data will be shown.

2   The Mexican Hat wavelet transform

Wavelets can be formally described as localized, oscillatory functions having zero average and values different from zero only within a limited region. Due to their properties, they can be used to characterize shape, location and strength of astronomical sources. Source detection algorithms based on wavelet transform involve the study of the correlation of scaled wavelet functions with 2-D images. Significantly non zero correlation coefficients will be observed only in presence of a source.

The wavelet transform of a two-dimensional image $f(x,y)$ is defined as:

$$w(x,y,a) = \int \int \psi(\frac{x-x'}{a}, \frac{y-y'}{a}) f(x',y') \; dx' \; dy' \tag{1}$$

where $\psi(\frac{x}{a}, \frac{y}{a})$ is the mother wavelet, x and y are the pixel coordinates, and a is the scale parameter. The most used mother wavelet in astrophysical image analysis is the *Mexican hat* (Figure 1). It is isotropically distributed and its 2-D expression is the following:

$$\psi(\frac{x}{a}, \frac{y}{a}) = \psi(\frac{r}{a}) = (2 - \frac{r^2}{a^2}) \; e^{-\frac{r^2}{2a^2}} \; , \quad (r^2 = x^2 + y^2) \tag{2}$$

It is appropriate when we deal with isotropic gaussian signals, because it is morphologically similar to a gaussian distribution, thus very efficient in detecting of point sources in optical, X-ray and γ-ray images, as the PSF of instruments are well described by gaussian functions.

3   Description of the algorithm

The algorithm we are going to describe has been designed to allow a fast and blind localization of the point sources, with only a small number of spurious detections, and their complete characterization (position, counts and spectral index).

The block diagram of the developed method is shown in Figure 2. It is an iterative procedure that produces as output a list of identified sources in input count maps, together with their position, counts, significance and relative errors.

Figure 1: 2-D mother wavelet *mexican Hat.*

Figure 2: A schematic picture of the algorithm steps

3.1 Estimation of the background

The main critical step is the construction of the background map, which is used to evaluate the detection threshold. It has to be evaluated *locally*, instead of *globally* because, as it has been evidenced from EGRET observation [1], the background emission shows several structures, whose size changes moving along the latitude axes in the sky map.

The background evaluation is carried out in 3 steps:
- smoothing of the input image by a gaussian filter, in order to reduce non uniformities;
- computation of an averaged background map (BG) through a median filter on large regions;
- *normalization* of the averaged map by the EGRET diffuse emission model in order to reproduce the typical background gradient and reduce spurious detections arising in correspondence of "structures" in the diffuse emission.

3.2 Computation of the threshold

The method used to calculate the threshold value in each pixel is derived from Damiani et al. [2]. They obtained a semi-analytical formula giving the relationship between the threshold value w_0 and the background photon density at a given scale and for a chosen threshold limit, expressed in term of σ of a gaussian distribution.

3.3   Sources detection and acceptance test

At the beginning, the wavelet transform map (WM) of the input images is computed at different scales a, where a ranges approximatively from the minimum value of the PSF to the maximum observed source size (a few of σ_{PSF}). All the pixels of the WM map whose value is over the threshold limit are flagged as belonging to source candidates. Then only "bright" candidates are accepted applying the following selection criterion: the signal and the background density are estimated in a cell of size equal to the selected scale, and their ratio (S/N) is computed. A minimum acceptance value for S/N is set: at first iteration the required ratio is the highest one and its value decreases at next stages, depending on the data set.

3.4   Fit and subtraction of detected sources

All sources detected at least at two consecutive scales are fitted by a single or a double gaussian, by a MINUIT routine and, if the fit converges, they are subtracted from the input images. The residual image is re-analyzed by the same algorithm; the iterative procedure ends when non more sources are detected. In this way faint or hidden sources can be enhanced after subtraction of bright candidates, since the background decreases (being less biased from "strong" signals).

3.5   Estimation of source parameters

The source parameters and relative errors (position and total number of counts) are derived from the fitting/subtraction procedure. The spectral index is obtained analyzing intensity maps of the source at different energy ranges and performing a linear regression of the flux (from the intensity maps fit) vs energy distribution (logarithmic values).

4   Results

The method has been applied to full sky 6-days simulated GLAST images, from the official GLAST-simulation by the Gleam framework [3]. In the simulation were included diffuse galactic and extragalactic emission, source from Third EGRET Catalog (3EG) and several faint blazars (as expected from Stecker and Salomon [4] predictions). In 6 day simulation mainly 3EG sources (263) are visible; our algorithm has produced 172 detections, of which only 12 spurious detection (no match with any simulated source). An example of detected sources along the galactic plane is given in Figure 3, while the spectral analysis for the Geminga pulsar is given in Figure 4.

A preliminary test has been made on EGRET combined data; only few pointed regions have been selected: the galactic center, Vela, 3c 279 and

Figure 3: Zoom on the galactic plane: blue boxes indicate a detected source while green boxes are the simulated sources.

Figure 4: Left: Spectral analysis of Geminga (6-day GLAST data) and comparison of the results with the simulated values (between brackets). Right: Spectral analysis of Crab pulsar (EGRET data) and comparison of the results with the Third EGRET Catalog values (between brackets).

Cygnus. An example of the identified sources in the Vela region is shown in Figure 5, while the spectral analysis for the Crab pulsar is given in Figure 4.

5   Conclusion

Our algorithm allows to obtain a preliminary list of candidate sources, quickly recognized, with an indicative estimation of their counts and position; all these information could provide the input for a more precise analysis. In this way the first step of a typical analysis algorithm (the detection) is performed through a fast, reliable and completely model-independent method, while the second part

Figure 5: Detected sources on EGRET data in Vela region. Detection from our algorithm are shown as white boxes centered at source position, while red and green circles indicate identified and unidentified 3EG sources respectively.

(the source characterization), even if already "tackled" in the proposed tool, could be refined by a classical method (i.e. Likelihood), more suitable for the scope.

The method has been applied for the detection of point sources, but it can be used for extended ones, searching for overthreshold contribution at large scales.

References

[1] S.D. Hunter et al., 1997, *ApJ*, **481**, 205

[2] F. Damiani, A. Maggio, G. Micela and S. Sciortino, 1997, *ApJ*, **483**, 350-369.

[3] P. Boinee et al., 2003, *Proc. of Science with the New Generation of High Energy Gamma-ray Experiments. Between Astrophysics and Astroparticle Physics*, Forum Editrice Universitaria, Udine

[4] M.H. Salamon, & F.W. Stecker, 1996, *ApJ*, **464**,600

GAMMA RAY BURSTS AND DATA CHALLENGE ONE: SEARCHING GRB IN ONE DAY OF SIMULATED GLAST DATA

NICOLA OMODEI [a],
ON BEHALF OF THE GLAST GRB AND SOLAR FLARE SCIENCE TEAM

[a] *INFN Sezione di Pisa,via F. Buonarroti 2, Pisa, Italy*

Abstract

GLAST (Gamma-ray Large Area Space Telescope) is a gamma-ray astronomy mission that will be launched in early 2007. The main instrument is the LAT (Large Area Telescope), a pair conversion telescope with sensitivity in the range 20 MeV-500 GeV. Data Challenge One (DC1) is the simulation of one day of observation of the entire gamma-ray sky by the LAT detector. The simulated data is similar to the real data, which allows for the development of scientific software. In this paper we present the GRB simulations and the detection algorithms developed by part of the GLAST GRB and Solar Flare Science Team[1]

---

[1]David Band, Jerry Bonnell, Monica Brigida, Johann Cohen-Tanugi, Riccardo Giannitrapani, Tune Kamae, Francesco Longo, Jay Norris, Nicola Omodei and Mikel Winai.

291

1   The Data Challenge One

The Large Area Telescope (LAT), the main detector onboard the GLAST satellite, will observe the sky between 20 MeV and 500 GeV. It is composed of a modular structure made by 16 identical towers. Each tower is composed of an hodoscopic calorimeter of 8.4 radiation length and of a silicon tracker module made of 19 stacked trays which provides 18 X-Y planes for the tracking of the electron-positron pair. The array of 4×4 towers is shielded by segmented scintillator tiles which provide the anti coincidence for rejection of charged particles. The LAT team has developed a full simulation environment[2], which allows the detailed study of the instrument performances and the development of scientific analysis software. The simulation starts from a detailed description of the sky. It takes into account the orbital motion of the satellite and computes the correct illumination of the detector. The incoming particles are then propagated into the detector using a montecarlo based on Geant4 tool. The digitized events are processed with the reconstruction tools. Time, direction and energy of each incoming gamma ray are computed and stored. The Data Challenge One (DC1) represented the first opportunity to test the complete simulation chain, and the first attempt to perform scientific analyses on simulated data.

1.1   The description of the sky and the Gamma-Ray Burst model

For DC1, only the gamma-ray sky has been simulated, while the cosmic-ray flux (about 10^4 times greater) was modeled separately for development of the background rejection algorithms, and that these algorithms were applied to the simulated gamma-ray data. The gamma-ray sky is made by a variety of sources: the software takes into account the relative fluxes and computes from which source arrives the next photon. The diffuse extragalactic source is an isotropic component while the galactic diffuse radiation has been obtained extrapolating the galactic map observed by EGRET at LAT energies. Furthermore, the third EGRET catalogue has been used to determine the contribution of all the point sources observed by EGRET. Similar simulated point sources fainter than could be detected by EGRET were also included. One of the most exciting target opportunities for the GLAST mission is the observation of GRBs, transient sources whose durations range between milliseconds and some hundreds of seconds. GRBs have typically a very complex temporal structure made of several spikes of the time scale of the order of milliseconds. Two different simulators for GRB have been developed for Data Challenge purposes. One is based on the physical fireball model[3] and has been used for simulating the first day of the DC1, the other is based on the phenomenological model and is also available in the GLAST software[5]. In the first day 21 bursts have been generated, one every $\sim$ 4000 seconds starting at $\sim 3000s$. The

Figure 1: Simulated light curve and spectrum from the GRB physical model. Left: LAT expected light curve. The histogram represents the arrival times of the extracted photons. Right: Filled line, from top to bottom: νF_ν, F_ν, N_ν. The dashed line is a fit with the Band function, with parameters:$\{\alpha = -0.86, \beta = -2.5, E_0 = 446.684 eV\}$. Crosses are the extracted photons.

bursts are isotropically distributed in the sky, thus some of those are outside the f.o.v. of the instrument and cannot be detected. The physical model[4] starts from the ejection of shells with different velocities. Their Lorentz factors are randomly generated allowing the possibility of internal inelastic shocks. Particles (electrons and positrons) are accelerated, and a randomly oriented magnetic field is built up in the shocked region due to repartitioning of the energy. Synchrotron emission is the main spectral component and the most efficient cooling mechanism. Inverse Compton scattering (SSC) is its natural extension at higher energies. The instantaneous spectrum is computed and the characteristic spiky temporal structure is reproduced. The GRB fluence is normalized at BATSE energy: all the simulated bursts have fluences between 10^{-7} and $10^{-5} erg/cm^2$ between 25 keV and 1 MeV. In a further step the software samples photon energies above a fixed threshold (typically 20 MeV) from the instantaneous spectrum. These photons are then processed by the Montecarlo. Figure 1 represents the light curve (left) and the integrated spectrum (right) for a typical GRB simulated by the GLAST GRB physical model.

2   Trigger and Alert algorithms

Several groups within the LAT collaboration are prototyping trigger and alert algorithms for detecting transient signals in DC1 data, and different algorithms have been studied. The idea of the **rate trigger** is simple: GRB are short

phenomena in time and their flux is higher than the flux coming from the gamma background. The rate trigger detects a transient if the differential flux exceeds a fixed threshold. We compute the count rate by fixing a window of M events:

$$R_j = \frac{M}{t_{M(j+1)} - t_{Mj}}, \tag{1}$$

where $t_{i \in [0,N]}$ is the temporal series of N events ($j \in [0, N/M]$). The first panel of Figure 2 shows the count rate for the simulated day for the entire field of view. The periodic oscillations are due to the scanning motion of the satellite across the galactic plane. The most intense GRBs (*time* $\sim$ 3000, 43000, 71000, 75000, 83000) are visible in the time history. The differential count rate is the quantity $R_{j+1} - R_j$ and it is shown in the second panel of Figure 2 with $M = 200$. The long period oscillations are not yet visible while short transient phenomena are enhanced by the differential operator. The third panel of Figure 2 represents the histogram of the differential count rate. The gamma background photons make up the exponential distribution, while Gamma Ray Bursts, for which the differential count rate is high, are the "outliers" of this distribution. This method is efficient for bright GRBs, for which the flux exceeds the background flux, while faint bursts, for which the flux is comparable to the gamma background, may not be triggered. An efficient improvement of the rate trigger is the **segmentation of the sky** in different regions where the rate trigger is successively applied. There are two ways for dividing the sky, depending on which coordinate system one chooses, the galactic coordinate system or the instrument system. The main difference between the two is that, the non stationarity of the background due to the orbital motion can be reflected as false trigger if the instrument coordinate system is chosen. A more interesting and complete scheme will be studied when background charged particles also will be introduced as Data Challenge source. Another algorithm has been developed by the GRB science team. The **Strawman GRB tracker trigger algorithm** makes maximal use of the unbinned photon data coming into the GRB buffer to form probabilities from the temporal and spatial information. A sliding window approach is used: a window of N_{range} photons is moved by N_{move}. The $N \times (N-1)$ distances on the sphere between the N_{range} photons are computed. Each of the N_{range} photons is considered the potential nucleus of a spatial cluster and the cluster with the smallest average distance for the retained photons is selected. For this cluster the chance spatial and temporal probabilities are computed. In particular, if R is the count rate, the joint log probability (JLP) is:

$$JLP = \sum \log_{10}[(1 - \cos(d_i))/2] + \sum \log_{10}[1 - (1 + R\Delta t_j) \exp(-R\Delta t_j)] \tag{2}$$

Figure 3 shows the evolution of the Joint Log Probability with time.

Figure 2: Top: count rate for the simulated day of the DC1 for the entire f.o.v. Middle: differential count rate. Bottom: histogram of the differential count rate. GRB are the outliers of the distribution.

Figure 3: Temporal evolution of the joint log probability. Triangles are triggered bursts.

Algorithm	Trigger/Generated
Rate Trigger	7/21
Rate Trigger in Inst. coord.	10/21
Rate Trigger in Gal. coord.	10/21
Strawman trigger Alg.	11/21

Table 1: Ratio between the triggered and the generated GRBs.

3   Results and conclusions

Different algorithms have been successfully applied for searching for transient signals in DC1 data. The general results are summarized in Tab.1. Bright bursts (with fluence greater than $10^{-5} erg/cm^2$ between 20 kev and 1 MeV) can be detected with simple and trivial algorithms. More sophisticated algorithms have to be developed for detecting faint GRBs. The segmentation of the sky into sub-regions gave good results, maintaining the algorithm easy and the execution fast. The best results in terms of triggered GRBs were obtained using the Strawman GRB tracker trigger algorithm, based on the joint log probability. Further studies will include the particle background, and the possibility to implement an on-board LAT alert algorithm. All of these items will be addressed for the next Data Challenge (DC2), in which one month of simulated data will be produced.

References

[1] R. Bellazzini et al., Nucl. Phys. B (Proc. Suppl.) 113 (2002) 303, 309

[2] P. Boinee et al., (2003), (astro-ph/0308120)

[3] T. Piran, Physics Reports 314 (1999) 575, 667 (astro-ph/9810256)

[4] http://www.pi.infn.it/∼omodei/GRBSimulator/GRBSimulation.html

[5] http://glast.stanford.edu/cgi-bin/cvsweb/SLAC/GRB/

THE SILICON TRACKER FOR THE GLAST MINI-TOWER

L. Baldini [a], R. Bagagli [a], R. Bellazzini [a], A. Brez [a], M. Kuss [a],
L. Latronico [a], M. Minuti [a], N. Omodei [a], M. Razzano [a], C. Sgro [a],
G. Spandre [a]

[a] INFN - Sezione di Pisa, via F. Buonarroti 2, Pisa, Italy

Abstract

The Gamma-ray Large Area Space Telescope (GLAST) is an international space mission that will study the high energy spectrum of the gamma-ray sky. The GLAST Mini-Tower is the first prototype, though on a reduced scale, of a flight tower module (including a silicon tracker, a CsI calorimeter and the corresponding data acquisition system) with full functionalities. In this paper we present the results of the tests performed on the Mini-Tracker before the integration with the calorimeter module.

1 Introduction

The Large Area Telescope (LAT), the main instrument onboard GLAST, is a gamma ray telescope based on the pair production effect. The LAT has a fully modular architecture: it consists of a 4×4 array of identical towers , each one including a high resolution silicon strip tracker [1], a CsI imaging calorimeter and a data acquisition module; the 16 towers are surrounded by an outer segmented Anti Coincidence Detector (ACD) ensuring the rejection of background due to charged particles.

The Mini-tower is the first prototype of a fully instrumented tower equipped with flight-like hardware, constituting a crucial step in the verification process of the overall design quality and effectiveness of the assembly procedures. The Mini-Tracker (figure 1) is made of 5 tray structures (19 in a full tower), which are the basic mechanical framework for 6 active planes (37 cm × 37 cm, including 16 flight silicon strip detectors each). The 6 detection planes (read

Figure 1: The GLAST Mini-Tracker, just before the assembly of the last sidewall. The front-end electronics boards (two are visible in the picture) are mounted on the sides of the trays - to minimize the gaps between adjacent towers - and connected to the silicon detectors by means of 90° pitch adapters. The power, control, trigger and data pass through 8 flex cables (two per side), providing full redundancy against single point failures to the electronics system [2].

by flight-like front end electronics) are arranged in 3 x-y pairs (with less than 2 mm spacing between each x plane and the following y plane), allowing the *three in a row* self triggering capability, which will be the main LAT Level 1 trigger primitive.

2   Test results

The GLAST Mini-Tracker has undergone extensive tests to verify the basic functionalities of the electronics system and the tracking performance of the entire instrument.

Basic system verification

The left panel of figure 2 shows the noise occupancy as a function of the threshold on the discriminators. The plot refers to the logical OR of the 1536 electronics channels which constitute one detection layer. We note that the occupancy value corresponding to the plateau at high threshold matches fairly well with the expected rate of accidental coincidences with cosmic rays.

Figure 2: Measured noise occupancy (left) and detection efficiency (right) for one of the silicon layers of the Mini-Tracker; note that the left panel refers to the logical OR of an entire detection plane. The average gain of the front-end electronics, allowing to convert the threshold level into the amount of released charge, is 100 mV/fC.

Figure 2 (right panel) also shows the detection efficiency for the same layer, measured with cosmic rays; the layer itself is excluded from the trigger and the events are analyzed under a full track reconstruction.

Together the two plots confirm that the system meets the design specifications with large working margins; in fact, at the nominal threshold setting (0.25 MIPs), the detection efficiency exceeds the 99% design level while the average single strip noise occupancy, extrapolated from the low threshold region, is as low as $\simeq 10^{-8}$.

Tracking performance

The tracking capabilities of the instrument have been verified by collecting data from cosmic rays. The full off-line analysis chain has been exercised using real data and the results have been compared to the full Monte Carlo simulation of the detector, showing a fairly good agreement with respect to all the relevant distributions (figure 3)

Figure 3: Hits distribution for one of the layers (left) and measured angular distribution (right) for cosmic rays. In both cases the black line represents the actual data, the blue crosses are the results of the full Monte Carlo simulation, and the red line the prediction of a simple analytical model.

3   Conclusions

A reduced scale, fully functional model of the silicon tracker for a GLAST flight tower has been constructed and intensively tested. The model has met all the specification with comfortable margins, demonstrating the effectiveness of the overall design. The assembly of the flight modules is ready to begin.

References

[1] R. Bellazzini et al., *The silicon-strip tracker of the Gamma ray Large Area Space Telescope*, Nuclear Instruments and Methods A523, Issues 1-1 (2003) 136

[2] D. Nelson, R. Johnson, *Conceptual design of the Tracker Electronics System*, LAT-SS-00168

THE GLAST TRACKER TEST AND DEVELOPMENT

F. Belli [a,b], M. Marchetti [a,b], A. Morselli [a,b], S. Russo [a,b]

[a] *Dipartimento di Fisica, Università di Roma "Tor Vergata",*
via della Ricerca Scientifica, Roma, Italy

[b] *INFN, Sezione di Roma II, via della Ricerca Scientifica, Roma, Italy*

Abstract

The GLAST (Gamma-ray Large Area Space Telescope) observatory is an astroparticle mission that will study gamma-rays emissions from a wide range of cosmological sources in the energy band extending from 20 MeV to more than 300 GeV. The silicon tracker is the heart of the photon detection system: we show here the assembly steps and performance test of its components.

1   The Gamma-ray Large Area Space Telescope (GLAST)

GLAST (Gamma-ray Large Area Telescope) [1] is a next generation high energy gamma ray observatory designed for making observations of celestial gamma ray sources in the energy band extending from 20 MeV to more than 300 GeV. In figure 1 is reported the energy range-timeline placement of the experiment. It follows in the footsteps of the CGRO-EGRET experiment, which was operational between 1991 and 1999.

The scientific goals of the experiment are:

Figure 1: Timeline schedule versus the energy range covered by present and future detectors in X and gamma-ray astrophysics

1. To understand the mechanisms of particle acceleration in AGNs, pulsars, and SNRs.

2. Resolve the gamma-ray sky: unidentified sources and diffuse emission.

3. Determine the high-energy behavior of gamma-ray bursts and transients.

4. Probe dark matter and early Universe.

5. Probe quantum gravity effects.

2   The Large Area Telescope (LAT) structure

The Large Area Telescope (LAT), the main instrument onboard GLAST, is a pair-conversion telescope that will measure direction and energy of photons over a broad energy range. It is structured as an array of 4x4 identical towers each equipped with: Si-strip Tracker Detectors and converters arranged in 18 XY tracking planes for the measurement of the photon direction; a segmented array

Some Dimensions are Distorted
for Clarity of Presentation

Complete GLAST
4 x 4 Array of Towers

1.73 m

Anticoincidence
Detector

Gamma
Ray

Tray Backbone

Tungsten (W)

Silicon

One Tower Module of GLAST

87.5 cm

12 Trays with 0.03
Radiation Length W Converters

4 Trays with 0.18
Radiation Length W Converters

2 Trays without
Converters

8.95 cm

Si Strip Detector

228 μm
Pitch

Preamps Mounted
on Vertical
Edge of Tray

Grid

Imaging Calorimeter
(8.5 rl)

6-2001

Figure 2: The LAT structure

Figure 3: Thermo-Vacuum test: the LAT ladders are mounted on the heating rack inside the vacuum chamber

of CsI(TI) crystals for the measurement of the photon energy (Calorimeter); a segmented Anticoincidence Detector (ACD) (figure 2).

The main characteristic are an energy range between 20 MeV and 300 GeV, a field of view of 3 sr, an energy resolution of 5% at 1 GeV, a point source sensitivity of $2x10^{-9}(phcm^{-2}s^{-1})$ at 0.1 GeV, an event dead-time of $20\mu s$ and a peak effective area of 10000 cm^2, for a required power of 600W and a payload weight of 3000 Kg.

3   Trays Thermo-Vacuum Test

The LAT trays are the panels that will support detectors, converters and electronics, composed of a carbon fiber structure surrounding an aluminium honeycomb core, with kapton bias circuits glued on their top and bottom faces. The main scope of the thermo-vacuum procedure is to check, on the LAT trays, the bias circuit adhesion to individuate eventual delamination under vacuum, due to air trapping, before electronics and detectors are mounted on them,

Figure 4: History of the expected and measured leakage currents of LAT Ladders. The values above 1000nA indicates a bad connection of the wafers within the ladder

with a cycle at $65(\pm 5)^\circ$C for 24 hours and at pressure < 0.01 bar for at least 1 hour. This will also permit removal of any surface impurities, if any, on the kapton bias circuits. To heat the trays, they are mounted in a metallic grid warmed by twelve 220 Ω resistors in which flows a 0.5 A current (see figure 3). The temperature is monitored in real time with eight sensors on the grid and ten or more floating on the trays. An automatic system for recording and control switches on or off the heating resistors depending on the grid detected temperature.

4   Silicon Ladders assembly and test

The silicon strip detectors on the LAT trays surfaces are composed by four parallel ladders: each one is the result of four consecutive six inches wafers, whose 380 microstrips are serially connected, with a delicate procedure of gluing, bonding and protective encapsulation ("Dam and Fill"). The connections and the characteristic of the device are then checked. A Karl Suss Probe Station PA 200 is used to perform measurements of:

1. The C-V characteristic for each microstrip and each ladder.

2. The I-V characteristic for each ladder.

4.1 Efficiency test with cosmic Rays

The trays are assembled in triple coincidence blocks and then they are mounted in one rack between three planes of two plastic scintillator detectors. Using cosmic rays as sources of particles it is possible to determine the efficiency of the Silicon Strip Detectors

4.2 Global results

Al the tests on the Silicon Strip Detectors showed a good agreement with the required parameters. The small differences between the expected values and measured ones indicates the good quality of the assembly procedure. We found:

1. An average depletion voltage of 63.553 V;

2. An average bulk capacitance at 150 V of 7505.5 pf;

3. An average leakage current at 150 V of 584.33 nA (see fig. 4);

4. a 10^{-5} bad strips fraction of the whole tested ones.

References

[1] Proposal for the Gamma-ray Large Area Space Telescope, SLAC-R-522 (1998).

A. Morselli, Very High Energy Phenomena in the Universe, Ed. Frontiers, 123, (1994).

P. Michelson, this conference

see also http://www-glast.stanford.edu/

γ-RAYS FROM NEUTRALINO ANNIHILATION

Lidia Pieri [a1], Nicolao Fornengo [a,b], Stefano Scopel [a2]

[a] *Dip. di Fisica Teorica, Università di Torino, via Pietro Giuria 1, Turin, Italy*

[b] *INFN, Sezione di Torino via Pietro Giuria 1, Turin, Italy*

Abstract

We predict γ-ray flux expected from neutralino annihilation in the Milky Way, in the Large Magellanic Cloud and in the Andromeda Galaxy in the frame of an effective minimal supersymmetric model and for different dark matter density profiles.

1 Introduction

The nature and the distribution of the dark matter in the universe are problems facing both particle physics and cosmology today.

Under the hypothesis of a dark matter composed by the lightest supersymmetric particle, which is the neutralino in most cases, many authors have considered their annihilation in our galaxy, as well as in the halos of

---

nearby galaxies (see [1] for a complete list of references). In this work we will implement the prediction of γ-ray flux in the frame of an effective minimal supersymmetric model.

2 γ-ray fluxes from neutralino annihilation

Following [1], we write the diffuse photon flux from neutralino annihilation in the galactic halo as:

$$\frac{d\Phi_\gamma}{dE_\gamma}(E_\gamma, \psi, \theta) = \frac{d\Phi^{\text{SUSY}}}{dE_\gamma}(E_\gamma) \times \Phi^{\text{cosmo}}(\psi, \theta) \tag{1}$$

The particle physics is embedded in the first term, which we will call "supersymmetric factor":

$$\frac{d\Phi^{\text{SUSY}}}{dE_\gamma}(E_\gamma) = \frac{1}{4\pi}\frac{\langle\sigma_{\text{ann}}v\rangle}{2m_\chi^2} \cdot \sum_f \frac{dN_\gamma^f}{dE_\gamma}B_f \tag{2}$$

where $\langle\sigma_{\text{ann}}v\rangle$ is the thermally-averaged neutralino self–annihilation cross–section times the relative velocity of the two annihilating particles, dN_γ^f/dE_γ is the differential photon spectrum for a given f-labeled annihilation final state with branching ratio B_f and m_χ is the neutralino mass.

Astrophysics and cosmology are considered in the "cosmological factor" given by the line–of–sight integral, defined as:

$$\Phi^{\text{cosmo}}(\psi, \theta) = \int_{\Delta\Omega(\psi,\theta)} d\Omega' \int_{\text{l.o.s}} \rho_\chi^2(r(\lambda, \psi'))d\lambda(r, \psi') \tag{3}$$

for the diffuse emission of our Galaxy, and

$$\Phi^{\text{cosmo}}(\psi, \theta) = \frac{1}{d^2} \int_0^{\min[R_G, r_{\max}(\Delta\Omega)]} 4\pi r^2 \rho_\chi^2(r)dr \tag{4}$$

for the emission from an extragalactic objects in the direction of ψ. $\rho_\chi(r)$ is the dark matter density profile, r is the galactocentric distance, related to the distance λ from the observer by $r = \sqrt{\lambda^2 + R_\odot^2 - 2\lambda R_\odot \cos\psi}$ ($R_\odot$ is the distance of the Sun from the galactic center) and $\Delta\Omega(\psi,\theta)$ is the solid angle of observation pointing in the direction of observation ψ and for an angular resolution of the detector θ. d is the distance of the external object from the observer, R_G is the radius of the extragalactic object and $r_{\max}(\Delta\Omega)$ is the maximal distance from the center of the external galaxy which is seen within the solid angle $\Delta\Omega(\psi,\theta)$.

As far as $\rho_\chi(r) \sim r^{-\alpha}$ is concerned, neither numerical simulations nor experimental data on galaxy rotation curves (see References in [1] were able

to constrain the inner slope α of the profile. Among the cited papers, cuspy profiles are bracketed between 1 (NFW97 profile) and 1.5 (M99 profile). An inner density core of radius 10^{-8} kpc has been taken into account in order to avoid divergences. Changing the inner core radius, or adding substructures can change considerably the result [1].

The upper left panel of Figure 1 shows the supersymmetric factor computed in the frame of an effective minimal supersymmetric model. The upper right panel shows the cosmological factor for the Milky Way, the Large Magellanic Cloud and the Andromeda galaxy. [1] The two factors have just to be multiplied in order to obtain physical γ-ray fluxes. It is done in the lower panels of Figure 1, where the predicted integrated γ-ray flux above 100 GeV is shown for the MW with a NFW97 profile (left) and for M31 with a M99 profile (right)

3 Conclusion

In this work we have given a recipe to predict γ-ray flux from neutralino annihilation in the Milky Way and in the brightest nearby galaxies. Such fluxes could be compared with recent and forthcoming data from the Galactic Center.

References

[1] N. Fornengo, L. Pieri and S. Scopel, hep-ph/0407342; L. Pieri and E. Branchini, Phys. Rev. D **69**, 043512 (2004).
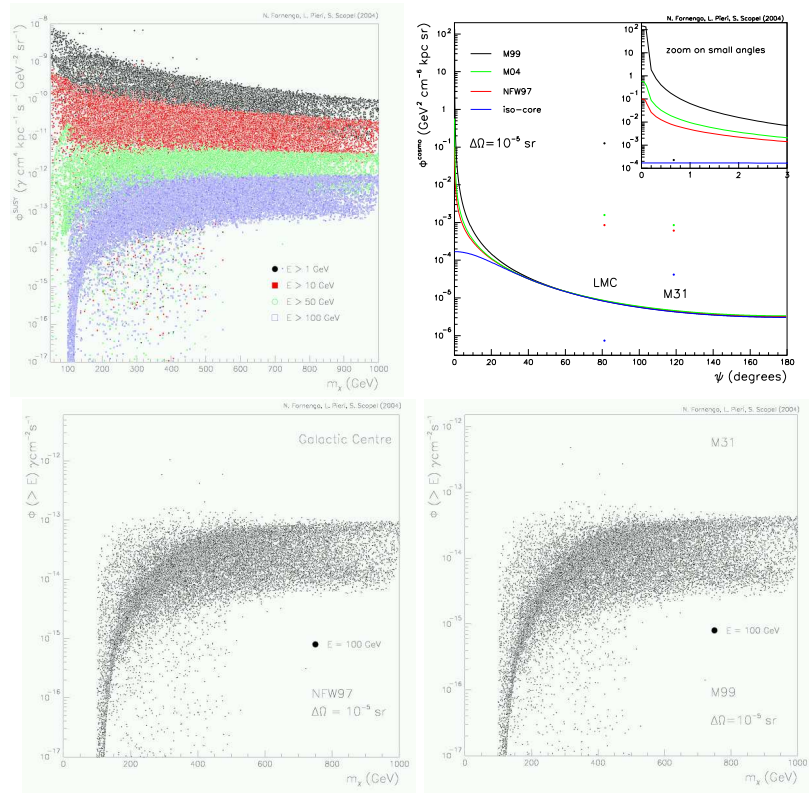
Figure 1: Upper left: Φ^{SUSY} calculated in the frame of an effective minimal supersymmetric model. Upper right: Φ^{cosmo} calculated for the Milky Way and two external galaxies (LMC and M31), for different dark matter profiles, for a solid angle $\Delta\Omega = 10^{-5}$ sr. The small boxes show a zoom at small angles toward the galactic center. A constant–density central region of radius $r_{\mathrm{cut}} = 10^{-8}$ kpc. Lower left: integrated γ-ray flux above 100 GeV predicted for the Galactic Center with a NFW97 profile. Lower right: integrated γ-ray flux above 100 GeV for M31 with a M99 profile. Figures are taken from [1]

Part VI

GAMMA RAYS AT GROUND

GALACTIC SOURCES OF VHE GAMMA RAYS

Werner Hofmann [a]

[a] *Max-Planck Institut für Kernphysik, Heidelberg, Germany*

Abstract

Recent developments in experimental TeV gamma ray astronomy of Galactic sources are summarized, covering the Crab nebula as a standard candle, pulsars and pulsar nebulae, gamma ray emission by supernova remnants, and the newly discovered gamma-ray source at the Galactic centre. For an earlier review, see e.g. [1]. A puzzle remains that some of the established southern TeV sources could not be confirmed in recent observations by the new H.E.S.S. instrument.

1 The northern sky: in good shape

I will cover only two Galactic northern sky sources, where new results have been presented: the Crab Nebula and the unidentified Cygnus TeV source.

1.1 The Crab nebula

The Crab Nebula is one of the best studied objects and continues to serve as standard candle to test the calibration of new gamma-ray instruments. New results have been released by the HEGRA collaboration, based on 400 h of data

collected between 1997 and 2002 [2]. The large statistics allow the extraction of an energy spectrum which covers two decades in energy – sub-TeV up to 100 TeV – and about 6 decades in flux (Fig. 1). The spectrum is quite well described by a power law with index $\Gamma = 2.62 \pm 0.02 \pm 0.05$ over the entire range. The measured spectrum can be reproduced in an Inverse Compton (IC) model if a new population of radio target photons is included [2]. Interestingly, the model predicts a spectral break just below the HEGRA energy range and preliminary CELESTE data covering the 50 to 400 GeV range indeed exhibit a flatter spectrum with $\Gamma = 1.64 \pm 0.26$ [3]. Among the new instruments, the MAGIC group has reported the detection of the Crab Nebula and the H.E.S.S. collaboration have, based on observations at large zenith angles, given a spectrum in the 500 GeV to 10 TeV range which is consistent with previous data.

1.2 The unidentified Cygnus TeV source

In 2002 the HEGRA collaboration published the discovery of the first unidentified TeV source [4] located in the Cygnus region, near the Cygnus OB2 association. Given the failure to clearly pinpoint supernova remnants as the source of cosmic rays, this discovery raised the possibility of a new class of cosmic accelerators, perhaps driven by shocks in the winds of the massive stars of Cygnus OB2, which release energy at a rate comparable to supernova explosions ($\approx 10^{51}$ ergs in 10^4 years [5]), but which have a much longer lifetime. Radio data and Chandra X-ray data do not show counterparts for the TeV source, with flux limits at the edge were an electronic origin could be ruled out [6, 7]. A final analysis of the HEGRA data [7] confirms the hard spectrum (photon index $\Gamma = 1.9 \pm 0.1 \pm 0.3$) and a source extension of $6.2' \pm 1.2' \pm 0.9'$. Compared to earlier results, where the source was treated as a point source, properly accounting for the size raises the flux above 1 TeV from 3% of the Crab flux to 5%. This source has now been confirmed by an analysis of Whipple archival data, resulting in a 3.3σ signal from the same location, albeit with a slightly larger flux (12% of the Crab flux) [8].

2 The southern sky: puzzles and discoveries

H.E.S.S. was the first of the next-generation Cherenkov instruments to report new results. While H.E.S.S. results concerning northern sources are in good agreement with previous data – the flux and spectrum of the Crab Nebula is reproduced, the AGN Mkn 421 was detected – H.E.S.S. results on the southern sky are at variance in particular with some of the earlier CANGAROO observations.
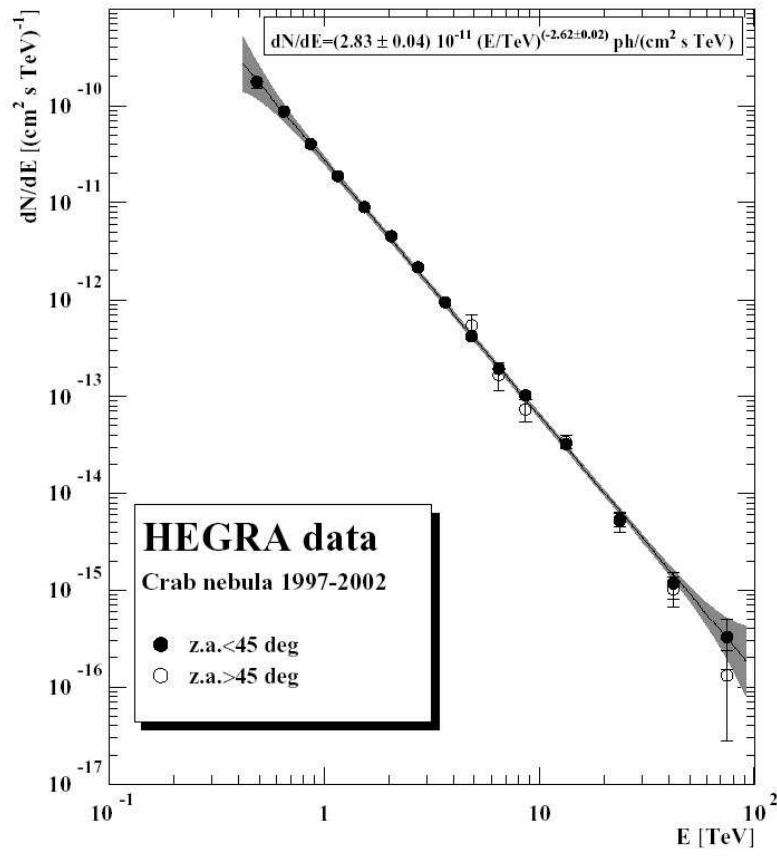
Figure 1: Gamma rays spectrum of the Crab Nebula, as measured by HEGRA, combining data at small and large zenith angles. Bands indicate systematic errors.
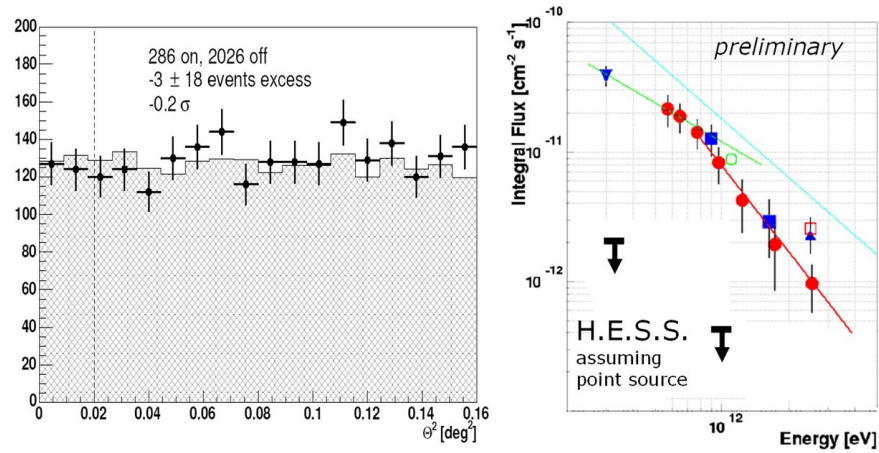
Figure 2: Left: distribution of gamma-ray candidates in the H.E.S.S. data relative to the direction to PSR 1706-44; shaded area shows background estimate. Right: Durham (triangle) and CANGAROO (circles, squares) measurements of the integral flux as a function of threshold energy, and new H.E.S.S. flux limits (preliminary).

2.1 Pulsars and pulsar wind nebulae

The pulsar PSR 1706-44 was detected with high significance by the CANGAROO I [9] and II telescopes [10], and was also seen by the Durham group [11]. At a flux of roughly 1/2 of the Crab flux, it was long considered as the southern equivalent of the Crab nebula. As noted by several authors, the high TeV flux is surprising [12, 13], given that the pulsar has a spindown luminosity of about 1% of the Crab pulsar, and the X-ray luminosity of the pulsar wind nebula is only 0.01% of the Crab. Unless one assumes that TeV gamma rays are emitted from a much larger volume than X-rays, the TeV flux cannot be explained in the framework of Inverse Compton scattering models, which predict an emission at a level of 10^{-2} to 10^{-3} of the Crab TeV flux [14].

H.E.S.S. data resulting from 14 h of observations with two telescopes during the commissioning phase show no indication of a signal from the direction of PSR 1706-44 (Fig. 2, left). Upper flux limits (Fig. 2, right) are about one order of magnitude below the fluxes reported earlier.

A possible explanation for the discrepancy is a time dependence; while not really expected for emission from a pulsar nebula, it cannot be excluded from first principles, given the compact size of the PSR 1706-44 nebula. Finally, one could argue that the object may not be a point source; since the H.E.S.S. instrument has a smaller point spread function and integrates over a smaller
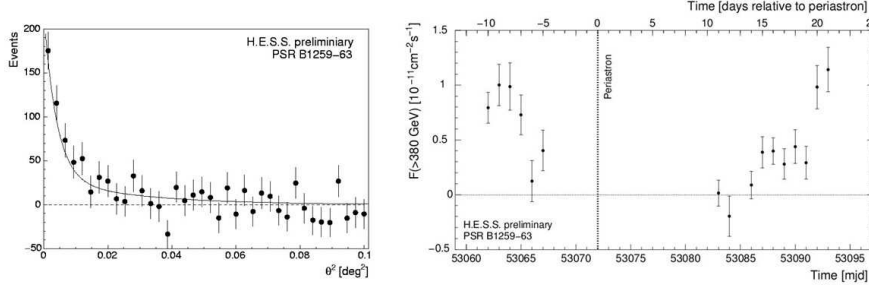
Figure 3: Left: excess of gamma-ray candidates in the H.E.S.S. data relative to the direction to PSR 1259-63. Right: Light curve (preliminary).

solid angle, this would reduce the detected flux. Use of a wider source region to match the CANGAROO psf, however, still results in upper limits which are well below the old flux.

The H.E.S.S. collaboration have recently reported the detection of the pulsar PSR B1259-63, a very interesting object.

PSR B1259-63 is a 48 ms pulsar in a highly eccentric orbit around a massive Be star with a disk-like outflow. Every 3.4 years, near periastron, the pulsar crosses the disk and is exposed to strong radiation fields and increased ambient density. Electrons or protons accelerated by the pulsar or by shocks in the wind or stellar outflow will, near periastron, find enhanced targets for the production of TeV gamma rays by the IC mechanism or by hadronic interactions, resulting in a modulation of the TeV gamma-ray flux with the orbital period of the pulsar [15, 16]. CANGAROO has reported upper limits for a section of the orbit far from periastron [16]. In the H.E.S.S data (Fig. 3) the pulsar is detected both before and after periastron, with 9σ and 7σ, respectively. Due to full moon, no data could be taken around periastron, but both the pre- and post-periastron data show a decrease in flux towards periastron, suggesting a flux minimum rather than a maximum. The average flux of PSR B1259-63 is about 7% of the Crab flux (above the 380 GeV threshold), the spectral index is 2.7 ± 0.3(stat). We note that PSR B1259-63 is the first variable galactic TeV source. Details are given in the contribution by M. Beilicke.

2.2   Gamma emission by supernova remnants

Supernova remnants (SNR) in the Galactic plane, as likely accelerators of cosmic rays and predicted TeV sources, are obviously a prime target for southern instruments, but already first data taken with H.E.S.S. on the supernova 1006 puzzled the community [17].

TeV gamma ray emission from one of the lobes of the SN 1006 remnant was detected by the first CANGAROO (3.8 m) telescope, reported in 1998 [18]. Follow-up observations with the CANGAROO II telescope resulted in a detection reported at the ICRC conference in 2001 [19]. The combined X-ray and TeV spectra can be modeled as synchrotron and IC emission of electrons with energies up to 100 TeV in a low (4 μG) magnetic field [20]. The H.E.S.S. collaboration, both with data from the first telescope alone, and using later multi-telescope data, find no indication for significant TeV emission in the entire SN 1006 field of view (Fig. 4, left); upper limits are derived for the original CANGAROO hotspot assuming both the CANGAROO and the (better) H.E.S.S. point spread function, and for the remnant as a whole. Upper flux limits are well below the CANGAROO flux and also below the flux reported for a tentative detection with the HEGRA CT1 telescope at higher energy [21] (Fig. 4, right). The only explanation consistent with all observations is a time variation of the flux on a scale of years; however, given the size of the remnant and its structures, such a rapid variation would be surprising. Also, very high fields of order mG would be required to cool an electron population quickly enough. Further data in the X-rays and new TeV data from CANGAROO III will hopefully resolve this puzzle. Models for the TeV emission of SN 1006 can accommodate a lower flux [22]: magnetic fields around 100 μG lower the electron density required to explain the detected X-rays and thereby lower the predicted IC flux below the detection limits. Hadronic contributions can be suppressed by assuming a low ambient interstellar gas density (0.1 cm^{-3}), which is consistent with all observations, and which, since it enters both in the proton injection rate in the shock and in the number of target protons to produce gamma rays, results in a much lower gamma ray flux than that predicted given the canonical density of 1 cm^{-3}.

The second classical TeV SNR is RX J1713.7-3946, again first detected by CANGAROO as a TeV hotspot coincident with one section of the X-ray SNR shell [23]. Using a single-zone IC model, it is difficult to simultaneously fit the X-ray spectra and the TeV spectra; a low magnetic field results in the correct TeV flux but predicts a harder TeV spectrum than observed [24]. Higher fields would soften the TeV spectra in relation to the X-ray spectra, but also suppress the TeV flux well below the measured flux. In consequence, the CANGAROO collaboration have claimed this as proof for a hadronic origin of the TeV gamma rays, and RX J1713.7-3946 as the first uniquely identified source of nuclear cosmic rays [24]. This interpretation has been questioned [25, 26], e.g. on the grounds that the gamma ray spectrum predicted for a hadronic source violates an EGRET upper limit – an argument which might be circumvented by fine-tuning the proton spectrum and the mix of hadronic and IC gamma rays. A more general argument is that given the highly structured (X-ray) SNR, a single-zone IC model is clearly oversimplified. If the magnetic field is high but
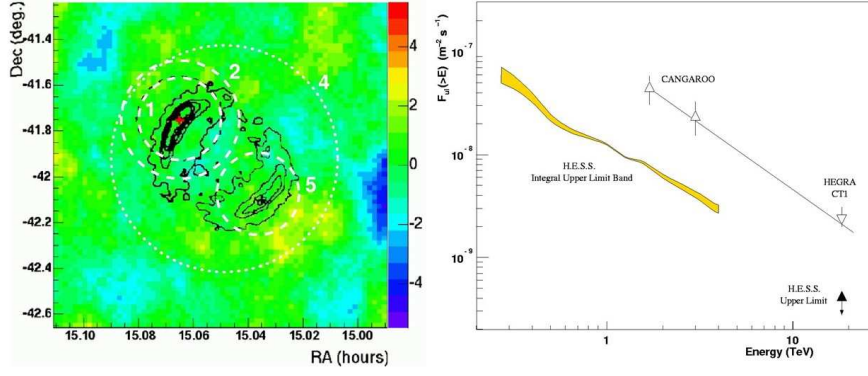
Figure 4: Left: H.E.S.S. sky map of the region around SN 1006, showing the excess significance as a function of source position. Black lines indicate X-ray countours, circle (2) the CANGAROO hotspot and circle (1) the H.E.S.S. psf. Right: H.E.S.S upper limits on the integral flux from the location of the CANGAROO hotspot, with an integration region corresponding to the CANGAROO psf (preliminary).

has a small filling factor, one can achieve softer TeV spectra, but maintain the high TeV intensity since IC gamma rays are emitted from a much larger volume than the X-rays [27]. More precise data from H.E.S.S. and CANGAROO III will help to address this issue.

2.3   The Galactic Centre

The Galactic Centre provides an environment with many potential TeV sources, ranging from mundane diffuse emission of cosmic rays interacting with the dense (10^3 cm^{-3}) gas to exotic processes such as curvature radiation from the black hole or dark matter (DM) annihilation. Recently, the CANGAROO group has reported the detection of TeV gamma rays from the Galactic Centre in data taken in 2001 and 2002 [28] (Fig. 5 left). Within the resolution of about 0.2°, the source location is consistent with Sgr A* (Fig. 5 middle). The gamma rays exhibit a rather soft energy spectrum, with a photon index $\Gamma = 4.6 \pm 0.5$ (Fig. 5 right). The spectrum can be interpreted both in terms of diffuse cosmic-ray-induced emission [28], or in terms of annihilation of (TeV) DM particles [28, 30], in the latter case, however, an enhanced density or annihilation cross section is required to explain the relatively high flux. Observations at large zenith angles with the Whipple telescope in the years 1995 through 2003 resulted in a marginal (3.7σ) detection at a threshold of 2.8 TeV [29], with a flux above the extrapolation of the CANGAROO spectrum. Within the statistical

and systematic errors, neither experiment finds evidence for variability, which otherwise could explain the difference in measured flux values.
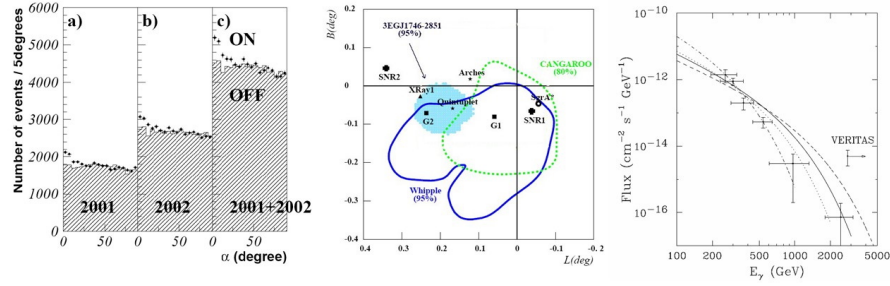
Figure 5: Left: Alpha distribution for the GANGAROO data of 2001 and 2002, showing an excess from the direction of the Galactic Centre. Middle: localization of the Galactic Centre source in the CANGAROO and Whipple data. From [30]. Right: Energy spectrum measured by CANGAROO and flux value from Whipple. Curves refer to dark matter annihilation of 1,2,3 and 5 TeV particles. From [30].

3   Concluding remarks

This contribution represents the results which were shown at the conference. In the time between the conference and the deadline for the report, a number of new results were released in particular by the H.E.S.S. collaboration, which include data for the Galactic Centre [31], with a gamma-ray spectrum which differs significantly from the CANGAROO spectrum, and the first resolved image of the supernova RX J1713.7-3946, where the shell structure in clearly visible in TeV gamma rays [32]. Details and further results can be found in extended versions of this report [33, 34].

References

[1] Weekes, T.C., Proc. 28th Int. Cosmic Ray Conf., Tsukuba, 2003, Univ. Academy Press, 1

[2] Aharonian, F., et al., ApJ **614**, 897 (2004)

[3] Piron, F., et al., in The Universe Viewed in Gamma Rays, Univ. Academy Press, 149

[4] Aharonian, F.A., et al., A&A **393**, L37 (2002)

 [5] Lozinskaya, T.A., Pravdikova, V.V., Finoguenov, A.V., Astron. Lett. **28**, 223 (2002)

 [6] Butt, Y.M., et al., ApJ **597**, 494 (2003)

 [7] Aharonian, F.A., et al., A&A, in press

 [8] Lang, M.J., et al., A&A **423**, 415 (2004)

 [9] Kifune, T., et al., ApJ **438**, L91 (1995)

[10] Kifune, T., Rapporteur talk at 28th Int. Cosmic Ray Conf., Tsukuba, 2003

[11] Chadwick, P., et al., Astropart. Phys. **9**, 131 (1998)

[12] Kushida, J., et al., Proc. 28th Int. Cosmic Ray Conf., Tsukuba, 2003, Univ. Academy Press, 2493

[13] Aharonian, F.A., Atoyan, A.M., Kifune, T., MNRAS **291**, 162 (1997)

[14] Sefako, R.P., De Jager, O., ApJ **593**, 1013 (2003), and De Jager, O., priv. comm.

[15] Kirk, J., Ball,, L., Skjœraasen, O., Astropart. Phys. **10**, 31 (1999)

[16] Kawachi, A., et al., ApJ **607**, 949 (2004)

[17] Masterson, C., Proc. 28th Int. Cosmic Ray Conf., Tsukuba, 2003, Univ. Academy Press, 2323

[18] Tanimori, T., et al., ApJ **497**, L25 (1998)

[19] Hara, S., et al., Proc. 27th Int. Cosmic Ray Conf., Hamburg, 2001

[20] Tanimori, T., et al., Proc. 27th Int. Cosmic Ray Conf., Hamburg, 2001

[21] Vitale, V., Proc. 28th Int. Cosmic Ray Conf., Tsukuba, 2003, Univ. Academy Press, 2389

[22] Völk, H.J., priv. comm.

[23] Muraishi, H., et al., A&A **354**, L57 (2000)

[24] Enomoto, R., et al., Nature **354**, 823 (2002)

[25] Reimer, O., Pohl, M., A&A **390**, L43 (2002)

[26] Butt, Y.M., et al., Nature **418** 499 (2002)

[27] Lazendic, J.S., et al., ApJ **602**, 271 (2004)

[28] Tsuchiya, K., et al., ApJ **606**, L115 (2004)

[29] Kosack, K., et al., ApJ **608**, L97 (2004)

[30] Hooper, D., et al., JCAP **0409**, 002 (2004)

[31] Aharonian, F.A., et al., A&A **425**, L13 (2004)

[32] Aharonian, F.A., et al., Nature **432**, 75 (2004)

[33] Hofmann, W., Proceedings of the Int. Symp. on High Energy Gamma Ray Astronomy, Heidelberg, 2004

[34] Hofmann, W., Proceedings of the Slac Summer Institute, 2004

THE H·E·S·S· EXPERIMENT: HIGH-ENERGY STEREOSCOPIC SYSTEM FOR VHE GAMMA-RAY ASTRONOMY

Michael Punch for the H·E·S·S· Collaboration

Physique Corpusculaire et Cosmologie, IN2P3/CNRS, Collège de France,
11 Place Marcelin Berthelot, F-75231 Paris Cedex 05, France

Abstract

H·E·S·S· (High Energy Stereoscopic System) Phase-I is comprised of four Imaging Atmospheric Cherenkov Telescopes (IACTs) for observation of galactic and cosmic sources of Very High Energy (VHE) gamma rays, with a significant improvement in sensitivity over, and a detection threshold below, that of previous IACTs.

Observations began with the installation of the first telescope in June, 2002, continued during the installation phase, and proceed now with full sensitivity since December, 2003. The telescope system has been carefully calibrated, and its performance compared to Monte Carlo simulations shows excellent agreement.

Galactic and Extra-galactic source observations are presented, in particular concerning the "Standard candle" in this domain—the Crab Nebula—and the Galactic source SN 1006 (see other talks in these proceedings for other Galactic source observations with H·E·S·S·) and the Active Galactic Nuclei (AGNs): PKS 2155-304 and Mkn 421.

1   The H·E·S·S· Telescope System

The H·E·S·S· detector for observation of > 100 GeV γ-ray s has been operating since June, 2002 in the Khomas highlands of Namibia ($23°$ S, $15°$ E, 1.8 km a.s.l.). In common with other IACTs, and in contrast to space-borne detectors, it benefits from a large collection area (~ 50000 m^2 compared to < 1 m^2 for satellite detectors), though with a relatively small field of view (a few degrees) and the restriction of observations to clear, moonless nights. It is, however, the first large-scale IACT system with a stereoscopic trigger and fast electronics, and so has unparalleled sensitivity in this domain.

The detector system consists of four IACTs in a square of side 120 m. Each telescope mount has a tessellated mirror dish of area 107 m^2 (382 Ø 60 cm facets), with a Cherenkov imaging camera (CIC) in the focal plane at 15 m. The mounts have a pointing precision of 8" while the mirror PSF is 1.3' (80% containment radius). The CIC contains 960 photo-multipliers (PMs) with $0.16°$ pixel-size, for a $5°$ field of view. Each PM is equipped with a "Winston cone" light guide to minimize dead-space between the PM sensitive areas and to cut down on albedo light (not coming from the mirror). Further details of the optical structure are given in [1, 2].

The read-out electronics are all contained within the CIC (which fits in a cube of side 1.5 m, weighing 900 kg). The modular construction of the CICs (60 "drawers" each of 16 PMs) permits their maintenance at this remote site. The read-out of the CIC is triggered when the signal from a number of PMs exceeds a trigger threshold in an effective ~ 1.3 ns trigger window. The PM signals, which are stored in an analogue memory while awaiting the trigger, are then read out, digitized, and integrated within a 16 ns window. The results are then sent from the CIC's on-board data-acquisition system to the control room via optical fibres.

Soon after the second telescope became operational in January 2003, a 'stereo' central trigger was implemented (June 2003), which retains events are only if multiple telescopes see the same cascade (see [3] for details). This decreases the dead-time for the individual telescopes, allowing the trigger threshold to be lowered (thus decreasing detector's energy threshold), while the multiple images improve the background-rejection capability and the angular and energy resolution of the system. The stereo trigger rate is ~ 300 Hz (single telscope rates ~ 800 Hz) for current trigger conditions.

Phase-I of H·E·S·S· was completed in December, 2003, with the addition of the fourth telescope, since which time the system has been operating at its full sensitivity. The energy threshold of the system is ~ 120 GeV for sources close to Zenith after background rejection cuts (~ 350 GeV for single-telescope mode) with an angular resolution improved to $0.06°$ (from $0.1°$) and allowing spectral measurements with an energy resolution of $\simeq 15\%$. See [4, 5] for further details of the H·E·S·S· detector system.

2   Calibration of the H·E·S·S· System

Calibration of IACTs is essential in order to properly estimate the physical characteristics (fluxes, spectra) of the γ-ray sources which are being measured. All elements of each telescope system (including mirrors, Winston cones, PMs, electronics, and the complete assembled CICs) were calibrated before installation in Namibia, and periodic calibrations continue.

The optics calibration (facet spot-size, and facet and Winston cone reflectivity) is described in [1] while the mirror facet alignment procedure and the resulting PSF are given in [2]. CCD cameras mounted at the centre of each mirror dish are used to align the facets and to measure the PSF of the dish using bright star images on the CIC lid. Thanks to the solid construction of the dish and mirror facet system, realignment is seldom necessary, though measurements are taken at least yearly. The absolute pointing can be verified by comparison of this CCD image of a star-field on the lid with the directly-viewed star-field in a second CCD camera mounted close to the first. A pointing precision down to 3" can be obtained using this information. This can be verified directly from the CIC, using information from the PM currents, but with somewhat lower precision. Both the PSF and pointing precision are above initial specifications.

The calibration of the H·E·S·S· CICs is described in [6]. The linearity of the channels has been verified over the dynamic range up to 1600 photo-electrons (γe). At the lower end of the dynamic range, the PMs and electronics allow the single-γe peak to be measured, thus providing a calibration of all of the detector system following the photocathode, allowing the gains of each channel to be periodically adjusted to compensate for PM aging. Calibration runs are taken every couple of nights, including measurement of the single-γe peak for all channels (using a pulsed LED in the CIC shelter), flat-fielding (relative gain) runs for all CICs (using a pulsed LED and filter system at the centre of each dish). Within standard data-taking runs, both the estimation of the ADC pedestals and the night-sky background can be made from the data itself. These calibration data are integrated in the data-analysis routines, and typical values are also included in the Monte Carlo simulations.

In addition, special calibration "muon runs" are taken every few nights. Muons from cosmic ray showers passing close to the detector give muon arcs, or full rings if they hit the mirror itself. The light emitted per metre by a muon of a given energy is a well-known quantity. The energy of the muon can be estimated from the diameter of the muon ring, and therefore such muon rings provide an absolute calibration of the detector system, including mirror, Winston cone, PM photo-cathodes and gains, and electronics. Indeed, the optical quality of the reflector can be measured with these muon rings, which should be narrow in width for a well-aligned telescope. For H·E·S·S· the measured width is $\sigma = 1.4'$ for muons well above the Cherenkov threshold. Only the atmosphere is not included in this calibration. The special "muon runs" are taken in single-

telescope mode (as most muons are eliminated by the stereo trigger) and are used to follow the detector evolution over time, for both the average over an entire CIC, and for individual channels (to a precision of $\sim 5\%$). A paper on the use of muon rings for the calibration of H·E·S·S· is in preparation.

3   The Crab Nebula with H·E·S·S· and Performance Verification

The Crab Nebula has been a standard candle of VHE γ-ray astronomy (as it is in many other wavelengths) since its discovery in 1988 by the Whipple group [7]. As a steady, bright source, it provides an ideal test beam of γ-ray s, which permits relative calibration between IACTs.

The Crab Nebula detection with the H·E·S·S· system while under construction, reported here, is based on observations taken with a 3-telescope system in October, 2003. These 4 hours of data are taken at large zenith angles (mean observation at $Z = 47°$), since the Crab is a standard Northern source. This gives a higher energy threshold of 325 GeV, but with an increased collection area. In the standard analysis of the data, γ-ray s are selected based on parameters determined from the images. *A priori* cuts are derived from Monte Carlo simulations to select γ-like events, while rejecting the much more abundant cosmic-ray induced background events. This analysis yields 53.5 σ in these data, with an event rate of 10.8 γ/minute.

Since the Crab Nebula is a known standard candle, the excess of γ-ray s above reference background data can be used to compare pre-cut parameter distributions with those which are predicted from our three independent sets of Monte Carlo simulations. This agreement is necessary in order to verify the effective collection area as a function of energy and the angular resolution of the system. The very good agreement seen for these comparisons confirms our understanding both of our telescopes' calibrations and our Monte Carlo simulations.

This detection significance of 26.6 $\sigma/\sqrt{\text{hr}}$, when extrapolated for sources close to Zenith observed by the full H·E·S·S· system, give a 1 Crab-level sensitivity (5σ detection) in only 30 seconds (1% Crab in 25 hrs). A preliminary spectrum as measured by H·E·S·S·, compared to previous experiments, is shown in Figure 1(a), and is well-fitted by a power law, with a differential index $\Gamma = 2.63 \pm 0.04^{\text{stat}} \pm 0.2^{\text{syst}}$ and an integral flux above 1 TeV of 1.98×10^{-12} photons·$\text{cm}^{-2}\text{s}^{-1}$. Subsequent observations with the full H·E·S·S· Phase-I system have confirmed this performance, and will be reported in a future paper.
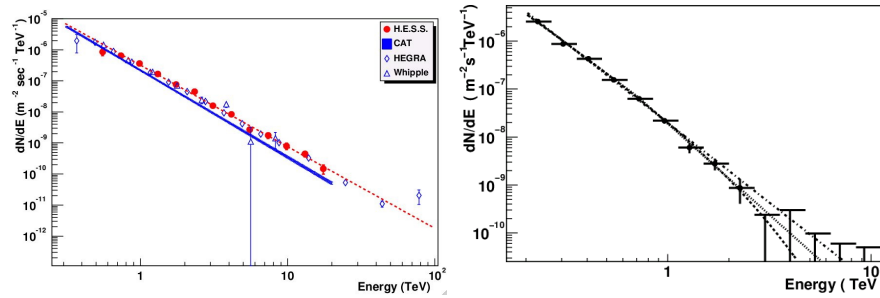
Figure 1: (a) Preliminary Crab Nebula γ-ray spectrum, together with results from CAT, HEGRA, and Whipple (the dashed line is the fit to the H·E·S·S· data). (b) Time-averaged energy spectrum of PKS 2155-304 for the 2003 stereo data. The lines represent best fits to a power law (dot-dash), power law with exponential cut-off (dashed), and a broken power law (dotted).

4   Observations of Other Galactic Sources with H·E·S·S·

In addition to the Crab Nebula, a number of Galactic source candidates have been observed with H·E·S·S·, with the most time (in descending order, up to Summer, 2004) given to: SN 1006 (107h), RX J1713.7-3946 (50h), PSR B1706-44 (43h), Vela (26h), Sgr A* (34h), Cen X-3 (32h).

The H·E·S·S· observations of PSR B1706-44 (upper limit) are covered elsewhere in these proceedings [8], as is the detection of the binary pulsar PSR B1259-63 [9]. The detection from the region around Sgr A* (Galactic Centre) is given in a recent paper [10], as is that of RX J1713.7-3946 [11]. Here, only the H·E·S·S· upper limit on SN 1006 will be presented.

4.1   H·E·S·S· Observations of SN 1006

SN 1006 is a young Shell-type Supernova remnant, and thus is a candidate as one of the sources for the acceleration of Cosmic Rays in the shock where the supernova ejecta encounters the interstellar medium. Observations in other wavebands, notably by the ASCA, RXTE, and *Chandra* X-ray satellites, indicate that electrons are accelerated up to 100 TeV in this source [12, 13], and so the acceleration of protons may also take place.

In the observation presented here, in 14 hours of data, no signal was seen, either from the whole remnant or from the hot-spot region (NE rim) from which emission was claimed by the CANGAROO collaboration using both their 3.8 m and 10 m (CANGAROO-II) IACTs [14, 15]. The H·E·S·S· preliminary upper limit (90% confidence level) [16] for the entire nebula is $< 8.94 \times 10^{-12}$ ph. cm^{-2}s^{-1} above 260 GeV, $< 0.64 \times 10^{-12}$ ph. cm^{-2}s^{-1} above 1.7 TeV from a region of radius 0.23° corresponding to the CANGAROO hotspot. This is an order

of magnitude below the latter's claim, thanks to the great improvement in sensitivity of H·E·S·S· over the previous generation of IACTs. The installation of the CANGAROO-III stereoscopic system (though currently without a stereo trigger) should increase their sensitivity, so new results from that detector are awaited.

Measurements in other wavebands provide some physical parameters of this source: distance 1.8–2.2 kpc, proton density $n_{\rm H} \simeq 0.05$–0.3 cm^{-3}, and a strongly enhanced magnetic field $B_{\rm int} = 120$–150 μG inferred from the broad-band synchrotron and X-ray structure measurements. When compared to emission models [17] using these parameters, which predict the VHE spectra from Inverse Compton emission of electrons and π^0 decay from proton interactions, and including the above magnetic field strength, our preliminary upper limit would favour the lower range of the allowed Remnant density as it greatly constrains the π^0 emission, which depends quadratically on $n_{\rm H}$. See [18] (these proceedings) for further details of these models as applied to this source and to Cas A.

5   Observations of AGNs with H·E·S·S·

Since the beginning of observations with the H·E·S·S· detector, many galactic and extragalactic sources have been studied. The observation of AGNs at the highest energies is a probe of the emission mechanisms in the jets of these sources, and studies of the their multi-wavelength spectral energy distributions and correlated variability between wavelength bands enable emission models (leptonic or hadronic) to be tested. In addition, as these VHE photons interact with the Intergalactic Infra-Red (IIR) background (to give an electron-positron pair) and are thus absorbed, they can also serve as a probe of this background (resulting mainly from early star formation) which is difficult to measure by direct means. However, this absorption limits the distance at which we can see AGNs up to a redshift of 0.5 at the H·E·S·S· detector threshold energy. The large detection area of H·E·S·S· allows us to measure spectral and temporal characteristics on hour timescales (depending on the strength of flares) for the sources seen.

Among the extra-galactic targets (with observing time up to Summer, 2004 in parentheses) are: PKS 2155-304 (92h), PKS 2005-489 (52h), M 87 (32h), NGC 253 (34h). Here we present results from two AGNs: PKS 2155-304 and Mkn 421 .

5.1   The AGN PKS 2155-304

PKS 2155-304 is the brightest AGN in the Southern Hemisphere, and has been well studied in many energy bands over the last 20 years. It has been previously detected in the VHE band [19]. With a redshift of $z = 0.117$ it is one of the

most distant VHE blazars, and therefore of interest not only for studies of this class of object, but also for IIR studies.

Initial observations were taken during the whole installation of H·E·S·S· Phase-I from July 2002 to October 2003, with an evolving detector threshold and sensitivity. Clear detections ($> 5\sigma$) are seen in each night's observations, and an overall signal of 45σ in 63 h of this mixed data, with ~ 1.2 γ/min, 10–60% Crab level, with variability on time-scales of months, days, and hours. The energy spectra are characterized by a steep power law with a time-averaged photon index of $\Gamma = 3.31 \pm 0.06^{\text{stat}} \pm 0.2^{\text{syst}}$, as shown in Figure 1(b).

Owing to a particularly high level seen by H·E·S·S· in October, 2003, we triggered our RXTE "target of opportunity" proposal on this source, enabling quasi-simultaneous observations to be taken between the two instruments. Short-term variations (< 30 min) are seen in both these datasets, and multi-wavelength correlations will be published in a forthcoming paper.

A H·E·S·S· multi-wavelength campaign with the PCA instrument on board the Rossi X-ray Timing Explorer (RXTE) was successfully completed in August, 2004, with the full four-telescope Phase-I array, and therefore full sensitivity, and these data are under analysis. This intense study of this source should yield insights into its inner workings.

5.2   The AGN Mkn 421

Mkn 421 was the first extra-galactic source detected at VHE energies [20]. It is the closest such source (at $z = 0.03$) and so is little affected by IIR absorption. With a declination $\delta \sim 38°$, it is still accessible to H·E·S·S· , though culminating at a Zenith angle above $60°$. Under these conditions, observations with the H·E·S·S· detector have a higher threshold, but a compensatory larger effective area (as the light-pool is geometrically larger for showers developing at a greater atmospheric slant distance), and so gives access to the highest energies of the spectrum.

In April of this year, a great increase in activity from this source was seen by the all-sky monitor aboard RXTE, reaching an historically-high level of 110 mCrab in mid-April. A multi-wavelength campaign was therefore triggered on this source, including other IACTs, radio and optical telescopes, and RXTE.

The H·E·S·S· observations, at an average Zenith angle of $62°$, provided a very clear signal in April, with 66σ in 9.7 h of data, yielding ~ 5.1 γ/min, and an estimated 1–2 Crab level. The flux clearly increases from the January level (6σ in 2.1 h, ~ 0.8 γ/min, 10–50% Crab level), and was also seen by other IACTs in the Northern hemisphere (Whipple, MAGIC). Shorter-term variations and correlations with other energy domains are currently under study.

6   Conclusions

Phase-I of H·E·S·S· has already provided many interesting new results, of which some of those from Galactic and Extra-Galactic sources are presented here and in other papers in these proceedings.

It will continue to provide exciting new results and promises to greatly expand the source catalogue at very high energies in the near future.

References

[1] K. Bernlöhr et al., *Astroparticle Physics* **20**, 111 (2003)

[2] R. Cornils et al., *Astroparticle Physics* **20**, 129 (2003)

[3] S. Funk et al., *Astroparticle Physics, accepted*

[4] W. Hofmann et al., *Proc. 28th ICRC* (Tsukuba) 2811 (2003)

[5] P. Vincent et al., *Proc. 28th ICRC* (Tsukuba) 2887 (2003)

[6] F. Aharonian et al., *Astroparticle Physics, accepted*

[7] T.C. Weekes et al., *Astrophysical Journal* **342**, 379 (1989)

[8] W. Hofmann et al., *these proceedings*

[9] M. Beilike et al., *these proceedings*

[10] F. Aharonian et al., *Astronomy and Astrophysics* **425**, L13 (2004)

[11] F. Aharonian et al., *Nature (in press)* (2004)

[12] K. Koyama et al., *Nature* **378**, 255 (1995)

[13] G.E. Allen, R. Petre, E.V. Gotthelf, *Astrophysical Journal* **588**, 739 (2001)

[14] T. Tanimori et al., *Astrophysical Journal Letters* **497**, L25 (1998)

[15] T. Tanimori et al., *Proc. 27th ICRC* (Hamburg) 2465 (2003)

[16] G. Rowell et al., *Proc. γ_{2004}* (Heidelberg) (*in press*) (2004)

[17] E.G. Berezhko, L.T. Ksenofontov, H.J. Völk, *Astronomy and Astrophysics* **395**, 943 (2004)

[18] G. Pühlhofer et al., *these proceedings*

[19] P. Chadwick et al., *Astrophysical Journal* **513**, 161 (1999)

[20] M. Punch et al., *Nature* **358**, 477 (1992)

WHIPPLE-VERITAS: A STATUS REPORT

F. KRENNRICH[1], I.H. BOND[2], P.J. BOYLE[3], S.M. BRADBURY[2], J.H. BUCKLEY[4],
D. CARTER-LEWIS[1], O. CELIK[5], P. COGAN[6], W. CUI[7], M. DANIEL[1],
I. DE LA CALLE PEREZ[2], C. DUKE[8], A. FALCONE[7], D.J. FEGAN[6], S.J. FEGAN[9],
J.P. FINLEY[7], L.F. FORTSON[3], J. GAIDOS[7], S. GAMMELL[6], K. GIBBS[9],
G.H. GILLANDERS[10], J. GRUBE[2], J. HALL[11], D. HANNA[12], A.M. HILLAS[2],
J. HOLDER[2], D. HORAN[9], T.B. HUMENSKY[3], M. JORDAN[4], G.E. KENNY[10],
M. KERTZMAN[13], D. KIEDA[11], J. KILDEA[12], J. KNAPP[2], K. KOSACK[4],
H. KRAWCZYNSKI[4], M.J. LANG[10], S. LEBOHEC[1,11], E. LINTON[3], J.
LLOYD-EVANS[2], A. MILOVANOVIC[2], P. MORIARTY[14], D. MÜLLER[3], T. NAGAI[11],
R.A. ONG[5], R. PALLASSINI[2], D. PETRY[15], B. POWER-MOONEY[6], J. QUINN[6],
K. RAGAN[12], P. REBILLOT[4], P.T. REYNOLDS[16], H.J. ROSE[2], M. SCHROEDTER[9],
G. SEMBROSKI[7], S.P. SWORDY[3], A. SYSON[2], V.V. VASSILIEV[11], S.P. WAKELY[3],
G. WALKER[11], T.C. WEEKES[9], J. ZWEERINK[5]

[1] *Iowa State University, Ames, IA, USA*

[2] *University of Leeds, Leeds, UK*

[3] *University of Chicago, Chicago, IL, USA*

[4] *Washington University, St. Louis, MO, USA*

[5] *University of California, Los Angeles, CA, USA*

[6] *National University of Ireland, Dublin, Ireland*

[7] *Purdue University, West Lafayette, IN, USA*

[8] *Grinnell College, Grinnell, IA, USA*

[9] *Smithsonian Astrophysical Observatory, USA*

[10] *National University of Ireland, Galway, Ireland*

[11] *University of Utah, Salt Lake City, UT, USA*

[12] *McGill University, Montreal, Quebec, Canada*

[13] *DePauw University, Greencastle, IN, USA*

[14] *Galway-Mayo Institute of Technology, Galway, Ireland*

[15] *University of Maryland Baltimore County and NASA/GSFC, USA*

[16] *Cork Institute of Technology, Cork, Ireland*

Abstract

Recent results from the Whipple 10 m gamma-ray telescope are presented including a tentative detection of the Galactic Center, a confirmation of the TeV unidentified source TeV J2032+4130 and an update on measurements of bazar spectra. Furthermore, we give a status report of the VERITAS project: we discuss the successful test of a prototype telescope and the rapid construction of a 4-telescope array on Kitt Peak, Arizona.

1   Introduction

The imaging atmospheric Cherenkov technique has rapidly advanced since the pioneering detection of the first TeV gamma-ray source, the Crab Nebula, by the Whipple collaboration in the late 1980s [23]. Although the Whipple 10 m gamma-ray telescope is now 36 years old, it still provides good sensitivity for gamma-ray observations in the northern hemisphere and it will be retired in the VERITAS era. We report science results from its most recent observations.

Stereoscopic imaging of air showers has been widely recognized as a key technique for providing better sensitivity for next generation ground-based based gamma-ray telescopes [9]. The VERITAS (Very Energetic Radiation Imaging Telescope Array System) collaboration is currently constructing VERITAS-4, an array of four imaging telescopes on Kitt Peak, located in southern Arizona. While VERITAS-4 is in the construction phase we report here first results on the performance of a prototype of the individual elements of VERITAS, showing that the design and technical specifications have been met.

2   Galactic Sources

2.1   Galactic Center

Observations of the Galactic Center have been pursued with the Whipple 10 m telescope over the time period of 1995 through 2003 ([3],[11]). The Galactic Center culminates at an elevation of 29° in the southern Arizona sky, therefore observations were taken at large zenith angles. This observing mode increases the energy threshold of the detector to 2.8 TeV. However, as shown previously for the Whipple 10 m telescope ([13],[17]), observations at large zenith angles also increase the collection area, yielding good sensitivity at multi-TeV energies as demonstrated for the Crab Nebula [13]. For sources with energy spectra harder than the Crab (dN/dE $\propto E^{-2.5}$), large zenith angle observations are

even more sensitive, because the ratio of source counts over cosmic-ray events increases with energy.

Since the Galactic Center data were taken over an extended period of time involving 3 different camera configurations, it was necessary to develop a new analysis method that allows the combination of data from eight years. Taking into account the different pixelations used in the camera and improvements of the point spread function of the telescope optics, it was possible to use scaled values of the image parameters for the analysis [12]. A total of 26 hours of on-source exposure have been used for this analysis.

Figure 1 shows the sky map of the excess events of gamma-ray events in the direction of the Galactic Center. An excess with a significance of 3.7 σ is present and coincides with the position of the Galactic Center. Since the region around the Galactic Center is relatively bright, related systematic effects from the different sky brightness between ON and OFF source runs were corrected in the analysis. However, remaining uncertainties could have effects on the number of excess events and the significance of the signal. The Galactic Center has been convincingly detected by the HESS collaboration [2] and has also been reported by the CANGAROO-II collaboration [22]. Further observations are underway to confirm the detection with the Whipple 10 m instrument and the VERITAS telescope array. The flux level at 2.8 TeV corresponds to 0.4 Crab, which is a factor of 3 higher than the corresponding flux point in the energy spectrum published by the HESS collaboration [2]. However, given the marginal significance of the Whipple detection of the Galactic Center, this result is not inconsistent with the HESS results.

2.2   TeV Unidentified Sources

The fortuitous detection of a gamma-ray source in the Cygnus region by the HEGRA collaboration [1] indicates the discovery of the first unidentified TeV source in the sky, TeV J2032+4130. The initial result is based on an extensive exposure time of 121 hours, raising the concern of possible systematic effects above what is usually expected from short exposures for which instrumental effects are better understood. Therefore, independent confirmation with another instrument is deemed important. The HEGRA collaboration was able to confirm the initial result by follow-up observations with now a total of 279 hours of observation time [20] yielding a significance of $\approx 7\sigma$. The integral flux of TeV J2032+4130 above 1 TeV is just 3% of the Crab which is at the sensitivity limit of second generation imaging atmospheric Cherenkov telescopes. Interestingly, the energy spectrum is rather hard with a differential spectral index of $1.9 \pm 0.3_{\text{stat}} \pm 0.3_{\text{syst}}$. The detection of this new source was unexpected; it was a result of a 2-dimensional analysis of the camera field of view around the direction of Cygnus X-3, which is just 0.6^o south of TeV J2032+4130.
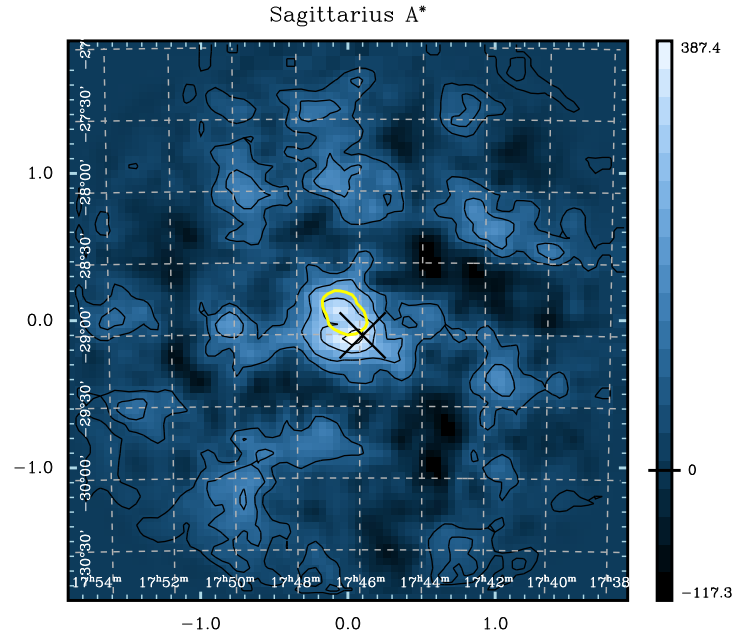
Figure 1: Showing the two dimensional distribution of the gamma-ray excess counts in the direction of the Galactic Center. The dark contour lines indicate the significance levels in steps of 1 σ. Also shown is the 99% confidence region for EGRET observations according to a recent analysis by Hooper et al. [10], however, for an earlier analysis see [16].

Archival data from the Whipple collaboration from the time period 1989/1990 in the direction of Cygnus X-3 allowed us to independently verify the reported source detection by HEGRA [1] . A total of 50.4 hours of observing time of Cygnus X-3 was used to search for the HEGRA source.

Figure 2 shows the excess significance of the skymap centered on the direction of Cygnus X-3 based on the Whipple observations [15]. A 4 σ excess is present near the HEGRA source location approximately 0.6^o north of Cygnus X-3. Accounting properly for the number of trial factors introduced by searching around the HEGRA position, the total significance is reduced to 3.5 σ. The excess appears in both years of observations, hence no variability is indicated by the data. Due to the relatively low significance of the detection it is not possible to determine the angular size of the source.

In summary, the first unidentified TeV gamma-ray source, TeV J2032+4130 has been confirmed by the Whipple 10 m telescope, although with marginal
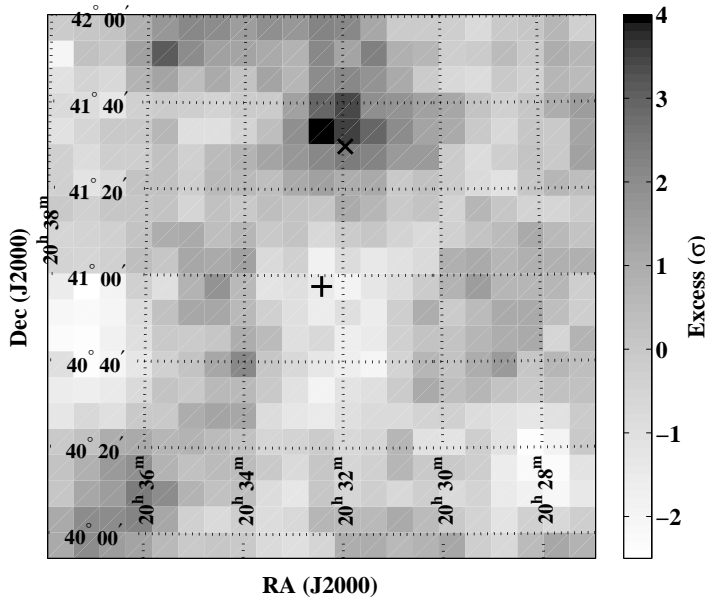
Figure 2: The skymap of the Cygnus X-3 region is shown in units of standard deviations of gamma-ray excess events. An excess with a significance of 3.3 σ is coincides with the position of TeV J2032+4130 as reported by the HEGRA collaboration. The cross nearby the excess corresponds to the HEGRA position, whereas the cross in the center indicates the position of Cygnus X-3.

significance. Observations with a next generation instrument, e.g., VERITAS-4 or MAGIC [5] are required to solve the origin of TeV J2032+4130 as a gamma-ray source and provide accurate identification with a counterpart at other wavelengths.

3   Extragalactic Sources: Gamma Ray Blazars

The Whipple 10 m telescope was used in an extensive survey searching for low redshift TeV gamma-ray blazars and was initially guided by the first EGRET catalog [8] of blazars at GeV energies. This led to the discovery of the first active galaxy, Mrk 421 in TeV gamma rays [19] . More refined search strategies selecting X-ray bright BL Lacs led to a number of detections of low redshift blazars (Mrk 501, 1ES2344+514, H1426+428 and 1ES1959+650) ranging from z=0.03 to 0.129. A major interest in blazar observations at TeV energies is to test particle acceleration models and gamma-ray emission models

in jets of active galactic nuclei. A recent overview describing properties of TeV blazars constraining gamma-ray production models in jets can be found in these proceedings in the paper by J. Buckley. The emphasis of this section will be the interaction of TeV gamma-ray beams with cosmological radiation fields, the cosmic near-IR and mid-IR background.

3.1 Gamma Ray Blazar Energy Spectra

TeV blazar observations can also be used to provide constraints to the intervening medium, in particular the diffuse extragalactic background light (EBL). A TeV photon can interact with a near-infrared photon of the EBL via pairproduction; the energy dependent cross section for a 1 TeV photon is maximal when interacting with a $\approx 1\mu$m soft photon. Because of the energy and distance dependence of this gamma-ray absorption effect, the observed energy spectra of blazars at various distances are attenuated by a different magnitude. In addition the shape of the imprinted absorption feature in the observed gamma-ray spectra also depends on the energy distribution of the EBL; its double-peak structure is well established. However, direct measurements of the EBL in the 5-60 μm wavelength regime are hampered by foreground emission from interplanetary dust, the EBL is largely uncertain in this wavelength regime. In fact, unfolding of TeV gamma-ray spectra of blazars at various redshifts may be the most promising method to gain information about the mid-IR part of the EBL spectrum.

Figure 3 shows the Whipple power spectra of the two nearby blazars Mrk 421 and Mrk 501, both at a redshift of ≈ 0.03, the more distant blazar 1ES1959+650 at a redshift of 0.048 and the most distant blazar H1426+428 at a redshift of 0.129. It is apparent that the two nearest blazars exhibit a hard spectrum (dN/dE $\propto E^{-1.95\pm0.07}$ and dN/dE $\propto E^{-2.14\pm0.03}$) terminated by a cutoff at approximately 4 TeV. The spectrum of 1ES1959+650 is steeper (dN/dE $\propto E^{-2.8\pm0.3}$) but statistics do not allow the unraveling of structure other than a power law. The energy spectrum of H1426+428 is even steeper (dN/dE $\propto E^{-3.5\pm0.6}$), again limited statistics prevent statements about the detailed spectral shape.

Although suggestive for EBL absorption, the energy spectra of Mrk 421 and Mrk 501 with the same characteristic cutoff energy, could present the intrinsic spectral shape of the two TeV gamma-ray sources. For example, Dwek & Krennrich [7] explore a wide range of EBL scenarios, which are allowed based on currently available direct measurements and limits, and reconstruct the absorption-corrected spectra of Mrk 421 and Mrk 501. These absorption-corrected spectra show that the source spectra could differ very little from the observed spectra except in the absolute flux level, which is almost certainly effected [7]. On the other hand, in case of EBL scenarios with a high energy density in the mid-IR, the observed cutoffs are mostly caused by the EBL. The
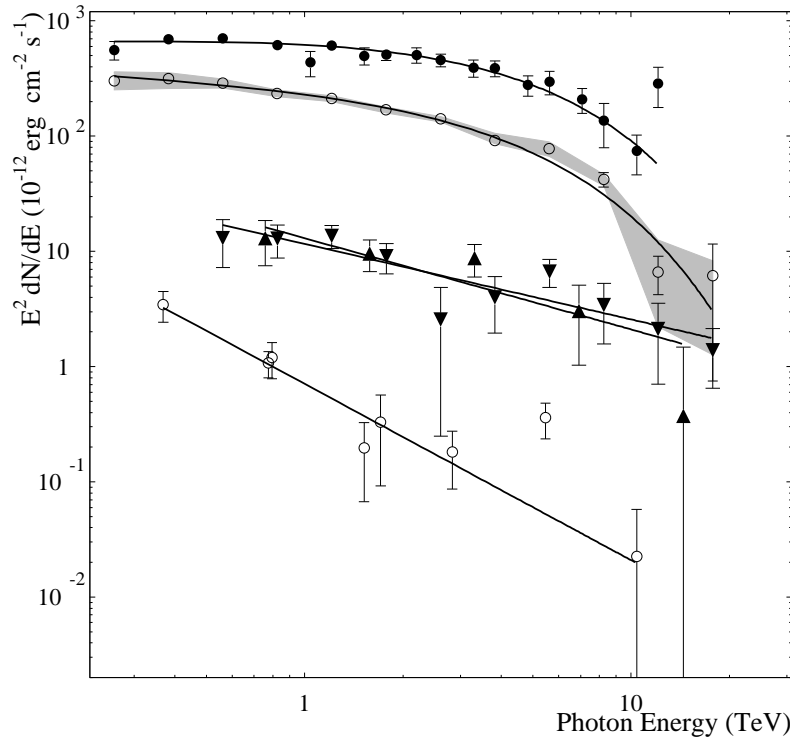
Figure 3: The energy spectra of Mrk 501 (filled circles) [21] , Mrk 421 (empty circles) [14] , 1ES1959+650 (triangles) [6] and H1426+428 (empty circles at bottom) [18] are shown.

absorption-corrected energy spectra of the TeV blazars Mrk 421 and Mrk 501 do show a limited range of luminosity peak energies between 0.5 TeV - 2 TeV, indicating that the power output of both objects peaks in the TeV range [7].

Limits to the EBL in the mid-IR have been derived from TeV observations, however, the ultimate goal of measuring the EBL over a range of 0.1 μm to 30 μm is still in its infancy and can likely be achieved with next generation imaging atmospheric Cherenkov telescopes.

Figure 4: A photomontage of the VERITAS telescope array currently under construction on Kitt Peak.

4   The VERITAS Project

VERITAS-4 is the next generation ground-based gamma-ray observatory in the U.S. and will be located in Horsehoe Canyon on Kitt Peak, in southern Arizona. The main objective of the design is to reach maximum sensitivity at 100 GeV - 10 TeV, providing excellent angular resolution (0.1º to 0.03º at 100 GeV and above 1 TeV, respectively) and good energy resolution (15% and 10% at 100 GeV and above 1 TeV, respectively). This can be achieved by stereoscopic imaging of air showers with 12 m diameter optical reflectors and imaging cameras with 499 photomultipliers in the focal plane. The field of view of each camera is 3.5° across.

The VERITAS-4 design consists of four 12 m diameter imaging Cherenkov telescopes, with three spaced on the corners of a triangle and one at the center with a distance of 80 m from the others. The mirror area of 100 m^2 for each telescope allows, e.g., for a total mirror area of 300 m^2 when three telescopes located in the Cherenkov light pool participate in a true array trigger. A true array trigger is possible by the use of a flash-adc system [4] with 8 μs memory depth, providing enough delay time for reaching a trigger decision based on Cherenkov light detected in each telescope. Utilizing the combined mirror area is essential for achieving the lowest possible trigger threshold and energy threshold.

The VERITAS collaboration has constructed and tested a prototype telescope at the basecamp of Whipple observatory. The prototype will become the first element of four telescopes forming the array. The reflector of the prototype telescope had been equipped with 80 mirrors (360 for a complete single VERITAS element) and a half camera in the focal plane. This prototype setup has allowed us to test the largely custom designed electronics (frontend, flash-adcs, discriminators and pattern trigger) and the optics of the VERITAS telescopes and verify performance specifications.

Figure 5: The prototype telescope for the VERITAS-4 telescopes.

The optics of the prototype meets expectations with a point spread function of 0.04° F.W.H.M., consistent with ray-tracing calculations of the prototype reflector. The optical support structure (OSS) with its quadrapot bypass structure, a design that passes the load from the telescope arms and camera to

a the positioner circumventing the OSS, meets our specifications.

The VERITAS-4 array is designed to use stereoscopic imaging and at the same time record the pulse shapes from the Cherenkov light flashes using a 500 MHz sampling rate flash-adc system. Imaging combined with timing is promising for the best possible shower reconstruction.

First results from observations of Mrk 421 in spring 2004 are reflected in Figure 6. Initiated by Whipple 10 m observations we were able to observe Mrk 421 in a high flaring state and carried out observations with the prototype telescope as well. In 19.2 hours an excess with a significance of 20.5σ has been detected. This demonstrates that the prototype is working well, although it contained only a half camera, less than a quarter of the mirror area and no light concentrators.
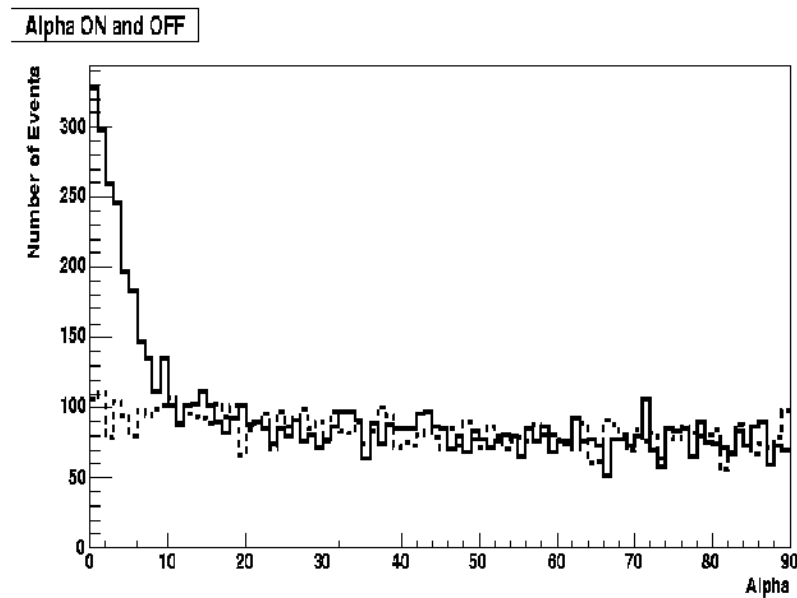

Figure 6: The alpha distribution of Mrk 421 observations (ON) and background events (OFF) showing an excess of 20.5 σ from19.2 hours of observations.

5 Summary

TeV gamma-ray observations with imaging atmospheric Cherenkov telescopes have reached a significant milestone for any astronomical technique: the

development of an order of magnitude more sensitive instruments and the discovery of unexpected sources of radiation occurring in the field of view. Whipple archival data has confirmed the detection of the first TeV unidentified source discovered by the HEGRA collaboration, a second generation instrument operated at its sensitivity limit.

Also at the sensitivity limit of the Whipple 10 m telescope is the Galactic Center, now unambiguously detected by the HESS collaboration; over a time period of 8 years and 26 hours of observations, a tentative detection with a significance the 3.7σ has been reported by the Whipple collaboration.

Furthermore, we give an update on the measurement of energy spectra of gamma-ray blazars with the 10 m telescope. There are several energy spectra available measured by the Whipple collaboration: Mrk 421 and Mrk 501 which exhibit a hard spectrum with a cutoff at 4 TeV, H1426+428 with a very steep spectrum and 1ES1959+650 with a spectral index between that of Mrk 421 and that of H1426+428. As to whether or not the cutoff for Mrk 421 and Mrk 501 is due to the EBL cannot be unambiguously decided. Recent studies of a wide range of EBL scenarios clearly show that an intrinsic cutoff as well as a cutoff due to the EBL are viable possibilities. However, all EBL scenarios imply substantial absorption above 0.5 TeV for the Mrk 421 and Mrk 501, indicating that the energy spectra of 1ES1959+650 and H1426+428 are strongly absorbed in that energy regime.

Finally, we show results from the construction of a prototype telescope that will be the basis for the elements of VERITAS-4. Tests of the optical support structure and point spread function indicate that the optics of the telescope is of excellent quality. Also the test of the mostly custom built electronics proved to be successful. A front-to-end test is given by a strong detection ($20.5\ \sigma$) of Mrk 421 in 19 hours of observation. VERITAS-4 is currently under constructed at Kitt Peak and is expected to start operating as a four telescope array in 2006.

References

[1] F.A. Aharonian et al., A&A, 393, L37 (2002).

[2] F.A. Aharonian et al., A&A, 425, L13 (2004).

[3] J.H. Buckley et al., Proceedings of the 25th ICRC (Durban), 3, 237 (1997).

[4] J.H. Buckley et al., Proceedings of the 29th ICRC (Tsukuba) (2003).

[5] J. Cortina et al., Proceedings of The II Workshop on Unidentified Gamma-Ray Sources (Hong Kong), in press, astro-ph/0407475 (2004).

[6] M. Daniel et al., submitted to ApJ (2004).

[7] E. Dwek & F. Krennrich, ApJ, in press, astro-ph/0406555 (2004).

 [8] C.E. Fichtel et al., ApJS, 94, 551 (1994).

 [9] W. Hofmann et al., these proceedings (2004).

[10] D. Hooper, & B. Dingus, astro-ph/0212509 (2002).

[11] K. Kosack et al., Proceedings of the 29th ICRC (Tsukuba) (2003).

[12] K. Kosack et al., ApJ, 608, 97 (2004).

[13] F. Krennrich et al., ApJ, 511, 149 (1999).

[14] F. Krennrich et al., ApJ, 560, L45 (2001).

[15] M.J. Lang et al., A&A, 423, 415-419 (2004).

[16] H. A. Mayer-Hasselwander et al., A&A, 335, 161 (1998).

[17] D. Petry et al., astro-ph/0108085 (2001).

[18] D. Petry et al., ApJ, 580, 104 (2002).

[19] M. Punch et al., Nature, 358, 477 (1992).

[20] G. Rowell et al., astro-ph/0307334 (2003).

[21] F.W. Samuelson et al., ApJ, 501, L17 (1998).

[22] D. Tsuchiya et al., ApJ, 604, L115 (2004).

[23] T.C. Weekes et al., ApJ, 342, 379 (1989).

[24] T.C. Weekes et al., Astropart. Phys., 17, 221 (2002).

FIRST RESULTS FROM MAGIC

Riccardo Paoletti[a,1]

[a] *Dipartimento di Fisica, Università di Siena & I.N.F.N. Sezione di Pisa, Italy*

Abstract

The MAGIC telescope has been designed to study the gamma ray astronomy in the 30-300 GeV energy range. With its 17 m diameter mirror it is the largest Cherenkov telescope currently operating. It started its operation in november 2003 and it is now in its commissioning phase. The first results are reported.

1   Introduction

The MAGIC (Major Atmospheric Gamma Imaging Cherenkov) telescope was originally proposed in early 1998[1]. In order to cover the energy gap between 10 and 300 GeV, left unexplored by EGRET and the first generation Cherenkov telescopes, the MAGIC telescope was designed to have the lowest achievable energy threshold.

The telescope is installed at the Roque de los Muchachos Observatory (ORM) at 2200 m asl (28.8^o north, 17.9^o west) on the Canary island of La Palma.

---

[1]On behalf of the MAGIC Collaboration (http://hegra1.mppmu.mpg.de/MAGICWeb/)

1.1   Frame and Drive System

The building of the mirror frame began in September 2001 and the whole frame structure was finished after few months (December 2001). The 17 m diameter $f/D = 1$ telescope frame is made by a nest of carbon fiber tubes specifically designed to achieve stiffness and light weight, about 20 tons, that add to the undercarriage weight to give a total weight of 40 tons.

The telescope drive system was installed during 2002. The position of the telescope is measured by three absolute shaft encoders that give a position accuracy is 0.02°. Thanks to the frame light weight, the telescope can reposition and track any point in the sky, like Gamma Ray Bursts locations, in about 20 seconds, well below the 30 seconds design goal. The pointing accuracy has been masured by using a CCD camera mounted on the reflector frame and it is better than 0.01° .

Figure 1: The MAGIC telescope on the inauguration day (2003/10/10). All the mirrors elements have now been installed.

1.2   Reflector and Active Mirror Control

The use of a parabolic shape is crucial to minimize the arrival time spread of the Cherenkov light flashes on the camera plane. In fact, the time structure of the Cherenkov pulses brings information of the parent particle and can be used to increase the signal to noise ratio with respect to the night-sky background light (NSB). The reflective surface is composed by a mosaic of 956 0.5×0.5 m^2 mirrors covering a total surface of 234 m^2. The alignment of the mirrors in the telescope surface is performed by using an artificial light source placed at a distance of 960 m and the overall spot has a FWHM of roughly half a pixel size ($< 0.05°$).

The deformations induced in the mirror surface by the telescope movement are corrected by an Active Mirror Control system by means of linear actuators. A laser module located in the center of the panel points to the camera plane and it is used as a reference spot for focusing. The corrected light spot of bright stars focused at infinity fits within one pixel (RMS of the Point Spread Function less than $0.1°$) for practically all elevation angles (greater than $\sim 30°$).

1.3   Camera System

The MAGIC camera has 1.5 m diameter, 450 kg weight and 3-4° FOV (see figure 2). The inner hexagonal area is composed by 397 0.1° FOV hemispherical photomultipliers of 1 inch diameter surrounded by 180 0.2° FOV PMTs of 1.5 inch diameter for a total of 577 PMTs. The time response FWHM is below 1 ns. The photocathode quantum efficiency is enhanced up to 30% and extended to the UV by a special coating of the surface using wavelength shifter [3]. Dedicated light collectors have been designed to let the photon double-cross the PMT photocathode for large acceptance angles. The camera was completed in summer 2002 after extensive testing and characterization. It was installed on the site in November 2002 and commissioned in March 2003.

1.4   Readout and Trigger Systems

The signals from the PMTs are amplified inside the camera enclosure and transmitted over 162 m long optical fibers using Vertical Cavity Emitting Laser Drivers (VCSELs, 850 nm wavelength) to reduce the weight and size of standard copper cables and to minimize the electromagnetic noise on the lines. In the electronics room the signal is split into two branches. The first branch passes through a software adjustable threshold discriminator that generates a digital signal for the trigger system. The second branch is stretched to 6 ns FWHM, amplified and sent to the readout system for digitization.

The digitization is performed by 8 bit 300 MHz Flash ADCs that continuously sample the analog signals and store the digital data into a 32 kByte

Figure 2: View of the MAGIC camera in park position.

long ring buffer. An event consists of 30 samples that are written to a 512 kByte long FIFO buffer at a maximum rate of 80 Mbyte/s. The readout of the ring buffer results in a dead time ~20 μs corresponding to less than 2% dead time at the design trigger rate of 1 kHz. The time and trigger information for each event are recorded by dedicated digital modules which are read out along with the FADC analog modules. The readout is controlled by a PCI card that saves the data on a RAID0 disk system at a rate up to 20 MByte/s.

MAGIC is equipped with a two-level trigger system with programmable logic [2]. The first level (L1T) applies tight time coincidence and simple next neighbour logic. The trigger is active in 19 hexagonal overlapping regions of 36 pixels each, to cover 325 of the inner pixels of the camera. The second level (L2T) can be used to perform a rough analysis and apply topological constraints on the event images. The individual pixel rates of the channels included in the trigger are monitored by 100 MHz scalers.

The L1T and L2T systems were installed and commissioned during the winter of 2003 as well as the whole computing system for the telescope control and DAQ.

2   Data Sample and Analysis

During last months operation most of the systems in the telescope have reached the expected performance. The telescope trigger rate has been found to vary smoothly with the discriminator threshold level as expected if it is dominated by cosmic rays and not by night sky background noise. Most of the data have been recorded with a threshold level around 4 photoelectrons (phe) and 4 Next-Neighbour Pixel trigger multiplicity.

It is worth mentioning that the telescope is still in its commissioning phase. All the results presented here are preliminary since the configuration and performance of the telescope are not the nominal ones yet and the analysis software is still in its development phase.

The data campaign in the period October 2003 to May 2004 has mainly concentrated on low zenith angle ($<40°$) observations of standard TeV candles like Crab Nebula, Mrk 421, Mrk 501, 1ES 1426 and 1ES 1959. A roughly equivalent amount of OFF source data have been recorded under the same conditions of the ON data for background substraction.

The preliminary analysis was performed only on very short data samples for which the weather conditions were excellent on the basis of the trigger rates and star extinction measurements, all the telescope hardware systems were performing nominally and the data have been already preprocessed and calibrated.

Standard Hillas analysis based on dynamic "supercuts" [4] has been applied. Further discrimination is obtained using the orientation of the shower image given by the ALPHA parameter.

A lower cut on the shower size of 2000 photons has been applied to select high energy showers for which a standard analysis based on the Hillas parameters is straightforward. However this increases substantially the analysis threshold as respect to the trigger threshold.

2.1   Crab Nebula

The Crab Nebula is a steady emitter at GeV and TeV energies. The γ-ray emission is produced by Inverse Compton (IC) scattering of a population of electrons that are accelerated in the plerion around the central pulsar. The spectrum of this source has been measured in the GeV range by EGRET and at energies above 300 GeV by a number of Cherenkov telescopes. The expected level of emission between 30 and 300 GeV makes it into an excellent calibration candle for MAGIC.

The Crab Nebula was observed during the winter months for about 20 hours under very different weather and instrumental conditions. A sample of Crab Nebula data of 60 minutes livetime at low zenith angle was selected. Fig. 3 displays the distribution of the *alpha* Hillas parameter for the ON and the
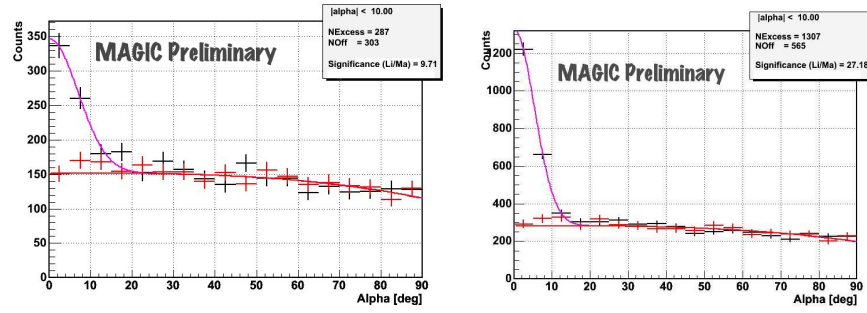
Figure 3: Alpha plot for the selected sample of Crab data (left) and for Mrk 421 data (2004/03/15).

corresponding OFF data. An excess is clearly visible at low *alpha*s. A signal of 287 gamma candidate events was observed over an expected background of 303 events corresponding to a significance of $\sim 10\sigma$.

2.2 Mrk 421

Mrk 421 is one of the so-called TeV BL Lacs that have been detected above 100 GeV. It undergoes the fastest flares that have been observed at these energies, with flux doubling times as short as 20 minutes. The very high energy emission is attributed to IC scattering of electrons that are accelerated in the base of the jet. The IC peak of the spectral energy distribution is probably around ~ 100 GeV. During 2004 the source has undergone an episode of intense flaring in X-rays. Since the correlation between the X-ray and the high energy emission is well established, this source was also an excellent candidate for MAGIC.

A small sample of 96 minutes in optimal conditions (night of March 14/15 2004) was analyzed. A total of 1307 excess events was observed over an expected background of 565 events. The significance of the detection is around 27σ. The excess in the alpha distribution was clearly visible even before any cuts. A false method analysis has confirmed that the detection and the position of the excess coincide with the source position after pointing corrections.

3 The Future

MAGIC as it stands now has always been thought as the first of a series of instruments aimed at reducing the energy threshold and increasing the sensitivity in the GeV energy range. The second instrument in this series is already under construction. It will have a reflector of the same size of

Figure 4: Artistic view of the future MAGIC installations in La Palma.

MAGIC but will incorporate a number of new techniques that will improve
its performance [5] like a fast digitizing system (with $>$2 GHz sampling rate),
light detectors with increased efficiency (e.g. HPDs or arrays of Geiger mode
SiPM). The frame for the second telescope is already under construction and
will be delivered to La Palma in 2005. The third instrument is ECO-1000 [6, 7],
a Cherenkov telescope with 1000 m^2 reflector surface (roughly four times larger
than MAGIC). ECO-1000 intends to take the Cherenkov Telescope technique
to its extreme and reduce the threshold down to 5 GeV with a sensitivity of
$\sim$3$\cdot$10^{-10}cm^{-2}s^{-1}. This is an energy range where it fully overlaps detectors
on board satellites like GLAST. Due to its large collection area and high flux
sensitivity, ECO-1000 is the ideal instrument to complement GLAST's huge
field of view in the study of transient sources.

4   Conclusions

The MAGIC telescope is a second generation Cherenkov telescope that
incorporates many technological improvements to explore the 10-300 GeV
energy window. Just after few months from installation and even if it is still
in the commissionig and calibration phase, the telescope has already detected

two very high energy sources, Crab and Mrk 421, with high significance. All the telescope sub-systems are working at their nominal performance, and are now undergoing extensive checks.

An estimate of the energy threshold of the telescope during this observation of the source's γ-ray flux is under way. An optimization of the selection cuts, e.g. the Cherenkov pulse time profile, is currently under study in order to improve the significance detection and to lower the analysis energy threshold.

MAGIC is now entering the normal regular operation. In the following months, the final system calibration will be over and the telescope will enter the discovery phase.

Acknowledgements

References

[1] J.A.. Barrio et al., The MAGIC Telescope Design Report, MPI Institute Report MPI-PhE/98-5 (March 1998)

[2] D. Bastieri et al., A Two Level Pattern Trigger for the MAGIC Telescope, Nuclear Instr. and Meth., A 461:521-523, 2001

[3] D. Paneque et al., A method to enhance the sensitivity of photomultipliers for Air Cherenkov Telescopes, Nuclear Instr. and Meth. A, in press.

[4] Fegan D. J., Gamma/hadron separation at TeV energies, J. Phys. G, 23:1013–1060, 1997.

[5] R. Mirzoyan et al., Technical Innovations for the MAGIC project, Proc. International Cosmic Ray Conference, Tokyo, 2003.

[6] Merck M. et al., Extending The Cherenkov Technique Down To An Energy Threshold of A Few GeV: The Ultimate Instrument For Ground-Based Gamma-Ray Astronomy, Proc. International Cosmic Ray Conference, Tokyo, 2003.

[7] Baixeras C. et al., Design studies for a European Gamma-ray Observatory, Preprint astro-ph/0403180

CANGAROO: OUTCOMES AND PROSPECT

Tadashi Kifune [a]

[a] *Faculty of Engineering, Shinshu University, Wakasato 4-17-1, Nagano, Nagano 380-8553, Japan*

Abstract

The CANGAROO project has been in operation over 10 years in Woomera, South Australia, searching for TeV γ-ray sources in the inner Galaxy. Discussed in this paper are the present status of TeV γ-ray emission from Galactic sources and prospect of the southern sky observation. Detection of TeV γ-rays such as from supernova remanants has provided key to locate the sites of accelerating cosmic rays, however, presenting questions and problems which are to be solved by the observations by CANGAROO III and H.E.S.S. projects.

1   Introduction

The window of seeing the Universe with VHE (very high energy) γ-rays was opened, thanks to the break-through about fifteen years ago. The use of IACT (imaging air Čerenkov telescope) has given the first firm evidence of TeV γ-ray signal from the Crab nebula [29], followed by discoveries of other sources of VHE γ-rays. The CANGAROO telescope was the first IACT in the southern

hemisphere and utilized to observe inner Galaxy where majority of acceleration sites of cosmic rays are to exist and to be found as sources of VHE γ-rays.

The current sensitivity of detecting VHE γ-rays is around $\sim 10^{-12}$ erg s^{-1} cm^{-2}, as determined by the area, $S \approx 10^8$ cm^2, of atmospheric Čerenkov lights illuminating on the ground and typical observation time $\sim 10^4$ s to accumulate sufficient number of γ-rays against backgrounds. The detection area S remains approximately constant and independent of γ-ray energy around ~ 1TeV. The method of IACT, thus, can be used even more effectively at lower γ-ray energies, since the energy spectrum of γ-ray photons $\propto E_\gamma^{-\alpha}$ with $\alpha > 2$ ensures more intense γ-ray fluxes at lower energies and γ-ray sources would exist more abundant at lower energies. Consequently, to reduce threshold energy of detectable γ-ray as low as or below 100 GeV is considered as the most promising way along which ground-based γ-ray astronomy will prosper. H.E.S.S. and CANGAROO projects have started operation of a system of IACTs of aperture $\sim$10m or larger with angular and energy resolution improved by stereoscopic observation.

2   Galactic Sources and CANGAROO Project

2.1   CANGAROO

The start of CANGAROO project is traced back to observation of atmospheric Čerenkov lights by three mirrors of diameter 2m, attempting to detect VHE γ-rays from SN1987A within a year after the supernova explosion. To improve and replace the observation of "drift scan" mode that can not track targets, a second-hand optical telescope of 3.8m diameter was given to the project kindly by National Astronomical Observatory of Japan. In order to fully utilize the good focusing property of the parabolic mirror, which is much better than one arcminute, the telescope was converted to IACT by installing a camera of 220 photomultiplier tubes to image atmospheric Čerenkov lights [10].

The observation with the 3.8m telescope started in 1992 and this phase of the project is called CANGAROO I. The threshold energy of detectable γ-rays was higher than 1 TeV though it had good angular resolution. To persue larger light collection area for lower γ-ray energy was of prime importance, and planned to construct was a new telescope of 7m diameter, which is composed of spherical mirrors of 80cm diameter. The 7m telescope commenced operation in 1998 and was later enlarged from 7m to 10m in 2000 by adding more number of mirrors. This period corresponds to CANGAROO II. Three more telescopes of 10m diameter were constructed to provide stereoscopic observation by four 10m telescopes. Operation of all the four telescopes was started in April 2004 as CANGAROO III.

2.2 General features of VHE γ-ray data and CANGAROO results

SNRs (supernova remnants) are considered to be the site of accelerating cosmic rays up to $\sim 10^{15}$eV and, as a result, are expected to emit VHE γ-rays. The EGRET result of 100MeV$\sim$10GeV γ-rays, of the Compton Gamma Ray Observatory launched in 1991, was thought to have prepared the targets for VHE γ-ray observation to aim at: Several unidentified EGRET sources are associated with SNR within its positional error circle and the energy spectra of γ-rays are hard with the power exponent consistent with ~ 2.0 as predicted for strong shock acceleration. The flux is, when extrapolated to TeV energy, high enough to be detectable. Observations, however, failed in detecting TeV γ-ray signal [22] from these EGRET sources.

Emission feature appears different between GeV and TeV γ-ray sources also in other types of objects: As for pulsars, GeV γ-rays are modulated by pulsar period as emitted from the pulsar magnetosphere, while TeV γ-rays are not modulated and interpreted as from pulsar nebula: In the case of active galactic nuclei, TeV blazars are rather a weak source of GeV γ-rays. The tendency of no correlation between GeV and TeV intensity can be attributed to radiation spectrum from electrons, as indicated by Fig.1. VHE γ-ray sky shines bright owing to abundant energetic electrons. In order to infer the
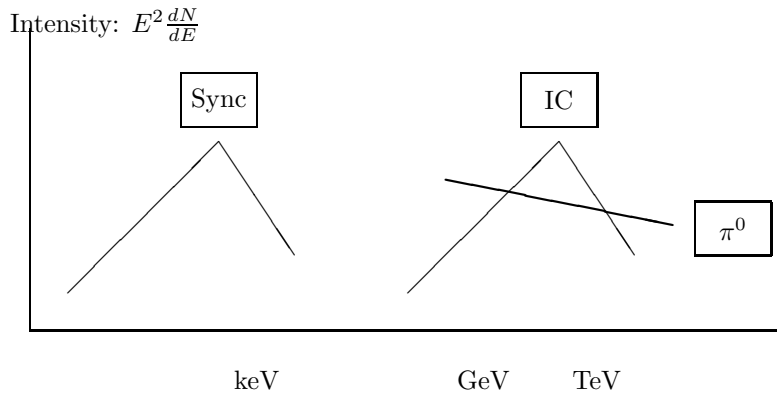
Figure 1: Schematic view of spectral energy distribution of TeV γ-ray sources. Hadronic γ-rays indicated by "π^0" are expected to have a monotonous spectrum from GeV to TeV energy in contrast to the case of electrons, which is characterized by two peaked distributions of synchrotron ("Sync") and inverse Compton processes ("IC"). In the vertical axis is plotted $E^2\,dN/dE$, where E and N are the energy and the number of photons, respectively.

mechanism of radiating TeV γ-ray, the first thing to try is to fit observed γ-ray flux with the spectral energy distribution of synchrotron and inverse Compton radiations, which is schematically illustrated in Fig.1. However, such a fit is a simplified view, and it is optimistic to expect that spectral energy distribution can be well calculated and fit presizely by the two energy spectrum of synchrotron and inverse Compton radiation. Magnetic field is generally not constant and uniform throughout emission region, the main emission regions of the two radiations may be generally deviated from each other, and other more effects. In fact, it is difficult to adjust parameters to make the observed VHE γ-ray flux consistent with the X-ray intensity in the case of PSR1706-44[1]. The true mechanism remains unclarified.

If radiation is from electron, TeV γ-ray sources are expected to be found more likely among X-ray bright objects rather than bright GeV sources, as Fig.1 explains. Thus, the target which CANGAROO chose was changed from EGRET sources of GeV γ-ray emission to X-ray bright SNRs of non-thermal energy spectrum,

Listed in Table 1 are the objects CANGAROO observed with results available in publication. The three pulsar nebulae in Table 1 appear disimilar to "the standard source", Crab nebula. In the case noted as Vela pulsar, VHE γ-rays could not be detected from the pulsar position but from a place deviated to the south-east by $0.13°$ [30]. It may be more adequate to classify the detection, not as pulsar nebula, but as "unidentified source" like TeV J2032+4130 in Cygnus region [3] and the emission near PSR1259-63 which H.E.S.S. observed [12].

The first report of VHE γ-rays emitted from SNR was from observation with the CANGAROO 3.8m telescope, on the bright spot of nonthermal X-rays in the north-west rim of SN 1006, and then followed by RXJ1713.7-3946, which was discovered as a X-ray bright SNR that resembles SN 1006 by the Rosat All-Sky Survey.

Interpretation of VHE γ-rays from the two SNRs is in dispute. The observed VHE γ-ray flux and spectral energy distribution of SN 1006 can be made consistent with synchrotron radiation in X-ray band, if magnetic field is as weak as $B \sim 6\mu G$, by assuming that γ-rays are from inverse Compton radiation of electrons colliding against 2.7K microwave background photons. Against this interpretation, it is argued that magnetic field B as strong as $\sim 100\mu G$ is preferred as *physically plausible* and the observed γ-rays are attributed to hadronic origin [4]. The spectral energy distribution of RXJ1713.7-3946 appears difficult to be fit by the synchrotron and inverse Compton radiation scheme, and was explained that VHE γ-rays observed are likely to be π^0 decay γ-rays from hadrons[9]. However, mutual cosistency among the multi wavelength data was argued to cast skepticism on the hadronic model [5]. Thus, widely accepted conclusion is left to future.

Table 1: CANGAROO results in publication

object	object[a]	phase/reference[b]	other group[c]
Crab	PN	CI[24]	many groups *e.g.*[29]
PSR1706-44	PN?	CI[16], CII[17]	D[6]; H−[11]
Vela	PN?	CI[30]	H−[12]
PSR1509-58	PN?	CI(?)[23]	
PSR1259-63	BP	CI, CII(−)[15]	H+[11]
W28	SNR?	CI(−)[22]	
SN1006	SNR	CI[25]	h[28], H−[11]
RXJ1713.7-3946	SNR	CI[18], CII[9]	H+[12]
Cen A	RG	CI(−)[21]	
PKS2155-304	blazar	CI(−)[20]	D[7], H+[8]
Mrk 421	blazar	CII[19]	many groups
NGC253	SBG	CII[13]	H−[12]
Galactic Center	?	CII[26]	H+[12]

(a) PN: pulsar nebula, BP: binary pulsar, RG: radio galaxy,
SBG: star burst galaxy
(b) CI, CII and CIII stand for the phase of CANGAROO project.
The mark (−): upper limit result, mark (?): marginal detection
(c) D: Durham. h: HEGRA. The mark H+ and H− indicate
H.E.S.S. results of confirming signal and upper limit, respectively

2.3 Origin of cosmic rays and prospect for ground-based γ-ray astronomy

The total number of VHE γ-ray sources is still ~ 10, but they consist of several different types of objects. In order to understand the processes of particle acceleration and VHE γ-ray radiation, more sources are required for each type of objects. Extended emission of TeV γ-rays has not yet detected from the Galactic disk, leaving it still unclear if contribution of point-like objects like SNRs could well explain cosmic rays which are confined in the Galactic disk with energy spectrum up to the knee energy of $\sim 10^{15}$ eV. It is necessary to compare the energy spectrum of γ-rays beyond multi TeV energy with cosmic ray spectrum. However, observation of γ-rays as high as 100TeV is difficult, leaving such attempt as unchallenged one of the frontiers of VHE γ-ray astronomy.

In longer wavelengths bands, many radiation sources reside below the sensitivity of IACT $\sim 10^{-12}$ erg s^{-1} cm^{-2}, suggesting that a considerable number of unknown VHE γ-ray sources are hidden at intensities weaker than the flux $\sim 10^{-12}$ erg s^{-1} cm^{-2}. Detection sensitivity of GeV γ-ray instruments

of $S \approx 1\text{m}^2$ is no better than that of IACT in VHE band, however the FOV (field of view) of GeV instruments is $\sim 1\text{sr}$, which is much larger than ~ 1 msr of IACT. The wide FOV has enabled longer exposure time on each object, resulting in ~ 300 sources which exceeds the number of TeV γ-ray sources by about one order of magnitude. IACT with larger FOV is an interesting next step of possibilities by which VHE γ-ray observation expands.

2.4 Southern sky and prospect of Galactic sources

The southern sky of VHE γ-rays is now viewed also by H.E.S.S.. However, some of CANGAROO results, for examples, VHE γ-rays from SN1006 and PSR1706-44 are so far not confirmed by H.E.S.S. [11]. In the case of GC (Galactic Center) and RXJ 1713.7-3946, the energy spectra considerably differ between CANGAROO and H.E.S.S. results[12].

There is still room of uncertainties in IACT technique. Fluxes estimated are, in general, affected by systematic errors in the procedures of data reduction; estimation of effective detection area, energy of γ-rays etc. On the other hand, X-ray emission from SN 1006 and RX J1713.7-3946 show a structure of extended emission having bright thin long filaments and spots [27]. VHE γ-rays are also likely to have a similar morphology but not exactly the same with X-rays. However, angular resolution of CANGAROO I and II was not good enough to match the X-ray map. The TeV γ-ray flux of SN 1006 was estimated by assuming point-like emission, and systematic error would change depending on unknown angular structure of γ-ray emission.

Detection of different fluxes from a common source are often caused by time-variable radiation. Angular spread of $\Delta\theta \sim 1'$ corresponds to $\sim 0.3\text{pc}$ at distance of 1kpc distance. Emission from this size, in principle, can vary during time scale as short as a year. In the case of plerions, variability of such time scale may be caused by pulsar and/or compact nebula.

Particle acceleration is believed to continue in SNRs for $\sim 10^3$ years or longer and to maintain stable γ-ray emission. Time scales, such as acceleration rate τ_{acc}, the life time τ_E of energy loss (in the case of electrons) and τ_{esc}, the escape time to outer region, are presumably balanced against each other, $\tau_{acc} \approx \tau_{esc}$, or τ_E, after averaged over the whole region of SNR, so that the process of acceleration and radiation stays stationary. However, morphology of arcminute scale of X-ray emission map implies that the time scales, τ_E and τ_{esc}, vary from place to place inside SNR. For examples, the synchrotron life time of electron is given by $\tau_{E,sync} = 3 \times 10^{16} \cdot B_{-6}^{-2} E_{10TeV}^{-1}$ sec, and the escape time τ_{esc} from a region of size x can be described as $\tau_{esc} \approx 3 \times 10^8 E_{10TeV}^{-1} B_{-6} x_{0.1pc}^2$ when Bohm diffusion assumed, where B_{-6}, E_{10TeV} and $x_{0.1pc}$ are magnetic field in μG, particle energy in the unit of 10TeV and size in 0.1pc, respectively. The electron life time can be as short as a year in the regeon of B as strong as 1mG, and, the transport time τ_{esc} can be a few years for a small size region of

~ 0.1pc and at weak magnetic field of $B \approx 1\mu$G in contrast to τ_E. As a result of such spatial variation of environmental conditions, the acceleration rate τ_{acc} could be affected to vary with position and time. Local intensity of VHE γ-rays from a bright small area may suffer from variation during observation period. Such possibility is to be examined by observation.

3   Summary

Galactic sources of VHE γ-rays have been studied by CANGAROO project for about 10 years, with VHE γ-ray sources reported as listed in Table 1. Among them, VHE γ-ray detection from SNR has presented key to solve the origin of cosmic rays. However, the number of SNRs reported to emit VHE γ-rays is only 3 until now, including Cas A which was detected by HEGRA group [2], and the intensity of diffuse VHE γ-rays from the Galactic disk yet remains to be observationally determined. We have still a long way to go before understanding from what types of objects and in what way cosmic rays are supplied and propagate, how and with what time scale and energy dependence they escape out of the Galactic disk. Operation of the system of four telescopes of CANGAROO III has been started in April 2004. The stereoscopic observation, together with the H.E.S.S.[12] project, will provide us with map of VHE γ-ray emission in angular accuracy of arcminutes. Comparison of emission morphology between X-ray and VHE γ-ray will be the main important task of IACT in the years to come, The results enable us to infer distribution of magnetic field, diffusion coefficient and so on. These informations will prepare answer for the intensity map and propagation of cosmic rays within each source and throughout the Galactic disk, finally to understand the meaning of the well known cosmic ray energy spectrum of $\propto E^{-2.7}$.

Discovery of unidentified sources of TeV γ-rays indicates that a wealth of unknown phenomena are hidden in the VHE γ-ray sky. *Unexpected discoveries are expected* from observations with $\sim 1'$ angular resolution and wide FOV. VHE γ-ray astronomy will continue to be exciting, new field.

References

[1] F.A. Aharonian, A.M. Atoyan, T. Kifune, *MNRAS*, 291, 162 (1997)

[2] F.A. Aharonian et al., *Astron Ap*, 370, 112(2001).

[3] F.A. Aharonian et al., *Astron Ap*, 393, L37(2002).

[4] E.G. Berezhko, L.T. Ksenofontov, H.J. Völk, *Astron Ap*, 395, 943(2002)

[5] Y.M. Butt et al., *Nature*, 418, 499(2002), O. Reimer, M. Pohl, *Astron Ap*. 390, L43(2002)

[6] P.M. Chadwick et al., *Astroparticle Physics*, 9, 131 (1998)

[7] P.M. Chadwick et al., *Ap J*, 513, 161 (1999)

[8] A. Djannati-Atai et al., *Proc. 28th Int. Cosmic Ray Conf. (Tsukuba)*, 5, 2575 (2003)

[9] R. Enomoto et al., *Nature*, 416, 823 (2002)

[10] T. Hara et al., *Nucl. Inst. Meth. in Phys. Res. A*, 332, 300 (1993)

[11] W. Hofmann, *talk in this conference* (2004)

[12] W. Hofmann, to appear in *Proc. of Int. Workshop γ2004(Heidelberg)* (2004)

[13] C. Itoh et al., *Astron Ap*, 396, L1 (2002), C. Itoh et al., *Astron Ap*, 402, 443 (2003)

[14] A. Kawachi et al., *Astroparticle Physics*, 14, 261 (2001)

[15] A. Kawachi et al., *Ap J*, 607, 949 (2004)

[16] T. Kifune et al., *Ap J*, 438, L91 (1995)

[17] J. Kushida et al., *Proc. 27th Int. Cosmic Ray Conf. (Hamburg)*, 438, L91 (2001)

[18] H. Muraishi et al., *Astron. Ap.*, 354, L57 (2000)

[19] S. Okumura et al., *Ap J*, 579, L9 (2002)

[20] M.D. Roberts et al., *Astron. Ap.*, 337, 25 (1998), *Astron. Ap.*, 343, 691 (1999)

[21] G.P. Rowell et al., *Astroparticle Physics*, 11, 217 (1999)

[22] G.P. Rowell et al., *Astron. Ap.*, 359, 337 (2000)

[23] T. Sako et al., *Ap J*, 537, 422 (2000)

[24] T. Tanimori et al., *Ap J*, 429, L61 (1994), T. Tanimori et al., *Ap J*, 492, L33 (1998)

[25] T. Tanimori et al., *Ap J*, 497, L25 (1998)

[26] K. Tsuchiya et al., *Ap J*, 606, L115 (2004)

[27] *e.g.* K. Uchiyama et al., *Ap J*, 571, 866 (2002)

[28] Vitale V. et al., *Proc. 28th Int. Cosmic Ray Conf. (Tsukuba)*, 4, 2389 (2003)

[29] T.C. Weekes et al., *Ap J*, 429, L61 (1994)

[30] T. Yoshikoshi et al., *Ap J*, 487, L65 (1997)

THE SOLAR TOWER ATMOSPHERIC CHERENKOV EFFECT EXPERIMENT

J. Kildea [a], A. Alabiso [b], D.A. Bramel [c], J. Carson [d],
C.E. Covault [b], D. Driscoll [b], P. Fortin [a], D.M. Gingrich [e],
D.S. Hanna [a], A. Jarvis [d], T. Lindner [a], R. Mukherjee [c],
C. Mueller [a], R.A. Ong [d], K. Ragan [a], R.A. Scalzo [f],
D.A. Williams [g], J. Zweerink [d]

[a] *Department of Physics, McGill University, 3600 University Street, Montreal, QC H3A 2T8, Canada*

[b] *Department of Physics, Case Western Reserve University, 10900 Euclid Avenue, Cleveland, OH 44106*

[c] *Department of Physics and Astronomy, Barnard College and Columbia University, New York, NY 10027*

[d] *Department of Physics and Astronomy, University of California at Los Angeles, 430 Portola Plaza, Box 951547, Los Angeles, CA 90095-1547*

[e] *Centre for Subatomic Research, University of Alberta, Edmonton, AB T6G 2N5, Canada.*

[f] *Lawrence Berkeley National Laboratory, MS 50R5008, 1 Cyclotron Road, Berkeley, CA 94720*

[g] *Santa Cruz Institute for Particle Physics, University of California at Santa Cruz, 1156 High Street, Santa Cruz, CA 95064*

Abstract

The Solar Tower Atmospheric Cherenkov Effect Experiment (STACEE) is a ground-based atmospheric Cherenkov telescope for the detection of very high energy gamma rays from Galactic and extra-galactic sources. By utilizing the large collection area provided by the solar mirrors of the National Solar Thermal Test Facility in Albuquerque, New Mexico, STACEE achieves a low energy threshold, around 100 GeV, for gamma-ray observations. We describe the STACEE detector and detail recent observations and results.

1 Introduction

The Solar Tower Atmospheric Cherenkov Effect Experiment is an atmospheric Cherenkov telescope that uses the facilities of the National Solar Thermal Test Facility (NSTTF) in Albuquerque, New Mexico for the detection of astrophysical gamma rays with energies in the range 50 GeV to $\sim$1 TeV. The NSTTF is a solar power research facility which includes a central receiver tower and an array of heliostats (solar mirrors). For solar power research, the heliostats are used to track the sun and concentrate its light onto the tower. STACEE is one of four atmospheric Cherenkov telescopes which were built to employ the optical facilities of this type of solar energy research installation; the others include CELESTE (the Cherenkov Low Energy Sampling and Timing Experiment) [1], GRAAL (Gamma-Ray Astronomy At ALmeria) [2], and Solar Two [3].

By utilizing the very large mirror area provided by the heliostats of the NSTTF (each heliostat has a surface area of $\sim$37 m^2) to collect the Cherenkov light emitted by atmospheric particle cascades, STACEE achieves an energy threshold of around 100 GeV for the detection of cosmic gamma rays; the energy threshold of an atmospheric Cherenkov telescope scales approximately as $A^{-1/2}$ [4] (A is the mirror area). This relatively low energy threshold, compared to the second generation of imaging atmospheric Cherenkov telescopes, allows STACEE to detect gamma rays in a poorly sampled energy regime, until recently inaccessible to both satellite and ground-based instruments. Furthermore, since the gamma-ray horizon extends further for lower energy gamma rays than it does for higher energy gamma rays, which are attenuated by the Extragalactic Background Light (EBL), STACEE has a richer set of extra-galactic target sources than the more traditional imaging Cherenkov experiments. As such STACEE observations have the potential to address fundamental astrophysical issues such as the unobserved cutoff in the pulsed emission spectra of gamma-ray pulsars and the EBL-induced cut-offs expected in AGN spectra.

2 The STACEE Detector

STACEE was commissioned in several stages, commencing in 1997 and completed in 2001. The first stage, STACEE-32, comprised an array of 32 heliostats and was used to detect the Crab nebula with high statistical significance [5]. The second stage, STACEE-48, completed in 2000 represented an upgrade from 32 to 48 heliostats and included a number of important improvements to the optics and electronics of the detector. STACEE-48 was used to detect flares from the blazar Markarian 421 during the spring of 2001 [6]. The final upgrade of STACEE to 64 heliostats, STACEE-64, was completed in the fall of 2001 and has been in regular operation since.
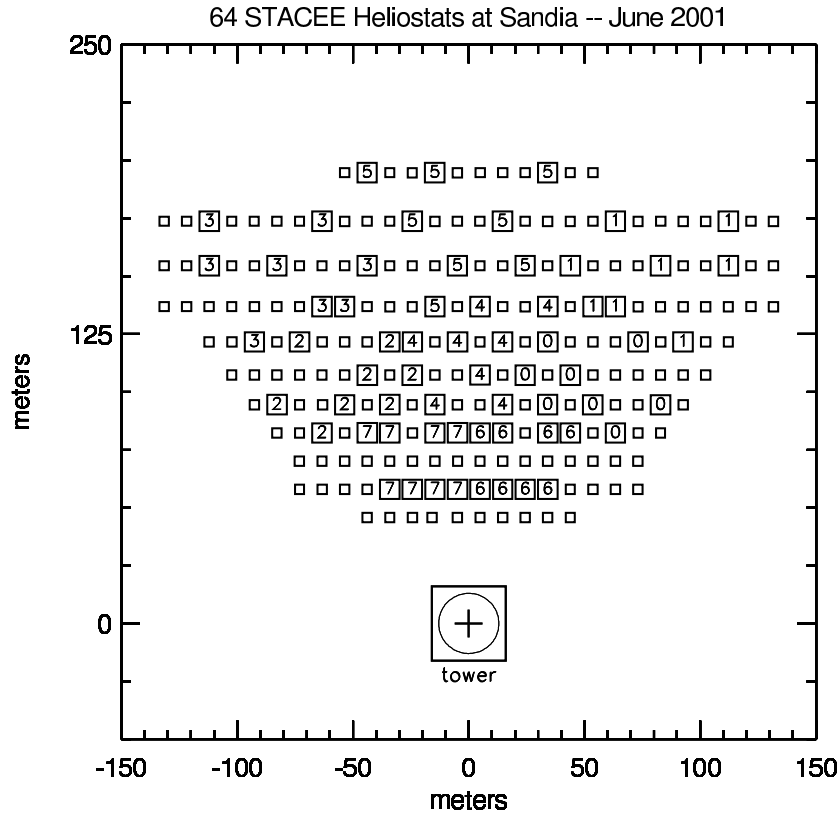

Figure 1: Map of the NSTTF heliostat field currently used by the STACEE experiment. Heliostats are numbered according to the trigger cluster to which they belong. The base of the NSTTF solar tower, which houses the STACEE optics and electronics, marks the origin of the coordinate system.

STACEE is essentially a wavefront sampling atmospheric Cherenkov detector, using as its primary optic an array of 64 heliostats. The heliostats are used to reflect Cherenkov light from extensive air showers onto 5 secondary mirrors located on the 200 ft solar tower adjacent to the heliostat field (see figure 1 for a map of the heliostat field currently used by STACEE). The secondary mirrors in turn focus the Cherenkov light onto a camera of 64 photomultiplier tubes. A one-to-one mapping between heliostats and PMTs allows the Cherenkov wavefront to be sampled independently at 64 different locations in the heliostat field. Extraneous background light from the night sky is reduced by using optical concentrators based on the DTIRC design [7] which widen the aperture of each PMT from 5 to 11 cm and limit their fields of view to include only light from the direction of the target heliostat.

Amplified and AC-coupled signals from the PMTs are fanned out to 8-bit FADCs (one per PMT) and to a three-level digital trigger and dynamic delay system. The first level of the trigger system provides fixed discrimination of the PMT pulses for input into a programmable delay pipeline. Dynamic delays are required to account for the combined effects of the sidereal motion of the source during observations and for the geometry of the Cherenkov wavefront, both of which result in time-of-flight differences for Cherenkov photons detected from different heliostats. The STACEE delay system is a custom built VME and FPGA based unit which provides programmable delays in 1 nanosecond steps over a one microsecond range [8]. The second and third levels of the trigger system demand sub-cluster and inter-cluster coincidences of the delayed pulses within a short time window, typically 16 nanoseconds. Trigger clusters are groups of eight heliostats which are located near each other on the heliostat field; STACEE-64 comprises eight such clusters (see figure 1). Cherenkov events which meet the trigger criteria are recorded for offline analysis, with a typical trigger rate of about 5 Hz.

The installation of FADCs represented a major part of the STACEE-64 upgrade. Fully digitized waveforms from each PMT provide valuable timing and pulse shape information for use in the wavefront sampling technique. The STACEE FADCs are a commercial system produced by *Acqiris, Inc* and are operated using custom software running on a real-time Linux operating system. Each FADC samples at 1 GHz with a dynamic range of 1 V.

STACEE uses non-event information such as atmospheric monitoring data, heliostat tracking data, PMT anode current monitoring data, and laser flasher calibration data in offline calibration and detector stability monitoring. A modification to the STACEE electronics system during the summer of 2004, to move the FADC system closer to the PMTs and to install new high-gain pre-amplifiers at the PMTs will allow STACEE to operate with a faster, cleaner, electronic system at a lower energy threshold during the upcoming seasons. Figure 2 presents an overview of the STACEE electronics and monitoring
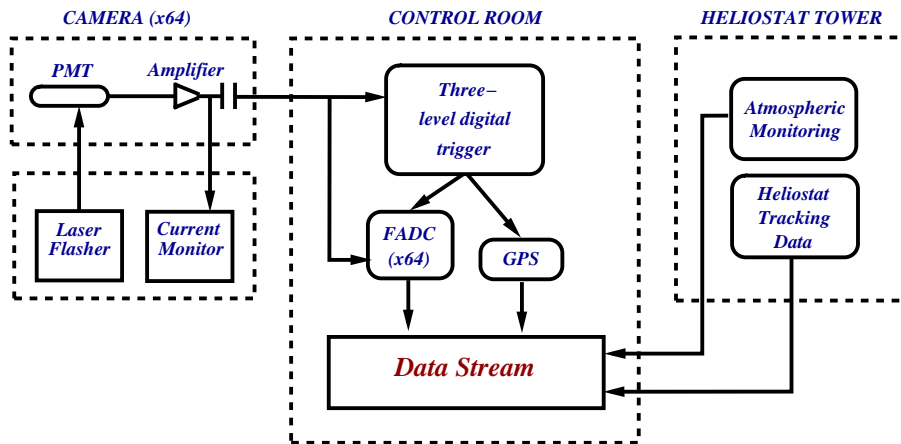
system.

Figure 2: Overview of the STACEE electronics and monitoring system. Cherenkov signals from all 64 PMTs are amplified and fanned out to a three-level dynamic delay and trigger and to a FADC system. Events which meet the trigger criteria are time-stamped by a GPS clock and written to the data stream. Monitoring and calibration data are also periodically written to the data stream.

3 Data Acquisition and Analysis

STACEE observations are conducted in ON/OFF mode. In this mode conterminous observations of the source and a control region of sky, at the same azimuth and elevation as the source, are undertaken. A gamma-ray signal from the source manifests itself as an excess of ON events. Any night-sky background brightness differences between the ON and OFF sky regions, which might otherwise introduce bias into the analysis, are accounted for through the use of software padding; the quieter ON or OFF FADC trace for a particular channel is padded up to the same noise level as its counterpart, through the use of a library of measured FADC noise traces.

As is the case for all atmospheric Cherenkov telescopes, the sensitivity of STACEE for the detection of gamma rays is limited by the abundant background flux of hadronic air showers. Unlike imaging Cherenkov telescopes, however, which reject hadronic events by exploiting pronounced differences between the focused images of gamma-ray and hadronic air showers, wavefront sampling experiments distinguish signal and background events on the basis of

subtle differences in the lateral and temporal profiles of their Cherenkov light pools. Event reconstruction for STACEE involves the fitting of the shower front after the application of necessary timing corrections, the use of simulated optical efficiency values to account for photon losses between heliostat and PMT, and the location of the impact point of the shower core on the heliostat field. An accurate knowledge of the shower core position is vitally important in order to reconstruct the direction of origin of the instigating photon and to allow for an estimate of its energy.

STACEE is currently experimenting with two independent methods for finding the shower core. The first method, detailed in [9], involves the generation of a large number of Monte-Carlo simulated charge templates which represent the charge at each PMT under various conditions. In the simulation process, the CORSIKA air shower simulation package [10] is used for the production of air shower events and custom ray-tracing and Monte-Carlo algorithms are used to simulate data generation. By finding the template which best matches a particular real event both an approximate core location and an estimate of the shower energy for that event are obtained. The templates used are compiled over a large range of energies, zenith angles, azimuth angles, and core locations. The mean core resolution for gamma-rays obtained using this method is about 22 m, when applied to simulated gamma-rays with energies between 20 GeV and 5 TeV generated on a spectrum of index -2.4.

The second method exploits the full pulse profile information provided by the STACEE FADCs and is independent of simulations. It locates the shower core using a simple centre-of-gravity calculation for the early part of the Cherenkov wavefront. Although a rather crude shower core position may be obtained by simply finding the centre-of-gravity of the complete Cherenkov wavefront, truncation of the front due to the finite size of the heliostat field typically degrades the accuracy of the result. It is fortuitous however, that the shape of the Cherenkov wavefront for gamma-ray showers around 100 GeV is approximately spherical. As such, while the complete light pool of a triggering shower can extend beyond the heliostat array, the early part of its Cherenkov wavefront (the first few nanoseconds) are likely to be contained within it. By accounting for the time-of-flight delays from the heliostats to the PMTs, and by applying a type of software trigger condition across each nanosecond sample of the FADC traces, the first nanosecond sample of the shower can be determined. With the beginning of the shower identified, the centre-of-gravity of the first few nanoseconds is calculable. The mean core resolution obtained using this method is $\sim$26 m for the same gamma-ray simulated events used in method 1.

4   Recent Observations

During the 2003/2004 observing season STACEE undertook observations of AGN, plerions/pulsars, and Gamma Ray Bursts (GRBs). In total 184 hours of on-source data were recorded of which 139 were spent observing blazars (namely W Comae, 3C 66A, H1426+428, OJ+287, and Markarian 421), 40 were dedicated to plerions/pulsars (the Crab nebula/pulsar) and 5 were GRB follow-up observations. An equal amount of time was spent on off-source observations.

While recent observations have not yielded any new source detections, the BL Lac object Markarian 421 was detected in a high state during the spring of 2004, at the level of about 6σ in approximately 11 hours of clean data. Work is ongoing to derive a spectrum from these data.

STACEE data on the BL Lac object W-Comae, detected by EGRET (spectral index $\alpha = 1.73$) but not by ground-based imaging telescopes operating above 250 GeV, have been used to produce upper limits on its gamma-ray flux [11]. Using 10.5 hours of STACEE W-Comae data 95% CL upper limits on the integral flux above 100 GeV for leptonic emission models and above 150 GeV for hadronic emission models were obtained. Although the leptonic models predict fluxes below the STACEE limits, extrapolations of the best-fit EGRET power law, and some synchrotron-proton hadronic models, predict fluxes close to or above the STACEE upper limits.

5   Conclusions

STACEE has undertaken regular observations of known and potential sources of TeV gamma rays since the STACEE-64 upgrade of 2001. A number of results have been produced using these data and future improvements are expected as the development of STACEE offline data analyses advances. Exploitation of important charge and timing information provided by the STACEE FADCs is just commencing and should provide significant improvements in sensitivity, through better gamma/hadron separation, for application to archival and future data. Given that STACEE is one of the lowest energy atmospheric Cherenkov telescopes operating in the northern hemisphere, and considering recent hardware improvements, which provide a faster, cleaner, detector with a lower energy threshold, the motivations to continue STACEE observations into the GLAST era (mid 2007) are stronger than ever.

References

[1] de Naurois, M., et al. 2002, Astrophysical Journal, 566, 343.

[2] Arqueros, F., et al. 2002, Astroparticle Physics 17 293.

[3] Tripathi, S. M., et al. 2002, BAAS, 34, 676.

[4] Weekes, T. C. 1988, Phys. Rep., 160, 1.

[5] Oser, S., et al. 2001, ApJ, 547, 949.

[6] Boone, L. M., et al. 2002, ApJ, 579, L5.

[7] Ning, X., Winston, R., & O'Gallagher, J. 1987, Appl. Opt., 26, 300.

[8] Martin, J.-P., & Ragan, K. 2000, Proc. IEEE, 12, 141.

[9] Scalzo, R. A., et al. 2003, Proceedings of the 28th International Cosmic Ray Conference, Tsukuba, Japan.

[10] Heck, D., Knapp, J., Capdevielle, J. N., Schatz, G., & Thou, T. 1999, Rep. FZKA 6019, Forschungszentrum Karlsruhe.

[11] Scalzo, R. A., et al. 2004, Astrophysical Journal, 607, 778.

CELESTE: DETECTING γ-RAYS ABOVE 30 GEV

Philippe Bruel [a]
for the CELESTE collaboration

[a] *Laboratoire Leprince-Ringuet, Ecole Polytechnique, 91128 Palaiseau, France*

Abstract

Since 2002, CELESTE has been running in an extended configuration. I report on the new results we have obtained on the Crab Nebula, Mrk421 and M31. I also present how we have improved our knowledge of the energy scale, and how we have reached a sensitivity of $\sim 6\sigma/\sqrt{h}$ on the Crab.

1 Introduction

The CELESTE experiment [1] (as STACEE [2]) was designed in 1996 to detect γ-rays in the energy range between 30 and 300 GeV, not covered by satellites and Cherenkov imagers. In 1999, CELESTE used 40 heliostats and in 2000 we detected the Crab Nebula [3] with a threshold of 60 GeV and a sensitivity of $\sim 3\sigma/\sqrt{h}$. Since 2000 we have improved several aspects of the experiment: we have increased the number of heliostats from 40 to 53 in 2002, we have reduced the systematic uncertainties and improved the sensitivity. Section 2 describes the CELESTE experiment. Section 3 is devoted to the knowledge of the energy scale. Section 4 describes the new data analysis, and the results on the Crab, Mrk421 and M31 are presented in section 5.

2   CELESTE

The CELESTE experiment uses 53 heliostats of a former solar plant at the THEMIS site (French Pyrénées) to detect γ-rays by sampling the Cherenkov light of their atmospheric showers. Each heliostat (54 m^2) reflects the light to the top of a tower, where the secondary optics and the photomultiplier tubes are located. The secondary optics allows the signals to be kept separate. Winston cones are placed at the entrance of each PMT such that the optical field of view of each heliostat is 10 mrad. This field of view is approximately the angular size of an electromagnetic shower in our energy range and helps to maximize the ratio of Cherenkov to night-sky light.

The heliostats are aimed at a single point, $P_{11\mathrm{km}}$, at 11 km above the ground and on the line passing through the center of the heliostat field in the direction of the observed source. In that configuration, the fields of view of the heliostats converge at the expected maximum point of Cherenkov emission for γ-ray showers in our energy range, allowing us to collect the largest number of photons.

The PMT signals are sent to the trigger electronics and the data acquisition system. The trigger system sums the individual analog signals by groups of 6 to 8 heliostats, and each sum enters a discriminator. A coincidence within 10 ns of at least 3 of the 6 groups is required to acquire the event. At each stage of the trigger, delays compensate for the changing optical path lengths. The trigger threshold is set above the night-sky light noise and is ~ 4.5 photoelectrons per heliostat. The trigger rate is ~ 25 Hz.

Each PMT signal is sent to a 1 GHz FADC (ETEP 301c). When a trigger occurs, a window of 100 samples (~ 100 ns) centered at the nominal Cherenkov pulse arrival time is read out. The photoelectron pulse width is ~ 4 ns.

The observations are made in the On-Off tracking mode: the observation of the source is followed or preceded by an observation at the same declination offset in right ascension by 20 minutes. The Off measurement is then used as a reference for the cosmic-ray background: the On-Off difference gives the source signal.

3   The knowledge of the energy scale

In order to reduce the uncertainty on the energy scale, we have improved our knowledge of the atmosphere and of the optical efficiency of CELESTE.

LIDAR

Since December 2001 a LIDAR [4] has been running at Themis. This LIDAR operates at two wavelengths: 532 nm (green) and 355 nm (UV). The data is used to extract the extinction profile up to ~ 15 km. The LIDAR allows us

to monitor the variations of the atmospheric opacity. So-called dust events (due to thick aerosol layers coming, for instance, from the Sahara) have been observed, in coincidence with other French network stations. During these dust events it has been possible to correlate the LIDAR measurements to the CELESTE trigger rate: the trigger rate clearly decreases as the atmospheric opacity increases, as expected. Apart from monitoring quick changes in the atmospheric conditions, LIDAR measurements have been used to derive a site-specific extinction parametrisation which we use in our simulation.

Photometry studies

The PMT anode currents are read out during observations and can be used to check the optical throughput and improve the quality of our simulation. The alignment of the heliostats are verified by mapping the images of bright stars: we measure these currents while spiraling around the star. Comparing these images to the ones obtained with the simulation showed us that we had to defocus the heliostats in the simulation. Furthermore, when a star is in the field of view of one heliostat, it is possible to compare the expected illumination to the one derived from the current measurement. This study showed us that we had a worse reflectivity than we thought. After these corrections, our simulation is in very good agreement with the observations.

4   Hadron rejection

Our first result on the Crab emission showed us that the discrimination between γ-ray induced showers and hadronic showers with CELESTE was not so easy. This was due to the narrow field of view of 10 mrad, which blurs the differences between electromagnetic and hadronic showers. We have tried to increase our sensitivity in two ways: a new pointing strategy and a new way of using the FADC data.

The veto pointing

In order to increase artificially the field of view, we have modified the pointing scheme: while 41 heliostats still aim the same point $P_{11\mathrm{km}}$, 12 other heliostats, called veto, aim 150 m aside, as seen in figure 1. Since γ-ray showers are more compact than hadron showers, no Cherenkov signal should be collected in the veto heliostats for a γ-ray shower. Thus, measuring a Cherenkov signal in a veto heliostat should be the signature of a hadronic shower. The figure 2 shows the distribution of N_{veto}, the number of veto heliostats with a significant Cherenkov signal, for simulated γ-rays and protons. We can see that $N_{veto} = 0$ for almost 100% of 50 GeV γ-rays, which is the case for only 30% of proton induced showers.
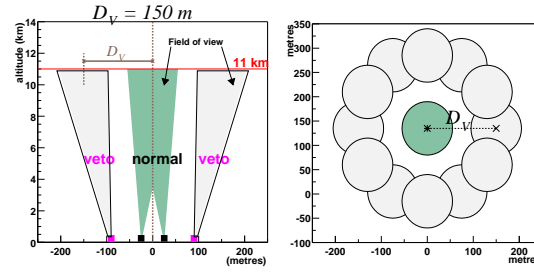
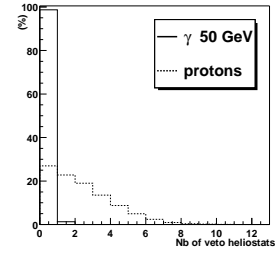Figure 1: Principle of the veto pointing. Side view (left) and top view (right).

Figure 2: N_{veto} for simulated γ-rays and protons.

Summing the individual FADC information

For γ-rays between 30 and 300 GeV, the Cherenkov wavefront is spherical and its center C_{11km} can be assumed to lie somewhere in the plane $\mathcal{P}$ perpendicular to the source direction and passing through the point P_{11km}. The analysis of the individual FADC channels can give the arrival time of the wavefront on each heliostat and it is thus possible to retrieve the position of C_{11km}. In order to check the sphericity of the wavefront, one can use the individual arrival times, or use the width of the sum of the individual FADC channels.

But at very low energy, it is hardly possible to detect any significant Cherenkov signals in the individual channels. In that case, only the sum of the individual FADC windows exhibits a significant Cherenkov signal. We face a problem since summing the individual signals in the most coherent way requires compensating for the propagation delays, which implies knowing the position of C_{11km}.

In order to overcome this difficulty we use the sum to find the position of C_{11km}. For each point C of the plane $\mathcal{P}$, we apply the corresponding propagation delays (*i.e.* assuming that the wavefront is spherical and centered on C) before summing and measure the height H and the width W of the sum. For the right delay corrections, that is to say when $C = C_{11km}$, the sum is the thinnest, or equivalently, the ratio H/W is the largest. The figure 3 shows the sum for one typical real event. The figure 4 shows how the ratio H/W varies in the plane $\mathcal{P}$ for one simulated 100 GeV gamma: this scan clearly exhibits a maximum which gives the position of C_{11km}. This method allows the determination of the core position with a resolution of $\sim$ 15 m.

The figure 5 shows what we obtain for a single simulated 500 GeV proton: the distribution of H/W is not as sharp as for a gamma, as we expect, since the Cherenkov wavefront of a hadron shower is not spherical . We have estimated how sharp the H/W distribution is by evaluating how much smaller H/W
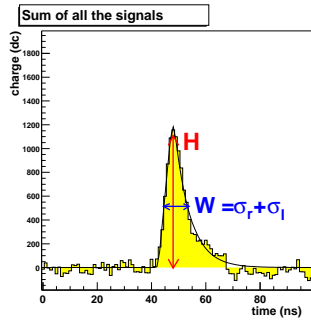
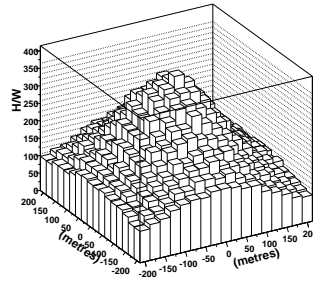Figure 3: The sum of the individual FADC windows for a typical real event.

Figure 4: Scan of H/W over the plane $\mathcal{P}$ for one simulated gamma. The maximum gives the position of $C_{11\text{km}}$.

is than its maximum value 200 m from $C_{11\text{km}}$. The resulting variable ξ is shown in figure 6. For γ-rays, ξ takes low values (corresponding to sharp H/W distributions), for Off data it has larger values.

5   Results

The Crab Nebula

After selection cuts, we have 5 hours of data on the Crab. The data set is small because the weather conditions at Themis have been particularly bad since 2002. The figure 7 shows the ξ distribution for On and Off data, and the On-Off difference. This difference exhibits a clear excess which is reproduced by the γ-ray simulation. Imposing $\xi < 0.35$ gives a significance of 14 σ. Also shown is the On-Off difference of N_{veto} after the $\xi < 0.35$ cut: the excess is mainly due to events for which $N_{veto} = 0$, as expected for γ-rays. Requiring that $\xi < 0.35$ and $N_{veto} = 0$ gives a significance of 13 σ. The sensitivity of this analysis is $5.8\sigma/\sqrt{h}$ and the signal/background ratio is $\sim 30\%$.

The figure 8 shows the energy distribution for a E^{-2} simulated spectrum at the transit of the Crab. We can see that the threshold after analysis cuts is still below 100 GeV, in spite of the optics degradation described in section 3.

Assuming that $E^2 \frac{dN}{dE} = kE^{\alpha + \beta \log_{10} E}$ and using the CAT spectrum [5] above 500 GeV, we have derived the integral flux of the Crab Nebula above 60 GeV: $I(E > 60 \text{ GeV}) = 10.2^{+3.2}_{-3.1} \times 10^{-6} \text{ph m}^{-2} \text{ s}^{-1}$. We have translated this measurement into a point in the $E^2 dN/dE$ plot. The figure 9 shows this new preliminary result, as well as our previous result and the results of EGRET and imagers.

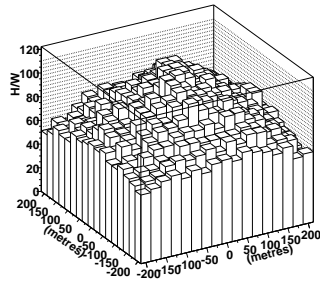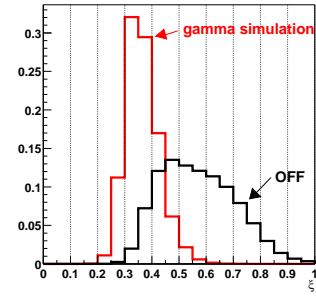Figure 5: Scan of H/W over the plane $\mathcal{P}$ for one simulated proton.

Figure 6: The ξ distribution for simulated gammas and Off data.

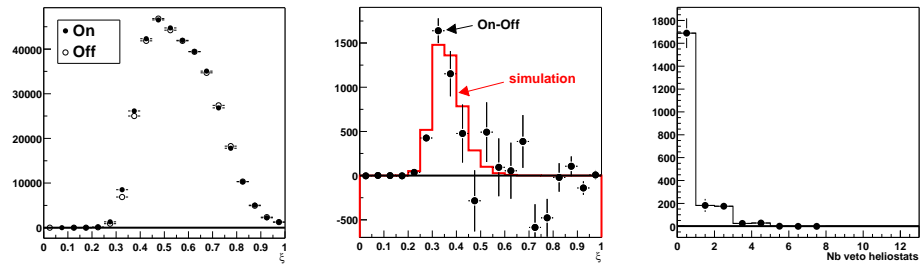Figure 7: Crab data: On and Off distribution of ξ, On-Off distribution of ξ, On-Off distribution of N_{veto} for $\xi < .35$.
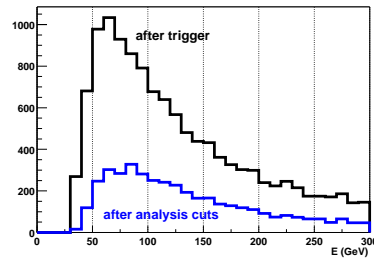

Figure 8: Energy distribution for a γ-ray E^{-2} simulated spectrum.
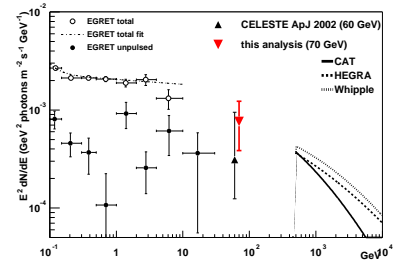
Figure 9: $E^2 dN/dE$ of the Crab.
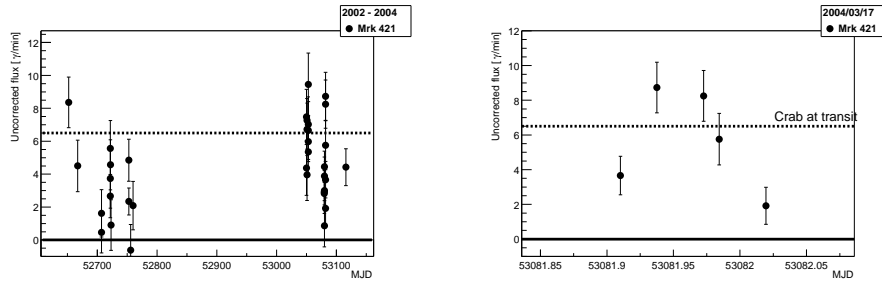
Figure 10: Light curve of Mrk421. Left: from January 2003 and April 2004. Right: one night (03/17/2004).

Markarian 421

After run selection, we have 10 hours of data on the blazar Markarian 421 between January 2003 and April 2004. After the cuts $\xi < 0.35$ and $N_{veto} = 0$, we have an excess of 19 σ. The figure 10 shows the uncorrected γ-ray rate for the entire observation period, and a zoom of a flaring night. It is interesting to note that the sensitivity reached by the new CELESTE analysis allows variability monitoring at the hour level.

Search for dark matter in M31

The possibility of γ-ray emission from M31 has been studied in [6], in the framework of neutralino annihilations. The rotation curve of M31 has been re-analysed with a more realistic mass-to-light ratio, leading to a spherical halo with a NFW profile. The supersymetric model predictions have been obtained with DarkSUSY and SUSPECT, in the minimal supergravity scenario (mSUGRA). In addition to standard phenomenological or theoretical constraints, we require the LSP relic density to verify $0.05 < \Omega_{\chi} h^2 < 0.2$.

After run selection, we have 10 hours of data. After analysis cuts, the On-Off difference is -0.9 σ, and we have derived an upper limit on the γ-ray flux above 50 GeV from M31. This upper limit is ~ 3 orders of magnitude above the predicted fluxes.

6   Conclusions

CELESTE ended the week after this conference, but analyses are still in progress and new results should come next. They will take benefit of the recent improvements: a better knowledge of the energy scale, a better simulation, smaller systematic uncertainties, and a sensitivity of $\sim 6\sigma/\sqrt{h}$ on the Crab.

For instance the new analysis will be applied to the data set obtained before 2002 (Crab, Mrk421 and Mrk501). CELESTE has already made spectrum measurements [7]. The energy resolution is $\sim 20\%$ above 100 GeV. New spectrum measurements of the Crab and Mrk 421 will be obtained with the new data set.

References

[1] E. Paré *et al.*, NIM A490 (2002) 71-89

[2] J. Kildea, this conference

[3] M. de Naurois, J. Holder *et al.*, ApJ 566 (2002) 343-357

[4] J. Bussons Gordo *et al.*, in preparation

[5] C. Masterson *et al.*, Proc. Gamma 2001 Conf. (Baltimore) 590-594

[6] A. Falvard *et al.*, Astropart.Phys. 20 (2004) 467-484

[7] F. Piron *et al.*, Proc. 28th ICRC (Tsukuba 2001) 2607-2610

STATUS OF THE ARGO-YBJ EXPERIMENT

P. Bernardini [a,b]

on behalf of the ARGO-YBJ Collaboration

[a] *Dipartimento di Fisica, Università di Lecce,*
via per Arnesano, 73100 Lecce, Italy

[b] *INFN, Sezione di Lecce, via per Arnesano, 73100 Lecce, Italy*

Abstract

The ARGO-YBJ experiment is devoted to the study of many issues in γ-astronomy and cosmic ray physics. The apparatus design is based on Resistive Plate Chambers operated in streamer mode and assembled in a single layer, fully covering a surface of $78 \times 74~m^2$ (the surface becomes $110 \times 100~m^2$ taking into account a partially instrumented ring). The mounting of the detector is going on in the YangBaJing Laboratory (Tibet, China) at $4300~m$ above the sea level. The present status of the experiment, the performances of the detector and some preliminary analysis of data will be presented.

1   Introduction

ARGO-YBJ is the acronym of *Astrophysical Radiation Ground-based Observatory - YangBaJing* and indicates a telescope optimized for the detection of small size air showers [1, 2] and located at the Yangbajing Cosmic Ray Laboratory (4300 m $a.s.l.$). The detector design is simply a single layer of Resistive Plate Chambers (RPCs) covering a large area and providing a detailed space-time image of the shower front.

Operated at high altitude this detector could image with high sensitivity and efficiency atmospheric showers initiated by primaries with energy in the range 100 $GeV \div 500\,TeV$. Therefore ARGO is a powerful tool to study cosmic γ-radiation at an energy threshold close to the limits of the satellite technology. Data gathered with ARGO will allow to face a wide range of fundamental issues:

- γ-ray astronomy, looking for point-like (galactic and extra-galactic) sources with an energy threshold of few hundreds GeV and for diffuse flux from Galactic plane and SuperNova Remnants;

- Gamma Ray Burst (GRB) physics, extending the satellite measurements over the $GeV - TeV$ energy range [3];

- Cosmic ray (CR) physics [4], that is measurements of proton/antiproton ratio at TeV energy, studies of spectrum and composition around the knee ($E > 10\,TeV$);

- Sun and Heliosphere physics ($E > 10\,GeV$), looking for CR modulation, monitoring the interplanetary magnetic field and observing flares of high energy gammas and neutrons from the Sun.

2   Main detector features and project performance

The active elements of the ARGO-YBJ detector are bakelite RPCs [5, 6] operated in streamer mode, with a mixture of argon (15%), isobutane (10%) and tetrafluoroethane (75%). The detector layout is shown in Fig. 1. The spatial measurement is gathered from strips ($6.5 \times 62\,cm^2$), the fast-OR signal from 8 strips (logical pad) provides the time measurement with a resolution of $\sim 1\,ns$.

The high space-time resolution allows to get a high granularity image of the shower front (an example in Fig. 2). The full coverage allows to decrease the energy threshold without losing shower details, therefore also small showers are detectable with this detector. The pointing resolution is expected to be better than $0.5°$. Moreover the large aperture and the high duty-cycle ensure the continuous monitoring of the sky in the declination band $-10° \div 70°$.
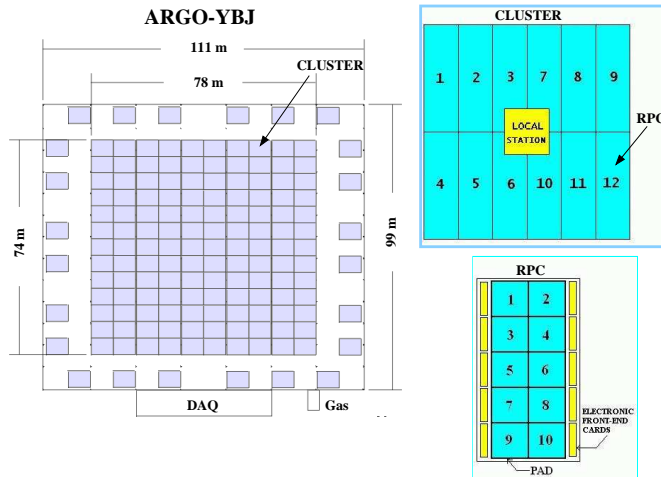
Figure 1: Layout of the detector

Two main kinds of trigger have been designed for the data-acquisition: the 'shower mode' and the 'scaler mode'. In the first one, a minimum pad multiplicity is required on the central carpet, with space/time consistency as for a shower front. In the 'scaler mode' the pad rate is measured from each cluster, with an integration time of 0.5 s. This last DAQ mode is devoted to the apparatus monitoring and the detection of unexpected increases in CR flux, as an effect of GRB, solar flares and so on.

3   Status of the experiment

The construction of the detector slowed up in 2003 because of the Severe Acute Respiratory Syndrome (SARS). Furthermore damages to the front-end electronics due to high density showers have been observed. This problem has been fixed thanks to the insertion of Zener diodes.

In the last months many cross-check measurements have been performed operating RPCs in Italy and in Tibet. Also an RPC telescope has been built in the YBJ laboratory. The goals of these measurements were the optimization of the gas mixture, the fine tuning of the electronics set-up and the monitoring of the RPC efficiency and stability.

Presently 16 cluster are in data-taking for many months with high stability and without significant damages. The RPC operation is also successfully monitored by a Detector Control System (DCS), able to record HV, currents, temperature, humidity, pressure and gas flow. Now the construction of the
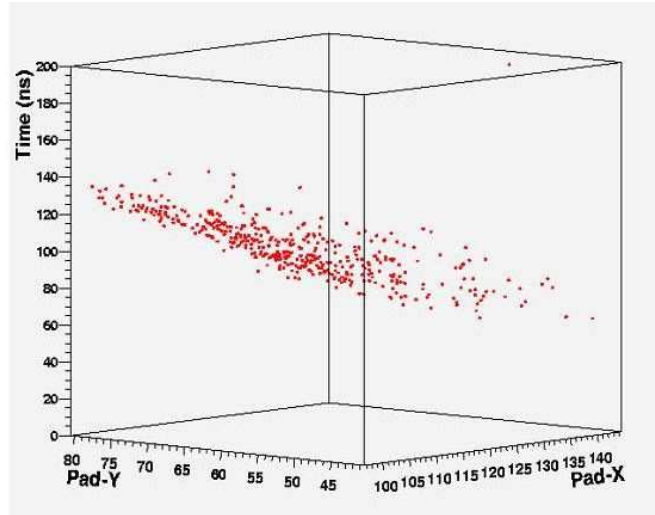
Figure 2: Display of a real event in space-time view

detector is going very fast and 48 clusters are expected to be operating within December 2004.

4 Detector performance and first measurements

Here the data collected in 'shower mode' with 6 clusters (260 m^2), after the modification of the front-end electronics, are presented. The analysis results are in full agreement with those of data collected in the past with 16 clusters, before electronics protection.

Rate measurements

In Fig. 3 differential and integral rates are plotted versus the hit multiplicity. The differential rate follows a power law with slope 2.5. This result demonstrates the physics consistency of the measurement and the agreement with what estimated on the basis of the CR spectrum. Also the rates of the different triggers are the expected ones and the distribution of the time difference between consecutive events (Fig. 4) confirms the regular operation of the detector.

Time calibration and angular resolution

Dedicated runs with high multiplicity trigger (more than 32 hits on each cluster) have been used for a preliminary time calibration. The goal of the procedure
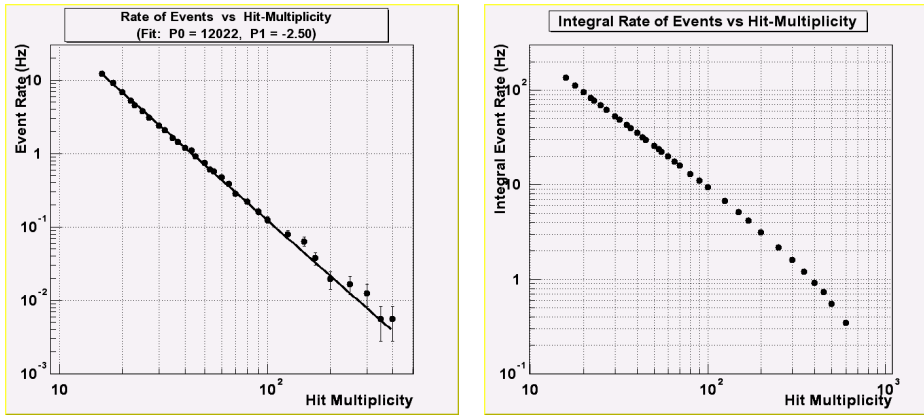
Figure 3: Differential and integral rates versus hit multiplicity (trigger condition: more than 15 hits)
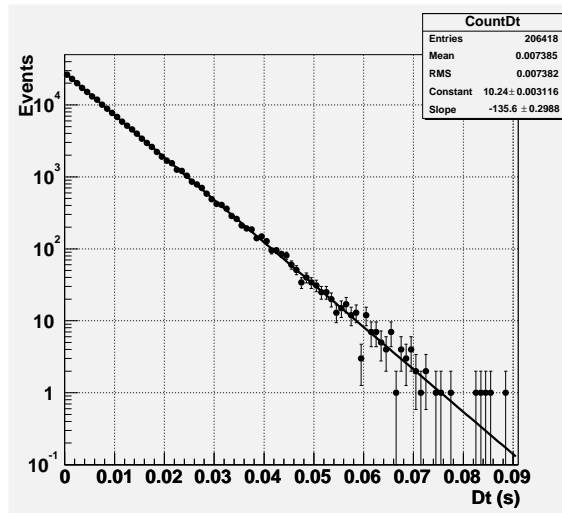
Figure 4: Time difference between events (trigger condition: more than 15 hits on each cluster)
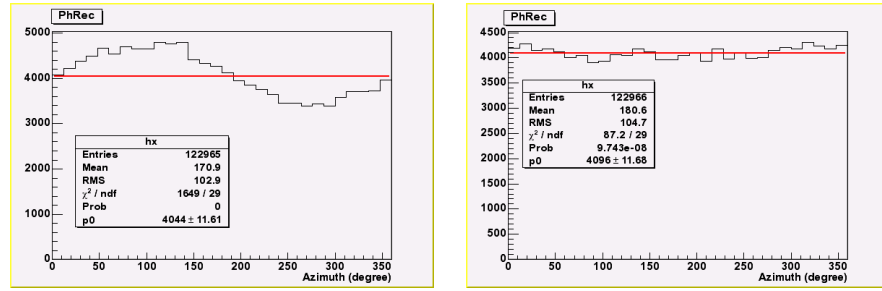
Figure 5: Azimuthal distribution before and after the time calibration. The χ^2 of the uniform fit is used as the estimator of the symmetry of the detector response

was to remove systematical time-offsets among the pads.

Corrections in the range $\pm 4\ ns$ have been introduced to minimize the time residuals, that is the difference between the time measured by the pad and the time of the shower estimated by the planar fit. After these corrections, the peak values of the residual distributions are very close to 0 ($|t_{peak}| < 0.2\ ns$).

The uniformity of the azimuthal distribution is another parameter taken into account in the calibration. A systematic correction of the time measurement has been introduced according to the method suggested in [7]. The effect of this second correction on the azimuthal distribution is shown in Fig. 5. Also the symmetry of the direction cosine distributions improves as an affect of this systematics correction.

The angular resolution of the 6-cluster carpet has been estimated by dividing the detector into two independent sub-arrays ("odd" and "even" pads) and studying the angular difference $\Delta\varphi$ between the reconstructed shower directions. The angular resolution depends on the width of the $\Delta\varphi$ distribution [1] and decreases with the hit multiplicity, as shown in Fig. 6.

Angular distributions of Extensive Air Showers

In the first plot of Fig. 7 the distribution of the reconstructed zenith angle θ is shown. In the second plot the quantity $sec\,\theta - 1$ is displayed. By means of the fit with the function $e^{-\alpha(sec\theta-1)}$ we get $\alpha = 4.678 \pm 0.016$. Then we estimate $(128.3 \pm 0.4)\ g/cm^2$ as attenuation length of showers, in excellent agreement with previous measurements [1].
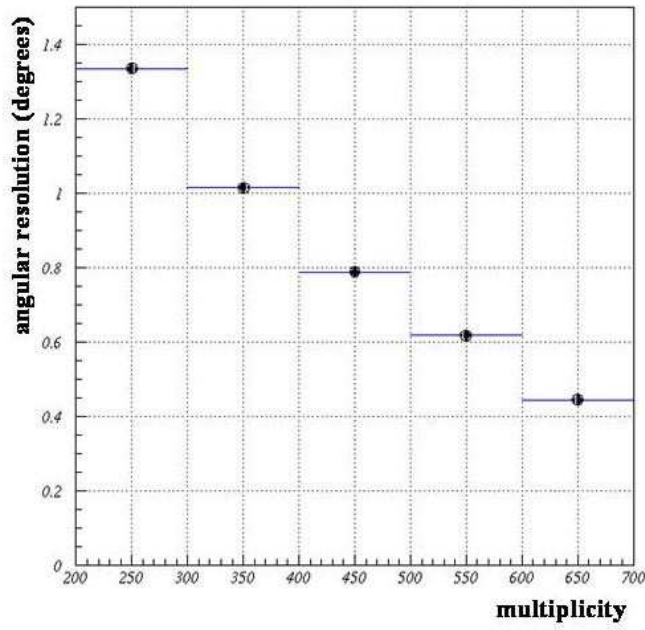
Figure 6: Angular resolution versus hit multiplicity
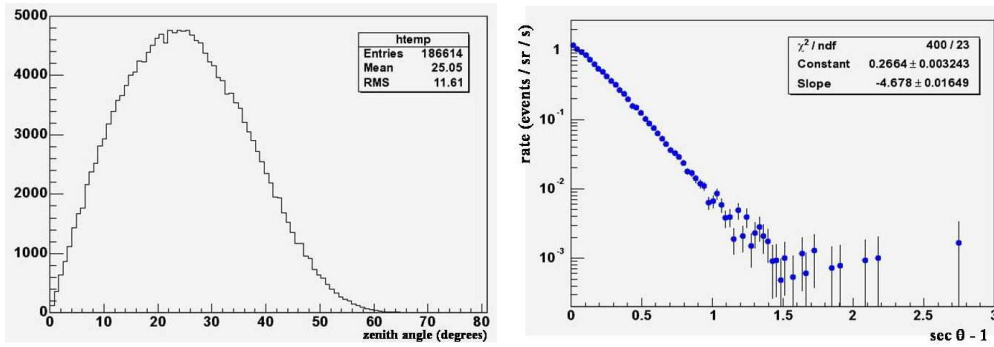
Figure 7: Distributions of the zenith angle θ and of the function $sec\ \theta - 1$

5   Conclusions

The construction of the ARGO-YBJ detector is going on. Some problems in the RPC front-end electronics have been studied and fixed. The data collected with portions of the apparatus have been used to check the detector performances and the analysis codes. The detector works as good as expected. Absolute trigger rates, shape of hit multiplicity distribution and preliminary shower reconstruction are consistent with the CR physics.

We foresee that 48 clusters ($\sim 2000 \; m^2$) will be in data-taking at the end of December 2004 and the central carpet will be completed within the begin of 2006. Stable data-taking and physics runs are expected already at the end of 2004. First physics results are close.

References

[1] C. Bacci et al. (ARGO-YBJ Collaboration), *Astroparticle Physics 17* (2002) 151

[2] ARGO Collaboration, Proceedings of the 25th International Cosmic Ray Conference (Durban), *5* (1997) 265 and 269

[3] ARGO-YBJ Collaboration, Workshop "Gamma Ray Bursts in the Afterglow Era", Rome (1998), in *Astronomy and Astrophysics, Suppl. Series 138* (1999) 597, also astro-ph/9904373

[4] L. Saggese et al. (ARGO-YBJ Collaboration), Proceedings of the 28th International Cosmic Ray Conference (Tsukuba), (2003) 263 [HE.1.2.9]

[5] ARGO-YBJ Collaboration, 6th International Conference on Advanced Technology and Particle Physics, Como (1998), in *Nucl. Phys. B (Proc. Suppl.) 78* (1999) 38

[6] C. Bacci et al. (ARGO-YBJ Collaboration), *Nuclear Instr. and Methods A 443* (2000) 342

[7] A.M. Elø, H. Arvela, Proceedings of 26th International Cosmic Ray Conference (Salt Lake City), **5** (1999) 320 [OG.4.4.07], 324 [OG.4.4.08] and 328 [OG.4.4.09]

DETAILED STUDY OF THE CRAB NEBULA AND PULSAR BETWEEN 500 GEV AND 80 TEV WITH THE HEGRA STEREOSCOPIC SYSTEM OF GROUND BASED GAMMA-RAY TELESCOPES

D. Horns[a], for the HEGRA collaboration[b]

[a] *Max-Planck Institut für Kernphysik, PO Box 103980, 69117 Heidelberg, Germany*

[b] *http://www-hegra.desy.de*

Abstract

The Crab supernova remnant has been observed regularly with the stereoscopic system of 5 imaging air Cherenkov telescopes that was part of the High Energy Gamma Ray Astronomy (HEGRA) experiment. In total, close to 400 hours of useful data have been collected from 1997 until 2002. The differential energy spectrum of the combined data-set can be approximated by a power-law type energy spectrum: $d\Phi/dE = \Phi_0 \cdot (E/\text{TeV})^\Gamma$, $\Phi_0 = (2.83 \pm 0.04_{\text{stat}} \pm 0.6_{\text{sys}}) \cdot 10^{-11}$ ph cm^{-2} s^{-1} TeV^{-1} and $\Gamma = -2.62 \pm 0.02_{\text{stat.}} \pm 0.05_{\text{sys.}}$. The spectrum extends up to energies of 80 TeV and is well matched by model calculations in the framework of inverse Compton scattering of various seed photons in the nebula including for the first time a recently detected compact emission region at mm-wavelengths. The average magnetic field in the emitting volume is determined to be $(161.6 \pm 0.8_{\text{stat}} \pm 18_{\text{sys}})$ μG. The presence of protons in the nebula is not required to explain the observed flux and upper limits on the injected power of protons are calculated being as low as 20 % of the total spin down luminosity for bulk Lorentz factors of the wind in the range of $10^4 - 10^6$. No indications for pulsed emission has been found and upper limits in differential bins of energy have been calculated reaching typically 1-3 % of the unpulsed component.

1 Introduction

Observations of the Crab pulsar and nebula have been carried out in every accessible wavelength band with ground and space based instruments. The source has been established as a TeV emitter with the advent of ground based Cherenkov imaging telescopes with sufficient sensitivity [Weekes et al.(1989)]. The historical lightcurve of the supernova explosion of 1054 A.D. is not conclusive with respect to the type of progenitor star and leaves many questions concerning the stellar evolution of the progenitor star unanswered [Stephenson]. At the present date, the observed remnant is of a plerionic type with a bright continuum emission and filamentary structures emitting mainly in lines in the near infrared and optical range.

The remaining compact central object is a pulsar with a period of 33 ms and a spin-down luminosity of $(\propto \dot{P}^3/P)\ 5 \cdot 10^{38}$ erg s^{-1}. The emitted power of the continuum peaks in the hard UV/ soft X-ray at $\approx 10^{37}$ erg s^{-1} (assuming a distance of 2 kpc). Given the kinetic energy of the spinning pulsar as the only available source of energy in the system, the spin-down luminosity is efficiently converted into radiation. There is no observational evidence for accretion onto the compact object as an alternative mechanism to feed energy into the system [Blackman & Perna(2004)].

Even though the Crab nebula is widely considered as the standard candle of TeV astronomy to calibrate the instruments' response, the object bears many unsolved problems of conversion of spin-down power, particle acceleration, and emission processes that deserve intense studying.

The observations of the the Crab nebula have been carried out with the HEGRA stereoscopic system of imaging air Cherenkov telescopes [Daum et al.(1997)]. The five 8.5 m^2 telescopes located on the island La Palma at 2 200 m height above sea level were operational from 1996 to 2002. The telescopes observed gamma-ray emission above energies of 500 GeV with an unprecedented sensitivity of 10^{-11} erg/(cm^2 s) at 1 TeV after one hour of observation. The angular resolution for individual events is on average better than 0.1° and for sufficiently strong sources like the Crab nebula, the origin of the gamma-rays is limited by systematic uncertainties of 25 arcseconds (0.007°) whereas the statistical error is as small as 3 arc seconds (0.0008°). The relative energy resolution for the analysis carried out here is better than 10 % at energies above threshold and increases to 15 % at threshold energies allowing for reliable and accurate spectroscopy.

2 Observations and data analysis

Throughout the entire life time of the HEGRA experiment, the Crab nebula has been observed regularly accumulating a total of 390 hours of selected observation time. The data are analysed using established techniques for
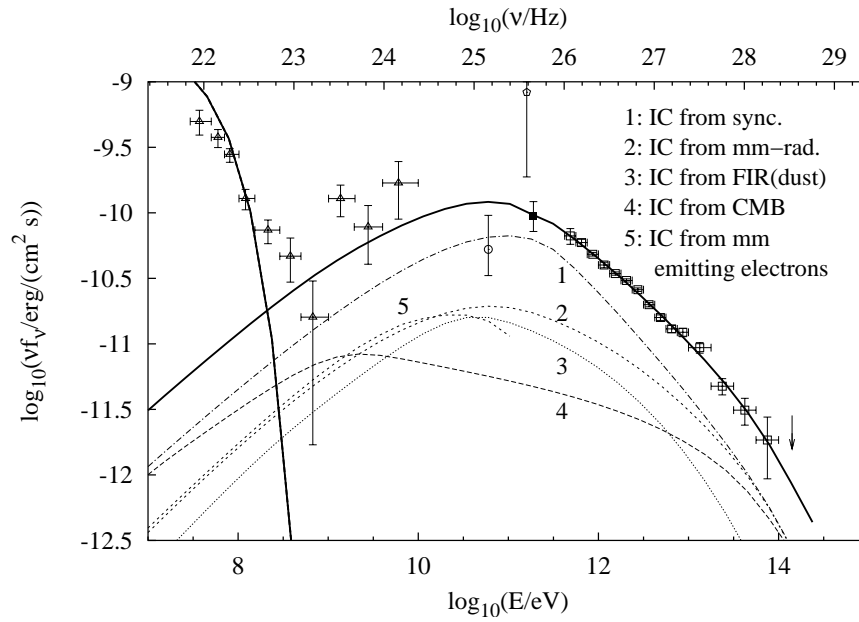
Figure 1: The HEGRA measurements (open boxes) are shown together with a compilation of other measurements and model calculations based upon inverse Compton emission from electrons on various seed photons.

calibration, reduction, and spectral reconstruction (see [Aharonian et al.(2004)] for details). Different event selection criteria have been employed for the various investigations carried out. The analysis described here is the reconstruction of the energy spectrum and search for pulsed emission from the pulsar. The instrument performed remarkably stable throughout the observations setting upper limits on systematic variations on the absolute energy calibration of the detectors to be less than 6 %.

3   Results

The energy spectrum is reasonably well described by a power-law: $d\Phi/dE = \Phi_0 \cdot (E/\text{TeV})^\Gamma$, $\Phi_0 = (2.83 \pm 0.04_{\text{stat}} \pm 0.6_{\text{sys}}) \cdot 10^{-11}$ ph cm^{-2} s^{-1} TeV^{-1} and $\Gamma = -2.62 \pm 0.02_{\text{stat.}} \pm 0.05_{\text{sys.}}$

The HEGRA energy spectrum at high energies is shown together with a compilation of observations in Figure 1. The HEGRA data cover a large dynamical range between 500 GeV and 80 TeV. Note, only observations at X-ray (RXTE and BeppoSAX satellites) and gamma-energies (CGRO satellite)

cover a comparable dynamical range and accuracy with a single instrument albeit with more than one type of detector onboard the satellite. The model calculations shown in Figure 1 include the inverse Compton emission from various seed photons present in the nebula; more details are given in [Aharonian et al.(2004), Horns & Aharonian(2004)]. Note, the representation of the data is following the approach of a spectral energy distribution (νf_ν) to emphasize the energy flux emitted at different energies.
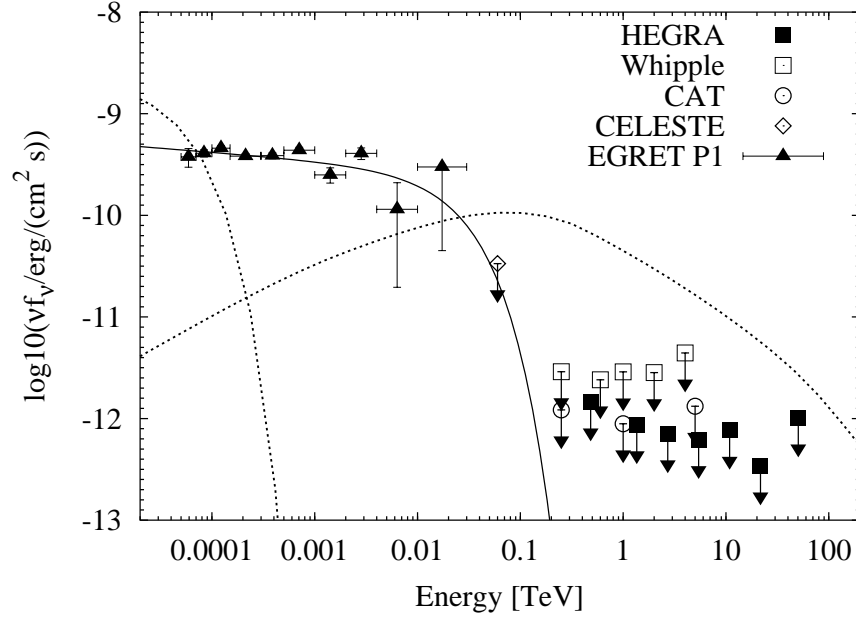
Figure 2: Result of a search for pulsed gamma-ray emission with HEGRA (upper limits indicated by filled squares). The integral upper limits quoted for the CAT, CELESTE, and Whipple group have been converted by assuming a differential spectral index of -2.4 at energies below 1 TeV and -2,6 above 1 TeV. For comparison, the energy spectrum for the main pulse as detected by the EGRET spark chamer is shown by filled triangles. The solid line is fit of a power-law function with photon index $\Gamma = -2.08$ and an exponential cut-off at 25 GeV to the EGRET data and the CELESTE upper-limit as suggested in [Durand(2003)]. The dotted line are the synchrotron and inverse Compton emission of the nebula as given by the model prediction explained in the text.

Besides the steady emission from the nebula, a pulsed component originating from the central compact object is searched for. The pulsed emission could be produced in the outer regions of the pulsar's magnetosphere

where the magnetic field and the ambient photon density is sufficiently low to allow high energy photons to escape the acceleration region.

The search for pulsed emission is carried out assuming that the high energy emission follows the same lightcurve as observed at radio wavelengths where the pulsar periods are studied regularly and the ephemerides are made public [Lyne et al.(2003)]. The analysis method employs a solar barycentric correction and a coherent overlay of the phase information of all events from the direction of the nebula. Besides a Pearson's χ^2-test of the resulting phasogram, more advanced search methods for pulses employing the sequence of phase informations of the events are employed: Rayleigh [Mardia(1972)] and Z_2^2 tests [Buccheri et al.(1983)] have been applied. In the absence of a signal, upper limits on the pulsed fraction during the main pulse are calculated for various energy bins and compared with other results in Figure 2. The upper limits are calculated in narrow energy intervals to look for narrow emission features expected in models where the pulsed emission is strongly suppressed as a consequence of pair production processes on the strong magnetic field and the intense radiation emitted by the pulsar's surface. The absorption effects are strongly energy dependent and may lead to narrow band emission features.

4   Discussion

The measurement of the energy spectrum of the Crab nebula up to the highest photon energies detected is of great importance to probe the composition of non-thermal particles present. Given the synchrotron nature of MeV photons and the observed emission up to 80 TeV, electrons of PeV energies are proven to exist in the nebula. Furthermore, the agreement of the inverse Compton model in the energy region covered by the observations is very good and allows to constrain immediately the average magnetic field to be $(161.6 \pm 0.8_{\mathrm{stat}} \pm 18_{\mathrm{sys}})$ μG. For the model considered, the magnetic field is assumed to be constant throughout the nebula which is a simplification convenient to carry out the calculations. However, given the fact that the bulk of the emission takes place in the downstream region of the standing reverse shock, only little variations of the magnetic field are expected in MHD solutions [Kennel & Coroniti(1984)].

Besides electrons, charged nuclei are generally expected to be accelerated as well. In some models, protons in the wind outflow are believed to be responsible for the acceleration of positrons in the downstream region [Arons(1995)] and inevitably be seen as a narrow energy band emission at high energies [Bednarek & Bartosik(2003), Amato, Guetta, & Blasi(2003)]. An additional component with an admixture of more than 20 % of the spin down power in the form of relativistic protons in the wind is excluded by the data.

References

[Aharonian et al.(2004)] Aharonian, F.A. et al. 2004, ApJ, 614 (in press)

[Amato, Guetta, & Blasi(2003)] Amato, E., Guetta, D., & Blasi, P. 2003, A&A, 402, 827

[Arons(1995)] Arons, J. 1995, in ASP Conf. Ser. 72, Millisecond Pulsars: A Decade of Surprise, ed. A.S. Fruchter, M. Tavani, D.C. Backer (San Francisco:ASP), 257

[Bednarek & Bartosik(2003)] Bednarek, W. & Bartosik, M. 2003, A&A, 405, 689

[Blackman & Perna(2004)] Blackman, E. G. & Perna, R. 2004, ApJ, 601, L71

[Buccheri et al.(1983)] Buccheri, R., Bennett, K., Bignami, G.F. et al. 1983, A&A, 128, 245

[Daum et al.(1997)] Daum, A., Hermann, G., Heß, M. et al. 1997, Astroparticle Physics 8, 1

[Durand(2003)] Durand, E. 2003, Thèse de doctorat, Université Sciences et technologies, Bordeaux I

[Horns & Aharonian(2004)] Horns, D. & Aharonian, F.A. 2004, ESA Special Publication SP-552 Proceedings of the 5th INTEGRAL Workshop in press

[Kennel & Coroniti(1984)] Kennel, C. F. & Coroniti, F. V. 1984, ApJ, 283, 710

[Lyne et al.(2003)] Lyne, A.G., Jordan, C.A, and Roberts, M.E. 2003, http://www.jb.man.ac.uk/~pulsar/crab.html

[Mardia(1972)] Mardia, K.V. 1972, *Statistics of Directional Data*, London: Academic Press

[Stephenson] Stephenson, F.R., & Green, D.A., 2002, (Oxford: Clarendon Press)

[Weekes et al.(1989)] Weekes, T. C., et al. 1989, ApJ , 342, 379

DETECTION OF THE BINARY SYSTEM PSR B1259-63/SS 2883 AT TEV ENERGIES WITH THE H.E.S.S. CHERENKOV TELESCOPES

M. Beilicke[a], for the H.E.S.S. collaboration[b]

[a] *Institut für Experimentalphysik, Universität Hamburg, Luruper Chaussee 149, D-22761 Hamburg, Germany*

[b] *http://www.mpi-hd.mpg.de/hfm/HESS/HESS.html*

Abstract

The first detection of the unique binary system PSR B1259-63/SS 2883 at TeV energies close to its 2004 periastron passage is reported. The observations have been performed with the array of four imaging atmospheric Cherenkov telescopes (IACTs) operated by the High Energy Stereoscopic System (H.E.S.S.) collaboration in Namibia. The observations were motivated by theoretical predictions of TeV emission with an expected maximum near the periastron passage. Following the detection in February/March 2004 the observations have been extended up to June 2004. In this paper the results of the observations between February, 26th and March, 5th 2004 taken before periastron are reported.

1 Introduction

The 48 ms radio pulsar PSR B1259-63 orbits its massive Be companion star SS 2883 ($\sim 10\,M_\odot$) on a highly eccentric orbit ($\epsilon \approx 0.87$) with a period of $\sim$ 3.4 years [1]. The system is located at $\alpha = 13^h 02^m 47^s.68$ and $\delta = -63°50'08''.6$ (J2000.0) at a distance of about 1.5 kpc [2]. The companion star is surrounded by a stellar matter outflow disk which is assumed to be inclined with respect to the orbital plane suggested by pulsar-timing data [3]. The distance between the pulsar and the companion star at periastron is only $\sim 23\,R_*$ whereas the matter disk of the companion star reaches out to nearly $20\,R_*$ (with R_* being the radius of the companion star). This geometry makes the PSR B1259-63/SS 2883 binary system a very unique and interesting object for studying the interaction of a pulsar wind with an environment of – due to the motion – varying matter and photon density.

The PSR B1259-63/SS 2883 system was observed at previous periastron passages in 1994 and 1997 at radio wavelength which yielded detection of only an unpulsed radio component for some weeks around periastron [4]. Also X-ray observations showed orbital dependency of the emission [5, 6] and suggest a synchrotron component produced by an electron population accelerated to very high energies. TeV emission has been predicted by different models: Inverse Compton (IC) scattering of the local companion star photon field by shock accelerated high energy electrons/positrons originating from the pulsar wind leading to TeV γ-emission up to $\sim 10^{-11}\,\mathrm{erg\,cm^{-2}\,s^{-1}}$ at 100 GeV [7]. Additionally, IC scattering in the unshocked pulsar wind can be taken into account [8]. More models exist (see for example references in [18]) partially taking into account the stellar disk geometry and nearly all of them predict a characteristic orbital dependency of the TeV γ-emission.

The PSR B1259-63/SS 2883 binary system has been observed at TeV energies with the CANGAROO experiment for the first time in 1994 with the 3.8 m telescope resulting in indications for TeV γ-ray emission ($\sim 4.8\,\sigma$ in 26.5 h of observations $\sim 120\,$d after periastron, but no signal in 8.6 h of observation near the 1994 periastron) [9]. A third observation campaign was done in 2000/2001 with the 10 m telescope resulting in upper limits of 0.13 Crab roughly 47 d and 0.54 Crab roughly 157 d after the 2000 periastron within 3.2 h resp. 10.4 h of observation [10], see also Fig. 1.

Recent observations at TeV energies have been performed with the 4 imaging atmospheric Cherenkov telescopes (IACTs) operated by the High Energy Stereoscopic System (H.E.S.S.) collaboration in Namibia [11]. Already the first observation period between February, 26th and March, 5th 2004 – close to the periastron passage of the binary system on March, 7th – led to a significant detection of the system at TeV energies [12] prompting the extension of the observations up to June 2004. In this paper the results of the H.E.S.S. pre-periastron 2004 data are reported.
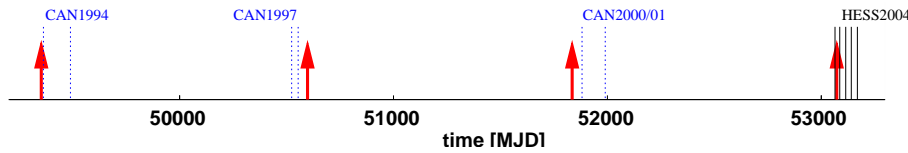
Figure 1: Illustration of the TeV observations of PSR B1259-63/SS 2883 over the past ten years. The arrows indicate the periastron passages of the system, the dotted lines mark the CANGAROO observations taken from [9, 10] and the solid vertical lines show the H.E.S.S. observations from March to June 2004; only the pre-periastron data is described in this paper.

2   Data analysis & results

2.1   Detector & data acquisition

Cherenkov telescopes record the Cherenkov light flash from extended air showers (EAS) initiated by high energy particles (γ-photons or hadrons) penetrating the earth's atmosphere. Each of the 4 H.E.S.S. telescopes has a $108 \, \text{m}^2$ tesselated mirror surface and is equipped with a 960 photomultiplier tube (PMT) camera with a field of view diameter of $\sim 5°$ [13]. The telescopes are operated in a stereoscopic (coincident) mode which means that an event is only read out if at least two telescopes have triggered [14]. This ensures that an event is always seen by more than one telescope and therefore allows the stereoscopic reconstruction of the shower geometry derived from the recorded Cherenkov images in each telescope [15]. The event-by-event angular resolution is $0.1°$ and the energy resolution about $15\,\%$ with an energy threshold of $100 \, \text{GeV}$ for observations close to the zenith. The data are taken in runs of $28 \, \text{min}$ duration in the moonless part of the nights in the so-called *wobble* mode displacing the telescopes tracking position with respect to the nominal object position by an alternating offset of $0.5°$ in Right Ascension or Declination allowing for an unbiased simultaneous background determination in the camera's field of view. Before the image analysis is applied the data are calibrated as described in [16].

2.2   Data set

Quality cuts have been applied to the data requiring stable weather and detector conditions. The PSR B1259-63/SS 2883 data reported in this paper have been taken between February, 26th and March, 5th 2004 and comprise $10.6 \, \text{h}$ of observation time. The periastron passage of the binary system was on March, 7th 2004. $8.6 \, \text{h}$ of the data passed the data quality cuts. The
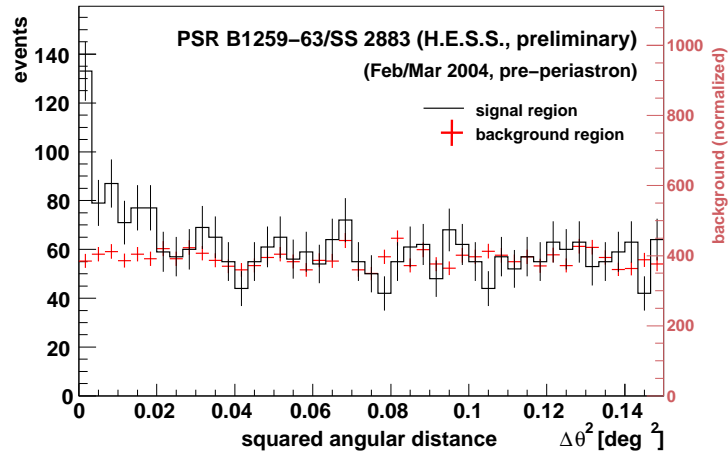
Figure 2: Number of events vs. the squared angular distance $\Delta\Theta^2$ between reconstructed shower direction and the nominal source position for the signal region (histogramm) and for the normalized background region (single points). The excess accumulating at small $\Delta\Theta^2$ values is compatible with a point-source which is expected for the given distance of the binary system.

observations were performed at zenith angles between $40°$ and $45°$ resulting in an energy threshold (pre-cuts) of $E_{\mathrm{thr}} \approx 200\,\mathrm{GeV}$. For the data presented here one of the four telescopes (CT01) was excluded from the analysis due to technical reasons.

2.3   Results

In the data set described above 168 ± 23 excess events from the direction of the PSR B1259-63/SS 2883 binary system have been recorded, corresponding to a significance of $8.2\,\sigma$ (calculated following [17]). The distribution of events as a function of the squared angular distance $\Delta\Theta^2$ measured between the reconstructed shower direction and the nominal source position (for the signal and the background region) is shown in Fig. 2. The integral flux above threshold of this observation has been estimated to be on the $5\,\%$ level of the Crab nebula flux. The skymap showing the 2D distribution of excess events in RA/Dec coordinates is shown in Fig. 3.

     These encouraging results triggered an extension of the H.E.S.S. observation campaign on PSR B1259-63/SS 2883 up to June 2004 with meanwhile more than $75\,\mathrm{h}$ of data. The results of this whole data set (including energy spectrum and lightcurve) will be described in an upcoming paper [18].
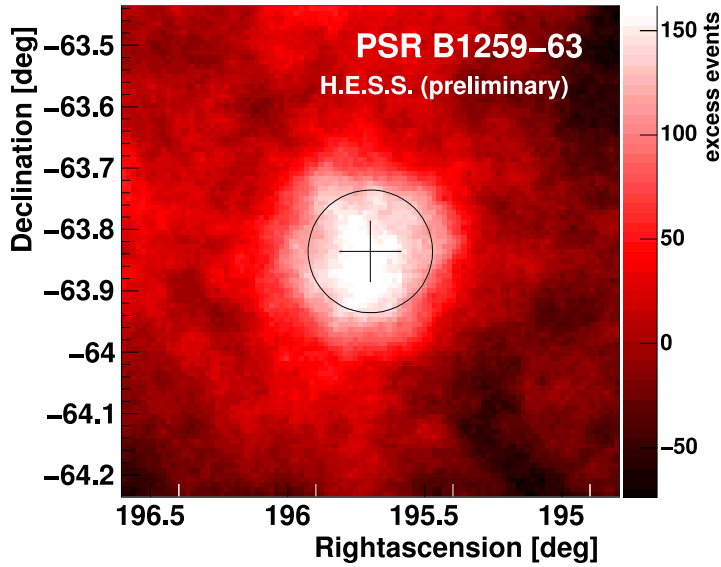
Figure 3: The 2D sky plot of excess events centered on the position of PSR B1259-63/SS 2883. The events are integrated within the angular cut of 0.14° for each bin. The circle indicates the event-by-event angular resolution of the H.E.S.S. telescopes.

3   Summary & Conclusion

The unique binary system PSR B1259-63/SS 2883 has been detected at TeV energies with the H.E.S.S. Cherenkov telescopes between February, 26th and March, 5th 2004 (near the periastron passage on March, 7th 2004) at an energy threshold of $E_{thr} \approx 200\,\mathrm{GeV}$ at the significance level of $\sim 8\,\sigma$. The measured integral flux above threshold was estimated to be on the 5 % level of the Crab nebula. This detection – being in agreement with the earlier reported upper limits by the CANGAROO collaboration [9] – gave rise to extend the H.E.S.S. observation campaign up to June 2004. The results of the whole data set including the energy spectrum and the lightcurve will be subject of an upcoming paper [18]. Together with observations at other wavelength the TeV observations allow for detailed comparisons between data and the various model predictions (i.e. [7, 8]). This might open a new window in the understanding of pulsar wind nebulae interactions with the surrounding environment which in this case is time-variable.

Acknowledgement

References

[1] Johnston, S., Manchester, R.N., Lyne, A.G., et al. (1992), *ApJ, 387, L37*

[2] Johnston, S., Manchester, R.N., Lyne, A.G., et al. (1994), *MNRAS, 268, 430*

[3] Wex, N., Johnston, S., Manchester, R.N., et al. (1998), *MNRAS, 298, 997*

[4] Johnston, S., Manchester, R.N., McConnell, D., and Campbell-Wilson, D. (1999), *MNRAS, 302, 277*

[5] Kaspi, V.M., Tavani, M., Nagase, F., et al. (1995), *ApJ, 453, 424*

[6] Hirayama, M., Cominsky, L.R., Kaspi, V.M., et al. (1999), *ApJ, 521, 718*

[7] Kirk, J., Ball, L., Skjæraasen, O. (1999), *Astropart. Phys., 10, 31*

[8] Ball, L., Kirk, J.G. (2000), *Astropart. Phys., 12, 335*

[9] Sako, T., Dazeley, S.A., Edwards, P.G., et al. (1997), *Proc. 25th ICRC, 3, 193*

[10] Kawachi, A., Naito, T., Patterson, J.R., et al. (2004), *ApJ, 607, 949*

[11] Punch, M. (2004), *Proc. FrontierScience2004, see these proceedings*

[12] Beilicke, M., Ouchrif, M., Rowell, G., Schlenker, S. (2004), *IAU Circular #8300*

[13] Vincent, P., Denance, J.-P., Huppert, J.-F., et al. (2003), *Proc. 28th ICRC (Tsukuba), Univ. Academy Press, Tokyo, p.2887*

[14] Funk, S., Hermann, G., Hinton, J., et al. (2004), *submitted to Astropart. Phys., see astro-ph/0408375*

[15] Aharonian, F., et al. (2004), *submitted to A&A (H.E.S.S. obs. of PKS2155-304)*

[16] Aharonian, F., et al. (2004), *submitted to Astropart. Phys., see astro-ph/0406658*

[17] Li, T., and Ma, Y. (1983), *ApJ, 272, 317*

[18] Aharonian, F., et al. (2004), *A&A, in preparation*

Part VII

VHE/UHE COSMIC RAYS

SPECTRUM FEATURES OF UHE PROTONS INTERACTING WITH CMB

V. BEREZINSKY

INFN, Laboratori Nazionali del Gran Sasso,67010 Assergi (AQ), Italy

Abstract

UHE extragalactic protons propagating through cosmic microwave background radiation (CMB) acquire the spectrum features in the form of the dip, bump and the Greisen-Zatsepin-Kuzmin (GZK) cutoff. The GZK cutoff is a steepening of the spectrum which occurs due to pion production in collisions with CMB photons. The GZK steepening is a model-dependent feature: it can be more flat in case of local overdensity of the sources and more steep in case of the local deficit. The protons do not disappear in interaction with CMB. They are only shifted to low energies and produce the *bump* of pile-up protons there. This *bump* is distinctly seen in the spectra of single sources, but since the bumps are located at different energies, they disappear in the diffuse spectra. The *dip* is produced due to e^+e^- pair-production in collision of protons with CMB photons. This feature is weakly model-dependent and is reliably predicted. The predicted dip is distinctly seen in the observational data, and thus it becomes the confirmed signature of UHE extragalactic protons propagating through CMB.

1   Introduction

The nature of signal carriers of UHECR is not yet established. The most natural primary particles are extragalactic protons. Due to interaction with the CMB radiation the UHE protons from extragalactic sources are predicted to have a sharp steepening of energy spectrum, so called GZK cutoff [1]. For uniformly distributed sources, the GZK cutoff is characterized by energy $E_{1/2}$, where the integral spectrum calculated with energy losses taken into account becomes twice lower than the power-law extrapolation from low energies [2] $E_{1/2} = 5.7 \times 10^{19}$ eV.

There are two other signatures of extragalactic protons in the spectrum: dip and bump [3, 2, 4, 5]. The dip is produced due $p + \gamma_{CMB} \rightarrow p + e^+ + e^-$ interaction at energy $E \sim 1 \times 10^{19}$ eV. The bump is produced by pile-up protons which loose energy in the GZK cutoff. As was demonstrated in [2], see also [5], the bump is clearly seen from a single source at large redshift z, but it practically disappears in the diffuse spectrum, because individual peaks are located at different energies. We shall demonstrate here that what is seen now in the observed spectrum as a broad bump is an artifact caused by multiplication of the spectrum to E^3.

A reliable feature in UHE proton spectrum is the dip produced by e^+e^- pair creation on CMB photons. It is less model dependent than GZK feature. Being relatively faint feature, it is however clearly seen in the spectra observed by AGASA, Fly's Eye, HiRes and Yakutsk arrays and can be considered as the confirmed signature of interaction of extragalactic UHE protons with CMB. This feature will be discussed in detail in this paper. The measurement of the atmospheric height of EAS maximum, x_{max}, in the HiRes experiment (see Fig.1) gives another evidence of pure proton composition at $E \geq 1 \times 10^{18}$ eV. Yakutsk data also favour the proton composition at $E \geq 1 \times 10^{18}$ eV [6], though the other methods of mass measurements show the mixed chemical composition [7].

At what energy the extragalactic component sets in?

According to the KASCADE data [8], the spectrum of galactic protons has a steepening at $E \approx 2.5 \times 10^{15}$ eV (the first knee), helium nuclei - at $E \approx 6 \times 10^{15}$ eV, and carbon nuclei - at $E \approx 1.5 \times 10^{16}$ eV. It confirms the rigidity-dependent confinement with critical rigidity $R_c = E_c/Z \approx 3 \times 10^{15}$ eV. Then galactic iron nuclei are expected to have the critical energy of confinement at $E_c \sim 1 \times 10^{17}$ eV, and extragalactic protons can naturally dominate at $E \approx 1 \times 10^{18}$ eV. This energy is close to the energy of the second knee (Akeno - 6×10^{17} eV, Fly's Eye - 4×10^{17} eV, HiRes - 7×10^{17} eV and Yakutsk - 8×10^{17} eV). The detailed analysis of transition from galactic to extragalactic component of CR is given in [9]. It favours the transition at $E \sim 1 \times 10^{18}$ eV. The model of galactic cosmic rays developed by Biermann et al [10] also predicts the second knee as the "end" of galactic cosmic rays (iron

nuclei) due to rigidity bending in wind-shell around SN. The extragalactic component became the dominant one at energy $E \sim 1 \times 10^{18}$ eV (see Fig.1 in [10]). The good candidates for the sources of observed UHE protons are
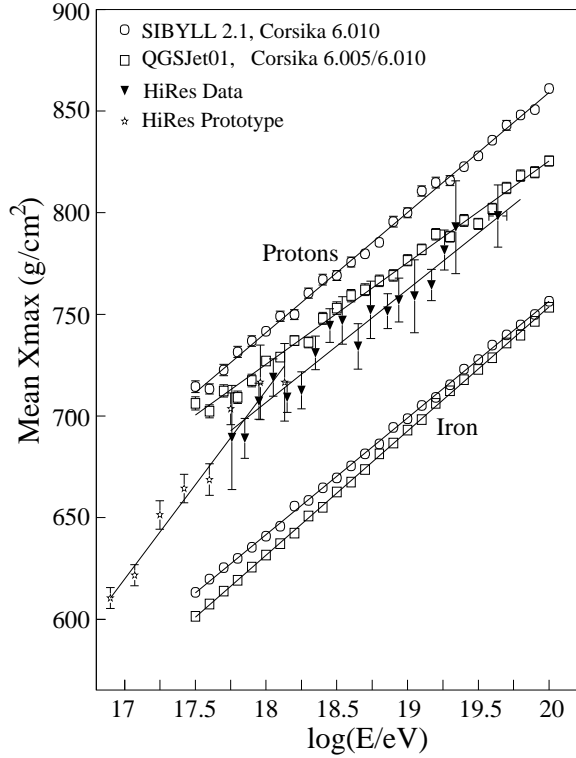
Figure 1: The HiRes data [11] on mass composition. The measured $x_{\max}$ at $E \gtrsim 1 \times 10^{18}$ eV (triangles) are in a good agreement with QGSJet-Corsika prediction for protons.

AGN. They can accelerate protons up to energy $E_{\max} \sim 10^{21}$ eV [12, 13, 14], they have power to provide the observed flux of UHE protons [15] and finally there observed the direct correlations [16] between directions of arrival of UHE particles with energies $(4 - 8) \times 10^{19}$ eV and directions to BL Lacs, which comprise some particular class of AGN.

Does it mean that UHECR puzzle has been already resolved in most conservative way?

In this model AGN cannot be the sources of observed particles with energy $E \geq 1 \times 10^{20}$ eV [17]: the attenuation length for a proton of this energy

is smaller than 135 Mpc, and correlation with AGN would be seen for all these particles, contrary to observations. The particles observed at $E \geq 1 \times 10^{20}$ eV, in particular those detected in AGASA, imply the presence of another component, e.g. produced by decays of superheavy DM.

2 $E_{1/2}$ as characteristic of the GZK cutoff.

$E_{1/2}$ is the energy where the flux calculated with energy losses becomes twice less than power-law extrapolation of integral spectrum. In Fig.2a the function $E^{(\gamma-1)}J(> E)$ is plotted as function of energy ($\gamma > \gamma_g$ is the effective index). For wide range of generation indices $2.1 \leq \gamma_g \leq 2.7$ the cutoff energy is the same, $E_{1/2} \approx 5.7 \times 10^{19}$ eV. We have determined $E_{1/2}$ from the Yakutsk data.
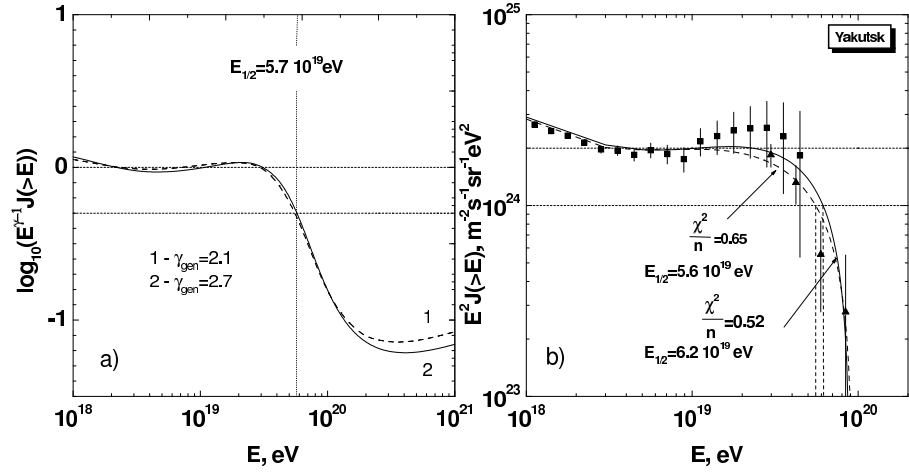
Figure 2: $E_{1/2}$ as numerical characteristic of the GZK cutoff. In panel a) the calculations for different γ_{gen} are presented. In panel b) $E_{1/2}$ is found from the integral spectrum of the Yakutsk array using two fits of the integral spectrum.

For this we found two fits of the Yakutsk integral spectrum with help of trial functions, as shown in Fig.2b. They have good χ^2/n equal to 0.65 and 0.52 (n is number of d.o.f.). The corresponding values of $E_{1/2}$, 5.6×10^{19} eV and 6.2×10^{19} eV, agree well with the theoretical value. Note, that in the fits above χ^2/n are the formal values from which probabilities cannot be calculated in the standard way, because the points in the integral spectrum are correlated quantities.

This analysis cannot be extended to the AGASA integral spectrum, because of too many events at the highest energies. Unfortunately, we do not have the

HiRes integral spectrum to perform the analysis as that above.
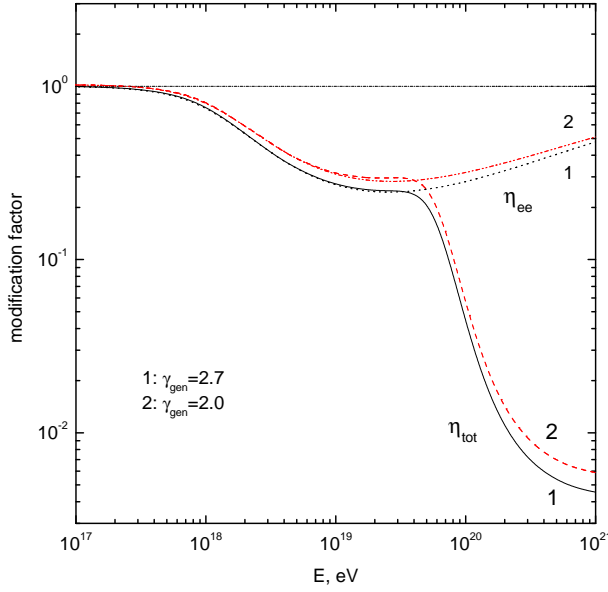
Figure 3: Modification factor for the power-law generation spectra with γ_g in a range 2.0 -2.7. Curve $\eta = 1$ corresponds to adiabatic energy losses only, curves η_{ee} corresponds to adiabatic and pair production energy losses and curves η_{tot} - to all energy losses included.

3   Bump in the diffuse spectrum

The analysis of the bump and dip is convenient to perform in terms of *modification factor* [2].

The modification factor is defined as a ratio of the spectrum $J_p(E)$, with all energy losses taken into account, to unmodified spectrum J_p^{unm}, where only adiabatic energy losses (red shift) are included.

$$\eta(E) = \frac{J_p(E)}{J_p^{\text{unm}}(E)}. \tag{1}$$

For the power-law generation spectrum $\propto E_g^{-\gamma_g}$ from the sources without cosmological evolution one obtains the unmodified spectrum as

$$J_p^{\text{unm}}(E) = \frac{c}{4\pi}(\gamma_g - 2)\mathcal{L}_0 E^{-\gamma_g} \int_0^{z_{\max}} dz \frac{dt}{dz}(1+z)^{-\gamma_g}, \tag{2}$$

where the observed energy E and emissivity $\mathcal{L}_0$ is measured in GeV and GeV/Mpc^{3}yr, respectively. The connection between dt and dz is given by usual cosmological expression. The flux $J_p(E)$ is calculated in [17] with all energy losses included. In Fig. 3 the modification factor is shown as function of energy for two spectrum indices $\gamma_g = 2.0$ and $\gamma_g = 2.7$. They do not differ much from each other because both numerator and denominator in Eq. (1) include factor $E^{-\gamma_g}$. Let us discuss first the bump. We see no indication of the bump in Fig. 3 at merging of $\eta_{ee}(E)$ and $\eta_{\mathrm{tot}}(E)$ curves, where it should be located. The absence of the bump in the *diffuse spectrum* can be easily understood. The bumps are clearly seen in the spectra of the single remote sources [2]. These bumps, located at different energies, produce a flat feature, when they are summed up in the diffuse spectrum. This effect can be illustrated by Fig. 4 from Ref. [2]. In Fig. 4 the diffuse flux is calculated in the model where sources are distributed uniformly in the sphere of radius $R_{\max}$ (or $z_{\max}$). When $z_{\max}$ are small (between 0.01 and 0.1) the bumps are seen in the diffuse spectra. When radius of the sphere becomes larger, the bumps merge producing the flat feature in the spectrum. If the diffuse spectrum is plotted as $E^3 J_p(E)$ this flat feature looks like a pseudo-bump.
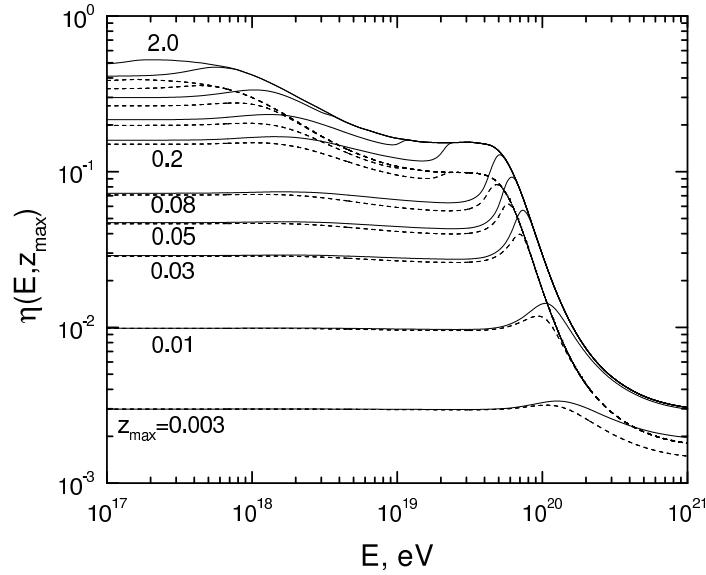
Figure 4: Disappearance of bumps in diffuse spectra (from Ref. [2]). The sources are distributed uniformly in the sphere of radius $R_{\max}$, corresponding to $z_{\max}$. The solid and dashed curves are for $\gamma_g = 2.7$ and $\gamma_g = 2.0$, respectively. The curves between $z_{\max} = 0.2$ and $z_{\max} = 2.0$ have $z_{\max} = 0.3$, 0.5, 1.0.

4   Dip as the signature of proton interaction with CMB.

The *dip* is more reliable signature of interaction of protons with CMB than
GZK feature. The shape of the GZK feature is strongly model-dependent: it
is more flat in case of local overdensity of the sources, and more steep in case
of their local deficit. It depends also on fluctuations in the distances between
sources inside the GZK sphere and on fluctuations of luminosities of the sources
there. The shape of the *dip* is fixed and has a specific form which is difficult to
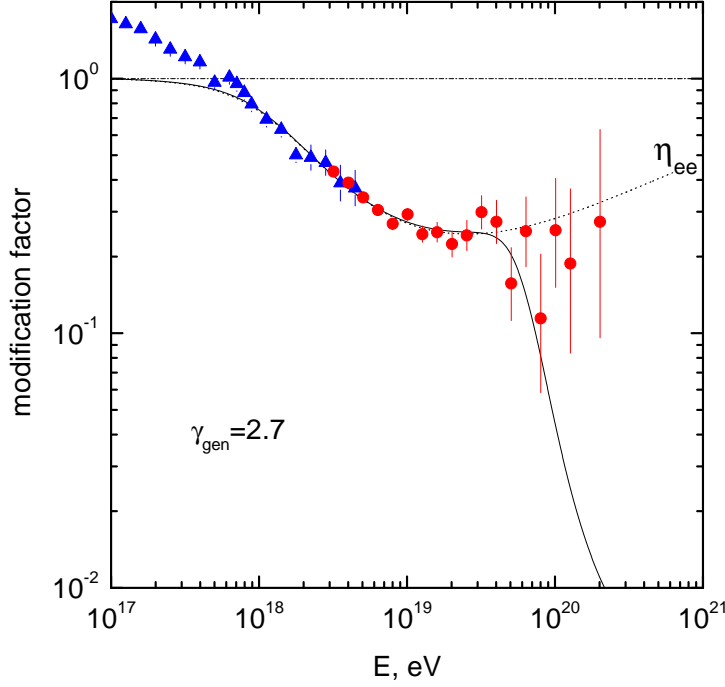
Figure 5: Predicted dip in comparison with the Akeno-AGASA data.

imitate by other mechnisms. The protons in the dip are collected from the large
volume with the linear size about 1000 Mpc and therefore the assumption of
uniform distribution of sources within this volume is well justified. In contrast
to this well predicted and specifically shaped feature, the cutoff, if discovered,
can be produced as the acceleration cutoff (steepening below $E_{\max}$). Since the
shape of both, GZK cutoff and acceleration cutoff, is model-dependent, it will
be difficult to argue in favour of any of them. The problem of identification of
the dip depends on the accuracy of observational data, which should confirm
the specific (and well predicted) shape of this feature. Do the present data
have the needed accuracy?
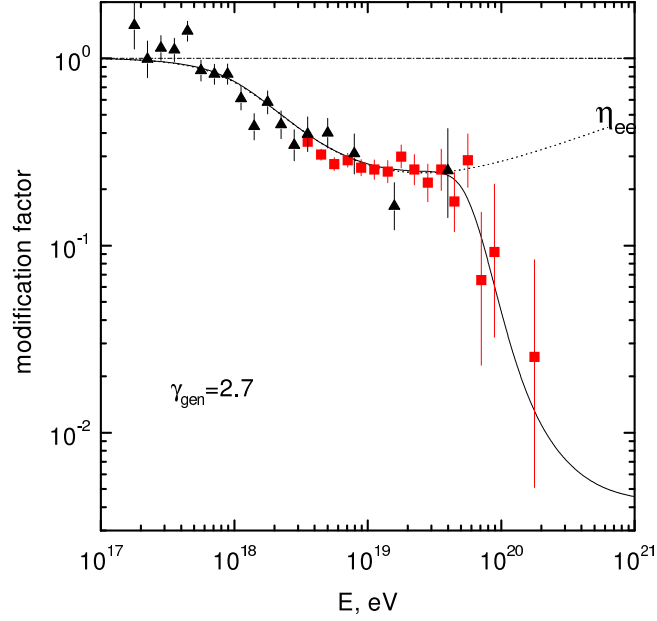
Figure 6: Predicted dip in comparison with the HiRes data.

The comparison of the calculated modification factor with that obtained from the Akeno-AGASA data, using $\gamma_g = 2.7$, is shown in Fig. 5. From Fig. 5 one observes the excellent agreement of predicted and observed modification factors for the dip.

In Fig. 5 one observes that at $E < 1 \times 10^{18}$ eV the agreement between calculated and observed modification factors becomes worse and at at $E \leq 4 \times 10^{17}$ observational modification factor becomes larger than 1. Since by definition $\eta(E) \leq 1$, it signals about appearance of another component of cosmic rays, which is most probably galactic cosmic rays. The condition $\eta > 1$ means the dominance of the new (galactic) component, the transition occurs at higher energy. To calculate χ^2 for the confirmation of the dip by Akeno-AGASA data, we choose the energy interval between 1×10^{18} eV (which is somewhat arbitrary in our analysis) and 4×10^{19} eV (the energy of intersection of $\eta_{ee}(E)$ and $\eta_{tot}(E)$). In calculations we used the Gaussian statistics for low-energy bins, and the Poisson statistics for the high energy bins of AGASA. It results in $\chi^2 = 19.06$. The number of Akeno-AGASA bins is 19. We use in calculations two free parameters: γ_g and the total normalization of spectrum. In effect, the confirmation of the dip is characterised by $\chi^2 = 19.06$ for d.o.f=17,

or χ^2/d.o.f.=1.12, very close to ideal value 1.0.

In Fig. 6 the comparison of modification factor with the HiRes data is shown. The agreement is also good.

The good agreement of the shape of the dip $\eta_{ee}(E)$ with observations is a strong evidence for extragalactic protons interacting with CMB. This evidence is confirmed by the HiRes data on the mass composition (see Fig. 1).

5   SuperGZK particles as a problem of astrophysical solution

The observed superGZK particles, i.e. those with energies higher than 1×10^{20} eV, impose a problem for astrophysical (acceleration) solution to origin of UHECR.

The "AGASA excess", namely 11 events with energy higher than 1×10^{20} eV, cannot be explained as extragalactic protons, nuclei or photons. While the spectrum up to 8×10^{19} eV is well explained as extragalactic protons with the GZK cutoff, the AGASA excess should be described as another component of UHECR, most probably connected with the new physics: superheavy dark matter, new signal carriers, like e.g. light stable hadron and strongly interacting neutrino, the Lorentz invariance violation etc.

The problem with superGZK particles is seen in other detectors, too. Apart from the AGASA events, there are five others: the golden FE event with $E \approx 3 \times 10^{20}$ eV, one HiRes event with $E \approx 1.8 \times 10^{20}$ eV and three Yakutsk events with $E \approx 1 \times 10^{20}$ eV. No sources are observed in the direction of these particles at the distance of order of attenuation length. The most severe problem is for the golden FE event: with attenuation length $l_{\mathrm{att}} = 21$ Mpc and the homogeneous magnetic field 1 nG on this scale, the deflection of particle is only 3.7°. Within this angle there are no remarkable sources at distance ~ 20 Mpc . SuperGZK particles can be explained by elementary-particle solutions, one of which is UHECR from Superheavy Dark Matter (SHDM), see reviews [18]. SHDM particles have masses $m_X \sim 10^{13} - 10^{14}$ GeV. They are produced at post-inflationary epoch gravitationally, when the Hubble constant $H(t) \gtrsim m_X$. To be (quasi)stable these particles should be protected by some symmetry from the fast decay. The example of such symmetry is a gauge discrete symmetry, like e.g. R-parity in case of neutralino. As any other cold DM the SHDM particles are accumulated in the halo with overdensity $\sim 2 \times 10^5$, and hence UHECR produced at the decays of these particles do not have the GZK cutoff. The spectrum of the produced UHE particles are nowdays reliably calculated. Since m_X is basically determined by cosmoligal density of SHDM Ω_m known from WMAP measurements, the only free parameter of the model is life-time τ_X of X-particles. Varying τ_X one can change the absolute flux of UHECR from SHDM, i.e. the normalization. In Fig. 7 the flux of UHECR is shown as the sum of two components: the astrophysical flux, most probaly from AGN,
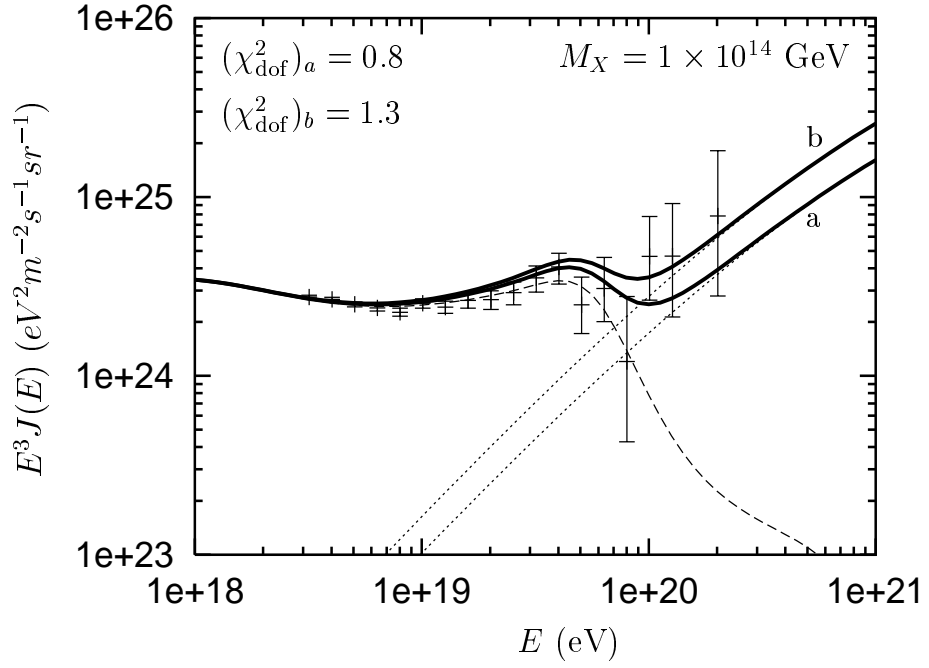
Figure 7: The astrophysical spectrum (dashed curve) and spectra from SHDM (dotted curves) [19], in comparison with AGASA data. The SHDM spectra are shown for two normalizations. The sum of two components is shown by the thick solid curves. The χ^2 values are given for the comparison of these two curves with the AGASA data at $E \geq 4 \times 10^{19}$ eV.

shown by dashed line and the flux from SHDM shown by dotted lines, according to calculations [19]. The AGASA spectrum, including the AGASA excess at $E \gtrsim 1 \times 10^{20}$ eV is well explained by the sum these fluxes shown by thick curves.

6 Conclusions

There are three signatures of UHE protons propagating through CMB: GZK cutoff, bump and dip.

The energy shape of the GZK feauture is very model dependent. The local excess of sources makes it flatter, and the deficit - steeper. The shape is affected by fluctuations of distances between the sources and of source luminosities. The cutoff, if discovered, can be produced as the acceleration cutoff (steepening

below the maximum energy of acceleration). Since the shape of both, the GZK cutoff and acceleration cutoff, is model-dependent, it will be difficult to argue in favour of any of them.

The *bump* is produced by pile-up protons, which are loosing the energy in photopion interactions and are accumulated at low energy, where the photopion energy losses become as low as pair-production energy losses. Such a bump is distinctly seen in calculation of spectrum from a single remote source. In the diffuse spectrum, since the individual peaks located at different energies, a flat spectrum feature is produced.

The *dip* is most remarkable feature of interaction with CMB. The protons in this energy region are collected from the distances ~ 1000 Mpc, with each radial interval dr providing the equal flux. All density irregularities and all fluctuations are averaged at this distance, and assumption of uniform distribution of sources with average distances between sources and average luminosities becomes quite reliable. The dip is confirmed by Akeno-AGASA and HiRes data with the great accuracy (see Figs 5 and 6). At energy $E > 4 \times 10^{19}$ eV the modification factor from Akeno data exceeds 1, and it signals the dominance of another CR component, most probably the galactic one. It agrees with transition of galactic to extragalactic component at the second knee $E \sim 1 \times 10^{18}$ eV.

How extragalactic magnetic field affects the calculated spectra features? The influence of magnetic field on spectrum strongly depends on the separation of the sources d. There is statement which has a status of the theorem [20]:

For uniform distribution of sources with separation much less than characteristic lengths of propagation, such as attenuation length l_{att} and the diffusion length l_{diff}, the diffuse spectrum of UHECR has an universal (standard) form independent of mode of propagation.

For the realistic intergalactic magnetic fields the spectrum is always universal, as was used in this paper.

The most probable astrophysical sources of UHECR are AGN. They can accelerate particles to $E_{max} \sim 1 \times 10^{21}$ eV and provide the needed emissivity of UHECR $\mathcal{L}_0 \sim 3 \times 10^{46}$ erg/Mpc^{3}yr. The correlation of UHE particles with directions to special type of AGN, Bl Lacs, is found in analysis of work [16].

The UHECR from AGN have a problem with superGZK particles with energies $E > 1 \times 10^{20}$ eV: (i) another component is needed for explanation of the AGASA excess, and (ii) no sources are observed in AGASA and other arrays in direction of superGZK particles. UHECR from SHDM can be one of the models explaining supeGZK particles (see Fig. 7 for description of the AGASA excess).

References

[1] K. Greisen, Phys. Rev. Lett., 16, 748 (1966); G.T. Zatsepin, V.A. Kuzmin, Pisma Zh. Experim. Theor. Phys. 4, 114 (1966).

[2] V.S. Berezinsky and S.I. Grigorieva, Astron.Astroph. 199, 1 (1988).

[3] C.T. Hill and D.N. Schramm, Phys. Rev. D 31, 564 (1985).

[4] S. Yoshida and M. Teshima, Progr. Theor. Phys. 89, 833 (1993).

[5] T. Stanev, R.Engel, A.Muecke, R.J. Protheroe and J.P. Rachen, Phys. Rev. D 62, 093005 (2000).

[6] A.V. Glushkov et al (Yakutsk collaboration) JETP Lett. 71, 97 (2000).

[7] A. Watson, these Proceedings.

[8] K.-H. Kampert et al (KASCADE collaboration) Proc. 27th ICRC, volume Invited, Rapporteur and Highlight papers, 240 (2001).

[9] V. Berezinsky, S. Grigorieva and B. Hnatyk, astro-ph/0403477 to be published in Astroparticle Physics.

[10] P.L. Biermann et al, 2003, astro-ph/0302201.

[11] G. Archbold and P.V. Sokolsky, Proc. of 28th ICRC, 405 (2003).

[12] P.L. Biermann P.L. and P.A. Streitmatter, Ap. J., 322, 643 (1987).

[13] W.H. Ipp and W.I. Axford, Astrophysical Aspects of Most Energetic Cosmic Rays (ed. M. Nagano), World Scientific, 273 (1991).

[14] J.P. Rachen and P.L. Biermann, Astron. Astroph. 272, 161 (1993).

[15] V. Berezinsky, A.Z. Gazizov and S.I. Grigorieva, hep-ph/0204357.

[16] P.G. Tinyakov and I.I. Tkachev I.I., JETP Lett., 74, 445 (2001).

[17] V. Berezinsky, A.Z. Gazizov and S.I. Grigorieva, astro-ph/0210095.

[18] V.A. Kuzmin and I.I. Tkachev, Phys. Rep. 320, 199 (199); V. Berezinsky, Nucl. Phys. (Proc. Suppl.) B87, 387 (2000).

[19] R. Aloisio, V. Berezinsky and M. Kachelriess, Phys. Rev. D69, 094023 (2004).

[20] R. Aloisio and V. Berezinsky, astro-ph/0403095 to be published in Ap.J 2004.

THEORETICAL ASPECTS OF ULTRA HIGH ENERGY COSMIC RAYS

P. BLASI [a]

[a] *INAF/Osservatorio Astrofisico di Arcetri,*
Largo E. Fermi, 5 - 50125 Firenze (Italy)

Abstract

The origin of the cosmic rays at energies in excess of 10^{20} eV is puzzling the scientific community for several decades now. The mystery adds to the general problem of understanding the nature of the bulk of cosmic rays, that are usually assumed to be accelerated within the Milky Way. Here we summarize the main elements of this puzzle and propose some possible avenues to interpret the present observations. The upcoming experiments for the detection of ultra high energy cosmic rays are expected to find answers to many of our current open questions, and in particular to identify the sources of the highest energy cosmic ray particles.

1 Introduction

Despite the wealth of data on the spectrum, anisotropy and chemical composition of cosmic rays, their origin is still a mystery. The spectrum extends to energies in excess of 10^{20} eV, with a knee at $\sim 10^{15}$ eV, but the nature of

this feature is also not clear, since it could be interpreted as a consequence of the propagation or of the acceleration within the sources. At sufficiently high energies the confinement of the Galaxy becomes inefficient and there must be a transition to an extragalactic origin, although much discussion is now ongoing on the energy where this transition takes place [2]. The crucial issue in this discussion is the chemical composition.

At present there is an almost complete consensus on the fact that cosmic rays with energy in excess of $\sim 10^{19}$ eV are generated in extragalactic sources. This implies that the sources must satisfy certain conditions on the propagation of cosmic rays on cosmological distances, which makes these so-called ultra-high energy cosmic rays (UHECRs) peculiar compared with the bulk of cosmic rays: indeed it was found in [3] that the main process that affects the propagation of cosmic rays at energies above 5×10^{19} eV is the production of pions in inelastic scatterings against the photons of the cosmic microwave background (CMB). At lower energies, the main channel for energy losses is proton pair production. The sharp drop in the loss length at energy $\sim 10^{20}$ eV due to the onset of the photopion production induces a feature in the spectrum of diffuse cosmic rays from extragalactic sources which is now known as the GZK feature, corresponding to a flux reduction at $E_c \sim 10^{20}$ eV. At energies $E > E_c$ only the nearby sources are visible, while the universe is almost transparent to photopion production at $E < E_c$. The detection of this GZK feature has occupied observers for almost four decades now, but another issue is equally important, namely the identification of a class of sources that may be able to accelerate cosmic rays to the extremely high observed energies.

This paper is structured as follows: in section 2 we briefly summarize the pieces of information that come from present and past experiments on UHECRs and the conclusions that can be derived from them on the sources of UHECRs; in section 3 we provide an incomplete list of plausible accelerators of cosmic rays to ZeV energies. We conclude in section 4.

2   What are present experiments telling us?

In this section we summarize three pieces of information that come from present and past experiments: 1) the spectrum of UHECRs in the range of energies $E > 10^{19}$ eV; 2) the small scale anisotropies; 3) the chemical composition.

The spectrum

Two effects seem evident in the spectra of UHECR as measured by AGASA and HiRes: the spectra show a systematic offset and the HiRes data look more compatible with the presence of a GZK feature than AGASA data do. We comment in the following on both these effects. The correct way to establish the statistical significance of a possible discrepancy between the two experiments is by carrying out numerical simulations of the propagation of UHECRs from

cosmologically distributed sources, with different assumptions on the injection spectrum. If the simulations are "constrained simulations", namely if the statistics of events, the statistical errors (and possible systematic errors) are forced to reproduce the observed ones, as was done in [4], the discrepancy between AGASA and HiRes can be quantified in a 2.6σ effect. This number is further reduced if the relative offset between AGASA and HiRes is attributed to a systematic error of 30% in the energy determination of the two experiments. It was demonstrated in [4] that if the relative discrepancy is shared in equal parts between the two experiments (15% each in opposite directions) not only the spectra are in good agreement in the energy region below 10^{20} eV, but the best fit injection spectrum is the same for the two sets of data. The low statistical significance of the discrepancy between AGASA and HiRes at energies in excess of 10^{20} eV is quite solid with respect to different ways of carrying out the analysis. Recently, the authors of Ref. [5] have performed a simulation similar to that described above but with the goal of finding the answer to the question "which fractions of realizations of the propagation of UHECRs with either AGASA statistics of events above 10^{19} eV correspond to the same number of events with $E > 10^{20}$ eV observed by AGASA?". In other words the authors address the question of whether there are realizations of the simulated propagation in which the GZK feature appears to be absent. Of 24000 realizazions of the propagation, adopting AGASA statistics of events above 10^{19} eV, 14 realizations had 11 or more events with energy above 10^{20} eV, corresponding to an effect at 3.2σ. If a systematic error of 15% in the energy determination of the AGASA events is assumed, then the number of events with energy above 10^{20} eV is 7, and the number of realizations with 7 or more events in the simulations was 240, corresponding to a 2.3σ effect.

These conclusions are all obtained by assuming that UHECRs are all extragalactic. A possible galactic component at energies around 10^{19} eV may have the effect of implying a flatter best fit injection spectrum for the highest energy events.

Small scale anisotropies (SSA)

Some anisotropies on the scale of a few degrees have been found in the AGASA data [6] in the form of doublets and triplets of events. For a truly diffuse distribution of sources these multiplets should appear only as a result of chance coincidences. This possibility appears to be disfavored, although some discussion is still ongoing [7] mainly concerning the way the data are treated for the analysis of the statistical significance. In Hires data there seems to be no indication of such anisotropies neither in the data obtained in the *mono* operation mode, nor in the *stereo* mode [8]. Whether this is compatible or not with the findings of AGASA due to the different statistics is still matter of investigation by several groups of scientists.

Clustering of events on small angular scales is the signature that UHECRs

are accelerated at astrophysical sources. Moreover, the number of multiplets with different multiplicities is an index of the density of sources, which makes small scale anisotropies a very important tool to have the first important clue to the nature of the sources.

Some attempts to estimate the number of sources of UHECRs in our cosmic neighborhood from the SSA found by AGASA have been carried out, adopting both semi-analytical and numerical approaches. An analytical tool to evaluate the chance coincidence probability for arbitrary statistics of events was proposed in [9]. A rigorous analysis of the clusters of events and of their energy dependence was given in [10]. In [11] the authors use an analytical method to estimate the density of the sources of UHECRs restricting their attention to the 14 events with energy above 10^{20} eV with one doublet. They obtain a rather uncertain estimate centered around 6×10^{-3} Mpc^{-3}. In [12] the energy losses are introduced through a function, derived numerically, that provides the probability of arrival of a particle from a source at a given distance. Again, only events with energy above 10^{20} eV are considered, therefore the analysis is based upon only one doublet of events out of 14 events. This causes extremely large uncertainties in the estimate of the source density, found to be $180^{+2730}_{-165} \times 10^{-3}$ Mpc^{-3}. No account of the statistical errors in the energy determination nor of the declination dependence of the acceptance of the experimental apparata is included in all these investigations. A complete calculation of the number density and luminosity of the sources of UHECRs with a full numerical simulation of the propagation was carried out in [13]. Such a calculation also accounted for the statistical errors in the energy determination and the declination dependence of the acceptance of the experiments involved. The number density of sources that fits the best the SSA observed by AGASA is $n_s \approx 10^{-5}$ Mpc^{-3}, although the error bars are large due to the limited statistics of clustered events in AGASA [13].

Chemical composition

The chemical composition of cosmic rays in the energy range of interest for our purposes is very poorly known. The old Fly's eye data pointed toward a heavy composition at energy 10^{18} eV, with a smooth transition to a light composition at higher energies. At 10^{19} eV these data seemed to favor a proton composition. The recent HiRes data on the other hand seem to suggest that this transition to a proton dominated composition occurs at lower energies, around 10^{18} eV. The content of heavy ions in the energy range above 10^{19} eV from Haverah Park can only be limited from above [17]. The possibility that the chemical composition may significantly change at energy 10^{18} eV was recently used in [2] to put forward the insightful proposal that the ankle is in fact a feature resulting from the propagation of UHECRs on cosmological distances.

3   Cosmic Zevatrons: a short list

Astrophysical sources distributed homogeneously in the universe, or following the observed density field [14] produce a spectrum of UHECRs with a GZK feature, more pronounced in general for steeper injection spectra [15]. Therefore the firm detection of this feature in the spectrum may serve as the most convincing evidence for an extragalactic astrophysical origin of UHECRs. Here we briefly summarize the potential sources of UHECRs and the acceleration processes that are supposed to be at work (a more complete review can be found in Ref. [16]).

3.1   Active and dead Galactic Nuclei

The term Active Galactic Nucleus (AGN) is used here to identify a very broad class of objects, characterized by the presence of a central massive black hole, and fueled by an accretion flow. When the fuel is almost exhausted, the AGN stops being active, leaving behind a *dead quasars* [19]. Cosmic rays can be accelerated in the central regions of AGNs, in the jets of some special class of AGNs and in the accretion disks of dead quasars. In the central regions og AGNs energy losses and diffusive confinement play together to limit the maximum energy to $10^6 - 10^7$ GeV [21]. Hot spots in F-R II radio galaxies appear to be more promising sites for the generation of UHECRs, due to the lower photon density and lower values of the magnetic field in the acceleration region [22]. The hot spot is terminated by a strong shock at which particles may be accelerated diffusively reaching a maximum energy that can be as high as 10^{21} eV or more for optimistic choices of the parameters. The propagation of UHECRs from active galactic nuclei was recently investigated by [18].

It has been proposed [19] that unipolar induction in dead quasars may energize charged particles to ultra high energies: in these objects energy losses due to photopion production and curvature radiation are expected to be less important than for active galaxies. Although dead quasars are not expected to be bright sources in the optical or radio bands, it has been proposed [20] that they show gamma ray emission, due to curvature radiation of UHECRs during the acceleration process. Unfortunately, at present no detailed calculation of the spectrum of UHECRs generated by dead quasars exists in the literature, so that it is difficult to predict in a more quantitative way the spectrum of particles detected at the Earth.

Other astrophysical objects may well be suitable candidates as sources of UHECRs, although a specific model may not have been worked out in the details. Recently, evidence has been found for a correlation of the arrival directions of cosmic rays with energy above 4×10^{19} eV with the spatial location of BL Lac objects [23]. Many of the BL Lacs are at large redshifts. The authors estimate the probability that the coincidence may occur by chance in one part

in 10^4. The correlation appears to be even more interesting after the recent claim [24] that a subsample of gamma ray loud BL Lac objects, probably seen even by EGRET, are in the direction of arrival of some ultra high energy cosmic rays.

3.2   Neutron Stars

Rapidly rotating strongly magnetized neutron stars are very efficient unipolar inductors, with an electromotive force (*emf*) that may reach 10^{21} V [25] between the polar region and the equator of the star. This potential is likely to be partially short-cut by the electron-positron pairs in the magnetosphere of the neutron star, so that the effective *emf* may be appreciably less. The *emf* is available in gap regions where the condition $\vec{E} \cdot \vec{B} = 0$ is violated [27]. The maximum achievable energy is typically around 10^{15} eV [1], mainly due to the limitation imposed by curvature radiation energy losses. In general, the presence of superstrong magnetic fields, such as those expected around magnetars and/or soft gamma ray repeaters, are unlikely to help to achieve higher energies, because although the *emf* gets larger, energy losses may also become more severe as well, unless quantum effects suppress the cross section for curvature or synchrotron radiation.

In [28] a phenomenological approach was taken to rule in favor of acceleration of heavy nuclei (as well as protons) to extremely high energies at the light cylinder of young neutron stars: it is well known that most energy lost by a spinning neutron star is not in the form of radiation [26], but is rather converted into kinetic energy of a relativistic wind. For a Crab-like pulsar, the Lorentz factor of the wind must be of the order of $\Gamma_W \sim 10^6 - 10^7$ [26], although it is not clear how this relativistic motion is achieved. If at the light cylinder a small pollution in the form of Iron nuclei or protons is present, the nuclei may acquire the same Lorentz factor of the wind, that for young neutron stars may well be in the useful range $\Gamma = 10^{10} - 10^{11}$. In order to escape freely from the plerion these nuclei should be able to cross the ejecta without suffering spallation and photodisintegration, which results in a constraint on the magnetic field of the neutron star and on its rotation period [28]. In case of Iron nuclei, the origin may be galactic, although this possibility does not appear to be favored by current data, due to the lack of evidence for anisotropy connected to the galactic disk. In other models in which the acceleration occurs due to reconnection [30], protons are accelerated in neutron stars in other galaxies. In this case, as usual, a GZK feature is expected in the spectrum at the Earth. A similar comment holds for the model presented in [29].

3.3 Gamma Ray Bursts

Cosmic rays may be accelerated diffusively at the relativistic shock front created by the relativistic fireball of a Gamma Ray Burst (GRB) [31, 32]. When the burst explodes in the interstellar medium, with magnetic field in the μG range, the maximum energy of the accelerated particles is [33] $E_{max} \approx 10^{15} eV B_\mu$, where B_μ is the magnetic field in μG. On the other hand, two of the models for GRBs currently in the literature, namely the binary neutron star merger [34] and the SupraNova model [35] predict that the GRB goes off in the relativistic wind of a neutron star, the so-called pulsar wind bubble (PWB), where the magnetic field is larger and the maximum energy in the 10^{20} eV range [36]. Acceleration of UHECRs in GRBs may also occur due to other plasma physics inspired processes, such as the wakefield acceleration proposed in [39].

If UHECRs are accelerated in GRBs, observations require the presence of an intergalactic magnetic field, in order to dilute in time the arrival of charged particles generated in the few GRB events occurring within ~ 100 Mpc.

In a magnetic field of $10^{-9} - 10^{-11}$ Gauss, the average deflection angle of UHECRs is smaller than the angular resolution of present experiments (2-3 degrees), therefore clusters of events are expected. If the observed multiplets are in fact the result of bursting sources, the higher energy particles should always reach the detector earlier than the lower energy ones. Although this condition is not satisfied by the AGASA clustered events, it was proposed [36] that fluctuations may in fact invert the order of arrival of particles with energy. The probability to obtain the observed multiplets simply due to statistical fluctuations has however not been calculated yet.

The energetic input of GRBs in the form of UHECRs was first investigated in [37, 38, 40]. If GRBs follow approximately the star-formation history, then the local rate of bursts should be unable to account for the observed flux of cosmic rays with energy above 10^{20} eV. The arguments in [37] were recently addressed in [36], where the burst rate and energy depositions were taken from recent literature [41, 42], and the spectra of UHECRs were calculated adopting a red-shift luminosity evolution of GRBs that follows Ref. [43]. The calculated energy injection rate found in [36] through comparison with the HiRes data at energies above 10^{17} eV, for an injection spectrum $E^{-2.2}$, is a factor ~ 6 larger than that available in gamma rays from GRBs (a factor 9 larger if the AGASA data are used). The mismatch is therefore still there, although it seems somewhat mitigated.

4   Conclusions and Discussion

We summarized the status of the field of UHECRs from the point of view of our theoretical understanding of the main issues related to their origin and propagation.

From the observational point of view, there are some open issues that need attention: 1) the spectra measured with different techniques appear to be not in perfect agreement, as discussed in section 2. It is likely that the main difference is due to a systematic error in the energy determination, and to limited statistics of events, but a final answer is still lacking. 3) After decades of measurements we still have a poor knowledge of the chemical composition of cosmic rays in the ultra-high energy range. 4) Despite the first hints of small scale anisotropies in the arrival directions of UHECRs, we still need a confirmation of this effect based on statistical grounds.

The upcoming Pierre Auger telescope and the spase-based initiatives such as EUSO and OWL have certainly the potential to answer many if not all of these questions.

There are mainly two fronts open in the search for the way Nature generates UHECRs: 1) understanding the basic principles involved in the acceleration processes that may allow some sources to accelerate particles up to energies as high as 10^{20} eV; 2) associating the UHECR emission to specific sources, possibly through multifrequency observations.

Acknowledgements

References

[1] V. S. Berezinsky, S.V. Bulanov, V. A. Dogiel, V. L. Ginzburg, and V. S. Ptuskin, Astrophysics of Cosmic Rays (Amsterdam: North Holland, 1990).

[2] V.S. Berezinsky, A. Gazizov, and S. Grigorieva, preprint astro-ph/0410650.

[3] K. Greisen, Phys. Rev. Lett. 16, 748 (1966); G. T. Zatsepin and V. A. Kuzmin, Sov. Phys. JETP Lett. 4, 78 (1966).

[4] D. De Marco, P. Blasi, and A.V. Olinto, Astropart. Phys. **20**, 53 (2003).

[5] D. De Marco, P. Blasi, and A.V. Olinto, in preparation.

[6] M. Takeda, et al., Astrophys. J. **522**, 225 (1999).

[7] C.B. Finley, and S. Westerhoff, preprint astro-ph/0309159.

[8] R.U. Abbasi, et al., Astroph. J. 610, L73 (2004)

[9] H. Goldgerg and T.J. Weiler, Phys. rev. **D64**, 056008 (2001).

[10] W.S. Burgett and M.R. O'Malley, Phys. Rev. **D67**, 092002 (2003).

[11] S.L. Dubovsky, P.G. Tinyakov and I.I. Tkachev, Phys. Rev. Lett. **85**, 1154 (2000).

[12] Z. Fodor and S.D. Katz, Phys.Rev. **D63**, 023002 (2001).

[13] P. Blasi, and D. De Marco, Astropart. Phys., Astropart. Phys. 20, 559 (2004).

[14] M. Blanton, P. Blasi, and A.V. Olinto, Astrop. Phys. 15, 275 (2001).

[15] V. Berezinsky and S. Grigorieva, Astron. Astroph. 199, 1 (1988).

[16] A.V. Olinto, Phys. Rep. **333**, 329 (2000).

[17] M. Ave, J.A. Hinton, R.A. Vazquez, A.A. Watson, A.A., and E. Zas, Phys. Rev. **D65**, 063007 (2002).

[18] V.Berezinsky, A.Z.Gazizov, and S.I.Grigorieva, preprint astro-ph/0210095.

[19] E. Boldt, and P. Ghosh, MNRAS 307, 491 (1999).

[20] A. Levinson, Phys. Rev. Lett. 85, 912 (2000).

[21] C.A. Norman, D.B. Melrose, and A. Achterberg, Astrophys. J. 454, 60 (2995).

[22] J.P. Rachen, and P.L. Biermann, A& A 272, 161 (1993).

[23] P.G. Tinyakov, I. I. Tkachev, JETP Lett. 74, 445 (2001); P. Tinyakov, and I. Tkachev, preprint astro-ph/0301336

[24] D. Gorbunov, P. Tinyakov, I. Tkachev and S. Troitsky, Astrophys. J. Lett. 577, 93 (2002).

[25] A. Venkatesan, Aparna M.C. Miller, and A.V. Olinto, Astrophys. J. 484, 323 (1997).

[26] C.F. Kennel, and F.V. Coroniti, Astrophys. J. 283, 694 (1984); C.F. Kennel, and F.V. Coroniti, Astrophys. J. 283, 710 (1984).

[27] M.A. Ruderman, and P.G. Sutherland, Astrophys. J. 196, 51 (1975); K.S. Chen, C. Ho, and M.A. Ruderman, Astrophys. J. 300, 500 (1986).

[28] P. Blasi, R. Epstein, and A.V. Olinto, Astrophys. J. Lett. 533, 123 (2000).

[29] J. Arons, Astroph. J. 589, 871 (2003).

[30] E.M. De Gouveia Dal Pino, and A. Lazarian, Astrophys. J. Lett. 536, 31 (2000).

[31] M. Vietri, Astrophys. J. 453, 883 (1995).

[32] E. Waxman, Phys. Rev. Lett. 75, 386 (1995).

[33] Y.A. Gallant, and A. Achterberg, MNRAS 305, L6 (1999).

[34] R. Narayan, P. Paczynski, and T. Piran, Astrophys. J. Lett. 395, L83 (1992).

[35] M. Vietri, and L. Stella, Astrophys. J. Lett. 507, 45 (1998).

[36] M. Vietri, D. De Marco, and D. Guetta, Astrophys.J. 592, 378 (2003).

[37] F.W. Stecker, Astropart. Phys. 14, 207 (2000).

[38] S.T. Scully, and F.W. Stecker, Astropart. Phys. 16, 271 (2002).

[39] P. Chen, T. Tajima, and Y. Takahashi, Phys. Rev. Lett. 89, 1101 (2002).

[40] V.S. Berezinsky, A.Z. Gazizov, and S.I. Grigorieva, preprint astro-ph/0204357.

[41] M. Schmidt, Astrophys. J. 552, 36 (2001).

[42] D. Frail, et al., Astrophys. J. Lett. 562, 55 (2001).

[43] C. Porciani, and P. Madau, Astrophys. J. 548, 522 (2001).

BLAZING CERENKOV FLASHES AT THE HORIZONS BY COSMIC RAYS AND NEUTRINOS INDUCED AIR-SHOWERS

Daniele Fargion [a,b]

[a] *Dipartimento di Fisica, Università di Roma "La Sapienza",*
Pl.A. Moro 2, Roma, Italy

[b] *INFN, Sezione di Roma I, Italy*

Abstract

High Energy Cosmic Rays (C.R.) versus Neutrino and Neutralino induced Air-Shower maybe tested at Horizons by their muons, gamma and Cerenkov blazing signals. Inclined and Horizontal C.R. Showers ($70^o - 90^o$ zenith angle) produce secondary ($\gamma, e^{\pm}$) mostly suppressed by high column atmosphere depth. The air column depth suppresses low energy Showers (TeV-PeV) and it dilutes higher energy (PeV-EeVs) ones. Indeed also earliest shower Cherenkov photons are diluted by large distances and by air opacity, while secondary penetrating, $\mu^{\pm}$ and their successive decay into $e^{\pm}, \gamma$, may revive additional Cerenkov lights. The larger horizontal distances widen the shower's cone while the geo-magnetic field open it in a very characteristic fan-like shape polarized by local field vector, making these elongated showers spread, fork-shaped diluted and more frequent, up to three order of magnitude (respect to vertical showers). GeVs γ telescopes at the top of the mountains or in Space may detect at horizons PeVs up to EeV and more energetic hadronic cosmic rays secondaries. Details on arrival

angle and column depth, shower shape, timing signature of photon flash intensity, may inform us on the altitude interaction and primary UHECR composition. Below the horizons, at zenith angle $(90^o - 99^o)$ among copious single albedo muons, rare up-going showers traced by muon $(e^{\pm},\gamma)$ bundles would give evidence of rare Earth-Skimming neutrinos, $\nu_\tau, \overline{\nu}_\tau$, at EeVs energies. They are arising by Tau Air-Showers (HorTaus) $(\nu_\tau + N \rightarrow \tau + X$, $\tau \rightarrow$ hadrons and/or electromagnetic shower). Their rate may be comparable with 6.3 PeVs $\overline{\nu}_e - e$ neutrino induced air-shower (mostly hadronic) originated above and also below horizons, in interposed atmosphere by W^- resonance at Glashow peak. Additional and complementary UHE SUSY $\chi^o + e \rightarrow \tilde{e} \rightarrow \chi^o + e$ at tens PeVs-EeV energy may blaze, as $\overline{\nu}_e - e \rightarrow W^-$ shower, by its characteristic electromagnetic signature. (These UHE χ^o are expected in topological defect scenarios for UHECRs). Their secondary shower blazing Cerenkov lights and distances might be disentangled from UHECR by Stereoscopic Telescopes such as Magic ones or Hess array experiment. The horizontal detection sensitivity of Magic in the present set up (if totally devoted to the Horizons Shower search) maybe already be comparable to AMANDA underground neutrino detector at PeVs energies.

1   UHECR Cerenkov Lights, Muons and Bundles at Horizons

Ultra High Energy Cosmic Rays (UHECR) Showers (from PeVs up to EeVs and above, mainly of hadronic nature) born at the high altitude in the atmosphere, may blaze (from the far edge) *above the horizon* toward Telescopes such as Magic one. The earliest gamma and Cerenkov lights produced while they propagate through the atmosphere are severely absorbed because of the deep horizontal atmosphere column depth $(10^4 - 5 \cdot 10^4 \ g \cdot cm^{-2}$), must anyway survive and also revive: indeed additional diluted but penetrating muon bundles (from the same by C.R. shower) are decaying not far from the Telescope into electrons which are source themselves of small Cerenkov lights . Also the same muon while hitting the Telescope may blaze a ring or arc of Cherenkov lights. These suppressed muon bundle secondaries,(about 10^{-3} times less abundant than the peak of the gamma shower photons) are arising at high altitude, at an horizontal distances $100 - 500$ km far from the observer (for a zenith angle $85^o - 91.5^o$ while at 2.2km. height); therefore these hard (tens-hundred GeV) muon shower bundles (from ten to millions muons from TeVs-EeVs C.R. primary) might spread in huge areas (tens- hundred km^2); they are partially bent by geo-magnetic fields and they are randomly scattered, often decaying at tens-hundred GeV energies, into electrons and consequent mini electromagnetic-showers traced by their optical Cerenkov flashes. These diluted (but spread and therefore better detectable) brief (nanosecond-microsecond)

optical signals may be captured as a cluster by largest telescope on ground as recent Stereoscopic Magic or Hess, Veritas arrays. Their Cerenkov flashes, single or clustered, must take place, at detection threshold, at least tens or hundreds times a night for Magic-like Telescope facing toward horizons $85^o - 90^o$. Their "guaranteed" discover may offer a new tool in CR and UHECR detection. Their primary hadronic signature might be hidden by the distance but its tail may arise in a new form by its secondary muon-electron-Cerenkov of electromagnetic nature. On the same time *below the horizons* a more rare (three-four order of magnitude) but more exciting PeV-EeVs Neutrino ν_τ Astronomy may arise by the Earth-Skimming Horizontal Tau Air-Showers (HorTaus); these UHE Taus are produced inside the Earth Crust by the primary UHE incoming neutrino ν_τ, $\overline{\nu}_\tau$, generated mainly by their muon-tau neutrino oscillations from galactic or cosmic sources,[6],[7],[8]. Finally just above or below the horizon edge, within a few hundred of km distances, it might also be observable the guaranteed and well tuned $\overline{\nu}_e$-$e \rightarrow W^- \rightarrow X$ air-showers at $6.3 PeV$ Glashow resonant peak energy; the W main hadronic (2/3) or leptonic and electromagnetic (1/3) signatures may be well observed and their rate might calibrate a new horizontal neutrino-multi-flavour Astronomy [6]. The $\overline{\nu}_e$-$e \rightarrow W^- \rightarrow X$ of nearby nature (respect to most far away ones at same zenith angle of hadronic nature) would be better revealed by a Stereoscopic Magic twin telescope or a Telescope array like Hess, Veritas. Additional Horizontal flashes might arise by Cosmic UHE $\chi_o + e \rightarrow \widetilde{e} \rightarrow \chi_o + e$ electromagnetic showers within most SUSY models, if UHECR are born in topological defect decay or in their annihilation, containing a relevant component of SUSY particles. The UHE $\chi_o + e \rightarrow \widetilde{e} \rightarrow \chi_o + e$ behaves (for light $\widetilde{e}$ masses around Z boson ones) as the Glashow resonant case [1]. Finally similar signals might be abundantly and better observed if UHE neutrinos share new extra-dimension (TeV gravity) interactions: in this case also neutrino-nucleons interaction may be an abundant source of PeVs-EeVs Horizontal Showers originated in Air [6]. The total amount of air inspected within the solid angle $2^o \cdot 2^o$ by MAGIC height at Horizons (360 km.) exceed $44 km^3$ but their consequent detectable beamed volume are corresponding to an isotropic narrower volume: V$= 1.36 \cdot 10^{-2}\ km^3$, nevertheless comparable (for Pevs $\overline{\nu}_e$-$e \rightarrow W^- \rightarrow X$ and EeVs ν_τ, $\overline{\nu}_\tau + N \rightarrow \tau \rightarrow$ showers) to the present AMANDA confident volume.

2   Blazing Cerenkov Flashes by Horizons Showers and Muons

The ultrahigh energy cosmic rays (UHECR) have been studied in the past mainly versus their secondaries (γ, $e^\pm$, $\mu^\pm$) collected vertically in large array detectors on the ground. This is due to the rare event rate of the UHECR in the atmosphere and due to the high altitude where the shower takes place,
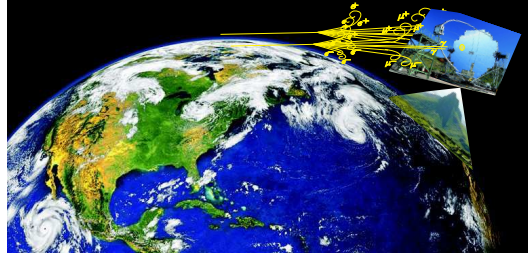
Figure 1: Schematic Picture of an Horizontal Cosmic Ray Air-Shower (superior track) (HAS), and an up-going Tau Air-Shower induced by EeV Earth-Skimming $\bar{\nu}_\tau, \nu_\tau$ HORTAU and their muons and Cerenkov lights blazing a Telescope as the Magic one. Also UHE $\bar{\nu}_e - e$ and $\chi^o - e$ Scattering in terrestrial horizontal atmosphere at tens PeVs energy may simulate HAS, but mostly at nearer distances respect largest EeV ones of hadron nature at horizon's edges.
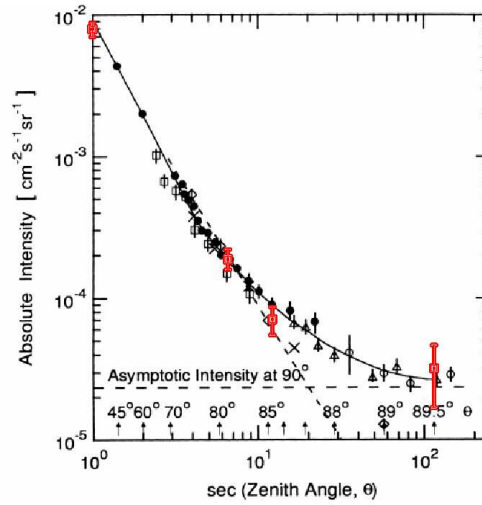
Figure 2: Observed Flux of Muons as a function of the zenith angle above (left [13],[12]) the horizons; for the muons below the horizons their flux at 91° zenith angle is two order of magnitude below $\simeq 10^{-7} cm^{-2} s^{-1} sr^{-1}$, as observed by NEVOD and Decor detectors in recent years. As the zenith angle increases the upward muons flux reduces further ; at 94° and ten GeV energy it is just four order below: $\simeq 10^{-9} cm^{-2} s^{-1} sr^{-1}$ [16],[17]; at higher energies (hundred GeVs) and larger zenith angle only muons induced by atmospheric neutrinos arises at $\simeq 2 - 3 \cdot 10^{-13} cm^{-2} s^{-1} sr^{-1}$ as well as Neutrino Tau induced Air-Shower (muon secondaries).

expand and amplify downward. On the contrary at the horizons the UHECR are hardly observable (but also rarely looked for). They are diluted both by the larger distances as well as by the exponential atmosphere opacity suppressing the electromagnetic (electron pairs and gamma) secondaries; also their rich optical Cerenkov signal is partially suppressed by the horizontal air opacity. However this suppression acts also as a useful filter leading to the choose of higher CR events; their Cerenkov lights will be scatter and partially transmitted ($1.8 \cdot 10^{-2}$ at 551 nm., $6.6 \cdot 10^{-4}$ at 445 nm.) depending on the exact zenith angle and seeing: assuming a suppression on average $5 \cdot 10^{-3}$ and the nominal Magic threshold at 30 GeV gamma energy, it does corresponds to a hadronic shower at far horizons (diluted by nearly three order of magnitude by larger distances) at an energy above $E_{CR} \simeq 6$ PeV. Their primary flux maybe estimated considering the known cosmic ray fluxes at same energy on the top of the atmosphere (both protons or helium) (see DICE Experiment referred in[12]) : $\phi_{CR}(E_{CR} = 6 \cdot 10^{15} eV) \simeq 9 \cdot 10^{-12} cm^{-2} s^{-1}$; the consequent event rate spread within a Shower Cerenkov angle $\Delta\theta = 1^o$ at a distance $d = 167 km \cdot \sqrt{\frac{h}{2.2km}}$ (zenith angle $\theta \simeq 87^o - 88^o$) corresponding to a wide shower area $[A = \pi \cdot (\Delta\theta \cdot d)^2 \simeq 2.7 \cdot 10^{11} cm^2 (\frac{d}{167km})^2]$, observed by a opening angle $[\Delta\Omega = (2^o \cdot 2^o)\pi \simeq 3.82 \cdot 10^{-3} sr.]$ is for a night of record ($[\Delta(t) = 4.32 \cdot 10^4 s]$):

$$N_{ev} = \phi_{CR}(E = 6 \cdot 10^{15} eV) \cdot A \cdot \Delta\Omega \cdot \Delta(t) \simeq 401/12h$$

Therefore one may foresee nearly every two minutes a far hadronic Cerenkov lightening Shower in Magic facing at the far horizons at zenith angle $87^o - 88^o$. Increasing the observer altitude h, the horizon zenith angle also grows: $\theta \simeq [90^o + 1.5^o \sqrt{\frac{h}{2.2km}}]$ In analogy at a more distant horizontal edges (standing at height $2.2km$ as for Magic, while observing at zenith angle $\theta \simeq 89^o - 91^o$ still above the horizons) the observation range d increases : $d = 167 \sqrt{\frac{h}{2.2km}} + 360km = 527km$; the consequent shower area widen by more than an order of magnitude (and more than three order respect to vertical showers) and the foreseen event number, now for much harder C.R. at $E_{CR} \geq 3 \cdot 10^{17} eV$, becomes:

$$N_{ev} = \phi_{CR}(E = 3 \cdot 10^{17} eV) \cdot A \cdot \Delta\Omega \cdot \Delta(t) \simeq 1.6/12h$$

Therefore at the far edges of the horizons $\theta \simeq 91.5^o$, once a night, an UHECR around EeV energies, blazes to the Magic (or Hess,Veritas, telescopes). At each of these far primary Cherenkov flash is associated a long trail of secondary muons in a very huge area; these muons eventually are also hitting inside the Telescope disk; their nearby showering, while decaying into electrons in flight, (source of tens-hundred GeVs mini-gamma showers) is also detectable at a rate discussed below.

3   Single-Multi muons: Arcs, Rings and γ Showers by $\mu^\pm \to e^\pm$

As already noted the main shower blazing photons from a CR may be also reborn or overlap with its secondary tens-hundred GeVs muons, either decaying in flight as a gamma flashes, or by direct Cerenkov muons lights painting arcs or rings while hitting the telescope. Indeed these secondary very penetrating muon bundles may reach hundreds km far distances ($\simeq 600km \cdot \frac{E_\mu}{100 \cdot GeV}$) away from the shower origin. To be more precise a part of the muon primary energy will dissipate along 360 km air-flight (nearly a hundred GeV energy), but a primary $130 - 150$ GeV. muon will reach a final $30 - 50$ GeV energy, just at minimal Magic threshold value. Let us remind the characteristic secondary abundance in a shower: $N_\mu \simeq 3 \cdot 10^5 \left(\frac{E_{CR}}{PeV}\right)^{0.85}$ These multiplicity are just at a minimal (GeV) energies [4]; for the harder (a hundred GeV) muons their number is (almost inversely proportionally to energy) reduced: $N_\mu(10^2 \cdot GeV) \simeq 1.3 \cdot 10^4 \left(\frac{E_{CR}}{6 \cdot PeV}\right)^{0.85}$ These values must be compared with the larger peak multiplicity (but much lower energy) of electro-magnetic shower nature: $N_{e^+e^-} \simeq 2 \cdot 10^7 \left(\frac{E_{CR}}{PeV}\right); N_\gamma \simeq 10^8 \left(\frac{E_{CR}}{PeV}\right)$. As mentioned most of these electromagnetic tail is lost (exponentially) at horizons (above slant depth of a few hundreds of $\frac{g}{cm^2}$)(out of the case of re-born, upgoing τ air-showers [8],[9]); therefore gamma-electron pairs are only partially regenerated by the penetrating muon decay in flight, $\mu^\pm \to \gamma, e^\pm$ as a parasite electromagnetic showering [3]. Indeed $\mu^\pm$ may decay in flight (let say at 100 GeV energy,at $2-3\%$ level within a $12-18$ km distances) and they may inject more and more lights, to their primary (far born) shower beam.

These tens-hundred GeVs horizontal muons and their associated mini-Cerenkov γ Showers have two main origin: (1) either a single muon mostly produced at hundreds km distance by a single (hundreds GeV-TeV parental) C.R. hadron primary (a very dominant component) or (2) rarer muon, part of a wider and spread horizontal muon bundle of large multiplicity born at TeVs-PeV or higher energies, as secondary of horizontal shower. Between the two cases there is a smooth link. A whole continuous spectrum of multiplicity begins from an unique muon up to a multi muon shower production. The dominant noisy "single" muons at hundred-GeV energies will loose memory of their primary low energy and hidden mini-shower, (a hundreds GeV or TeVs hadrons); a single muon will blaze just alone. The muon "single" rings or arcs frequency is larger (than muon bundles ones) and it is based on solid observational data ([13] ; [12],as shown in fig.2 and references on MUTRON experiment therein); these "noise" event number is:

$$N_{ev} = \phi_\mu(E \simeq 10^2 eV) \cdot A_{Magic} \cdot \Delta\Omega \cdot \Delta(t) \simeq 120/12h$$

The additional gamma mini-showers around the telescope due to a decay (at a probability $p \simeq 0.02$) of those muons in flight, recorded within a larger collecting

Area $A_\gamma \geq 10^9 cm^2$ is even a more frequent (by a factor ≥ 8) noisy signal:

$$N_{ev} \geq \phi_\mu(E \simeq 10^2 eV) \cdot p \cdot A_\gamma \cdot \Delta\Omega \cdot \Delta(t) \simeq 960/12h$$

These single background gamma-showers must take place nearly once a minute (in an silent hadronic background) and they are an useful tool to be used as a prompt meter of the Horizontal C.R. verification.

On the contrary PeVs (or higher energy) CR shower Cerenkov lights maybe observed, more rarely, in coincidence both by their primary and by their later secondary arc and gamma mini-shower. Their $30-100$ GeV energetic muons are flying nearly undeflected $\Delta\theta \leq 1.6^o \cdot \frac{100 \cdot GeV}{E_\mu} \frac{d}{300km}$ for a characteristic horizons distances d , partially bent by geo-magnetic 0.3 Gauss fields; as mentioned, to flight through the whole horizontal air column depth (360 km equivalent to 360 water depth) the muon lose nearly 100 GeV; consequently the origination muon energy should be a little above this threshold to be observed by Magic: (at least $130 - 150$ GeV along most of the flights). The deflection angle is therefore a small one: $\Delta\theta \leq 1^o \cdot \frac{150 \cdot GeV}{E_\mu} \frac{d}{300km}$). Magic telescope area ($A = 2.5 \cdot 10^6 cm^2$) may record at first approximation the following event number of direct muon hitting the Telescope, flashing as rings and arcs, each night:

$$N_{ev} = \phi_{CR}(E = 6 \cdot 10^{15} eV) \cdot N_\mu(10^2 \cdot GeV) \cdot A_{Magic} \cdot \Delta\Omega \cdot \Delta(t) \simeq 45/12h$$

to be correlated (at 11% probability) with the above results of 401 primary Cerenkov flashes at the far distances. As already mentioned before, in addition the same muons are decaying in flight at a minimal probability 2% leading to a mini-gamma-shower event number in a quite wider area ($A_\gamma = 10^9 cm$):

$$N_{ev} = \phi_{CR}(E = 6 \cdot 10^{15} eV) \cdot N_\mu(10^2 \cdot GeV) \cdot p \cdot A_\gamma \cdot \Delta\Omega \cdot \Delta(t) \simeq 360/12h$$

Therefore , in conclusion, at $87^o - 88^o$ zenith angle, there are a flow of primary $E_{C.R} \simeq 6 \cdot 10^{16} eV$ C.R. whose earliest showers and consequent secondary muon-arcs as well as nearby muon-electron mini-shower take place at comparable (one every 120 s.) rate. These *certain* clustered signals offer an unique tool for gauging and calibrating Magic (as well as Hess,Cangaroo,Veritas Cerenkov Telescope Arrays) for Horizontal High Energy Cosmic Ray Showers. Some more rare event may contain at once both Rings,Arcs and tail of gamma shower and Cerenkov of far primary shower. It is possible to estimate also the observable muons-electron-Cerenkov photons from up-going Albedo muons observed by recent ground experiments [16] [17]: their flux is already suppressed at zenith angle 91° by at least two order of magnitude and by four order for up-going zenith angles 94°. Pairs or bundles are nevertheless more rare (up to $\phi_\mu \leq 3 \cdot 10^{-13} cm^{-2} s^{-1} sr^{-1}$ [16] [17]). They are never associated to up-going shower out of the case of tau air-showers or by nearby Glashow $\bar{\nu}_e - e \rightarrow W^-$ and comparable $\chi^o + e \rightarrow \tilde{e}$ detectable by stereoscopic Magic or Hess array telescopes, selecting and evaluating their column depth origination, just discussed below.

4   UHE $\bar{\nu}_e - e \to W^-$ and $\chi^o + e \to \tilde{e}$ resonances versus τ air-showers

The appearance of horizontal UHE $\bar{\nu}_\tau \; \nu_\tau \to \tau$ air-showers (Hortaus or Earth-Skimming neutrinos) has been widely studied [5], [6], [2], [10], [7], [8], [14], [18], [15], [9]; their rise from the Earth is source of rare clear signals for neutrino UHE astronomy (see fig.3). However also horizontal events by UHE 6.3 PeV, Glashow $\bar{\nu}_e - e \to W^-$ and a possible comparable SUSY $\chi^o + e \to \tilde{e}$ [1] hitting and showering in air have non negligible event number:

$$N_{ev} = \phi_{\bar{\nu}_e}(E = 6 \cdot 10^{15} eV) \cdot A \cdot \Delta\Omega \cdot \Delta(t) \simeq 5.2 \cdot 10^{-4}/12h$$

assuming the minimal GZK neutrino flux : $\phi_{\bar{\nu}_e}(E = 6 \cdot 10^{15} eV) \simeq 5 \cdot 10^{-15}$ eV $cm^{-2}s^{-1}sr^{-1}$; the energy flux is $\phi_{\bar{\nu}_e} \cdot E_{\bar{\nu}_e} \simeq 30$ eV $cm^{-2}s^{-1}sr^{-1}$.(We assume an observing distance at the horizons $d = 167km \cdot \sqrt{\frac{h}{2.2km}}$.) Therefore during a year of night records and such a minimal GZK flux, a crown array of a 90 Magic-like telescopes on $2 \cdot \pi = 360^o$ circle facing the horizons, would discover an event number comparable to a Km^3 detector, (nearly a dozen events a year). Indeed Magic facing at the Horizons as it is, offer a detection comparable to present AMANDA $\simeq 1\%Km^3$ effective volume. In conclusion while Magic looking up see down-ward γ tens GeVs Astronomy, Magic facing the Horizons may well see far UHE (PeVs-EeVs) CR, and rarely, along the edge, GZK $\bar{\nu}_e - e \to W^-$ neutrinos showering in air, as well as charged current $\nu_\tau + N \to \tau^-$,$\bar{\nu}_\tau + N \to \tau^+$ whose decay in flight while in air leads to Hortau air-showers. Even SUSY $\chi^o + e \to \tilde{e} \to \chi^o + e$ lights in the sky (with showers) may blaze on the far frontier of the Earth.

References

[1] Datta A., Fargion D., Mele B. hep-ph/0410176

[2] Bertou, X. et. all 2002, Astropart. Phys., 17, 183

[3] Cillis, A.N., & Sciutto, S.J., 2001, Phys. Rev. D64, 013010

[4] Cronin, J.W., 2004, TauP Proceedings, Seattle 2003; astro-ph/0402487

[5] Fargion, D., Aiello,et.all. 1999, 26th ICRC HE6.1.10,396-398

[6] Fargion, D., 2002, ApJ, 570, 909; see astro-ph/0002453/9704205

[7] Fargion, D. et.all. 2003 Devel.Astrophysics., 1, 395 astro-ph/0303233.

[8] Fargion D., De Sanctis Lucentini, P.G., De Santis, M., Grossi, M., 2004, ApJ, 613, 1285; hep-ph/0305128.

$$\frac{dN_\tau}{d\theta\, d\varphi\, dt\, dA\, dE} E \;[cm^{-2}\; sec^{-1}\; sr^{-1}]$$
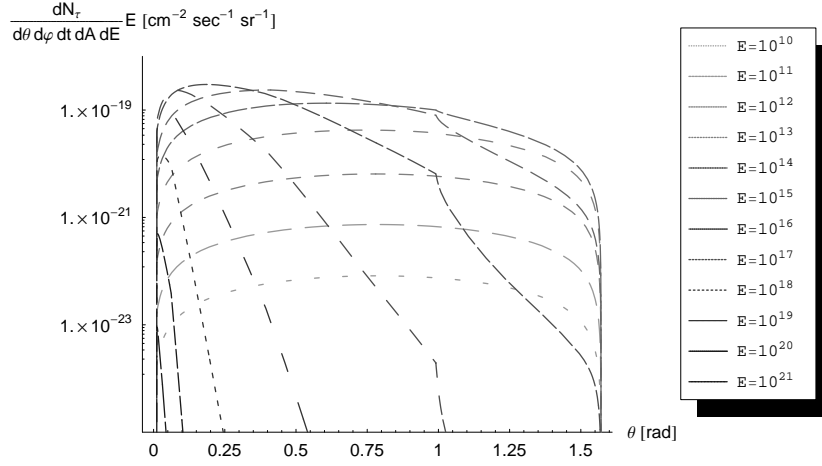
Figure 3: Tau Air-Showers rates angular distribution, by Earth Skimming Neutrino τ inside the rock, assuming a rock surface density; the UHE E_{ν_τ} energies are shown in eV unity. The incoming neutrino flux is a minimal GZK flux (for combined ν_τ and $\bar{\nu}_\tau$) at $\phi_{\nu\tau} \cdot E_{\nu_\tau} \simeq 50$ eV $cm^{-2}s^{-1}sr^{-1}$; [9]

$$\frac{dN_\mu}{d\theta\, d\varphi\, dt dA\, dE} E \;[cm^{-2}\; sec^{-1}\; sr^{-1}]$$
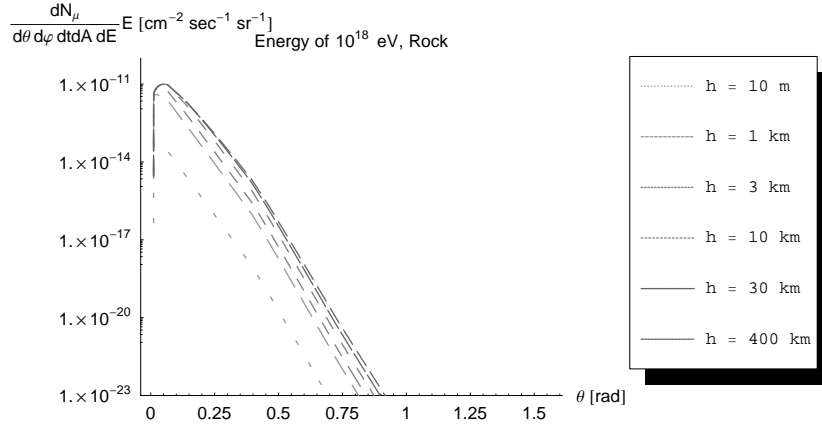
Figure 4: Consequent Muons Secondary (by Tau Air-Showers) rate angular distribution at different observer height, at 10^{18}eV energy, exceeding (at horizontal zenith angle $\theta \simeq 93 - 97^o$) even the same atmospheric neutrino induced up-going muon flux $\phi_\mu \simeq 3\cdot10^{-13}\cdot cm^{-2}s^{-1}sr^{-1}$. The incoming neutrino flux is a minimal GZK flux (for combined ν_τ and $\bar{\nu}_\tau$) at $\phi_{\nu\tau} \cdot E_{\nu_\tau} \simeq 50$ eV $cm^{-2}s^{-1}sr^{-1}$; [9]

[9] Fargion D. De Santis, M. et al., Nuclear Physics B (Proc. Suppl.), 136 ,119(2004)

[10] Feng, J.L., Fisher, P., Wilczek, F., & Yu, T.M., 2002, Phys. Rev. Lett. 88, 161102; hep-ph/0105067

[11] Gandhi, R., Quigg, C., Reno, M.H., Sarcevic, I., 1998, Phys. Rev. D., 58, 093009

[12] P.K.F. Grieder , Cosmic Rays at Earth, Elsevier 2001

[13] Iori, M., Sergi, A., Fargion, D., 2004, astro-ph/0409159

[14] Jones, J. et all. 2004 Phys. Rev. D , 69, 033004

[15] Tseng, J.J, Yeh, T.W., Athar et all. 2003, Phys. Rev. D68, 063003

[16] I.I. Yashin et al., ICRC28 (2003), 1195.

[17] I.I. Yashin et al, ICRC28 (2003), 1147.

[18] Yoshida, S.,et all 2004, Phys. Rev. D69, 103004;

EUSO: A SPACE-BORNE EXPERIMENT FOR UHECR OBSERVATION

Alessandro Petrolini [a]

[a] *Dipartimento di Fisica dell'Università di Genova and
INFN Sezione di Genova,
Via Dodecaneso 33, I-16146 Genova, Italy.
e-mail: Alessandro.Petrolini@ge.infn.it.*

Abstract

The *EUSO* experiment is currently under study by ESA for a possible installation on the International Space Station. The experiment is designed to observe, by means of a space-based apparatus, the Extensive Air Showers produced in the atmosphere by Ultra High-Energy Cosmic Rays. The design of a large aperture, large field of view, fast and high granularity, single-photon Photo-Detector, sensitive in the near UV and suitable for a few years of operation in space, is a challenging task. The basic aspects of the current concept of the *EUSO* mission, based on the presently known requirements and constraints will be described.

The *EUSO* experiment can be considered the precursor and pioneer of a new generation of experiments in the UHECR field aiming to go beyond what is practically achievable at the Earth surface.

1   Ultra High Energy Cosmic Rays

The interpretation of the phenomenology of the Ultra High Energy Cosmic Rays (UHECR) is one of the most challenging topics of modern astro-particle physics [1]. UHECR reach the Earth with a low flux (of the order of $F \approx 0.01$ particle year $^{-1}$ km^{-2} sr^{-1} for particle with an energy $E \gtrsim 10^{20}$ eV) and therefore a complex and sophisticated experimental apparatus is required to observe them.

The *EUSO* (Extreme Universe Space Observatory) experiment, proposed to the European Space Agency (ESA) for installation on the International Space Station (ISS), has just finished its phase A study (the feasibility study).

The experiment goal is the study of the Cosmic Rays in ultra high energy part ($E \gtrsim 5 \cdot 10^{19}$ eV) of the energy spectrum, by observing, from Space, the Extensive Air Showers (EAS) produced by the interaction of the primary UHECR with the atmosphere. This is accomplished by installing *EUSO* on the ISS, looking down to nadir during night-time.

The phase A study has demonstrated the technical feasibility, with up-to-date technology, of a scientific apparatus satisfying the *EUSO* scientific objectives.

2   The observational technique

EUSO is an implementation of the *AirWatch concept*, originally proposed by John Linsley more than twenty years ago [2]: to observe EAS from Space, as shown in Figure 1.

An EAS can be detected by observing the air scintillation light, isotropically produced during the EAS development, and proportional, at any point along the EAS development, to the number of charged particles in the EAS. The additional observation of the diffusely reflected Cherenkov light (reflected either by land, sea or clouds) provides additional information. Therefore it is possible to estimate the energy and arrival direction of the primary UHECR, and to gather information about its nature. The atmosphere acts as a calorimeter (passive, continuously changing and outside human control).

Any given EAS will be seen as a point moving with a direction and angular velocity depending on the EAS direction. The peculiar characteristics of the EAS, including the kinematical ones, allow one to distinguish them from the various backgrounds, because those have a typically different space-time development.

Key points of the observational technique are the following.

- A large instantaneous geometrical aperture can be obtained ($\mathcal{A}_{\mathrm{GEO}} \gtrsim 2.1 \cdot 10^5$ km^2 sr, at least), thanks to the large distance ($\gtrsim 400$ km) and depending on the Instrument Field of View ($\gamma \gtrsim 20°$). A large mass
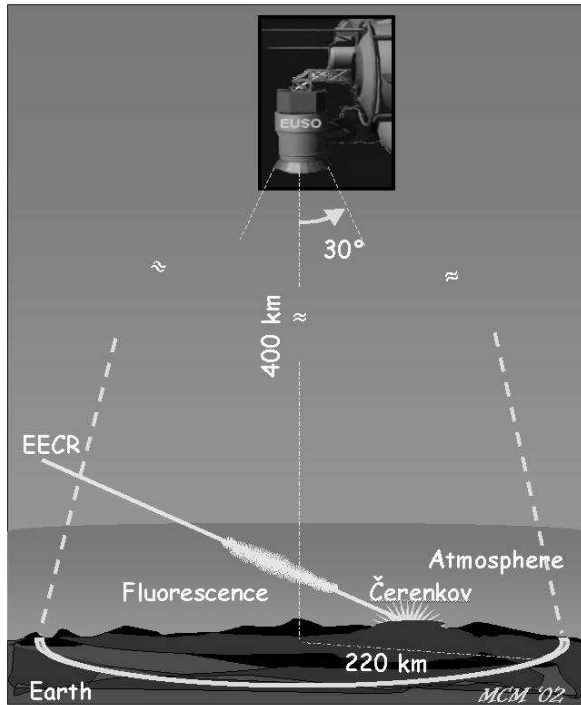
Figure 1: The *EUSO* observational approach.

of atmosphere (the calorimeter medium) can therefore be observed. The estimated duty cycle is in the range $\approx (0.05 \div 0.20)$.

- Detection of EAS produced by weakly interacting primary particles, starting to shower deeply in the atmosphere, is possible, by the direct observation of the EAS development and starting point.
- All sky coverage is possible with one single apparatus.
- The approach is complementary to the ground-based one. In fact the Space experiments are best suited for the observation of higher energy cosmic rays with respect to ground-based experiments. However an overlap of the observed energy spectrum with the one known from ground-based experiments is required for a better comparison. A larger geometrical

aperture is obtained from Space experiments with respect to ground-based experiments. The systematic effects are different in the two approaches.

2.1 The signal

The scintillation light, mainly emitted in the $330\,\mathrm{nm} \div 400\,\mathrm{nm}$ wavelength range, is isotropic and proportional, at any point, to the number of charged particles in the EAS, largely dominated by electrons and positrons. The total amount of light produced is proportional to the primary particle energy and the shape of the EAS profile (in particular the atmospheric depth of the EAS maximum) contains information about the primary particle identity. In this wavelength range the atmosphere is relatively transparent, down to $\lambda \approx 330\,\mathrm{nm}$ where the ozone absorption becomes strong. However the scintillation signal turns out to be rather weak, due to the large distance, making the task a challenging one. The typical number of detected photons from a proton EAS with $E \approx 10^{20}$ eV, for an *EUSO*-like apparatus, is of the order of $10^2 \div 10^3$ depending on the EAS inclination with respect to ground. The time duration of the signal spans the range from tens to hundreds of μs, again depending on the EAS inclination with respect to ground.

The possible observation of the Cherenkov light diffusely reflected by the Earth (by land, sea or clouds) will help the determination of the EAS parameters. While the amount of observed Cherenkov photons depends on the reflectance and geometry of the impact surface, the directionality of the Cherenkov beam provides a precise extrapolation of the EAS direction to the first reflecting surface.

2.2 The main background contributions

A selective and efficient trigger is required to distinguish the EAS from the background. Many different kind of backgrounds are expected including: the night-glow, man-made lights, auroras, natural photo-chemical effects (in atmosphere, sea and land), low-energy cosmic rays, reflected moon-light and star-light. However the typical characteristics of EAS are quite different from the background ones, in particular the kinematic characteristics. The backgrounds, for instance, typically have a time-scale of the order of ms. Another type of background is the random night-glow, currently estimated, for *EUSO*, in the range $B \approx (3 \div 9) \cdot 10^{11}$ photons m^{-2} s^{-1} sr^{-1}, in the wavelength range $330\,\mathrm{nm} \le \lambda \le 400\,\mathrm{nm}$ at $h \approx 400$ km height, depending on various factors. The random night-glow background in *EUSO* is estimated to be $30 \div 100$ GHz over the full FoV.

3   The *EUSO* Instrument

The design of an Instrument to look from Space to the EAS produced in the atmosphere by UHECR is a challenging task mainly because the UHECR flux reaching the Earth is very small, the observable signal is very faint and the apparatus has to operate in Space [3]. The engineering is very complex and the engineering design has a strong and critical impact on the scientific performance of the Instrument. This is caused by the tight Instrument requirements deriving from the Science requirements.

The *EUSO* Instrument is basically a fast digital camera, operating in the near-UV wavelength range, with large aperture and FoV. The main Instrument requirements are the following.

- The Instrument must collect as many photons as possible, in order to be able to detect the faint signal from the less energetic EAS and to discriminate it from the background. As a consequence a large aperture is required, as well as a good transmission of the optical elements and good photon detection efficiency in the 330 nm ÷ 400 nm wavelength range. In fact a sufficiently low lower energy threshold is mandatory to connect the energy spectrum observed by *EUSO* with the observations by ground-based experiments, operating in a lower energy range.
- A large Field of View (FoV) is required to be able to observe a mass of atmosphere as large as possible, thus increasing the expected event rates.
- The physics requirements can be satisfied with a system having an angular granularity sufficient to ensure an angular resolution on the EAS direction of $\Delta\alpha \approx 1°$.
- A single-photon detector is required, fast enough to be able to follow the space-time development of the EAS (sampling time below $\approx 0.1\ \mu$s) and reconstruct the EAS kinematical parameters from one single observation point.
- A low noise and good signal to noise ratio are required to detect the faint signal produced by the less energetic EAS and discriminate it from the background. Small cross-talk and after-pulse rate are required to avoid degradation of the energy and angular resolution.
- An efficient and reliable trigger system, capable of a good background rejection, is required to cope with the limited data storage, data transfer and computing capabilities available on-board.
- All the constraints and requirements related to the Space mission have to be accounted for. Mandatory characteristics are therefore: a compact and robust system with low mass, volume and power consumption, good reliability and time stability, radiation hardness and low sensitivity to magnetic fields of the order of the gauss.
- A system is required to protect the Instrument from possibly dangerous

environmental factors, including intense light.

3.1 The main Instrument parameters

The *EUSO* Instrument is made of a main optics, to collect and focus the incoming light, and a photo-detector, on the Focal Surface (FS), to detect the photons collected by the optics. The present provisional *EUSO* parameters and design goals are summarized in Table 3.1.

The main *EUSO* parameters and design goals	
ISS average orbit height	$H \approx 430$ km (at year 2010)
ISS orbit inclination	$i = 51.6°$
Orbital period	$T_0 \simeq 90$ min
Operating wavelength range (WR)	$\{330\,\text{nm} \leq \lambda \leq 400\,\text{nm}\}$
Observation duty cycle	$\eta \simeq (0.10 \div 0.20)$
Operational lifetime	at least three full years
Instrument field of view (half-angle)	$FoV \simeq 30° \equiv \gamma$
Effective aperture at high-energy	$\simeq (6 \div 9) \cdot 10^4$ km^{2}sr
Angular granularity	$\Delta\alpha \simeq 0.1°$
Optics maximum diameter	$D_M \simeq 2.5$ m
Optics aperture (entrance pupil diameter)	$D \simeq 2$ m
Optics $f/\#$	$f/\# \leq 1.25$
Optics spot size diameter on the FS	$3\,\text{mm} \div 6\,\text{mm}$
Average transmission of the optics	$K_{opt} \approx 0.5$
Average photo-detector detection efficiency	$\varepsilon_{det} \approx 0.1$
Pixel dimensions	$\approx 3 \div 6$ mm
Number of channels	$\approx 1 \cdot 10^5 \div 4 \cdot 10^5$
Average atmospheric transmission (in WR)	$K_{atm} \gtrsim 0.4$
Background (in WR at ≈ 400 km height)	$(3 \div 9) \cdot 10^{11}$ m^{-2} s^{-1} sr^{-1}

3.2 The Atmospheric Sounding

The knowledge of the atmospheric properties on a event by event basis is important in order to improve the data quality, energy resolution and primary particle identification, in particular. For this reason a LIDAR to perform atmospheric properties sounding has been added to the current experimental apparatus. This will allow to determine the atmospheric properties relevant to the reconstruction of the triggered events, thus greatly improving the data quality.

4   Scientific activities to support the development of a Space-based observatory

A number of activities are required to provide information necessary/useful for a better design and optimization of a space-based experiment and to help the data-set interpretation such as:

- measurement of the fluorescence yield (many efforts are on-going);
- measurement of the Cherenkov light albedo from land, water and clouds under different relevant conditions (efforts are on-going: the ULTRA experiment [4]);
- a dedicated measurement of the diffuse background from space, to improve the current knowledge is probably necessary.

5   Conclusions

After the Pierre Auger project (both south and north Observatories) and Telescope Array will have clarified the UHECR properties around the GZK-cutoff region a different approach is probably needed to explore the higher energies.

The full understanding of the space-based approach, proposed more than 20 years ago, is now reaching its maturity, and it is now ready to pass into the implementation Phase.

The *EUSO* project has just finishing its phase A study. During phase A a preliminary conceptual design of the Instrument has been developed, capable to fulfill the Scientific requirements. The positive outcome of the *EUSO* phase A study from the scientific and technical point of view has demonstrated that the construction of an *EUSO*-like apparatus is a technically achievable goal with up-to-date technology. The Cosmic Rays physics community started to learn how to do such a kind of Experiment/Mission, thanks to the opportunity provided by the *EUSO* phase A.

EUSO is an energy range which makes it an experiment complementary to present and forthcoming ground-based experiments, the Pierre Auger Observatory and Telescope Array in particular. The Observational Approach implemented by *EUSO* makes it the precursor and pioneer of a new generation of experiments in the UHECR field.

The design of an *EUSO*-like Instrument is a real challenge due to the many (scientific and technical) requirements and constraints. Unconventional solutions might be required under many respects.

UHECR observation from space is a challenging task, requiring a huge and well-coordinated effort by the whole Cosmic Rays physics community.

6   Acknowledgements

References

[1] A. Watson, these proceedings;
V. Berezinsky, these proceedings;
P. Blasi, these proceedings.

[2] J. Linsley, *Call for Projects and Ideas in High Energy Astrophysics*, 1979.

[3] The AirWatch Collaboration, Workshop on Observing Giant Cosmic Ray Air Showers, AIP Conf. Proc., 433, 353-357, (1998); The AirWatch Collaboration, Proc. SPIE 3445, 486, (1998); R. Stalio et al., Proc. 26th ICRC 2, 403 (1999); K. Arisaka, *Optimization of OWL-AirWatch Optics and Photo-Detectors*, 28/12/1999, available at `http://www.physics.ucla.edu/ arisaka/`; M. Ameri et al., *Study report on the EUSO photo-detector design*, Report INFN/AE-01/04, April 2001; O. Catalano, Il Nuovo Cimento 24C, n. 3, (2001), pag. 445; M. Ameri et al., Proc. 27th ICRC (2001), Hamburg, August 2001; A. Petrolini, Nucl. Phys. Proc. Suppl. 113 (2002) 329.

[4] O. Catalano et al., *ULTRA: UV Light Transmission and Reflection in the Atmosphere*, funded by INFN.

A SPACE OBSERVATORY FOR ULTRA HIGH ENERGY NEUTRINOS

P. Mazzinghi [a], V. Bratina [a], P. Spillantini [b], S. Bottai [b]

[a] *INOA, Istituto Nazionale di Ottica Applicata,*
L.go E. Fermi 6, Firenze, Italy

[b] *INFN, Sezione di Firenze, via Sansone 1, Sesto Fiorentino, Italy*

Abstract

The physics of High Energy Cosmic Rays (HECR) will be deeply investigated by next generation of space detectors. For the Ultra High Energy Neutrino (UHEN) astronomy such detectors will probably exhibit a lack of statistics and a further increase of sensitivity will be necessary for this goal. A presentation of possible optical configuration for high energy neutrinos collection is given.

1 Introduction

Today's systems for HECR detection through induced fluorescence consist of a very large arrays of detectors (e.g. scintillators, Cherenkov detectors) deployed on the ground over many square kilometers [1][2][3] each one observing a small portion of the sky. By combining the field of view of all of these mirrors, the necessary aperture needed to detect events efficiently is provided. However,

the flux of the HECRs above 10^{19} eV is low, and the rate of the detectable neutrino events is far less, that a very large target is necessary. Only a few decades of events, above the knee of the spectrum have been observed so far, which represent a poor statistics. For instance, the HiRes fluorescence detector has an effective aperture of 1000 km^2 sr, while the Pierre Auger Observatory under construction will have an aperture of 7000 km^2 sr. The two ground based observatories will probably detect tens of events with energy greater than 10^{20} eV per year, but still not enough to build a significant statistics.

An ultra high energy particle observatory would benefit from being lifted into space as a larger portion of atmosphere will be observable. Fluorescence signals will be detected by looking downwards at the dark Earth's atmosphere from a free flyer in a Low Earth Orbit or from a platform like the ISS. Light will be imaging onto a focal surface detector, and the segmentation and the time resolution will allow the precise reconstruction of the arrival direction. Such an instrument will be monitoring approximately $3 million$ km^2 sr of atmosphere and will be collecting about 3000 events per year with energy greater than 10^{20} eV.

Different optical design approaches for the optics of a suitable space observatory for UHEN's have been suggested, and a reflecting mirror with a Schmidt corrector seems to match most of the needed optical technical requirements. Nevertheless, a single mirror allows a considerable cost and mass reduction. A single mirror will be providing a large field of view and a large collecting area, in order to monitor a sufficiently large portion of Earth's surface, and to collect enough fluorescence light from orbit. The Schmidt telescope, one of the best known reflectors, well matches both those characteristics, and appears as an appropriate solution to solve the problem. Existing Schmidt telescopes do not meet the dimension needed for this kind of space application. Pursuing this way, it is therefore also a technology challenge, which may open the view to many new applications for space astrophysics.

2   The problem of neutrino detection

The discovery of cosmic ray particles with energy greater than 10^{20} eV (Extreme High Energy Cosmic Rays -"EHECR") [4] has opened a new perspective for Astrophysics showing the existence of either unexpected extremely powerful acceleration mechanisms ("bottom-up") or more fundamental phenomena of emission/creation closely related to the primordial structure of the Universe ("top-down"). Furthermore if EHECR are hadrons or nuclei, the energy loss due to their interaction with the cosmic microwave background radiation (Greisen-Zatsepin-Kuzmin cut-off (GZK)) raises the fundamental question concerning the distance travelled by such particles. In case of uniform distribution of sources in the Universe, due to

GZK cut-off, the observed spectrum should end around 10^{20} eV. In general if sources yield hadronic EHECR, they produce as well photons and neutrinos of comparable energy. Furthermore the GZK mechanism will guarantee a neutrino flux which arise from the interaction of protons with the cosmic microwave background radiation [5] (Fig. 1). Such neutrinos (called GZK neutrinos) are able to travel for almost the entire universe and carry the information about very far Extreme Energy proton sources. Their detection will open a new window in neutrino astronomy, complementary to neutrino astronomy performed by neutrino telescopes at lower energy. The GZK neutrino direction will be almost the same than proton direction and the angular deviation respect to the sources direction will be affected by the intergalactic magnetic fields encountered by the protons.
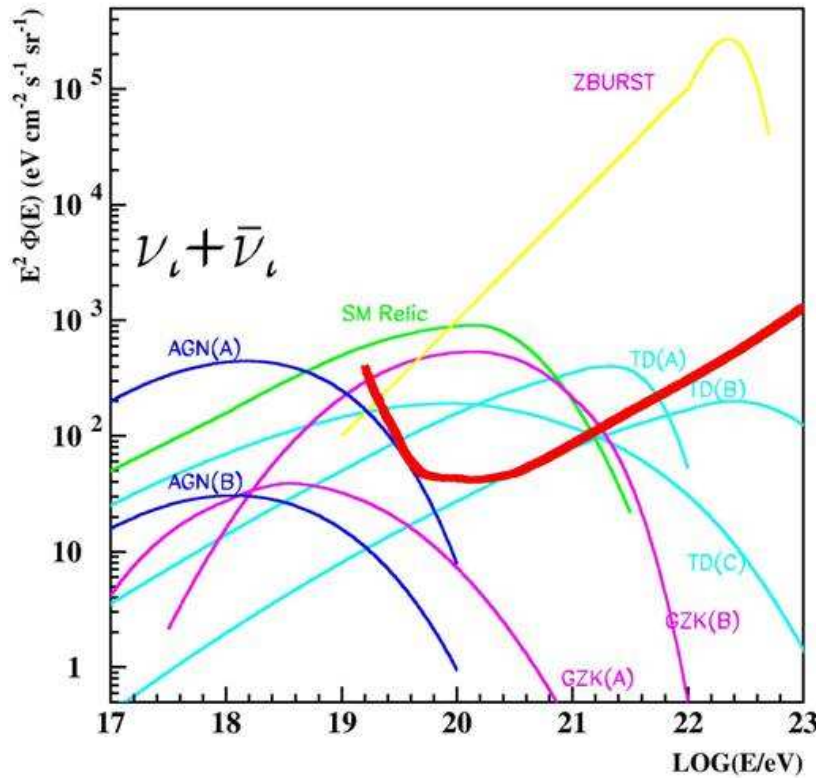

Figure 1: Fluxes of neutrinos from various models. GZK (B) and GZK(A) are respectively the "maximum" and "minimum" GZK neutrino fluxes per flavour considered in this work. The broad line is the EUSO limit

Due to the very small value of the EECR and neutrino fluxes, their detection require the indirect observation through their atmospheric induced showers (EAS) and very lage detectors. The outcoming generation of such EECR detectors plans to look at the EAS from space observatories. From the space it is possible to observe the fluorescence light emitted in the terrestrial atmosphere by the gigantic showers produced by extreme energy cosmic rays. Several experiment have been proposed for performing such an observation from orbiting spacecrafts (AIRWATCH concept) : TUS [6] on board of a Russian satellite, OWL [7] (proposed by NASA physicists) on board of two satellites in order to obtain a stereoscopic view of the shower, KLYPVE [5] on board of the Russian section of the International Space Station (ISS) and EUSO [8] as external payload attachment to the European module Columbus of the ISS. Assuming the average altitude of the ISS at 400 km, the full coverage FOV is 140.8^o, the area of the corresponding observed terrestrial surface $\approx 1.5 \cdot 10^7$ km^2, and the mass of the corresponding volume of air $\approx 150 \cdot 10^{12}$ t. The realization of a neutrino observatory can be pursued acting in two directions: (a) going down in the energy threshold for the observation of the atmospheric showers, thus profiting of the expected increase of the rates in the lower energy region, where the flux is much higher; (b) and/or increasing the FOV for including in the observation as much as possible area of the terrestrial surface. In order to decrease the energy threshold we can both increase the diameter of the optical system collecting the fluorescence light, and the efficiency of the sensors in converting this light in an electric signal.

3   Optical design proposals

The optical configuration of a system for UHEN detection is determined by several factors. An important constraint is given by the aperture of the system, which is linked to the number of events to be detected. The choice of the Entrance Pupil Diameter (EPD) is driven by radiometric consideration. For the purpose of UHEN detection, an $EPD > 5m$ has to be considered. The larger the EPD, the lower the energy threshold of particles under investigation, but the signal is also affected by the geometry, as a vignetting factors enters the intensity formula:

$$S \propto \cos 2a \cdot \frac{EPD}{H} \tag{1}$$

S=detected signal, a=angle from optical axis, EPD=Entrance Pupil Diameter, H=orbit height

Moreover the EPD and the height of the orbit scale inversely: increasing the height of the orbit to increase observed area requires scaling EPD. Signal is also proportional to the overall transmission of the optics, including transmission

and diffusion of eventual refractive elements, reflectivity and diffusion of mirrors and obscuration by focal plane and other optical and mechanical elements The overall dimension of the photon detector area is given as a function of the FOV and of the focal length:

$$D = 2 \cdot f \cdot \sin \frac{\theta_{FOV}}{2} \qquad (2)$$

θ_{FOV} = overall field of view, f = focal length of the system.

From eq (2) it is clear that in order to keep the detector Diameter as small as possible, reducing so the overall weight of the telescope, one need short focal length. The picture is much more clear by introducing the $F/\sharp$ parameter: $F/\sharp = f/EPD$. A small detector diameter is guaranteed by fast optical systems:

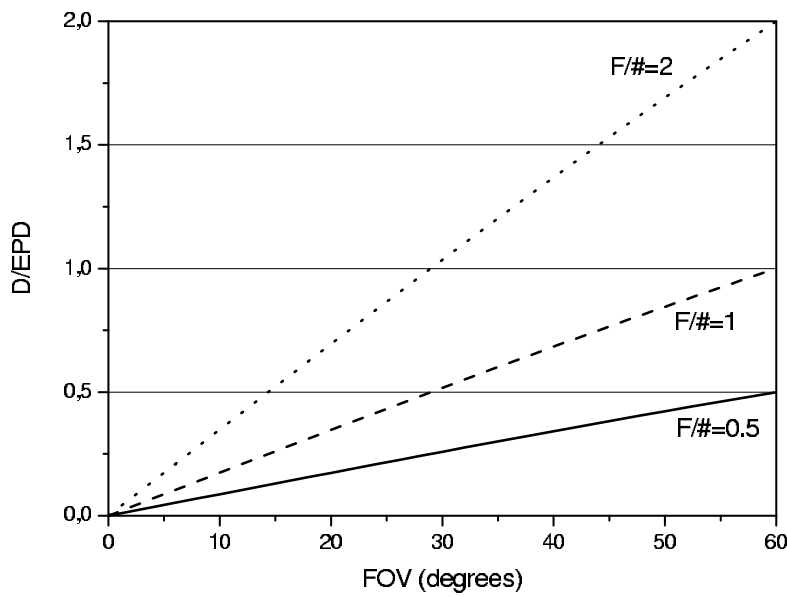$$D = 2 \cdot EPD \cdot F/\sharp \cdot \sin \frac{\theta_{FOV}}{2} \qquad (3)$$

Figure 2: Detector diameter and FOV

Figure 2 can help in choosing an optical configuration with smaller FOV or smaller $F/\sharp$. With FOV=60° and $F/\sharp = 1$, the detector is as large as the EPD! Since it is very rare finding in literature examples of optical systems with $F/\sharp <$

Table 1: optical design data

Parameter	Value
EPD	$5m$
resolution on ground	$0.1km$
orbit height	$400km$
$F/\sharp$	1
FOV	$\pm25°$

0.5, it appears clear that an optical configuration suitable for UHEN detection should rather accept a 20-25° halfangle FOV. The typical radial extension of a shower of particles induced as the cosmic rays and neutrinos interact with the atmosphere is about 1 km , while the streak of scintillation light spreads over $10 - 30$ km in length along its passage in the atmosphere. In order to observe the lights streak along its entire path, several spots shall be detected. When viewed continuously, the scintillation flash moves on a straight path with the speed of light, and the light recorded in the track is proportional to the Primary energy. The ideal configuration would therefore be that each detector pixel covers on ground an area of about 1 km2 in size corresponding to the dimension of the extended shower of particles caused by cosmic ray hit. On the other hand, the ground resolution is inversely proportional to $F/\sharp$:

$$groundresolution = H \cdot \frac{S_D}{f} = H \cdot \frac{S_D}{EPD \cdot F/\sharp} \propto \frac{S_D}{F/\sharp} \qquad (4)$$

where S_D is the dimension of the spot. A good ground resolution can not match a small $F/\sharp$ and therefore a large FOV. Once again, the solution with a limited FOV is advisable. The actual resolution is usually worse, as it is affected by the aberration of the optics. Since here we are far from the diffraction limit, we can accept a highly aberrated system. The best image spot size given by the configuration selected can be easily calculated by geometrical considerations. For the values given in table 1, the smaller achievable spot size is 14 mm. The result is independent of the optics, the spots are usually larger because of aberrations. Baring in mind the basic optical data stored in table 1, one can set up a preliminary design of the optics based on a spherical primary mirror configuration. Optimization and analysis done by ray-tracing technique aimed at maintaining the spot diagram diameter within the needed pixel size dimension to match the desired resolution, assuring at the same time a good vignetting factor and a high amount of energy falling into RMS spot radius. The RMS spot radius was calculated with reference to the centroid, the central ray of the distribution of rays traced, and computed through a Gaussian quadrature

algorithm. The ground resolution obtained with pure reflecting systems is very poor. Even if we limit the halfangle FOV to 15°, the resolution obtained is more than twice what we need (figure 3). The reason is that a concave spherical mirror is always affected by spherical aberration. The Schmidt configuration introduces a corrector which enable to reduce consistently the optical aberration. Such a system, optimized on axis, leads to excellent results for little deviation from the optical axis, while it shows a rapid fall of the performance as marginal fields become dominant. Since a good performance on axis is not crucial, another optimization can be performed, in order to preserve the desired RMS spot radius (and consequently on ground resolution) even at larger angles, where the dimension of spot diagrams are homogeneous over the entire field. A more detailed analysis [9] reveals that there are some differences depending on the wavelength, resulting in a smaller spot dimension for a higher wavelength. Different curves start to match together for angles of about 18°, which is also the value on the X axis in figure 3 when all the curves related to the Schmidt configuration start to increase upwards. The performance of the system may be further improved by using an aspherical mirror as a primary. Although the manufacturing of an aspheric surface of large dimensions is not straightforward, the achievement obtained with such a mirror is notable.
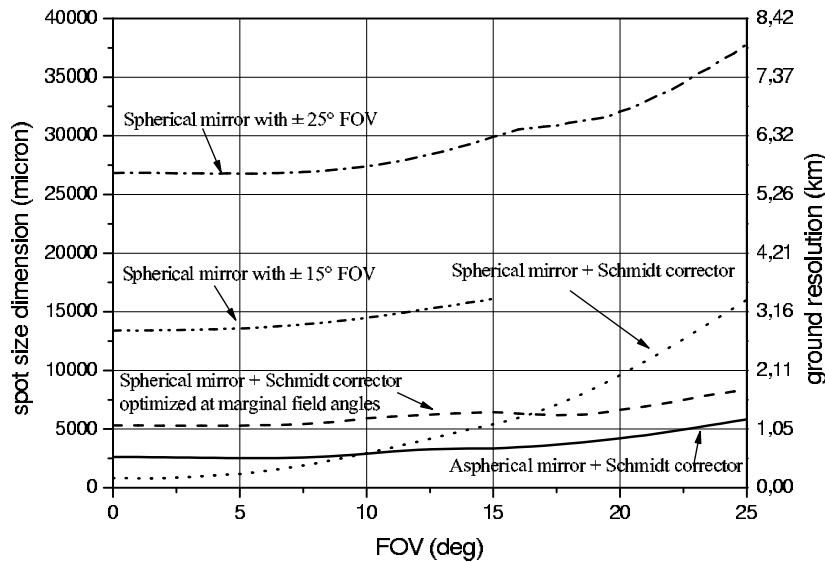

Figure 3: resolution of 5 m EPD reflecting systems

4   Technological issues

Multiple mirrors seem to be a reasonable approach for optical telescopes with large apertures. Small segments have potential for lightweight and low-cost telescope mirrors. Moreover, the optical configuration here presented is considerably large, exceeding the dimensions of the available spacecraft for space transportation, therefore a segmented mirror to be open once in orbit appears to be a suitable solution. The simplest deployment mechanism consists in dividing the mirror into a fixed center structure, about the same size of the focal plane, surrounded by a "petal" structure holding the remaining mirror. The whole could be closed around the focal plane and the corrector plate, achieving a compact cylindrical structure with a diameter close to that of the entrance pupil. The length will result about twice the focal length, or even less if a system to reduce the distance from the mirror to the focal plane is reduced.

Possible deployment techniques are still under review. Beyond the easiest self-deployment technique, it may be worth to remind that such a system could also be assembled by robots on the Shuttle or by robotic arms available on ISS. Furthermore, after assembling on ISS the system can be either remain attached to the station as an external payload or moved to a different orbit as a free flyer. NASDA's Engineering Test Satellite ETS-VIII is a technology test for large-Scale Deployable Reflectors, mainly devoted to mobile satellite communications from geostationary orbit, with an overall extension of 40 m.

The main limitation to the aperture dimension for a Schmidt-type telescope is the refracting material of the plate corrector, which can collapse upon its own weight. Recently proposed optical design solutions for Schmidt-type telescopes demonstrated that a combination of segmented mirrors and refractive surfaces, driven by active optics elements, can overcome this problem, resulting in very high aperture Schmidt telescope (up to 4m in diameter). The tolerances involved in the mechanical deployment system are not stringent for the present design, because of the relatively large spot dimensions. The angular tolerances for the mirror surface result to be several mrad, easily achievable with mechanical systems without any in-orbit adjustment. Requirements on the mirror alignment tolerances are then much more relaxed with respect to a classical telescope for astronomical observation or other imaging optical systems. The fact that mirrors can be supported from behind is an additional advantage in the mechanical design.

A possible technology for the mirror in such design could the nickel electroforming replica. The replication technique by nickel electroforming is a well known technology used to obtain thin, lightweight and good quality mirrors[10]. Further advances in this technology may provide significant reductions in the thickness and consequently weight of the mirrors. These results have been achieved without degradation of the mirror optical quality and this technique is still far from being fully exploited. The electroforming

technique is ideally suited for the production of many identical mirrors from one master, all being then assembled together to form a segmented, deployable axis symmetrical reflector, with considerable gain in terms of costs and weight. The thermal properties of metallic mirrors will induce uniform temperature changes due to the space environment, preventing from eventual radiation induced aberration, a typical problem one has to deal with in space, when other material like plastics is used. Metals present predictable thermal properties, enabling to predict the performance of the mirror at a wide range of temperatures with a high degree of reliability.

5   Conclusion

An UHEN observatory from space can be built with large mirrors, and the construction is already possible with existing technologies, scaling the dimension in order to get a higher signal, and hence a lower energy threshold. The orbit can also be higher, increasing the observed area downward. Better performance is obtained with a design including an aspherical primary mirror, yielding either to a possible significant reduction of the total mass of the system by reducing the size of every single pixel or to a higher limiting FOV by maintaining a greater spot size radius. Several construction technology may be considered for the manufacturing of the telescope, amongst them, replication by nickel electroforming is a widely used technique for producing cost effective and light weight optics for space applications.

References

[1] "The Pierre Auger Project Design Report," Fermilab, 1996

[2] D.J. Bird et al., "The Cosmic Ray Energy Spectrum Observed by the Fly's Eye" Ap.J., 424, 491, 1993.

[3] N. Chiba et al., "Akeno Giant Air Shower Array (AGASA) covering 100 km2 area", Nucl. Instr. Methods, A311, 338-349, 1992

[4] D. J. Bird et al.: Phys. Rev. Lett. 71 (1993) 3401; N. Hayashida et al.: Phys. Rev. Lett. 73 (1994) 3491. M. Takeda et al. Phys. Rev. Lett. 81 (1998) 1163

[5] Oleg E. Kalashev et al. Phys.Rev.D66:063004,2002

[6] B.A. Khrenov et al. "Space program KOSMOPETL ....." Metepec 2000, Observing ultrahigh energy cosmic rays from space and earth 57-75

[7] R.E. Streitmatter for the OWL collaboration. "Orbiting Wide Angle Light-Collectors (OWL) : Observing Cosmic Rays from Space" College Park 1997, Observing giant cosmic ray air showers 95-107.

[8] L. Scarsi et al., "Extreme Universe Space Observatory", proposal to ESA for the F2/F3 missions ; ESA and EUSO Team, "Extreme Universe Space Observatory - Report on the accommodation of EUSO on the Columbus Exposed Payload Facility" ESA/MSM-GU/2000.462/AP/RDA December 2000, O. Catalano et al. ICRC 2003 HE1.5 pg. 1081

[9] P.Mazzinghi, V.Bratina, "Wide-field reflector for the detection of HECR from space", SPIE Proceedings 5166, UV/Optical/IR Space Telescopes: Innovative Technologies and Concepts

[10] A. Valenzuela et al., "Cost Effective Ultra Light Weight Mirrors" Proceedings Ultra Lightweight Optics Challenge, Pasadena, (1999)

THE PIERRE AUGER OBSERVATORY: A PROGRESS REPORT

SERGIO PETRERA [a]
FOR THE PIERRE AUGER COLLABORATION

[a] *INFN and Dipartimento di Fisica, Università di L'Aquila,
via Vetoio, 67010, Italy*

Abstract

The Pierre Auger Observatory is in advanced stage of construction in the southern site of Malargüe, Argentina. This progress report mainly focuses on hybrid events, a remarkable subset of cosmic ray events which are simultaneously detected by both Surface Detector and Fluorescence Detector subsystems. The hybrid method and its performances are presented.

1 Introduction

The Pierre Auger Observatory [1] is an international experiment with the goal of exploring with unprecedented statistics the cosmic ray spectrum above 10^{19} eV. Of particular interest are cosmic ray particles with energy $> 10^{20}$ eV. At these energies they interact with cosmic microwave background radiation thus generating a spectrum cutoff, known as GZK effect [2]. This effect attenuates

the particle flux except if their sources are in our cosmological neighborhood ($<$ 100 Mpc). Furthermore protons of these energies may point back to the source and open a new kind of astronomy with charged particles.

The extremely low rate, a few particles per km^2 sr century, of cosmic rays above the GZK cutoff requires a large area detector. The Auger Southern Observatory, in advanced stage of construction close to the town of Malargüe, Province of Mendoza, Argentina, covers an area of 3000 km^2.

Cosmic rays are detected by the Auger Observatory with two different experimental techniques. The Surface Detector (SD), a giant array of 1600 water Cherenkov tanks, placed over the Observatory area with a spacing of 1.5 km, measures the shower particle density and arrival times at ground level. Presently about one third of the SD tanks are already taking data.

The Fluorescence Detector (FD), composed by a set of 24 telescopes, simultaneously measures the longitudinal development of the cosmic ray shower in the atmosphere above ground. The telescopes are arranged in fou r peripheral buildings (Eyes), each housing 6 telescopes, overlooking the SD array. The first two buildings at Los Leones and Coihueco are completed, with their 12 FD telescopes taking data. The Los Morados building is under construction.

Numerous data are being collected by Auger. Preliminary analyses based on either subsystems show good consistency and comprehension of the whole detector. In this stage, particular attention is devoted to hybrid detection, i.e. with the cosmic ray observed simultaneosly by the array tanks and the fluorescence telescopes. This allows high precision energy and arrival direction determination and deeper understanding of the systematics of energy scale of the two techniques. This progress report will focus on hybrid reconstruction method and its application to preliminary data. Other features of Auger data analysis are given in [3].

2   The Surface Detector

The Surface Detector (SD) is made of water Cherenkov tanks. The tanks have 3.6 m diameter and 1.2 m height to contain 12 m^3 of clean water viewed by three 9" photomultiplier tubes (PMT). A solar panel and a buffer battery provide electric power for the local intelligent electronics, GPS synchronization system and wireless LAN communication. A picture of one tank in the field, showing its main components, is shown in Figure 1.

Cosmic ray muons produce an essential calibration signal of about 80 photoelectrons in one PMT. The signals are continuously digitised with 16 bit dynamic range at 40 MHz sampling rate and temporarily stored in local memory. The time structure of PMT pulses carries rich information related to the mass of the primary particle. The trigger conditions include a *threshold trigger* (one or more FADC counts above 3.2 Vertical Equivalent Muon [*VEM*]
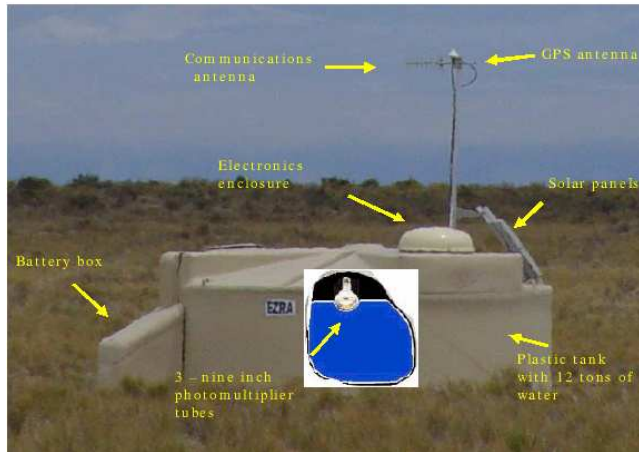
Figure 1: A SD tank in the field. The main components of the detector are sketched in the figure.

in each of 4 or more tanks) and a *time over threshold trigger* (12 FADC bins exceeding 0.2 VEM in sliding window of 3 μs in each of 3 or more tanks) Detection efficiency will begin around 10^{18} eV and reach 100% at 10^{19} eV.

3 The Fluorescence Detector

The Fluorescence Detection method is based on the measurement of fluorescence photons emitted from the shower in its development through the atmosphere. The nitrogen molecules excited by shower particles emit isotropically fluorescence photons, with wavelengths between 300 to 400 nm. The fluorescence yield is ≈ 4 photons per electron traversing one meter of atmosphere, approximately constant as a function of altitude. The fluorescence light is collected by a large mirror and focused on a pixellated surface. The arrival direction of the cosmic ray is then reconstructed from the pixel directions and signal times.

The Fluorescence Detector (FD) consists of 24 wide-angle Schmidt telescopes grouped in four stations. Each telescope (see Figure 2) has a 30° field of view in azimuth and vertical angle. The four stations at the perimeter of the surface array consist of six telescopes each for a 180° field of view inward over the array. A picture of one of the FD telescopes installed in the Los Leones building is shown in Figure 2.

Each telescope is formed by segments to obtain a total surface of 12 m^2 on a radius of curvature of 3.40 m. The aperture has a diameter of 2.2 m and is equipped with optical filters and a corrector lens. In the focal surface
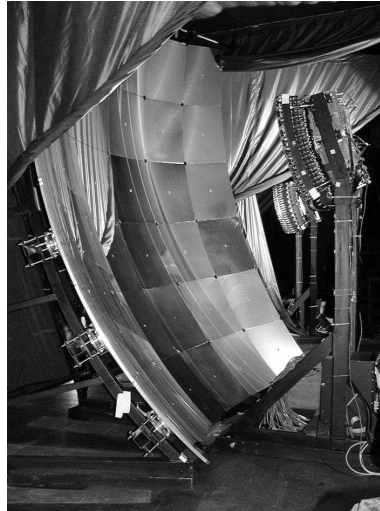
Figure 2: The FD telescope: on the left the spherical mirror with square shaped segments, on the right the PMT camera. The adjacent telescope's camera is also seen in the background.

a photomultiplier camera detects the light on 20×22 pixels. Each pixel covers $1.5° \times 1.5°$ and the total number of photomultipliers in the FD system is 13,200. PMT signals are continuously digitised at 10 MHz sampling rate with 15 bit dynamic range. The FPGA-based trigger system is designed to filter out shower traces from the random background of 100 Hz per PMT.

The absolute calibration of the detector follows an end-to-end approach, based on the uniform illumination of the pixels from a calibrated light source. This is obtained with a "drum" illuminator consisting of a pulsed UV LED embedded in a small cylinder of teflon and illuminating the interior of a 2.5 m diameter cylindrical drum, 1.4 m deep. The drum is positioned at the entrance aperture of the telescope under calibration. Relative optical calibration is also used to monitor time variations in the telescopes calibration during the periods of data taking.

Finally, attention is given to atmospheric monitoring, making use of laser beams, LIDAR's, calibrated light sources and continuous recording of weather conditions. Special efforts are being made to determine the air fluorescence efficiency and its dependence on relevant conditions.

4 Hybrid reconstruction

4.1 Geometry reconstruction

FD shower axis reconstruction proceeds in two stages. First, the shower detector plane (SDP) is derived from the angular pattern of hit FD pixels. The SDP is the plane containing the shower axis and the FD. Second, the shower spot angular motion is used to determine the orientation and location of the shower axis in the SDP. The axis is most conveniently described in terms of the SDP normal $\hat{n}_{SDP}$, the perpendicular distance from the FD to shower axis R_p, the angle χ_0 that the axis makes with the horizontal, in the SDP, and t_0 the time at which the shower passes closest to the FD. We call this the "mono" geometric reconstruction method because it relies on information from a single FD telescope. The time information of the pixels is then used for the reconstruction of the shower axis within the SDP. For a given geometry, the arrival time of light onto the pixel i, at angle χ_i, is given by the following expression

$$t_i = t_0 + \frac{R_p}{c} tan[(\chi_0 - \chi_i)/2], \tag{1}$$

The mono procedure suffers from having to find three geometric parameters (R_p, χ_0 and t_0) from a nearly linear relationship between spot position and time. The Auger hybrid procedure solves this problem by exploiting the time of shower front arrival at one or more SD stations. An effective reduction of the fit parameters is accomplished by specifying the time t_0 at which the shower front reaches the position of closest approach, which is related to the ground array tank time t_{GND}, its position $\vec{R}_{GND}$ and the shower axis unit vector $\hat{S}$ by the equation:

$$t_0 = t_{GND} - (\vec{R}_{GND} \cdot \hat{S})/c. \tag{2}$$

Fitting strategies which use only the timing information from the highest signal tank have been studied, as well as others using all the tanks in the event. In Figure 3, the time as a function of χ_i is shown for the hybrid event, with stars representing FD data, and the full line representing the best fit to the hybrid hypothesis. The tanks data are also represented on the same figure as open dots. The event is reconstructed as having a zenith angle of $35°$, and core location at 15 km from the Los Leones telescope. The event as seen by the array is shown in Figure 4. Ten tanks, represented as circles of radius proportional to the logarithm of the energy deposited, are included in the reconstruction. This event was also partly seen by a Coihueco telescope. In this case, the intersection of the SDP's provides an independent, purely geometrical ("stereo") determination of the shower direction and core position. The hybrid reconstruction and the "stereo" one are compatible within a few tenths of a degree, consistent with the expected hybrid accuracy on the shower direction reconstruction.
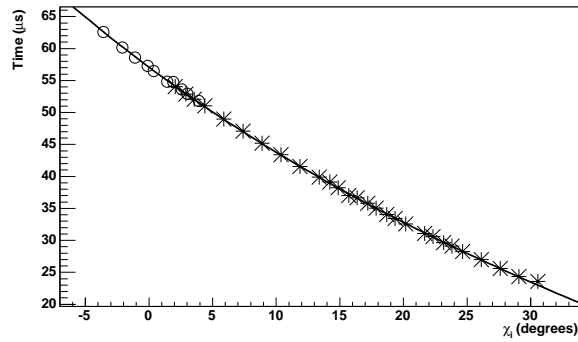
Figure 3: Time vs angle correlation for the hybrid event: stars represent FD data, open dots SD data, and the line is the results of the best fit to the hybrid geometry.

Particular attention is being paid to the systematic uncertainties associated to the basic detector measured quantities. The determination of the SDP relies on the FD pixels directions, and it is thus affected by possible misalignments of the telescopes with respect to their nominal direction. Detailed analyses of the reconstructed path of stars on the FD cameras, as well as of the reconstruction of laser shots fired in a known direction, indicate that the alignment is better than $0.1°$. The synchronization of the SD stations is given by the GPS receivers installed in each tank. A direct measurement of the SD/FD synchronization is provided by the CLF (Central Laser Facility) which fires periodically the
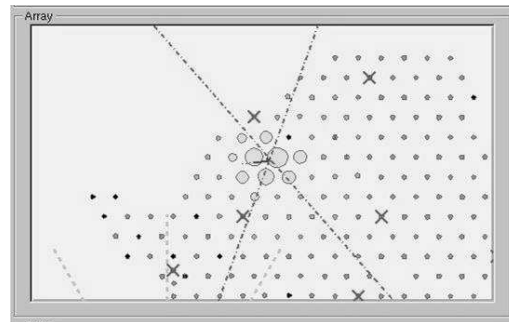

Figure 4: The hybrid event detected by the array. Tanks are represented by circles of radius proportional to the logarithm of the energy deposited. Dashed-dotted lines represent the intersection between the ground plane and the shower detector planes reconstructed by the telescopes.

FD with shower-like tracks and injects laser pulses into a tank placed next to the laser facility for this purpose. The tank's measurement of the pulse emission time can then be compared with the FD determination of the same pulse emission time. Differences of only a few hundreds of ns were found, and are corrected for in the data analysis.

4.2   Shower energy

In this phase of the analysis, shower energy estimation follows the independent procedures used in SD and FD detection. Nonetheless hybrid detection provides a remarkable constraint through the common geometry obtained with the hybrid fitting method described above.

In the Surface Detector energy is estimated from the lateral distribution function (LDF). This can be obtained from the measured signals at the water tanks as a function of the distance to the shower core. The measured LDF of the hybrid event is shown in Figure 5. The value of the LDF at 1000 m (S_{1000}) is correlated to the primary cosmic ray energy, giving about $2 \cdot 10^{19}$ eV.

The FD profile reconstruction procedure uses as input the calibrated ADC traces in all pixels. Using the reconstructed geometry of the shower axis and a model of aerosol scattering in the atmosphere is then possible to transform the light received at the detector to the light emitted from the shower axis as a function of slant depth (in g/cm^2). The Cherenkov light contamination, both direct and (Rayleigh and Mie) scattered, is subtracted from the profile [1]. The fluorescence light emitted from a volume of air is proportional to the energy dissipated by the shower particles in that volume. The integral of the light signal is thus proportional to the shower energy. The reconstructed longitudinal profile of the hybrid event, together with a fit to a Gaisser-Hillas function, is shown in Figure 6.

The estimated energy from the FD profile reconstruction for this hybrid event was also about $2 \cdot 10^{19}$ eV, in agreement with the S_{1000} determination.

Several hundreds of good quality hybrid events have been collected so far, and their number is continuously increasing with the progress of tanks and telescopes installation. Preliminary analysis show consistency between the energy estimates of the Fluorescence and Surface Detector.

5   Conclusions

The southern site of the Pierre Auger Observatory is in advanced stage of construction. Presently about one third of the Surface Detector and one half of the Fluorescence Detector are taking routinely data. The hybrid performances of the detector have been studied with dedicated field measurements and a first sample of events. The simultaneous measurement of the shower energy by two independent techniques, which is a unique feature of the Auger experiment,
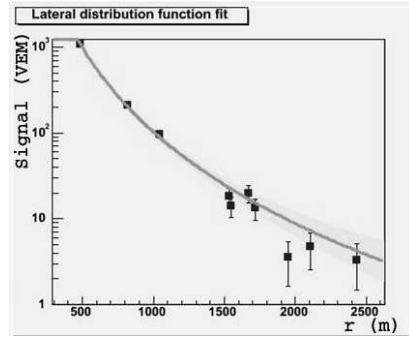
Figure 5: Reconstructed LDF for the hybrid event: the signal measured for each tank, expressed in Vertical Equivalent Muon (VEM) is plotted as a function of the tank distance to the shower core.
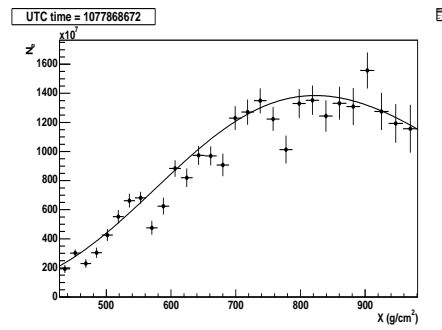

Figure 6: The reconstructed longitudinal profile of the hybrid event: the number of shower particles as a function of the slant depth.

provides intercalibration and strengthen the knowledge of the absolute energy scale, which is of primary importance in the study of the GZK cutoff.

References

[1] The AUGER Collaboration, "Properties and performances of the prototype instrument for the Pierre Auger Observatory", Nucl. Instr. Meth. A523 (2004) 50-95

[2] K. Greisen, Phys. Rev. Lett. 16 (1966) 748;
G.T. Zatsepin, V.A. Kuzmin, Sov. Phys. JETP Lett. 4 (1966) 78.

[3] A. A. Watson, contribution to this conference

COSMIC RAYS IN THE PEV RANGE: RESULTS FROM KASCADE

A. Haungs[1], T. Antoni[2], W.D. Apel[1], F. Badea[1], K. Bekk[1], A. Bercuci[3],
M. Bertaina[4], H. Blümer[1,2], H. Bozdog[1], I.M. Brancus[3], M. Brüggemann[5],
P. Buchholz[5], C. Büttner[2], A. Chiavassa[4], A. Chilingarian[6],
K. Daumiller[1], P. Doll[1], R. Engel[1], J. Engler[1], F. Fessler[1], P.L. Ghia[7],
H.J. Gils[1], R. Glasstetter[8], D. Heck[1], J.R. Hörandel[2], K.-H. Kampert[8],
H.O. Klages[1], Y. Kolotaev[5], G. Maier[1], H.J. Mathes[1], H.J. Mayer[1],
J. Milke[1], C. Morello[7], M. Müller[1], G. Navarra[4], R. Obenland[1],
J. Oehlschläger[1], S. Ostapchenko[1], S. Over[5], M. Petcu[3], S. Plewnia[1],
H. Rebel[1], A. Risse[9], M. Risse[1], M. Roth[2], G. Schatz[1], H. Schieler[1],
J. Scholz[1], T. Thouw[1], G. Toma[3], G.C. Trinchero[7], H. Ulrich[1],
S. Valchierotti[4], J. van Buren[1], A. Vardanyan[6], W. Walkowiak[5],
A. Weindl[1], J. Wochele[1], J. Zabierowski[9], S. Zagromski[1], D. Zimmermann[5]

[1] *Institut für Kernphysik, Forschungszentrum Karlsruhe, Germany*

[2] *Institut für Experimentelle Kernphysik, Universität Karlsruhe, Germany*

[3] *Nat. Inst. Physics and Nuclear Engineering, Bucharest, Romania*

[4] *Dipartimento di Fisica Generale dell'Università, Torino, Italy*

[5] *Fachbereich Physik, Universität Siegen, Germany*

[6] *Cosmic Ray Division, Yerevan Physics Institute, Armenia*

[7] *Istituto di Fisica dello Spazio Interplanetario, CNR, Torino, Italy*

[8] *Fachbereich Physik, Universität Wuppertal, Germany*

[9] *Soltan Institute for Nuclear Studies, Lodz, Poland*

Abstract

KASCADE is determining flux spectra for different primary mass groups to disentangle the knee feature of the primary cosmic-ray energy spectrum. The energy spectra of the light element groups result in a knee-like bending and a steepening above the knee. The topology of the individual knee positions show a dependency on the primary particle. To quantify this dependence the KASCADE array is now extended by a factor of 10 in area. The major goal of the new KASCADE-Grande array is the observation of the 'iron-knee' in the cosmic-ray spectrum at around 100 PeV which is expected following from the KASCADE results presented below.

1   Introduction

The all-particle energy spectrum of cosmic rays shows a distinctive feature at few PeV, known as the *knee*, where the spectral index changes from -2.7 to approximately -3.1. At that energy direct measurements are presently not possible due to the low flux, but indirect measurements observing extensive air showers (EAS) are performed. Astrophysical scenarios like the change of the acceleration mechanisms at the cosmic ray sources (supernova remnants, pulsars, etc.) or effects of the transport mechanisms inside the Galaxy (diffusion with escape probabilities) are conceivable for the origin of the knee as well as particle physics reasons like a new kind of hadronic interaction inside the atmosphere or during the transport through the interstellar medium.

Despite of 50 years of EAS measurements the origin of the kink is still not clear, as the disentanglement of the threefold problem of estimate of energy and mass plus the understanding of the air-shower development in the Earth's atmosphere remains an experimental challenge. To solve the puzzle the access is to reconstruct energy spectra of individual elements (or mass groups), accompanied by a careful investigation of the hadronic interaction mechanisms driving the air-shower development. For a detailed discussion of the subject see a recent review [1].

The KASCADE (KArlsruhe Shower Core and Array DEtector) experiment [2] approaches this goal by measuring as much as possible redundant information from each single air-shower event. The multi-detector system allows to measure the total electron and muon numbers ($E_\mu > 240\,\mathrm{MeV}$) of the shower separately using an array of 252 detector stations containing shielded and unshielded detectors at the same place in a grid of $200 \times 200\,\mathrm{m}^2$. The excellent time resolution of the detectors allows also decent investigations of the arrival directions of the showers in searching large scale anisotropies and, if exist, cosmic ray point sources. Additionally muon densities at three more different
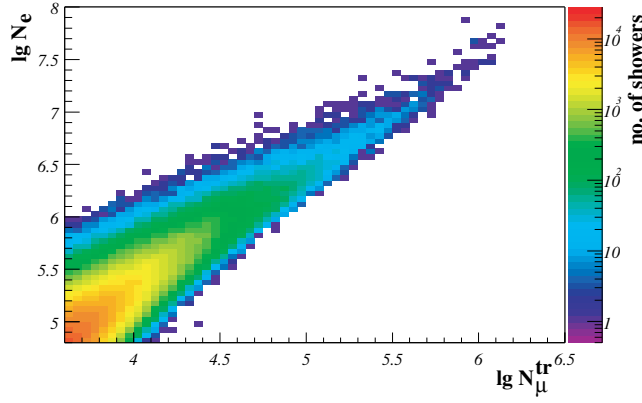
Figure 1: Two dimensional electron (N_e) vs. muon (N_μ^{tr}, i.e. number of muons in 40-200m core distance) number spectrum measured by the KASCADE array. Only showers with zenith angle $<18°$ are included.

muon energy thresholds and the hadronic core of the shower by a $300\,\mathrm{m}^2$ iron sampling calorimeter are measured. These redundant information is mainly used for tests and improvements on the hadronic interaction models unavoidably needed for the interpretation of air shower data.

In the following we present the results of KASCADE, in particular an unfolding of the measured two-dimensional electron vs. muon number spectrum into energy spectra of five primary mass groups. The results motivate the extension of KASCADE to measure higher primary energies, which will be realized by KASCADE-Grande.

Covering a wide energy range KASCADE-Grande is also the ideal test-ground for the development of new techniques of air-shower detection. With this view, recently an array of dipol-antennas for measuring the radio emission in the Atmosphere by high-energy cosmic rays were put into operation.

2   KASCADE results

2.1   Energy spectra of individual mass groups

The content of each cell of the two-dimensional spectrum of electron number vs. muon number (Fig. 1) is the sum of contributions from the 5 considered primary elements. Hence the inverse problem $g(y) = \int K(y,x)p(x)dx$ with $y = (N_e, N_\mu^{\mathrm{tr}})$ and $x = (E, A)$ has to be solved. This problem results in a system of coupled Fredholm integral equations of the form

$$\frac{dJ}{d \lg N_e \, d \lg N_\mu^{tr}} = \sum_A \int_{-\infty}^{+\infty} \frac{d J_A}{d \lg E} \cdot p_A(\lg N_e , \lg N_\mu^{tr} \mid \lg E) \cdot d \lg E$$
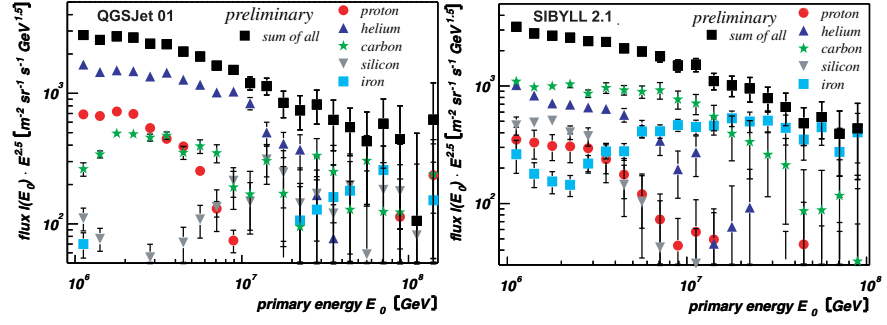
Figure 2: Result of the unfolding procedure. Left: based on QGSJet 01; right: based on SIBYLL 2.1.

where the probability p_A

$$p_A(\lg N_e, \lg N_\mu^{tr} \mid \lg E) = \int\limits_{-\infty}^{+\infty} k_A(\lg N_e^t, \lg N_\mu^t) d \lg N_e^t \, d \lg N_\mu^t$$

is a further integral with the kernel function $k_A = r_A \cdot \epsilon_A \cdot s_A$ factorized into three parts. The quantity r_A describes the shower fluctuations, i.e. the distribution of electron and muon number for given primary energy and mass. The quantity ϵ_A describes the trigger efficiency of the experiment, and s_A describes the reconstruction probabilities, i.e. the distribution of reconstructed N_e and N_μ^{tr} for given true numbers of electrons and muons. The probabilities p_A are obtained by parameterizations of Monte Carlo simulations for fixed energies using a moderate thinning procedure as well as fully simulated showers as input of the detector simulations.

The procedure is tested by using random initial spectra generated by Monte Carlo simulations. It shows that knee positions and slopes of the initial spectra can be reproduced and that the discrimination between the five primary mass groups is sufficient. For proofing the unfolding procedure, different mathematical ways of unfolding (Gold-algorithm, Bayes analyses, etc.) have been compared and the results are consistent [3].

The application of the unfolding procedure to the data is performed on basis of two different hadronic interaction models (QGSJet 01 [4], SIBYLL 2.1 [5]) as options embedded in CORSIKA [6] for the reconstruction of the kernel functions [7].

By applying the above described procedures to the experimental data energy spectra are obtained as displayed in Fig. 2. Knee like features are clearly visible in the all particle spectrum as well as in the spectra of primary proton and helium. This demonstrates that the elemental composition of cosmic rays is dominated by light components below the knee and dominated by a heavy component above the knee feature. Thus the knee feature originates from a

decreasing flux of the light primary particles. This observation corroborates results of the analysis of muon density measurements at KASCADE [8], which are performed independently of the unfolding procedure.

2.2   Inaccuracy of hadronic interaction models

Comparing the unfolding results based on the two different hadronic interaction models, the model dependence when interpreting the data is obvious. The first interaction of the primary particle in the atmosphere is inaccessible for the present man made accelerator experiments in both, in the energy and in the kinematic region of the extreme forward direction. Hence modeling these interactions underlies assumptions from particle physics theory and extrapolations resulting in large uncertainties, which are reflected by the discrepancies of the results presented here. Hints for the inadequate description of the hadronic interactions at the atmosphere are also given by additional KASCADE data analyses taking the advantage of the multi-detector information, i.e. investigations of the hadron component in air-showers with the KASCADE hadron calorimeter [9] and comparing muon densities for different muon energy thresholds [10]. These investigations show that none of the present hadronic interaction models are able to describe all the KASCADE data consistently (on a level of a few percent). Recently some efforts are made to sample the information from accelerator experiments and cosmic ray investigations [11, 12] to improve the hadronic interaction models.

2.3   Search for anisotropies and point sources

Investigation of anisotropies in the arrival directions of the cosmic rays give additional information on the cosmic ray origin and of their propagation. Depending on the model of the origin of the knee one expects large-scale anisotropies on a scale of 10^{-4} to 10^{-2} in the energy region of the knee and depending on the assumed structure of the galactic magnetic field. For example in Fig. 3 (left panel) the predictions from calculations of Candia et al. [13] are compared with the limits of anisotropy given by KASCADE results [14]. The KASCADE limits were obtained by investigations of the Rayleigh amplitudes and phases of the first harmonics. Taking into account possible nearby sources of galactic cosmic rays like the Vela Supernova remnant [15] the limits of KASCADE already exclude certain model predictions. But for a complete picture the investigations have to be performed with air shower samples of the different mass groups which need a higher statistics in measurements.

Interest for looking to point sources in the KASCADE data sample is given by the possibility of unknown near-by sources, where the deflection of the charged cosmic rays would be small or by sources emitting neutral particles like high-energy gammas or neutrons. Due to their small decay length the latter ones are
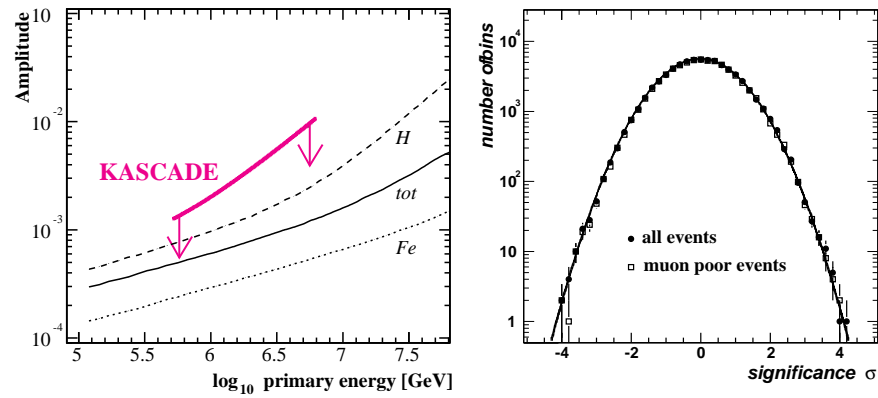
Figure 3: Left: Rayleigh amplitude of the harmonic analyses of the KASCADE data [14] (limit on a 95% confidence level). Right: Significance distributions for searching point sources on the sky map seen by the KASCADE experiment [16].

of interest for near-by sources only. Fig. 3 (right panel) shows the distribution of significances for a deviation of the flux from the expected background for all bins of the visible sky of KASCADE. Shown are the distributions for the full sample of air showers as well as for a sample of "muon-poor" showers which is a sample with an enhanced number of candidates of γ-ray induced events. No significant excess was found in both samples [16].

3   KASCADE-Grande

To solve the puzzle of the origin of the knee data extending to higher primary energy is obviously required. For example a confirmation of the dependence of the knee positions for the various elemental groups the experimental observation of an 'iron-knee', expected at around 100 PeV primary energy is required. For that purpose the KASCADE experiment has been enlarged by an installation of additional 45 detector stations (37 as Grande array plus 8 as Piccolo trigger array) in a grid of $700 \times 700 \, \mathrm{m}^2$. In the present configuration KASCADE-Grande consists of sensitive detectors of an area of $965 \, \mathrm{m}^2$ for the electron component, of $1070 \, \mathrm{m}^2$ for measuring muons at four different energy thresholds, and of $300 \, \mathrm{m}^2$ for hadron detection. Thus KASCADE-Grande displays the full capability of a multi-detector experiment [17] and continue to measure high-quality data as the original KASCADE experiment.

4   Radio measurements with LOPES

LOPES is a small array of radio antenna to operate in conjunction with KASCADE-Grande in order to calibrate the radio emission from cosmic ray air showers. At present, LOPES operates 10 dipole antennas in coincidence with KASCADE [18]. The antennas are positioned between the array detectors of KASCADE and data are collected when a special trigger for very high-energy events is received from the KASCADE array. The antennas are operated in the frequency range of 40-80 MHz. For several air-shower events a coincident and coherent signal has been found in the data of the radio antenna and a preliminary analysis has already been performed [19]. The main goal of further investigations is to calibrate the radio signal with help of the observables of the individual air-showers given by KASCADE-Grande.

5   Conclusions

Due to the uncertainties of the results described above, in particular arising from the inadequacy of the hadronic interaction models, still there are only weak constraints for astrophysical models to explain the knee in the primary cosmic ray energy spectrum. Hence most of the current models cannot be excluded by the present measurements. In future, by having the data of the KASCADE-Grande experiment and by improving the hadronic interaction models better constraints especially at higher primary energies are expected. Thus cosmic ray physics at energies around the knee remains a vital field of research with high scientific interest.

References

[1] A.Haungs, H.Rebel, M.Roth, Rep.Prog.Phys.**66**,(2003),1145

[2] T.Antoni et al. KASCADE coll., Nucl. Instr. Meth. A **513** (2003) 429

[3] H.Ulrich et al., Nucl.Phys.B (Proc.Suppl.) **122**, (2003), 218

[4] N.N.Kalmykov, S.S.Ostapchenko, Yad.Fiz. **56**, (1993), 105

[5] R.Engel et al., 26thICRC(Salt Lake City) **1**, (1999), 415

[6] D.Heck et al., Rep.FZKA 6019, Forschungszentrum Karlsruhe (1998)

[7]   M.Roth, H.Ulrich et al., 28^{th}ICRC(Tsukuba) **1**, (2003), 131

[8]   T.Antoni et al.-KASCADE coll., Astrop.Phys. **16**, (2002), 373

[9]   J.Milke et al., Nucl.Phys.B (Proc.Suppl.) **122**, (2003), 388

[10] A.Haungs et al., Nucl.Phys.B (Proc.Suppl.) **122**, (2003), 384

[11] R.Engel et al., Nucl.Phys.B (Proc.Suppl.) **122**, (2003), 437

[12] H.Rebel, Proc. of the 23rd Int. Workshop on Nucl. Theory, Bulgarian
       Academy of Sciences, Rila Mountains, June (2004)

[13] J.Candia et al., J. Cosmol. Astropart. Phys. **5**, (2003), 3

[14] T.Antoni et al. - KASCADE coll., Astrophys. J. **604**, (2004), 687

[15] V.Ptuskin, Int.Symp.HE Gamma-Ray Astron. Heidelberg, July (2004)

[16] T.Antoni et al. - KASCADE coll., Astrophys. J. **608**, (2004), 865

[17] A.Haungs et al. - KASCADE-Grande coll., 28^{th}ICRC(Tsukuba) **2**, (2003),
       985

[18] A.Horneffer et al., 28th ICRC(Tsukuba) **2**, (2003), 969

[19] A.Horneffer et al., Proc. of SPIE conference, Glasgow (2004), in press.

HIGH ENERGY COSMIC RAY STUDIES: FINAL RESULTS FROM EAS-TOP

Gianni Navarra [a,b] for the EAS-TOP Collaboration

[a] *Dipartimento di Fisica Generale, Università di Torino*

[b] *INFN, Sezione di Torino, via P. Giuria, 1 10125 Torino, Italy*

Abstract

We present the results of the EAS-TOP experiment in the study of cosmic rays in the energy region 10^{12}-10^{16} eV concerning the primary spectrum, composition and anisotropy. The analysis of very inclined air showers, and their application to high energy neutrino physics are discussed.

1 Introduction

The EAS-TOP experiment has been planned for the study of cosmic rays, and of some aspects of hadronic interactions and Extensive Air Shower (EAS) properties, in the energy region overlapping the *direct* measurements and extending above the *knee* in the primary spectrum (10^{12}-10^{16} eV), i.e. the range which is usually considered to represent the high energy galactic radiation. The array (fig. 1) included detectors of the electromagnetic (35 modules, 10 m^2 of scintillators each), hadron + muon (144 m^2 of streamer tubes + Fe absorber, for $E_h > 50$ GeV and $E_\mu > 1$ GeV), Cherenkov
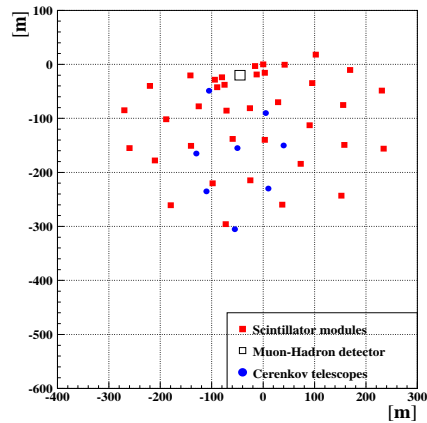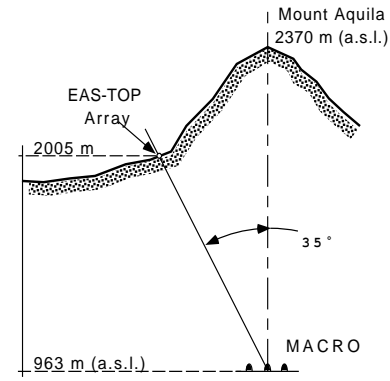
Figure 1: The EAS-TOP array.

Figure 2: The EAS-TOP location with respect to the underground Gran Sasso Laboratories.

light (7 telescopes) components of EAS[1], and, due to its location above the underground Gran Sasso laboratories (fig. 2), could run in coincidence with the TeV muon detectors MACRO and LVD. All the interpretations discussed in the following have been obtained through simulations based on QGSJET[2] as implemented in CORSIKA[3].

2   The spectra and composition

The connection with the *direct* measurements is summarized in figs. 2[4] and 2[5]. In fig. 2 the proton flux as derived from the single hadron measurements is shown, compared with the direct data. In fig. 2 the atmospheric Cherenkov light yield at core distance $125 < r < 145$ m for events recorded in coincidence with MACRO[1] is reported. Such photon density (which is proportional to the primary energy and is sensitive to the light components) is compared with the expectation from the JACEE[6] and RUNJOB[7] spectra. It results that the p-flux agrees with the *direct* data[4], and the (p+He) and (p+He+CNO) ones are consistent with the JACEE observations[5]. By using the p-flux obtained from the quoted measurements, we obtain (at 250 TeV): J(p):J(He):J(CNO)=(0.20 ± 0.08):(0.58 ± 0.19):(0.22 ± 0.17), i.e. in the 100 TeV region the He flux overcomes the p one (in agreement, at PeV energies, with the $N_e - N_\mu$ data [8]).

---

[1]The collaboration with MACRO has been determinant for reaching part of these results.
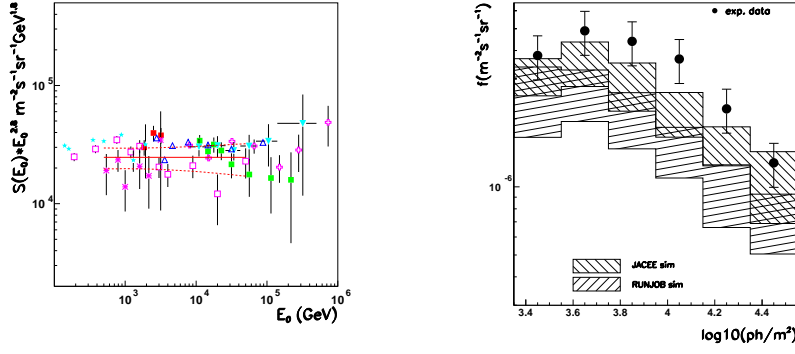
Figure 3: (On the left) The primary proton spectrum obtained from the hadron flux (continuous line). The dotted lines represent the 1 s.d. statistical and systematic errors.

Figure 4: (On the right) Comparison between the experimental C.l. photon numbers, for events in coincidence with MACRO, and the expectations from the JACEE and RUNJOB spectra.

The *knee* as observed in the N_e spectrum is shown in fig. 2[9]. In such region, the spectra of *light* (p,He), *intermediate* (CNO), and *heavy* (Fe) primaries are obtained by fitting the muon number distributions in intervals of N_e[8]. The expression minimized is: $\chi^2 = \sum_{i=1}^{M} \frac{[f^d(i) - f^s(i)]^2}{\sigma(i)^2}$ where: $f^d(i)$ is the experimental fraction of events falling in the N_e channel i; $f^s(i) = \alpha_L f_L(i) + \alpha_I f_I(i) + \alpha_H f_H(i)$ is the theoretical expression in which α_L, α_I and α_H are the fit parameters representing the relative abundances of the *light*, *intermediate* and *heavy* mass groups; $f_L(i)$, $f_I(i)$ and $f_H(i)$ are obtained through simulations based on QGSJET for primary spectra with slopes $\gamma = 2.75$, and $\sigma(i)$ is the error on the theoretical expression. Results of the fits as relative abundances (vs. N_e) are reported in fig. 2. The energy range between 10^{15} and 10^{16} eV is therefore characterized by an average steeper spectrum of the lighter ($\gamma_{p,He} > 3.1$), and then of the medium component ($\gamma_{CNO} \approx 2.75$), while the heaviest one is unchanged ($\gamma_{Fe} = 2.3 \div 2.5$). The overall energy spectrum as measured by EAS-TOP in the energy region $10^{12} - 10^{16}$ eV is shown in fig. 7. The intensities at 10^{15} eV are consistent with the extrapolations from direct measurements. In ref.[8] it has been shown that some main features of the conclusions, as the helium *dominance* in the knee region, and the *increasing average mass* of the primaries do not depend on the specific hadronic interaction model used inside CORSIKA.

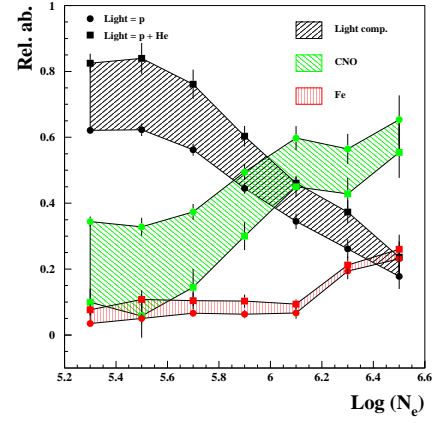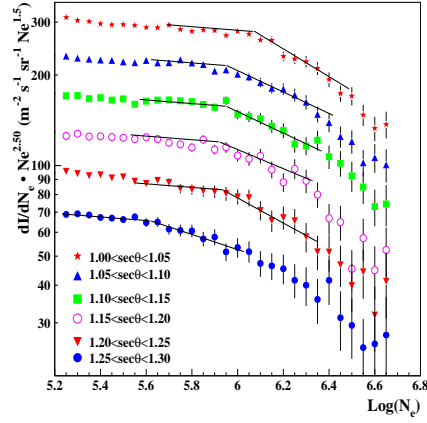Since the main differences between the hadronic interaction models would

Figure 5: (On the left) Differential shower size spectra measured at different zenith angles (i.e. atmospheric depths), showing the *knee* position, and its shift with zenith angle.

Figure 6: (On the right) Relative abundances of the three mass groups in different intervals of shower sizes.

finally manifest into different energy distributions of the secondaries, an independent check of the model used is provided by a similar $N_e - N_\mu$ analysis performed by means of the $E_\mu > 1.3$ TeV muons recorded by MACRO. The obtained spectra of the *light* and *heavy* components are shown in fig. 3: as for the GeV muon analysis the *knee* results from the steepening of the spectrum of the *light* component [10]. This demonstrates the consistency of QGSJET in describing the shower properties over a wide energy range of the secondaries.

3   The anisotropy

A crucial test of the possibility that the *knee* feature is due to the decreasing galactic containment is provided by the anisotropy data. The anisotropy is measured at primary energy $E_0 \approx$ 100-200 TeV, with amplitude $A(\delta=0) = (3.7 \pm 0.6) \ 10^{-4}$ and phase $\phi = (1.8 \pm 0.5)$ hrs LST. The lower statistics does not allow measurements with equal accuracy at higher energies. Upper limits have been obtained (see fig. 3), that exclude an increasing amplitude of the anisotropy with energy dependence stronger than $A \propto E_0^{0.3}$[11].

A systematic search for γ-ray sources has been performed, looking for different candidates[12]: Pulsars, SNRs, X-ray binaries, BL Lac objects, galactic disc, diffuse flux, and over the whole visible sky, for steady and
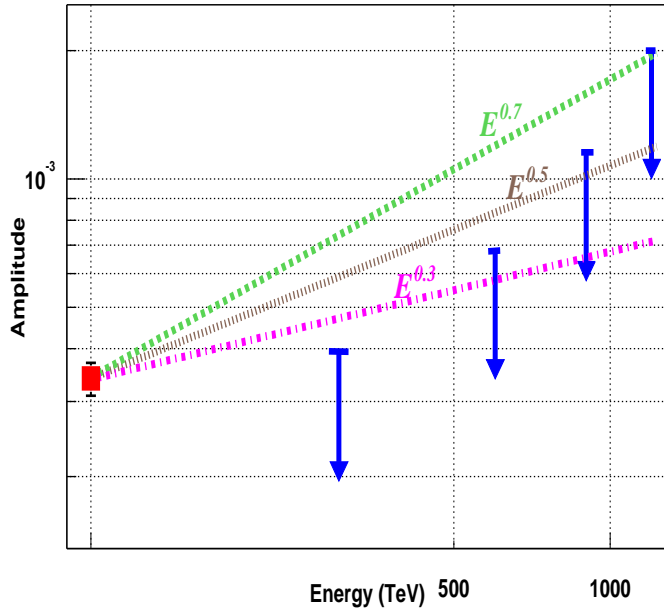
Figure 7: Overall energy spectrum as measured by EAS-TOP in the energy region $10^{12} - 10^{16}$ eV. The direct data, and the techniques are also given.

transient emissions. No DC emission has been detected; the values of the energy thresholds and the obtained upper limits depend on the source declination. As examples, the 90% c.l. upper limits obtained from the Crab Nebula are $\Phi(> 20\text{TeV}) < 2.6 \cdot 10^{-13}\text{cm}^{-2}\text{s}^{-1}$, and $\Phi(> 100\text{TeV}) < 3.9 \cdot 10^{-14}\text{cm}^{-2}\text{s}^{-1}$.

4 Penetrating showers (HAS)

The detection of EAS at very large zenith angles can be a tool for the search of UHE penetrating particles and neutrinos from cosmic ray sources[13]. In the e.m. EAS-TOP detector, at zenith angles $\theta > 65°$, an excess of events is observed above the rate of EAS as expected from their attenuation length in the atmosphere (fig. 4). The physical nature of the anomalous arrival directions of HAS is confirmed by: a) the absence of events from the direction of the sky shaded by the top of the mountain on which the array is located (fig. 4), and b) the dependence of the barometric coefficient ($\beta = (1/n)dn/dp$) on zenith angle: the deviation from the $k/sec\theta$ law indicates the presence of
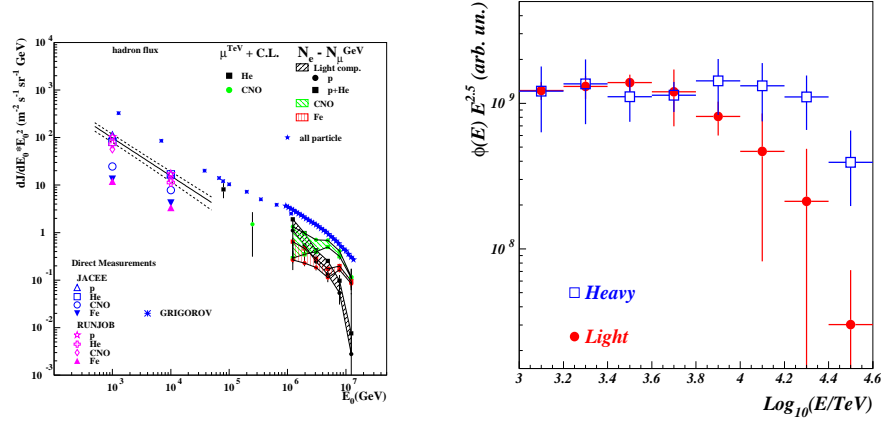
Figure 8: (On the left) *Light* (p+He) and *heavy* (Mg+Fe) primary spectra as obtained from the fits to the TeV muon multiplicity distributions (by MACRO) in different bins of N_e (by EAS-TOP).

Figure 9: (On the right) The amplitude of the measured anisotropy at 100-200 TeV, and the upper limits at higher energies.

a *non − attenuated* EAS component amounting to about 30% of the total EAS flux at 70°, and dominating at larger zenith angles (fig. 4). A clue to the understanding of such events is provided by their muon content recorded by the tracking μ-detector: in 575 days, 37 events have been recorded with $\theta \geq 75°$[14]. Very few of such showers have a negligible content of muons i.e. could be μ-poor as expected for μ induced showers in the atmosphere. The 2 over 37 events with no muon in the μ-detector correspond to events with small energy losses in the scintillators, compatible with the absence of muons in the tracking module respectively at 1. and 3.5 s.d.. For all other events, the muon density ($\rho_\mu \approx \bar{n}_\mu / A_\mu \approx 0.3$ μ m^{-2}) is comparable with the total density of charged particles measured by the scintillators. The charged particle density, measured by the scintillator detector ($\Delta E / \Delta E_{m.i.p.}$), and the muon density measured by the tracking detector at the same core distances are compared in fig. 13: all experimental points lay inside a ± 2 s.d. interval around the 1 to 1 correlation line. This is expected from *pure* muon showers, with a marginal content of electrons, i.e. from primaries having interacted very far in the atmosphere. Inside the uncertainties on the primary spectrum and composition, the experimental event rate and multiplicity distribution are fairly well explained by a simulation based on CORSIKA-QGSJET. It appears that events with detected muon multiplicities $N_\mu \geq 10$ are due to primaries
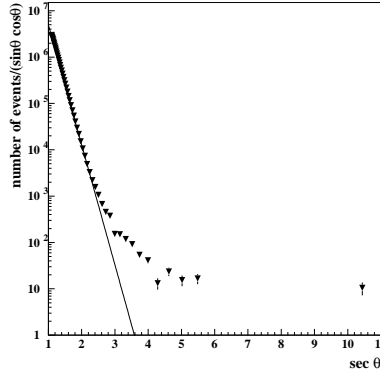
Figure 10: (On the left) The zenith angle distribution of a sample of EAS as measured by the EAS-TOP e.m. array.
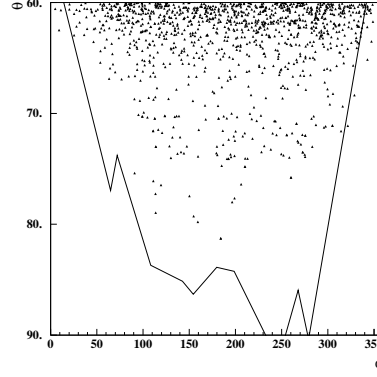
Figure 11: (On the right) The arrival directions of very inclined events, with respect to the mountain profile.

with typical energy $E_0 \approx 10^{17}$ eV, detected at core distances $r \approx 500$ m, the total muon number for such events being $N_\mu \geq 10^4$. UHE cosmic neutrinos produce showers with muon content lower or similar to ordinary cosmic ray showers. In fig. 13 a $\rho_\mu = 0.1\rho_{\mu+e}$ line is drawn, as an upper limit to the muon content of neutrino induced showers. For none of the events the quoted limit is exceeded, providing an upper limit to the diffuse neutrino intensity (at 90 % c.l.), for $E_\nu \approx 10^5$ GeV: $\frac{dI_\nu}{dE_\nu} < 8.5 \times 10^{-14}(\frac{10^5}{E_\nu})^2 \mathrm{cm}^{-2}\mathrm{s}^{-1}\mathrm{sr}^{-1}\mathrm{GeV}^{-1}$ and for resonant events ($E_{\bar{\nu}_e} = 6.4 \cdot 10^6$ GeV): $\frac{dI_{\bar{\nu}_e}}{dE_{\bar{\nu}_e}} < 4.3 \times 10^{-18}\mathrm{cm}^{-2}\mathrm{s}^{-1}\mathrm{sr}^{-1}\mathrm{GeV}^{-1}$.

References

[1] EAS-TOP Coll, N.I.M., A 336 (1993) 310; N.I.M., A 420 (1999) 117; Il Nuovo Cimento, 105A (1992) 1807

[2] N.N. Kalmykov et al., Nucl. Phys. B, 52B (1997) 17

[3] D. Heck et al, FZK-Report 6019 (1998)

[4] EAS-TOP Coll, Astrop. Phys., 19 (2003) 329

[5] EAS-TOP and MACRO Colls, Astrop. Phys., 21 (2004) 223

[6] K. Asakimori et al., Ap.J., 502 (1998) 278
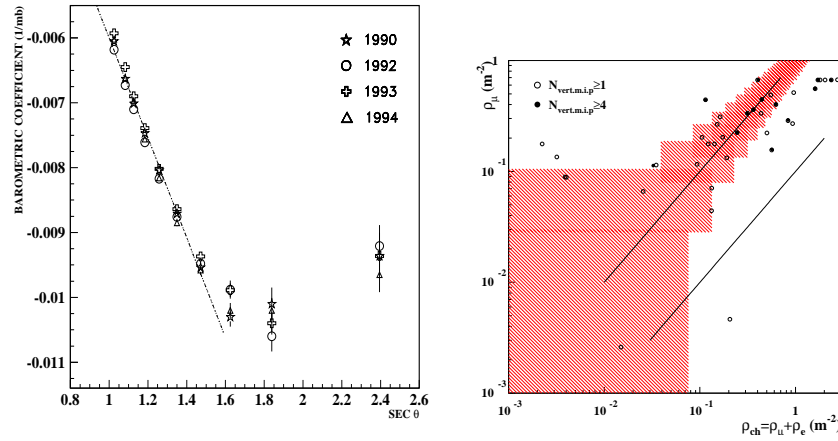
Figure 12: (On the left) Barometric coefficient as a function of zenith angle.

Figure 13: (On the right) Particle density as measured by the scintillator and tracking detectors. 1 s.d. error boxes are shown.

[7] A. V. Apanasenko et al., Astrop. Phys., 16 (2001) 13

[8] EAS-TOP Coll, Astrop. Phys., 21 (2004) 583

[9] EAS-TOP Coll, Astrop. Phys., 10 (1999) 1

[10] EAS-TOP and MACRO Colls, Astrop. Phys., 20 (2004) 641

[11] EAS-TOP Coll, Ap. J., 470 (1996) 501; Proc. 28th ICRC, 1 (2003) 183

[12] EAS-TOP Coll, Astrop. Phys., 3 (1994) 1; Astrop. Phys., 6 (1996) 71; Ap. J., 397 (1992) 148; Ap. J., 469 (1996) 305; Proc. 26th ICRC, 4 (1999) 68; Proc. 27th ICRC, 6 (2001) 2411

[13] EAS-TOP Coll, Phys. Lett. B, 333 (1994) 555

[14] EAS-TOP Coll, Proc. 26th ICRC, 2 (1999) 24

THE ATMOSPHERIC MONITORING FOR THE PIERRE AUGER OBSERVATORY

Michela Chiosso [a,b], for the Pierre Auger Observatory [c]

[a] *Dipartimento di Fisica Sperimentale, Università degli Studi di Torino, via Pietro Giuria 1, Torino, Italy*

[b] *INFN, Sezione di Torino, via Pietro Giuria 1, Torino, Italy*

[c] *Observatorio Pierre Auger, Malargüe, (5613) Mendoza, Argentina*

Abstract

The Pierre Auger Observatory has been designed to compound the puzzle on the ultra-high energy cosmic rays, combining the advantages of two different techniques: the Ground Array and the Fluorescence Detector (FD), both detecting the Extensive Air Showers (EAS) generated by the primaries. The Fluorescence Detector uses the atmosphere as an electromagnetic calorimeter: it is then crucial an accurate calibration of this calorimeter. Many atmospheric monitoring techniques and devices are under study and implementation on the South Auger Site, in Malargüe, Argentina, to get the most through understanding of atmospheric composition and properties. In this paper are described the most relevant of these devices, their functioning principles and application.

471

1 Introduction

A fluorescence detector observes and records the longitudinal development of an extensive air shower passing in the atmosphere through its field of view. With respect to the Ground Array, which detects directly those particles of the shower which survive down to the detection level, the fluorescence eye detects the fluorescence photons, emitted by de-excitation of atmospheric nitrogen molecules and ions, previously excited from the charged particles of the shower. At different stages the atmosphere may affect the final reconstruction of the shower longitudinal profile, that is expressed in terms of number of shower charged particles as function of the atmospheric depth. First, the shower development depends on amount of air traversed, which is given by atmospheric density, varying with altitude, $\rho(h)$. Second, the EAS development versus geometrical height, as it arises from the Auger Fluorescence Detector experimental setup, has to be converted into EAS development versus atmospheric depth, and this transformation from altitude to grammage (that is the total amount of matter traversed) depends on the vertical distribution of density. Third, the fluorescence yield, that is defined as the number of fluorescence photons produced by a charged particle per meter of travel in air, varies with air pressure and temperature, hence it is necessary to know profiles of temperature and pressure to calculate the emitted light curve in atmosphere. Finally, the light suffers attenuation processes, due to scattering and absorption in atmosphere, along its path from the source point at shower track towards the telescope, and the transmission factor depends again on atmospheric properties. Thus, it is central to the mission of the Pierre Auger Project, of providing a reliable air shower energy scale and resolution, to measure with grate accuracy and monitor with time the atmospheric properties, which must enter as inputs in the analysis of the fluorescence data. The atmospheric monitoring systems deployed on the southern site of the Pierre Auger Observatory include LIDARs, central steerable laser, cloud monitors, horizontal attenuation length monitors, phase function monitors, weather stations, and radiosondes.

2 Monitoring Systems

2.1 Radiosondes and Meteorological Stations

The amount of traversed air is usually given as grammage or atmospheric depth profile $X(h)[g/cm^2]$, which is defined as:

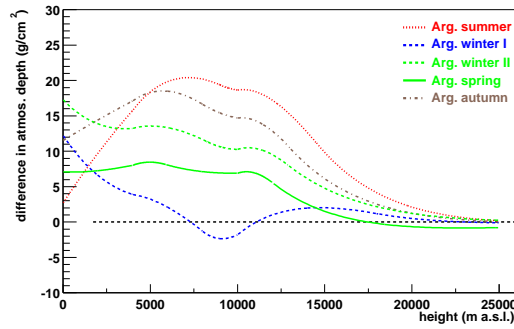$$X(h) = \int_h^\infty \rho(z)dz \qquad (1)$$

Figure 1: Percentage difference in grammage profiles to the US-Standard Model.

Since the air density can not be measured directly, it can be derived from the ideal gas law, once measured air pressure, P, and temperature T:

$$\rho(P,T) = \frac{P \cdot M_{mol}}{R\,T},\qquad(2)$$

with M_{mol} the molar mass of air, R the universal gas constant. The pressure and temperature profiles are measured by meteorological stations at ground level, whereas radiosondes suspended to small balloons provide same measurements as function of height up to typical maximum altitude between 20 km and 30 km. There is one weather station per each fluorescence eye and one at the center of site. They provide daily ground measurements of temperature, relative humidity, wind speed and direction, solar radiance and pressure. The radiosondes are standard meteorological sondes with GPS option. They are launched using helium filled balloons, and a radio ground station receives raw data, including mainly measurements of temperature, pressure and humidity, but also wind speed and direction and the balloon position with respect to the ground station. Based on these data and data from weather stations, the air density and grammage as function of height are provided. Measurement campaigns performed on the Auger site since August 2002, during the local winter, spring and summer, on night and day, produced results which have been compaired to the US Standard Atmosphere Model profile and other standard profiles, showing not negligible differences that affect the final determination of the longitudinal shower development (see fig.(1)).

2.2   LIDAR Stations and Central Laser Facility

The attenuation processes that light undergo in the atmosphere are elastic Rayleigh (molecular) and Mie (areosol) scatterings, inelastic Raman scattering and gas absorption. While the gas absorption is rather negligible for fluorescence light and the Raman scattering has very small cross section

compaired to eleastic scattering, Rayleigh and Mie scatterings may affect the transmission efficiency of fluorescence photons from the EAS to the detector. Thus, an accurate measurement of this atmospheric transmission function, $T(r) = T_{mol}(r) \cdot T_{aer}(r)$, is crucial for the final determination of the energy of the primary particle.

Located at each of the four fluorescence sites, the Lidar stations are able to probe directly the shower-detector atmospheric path. Each Auger LIDAR system consists of a pulsed laser beam at 355 nm and of a receiver telescope with three mirrors, one dedicated to Raman scattering detection, the others collecting the elastic backscattered photons on to a photomultiplier tube; incoming light is recorded as a function of time. The so called lidar equation describes the instantaneous received power at time t, P(r), as a function of the instantaneous trasmitted power at time t_0, P_0 [1]:

$$P(r) = P_0 \cdot \frac{c\Delta T}{2} \cdot \frac{A}{4\pi r^2} \cdot \beta_\pi^\lambda(r) \cdot e^{-2\int_0^r \alpha_\pi^\lambda(R)dR} \, , where \tag{3}$$

1. $\beta_\pi^\lambda(r) = \beta_{mol}^\lambda(r) + \beta_{aer}^\lambda(r)$ is the backscatter coefficient:

$$\beta_\pi^\lambda(r) = N_{mol}(z)\sigma_{mol}f_{rayleigh}(180°) + N_{aer}(z)\sigma_{aer}f_{mie}(180°), \tag{4}$$

with $f_{rayleigh}$ and f_{mie} the angular scattering distribution functions, also called Rayleigh and Mie phase functions.

2. $\alpha_\pi^\lambda(R) = N_{mol}(z)\sigma_{mol} + N_{aer}(z)\sigma_{aer}$ is the extinction coefficient, and the transmission function is:

$$T(r) = e^{-\int_0^r \alpha_\pi^\lambda(R)dR} \tag{5}$$

Both molecular and aerosols extinction coefficients may be factorized into a height dependent factor, the particles density $\rho(z)$, and in a wavelength dependent term, the horizontal attenuation length $\Lambda(\lambda)$:

$$\alpha_\pi^\lambda(R) = \frac{1}{sin\alpha}\frac{\rho_a(r)dr}{\Lambda_a(\lambda)}, \tag{6}$$

where $\frac{1}{sin\alpha}$ is the slant factor. The first LIDAR station was installed in Los Leones and started to take data in February 2002. Presently, two LIDAR Stations (in Los Leones and Coihueco), are completed and operational, a third one (in Los Morados) is very near to be completed. The Central Laser Facility (CLF) is based on the same functioning principle of LIDAR, but here the receiving system is the Fluorescence Detector itself. It is a remotely controlled laser setup (355 nm) at the center of the array, conceived to provide again measurements of the aerosol vertical depth versus height, but with different uncertainties from the backscatter LIDAR, and measurement of the horizontal uniformity across the aperture of the array.

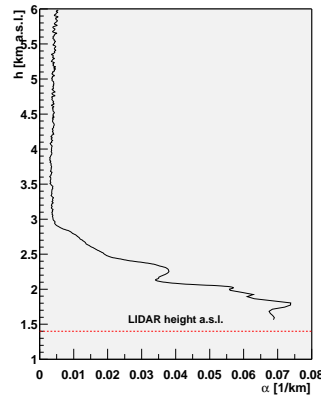The CLF started to be operated regularly since November 2003.

Figure 2: Aerosol extinction coefficient as function of height measured with the LIDAR system at the Los Leones site.

2.3   Horizontal Attenuation Length Monitor (HAM)

The first system was installed in May 2001. It consists of a stable DC light source, located in Coihueco, and a UV sensitive CCD camera, placed in Los Leones site. It records the horizontal attenuation lengths at several wavelengths, 365 nm, 405 nm, 436 nm, and 542 nm, by use of interference filters. The total horizontal attenuation length is obtained by ratio of flux measured at large distance ($\sim$ 50 km) from the source to flux measured at a very small distance, used as calibration point.

2.4   Aerosol Phase Function Monitor (APF)

To estimate the contribution to the fluorescence signal that may derived from multiple-scattering processes in air and, on the opposite, the contamination from almost scattered , rather than direct, Cherenkov photons (unless the shower is directed towards the detector line of sight) it is necessary to measure the aerosol extinction length, $\Lambda_a(z, \lambda)$, and the aerosol phase function, $\frac{1}{\sigma_a}(\frac{d\sigma_a}{d\Omega})$. $\Lambda_a(z, \lambda)$ is obtained from LIDAR measurements, whereas the APF measures the normalized aerosol differential scattering cross section as a function of the scattering angle from the initial light direction. The apparatus, installed in March 2003, about $\sim$ 1.3 km far from the Coihueco fluorescence building, consists of three separate light sources (330 nm, 360 nm, 390 nm) pulsing light beams across the field of view of the fluorescence detector, which records the light scattered out of the beam over the desired range of scattering angles (between 20° and 160°).

2.5 Cloud Cameras

Clouds may affect in an unpredictable way the detection of an EAS by fluorescence detector. The Cloud Cameras allow to monitor the presence of clouds over the Auger array. The detection of clouds is possible by their strong infrared emission against a much weaker clear sky background. The apparatus is based on the Raytheon Control-IR 2000B digital camera with a spectral range between 7 and 14 μm, and a field of view of 45° x 36°. Mounted on a steerable support, it can provide a scan of the field of view of the fluorescence telescopes, or a full-sky image, or, triggered by the fluorescence detector, a picture of a given direction where an high energy air shower has just developed.

3 Conclusion

The main components of the Auger atmospheric monitoring system have been already deployed and tested on-site. To minimize systematic uncertainties, all the atmospheric measurements are made at least by two different indipendent techniques: the horizontal attenuation length obtained from HAM may be compaired with the results of horizontal LIDAR measurement. The CLF may cross-check the LIDAR in aerosol optical depth measurements. Both LIDAR and Cloud IR Camera may perform the $"Shoot - theShower"$, to provide real-time monitoring just along the track of a high energy shower, after they have received a trigger from the Fluorescence Detector. The radiosondes measurements of atmospheric profiles are cross-checked by measurement at ground level by weather stations. The corrections due to scattered Cherenkov light, and multi-scattering processes are determined by APF and HAM measurements. The main goal is to reduce the atmospheric contribution to the shower energy uncertainty to $\sim 10\%$.

References

[1] A. Filipcic et al., *Pierre Auger Atmospheric-Monitoring Lidar System* Proc. of 27th ICRC, 2, 784

[2] M. Mostafá et al., *Atmospheric Monitoring for the Pierre Auger Fluorescence Detector* Proc. of 28th ICRC, 2003

[3] B. Keilhauer et al., *Results of the first balloon measurements above the Pampa Amarillia* Proc. of 28th ICRC, and Auger Note GAP-2003-009

[4] J.A.J. Matthews, M. Mostafá, *APF light sources for the Auger Southern Observatory* Proc. of 28th ICRC, 2003

IMPROVING THE COLLECTION EFFICIENCY OF EUSO FOCAL SURFACE DETECTORS

L. GAMBICORTI [a,b], V. BRATINA [d,b], A. GHERARDI [b], G. CORTI [a],
R. CIARANFI [b], P. MAZZINGHI [d,b], E. PACE [a,b]

[a] *Dipartimento di Astronomia e Scienza dello Spazio, Università di Firenze,
L.go E. Fermi 2, Firenze, Italy*

[b] *INFN, Sezione di Firenze, via Sansone 1, Sesto Fiorentino, Italy*

[c] *Dipartimento di Fisica, Università di Firenze,
via Sansone 1, Sesto Fiorentino, Italy*

[d] *INOA, Istituto Nazionale di Ottica Applicata,
L.go E. Fermi 6, Firenze, Italy*

Abstract

The *Extreme Universe Space Observatory* (EUSO) on the International
Space Station (ISS) will detect the Extreme Energy Cosmic Rays (EECRs
with $E > 4 \times 10^{19}$ eV) and the high energy cosmic neutrino flux looking at
the streak of fluorescence light produced when the particles interact with
the Earth's atmosphere. The photo-detector of EUSO experiment will
consist of several Multi-Anode PhotoMultipliers (MAPMTs) arranged
on the hemispherical focal surface. The experimental group in Florence
has carried out the task of improving the collection efficiency of the
MAPMT that is a common problem to cosmic-rays and neutrino physics
experiments. The first solution was a 64-channel PMT with a collection
efficiency of 45%, which was improved to 65% using light collectors or
optical adapters. A second solution was proposed using an electrostatic-
focusing PMT, which provide an efficiency of 74%. Then, our group

was engaged in finding out innovative solutions to enhance this efficiency exceeding 90%, including a band pass filter and keeping the mass below 25 g. An innovative imaging optical adapter that improves radiometric efficiency - taking into account the band pass filter and lens absorption and light reflection - up to 94% in the $330 \div 400$ nm spectral range will be presented. In addition, the signal observed from the single-photoelectron distribution curve shows a secondary peak at smaller gains due to the photoemission from the first dynode. It will be discussed its contribution to the detector efficiency and the problems concerning the selection of the threshold that is related to the presence of this peak.

1 Introduction

EUSO telescope will observe the Earth's atmosphere under a 60° full field-of-view from its location, as external payload, onboard the ISS, at about 400 km altitude. EUSO is planned to observe 1000 events in 3 yr, that is a huge expected number with respect to the current 17 after 40 yr [1]. The optical system of EUSO consists in 2 Fresnel lenses and a curved focal surface of 5 squared meters of area in which will be placed thousands of MAPMT detectors, organized in module structure to reduce defocusing effects and losses in the geometrical acceptance due to dead regions between the close packed devices. The aim of this paper is to describe some solutions to increase the photon collection efficiency of the EUSO focal surface detectors.

2 EUSO detectors

A detector proposed for the EUSO telescope is the R8900-03-M36, a Multi-Anode PhotoMultiplier Tube (MAPMT) from Hamamatsu Corp., having 6x6 pixels. The baseline at the beginning of phase-A of the EUSO experiment was the R7900-M64 [2], a 64-anodes MAPMT still from Hamamatsu Corp., having a sensitive area of 45% with respect to its total area. The R8900-03-M36 model is a modified version of the R7900 MAPMT in which has been introduced electrostatic focusing increases the MAPMT sensitive area up to 84% with respect to the total area of the detector. However, if we consider a MAPMT holder to insert it in the focal surface and we assume a spacing such that the section occupied by each photomultiplier is increased up to 27 mm, the collection efficiency is 79% [3]. The sensitivity is distributed in the visible and near-UV wavelength regions and the quantum efficiency is peaking at 420 nm [4]. The near-UV photons in the wavelength region of $330 \div 400$ nm will be selectively detected by employing optical filters on the top of MAPMT units.
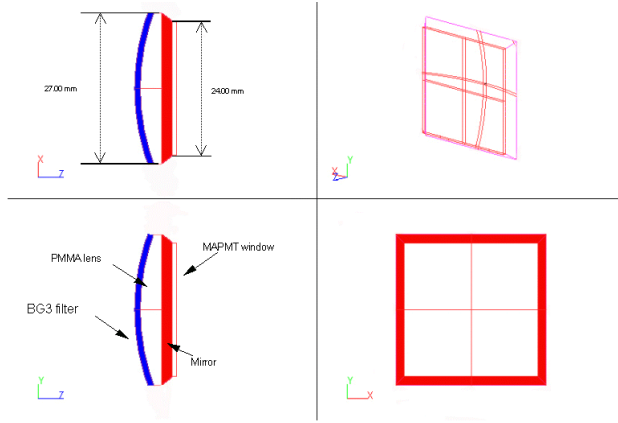
Figure 1: *Views and sections of filter lens with BG3-MgF$_2$ filter and mirror. BG3 curved filter of thickness 1 mm is glued on front of hemispherical dome of PMMA lens and covered with a thin layer of MgF$_2$. On back represented the empty pyramid made of 4 mirrors.*

In order to improve the collection efficiency they need optical adapters to focus the photons only on the sensitive area.

3   EUSO adapters

To improve the collection efficiency of the MAPMT R7600-M64 or M16 we have carried out the simulations of different type of non-imaging adapters using ray-tracing programs. Those adapters, named Compound Parabolic Concentrator (CPC), are Winston cones designed with a parabolic shape and a cylindrical simmetry on each detector pixel [5]. The efficiency of single solid CPC anachieve 99%, but being the CPC circular with respect to squared pixel, they cover only the 78.5% of the sensitive area, that represents the real collection efficiency [6, 7]. In the last year it has been developed the new detector R8900-03-M25/M36 with electrostatic focousing. The greater ratio between sensitive and total area of this new detector allows the use of a thinner hemispheric lens as adapter [8]. We have carried out studies to define an adapter with imaging capability to filtering the incident radiation, collecting photons on the sensitive area of the detector. The UV filter is required to stop unwanted radiation, out of the wavelength range $300 \div 400$ nm and to improve the detector signal-to-noise ratio [9]. Glass BG3 from Schott has been selected as the baseline filter for EUSO. This filter will have a multi-layer, coating that cuts off transmission sharply above 400 nm and is anti-reflective in the region of interest. Filter lens collector is composed of an hemispherical dome of squared section, having side 27 mm (Fig.1).
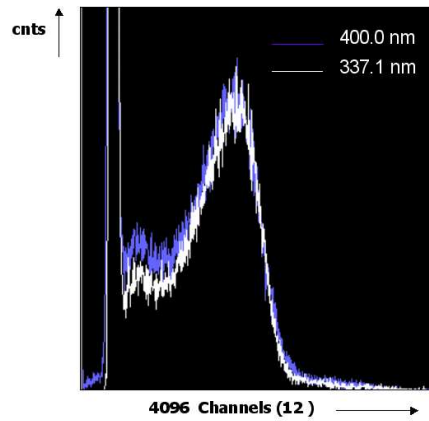
Figure 2: *The signal observed from the single-photoelectron distribution curve of the peaks separation measured. The distribution obtained with our detector presents a better separation between the noise pedestal and the signal.*

This dome is formed by 1 mm thick BG3 filter glass glued on an hemispherical lens of UV-grade Poly-Metyl-Metha-Acrylate (PMMA), a plastic material, the same used in EUSO for Fresnel lenses, which has transmittance 0.99 in the whole spectral range of interest. The glue is a UV transmitting layer of Epotek 301-2. Then, 4 small mirrors forming a reflecting truncated pyramid, are arranged below the lens, in order to collect all the escaping photons and to fit the lens size with the sensitive area of the detector, having a 24 mm side. The mirror reflectivity has been assumed of 98% that can be achieved using a layer of aluminum coated with a thin layer of MgF_2. Lateral sides of the hemispherical lens are also metallized to improve the collecting capabilities and to avoid cross-talk between neighbouring collectors [10]. The Schott BG3 absorption filter has been selected as the baseline filter for EUSO but its transmittance window is extended up to 500 nm. This *blue leak* must be strongly reduced and the transmittance limited to the region of interest, in order to reject the background signal from this spectral region. This can be achieved by coating the BG3 front surface with a multi-layer of dielectrics. The results of one of our studies on interference filters [11] show that multilayer coatings of MgF_2/HfO_2 can limit effectively the pass band of the BG3 filter glass to the $300 \div 420$ nm region. Another constraint to design the optical adapters is represented by the allowed maximum total weight below 25 kg because EUSO focal surface is composed of 5544 detectors and as many filter lenses must be placed in front of them. The calculation shows that the total weight of adapters system is 20.7 kg, taking into account the density values of the used materials. The performance of this filter lens coupled to the MAPMT has been simulated and estimated both the geometric and radiometric efficiency. Geometric efficiency is the ratio

Table 1: *Geometric and radiometric efficiency of filter lens adapter*

$\lambda(nm)$	Geometric efficiency %	Radiometric efficiency %
337	99.5	94.7
347	99.5	95.6
337	99.5	94.4

between the number of photons collected from the overall system (adapter + detector) and the total number of incident photons. Radiometric efficiency is a measure of the fraction of energy collected on the sensitive area with respect to the total energy impinging on the detector. Radiometric efficiency is the most important parameter to evaluate the collection efficiency because it includes the properties of the materials, such as for example optical absorption. Ray-tracing simulations of the filter lens coupled to the UV glass sealing the MAPMT has been performed using the code OptiCAD8. The performance of the system is obtained considering the main wavelengths of the atmospheric nitrogen fluorescence, i.e., 337 nm, 357 nm and 391 nm. Data on optical and physical properties of the BG3 filter glasses are available from Schott, providing designers with a specific software code, FILTER'99. Results of simulation are shown in Tab.1.

4   Conclusion

The results are very encouraging and show that a very small fraction of the photon flux impinging on the detector can be lost, even including the UV filter; the lens weight is very small, so that the total weight of the optical adapters on the EUSO focal surface is well within the specifications. The next step of this work will be to produce some prototypes and to carry out UV testing measurements to assess their real optical performance. In the new EUSO laboratory of the Florence Group the R7900-M64, a 64-anodes MAPMT, has been tested. The signal observed from the single-photoelectron distribution curve shows a secondary peak at smaller gains due to the photoemission from the first dynode. The MAPMT's spectrum is expected with a peaks separation of $100 \div 200$ channels. In fact, each preamplifier's channel has a different gain value (variable from 150 to 250), which optimizes the circuit performances; the MAPMT gain (at -900V voltage supply) is $\sim 10^6$. To see the real separations in the spectrum, we sent to preamplifier a charge quantity equivalent to one up to five photons: we measured the calculated peaks separation. The pulse height distribution of the MAPMT response to a single photon is obtained by irradiating only one pixel using the source that emits 60-ns light pulses

with amplitude of 1.60V (putting a Teflon filter between the LED and the detector) [12]. The distribution obtained with our detector presents a better separation between the noise pedestal and the signal: this means that it is easier to discriminate the signal from the noise counts; besides, as we can see, the observed separation peaks is near the expected values.

References

[1] *EUSO Extreme Universe Space Observatory* Original Proposal for the ESA F2/F3 Missions, (January 2000)

[2] *Multi-anode Photo-Multiplier tube R7600*, Hamamatsu Photonics K. K., Electron Tube Center, 314-5, Shimokanzo, Toyooka-village, Iwata-gun, Shizuoka-ken, 438-0193, Japan; http://www.hamamatsu.com.

[3] *Multi-anode Photo-Multiplier tube R8900*, Hamamatsu Photonics K. K., Electron Tube Center, 314-5, Shimokanzo, Toyooka-village, Iwata-gun, Shizuoka-ken, 438-0193, Japan; http://www.hamamatsu.com.

[4] N.Sakaki and EUSO-Japan collaboration,*EUSO-J Doc.* , No. 011 (2002).

[5] P. Mazzinghi, V. Bratina. *Concentration of radiation on EUSO focal plane detectors: theoretical limitations and practical implementation* EUSO Tech. Rep., EUSO-Florence collaboration, (2000)

[6] A. Petrolini. *A comparative study of light collector systems for use with multi-anode photo-multipliers*, Nuclear Instruments and Methods in Physics Research A 497 (2003) 314-330

[7] V. Bratina, P.Mazzinghi, L.Gambicorti, *Overview of possible optical adapter for EUSO*, Proc. Spie Vol. 5164, UV/EUV and Visible Space Instrumentation for Astronomy II; Oswald H. Siegmund; Ed. (2003) 100-112

[8] P. Mazzinghi, V. Bratina, *Optical adapters EUSO focal surface: lens system* EUSO Thech. Rep., EUSO-Florence collaboration, (2000)

[9] L. Gambicorti, V. Bratina, P. Mazzinghi, E. Pace, and M. Focardi, *Improved collection efficiency of the MAPMT R8900 by UV filter optical adapters*, EUSO-IT Tech. Rep., TR2-2003, January 2003.

[10] L. Gambicorti, V. Bratina, P. Mazzinghi, E. Pace, *UV filtering optical adapters to enhance the collection efficiency of MAPMT R8900*, EUSO-IT Tech. Rep., TR4-2003, May 2003.

[11] L.Gambicorti, P. Mazzinghi, E. Pace, *EUSO Optical adapters: Comparison between UV filtering optical adapters optimized for EUSO focal surface*, EUSO-FS-Rep. 012, 20 July 2004.

[12] A. Gherardi, R. Ciaranfi, E. Pace, S. Bottai, G. Landi, *Preliminary analysis of the R7600-03-M64 MAPMT response to the nitrogen UV emission wavelength*, EUSO-IT DFF 402/5/03, (2003)

Part VIII

GRAVITATIONAL WAVES AND FUNDAMENTAL PHYSICS IN SPACE

DETECTION TECHNIQUES FOR GRAVITATIONAL WAVES

Eugenio Coccia [a,b], Alessio Rocchi [a]

[a] *Dipartimento di Fisica, Università di Roma "Tor Vergata" e INFN Sezione di Roma II, via della Ricerca Scientifica, Roma, Italy*

[b] *INFN, Laboratori Nazionali del Gran Sasso, I-67010 Assergi, L'Aquila, Italy*

Abstract

In this paper we report on the present techniques adopted in the search for gravitational waves with earth-based detectors. The principles and the main techinques adopted by resonant-mass and interferometric detectors are examined.

1 Introduction

Gravitational waves (GW in the following) are predicted by Einstein's General Relativity. According to the same theory, they represent a time-dependent distortion of the local space-time and are supposed to propagate at the speed of light. Analogous in many ways to electromagnetic waves, GW are produced by the acceleration of masses, but while only a single charge is needed to produce electromagnetic waves, at least two point-like masses are required for GW. Due to the low value of the coupling constant of the gravitational field,

as Einstein himself stated, it practically is impossible to produce detectable GW in a laboratory. So, only astronomical scale events, such as supernovae, merging of binary systems or spinning neutron stars, are supposed to emit GW with a detectable amplitude. Direct detection of GW from astrophysical sources will fund a new kind of astronomy.

Astrophysical sources of GW [1, 2] can be grouped into three classes: transients, continuous and stochastic waves. To the first class belong the GW bursts, which are high energy emissions lasting a very short time, of the order of a few milliseconds. This kind of sources includes collapsing star into a neutron star or a black hole. Transient GW are also due to to the final inspiral phase, coalescence and merging of compact binary systems. The non-spherically simmetric collapse of a star of $M = 6M_\odot$ at the centre of our Galaxy would produce waves with a relative amplitude on Earth of $h_0 \sim 3 \cdot 10^{-17}$ [3]. But the expected rate of these events is a few over a century. If we consider a bigger volume, as big as to include the Virgo Cluster, the rate would grow to 1 event/week, but the strenght of the waves would decrease to $h_0 \sim 1.4 \cdot 10^{-20}$ [3]. Continuous waves differ from bursts, because they last longer but the energy emitted is orders of magnitude smaller. Tipical sources of continuous waves are rotating compact objects or binary systems, e.g. the pulsar PSR 0532, in the Crab Nebula, would emit GW with an amplitude of the order of $h_0 \sim 10^{-26}$ [4]. The stochastic background can have two origins: as a relic of the time when the gravitons decoupled from matter (analogous to the CMB); a pop-corn like signal due to the superposition of the radiation emitted by a large population of collapsing objects in all the galaxies. The spectrum of primordial stochastic background extends through the entire frequency range [1], from $f \sim 10^{-18}$ Hz to $f \sim 1 - 10^4$ Hz and beyond. Constraints on the amplitude of this background come from Nucleosyntesis and the CMB anisotropy. See Table (1).

2 Resonant mass detectors

Resonant-mass antennas for gravitational radiation were pioneered by Joseph Weber about 40 years ago [5], and have been pushed to ever higher sensitivity by a number of research groups since then. At present there are four of such antennas [6], operating with a noise level for broad-band gravity-waves bursts of $h \simeq 6 \times 10^{-19}$.

A resonant-mass antenna consists of a solid body that (heuristically speaking) rings like a bell when a GW hits it. This body is usually a cylinder, but at least two spheres are being built [7, 8]. The resonant mass is typically made of an alloy of aluminum and weighs several tons, but some have been made of niobium or single-crystal silicon or sapphire. To reduce thermal noise, the resonant mass is usually cooled to liquid-helium temperatures or below.

The resonant-mass antenna is instrumented with an electromagnetic

Table 1: Gravitational waves sources, detection methods and main projects and detectors.

Frequency	Sources	Detection method and projects
10^{-16} Hz	Primordial	Anisotropy of CBR Background Radiation
10^{-9} Hz	Primordial Cosmic Strings	Timing of ms pulsars
10^{-4} to 10^{-1} Hz	Binary stars Supermassive BH(10^3-10^7 M$_\odot$)	Doppler tracking of Spacecraft Laser interferometers in Space LISA
$10 - 10^3$ Hz	Inspiral of NS and BH binaries (1 - 10^3 M$_\odot$) Supernovae Pulsars	Laser interferometers on Earth LIGO, VIRGO, GEO600, TAMA
10^3 Hz	Coalescence of NS and BH binaries Supernovae ms Pulsars	Cryogenic resonant detectors ALLEGRO, AURIGA, EXPLORER, NAUTILUS, MiniGRAIL, Mario Schenberg

transducer and electronics, which monitor the amplitude and phase of one or more of the mass's normal modes. When a GW passes through the mass, its frequency components near each normal-mode frequency f_0 drive that mode, changing its amplitude and phase; and the time evolution of the changes is measured within the bandwidth Δf by the transducer and electronics. In the past, resonant-mass antennas were narrow-band devices ($\Delta f / f_0 \ll 1$), but in the last few years, the efforts of researchers managed to increase the bandwidth [9, 10].

2.1   Cylindrical Antennas

Any vibrational mode of a resonant body that has a mass quadrupole moment, such as the fundamental longitudinal mode of a cylindrical antenna, can be excited by a GW with nonzero energy spectral density at the mode eigenfrequency.

The size of a resonant antenna is determined by the frequency and the

velocity of sound v_s in the material used. Since v_s is always orders of magnitude less than the speed of propagation of GW, resonant-mass antennas are always much smaller than the wavelength of the radiation. Typical antennas are cylindrical bars made of alluminum with a fundamental longitudinal resonance in the frequency band around 1 kHz.

Because of the forces responsible for the antenna's elasticity, the GW performes work and, in the case of a thin cylindrical bar, deposits energy only in the odd-order longitudinal modes. Because of the quadrupole nature of the radiation, the even-order modes are not excited.

The mechanical oscillation induced in the antenna by the interaction with the GW is transformed into an electrical signal by a motion or strain transducer and then amplified by an electronic amplifier.

Bars were the first GW antennas to be operated, and one of the reasons for this choice is the simplicity of the model and of fabrication. Since Weber time, the conceptual scheme of the detector has not been modified, but, thanks to technological progress, the energy sensitivity of these detectors has improved by a factor of 10^4.

2.2 The future of resonant-mass detectors

The next generation of resonant-mass GW detectors will have spherical shape. At present, two of these detectors are being built, MiniGRAIL [7] (Leiden, The Netherlands) and Mario Schenberg [8] (Sao Paulo, Brasil). Both are spheres made of an alloy of copper and aluminum with a diameter of 65 cm and a mass of 1150 kg and a resonant frequency of about 3 kHz. The goal sensitivity of these detectors is $h \simeq 10^{-20}$.

Spheres have several advantages with respect to bars. First of all, a spherical detector is omni-directional, it is equally sensitive to a wave from any direction and it can also measure the polarization state of the wave. A single sphere is able to determine the source direction [12]. Besides, as will be shown below, the energy cross-section of a sphere is about 70 times larger than a typical bar at the same resonant frequency. Furthermore, the spherical geometry can, in principle, help in discriminating between different metric theories of gravity [11].

The total cross section of a sphere for each quadrupolar mode is given by [12]

$$\sigma_n = F_n \frac{G}{c^3} M_s v_s^2 \qquad (1)$$

where n is the order of the quadrupole mode, M_s is the sphere mass, v_s the sound velocity and F_n is an dimensionless coefficient characteristic of each quadrupole mode. It is interesting to note that the cross section of the second-order quadrupolar mode is only a factor 2.61 lower than that of the first-order

quadrupole mode. This means this detector can potentially be used at two frequencies.

It has been known for some time that a sphere has a gravitational cross section larger than that of an equivalent bar at the same frequency [12] for a single component of the gravitational tensor, a factor 18 if referred to the present bars. Moreover a sphere can detect all 5 indipendent components of the gravitational strain tensor, compared to only one for the bar. For a bar detector, it is well known that averaging over source direction and polarization [12] leads to a loss of energy resolution, compared to the optimum, by a factor $15/4 = 3.7$. Thus the net result is that the angle-averaged energy resolution of a sphere is $3.7 \times 18 = 67$ times better than the present bar detector (or about 8 times in h).
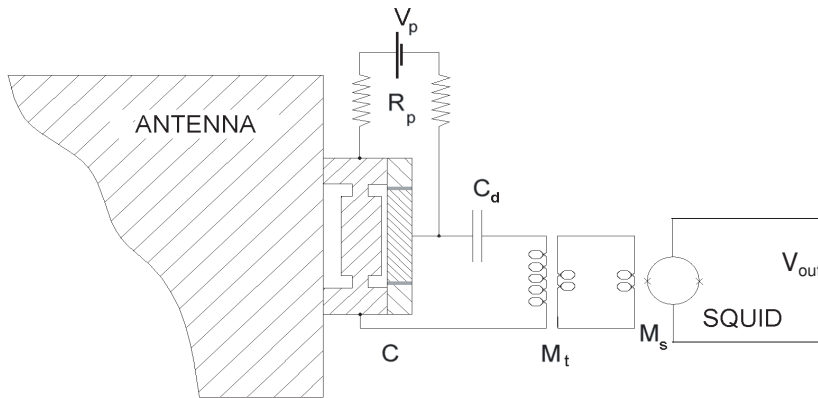

Figure 1: The read-out system of the Rome gravitational wave detectors.

A "dual" resonator GW detector is formed of two mechanical massive resonators both sensitive to GW and whose relative vibrations are measured by non-resonant readouts [13]. Configuration as two nested spheres, an inner solid one and a hollow outer one, or two nested cylinders have been considered. The frequency of the first quadrupolar mode of the external resonator is lower than that of the inner one, thus, the two resonators are differently driven by the GW.

"Dual" resonators promise, both high sensitivity and wide bandwidth, of the order of one kHz, at about 2 kHz. A research and development activity is

started.

2.3   Read-out and noise sources

After a signal has been picked up by the antenna, it must be amplified and recorded for analysis. The only viable way to achieve this is to transform the signal into electromagnetic energy, and then use state-of-the-art techniques for electromagnetic amplification and read-out.

The electromechanical transducer can be represented with the components of the Z_{ij} matrix which connects the input variables (force $f(t)$ acting on the transducer and velocity $\dot{x}(t)$ of the transducer mechanical parts) with the output variables (voltage $v(t)$ and current $i(t)$):

$$f(t) = Z_{11}\dot{x}(t) + Z_{12}i(t) \tag{2}$$
$$v(t) = Z_{21}\dot{x}(t) + Z_{22}i(t) \tag{3}$$

An important parameter is the ratio β of the electrical energy in the transducer to the total energy in the resonant body:

$$\beta = \frac{1}{m\omega}\frac{|Z_{21}|^2}{Z_{22}} \tag{4}$$

The principle of all transducers is to store electromagnetic energy in a very small volume, usually a narrow gap, one of the walls of which is part of the antenna. The motions of this wall, arising from vibrations in the antenna, induce a modulation of this energy which is detected and amplified as an electrical signal. Transducers of the sensitivity required to detect the extremely small signals of GW are not available commercially. Development of transducers and components of the read-out system are therefore an important part of the R&D efforts of all GW experiments.

Strain transducers are classified as belonging to the following three categories: capacitive (electrostatic), inductive (magnetostatic), optical (electromagnetic). Piezo-electric, magnetostrictive and μ-wave cavities are respective examples of such transducers. We can also distinguish between passive and active transducers. Passive transducers are linear transducers in which the source of energy in the gap is a permanent field, either electric or magnetic or both. These transducers preserve a linear phase and amplitude relation between input and output. Because of their relatively simple construction they are widely used. In active transducer the gap is fed with an oscillating bias field at high frequency ω_p. The mechanical vibration of frequency ω_0 modulates the phase of this oscillating field and produces side-bands which contain the information of the mechanical signal. Good performance of this type of transducer is expected because of the gain ω_p/ω_0

resulting from the conversion of the pump frequency ω_p into the antenna frequency ω_0.

An important breakthrough in increasing the sensitivity of resonant-mass detectors was achieved when resonant transducers (which can be active or passive) were introduced [14]. In a resonant mass transducer an oscillator with a small effective mass m_t is coupled in resonance with the antenna, which has a large effective mass m. The maximum amplitude of the motion of the small oscillator will then be increased by a factor $\sqrt{m/m_t}$ relative to the amplitude of the antenna. In the expression of β the antenna mass is thus replaced by the transducer mass.

Several groups have analyzed resonant transducers and have developed their own designs [14, 15, 16, 17, 18]. The transducer is connected to an electrical amplifier whose noise can be characterized by two parameters. The two parameters are, usually, the power spectra of the voltage and current noise, V_n^2 and I_n^2, or their following combinations:

$$T_n = \frac{\sqrt{V_n^2 I_n^2}}{K} \tag{5}$$

$$R_n = \sqrt{\frac{V_n^2}{I_n^2}} \tag{6}$$

T_n is called the amplifier noise temperature and R_n the amplifier noise resistance. Another parameter, useful to express the matching between transducer and amplifier, is

$$\lambda = \frac{R_n}{|Z_{22}|} \tag{7}$$

A large fraction of the technological complexity of resonant mass detectors results from the optimization of the quantities β, T_n and R_n.

2.4   Noise

Two classes of noise sources have to be considered in the sensitivity analysis of a GW antenna:

- the intrinsic noise sources such as the thermal and electronic ones, which have Gaussian statistics and can be accurately modeled, and

- the external noise sources such as seismic noise and disturbances from cosmic rays, which are more difficult to characterize because they are non-Gaussian and often also non-stationary.

The depth of the peaks in Figure (2) is directly proportional to the thermodinamical temperature of the bar. So cooling the detector to cryogenic
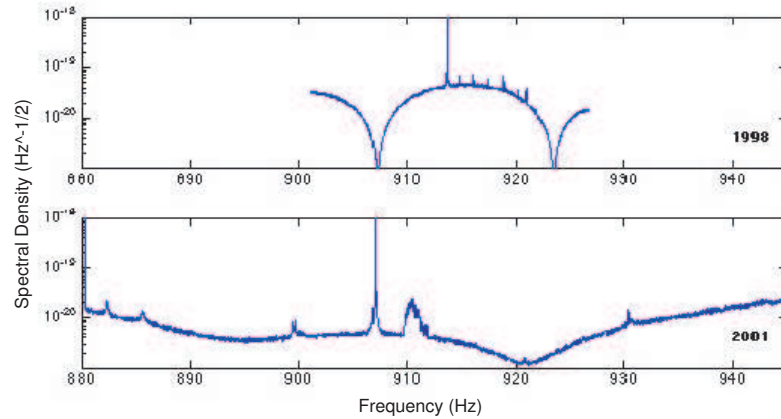
Figure 2: The strain sensitivity curve for the EXPLORER detector.

and ultracryogenic temperatures is, first of all, an effective way to reduce thermal noise and to improve the sensitivity of the antenna. This involves the use of low temperature techniques [19].

The useful bandwidth of the detector is, roughly speaking, given by the ratio β/T_n. This means that the effort of the groups must be focused on better transducers [18] and low noise amplifiers. The device that, in the kHz region, has the best performances in terms of T_n is the d.c. SQUID, which is capable of getting very close to the quantum limit [20, 21].

The last noise source, which the experimentalist can take care of, is seismic noise. Through FEM analysis, suspension systems with attenuation factors of more then 250 dB can be designed and used on real detectors.

The effects of other external unmodeled noises can be efficiently eliminated by coincidence measurements with several detectors located far away from each other.

3 Interferometric detectors

Interferometric detectors presently in operation are GEO600 [24] in Germany, LIGO [22] in the US, and TAMA300 [25] in Japan, while VIRGO [23] in Italy is in the commissioning phase. The basic idea behind this kind of GW detector is the Michelson interferometer. The simplest design uses light that passes up and down each arm once. Real detectors are designed to store the light in each arm for longer than just one reflection: the optimum storage time of the light is half of the period of the GW (Ex. 200 Hz wave, $t_{stor} \sim 3$ ms $\Rightarrow$ L=1000 Km). The impracticality of very long arms has led to the development of schemes for folding a long optical path into a shorter length: delay lines and Fabry-Perot
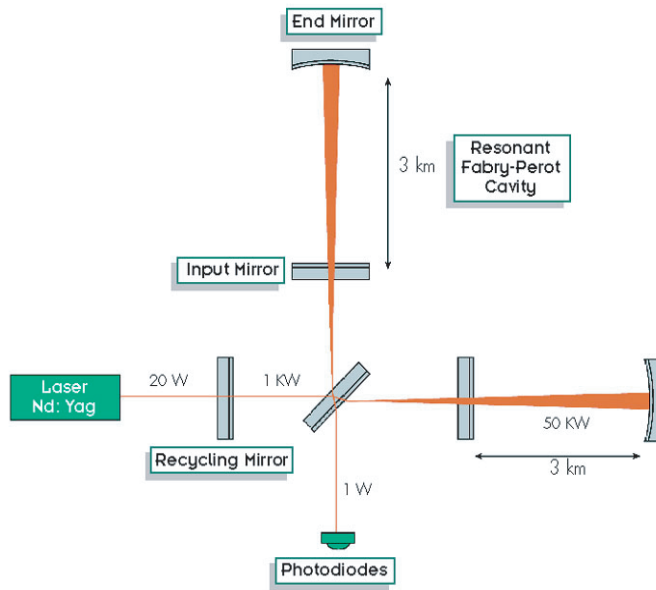
Figure 3: A schematic diagram of a laser interferometer gravitational wave detector.

cavities.

A laser interferometer gravitational detector consists of masses that hang from vibration-isolated supports (shown in figure (3) is the optical system to monitor the separation between the masses). Two masses are close to each other, at the corner of an "L", and one mass is at the end of each of L's long arms. The arms lengths are nearly equal, $L_1 \approx L_2 = L$. When a GW, of amplitude $h(t)$, with frequencies higher than the masses' pendulum frequency (≈ 1 Hz), passes through the detector, it changes each arm length by a quantity equal to $\frac{1}{2}h(t)L_{1,2}$, thereby changing the arm-length difference, $\Delta L \equiv L_1 - L_2$. That change is monitored by laser interferometry in such a way that the variations in the output of the photodiode (the interferometers output) are directly proportional to $\Delta L(t)$.

The interferometer's output is a linear combination of the two wave fields h_+ and $h_\times$:

$$\frac{\Delta L(t)}{L} = F_+ h_+ + F_\times h_\times \equiv h(t) \tag{8}$$

The coefficients F_+ and $F_\times$ are of the order of unity and depend in a quadrupolar manner on the direction to the source and the orientation of the detector [4].

Test masses are made of transparent fused silica, though other materials

might be used in the future. The masses' inner face are covered with high-reflectivity dielectric coating to fit the mirror requirements, while the masses outer faces are covered with anti-reflection coatings. The two mirrors facing each other on each arm form a Fabry-Perot cavity. A beam splitter splits a carefully prepared laser beam in two, and directs the resulting beams down the two arms. Each beam penetrates through the antireflection coating of its arm's corner mass, through the mass, and through the dielectric coating (the mirror); and thereby - with the length of the arm's Fabry-Perot cavity adjusted to be nearly an integral number of half wavelengths of light - the beam gets trapped in the cavity. Since the cavity's end mirror has much higher reflectivity than its corner mirror, most of the light impinging on the cavity is reflected backwards, and then hits the beam splitter where it recombines with light from the other arm. The output of the interferometer is kept on the dark fringe, so most of the recombined light would go back toward the laser but it is returned to the interferometer by a "light-recycling mirror".

The large magnitude of the low frequency seismic noise makes a "passive" interferometer design unworkable. The key is to use a *feedback* to keep the interferometer fixed at a chosen operating point (the dark fringe). The feedback is made of

- a sensor, producing an error signal measuring how far you are from the desired operating point;

- an actuator, a device that takes the error signal as input and that supplies the feedback influence to bring the interferometer toward this point.

When a GW hits the detector, changing the lengths L_1 and L_2 of the two cavities, it shifts each cavity's resonant frequency slightly relative to the laser frequency, and thereby changes the phase of the light in the cavity and the phase of the light that is reflected by the cavity toward the beam splitter. Corrispondingly, the relative phase of the two beams returning to the splitter is altered by an amount $\Delta\Phi \propto \Delta L$, and this relative phase shift causes a change in the intensity of the recombined light at the photodiode, $\Delta I_{pd} \propto \Delta\Phi \propto \Delta L \propto h(t)$. Thus, the change of photodiode output current is directly proportional to the GW amplitude $h(t)$. This method of monitoring $h(t)$ is capable of very high sensitivity.

4 Interferometers' noises

The significance of the various noise sources for the final design of a fully optimized interferometer to broad band GW is shown in Figure (4). At low frequencies, the sensitivity will be limited by seismic noise, at intermediate frequencies by the thermal noise of the mirror suspension, and at high frequencies by photon shot noise.
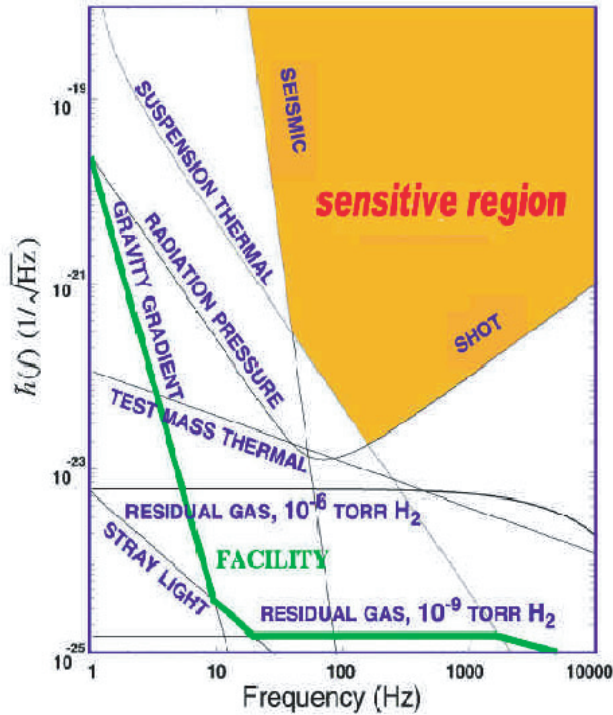
Figure 4: Noise sources limiting the sensitive region of earth-based interferometers.

4.1 Seismic noise

At the frequency of 1 kHz, the displacement due to seismic ground motion is about 10^7 times larger than any possible signal due to GW. Thus, an effective way to isolate the test masses is required. Some very promising work on passive isolation has been done in the VIRGO Project. The Superattenuator [26] has been designed on the working principle of a multistage pendulum. With this solution a very good reduction of the seismic noise transmission to the test masses in all degrees of freedom has been obtained, extending the detection band in the low-frequency region down to a few hertz [27]. The system consists of an inverted pendulum, the seismic filters (six and two in the long and short SA chains, respectively) connected to each other by metallic suspension wires and the last stage or payload. A more detailed description of each element including the short suspension system can be found in [26].

To the last stage of the SA chain is hung a mechanical filter; it consists of a marionette, a reference mass and a mirror. The marionette has been designed with four wings on which four small permanent magnets are attached. In front

of these magnets four coils are placed. They are attached to the end of four aluminium pipes fixed on the bottom part of the previous filter. In this way the magnet-coil system and the marionette allow the control of the interferometer optical component in four degrees of freedom: the displacement along the beam direction (z) and the horizontal direction perpendicular to the beam (x), the rotation around the vertical axis (θ_y) and the rotation around the horizontal axis perpendicular to the beam (θ_x). From the marionette two pairs of thin wires start. The first pair supports the mirror and the second one supports the reference mass forming the last stage with a pendulum length of 0.7 m.

4.2   Thermal noise

Thermal noise is mostly important on the last stage of the suspension system. This is usually a simple wire pendulum made of a sling supporting the mirror. The resonance frequency is about 1 Hz and the frequency window of observation is usually above this frequency. The spectral density of apparent strain noise due to this effect is given by

$$\tilde{h} \approx \sqrt{\frac{16kT\omega_0}{mQ_S\omega^4 l^2}} \tag{9}$$

where m is the mirror mass, ω_0 the resonant frequency and Q_S the mechanical quality factor of the suspension pendulum. This Q can be much higher than the internal Q of the wire material because most of the energy of the pendulum is in the form of potential and kinetic energy of the swinging bob and not in the elastic energy of a bent wire. But it is extremely important that the wire support points be properly designed to avoid friction. Pendulum Q_S as high as 10^7 have been experimentally observed.

4.3   Shot noise

The sensitivity of a simple Michelson interferometer in the high frequency region is limited by photon shot noise to [28]

$$h \approx 2.4 \times 10^{-21} \left[\frac{\epsilon I_0}{50\,\text{W}}\right]^{-1/2} \left[\frac{f}{1\,\text{kHz}}\right]^{3/2} \tag{10}$$

where ϵ is the quantum efficiency of the detector, I_0 is the laser output power and f is the center frequency of the burst. Green light and a bandwidth of half the center frequency have been assumed in Equation (10). The first problem to be solved is thus the construction of a laser with sufficient output power in a stable sigle transverse and longitudinal mode.

   This problem has been overcome in two ways: developing high power solid-state Nd:YAG lasers and recycling, which can be power and/or signal recycling.

Power recycling makes use of the fact that the interferometer output is held on a dark fringe by a feedback loop and almost all the light goes back towards the input. By placing a mirror in the input of the interferometer, a resonant optical cavity can be formed that uses the whole locked interferometer as an end mirror. So the circulating light power will be higher than the laser power by the inverse of the losses in the interferometer.

Signal recycling works similarly, except that it leads to a resonant enhancement of the signal instead of the light. By placing a mirror in the output port of the interferometer, a resonant cavity for the signal is formed. Depending on the reflectivity of this mirror, the detector can be made to operate narrow-band or wide-band and by changing the position of the mirror, the interferometer can be tuned to specific frequencies.

A combination of the above techniques is also possible, leading to the so called Dual Recycling. In this case, under the same assumptions as for Equation (10), the shot-noise limited sensitivity becomes [28]

$$ h \approx 10^{-22} \left[\frac{\epsilon I_0}{50\,\mathrm{W}} \right]^{-1/2} \left[\frac{f}{1\,\mathrm{kHz}} \right] \left[\frac{1-R}{5 \times 10^{-5}} \right]^{1/2} \left[\frac{l}{3\,\mathrm{km}} \right]^{-1/2} \qquad (11) $$

where R is the reflectivity of the signal mirror. It is clear that, in order to make these detectors work, mirrors with extremely small losses are needed. This requires substrates with a microroughness of the order of an Ångström and reflective coatings with very small scatter and absorption. The effort of the last few years has focused on the problem of building highly polished surfaces and high reflecivity coatings. Nowadays, mirrors with reflection losses of much less than 50 parts per million are available.

5   Conclusions

Various technological aspects are pushed at the limit in the search for GW. Techniques based on resonant-mass and interferometer configurations are mature to explore a new astronomical window.

We can confidently say that today the strongest sources in our Galaxy will not pass unnoticed to earth-based GW detectors. This fact is extremely important as the search for GW is based on the technique of coincidences among two or more detectors.

Large interferometers are ambitious and promise a good rate of events in the next years. The future competitivity of resonant-mass detectors with advanced interferometers is connected to the possibility of overcoming the narrow band barrier ("dual" concept [13]) and the detector directionality (omnidirectional spheres [7, 8]).

References

[1] K. S. Thorne, "*Gravitational Waves*", *Proceedings of the Snowball 95 Summer Study on Particle and Nuclear Astrophysics and Cosmology*, eds. E. W. Kolb and R. Peccei (World Scientific, Singapore).

[2] B. F. Schutz, Class. Quantum Grav. **16**, A131-A156 (1999).

[3] K. Kokkotas, Class. Quant. Grav. **21**, S501-S508 (2004).

[4] K.S. Thorne, in S.W. Hawking and W. Israel, editors, *Three Hundred Years of Gravitation*, pages 330-458. Cambridge University Press (1987)

[5] J. Weber, Phys. Rev. **117**, 306 (1960).

[6] P. Astone *et al.*, Phys. Rev. D **68**, 022001 (2003)

[7] A. de Waard *et al.*, Class. Quantum Grav. **20**, S143-S151 (2003).

[8] O.D. Aguiar *et al.*, Braz. J. Phys. **32**, 866-868 (2002).

[9] J.P. Zendri *et al.*, Class. Quantum Grav. **19**, 1991-1996 (2002)

[10] P. Astone *et al.*, Phys. Rev. Lett. **91**, 11 (2003).

[11] M. Bianchi *et al.*, Class. Quantum Grav. **13**, 2865 (1996).

[12] S. M. Merkowitz, W. Johnson, Phys. Rev. D **51**, 2546 (1995).

[13] M. Cerdonio *et al.*, Phys. Rev. Lett. **87**, 031101 (2001).

[14] H. J. Paik, J. of Appl. Phys. **47**, 1168 (1976).

[15] J-P. Richard, Rev. Sci. Instrum. **47**, 423 (1976).

[16] P. Rapagnani, Nuovo Cimento **5C**, 385 (1982).

[17] J-P. Richard, Phys. Rev. Lett. **521**, 165 (1984).

[18] M. Bassan, Y. Minenkov, R. Simonetti, "*Proceedings of the VIRGO Conference*", F. Fidecaro and I. Ciufolini editors (World Scientific, Singapore, 1997).

[19] P. Astone *et al.*, Astropart. Phys. **7**, 231-243 (1997).

[20] P. Carelli *et al.*, Appl. Phys. Lett. **72**, (1998).

[21] P. Falferi *et al.*, Appl. Phys. Lett. **82**, 931 (2003).

[22] R. E. Vogt, *The U.S. LIGO Project*, in "International Report LIGO", pagg. 91-97, Caltech (USA) 1991.

[23] F. Acernese *et al.*, Class. Quantum Grav. **20**, S609-S616 (2003).

[24] M. Hewitson *et al.*, Class. Quantum Grav. **20**, S581-S591 (2003).

[25] M. Ando *et al.*, Class. Quantum Grav. **19**, 1409-1412 (2002).

[26] The VIRGO Collaboration, *VIRGO Final Design*, ETS Pisa, Italy (1995)

[27] G. Ballardin *et al.*, Rev. Sci. Instrum. **72**, 3643-3652 (2001).

[28] K. Danzmann, "*Proceedings of the Thirteenth International Conference On General Relativity and Gravitation*", R. J. Gleiser, C. N. Kozameh and O. M. Moreschi editors (Institute of Physics Publishing, London, 1993).

LARES/WEBER-SAT, FRAME-DRAGGING AND FUNDAMENTAL PHYSICS

Ignazio Ciufolini [a], Antonio Paolozzi [b] Douglas G. Currie [c]
Erricos C. Pavlis [d]

[a] Dipartimento di Ingegneria dell'Innovazione, Università di Lecce,
via Monteroni, 73100 Lecce, Italy

[b] Dipartimento di Ingegneria Aerospaziale e Astronautica Università "La Sapienza",
Via Eudossiana 18, 00184 Roma, Italy,

[c] Department of Physics, University of Maryland, College Park, MD, USA

[d] Joint Center for Earth Systems Technology University of Maryland
Baltimore County and NASA Goddard/926 1000 Hilltop Circle, Baltimore, MD
21250, USA

Abstract

After a brief introduction on the scientific objectives of the LARES/
WEBER-SAT satellite we present the recent measurement of the Lense-
Thirring effect using the nodes of the LAGEOS and LAGEOS 2 satellites
and using the Earth gravity model EIGENGRACE02S obtained by the
GRACE space mission. Finally, we describe an interesting possibility of
testing the Brane-World unified theory of fundamental interactions by
the use of a specially designed LARES/WEBER-SAT satellite.

499

1   Introduction

The scientific objectives of the LARES mission are:

(1) High precision tests of Einstein's theory of general relativity, in particular, (1a) a $\sim 1\%$ measurement of the frame-dragging effect due to the angular momentum of a body, i.e., the Lense-Thirring effect, and test of the Earth's gravitomagnetic field. The Lense-Thirring effect [1, 2] is a tiny shift of the orbit of a test-particle. Frame-dragging, gravitomagnetic field and Lense-Thirring effect are theoretical predictions of Einstein's theory of general relativity (see, e.g., ref. [3]). (1b) A High precision test [4] of large distance infrared modification of gravity recently proposed by Dvali [5] to explain the dark-energy problem (a study will be required to precisely assess the achievable level of accuracy), see below. An improved high precision test of the inverse square law for very weak-field gravity and improved test of the equivalence principle (see the Italian Space Agency LARES phase A study [6]). A $\sim 10^{-3}$ measurement of the gravito-electric general relativistic perigee precession of the WEBER-SAT and a high precision measurement of the corresponding combination of the PPN (Parametrized-Post-Newtonian) parameters β and γ [10, 11]. This test will be achieved in the field of Earth with a range of about 10000 km, more accurate tests of β and γ are achieved in the field of Sun but with a much longer range. The PPN parameters β and γ test Einstein's theory of gravitation versus other metric theories of gravitation. (1d) Other tests of general relativity and gravitation (see LARES phase A study [6]).

(2) Measurements and improved determinations in geodesy and geodynamics. Cannonball type satellites have been used in Geodesy ever since the dawn of the space age, being nearly perfect targets for precise distance measurements from stations located on Earth's surface. Initially the accuracy was very low, only at the meter level, but with the current state-of-the-art laser systems, we can measure these distances to better than one centimeter with a single shot, and well below the one millimeter for a "normal point" average of several hundreds or even thousands of rapid firings (2 kHz systems are now already deployed and operational). This increased accuracy allows us to determine the origin, scale and orientation of the Terrestrial Reference Frame with very high accuracy [7], [8], a fundamental requirement for future climate change research, and contribute significantly in fundamental physics research [9].

The launch of an additional cannonball target will be a great addition to the relatively small and aging "constellation" of such targets already in orbit. It is however a very much needed addition because it enables the increase of tracking opportunities by a weather-dependent system such as the laser ranging network. The new target will also allow for a better temporal distribution of the tracking data making possible a more robust observation of the minute rotational (orientation) variations of Earth under the quasi-inertial

frame realized by the satellite orbits. Finally, the temporal variations of the long-wavelength harmonics, especially the zonals, of the gravitational field of Earth, are proxies of global change and interactions between the solid part of Earth, its atmosphere, hydrosphere and ice sheets [22]. The secular and long period variations in these terms are almost uniquely determined from laser ranging observations to these cannonball targets. The more targets available, the more accurate, robust are the corresponding estimates. Furthermore, we can observe more harmonics with more targets placed in differently inclined orbits.

Frame-dragging may be thought of as an aspect of the Einstein's principle of equivalence stating that, in a sufficiently small neighbourhood of a spacetime point, the effects of gravitation are not observable inside a freely falling frame, i.e. inside the so-called "Einstein elevator" [3]. The basic aspect of the equivalence principle is the equality of inertial and gravitational mass, which is one of the best tested principles of physics, measured to date with an accuracy of about 10^{-13}. However, the axes of a freely falling frame, where the equivalence principle holds, are not fixed relative to "distant inertial space", i.e. with respect to "distant fixed stars", but they are "dragged" by any moving mass. For example, they are dragged by a rotating mass; this is the "dragging of inertial frames" or "frame-dragging" as Einstein called it in 1913. In the near future the Gravity Probe B (GP-B) mission will try to measure frame-dragging, with unprecedent accuracy, on small super-conducting gyroscopes (the axes of the frames where the equivalence principle holds) orbiting around the Earth. GP-B will collect data, over a period of about one year only, that will then be analyzed to measure frame-dragging. However, the WEBER-SAT will collect data for a period of virtually hundreds of years (being a totally passive satellite with a very small orbital decay). These data could then be analyzed again in the future using the future improved gravitational models, in order to obtain much improved tests of frame-dragging and of other gravitational effects.

The orbit of a test-particle, such as a small satellite, is also a kind of gyroscope. Indeed, two of the orbital elements of a test-particle behave as "gyroscopes": the node and the pericenter (neglecting all the other perturbations).

Frame-dragging, gravitomagnetic field and Lense-Thirring effect have been described in several papers and studies, see for example ref. [3] and the ASI LARES phase A study [6].

Here we just point out that the Gravity Probe B experiment will try to measure the gravitomagnetic effect generated by the angular momentum of the Earth on a *gyroscope*, whereas the WEBER-SAT should measure the Earth's angular momentum effect on the orbit of a test particle. In some alternative theories the two effects may be different as in the case of a non-metric theory

with asymmetric connection, such as the Cartan theory with torsion, that may affect in a different way the orbit of a test-particle and of a gyroscope (see ref. [3]).

2   A recent measurement of the Lense-Thirring effect using the LAGEOS satellites

Let us briefly report a recent measurement of the Lense-Thirring effect on the two Earth satellites LAGEOS and LAGEOS 2 [12]. We measured the Earth frame-dragging to be 99 % of the value predicted by general relativity; the uncertainty of this measurement was ±5 % including all the known errors and ±10 % allowing for underestimated and unknown error sources.

Recently, by analysing the uncertainties in the spherical harmonic coefficients of the recent Earth gravity model EIGEN-GRACE02S obtained by the NASA space mission GRACE [13, 14], we found that the only relevant uncertainty in the orbit of the LAGEOS satellites [15], comparing it with the magnitude of the Lense-Thirring effect, is the one, δJ_2, in the Earth quadrupole moment, J_2, which describes the Earth oblateness. In the EIGEN-GRACE02S model, the relative uncertainty $\delta J_2/J_2$ is about 10^{-7}. This uncertainty corresponds on the orbits of the LAGEOS satellites to a shift of the node larger than a few times the Lense-Thirring effect. However, the orbital uncertainty due to all the other harmonics is only a few percent of the general relativity shift. Therefore, in order to eliminate the orbital uncertainty due to δJ_2 and in order to solve for the Lense-Thirring effect, it is necessary and sufficient to use only two observables. The two orbital observables we have analyzed are the two nodes of the LAGEOS satellites [16, 17, 18]. After modelling all the orbital perturbations, apart from the Lense-Thirring effect, we are able to predict the LAGEOS satellites' orbit with an error (root-mean-square of the residuals) of about 3 cm for a 15 day arc, corresponding to about fraction of a half millisecond of arc at the LAGEOS satellites altitude. The Lense-Thirring effect is in contrast 31 milliarcsec/yr on the LAGEOS node and 31.5 milliarcsec/yr on the LAGEOS 2 node, as calculated by the Lense-Thirring formula. The residual (calculated minus observed) nodal rate of the LAGEOS satellites, $\dot{\Omega}_{residual}$, is therefore: (residual nodal rate) = (nodal rate from δJ_2 error) + (nodal rate from other δJ_{2n} errors) + (Lense-Thirring effect) + (other smaller modelling errors), where the δJ_{2n} are the errors in the Earth even zonal harmonic coefficients, J_{2n}, of degree $2n$. We can then solve for the Lense-Thirring effect the system of the two observed residual nodal rates for the Lense-Thirring effect and simultaneously eliminate the error due to the δJ_{2n} uncertainty. The maximum error in the combination of the residuals due to the δJ_{2n} is 4 % of the Lense-Thirring effect.

In Ref. [12] is reported the analysis (using the orbital estimator GEODYN

[19]) of nearly eleven years of laser-ranging data, from January 1993 to December 2003, corresponding to about one million of normal points, i.e., to about 100 million laser ranging observations from more than 50 ILRS stations distributed all over the world [20].

In Fig. 1 we show the observed residuals of the nodal longitudes of the LAGEOS satellites, combined according to the formula to cancel the δJ_2 uncertainty [12]. The best fit line through the raw residuals in Fig. 1a (one-parameter fit) has a slope of 47.4 milliarcsec/yr; the root-mean-square of these post-fit residuals is 15 milliarcsec. In Fig. 1b are the residuals after removal of six main frequencies, corresponding to a thirteen-parameter fit with a secular trend plus phase and amplitude of six main signals with periods of 1044, 905, 281, 569, 111 and (see Method) 284.5 days. In this case the secular trend is 47.9 milliarcsec/yr, however the root-mean-square of these post-fit residuals is 6 milliarcsec only. In Fig. 1c is the Lense-Thirring effect predicted by general relativity for the combination of the LAGEOS nodal longitudes, which amounts to 48.2 milliarcsec/yr. Therefore, corresponding to the thirteen parameter fit of Fig. 1b, the observed Lense-Thirring effect is 47.9 milliarcsec/yr, corresponding to 99 % of the general relativistic prediction. In conclusion, this analysis confirms the Einstein's theory predictions of frame-dragging and Lense-Thirring effect [12]. The total uncertainty of our measurement is, including systematic errors, ±5% of the Lense-Thirring effect and ±10% allowing for underestimated and unknown error sources. For example, if we consider the time-independent gravitational error (root-sum-square) to be three times larger we get a corresponding error of 9 % and a total uncertainty of less than 10 %.

3 Some geodetic results using the LAGEOS satellites and the EIGENGRACE02S model

Using the method of analysis of about 11 years of satellite ranging observations reported in the previous section, in addition to the accurate determination of the Lense-Thirring effect, an anomalous variation in the Earth gravity field since 1998 was observed [21] that was clearly identified as an anomalous increase in the Earth quadrupole moment. The trend in the nodal longitudes of both satellites distinctly showed a variation in the Earth gravity field since 1998. This effect was proved [21] to be due to an increase in the J_2 coefficient, indeed, combining the node residuals according to the formula to eliminate the J_2 perturbation only, the effect disappeared. The anomalous trend observed using EIGEN-GRACE02S was also accurately reproduced using the previous EGM96 Earth gravity model and the recent EIGEN-2 model due to the CHAMP satellite. This result confirms the measured relative increase of J_2 of the order of 10^{-11} that was recently reported [22]. The Earth mass redistribution associated with this phenomenon is so far not clearly understood.
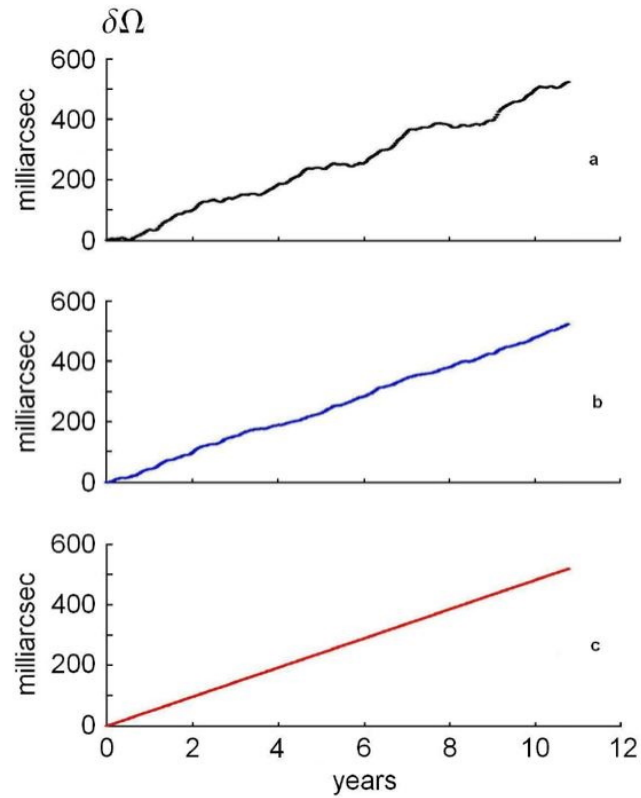
Figure 1: Observed orbital residuals of the LAGEOS satellites. The residual nodal longitudes of the LAGEOS satellites were combined according to the equation to cancel the δJ_2 uncertainty. In Fig. 1a is the raw, observed, residual nodal longitude of the LAGEOS satellites without removal of any signal, whereas in Fig. 1b is the observed residual nodal longitude after removal of six periodic signals. The best-fit line (thirteen parameter fit) through these observed residuals has a slope of 47.9 milliarcsec/yr. In Fig. 1c is the theoretical Lense-Thirring prediction of Einstein's general relativity for the combination [6] of the nodal longitudes of the LAGEOS satellites, its slope is 48.2 milliarcsec/yr.

It is important to stress that together with the measurement of the Lense-Thirring effect, it was also measured the effect of the variations of J_2, J_4 and J_6 on the nodes of the LAGEOS satellites. In [23] it is indeed reported an effective (i.e. including the effect of the higher even zonal harmonics) value of $\dot{J}_4^{Effective} \cong 1.5 \cdot 10^{-11}$. In the EIGENGRACE02S model, obtained by the GRACE mission only, the Earth gravity field was measured during the period 2002-2003. Corrections due to $\dot{J}_2$ and $\dot{J}_4$ were then applied to this 2002-2003 measurement in order to obtain a gravity field model antecedent to 2002-2003. These values of $\dot{J}_2$ and $\dot{J}_4$ used by the GFZ team are $\dot{J}_2 = 2.6 \cdot 10^{-11}$ and $\dot{J}_4 = 1.41 \cdot 10^{-11}$ and they were measured on the basis of completely independent 30-year observations before 2002. In ref. [23] are reported the orbital analyses using the orbital estimator GEODYN with and without a contribution of $\dot{J}_4 = 1.41 \cdot 10^{-11}$. First, it is important to stress that in the case of *not* applying this $\dot{J}_4$ correction to the orbital analysis, it can be clearly seen, by visual inspection, a hump in the combined residuals. Indeed, the effect of the time variation $\dot{J}_4$ shows up as a quadratic effect in the cumulative nodal longitude of the LAGEOS satellites, therefore the combined residuals of LAGEOS and LAGEOS 2 were fitted with a parabola, together with a straight line and with the main periodic terms. Then, by fitting the raw residuals obtained *without* any $\dot{J}_4$, it was measured a $\dot{J}_4^{Effective} \cong 1.5 \cdot 10^{-11}$, which includes the effect of $\dot{J}_6$ and of higher even zonal harmonics. On other hand, in the analysis of the combined residuals obtained with the EIGENGRACE02S correction of $\dot{J}_4 = 1.41 \cdot 10^{-11}$, it was measured a $\dot{J}_4^{Effective}$ of less than $0.1 \cdot 10^{-11}$, in complete agreement with the previous case. It is finally important to stress that this small value of the unmodelled quadratic effects in our nodal combination due to the unmodelled $\dot{J}_{2n}$ effects (with $2n \geq 4$) corresponds to a change in the measured value of the Lense-Thirring effect of about 1 %. In other words using the value of $\dot{J}_4^{Effective} = 1.5 \cdot 10^{-11}$ that we obtained from fitting the combined residuals (which is about 6 % larger than the value $\dot{J}_4 = 1.41 \cdot 10^{-11}$ given in the EIGENGRACE02S model) resulted in a change of the measured value of frame-dragging by about 1 % only with respect to the case of using $\dot{J}_4 = 1.41 \cdot 10^{-11}$; in conclusion this 1 % variation fully agrees with the error analysis given in [12].

4 On the possibility of testing Brane-World theories with WEBER-SAT/LARES

Let us now briefly describe the possibility of probing some recently proposed modifications of gravity using the Runge-Lenz vector, i.e., the perigee of WEBER-SAT [4].

In Newtonian mechanics, the orbital angular momentum of a satellite and its nodal line, the intersection of its orbital plane with the equatorial plane

of the central body, maintain a constant direction relative to "distant inertial space" for a motion under a central force. The Runge-Lenz vector, joining the focus and the pericenter of the orbit of a satellite, has also a constant direction relative to "distant inertial space" for a motion under a central force dependent on the inverse of the squared distance from the central body. Using the technique of laser-ranging with retro-reflectors to send back the short laser pulses, to this date we are able to measure distances with a precision of a few cm to a point on the Moon and of a few millimeters to a small artificial satellite. The instantaneous position of the LAGEOS satellites can be measured with an uncertainty of a few millimeters and their orbits, with semi-major axes $a_{LAGEOS} \cong 12270$ km and $a_{LAGEOS\ II} \cong 12210$ km, can be predicted, over 15 day periods, with a root-mean-square of the range residuals of a few cm. This uncertainty in the calculated orbits of the LAGEOS satellites is due to errors in modelling their orbital perturbations and, in particular, in modelling the deviations from spherical symmetry of the Earth's gravity field, described by a spherical harmonics expansion of the Earth's potential. However, to date, the terrestrial gravity field is determined with impressive accuracy, in particular with the dedicated satellites CHAMP and especially GRACE [13]. Regarding the perigee, the observable quantity is $ea\dot{\omega}$, where e is the orbital eccentricity of the satellite and, ω, the argument of perigee, that is the angle on its orbital plane measuring the departure of the satellite perigee from the equatorial plane of Earth. Therefore, we can increase the measurement precision by considering orbits with larger eccentricities.

Motivated by the cosmological dark energy problem, Dvali recently proposed string theories leading, among other things, to weak field modifications of gravity [5]. One of the interesting observational consequences of the large distance infrared modification of gravity pointed out by Dvali is the anomalous shift of the pericenter of a test particle. The anomalous perihelion precession predicted by this gravity modification for the Moon perigee is:

$$\delta\phi = -[(3\pi\sqrt{2}/4)r^{3/2}]/(r_c r_g^{1/2}) \ rad/orbit \qquad (1)$$

Where, $r_g = 0.886 cm$ is the gravitational radius of the Earth, r is the Earth-satellite distance and $r_c = 6Gpc$ is the gravity modification parameter that gives the observed galaxies acceleration without dark energy [5]. $\delta\phi = 1.4 \cdot 10^{-12}$ rad/orbit for the Moon.

Therefore in the case of the WEBER-SAT satellite with a semimajor axis of about 12270 km this effect would amount to 0.004 milliarcsec/yr only.

Since this effect of infrared gravity modification is proportional to the 3/2 power of the semi-major axis and however the number of orbits per year goes as the -3/2 power of the semi-major axis, in terms of radians per year the perigee shift is the same for both the Moon and WEBER-SAT, i.e. $1.9 \cdot 10^{-11}$ rad/yr. Therefore, we [4] simply need to consider what can be gained, or lost, with the

use of WEBER-SAT versus the Moon. In regard to the measurement precision, the ranging precision is very roughly proportional to the range distance, i.e. is a few cm for the Moon and a few millimeters for the WEBER-SAT, then since the shift of the perigee at the satellite altitude is $1.9 \cdot 10^{-11}$ rad/yr times the semi-major axis, the ratio of ranging precision to the effect to be measured is roughly the same for both the Moon and WEBER-SAT, even though slightly more favorable for the Moon. However, since the recovery of the perigee shift is proportional to the eccentricity of the satellite, we could orbit the WEBER-SAT satellite with a much larger eccentricity than the one of the Moon and therefore we could make the measurement of the perigee shift of the WEBER-SAT more *precise* than the one of the Moon.

However, critical are the *systematic errors* acting on the WEBER-SAT:

(a) the impact of the modelling uncertainties in the gravitational perturbations is critical for the WEBER-SAT satellite indeed the zonal harmonics of the Earth gravity field produce a perigee shift that is a function of the inverse powers of the semi-major axis, a: $1/a^{(2n+3/2)}$, for each even zonal harmonic coefficient J_{2n} with n integer. However, considering the improvements in the future Earth gravity models from the mission CHAMP, GRACE and GOCE, the future uncertainty in the perigee shift due to gravitational perturbations should drastically decrease.

There is also an interesting possibility to choose a different orbit for WEBER-SAT, not at 70 degrees of inclination, but for example with the special inclination of about 63.4 degrees, (of the type of the Molniya orbits) at which a satellite would have a null perigee shift due to the Earth's quadrupole moment J_2. In this way we would be able to cancel the major part of the J_{2n} uncertainties to measure the perigee, but we will lose some accuracy in the measurement of the Lense-Thirring effect on the node, even though the use of LAGEOS and LAGEOS II, together with WEBER-SAT, and the future improvements in the accuracy of the Earth's gravity models should not make this Lense-Thirring measurement much worst than a 1 % measurement (this possibility has to be further investigated) and furthermore, in this case, the Lense-Thirring effect could be measured using the WEBER-SAT perigee.

The impact of the modelling uncertainties in the non-gravitational perturbations is also critical for the WEBER-SAT satellite indeed the crucial factor is the cross-sectional area to mass ratio. In other words the acceleration produced by a non-gravitational force (such as radiation pressure) acting on a satellite is proportional to its cross sectional area and inversely proportional to its mass. Then this ratio is roughly proportional to the inverse of the radius of the considered satellites. Then for the Moon is very small whereas for WEBER-SAT may be a critical source of error.

These forces could be reduced by (a) a much denser and larger satellite than the one of the original proposal (although by increasing the cost of the mission);

(b) the non-gravitational perturbations of the perigee could also be reduced through the use of a much more eccentric orbit and (c) the mismodelling of the radiation pressure perturbations could be reduced by special optical and thermal tests performed on the WEBER-SAT satellite and through the measurement of its spin axis and rotational rate, once in orbit. Finally, we also mention the possibility of a drag free system, that implies acceleration sensors and propulsion systems on board, or of a spherical satellite made of a material transparent to most of the radiation; similar spherical retro-reflectors have been tested by the Russian space agency.

5   The WEBERSAT satellite

WEBERSAT satellite is a very simple satellite. In fact it is passive and does not require telemetry, attitude control, power, downlink, etc... On the other hand it has very demanding requirements. As mentioned earlier, the surface-to-mass ratio should be the lowest possible but also the satellite size must be maintained small to keep launch cost reasonable. Unfortunately the two requirements play opposite roles, in fact the abovementioned ratio is roughly inversely proportional to the radius. Another important aspect to be considered is the visibility of the satellite. There are more than 40 laser ranging stations in the world with different ranging capabilities. From some stations such as the one in Matera, in Italy, one can reach the Cube Corner Reflectors (CCRs) deployed on the Moon by the astronauts of the Apollo missions and get the signal back. Other stations are instead more limited. The amount of light reflected by the CCR is a function of the satellite altitude as well as of the satellite radius. In fact for a satellite the size of LAGEOS (60 cm in diameter) there are in average about 7 CCRs capable of reflecting the light, while for a satellite the size of LARES (30 cm in diameter) we have only 2 CCRs in "active" condition. Presently we reached a good compromise between surface-to-mass ratio, visibility and weight, by choosing a diameter of about 30 cm for the satellite.

In order to optimize the orbit for testing Brane-World theories, it is recommended, as mentioned earlier, a very eccentric orbit. The most economical one might be a Geostationary Transfer Orbit (GTO) typically used for commercial satellites, being a secondary payload for a commercial launch a convenient solution. Most commercial satellites are in a geostationary orbit, with low eccentricity. Our release would have to be during the transfer trajectory so that it has a high eccentricity. However the perigee should perhaps be raised from 600 km to at least 2000 km to reduce the inhomogeneous drag effects on the motion of the perigee (this problem has to be further studied). Part of the GTO orbit has an altitude of 36.000 km which is far beyond the capability of many laser ranging stations. In case this orbit will be considered,
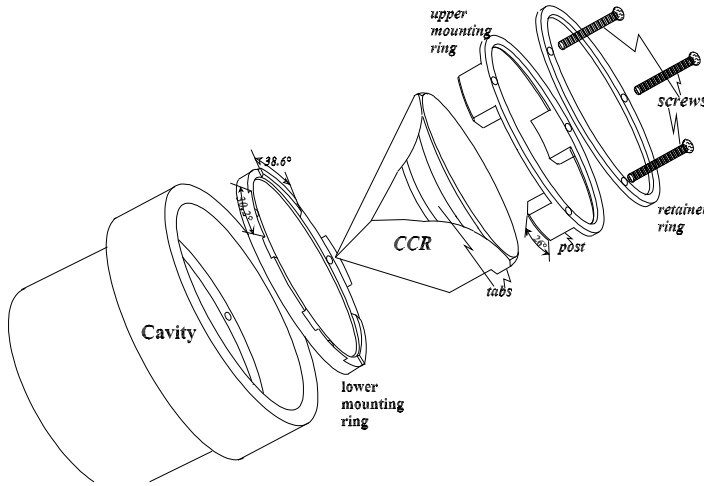
Figure 2: CCR mounting system.

one has to evaluate if a scarcity of data in the higher part of the orbit itself will be acceptable. Also the eccentricity enters in the equations, but the very accurate determination of this parameter is probably not as critical and fewer data points on the higher part of the orbit may suffice. A GTO orbit may therefore be a convenient choice to reduce the errors in the measurement of the perigee rate.

Another mitigation measure can be taken on another important source of error: the thermal thrust. The effect of thermal thrust on the node of a laser ranged satellite is relatively small, considering that this perturbation is also well modelled. The unmodelled effect on the perigee is much larger and probably bigger than the drift expected from Brane-World theories. In this last case improved modeling of thermal thrust is not enough, it is in fact required also an improved design of the satellite or even a dramatic change of it. Since thermal thrust is induced by thermal gradients on the satellite surface, thermal exchange between the several components of the satellite has to be increased. In Fig. 2 are reported the main components of the satellite (conventional design) which are: satellite cavity, CCR, plastic mounting rings, aluminum retainer ring and three screws. In [24] one can see that the estimated temperatures are quite different for the several components. In Table 1 are reported the approximate values of the component temperatures in two extreme conditions in the case of spin axis toward the Sun.

The major differences can be observed between the aluminum retainer ring and the CCRs. Also significant is the temperature difference between

	Sunlit pole	Dark pole
Satellite structure	300 K	300 K
Lower plastic mounting ring	307 K	290 K
Upper plastic mounting ring	343 K	280 K
Aluminum retainer ring	355 K	280 K
CCR	290 K	250 K

Table 1: Temperature distrubution on LAGEOS components

CCRs and satellite. Now this is certainly due to the absence of direct contact between the CCR and the metallic structure of the satellite. As suggested in [6] an improvement of thermal exchange between CCRs and satellite may be obtained by optimizing the emissivity and absorptivity of the CCR cavity and the three back surfaces of the CCR. That can be obtained by a proper choice of thin film to be deposited on the mentioned surfaces. This process will increase the heat exchange through radiation. Other mitigating measures have to be taken to reduce all the thermal conductances present in the satellite such as those between retainer aluminum rings and satellite. A further source of error is due to the satellite eclipses. Increasing the thermal capacity of the aluminum retainer rings by making them thicker for instance, one can reduce temperature variations during the eclipse [6]. A careful evaluation of temperature distribution through heat transfer analysis and dedicated tests need to be performed. A radical change in the design of WEBERSAT is being evaluated to reduce drastically temperature gradients on the satellite. The idea is that of eliminating the major cause of those temperature gradients i.e., thermal contact resistance and gaps between satellite components. This last aspect is very difficult to eliminate when one of the components is made of glass and the other of metal. Putting these two materials, with different thermal expansion coefficient, in intimate contact may jeopardize the integrity of the CCR. The more direct way to cope with this aspect is considering a full metal solution for the satellite. This means that the CCR should be carved directly on the spherical surface of a single piece satellite. Having a small satellite (a little bigger than a basket ball) made of high thermal conductivity material will drastically reduce the problems concerning thermal thrust. Temperature gradients will be reduced by about one to two orders of magnitudes. On the other hand with the full metal solution eddy currents will flow more easily and by interacting with the Earth magnetic field will cause the spin down torque to be more severe than in the LAGEOS satellites. By using a special tungsten alloy, characterized by a sufficiently low electrical conductivity (but still high thermal conductivity), the spin down torque can be mitigated. This is an advantage since modeling of thermal thrust in the rapid spin case for the satellite is more accurate. The baseline density for the satellite is at least

15.000 kg/m^3. Since with such a high density the spin down rate will be lower, the rapid spin case for WEBERSAT/LARES will last anyway many years after orbital injection. Another problem with this solution is the difficulty of getting the satellite attitude from ground observation of solar glints. These are solar reflections that can be obtained from the front surface of the silica glass CCRs. In order to reach the Brane world sensitivity it may be required to have anyway attitude information. For sure from some stations (MLRO for instance) by simply looking at the shape of the return laser beam it is possible to obtain the rotation rate. Furthermore by improving the photometric measurements it will be possible to recover spin axis orientation, and consequently thermal force direction, also in the case of full metal solution. But the big problem is the difficulty of machining the hollow CCRs on the spherical surface. The main reason is that the surface is concave and the requirements very strict: back surface angles with a tolerance of only 0.5 arcsec [25] and metallic surface polished to optical quality. It is obvious that special optical set up has to be arranged, possibly in the vicinity of the tooling machine, in order to check, in almost real time, the fulfillment of the requirements. There is also an issue concerning the retroreflecting efficiency of the hollow CCR. The conventional CCR has a reflection optical performance that decays with the cosine of the impinging angle from the normal. This is partly due to total internal reflection condition partly failing at larger angles. The hollow CCR also decays with cosine of the impinging angle. However, at large angles, there will be no failure of the total internal reflection. On the other hand, there will be absorption due to the metallic surface. For alumimun, this will be about 30% loss. However special coatings may help this.

References

[1] J. Lense and H. Thirring, *Phys. Z.* **19**, 156 (1918).

[2] Thirring H *Z. Phys.* **19**, 33 (1918).

[3] I. Ciufolini and J.A. Wheeler, *Gravitation and Inertia* (Princeton University Press, Princeton, New Jersey, 1995).

[4] I. Ciufolini, Introduction to the INFN study on WEBER-SAT, to be published (2004). See also: arXiv:gr-qc/0412001 v1, 1 Dec 2004.

[5] Dvali, G., Talk given at Nobel Symposium on Cosmology and String Theory, August 03, Sigtuna, Sweden (2004), arXiv:hep-th/0402130.

[6] I. Ciufolini, A. Paolozzi, et al. *LARES phase A study for ASI* (1998).

[7] Pavlis, E. C., Dynamical Determination of Origin and Scale in the Earth System from Satellite Laser Ranging, in Vistas for Geodesy in the New Millennium, proceedings of the 2001 International Association of Geodesy Scientific Assembly, Budapest, Hungary, September 2-7, 2001, J. Adam and K.-P. Schwarz (eds.), Springer-Verlag, New York, pp. 36-41, (2002).

[8] Pavlis, E. C., Monitoring the origin of the TRF with space geodetic techniques, S. Klosko, C. Noll and M. Pearlman (eds.), Proceedings of the 13th International Laser Ranging Workshop, Washington DC, USA, October 7-11, NASA CP 2003-212248, NASA Goddard, Greenbelt, MD, October (2003).

[9] Pavlis, E. C., Geodetic Contributions to Gravitational Experiments in Space, in Recent Developments in General Relativity, Genoa 2000, R. Cianci, R. Collina, M. Francaviglia, P. Fre, pp. 217-233, Springer-Verlag, Milan, (2002).

[10] Misner, C.W., Thorne, K.S., and Wheeler, J.A. *Gravitation* (Freeman, San Francisco, 1973).

[11] Weinberg S, *Gravitation and Cosmology: Principles and Applications of the General Theory of Relativity* (Wiley, New York, 1972).

[12] I. Ciufolini and E. C. Pavlis, *Letters to Nature*, **431**, 958 (2004).

[13] Reigber, C., Schmidt, R., Flechtner, F., König, R., Meyer, U., Neumayer, K.H., Schwintzer, P., Zhu, S.Y. An Earth gravity field model complete to degree and order 150 from GRACE: EIGEN-GRACE02S, Journal of Geodynamics, in press (2004). The EIGEN-GRACE02S gravity field coefficients and their calibrated errors are available at: http://op.gfz-potsdam.de/grace/index_GRACE.html 18.

[14] Tapley, B. D., The GRACE Mission: Status and Performance Assessment, Eos. Trans. AGU, 83(47), Fall Meet. Suppl., Abstract G12B-01 (2002).

[15] P. Bender and C. C. Goad, *The use of satellites for geodesy and geodynamics*, in *Proceedings of the Second International Symposium on the Use of Artificial Satellites for Geodesy and Geodynamics*, Vol. II, G. Veis and E. Livieratos, eds. (National Technical University of Athens, 1979), p. 145.

[16] I. Ciufolini, *Phys. Rev. Lett.* **56**, 278 (1986).

[17] I. Ciufolini, *Int. J. Mod. Phys. A* **4**, 3083 (1989). See also: B. Tapley, I. Ciufolini, J.C. Ries, R.J. Eanes, M.M. Watkins, *NASA-ASI Study on LAGEOS III*, CSR-UT publication n. CSR-89-3, Austin, Texas (1989).

[18] I. Ciufolini, *Nuovo Cimento A* **109**, 1709 (1996).

[19] Pavlis, D. E., et al., GEODYN Systems Description, Vol. 3 (NASA GSFC, Greenbelt, MD, 1998).

[20] ILRS 2003, Annual report of the International Laser Ranging Service, Klosko, S., Noll, C. and Pearlman, M., eds. Proc. of the 13th International Laser Ranging Workshop, (Washington DC, October 2003), NASA CP 2003-212248 (NASA Goddard, Greenbelt, MD, 2003).

[21] I. Ciufolini, E. C. Pavlis and R. Peron, to be published (2004)

[22] Cox, C.M., Chao, B., *Science* **297**, 831 (2002).

[23] I. Ciufolini et al., to be published (2004).

[24] Slabinski V.J., "A numerical solution for LAGEOS thermal thrust: the rapid-spin case", Celestial Mechanics and Dynamical Astronomy, 66: 131 (1997).

[25] Johnson C.W., Lundquist C.A., Zurasky L.J. "The LAGEOS satellite", presented at the International Astronautical Federation, XXVIIth Congress, Anheim, CA, Oct. 10-16 (1976).

MEASUREMENT OF RELATIVISTIC EFFECTS IN THE ORBITS OF LAGEOS AND LAGEOS II SATELLITES

Roberto Peron [a,b]

[a] *Dipartimento di Fisica, Università di Lecce, Via Arnesano, 73100 Lecce, Italy*

[b] *INFN, Sezione di Lecce*

Abstract

We present here the results of a recent analysis focused on the study of the nodal secular precession in the orbits of LAGEOS and LAGEOS II satellites caused by the gravitomagnetic field of Earth. This phenomenon (also called Lense–Thirring effect) is a consequence of dragging of inertial frames due to mass–energy currents. This study is made possible by the technique of Satellite Laser Ranging (SLR), that allows a higher accuracy in orbital determination of geodetic satellites like LAGEOS (below 1 cm accuracy in single–shot range, sub–millimeter for normal points). The analysis was carried out with the GEODYN II software, using the most recent models, in particular for gravitational geopotential (CHAMP– and GRACE–derived).

513

1   Introduction

The theory of general relativity by Albert Einstein, almost a century after its development, continues to challenge theoretical and experimental physicists, who are keeping to discover its consequences. The field charachter of this theory gives rise to a series of phenomena, who have their common counterpart in electromagnetic theory. Gravitational waves are a well-known consequence of the theory, and a number of experiments are in course to detect them. Gravitomagnetic effects are another consequence, equally worth of being tested.

General relativity predicts that a current of mass–energy would produce an effect on nearby test particles, analogous to the Lorentz force exerted on test charges by electromagnetic currents. This interaction is called *Gravitomagnetism* for this analogy with (electro)magnetism, and is of pure gravitational origin. The intensity of this "force" turns out to be very tiny in the weak–field, slow–motion regime we can directly sense in the solar system. We can see this from the formulæ calculated in 1918 by J. Lense and H. Thirring [10] for the secular effects on nodal longitude and argument of perigee of a test mass orbiting around a spinning spherical mass (*Lense–Thirring effect*):

$$\dot{\Omega}^{L-T} = \frac{2GJ}{c^2 a^3 (1-e^2)^{3/2}} \tag{1}$$

$$\dot{\omega}^{L-T} = \frac{-6GJ}{c^2 a^3 (1-e^2)^{3/2}} \cos I \tag{2}$$

where $\dot{\Omega}$ and $\dot{\omega}$ are the nodal and perigee rates respectively, a the semimajor axis of the orbit, e its eccentricity, I its inclination, and J is the angular momentum of the rotating body. When applied to a typical setting — and artificial satellite orbiting around Earth at an altitude of ~ 10000 km — they give values of the order of tens of mas/year, where mas denotes a millisecond of arc. Such a rate causes a shifting of the satellite orbit of some meters per year. This has to be compared with the distance between the satellite and measuring stations on Earth surface (of the order of semimajor axis). It is evident the great accuracy required in orbit recovery to be able to extract the gravitomagnetic relativistic signal.

Such an accuracy is available by the use of *Satellite Laser Ranging* (*SLR*) tecnique, in conjunction with a series of models to describe all other effects that could mask the gravitomagnetic precession. Of course, this tecnique is useful for measuring other relativistic effects on the satellite orbit, as well as other physical processes in geodesy and geodynamics.

In the following, we will describe a measurement of Lense–Thirring effect on the orbits of LAGEOS and LAGEOS II laser ranged satellites with Geodyn II software. We will discuss the procedure and models implied with this measurement, together with some problems related to data analysis and

perturbation modeling; we will conclude with a geophysical "application", to show the broad scientific use of laser ranging data.

2 Data reduction and residual analysis

The foundations of our work lie in the analysis of laser ranging data of LAGEOS and LAGEOS II satellites. These satellites are completely passive and covered by Corner Cube Retroreflectors (CCR) that reflect back laser pulses sent by a network of station on Earth (International Laser Ranging Service — ILRS). The total round–trip time of the pulse (as measured by very precise clocks at the stations) is used to compute the istantaneous distance station–satellite. The knowledge of a number of these observations enables the reconstruction of satellite orbit, usually with a numerical fitting procedure.

The precision of the normal point laser observations is remarkable: $\sim$ mm. This has to be compared with the mean distance station–satellite: $\sim$ 8000 km. So in principle one could recover the orbit with the same degree of accuracy. In practice, the effective ability in doing this recovery depends on the dynamical modeling of satellite behaviour: with a good functional dependence on the relevant parameters, the fit will end up to be better. As will be explained later, currently we can achieve an accuracy of $\sim$ 2 cm post–fit in range.

Range data are analysed using Geodyn II software (NASA GSFC) [15]. The selected time period is divided in chunks called *arcs*; for each of them a data reduction procedure is employed. In particular we have:

- Up–to–date models to describe the dynamics of satellite

- State vector $(\vec{x}, \dot{\vec{x}})$ and other parameters estimated through an iterative procedure

- Lenght of an arc: 15 days

From the knowledge of the state vector for each satellite a series of so–called *residuals* is derived; a residual for a given physical quantity is defined as the difference between observed and calculated value for that quantity. It gives a measure of how much better the set (models, estimated parameters) follows real data. The residuals contain all the features of satellite motion bad modeled or not modeled at all.

By analysing a residual time series one can separate secular and periodical effects, and try to gain knowledge about the unknown (not modeled) part of satellite dynamics. In our case, not including the gravitomagnetic "force" into the set of dynamical models, we hope of recovering the Lense–Thirring effect as a secular trend in residual behaviour.

The set of models included in the data reduction contains the perturbations of gravitational and non–gravitational origin acting on each satellite (apart —

as said before — the gravitomagnetic "force") and every other information useful to process the data, as the atmospheric delay corrections or the Earth Orientation Parameters (EOP) for a correct integration of the equations of motion in a quasi–inertial frame.

3   Measurement of Lense–Thirring effect

The detection of the secular trend related to Lense–Thirring effect is feasible only with a careful check of all the sources of error associated with the orbit determination process. In particular, the most relevant errors are due to the lowest degree even zonal spherical harmonics in the expansion of geopotential [6]. Thanks to recent improvements in accuracy achieved by the new geopotential models [17], only the error related to coefficient C_{20} (Earth quadrupole) is critical. We can use the formula (see also [4])

$$\left(\dot{\Omega}_I^{L-T} - \frac{N_2^I}{N_2^{II}}\dot{\Omega}_{II}^{L-T}\right)\mu = \delta\dot{\Omega}_I - \frac{N_2^I}{N_2^{II}}\delta\dot{\Omega}_{II} \tag{3}$$

to remove this source of error, combining the nodal residuals of both LAGEOS satellites. Here μ is the parameter measuring the intensity of gravitomagnetic "force" (0 in Newtonian physics, 1 in general relativity), $\delta\dot{\Omega}_I$, $\delta\dot{\Omega}_{II}$ are the nodal residuals of the two satellites, and N_2^I, N_2^{II} are coefficients related to the orbital elements of the satellites.

In Figure 1 are shown the combined residuals following (3) for a period of nine years, starting from the beginning of 1993, using the recently released model EIGEN-GRACE02 [17] (see also [7, 8]). We can see clearly the secular trend which, apart the mismodeling, can be associated with the Lense–Thirring effect. This results fully confirms previous works [3, 5, 6].

4   Rôle of non–gravitational perturbations

In the modeling of satellite dynamical behaviour, an important rôle is played by the forces of non–gravitational origin. These forces are due to the interaction of the satellite with the environment surrounding it. The satellite is subject to the impact of eletromagnetic radiation from Sun and Earth, of interplanetary dust and could hit micrometeorites; it can emit infrared radiation. Among the vast class of these phenomena, two effects are of major impact on our measurement: direct solar radiation pressure and Yarkovsky–Schach effect.

Direct solar radiation pressure is a perturbation caused by reflection–diffusion–absorption of solar photons by the surface of satellite. For a spherical satellite, the resultant acceleration is given by (see [11])

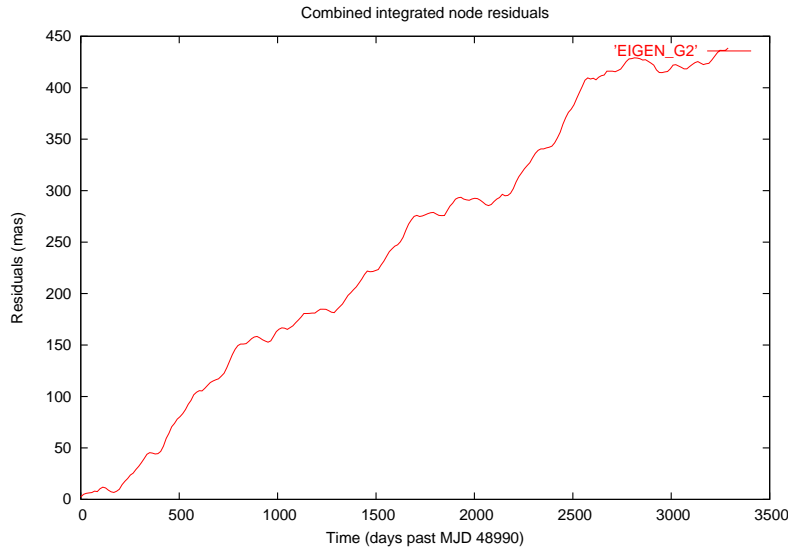$$\vec{a}_\odot = -C_R \frac{A\Phi_\odot}{mc}\left(\frac{1AU}{r}\right)^2\hat{s} \tag{4}$$

Figure 1: Combined integrated nodal residuals.

where A is the cross–section of satellite, m its mass, r the Sun–satellite distance ($\sim$ Sun–Earth distance), $\hat{s}$ the satellite–Sun unit vector, $\Phi_\odot$ is the solar constant and C_R is the so–called *radiation coefficient*, which is an empirical measure of the optical properties of the satellite surface. This perturbation (the strongest among the non–gravitational ones) is well modeled, but it remains an open issue regarding a possible time variation of C_R. Indeed, this parameter is adjusted in the orbit determination process, and there are evidences of a possible variation of it in case of LAGEOS II [13].

Yarkovsky–Schach effect is due to anisotropic emission of infrared radiation by the satellite (which is warmed by the Sun). In the fast rotation approximation, the resultant acceleration is given by (see [12])

$$\vec{a}_{Yar} = -\gamma\Gamma(\zeta)\cos(\xi)\hat{S} \tag{5}$$

with $\gamma = \frac{16}{9}\frac{\epsilon_{ir}\sigma}{mc}\pi R^2 T_0^3 \Delta T$, where $\Gamma(\zeta)$ is the physical shadow function ($\zeta = \omega + f$), ξ the angle between the Sun direction and the satellite spin axis, $\hat{S}$ the spin direction of the satellite, ϵ_{ir} the retroreflectors infrared emissivity, σ the Stefan–Boltzmann constant, R is the radiu of the satellite, T_0 its average temperature and ΔT is the temperature difference between its two emispheres. This perturbation is effective for perigee behaviour (so it's not relevant for the two–nodes solution), and its modeling is much more difficult, due to the

dependence on $\hat{S}$, whose temporal evolution is still an open problem [1].

Perturbative study of these two forces reveals several common frequencies [11, 12]. So great care is required in the analysis of residuals: an effect thought to be due to a force could really be caused by another effect.

It is common practice in orbit parameter estimation to introduce so–called *empirical accelerations*, to take into account small not modeled perturbations. This leads to an improvement of the fit, but at the risk of absorbing important signal. In our analysis we usually estimate only the T (transverse) component of this acceleration, obtaining values for the constant part of $\sim 10^{-12}$ m/s^2. The use of the T component causes no problem in the estimate of the nodal longitude, since the nodal rate depends only on the out–of–plane W component, as we can see from the corresponding Gauss perturbative equation [2, 14]:

$$\dot{\Omega} = \frac{W}{H \sin I} r \sin(\omega + f). \tag{6}$$

Here H is the osculating angular momentum (per unit of reduced mass) of the system, r the Earth–satellite distance, ω the argument of perigee and f the true anomaly.

We also tried not to include these empirical accelerations. Apart from observing a worst post–fit RMS, we noticed that the "power" of the signal due to solar radiation pressure could cause a non–physical estimate of C_R. The question of a possible time variation of this parameter is still open, and we are working in this direction.

5 A geophysical "application"

SLR tecniques are a useful tool for sensing time variations of geopotential coefficients. These variations could be due to:

- Tides

- Secular variations (*postglacial rebound*)

- Mass transport (oceans ↔ atmosphere)

The importance of these processes is more and more recognized, in conjunction for example with global warming issues. In our residual time series we see these processes at work. In particular, we noticed — starting from about 1999 — a sensible variation of nodal rate, that seems to be due to an abrupt change in quadrupole rate [9]. The causes of this change are uncertain, perhaps related to mantel or ocean mass transport. Our observation of this phenomenon, anyway, is an important confirmation of the validity of our analysis procedure.

6   Conclusions

The observing and analysis tecniques based on Satellite Laser Ranging are a valuable tool for the study of phenomena in the Earth environment. The intrinsic precision of laser measurements, coupled with complex models of gravitational and non–gravitational effects acting on passive satellites like LAGEOS, makes possible the measurement of tiny relativistic effects, in particular the Lense–Thirring effect. As a by–product of this work, useful geophysical and geodynamical information can be extracted by the residual time series obtained from the analysis of range data.

Aknowledgements

References

[1] J. I. Andrés *et al.*, J. Geophys. Res. **109 B**, 06403 (2004)

[2] B. Bertotti, P. Farinella and D. Vokrouhlický, *Physics of the Solar System*, Kluwer, Dordrecht, 2003

[3] I. Ciufolini *et al.*, Nuovo Cim. **A 109**, 575 (1996)

[4] I. Ciufolini, Nuovo Cim. **A 109**, 1709 (1996)

[5] I. Ciufolini *et al.*, Class. Quantum Grav. **14**, 2701 (1997)

[6] I. Ciufolini *et al.*, Science **279**, 2100 (1998)

[7] I. Ciufolini *et al.*, New Astron., to be published

[8] I. Ciufolini *et al.*, Science, to be published

[9] M. Cox and B. F. Chao, Science **297**, 831-833 (2002)

[10] J. Lense and H. Thirring, transl. B. Mashhoon *et al.*, Gen. Rel. Grav. **16**, 711 (1984)

[11] D. M. Lucchesi, Planet. Space Sci. **49**, 447 (2001)

[12] D. M. Lucchesi, Planet. Space Sci. **50**, 1067 (2002)

[13] D. M. Lucchesi *et al.*, Planet. Space Sci. **52**, 699 (2004)

[14] A. Milani, A. M. Nobili and P. Farinella, *Non-gravitational perturbations and satellite geodesy*, Adam Hilger, Bristol, 1987

[15] D. E. Pavlis *et al.*, *GEODYN operations manuals*, contractor report, Raytheon, ITSS, Landover MD, 1998

[16] C. Reigber *et al.*, Adv. Space Res. **31(8)**, 1883 (2003)

[17] C. Reigber *et al.*, Journal of Geodynamics (2004), in press

LIGHT FLASH OBSERVATIONS IN SPACE: FROM APOLLO TO THE INTERNATIONAL SPACE STATION

Marco Casolino [a,b]

[a] INFN, Sezione di Roma II, via della Ricerca Scientifica, Roma, Italy

[b] Dipartimento di Fisica, Università di Roma "Tor Vergata",
via della Ricerca Scientifica, Roma, Italy

Abstract

Light Flashes are abnormal visual sensations caused by the interaction of high energy particles with the human visual apparatus. They were originally predicted in 1952 and observed on almost all space missions. From the '70s a number of dedicated observations in space and on ground (using accelerator beams) in a controlled environment have been carried forth to study this phenomenon. In this work we briefly summarize the observations and results obtained in more than 30 years of research in space.

1 Introduction

Light Flashes (LF) are abnormal visual perceptions thought to originate from the interaction of cosmic radiation with the human visual system. They

are described to occur in a variety of shapes (streaks, star-like flashes, etc.) apparently differing from the diffuse glow reported by patients subjected to X-ray exposure. Usually these flashes are observed after a period of dark adaptation of the eye, although some subjects have reported events even under normal lighting conditions. Frequency, type and shape are greatly dependent on the observer; in addition it is usually necessary to brief the astronauts on what to expect in order for them not to discount LF without paying attention to them. After being instructed most (but not all) astronauts were able to observe this phenomenon. LF were originally predicted by Tobias[1] in 1952[1] before the first space flights and before a detailed knowledge of cosmic ray radiation was available.

(1969) and were subsequently reported on Apollo 12 and 13 missions, resulting in the first dedicated observation sessions on Apollo 14 and 15. On Apollo 16 and 17, LF observation sessions were carried out in using the ALFMED[2] (Apollo Light Flash Moving Emulsion Detector) experiment, consisting of an helmet with cosmic ray sensible emulsion plates to correlate passage of particles with the astronauts' visual system. Average LF observation rate for the Apollo missions was 0.23 LF/min[2], compatible with the hypothesis of cosmic ray nuclei interacting with the human visual system[3]. LF frequency during translunar coasting (going toward the Moon) was higher (0.39 LF/min) than that (0.34 LF/min) during transearth coasting (coming back to Earth). This phenomenon was particularly manifest during the Apollo 17 transearth phase, where none of the three astronauts observed any LF. In addition to the lower LF frequency, dark adaptation time in the former case was lower (11 min) than in the latter (22.6 min). Studies of correlation with the relative position of the spacecraft, the moon and the geomagnetic field, solar activity or other phenomena were done, but none was found.

In 1974 LF were investigated in low Earth orbit on board Skylab[4]. Two observation sessions by the pilot of Skylab 4 mission were performed: the first (70 minutes on day 74 of the mission) passed through the edge of the South Atlantic Anomaly and reached higher geomagnetic latitudes; the second (55

---

[1]We quote the most significant passage notable for its validity up to now:

> Of particular interest here is the retina. The dark adapted retina can detect even x-ray ionization (al bluish diffuse light). It is conceivable that very densely ionizing tracks would produce small flash-like light sensations. If the retina, fibers of the optic nerve, and certain brain cells are regarded as performing as a unit, there is a possibility for greater damage to vision than to either component of the visual system, since vision from a given sensitive element of the retina might be affected, if either the retina, or the impulse carrying nerve fibers and synapses or brain cells were affected.

[2]These are up to now the only sessions (and the only human missions) performed outside the geomagnetic shielding.

minutes on day 81) passed through the center of the South Atlantic Anomaly. In both cases a large number (112) of flashes were observed during the passage in the SAA (a total of 12 minutes), mostly during the second session where the anterior-posterior axis of the head of the astronaut was parallel to the local magnetic field, suggesting an important contribution by trapped protons. Also marginal evidence for a latitude effect was reported but not deemed conclusive at the time.

Light Flashes were also observed in 1975 in the framework of the Apollo-Soyuz Test Project[5, 6] (ASTP). Also in this case two sessions were planned and resulted in the observation of a total of 82 flashes. The frequency of flashes was strongly dependent on latitude, showing an increase at high latitude regions where particle flux is higher due to the lower geomagnetic shielding (which allows lower energy particles to reach low earth orbit). Contrary to the Skylab, no flashes where observed in the SAA. This was explained in terms of the lower altitude (225 km on Apollo-Soyuz and 443 km on Skylab) and the higher shielding of the Apollo capsule respect to the Skylab: these two causes concurred to reduce trapped proton flux in the Anomaly region.

2   Ground based investigations: 1970-1975

During space observations a number of ground experiments was also performed using low intensity particle beams and cosmic rays on human subjects. LF were first observed on a beam of 3 MeV neutrons[7] and subsequently with 14 MeV neutrons[8] (but not with 3 MeV neutrons in the same experimental conditions) and 300 MeV neutrons (but not with 1.5 GeV/c pions), suggesting that the production of knock-on protons could be involved in this effect. Tests on cosmic muons resulted in observation [10, 11] of the phenomenon, clearly observed on a 6 GeV muon beam[12]. Another 7 MeV muon experiment reported the observation of LF with a dark center[13], subsequently observed in space on Apollo[2] and proposing the generation of Cherenkov radiation emission in the eye as the process involved. The use of Carbon beams of 595 MeV/n and 470 MeV/n resulted[15] in the observation of LF in both cases but with a higher rate at the higher energy, which was above the threshold for Cherenkov radiation[14]. Another experiment, which scanned different regions of the eye with a nitrogen beam, observed LFs when the beam was pointed at the posterior part of the eye and thus was in favor of a direct ionization of the retina[16].

LF observed in space may thus be due to one or more of the following processes: 1) Direct retinal ionizaton by highly ionizing particles; 2) Chrenkov light emission in the eye bulb; 3) Proton (or neutron) nuclear interaction in the eye producing an hadronic shower which in turn stimulates the retina.

3   The Sileye experiments:1995-2004

Light Flash research in space was resumed on board Mir Space Station with the Sileye experiments, which placed two detectors (Sileye-1 in 1995 and Sileye-2 in 1998) and involved 6 cosmonauts if LF observations between 1995 and 1999.

Both detectors share the same philosphy of the previous devices. They consist in an helmet which contains a cosmic ray silicon tracking detector: the cosmonaut wears the helmet (with a light shielding mask), undergoes a period of adaptation to darkness conditions and pushes a button when he observes an LF. In parallel the silicon detector[17] measures cosmic rays above 40MeV/n from protons to Iron. The Sileye experiment has up to now involved 7 cosmonauts in 35 LF observation sessions. Results of the observations are resumed in Table 1 and compared with previous observations: it is possbile to see how LF perception on board Mir is lower than that observed on previous experiments (0.13 LF/min). This is probably due to a lower orbit and and higher shielding of the station.

A correlation between nuclear events with track direction and timing compatible with LF observations by the cosmonauts was observed in the case of 8 events (5 due to light nuclei: $Z \leq 5$ and 2 due to $Z = 8$ and one with $Z = 24$)[18]. The ratio of these events with the total number of flashes is consistent with the portion of the eye covered by the detector (8%).

From an analysis of the LF observed on Mir it is possible to see a linear dependence between particle flux and LF outside the SAA[19]. In the region of the Anomaly the LF increase is not proportional to the high flux increase of trapped protons. However LF rate in the Anomaly ($0.15 \pm 0.03 \, min^{-1}$) is higher than what found outside ($0.6 \pm 0.03 \, min^{-1}$), an evidence that galactic nuclei (which do not increase in fluence in the SAA) cannot be the only cause of LF. These observations prove that there are at least two distinct causes of LF, involving different physical phenomena: the first is probably due to direct nuclear ionization by galactic nuclei and therefore exhibits the latitudinal dependence due to the varying geomagnetic cutoff. The second component is due to proton nuclear interactions in the cosmonauts' visual apparatus. Due to the lower cross section, the role of protons is "seen" only in the Anomaly[3].

Sileye-2 reentered the atmosphere together with Mir in March 2001; LF research continued with the experiment Sileye-3/Alteino on board the International Space Station during the Soyuz-34 mission. In this case, an advanced version of the cosmic ray detector was used together with an electroencephalograph to monitor brain activity of the cosmonaut during the mission. Data analysis is currently in progress but the LF frequency was found

---

[3]On Shuttle flights for Hubble servicing missions, where the altitude is higher, LF have been reported with an higher rate and were even observed in the absence of dark adaptation.

Cosmonaut / Mission	Numb. sess.	Dark adapt. time (min)	Sess. length (after D.A.) (min)	LF Obs.	LF rate (LF/min)	Shielding (g/cm2) / height (km)
Cosm. 1	2	12±7	112	28	0.25±0.04	
Cosm. 2	1	23	26	9	0.34±0.11	
Cosm. 3	5	13±3	239	20	0.08±0.02	
Cosm. 4	11	13± 9	673	79	0.12±0.01	
Sileye-2 tot. (1998-1999)	19	13.5±8	1050	145	0.13±0.01	> 0.81 300-400 [18, 19]
Sileye-1 tot. (1995-1996)	9		492	87	0.18±0.02	> 0.81 300-400 [18]
ASTP (1975)	2	≃ 15	180	82	0.46±0.05§	3-3.5 (0.27π sr) 3.5-5.5 (0.77 π sr) 225 [6]
Skylab-4 (1974)	2	≃ 10	125	168	1.3±0.1	1.5-2.0 (1.5π sr) 443 [4]
Apollo 14-17 (1971-1972)	20	19±9‡	1161	268	0.23±0.1†	3-3.5 (0.27πsr) 3.5-5.5 (0.77π sr) (Earth-Moon) [2]

Table 1: Sileye-2 LF results obtained with the four cosmonauts involved. Combined data are compared with previous missions. *Notes: §112 LF were observed in the 12 min transit in SAA. ‡ Translunar coast sessions had a lower DA (11.0 min) and higher LF rate (mean time between events 2.58 min) than transearth coast sessions (DA 22.6 min, mean time 2.91). † Takes into account that during Apollo 17 transearth session there were no LF observations by the three astronauts. If these three sessions are excluded the rate rises to 0.27±0.02 LF/min.*

to be coherent with that observed with Mir[20].

The device is still on board ISS for future use: it will be followed by Altea: a larger facility to study cosmic rays, Light Flashes and the effect of space environment on visual sensations of the astronauts.

References

[1] C. A. Tobias *J. Aviat. Med.* **23** 345, (1952).

[2] L. S. Pinsky, W. Z. Osborne, J. V., R. E., Benson, L. F., Thompson, *Science*, **183**, 957 (1974).

[3] W. Z. Osborne, L. S. Pinsky, J. V. Bailey, *N*ASA SP-368, **355** (1975).

[4] R. A. Hoffman, L. A. Pinsky, W. Z. Osborne, J. Z. Bailey, *N*ASA SP-377, **133** (1977).

[5] T. F. Budinger, et. al, *N*ASA TM X-58173, **13-1** (1976).

[6] T. F. Budinger, et. al, *N*ASA SP-412, **193** (1977).

[7] J. H. Fremlin, *N*ew Scientist, **47**, 42 (1970).

[8] W. N. Charman, J. A. Dennis, G. G. Fazio, J. V. Jelley,*N*ature, **230**, 522 (1971).

[9] C. A. Tobias, T. F. Budinger, J. T. Lyman, *N*ature, **230**, 596 (1971).

[10] F. J. D'Arcy, N. A. Porter N. A., *N*ature, **196**, 1013 (1962).

[11] W. N. Charman, C. M. Rowlands, *N*ature, **232**, 574 (1972).

[12] P. J. McNulty, *N*ature, **234**, 110 (1971).

[13] P. J. McNulty, V. P. Pease, V. P. Bond, *S*cience, **189**, 453 (1975).

[14] G. G. Fazio, J. V. Jelley, W. N. Charman, *N*ature, **228**, 260 (1970).

[15] P. J. McNulty, V. P. Pease, V. P. Bond, *S*cience, **201**, 342 (1978).

[16] T. F. Budinger, J. T. Lyman, C. A. Tobias, *Nature*, **239**, 209 (1972).

[17] V. Bidoli, M. Casolino, E. De Grandis, *et al.*, **J. Phys. G**, **27**, 2051 (2001).

[18] S. Avdeev, V. Bidoli, M. Casolino, *et al.*, *A*cta Astronautica, **50**, 81, 511 (2002).

[19] M. Casolino, *et al.*, *N*ature, **422**, 680 (2003).

[20] A. Popov, private communication, 2004.

TESTING FOR THE PIONEER ANOMALY ON A PLUTO EXPLORATION MISSION

Andreas Rathke [a]

[a] *ESA Advanced Concepts Team (DG-X), ESTEC, Noordwijk, The Netherlands*

Abstract

The Doppler-tracking data of the Pioneer 10 and 11 spacecraft show an unmodelled constant acceleration in the direction of the inner Solar System. An overview of the phenomenon, commonly dubbed the Pioneer anomaly, is given and the possibility for an experimental test of the anomaly as a secondary goal of an upcoming space mission is discussed using a putative Pluto orbiter probe as a paradigm.

1 Introduction

The orbit reconstruction from the Doppler tracking data of the hyperbolic trajectory away from the Sun of the Pioneer 10 and 11 probes shows an anomalous deceleration of both spacecraft of the order of $10^{-9}\,\mathrm{m/s^2}$. Even before the Jupiter swing-by, an unmodelled acceleration of that order [2] had been noticed for Pioneer 10. It had however been attributed to gas leaks and a mismodelling of the solar radiation force. Such patterns of explanation became unsatisfactory for the post swing-by hyperbolic arc due to the decrease of the solar radiation pressure inversely proportional to the square of the distance
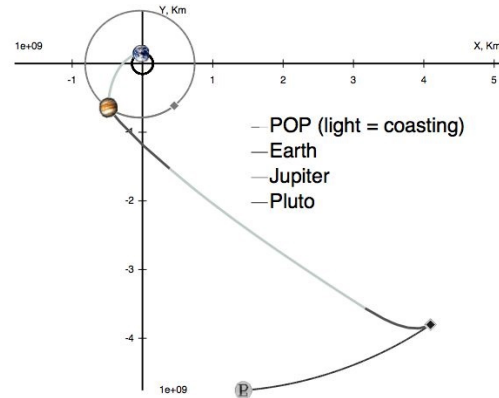
Figure 1: View of POP.   Figure 2: The trajectory of POP.

from the Sun and the quiet state of the spacecraft, which should reduce any gas leaks. The anomaly on both probes has been subject to three independent analyses [1, 3]. The result of all investigations is that an anomalous Doppler blueshift is present in the data from both craft of approximately 1.1×10^{-8} Hz/s corresponding to an apparent deceleration of the spacecraft of approximately 8×10^{-10} m/s^2. From Doppler data alone, it is not possible to distinguish between an anomalous frequency shift of the radio signal or a real deceleration of the spacecraft.

The principle investigators of the anomaly have conducted a thorough investigation of possible biases and concluded that no conventional effect is likely to have caused the anomaly [1]. Meanwhile, there exists an ample body of literature discussing various aspects of possible systematic effects, without definitive conclusion.

Although the Pioneer anomaly (PA) is an effect at the edge of what is detectable with radiometric tracking of a deep-space probe, it is huge in physical terms: The anomaly exceeds the general-relativistic corrections to Newtonian motion by five orders of magnitude (at 50 AU). A gravitational origin of the deceleration of the Pioneer probes is however hard to imagine, since no corresponding anomaly is seen in the orbits of Uranus and Neptune. Hence, a gravitational anomalous deceleration would indicate a violation of the weak equivalence principle.

Considering the efforts that have been undertaken to find a conventional explanation of the PA, it seems likely that only an experiment will finally be able to determine the nature of the effect. A mission to perform an investigation of the PA has to exceed the navigational accuracy of the Pioneers. In particular, the systematic errors in the modelling of onboard generated forces must not exceed a few percent of the Pioneers' anomalous deceleration and the test should take place in the outer part of the Solar system so that external

disturbances are minimised.

The spacecraft currently in operation or in design are not capable to fulfil these requirements. Hence, a PA test will have to be performed by a mission which takes into account the experiment already in an early stage of its design process. We discuss in the following how the test requirements can be achieved on a mission which has a test of the PA only as a secondary goal. Considering a non-dedicated mission as a first choice seems reasonable in view of the high cost of a mission to the outer Solar system.

2   The Pluto orbiter probe

To make our considerations about the implementation of a PA test as tangible as possible we consider its realisation onboard of a low-mass, low-thrust mission to Pluto. A study of such a mission has been undertaken recently in ESA's Advanced Concepts Team and detailed results of the system design and trajectory design have been presented in [4].

The goal of the Pluto-orbiter-probe (POP) study was to design a spacecraft that would reach a low circular orbit around Pluto, 1000 km above its surface, using only hardware that will already be space-qualified by the launch date. The capability of entering a Pluto orbit is provided by a nuclear electric propulsion system. The trajectory will incorporate a Jupiter gravity assist. The envisaged launch date is in 2016, arrival at Pluto would be 18 years later in 2034. The spacecraft's wet mass is 837 kg, and the dry mass 516 kg. This would enable a launch with a heavy launcher with an Earth escape velocity of 10 km/s. The science payload will have a mass of 20 kg and will feature a multi-spectral imaging camera, a near-infrared spectrometer, an X-ray spectrometer, a bolometer and the provision to use the communication antenna also as a synthetic-aperture RADAR.

The central part of POP (Fig. 1) is a cylindrical spacecraft bus of 1.85 m length and 1.2 m diameter. The 2.5 m diameter Ka-band (32 GHz) high-gain antenna is located at one end of the bus. The other end of the spacecraft bus houses the propulsion system. It consists of four radioisotope thermoelectric generators (RTG's) on short booms inclined $45°$ to the axis of the bus, a toroidal tank for the Xenon propellant and the four QinetiQ T5 ion thruster main engines. Attitude control is provided by 10 hollow-cathode thrusters, which use the same power-processing unit and propellant supply as the main engines.

The trajectory of POP (Fig. 2) has a hyperbolic coast phase of 18 AU length before the braking burn for the Pluto orbit capture begins. This coast phase will last 7.4 years. During this time the spacecraft will transverse a radial distance between 13.4 AU and 30.4 AU from the Sun. The mass of POP will then be about 760 kg.

POP is envisaged to employ two different attitude-control modes during

different parts of its journey. When the main engines of POP are thrusting and during the swing-by the craft will be three-axis stabilised in order improve pointing accuracy. The same is the case in Pluto orbit where reorientation requirements demand three-axis control. During long coasts, however, spin stabilisation will be employed. This has the practical benefit of enhancing the lifetime of the momentum wheels and, thus, saves mass. The rotational speed will be very low during the coast, ca. 0.5 rpm, so that attitude acquisition can still be preformed by the star trackers to be used in 3-axis stabilised mode. Hence, no additional attitude acquisition hardware will be necessary during the spinning mode and it can be realised at no additional spacecraft mass. Spin stabilisation during the coast is a crucial factor to enable a test of the PA as it reduces the number of attitude control manoeuvres to one every few weeks and hence minimises onboard generated accelerations.

3   Measurement strategy

With a new mission, the search for a PA-like effect will still rely on radio-tracking. Nevertheless, considerable advances over the precision of the Pioneer data are achievable with present-day telecommunication hardware. The major improvement comes from the use of sequential ranging in addition to Doppler tracking. The information from sequential ranging relies on the group velocity of the signal, whereas the information from Doppler tracking relies on the phase velocity. Sequential ranging is hence insensitive to a gravitational effect on the radio signal, which would be non-dispersive. The usage of both methods allows an anomalous blueshift of the radio signal to be detected which would affect the Doppler signal only. Another advantage of sequential ranging is that it allows a considerably more precise orbit determination than Doppler tracking. Interestingly, Delta differential one-way ranging does not add to the performance of a PA test [5].

For the POP trajectory, the tracking will be precise enough to distinguish between a "drag force" in the direction opposite to the velocity vector, and a force pointing towards the centre of the Solar system. However, despite the high accuracy of tracking techniques, a discrimination between an Earth and Sun pointing deceleration does not seem possible with POP. The distinction would be made by the search for an annual modulation of the Earth-pointing component of the acceleration, revealing that the force on the spacecraft originates from the Sun. For the POP trajectory, the modulation of a Sun-pointing anomaly would be $\lesssim 0.3\%$. Whereas this is still detectable, the modulation is too low to show up in the background noise caused by onboard generated systematics (see next section). Nevertheless the most plausible origins of an anomaly can be discriminated by the combination of Doppler-tracking and sequential ranging because an Earth-pointing anomaly should

always be caused by a blueshift and not by an acceleration of the spacecraft.

4   Overcoming systematics

For a new mission the magnitude of the anomaly will in general not coincide with the value from the Pioneer probes but will most likely be influenced by the spacecraft design. Most importantly, the magnitude of the putative anomaly depends on the mass of the satellite for a real acceleration.

For a conventional force, the anomalous acceleration will be inversely proportional to the mass of the satellite, in accordance with Newton's second principle. For POP, which is roughly three times as heavy as the Pioneer probes during the coast, this would reduce a putative anomaly to $3 \times 10^{-10}\,\mathrm{m/s^2}$. A mass dependence should be present for a gravitational force as well, because an explanation in terms of modified gravitation requires a violation of the weak equivalence principle. If the PA is a blueshift of light, the spacecraft mass will not influence the magnitude of the anomaly.

Lacking a conclusive theoretical model of the anomaly, no firm prediction for the magnitude of the anomaly, that one should expect, can be given. Thus the spacecraft design has to reduce acceleration systematics as far as possible or provide means to precisely determine the systematics. With this goal in mind, we review the major potential sources of systematics and how they are controlled on POP.

Fuel leakage is much easier to reduce for an electric propulsion system than a chemical one. The reason is that the propellant for all engines, both main and attitude control, is taken from the same tank through the same pressure regulator. Low leakage rates can easily (and for a moderate mass budget) be achieved by stacking several regulators in a row. In this way the maximal acceleration of POP due to fuel leakage can be reduced to $\sim 0.1\%$ of the PA.

Whereas electric propulsion systems have a considerable advantage concerning fuel leakage, they have the major drawback of requiring high electrical power. For POP, this results in 17,000 W of heat, which has to be dissipated by the radiator fins on the RTG's. Reflection of RTG thermal radiation by the spacecraft bus and antenna will generate a deceleration of $8.5 \times 10^{-10}\,\mathrm{m/s^2}$, the magnitude of the PA. This force can, however, be discriminated from other effects because it will decay with the half-life of the Pu in the RTG's by an amount of 6% during the measurement coast.

The radiation force by the 55 W antenna beam would lead to an acceleration of $2.5 \times 10^{-10}\,\mathrm{m/s^2}$. This force can be controlled by changing the transmission power during the coast and measuring the change in the acceleration of the craft. The reduction in data transmission rate, which accompanies a reduction of the power is not a problem as only a small amount of housekeeping data needs to be sent during the cruise.

The Solar radiation force is less important on POP than it was on the Pioneers and reduces to $1\,\%$ of the PA at the end of the coast.

Overall the systematic accelerations of POP can be controlled or modelled to $10^{-11}\,\mathrm{m/s^2}$. With this level of systematics it becomes possible to unambiguously detect an anomalous force or blueshift of PA magnitude.

5 Summary and conclusions

With the current status of our knowledge it would be premature to consider the PA as a manifestation of a new physics. Rather, an incorrectly modelled conventional force seems the most likely origin for the anomaly. Most lines of "explanations" of the PA in terms of "new physics" are not stringent, e. g. it is not at all clear how to circumvent the constraints from planet orbits if a real force is present. Even without a satisfactory model of the anomaly at hand, we found that a test for all currently discussed causes of the PA is possible. The test can be incorporated in a planetary exploration mission to Pluto at practically no cost in launch mass, if the objective of the PA test is taken into account during the design of the spacecraft right from the beginning. Other non-dedicated options for a PA test will be discussed elsewhere [5].

References

[1] J. D. Anderson, P. A. Laing, E. L. Lau, A. S. Liu, M. M. Nieto and S. G. Turyshev, Phys. Rev. Lett. **81** (1998) 2858 [arXiv:gr-qc/9808081], Phys. Rev. D **65** (2002) 082004 [arXiv:gr-qc/0104064].

[2] G. W. Null, AJ **81** (1976) 1153.

[3] C. B. Markwardt, arXiv:gr-qc/0208046.

[4] T. Bondo et al, "Preliminary Design of an Advanced Mission to Pluto". Proceeding of the 24th ISTS, Miyazaki, Japan, June 2004 (to appear), http://www.esa.int/gsp/ACT/doc/ACT-RPR-4200-ISTS2004.pdf

[5] D. Izzo and A. Rathke, "Options for a non-dedicated test of the Pioneer anomaly", in preparation.

THE NASA PROGRAMS IN PARTICLE ASTROPHYSICS

JONATHAN F. ORMES [a], DONALD A. KNIFFEN [b]

[a] *NASA Goddard Space Flight Center, retired*
now at the University of Denver, Denver, CO

[b] *NASA Headquarters, Washington, DC*

Abstract

In this talk we describe on-going and future efforts within NASA in its particle astrophysics program. Emphasis will be on the Beyond Einstein program to study gravitational waves, dark matter, dark energy and x-ray emission around black holes.

1 Introduction

The conference organizers were interested in having the participants understand the national priorities for particle astrophysics and cosmology. In the USA, most of this research is part of NASA's space science program. The discussion is timely because the NASA mission is currently under discussion and reprioritization.

The NASA Vision and Mission statements are given in Figure 1. Note the emphasis on the search for life and the role played by concern for life on Earth.

Figure 1: The NASA 2004 vision and mission statements

This vision for NASA includes trying to understand where we came from and what will happen to us in the long run. Education and the inspiration of young people is an important component of all NASA programs and a priority of the US to create a scientifically and technically literate population well prepared for the challenges of the 21st century.

In understanding the current discussion within NASA for the future of its space science programs, one must recall the crisis caused by the loss of Columbia and her crew. A national panel undertook the challenge of helping the Nation and NASA to understand what went wrong and how to prevent it happening again. The board was known as the Columbia Accident Investigation Board (CAIB) and their findings were documented in a report known as "the CAIB report". The findings were critical of not only NASA but the administration and the US Congress for failing to have a clearly defined goal for the space program, in particular the human space flight part of the program that dominates the NASA budget and program.

In January 2004, President Bush responded by elucidating the goal of exploration of the solar system. He said "The cause of exploration and discovery is not an option we choose; it is a desire written in the human heart." And he set return of humans to the moon first and then to Mars as the next steps for human flight program. There were four main points:

• Implement a sustained and affordable human and robotic program to explore the solar system and beyond

  • Extend human presence across the solar system, starting with a human

return to the Moon by the year 2020, in preparation for human exploration of Mars and other destinations;

• Develop the innovative technologies, knowledge, and infrastructures both to explore and to support decisions about the destinations for human exploration; and

• Promote international and commercial participation in exploration to further U.S. scientific, security, and economic interests.

THE FUNDAMENTAL GOAL OF THIS VISION IS TO ADVANCE U.S. SCIENTIFIC, SECURITY, AND ECONOMIC INTEREST THROUGH A ROBUST SPACE EXPLORATION PROGRAM

From A Renewed Spirit of Discovery

The President's Vision of the U.S. Space Exploration

That NASA needed such a direction is not in debate, but the details of how to accomplish it are. It is an expensive proposition. In contrast to President Kennedy's original goal of landing someone on the moon and returning him/her safely to Earth by the end of a decade (the 1960s), this goal is to be accomplished with a fixed annual budget at a level that can be sustained over the long haul, one administration after another. The timetable and implementation details are set out as indicated below.

• Complete the International Space Station and then retire the Space Shuttle at the end of this decade.

• U.S. ISS research emphasis on space environment, astronaut health, and countermeasures.

• Develop a crew exploration vehicle for deep space.

• Lunar exploration to enable sustained human and robotic exploration of Mars and elsewhere.

• By 2008, initiate a series of robotic missions.

• Extended human expedition to the lunar surface as early as 2015, but no later than the year 2020.

• Conduct science activities in support of exploration goals

• Conduct robotic exploration of Mars to search for evidence of life and prepare for human exploration.

• Conduct robotic exploration across the solar system (Jupiter's moons, asteroids) to search for evidence of life and resources.

• Conduct telescope searches for Earth-like planets and habitable environments around other stars.

NASA is currently reorganizing to meet the objectives of this exploration initiative. To see what might be the directions of future space research efforts we can look at the plans that have been put into place previously. NASA Office of Space Science was divided into four research theme areas: Astronomical Search for Origins, Solar System Exploration, Sun Earth Connections and

Structure and Evolution of the Universe. Each theme had a roadmap developed in concert with the scientific communities involved that provided the input to a Space Science Enterprise Strategy that was updated every three years. There is considerable political interest and support for the general idea that when people look back on the 21st century with the perspective of history it will be known as the century where life was discovered elsewhere in solar system and probably on a planet around a nearby star. This parallels the tremendous progress being made in understanding life on Earth, genes and other biology of living things. NASA's focus will be something along the following lines:

- How does the sun affect life on Earth?
- How did living organisms arise?
- How do planets form and evolve?
- What is it like elsewhere in the solar system? Could human beings survive there?

The interests represented by the subject matter of this conference fall primarily in the Structure and Evolution of the Universe (SEU) theme area. We will not consider the other theme areas further in this paper except to say that the alignment of the other areas with the President's new vision is more obvious than that of the SEU theme. The SEU theme has a partial approval for the program laid out in its Beyond Einstein roadmap. It is partial in the sense that there is startup money for major programs (LISA and Constellation-X), as we will discuss further below. However, funding for these programs has barely started (it is still easy for these budgets to be cut and/or the programs seriously delayed) and all the other smaller missions remain unfunded and accepted for approval in principle only.

Because the expenditure of large amounts of the public funds is necessary to sustain these programs, they must have public support. We believe the strongest case for this rests on finding ways to involve the public. Few of us will actually leave the planet; the remainder must experience this vicariously through what we call virtual journeys. The SEU theme represents virtual journeys to the edges of space and time. We go there with our sensing instruments and attempt to understand what is happening there in these remote (both in space and time) places: the beginning of the universe, the edges of black holes to explore and try to find answers to questions that are as old as human curiosity. Such questions are now becoming subject to quantitative scientific investigation.

- How did the Universe begin?
- Does time have a beginning and an end?
- Does space have edges?

NASA missions under development

Let us turn now to a discussion of NASA missions under development and planned for the SEU theme. The flagship mission is the James Webb Space
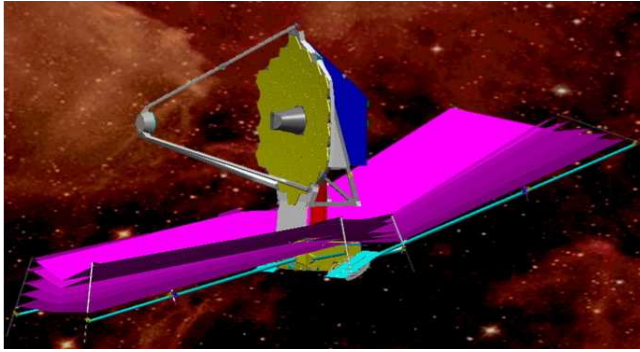
Figure 2: The James Webb Space Telescope

Telescope (Figure 2). Its objective is to find and study the first light from the first generation stars in the universe. Because of the redshift, this light will be appear to us to be in the near to mid-infra-red. It has three cameras, a near infra-red camera (NIRCam) being built in North America by a US/Canadian team, a near infra-red spectrometer (NIRSpec) being built primarily in Europe and a mid infra-red instrument being built by a NASA/ESA consortium. The specific scientific questions being addressed are:

• How and from what were galaxies assembled?

• What is the history of star birth, heavy element production, and the enrichment of the intergalactic material?

• How were giant black holes created and what is their role in the universe?

Beyond Einstein

The Beyond Einstein Program addresses questions with a more fundamental physics emphasis:

• What powered the big bang?

• What happens at the edge of a black hole?

• What is dark energy?

As is well known to the audience of this talk, there were three startling predictions buried in Einstein's equations for general relativity. They predicted the expansion of the universe, the existence of black holes and dark energy acting against the gravitational attraction of the matter of the universe causing it's expansion to accelerate. These predictions, not clearly recognized by Einstein himself until they were actually observed, have all been measured, the last only within the past 5-6 years. His theory fails to explain the very phenomena predicted. The Beyond Einstein initiative is an attempt to understand the physics that comes out of his equation.

These questions have motivated the planning and technology development
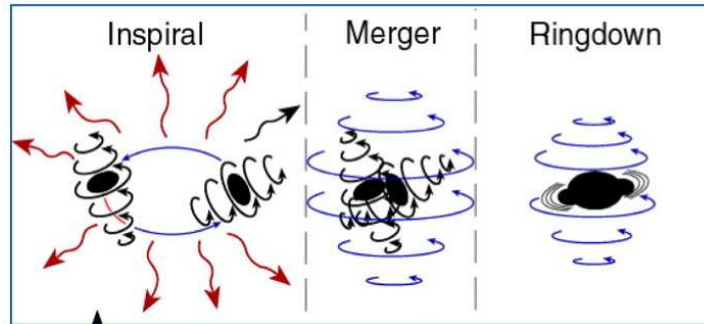
Figure 3: The three phases of a black hole merger

for the Laser Interferometric Space Array (LISA) to probe the universe for low frequency gravitational waves and the Constellation X-ray mission, a very high throughput broad-band X-ray spectrometer to study hot plasmas near black holes and in many other astrophysical environments. LISA uses a laser based Michelson interferometer to monitor the separation between proof masses in separate spacecraft. The array consists of three spacecraft separated by 5 million km that follow the Earth around the sun. The orbits are inclined such that they form a triangular pattern. Within each spacecraft there are two freely falling test masses protected from external forces by the spacecraft to make possible drag free operations. Changes in the distance between the spacecraft are measured with precision of 4 pico-meter RMS over 100 seconds. This level of change should make it possible to detect the passage of gravitational waves and determine their direction. A flight demonstration of the critical hardware is in preparation. LISA should be able to see inspiraling supermassive black holes ($\sim 10^5 - 10^7 \ M_\odot$) resulting from mergers of galaxies or pre-galactic structures out beyond z 20. The event rate prediction is sensitive to dynamical friction that would bring the two SMBHs close enough together to merge. If most galaxies have undergone a SMBH-SMBH merger, then the event rate would be reasonable ($\sim$ 1 per year).

Figure 3 illustrates what LISA is capable of doing. The signature of the gravitational waves expected from the merger of two massive objects (in the illustration two black holes) can be calculated in a relatively straightforward manner, as can the post merger ringdown and settling of the combined system. The physics of the black holes themselves is probed by the details of their gravitational signal during the merger itself. Computing the detailed waveforms expected during mergers requires highly sophisticated general relativistic computer modeling.

The measurement of the emission of the iron K-line from the gas heated to millions of degrees by falling into the potential well of a black hole has

the potential to observe the effects of general relativity in a very strong gravitational field, something that is impossible to do on Earth, or even anywhere in our solar system. There are effects of gas motion in the orbits close to the event horizon of the hole, the gravitational redshift due to the mass of the hole itself, effects due to the energy and dragging of the frame of reference associated with the spin of the hole, etc. that can be sorted out by measuring the X-ray emissions from many black holes. We note that it is only within the past 15 years or so that the existence of black holes has been established to the satisfaction of the full scientific community. Prior to the early 1990s, black holes usually had the qualifier "candidate" or "putative" attached.

Con-X will also be able to study the dark energy distribution the Universe by studying clusters of galaxies and large-scale structure. Also planned is a study of the production and recycling of the elements from supernova into the interstellar medium.

Con-X will have 25-100 times the sensitivity of currently flying missions for doing high resolution spectroscopy in the 0.25 to 10 keV band. It consists of four satellites at L2 operating as one. This also allows highly efficient viewing of sources. All the technology to enable the mission is well along.

Beyond Einstein Probes

We don't know what 95% of the universe is made of. Recent results from the Wilkinson Micro-wave Anisotropy Probe (WMAP) have shown that only 5% is accounted for by ordinary matter. We need another 25% to account for the gravitational binding of galaxies and the larger collections of galaxies and structures composed of galaxies. The remaining 70% of the energy content is associated with the energy of acceleration. The term dark is used in both cases to hide our ignorance. This is illustrated in Figure 4. The long-term experimental goal will be to look for the polarization of the gravitational waves that come from the big bang. More immediately, we can look for the imprint they make on the microwave background.

In addition to these major missions, the Beyond Einstein roadmap envisions 3 probes, one for studying dark energy, a second to probe the epoch of inflation and another for doing a census of black holes. The Probes were originally conceived as competed PI led missions in which the implementation approach would be determined by peer reviewed competition, would cost in the neighborhood of $350-$500 M each and be launched at the rate of one every 3-4 years. There is strong interest in these missions by the Department of Energy and the National Science Foundation, and so the exact character of the missions may evolve as these partnerships are worked out in detail.

The order in which the Einstein Probes are flown will be determined by both science priority and technological readiness. In any case, these are important and timely scientific missions. Even if NASA should decide to focus on other
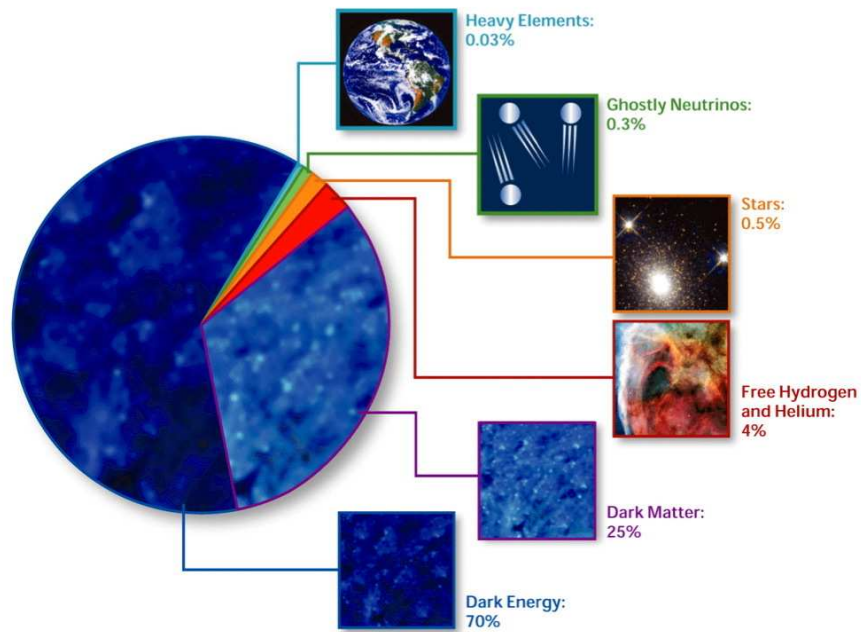
Figure 4: What the Universe is made of

priorities, they will be done in one form another by the international scientific community.

Summary

The future of the NASA program in particle astrophysics is somewhat uncertain. The science is compelling and, in the long run, there is no holding back the pressure for scientific progress in studying black holes, physics in the limit of strong gravity, the formation of structure (planets, stars, galaxies, galaxy clusters and galaxy superclusters) on all scales. The astronomy of dust and molecules, the formation of comets, and the origin of prebiotic species in space will be the thrust of new missions. The physics of particle acceleration and the interrelationships of matter, plasma and photons all form the subject of astrophysics. The variation with time, the complexity as one looks at objects in the sky with higher and higher resolution and the complexity of dynamical rotational systems with magnetic fields will provide grist for the mill of scientific study for years to come.

PHYSICS AND ASTROPHYSICS IN SPACE: FROM PRESENT TO THE FUTURE

Piero Spillantini [a,b]

[a] *Dipartimento di Fisica, Università di Firenze ,*
via Sansone 1, Sesto Fiorentino, Italy

[b] *INFN, Sezione di Firenze, via Sansone 1, Sesto Fiorentino, Italy*

1 Introduction: from the past to the future

My duty of summarizing the works of this conference and discussing the future perspectives is greatly simplified by the previous talks of this session, which gave an exhaustive picture of the present and future space programs in Cosmology, Gravitational Waves and Fundamental Physics, and left me to deal with gamma rays and cosmic rays in space, a water where I am more used to swim. In these waters we cannot afford the future without going through the past. And for the past I will not go back to the pioneer research in these fields, but to the more recent 80's. In the 70's the realization of the Space Shuttle allowed a huge jump in the space access. At the end of the 70's several observatories in space were planned for the continuous and simultaneous observation of the Universe in the whole electromagnetic spectrum, complemented by the simultaneous observation of the charged component in its whole energy range, from the a few tens MeV up to the UHECRs [1]. It was the Astrophysics and Astronomy program of the NASA administration represented in fig. 1, adapted from the cover of the brochure that NASA dedicated to the Great Observatories: besides the 4 space Great Observatories and the Very Long Base Interferometer on ground dedicated to the various wavelength ranges of the electromagnetic spectrum to CR facilities were foreseen: the Advanced Composition Explorer (ACE) [2] for measuring the energy spectra of rare elements and radioactive isotopes at low energy, far away from the influence of the terrestrial magnetic
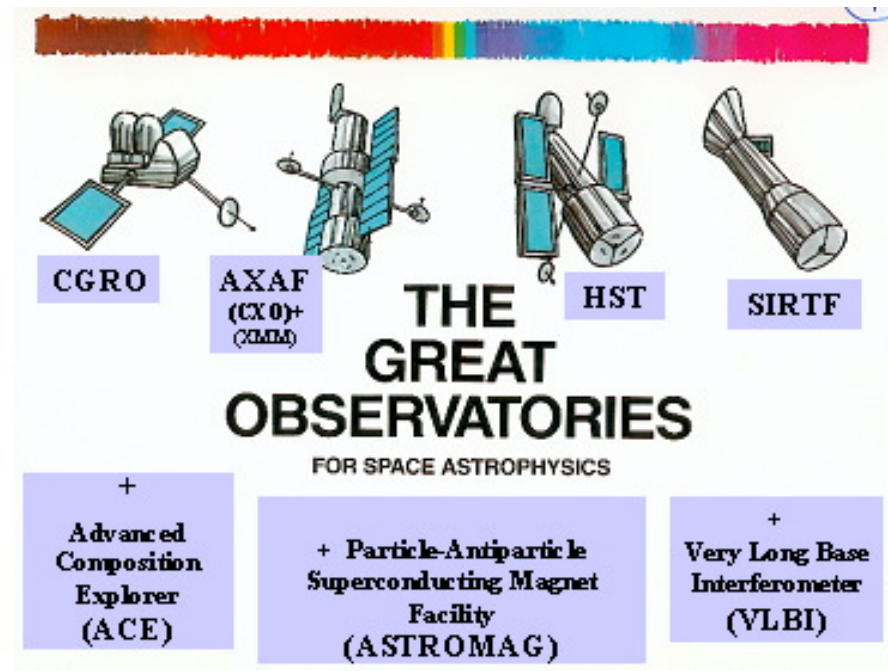
Figure 1: The Great Observatories for space astrophysics and the CR program

field, and the Particle-Antiparticle Superconducting Magnet Facility, initially foreseen for a free flier, and moved with the new name ASTROMAG [3] as a facility offered by NASA on board of the Freedom Space Station (FSS) after the announcement of its construction by the President of USA, Ronald Reagan, in 1983.

2 The 1985-1995 CR program of NASA

Appointing our attention to the cosmic ray part, it is of keen interest to examine today, twenty years later, the CR research program for the 1985-1995 decade [4] elaborated by NASA according to the recommendation of its Cosmic Ray Working Group [5]. It was a very complete and far-reaching program, still nowadays neither accomplished nor fully afforded for the next future. The summary page of this program is reproduced in fig. 2.

Already one year after its release the Challenger tragedy gave a halt lasting several years to the USA access to space, and several aspects of the CR program were vanished. The consequent reconsideration of the assembling of structures in space hampered the realization of the Freedom Space Station (FSS), such
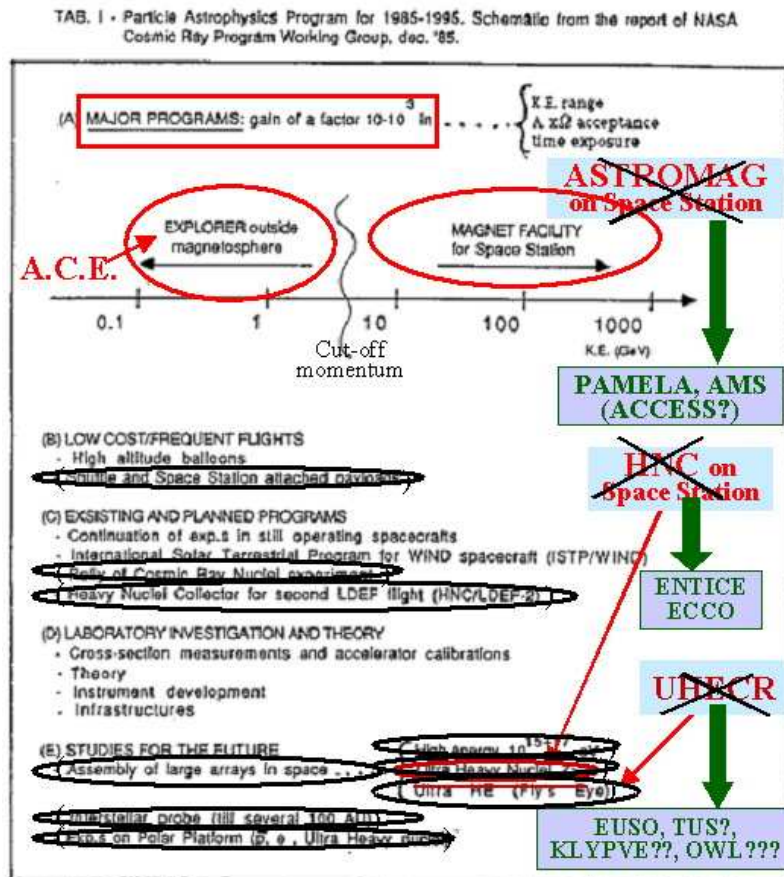
Figure 2: Particle Astrophysics Program for 1985-1995

as it was designed at that time, as well as the study of systems to be deployed
or assembled in space, among them the systems for observing from space the
UHECRs by the shower fluorescence of their showers.

Because of the Challenger disaster the FSS program was delayed and
finally stopped in 1991. The consequences of this were devastating for the
gamma and CR programs: the Heavy Nuclei Collector (HNC) [6] and the
superconducting spectrometer for high energy CRs ASTROMAG [3], planned
as facilities on board of the FSS, were cancelled, with the consequent dispersion
of the programs and of the teams. In fig. 2, reproducing the original page of
the summary of the program, the items postponed or cancelled because of the
Challenger disaster are circled in an ellipse. On the right side of the figure
the names of the stopped facilities and studies are added, indicated by a cross;

the arrows starting from these items point to a box with the acronyms of the experiments nowadays planned for recovering the original observational program.

It is important to remark at this point that the study of the ASTROMAG facility and the elaboration of its experimental program collected in one large international working group scientists from USA, Europe and Japan, allowing their small teams to converge in larger international collaborations joining several experimental techniques and many researchers, in a style similar to that operating in the Elementary Particle field. This is the main heritage of that period, also because the experimental program for the ASTROMAG facility included several important thematic typical of Astrophysics as well, for the first time, touching fundamental themes of the Elementary Particle physics. It is not exaggerated to say that it signaled the birthday of the Particle Astrophysics in space as presently we intend it.

3   The realization of the NASA program slows down

It is well known that the difficulties of the whole NASA space program at the end of the eighties and beginning of the nineties greatly affected the realization of the Great Observatories program. After the launch in 1990 of the HST optical observatory and of the CGRO for the gamma rays in 1991, the AXAF observatory, too difficult and expensive for performing the X-ray source spectroscopy and the search for faint sources by the same instrument, was shared with ESA and the two new instruments, CXO for the search of faint objects and XMM for the spectroscopy, were flown much later, both in 1999. Finally the IR Observatory SIRFT could be launched only last year, in 2003. Less known is that, after that in the meantime the CGRO had to terminate its mission in 2000, and the lack of the ASTROGAM instrument planned for the ASTROMAG facility left the gamma ray spectrum gap between 10 and 300 GeV unexplored, and nowadays we still are waiting for the GLAST mission for covering this gap.

Also one of the two main points of the CR program (item (A) in fig. 2), ACE, first proposed in 1983, had to wait several years to be finally launched in 1997. Nothing to do instead for the ASTROMAG facility, as well as for the HNC, both cancelled for the stop of their vehicle, the FSS. Many important observational programs were left, and still are, not afforded:

(a) the systematic measurement of the energy spectra of elements and isotopes beyond one GeV/nucleon, main thematic of the LISA proposal [7];

(b) the measurement of the elementary particles and antiparticles energy spectra up to very high energies and the search for antinuclei, main thematic of the WIZARD proposal [8];

(c) the elemental composition in the knee region, to which was dedicated the MAGIC/SCINATT proposal [9];

(d) the fluxes of the Ultra Heavy Nuclei beyond the iron group, up to the actinides group, for counting the supernovae rate in the Galaxy and evaluating the contribution of slow and rapid processes to their formation, thematic of the HNC facility;

(e) besides the above mentioned very high energy gamma ray observation.

4   CR and gamma ray themes implemented in the meantime or on the way in the next future.

What happened of these observations during in the following fifteen years?

(a) The measurement of the elemental and isotopic energy spectra was afforded by Japan-USA collaboration by ballooning. The superconducting spectrometer ISOMAX [10] that they realized with an activity lasted several years for improving the quality and the covered energy range was lost by accident and never reconstructed. This chapter of physics, fundamental for the understanding the structure and the evolution of the Galaxy is still unexplored, and there are no plans for it in the future; important, but anyway partial and scanty results will be obtained in next years by the PAMELA [11] and AMS [12] spectrometers as by products, but they could not recover the abundant wealth of results promised by LISA (see fig. 3).

(b) Much better it will be in few years the situation for the particle and antiparticle spectra and the search for antinuclei: after having exploited all the possibility allowed by a long ballooning activity, the two magnetic telescopes PAMELA and AMS promise to fill the observational gap left by the WIZARD proposal, while the BESS [13] spectrometer will define the observational situation by long duration ballooning in the low energy portion of the spectra.

(c) The situation for the elemental composition at the knee is instead in a much less promising status: many balloon missions were and still are slowly and patiently collecting information in the region up to 10^{14} eV, but the needed 10^{15} frontier is well beyond their possibilities, as well also beyond the possibility of the Ultra Long Duration Ballooning (ULDB) programs of the CREAM [14] and ATIC [15]experiments. Several enterprises were proposed for observations in orbit (NUCLEON [16], INCA [17], PROTON5 [18], ACCESS [19]), perhaps too many for allowing to have at least one in space. A possible convergence of all the proponent groups in one single enterprise could open the way toward its realization, but it will not be for now or for the near future. A significant step forward
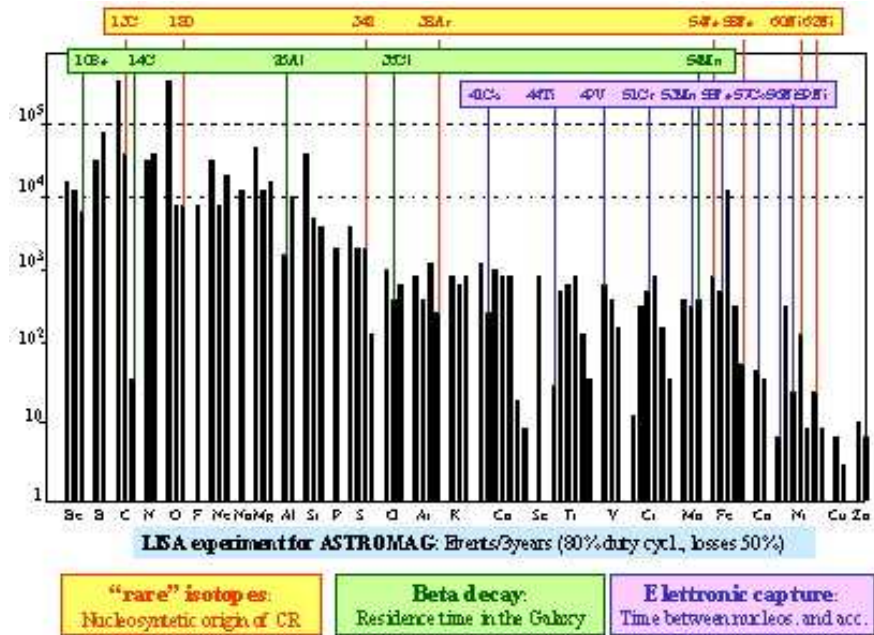
Figure 3: Expected rates for isotopes for the LISA experiment

could be given by the NUCLEON, which has a somewhat limited mass and acceptance, but it is the only one that seems to have a concrete flight opportunity in the next 4 or 5 years.

(d) A Heavy Nuclei Explorer (HNX) [20] is in the plan of NASA for recovering the physics of the HNC for the FSS, but as long as we know now still didn't go beyond the feasibility study status.

(e) About the gamma ray program, with AGILE [21] and GLAST [22] to be flown in next few years, we said above.

(f) What about the last important item of CR observation left behind, the UHECRs? For several years there was only the OWL [23] concept put at the end of the road map proposed by the SEUS committee of NASA. New concepts came out in last years in Europe (EUSO [24]) and Russia (TUS [25] and KLYPVE [26]). The EUSO proposal was selected by ESA for a phase A study just concluded. The EUSO instrument should be accommodated on board of the ISS and avoid the difficulties connected with the assembling and deploying structures in space which halted this kind of studies after the Challenger disaster. It should take data for at least 3 years, giving about 1000 events around and beyond 10^{20} eV energy. This experiment, together with the AUGER [27] experiment on ground,

is a huge step forward for understanding the fundamental mechanisms responsible of the ultra high energy acceleration in the Universe, and the related questions of fundamental physics. Perhaps it could be not conclusive for answering to all the open problems, however any possible follow-up experiment could hardly substantially improve the statistics and quality of data, and EUSO must now be regarded as a unique occasion for pushing forward our exploration in the extreme energy region.

5   What "space" still for the "particle astrophysics" in space?

Let now try to understand what could be the development of particle astrophysics in space in the future, say 10 or more years from now.

5.1   The high energy gama rays

For what concerns gamma rays after a long preparatory period the experiments AGILE and GLAST in space will retrieve the ASTROGAM [28] program on ASTROMAG, planned in the 80's for covering the energy gap between EGRET [29] on CGRO (10 GeV) and the ground experiments (about 300 GeV). The evolution of the many ground based experiments promises to fill the energy gap with complementary observations.

A new step forward after the INTEGRAL [30], AGILE, GLAST and SWIFT [31] mission is not foreseen in the far future, at least as long as new ideas allow to substantially improve the angular resolution. An observatory of the CGRO class could strengthen the planned instruments and possibly save part of the investment, but presently no people or organization has the means and the strength to think to an observatory.

5.2   The cosmic rays up to a few GeV/nucleon

For what concerns the low energy CRs, up to a few GeV/nucleon, ACE is continuing its mission supplying a flood of data, fundamental tools for the astrophysics of the Galaxy.

An interstellar probe touching the frontiers of the heliosphere and beyond would be a fundamental instrument for understanding the acceleration mechanisms of CRs in their interaction with plasmas. Several groups have proposed it in the past and its study also appeared in the CR above-mentioned program of NASA (item (E) in fig. 2). However its realization is improbable if in the future new propulsion techniques will not allow to reach the limits of the heliosphere in much less than the thirty and more years presently foreseen.

5.3   The cosmic between a few GeV/nucleon and several TeV/nucleon

It is in the energy range between a few GeV/nucleon and several TeV/nucleon that the "Particle Physics" new theories can enter in the CR observations. For what concerns the rare particles and antiparticle components of CRs important but not conclusive results were obtained, mainly in the last decade, by ballooning.   They are however not conclusive for what concerns the antiparticle energy spectra, either because of the limited statistics and the residual atmosphere background or because the possible contribution of the so-called new physics channels can become sensible at energies higher than those reachable by ballooning.

A real "new era" will be opened in this theme by the PAMELA and AMS-2 experiments in space, which before the end of this decade should supply the positron and antiproton energy spectra up to several hundred GeV, well inside the energy region where new effects could be expected. These experiments will also hunt for antinuclei at high energy and with unprecedented sensitivity. No plans at the moment are foreseen for the far future, either because the development direction should be indicated by the expected results, or because in any case a huge instrumental effort would result in a not correspondly increase of the acceptance and of the covered energy range.

As above noted, after the loss of the ISOMAX instrument new results for rare event energy spectra and isotopic energy spectra will be obtained only as by-product of the PAMELA and AMS experiment. The quality and quantity of expected result is important, also if far away from the wealth of the results expected by the old LISA proposal (see again fig. 3). As already remarked no plan exist for recovering such physics theme also in the far future, the main difficulty being the dispersion of the interested community in other enterprises.

Also the measurement of the fluxes of the high Z nuclei, and of the actinides group in particular, seems difficult to be recovered, and the ECCO [32] and ENTICE [33] proposals on the HNX explorer are still pending in the NASA program.

Finally a specific comment must be dedicated to the many experiments on ground and in space dedicated to the study of the so-called "knee" region of the CR energy spectrum, i.e. between 10^{13} and 10^{16} eV. The ground experiments are improving their instrumentation as well as the interpretation computational machinery, but still give inconclusive results for what concerns the main goal of their activity, i.e. the energy spectra of the separate elements. From space the answer to this problem should be straightforward, but the steep energy spectrum of the flux requires an instrument accepting particles on a few $m^2 sr$ for several years. Several concepts of such an instrument were presented in USA (ACCESS in a two versions) and in Russia (INCA, PROTON5), but no one obtained until now a support going beyond the feasibility study. The impression is that the interested community has some difficulty to work together toward

one international project, a needed approach for being supported by several space agencies and institutions. In this situation the research must relay on ballooning. In Antarctic continent the JACEE collaboration going on with its periodic long duration balloon (LDB) launches, while the CREAM collaboration planned several ultra long duration balloon (ULDB) launches in next years, but for the moment must wait the setting up of this new technique. It is in any case a long and patient work that will require one or more decades to reach the statistical relevance useful to answering to the afforded physics questions. A noticeable step forward promise to be given in the meantime by the NUCLEON experiment on board of the Resurs-DK satellite, mainly supported by Russian agencies, conceived for catching a suitable occasion of launch and as prototype of a possible larger instrument for definitively solving the "knee" problem.

6   A new actor on the scene?

The possibility of observing large statistics of UHECR events focused the attention on the already long ago foreseen GKZ effect produced by the interactions of the UHECR with the cosmic microwave background (CMB), with consequent degradation of their energy and generation of a high flux of UHE neutrinos. Because of this origin these neutrinos are called "cosmogenic". Their flux can be foreseen with an approximation of about one order of magnitude [34], and can be considered the "less uncertain" flux among the neutrino fluxes expected by many different models proposed in Astrophysics and Elementary Particle physics (see fig. 4). Surely the neutrinos as probes of the deep Universe are the most promising particles. Their interaction length is, also at UHE, one order longer than the dimensions of the Universe, and therefore their observation opens the door to a new powerful astronomical tool. On the basis of the results of the phase A study of EUSO it can easily evaluated that a neutrino observatory suitable to give between 10 and 100 observed neutrinos per year could have parameters for the detector not far away from those of the EUSO instrument if a dedicated optical system for collecting the fluorescence light of the neutrino produced showers would be provided.

In fig. 5, (from [35]) the EUSO parameters are compared with those of a possible neutrino observatory for several values of the FoV of the optical system, and assuming that in the following 10-15 year the efficiency of the light detectors in the region of the fluorescence wavelengths could reach 50% (laboratory prototypes are not far away from this value). Probably the definition of a mission dedicated to the realization of a UHE neutrino observatory should wait for the accomplishment of the EUSO mission. In any case it will be necessary that all the teams nowadays proposing several approaches for the
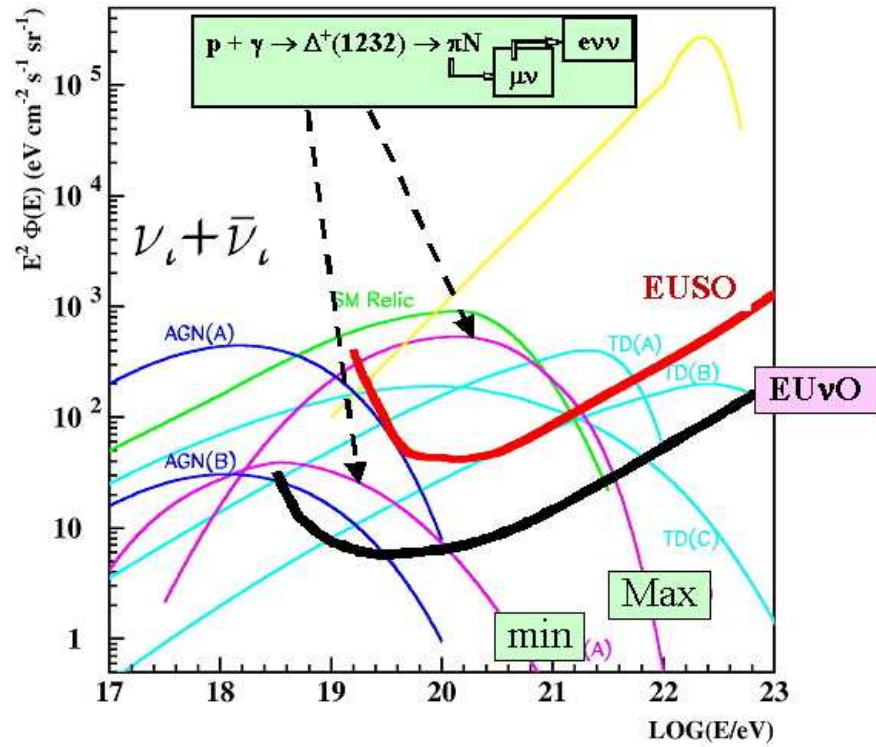
Figure 4: Neutrino fluxes foreseenby different models

UHECR observation from orbit join in one collaboration team.

7   The other (old) actors, and final considerations.

Other important themes, some of them very old, are present in Physics and Astrophysics in Space, and make the whole field so exiting and rewarding.

We heard fascinating talks in the days of the symposium, with the CMB experiments grasping toward the primordial "seeds" of the Universe, the Gravitational Wave (GW) detection seeking to observe from very near the Big-Bang, Fundamental Physics experiments questioning General Relativity and other fundamental laws of nature, and the new observatories for IR, Optical and X radiation in service and in program promising a wealth of information overlapping with topics of fundamental physics. For all these themes several missions are in program for the next as well for the far future, and a wide and exhaustive panorama was described in the previous talks of this session of the

	EUSO like		Multi-mirror		
H (km)	400		400		
Total FoV (°)	60		90		
Radius on ground (km)	235		413		
Area on ground (10^3km^2)	173		536		
Pixel on ground (km * km)	0.8 x 0.8		1.6 x 1.6		
Ø pixel on detector (cm)	0.6		2.0		
Area/pixel (≈n. of pixels)	270k		238k		
Pupil diameter (m)	2.0	2.0	5.0	7.5	10.0
Photo detection efficiency	20%	50%	50%	50%	50%
E threshold (EeV)	50	20	5.5	3.2	2.3
Proton events/year,					
GKZ + uniform source distrib.	1200	8000	300k	900k	1800k
with E_p >100 EeV)	100	100	310	310	310
Neutrino events per year (≈min)	**0.6**	**1.5**	**18**	**30**	**42**
Neutrino events per year (≈Max)	**12**	**18**	**108**	**120**	**138**

Figure 5: EUSO parameters compared with the parameters of a possible neutrino observatory for several values of the FoV of the optical system

symposium.

What about gamma ray and CR physics in space in this context?

For high energy gamma astrophysics I can say as conclusive remark that a lot of work is in progress and is in program, also if not necessarily from space, but there are not "vision" proposed for the far future.

For CRs many important themes left back from the past wait to be afforded, however no programs have been formulated for the far future, in some cases (as for antinuclei and antiparticles) waiting for the coming results of the planned experiments, but also waiting for an enlargement and better convergence of the CR community. The new fact for the far future is linked to the new "actor", neutrino observation from space. An UHE neutrino observatory can be envisaged, and this could be a sufficient reason for attracting several teams to collaborate in one mission dedicated to its realization.

References

[1] Field Committee on Space Astronomy and Astrophysics of the National Research Council of the National Academy of Sciences, *A Strategy for*

Space Astronomy and Astrophysics for the 1980's, National Academy of Sciences report, 1979.

[2] E.C. Stone et al., Space Science Reviews, 86 (1998) 285.

[3] M.A. Green et al., IEEE Transactions in Magnetics, MAG-23, n.2 (1987) 1240. - T. Bowen et al., *Review of NASA Particle Astrophysics Magnetic Facility Study Team: ASTROMAG*, May 1988. - G.Basini et al., IEEE Transactions in Magnetics, MAG-24, n.2 (1988) 1015. - G. Basini et al., Il Nuovo Cimento, 102B (1988) n.5.

[4] Cosmic Ray Program Working Group, *The Particle Astrophysics Program for 1985-1995*, NASA report, October 1985.

[5] Cosmic Ray Program Working Group, *Cosmic Ray Program for the 1980's*, NASA report, August 1982.

[6] P.B. Price, Particle astrophysics - *The NASA cosmic ray program for the 1990s and beyond (A92-20526 06-93)*, New York, 1990, American Institute of Physics, pp 63-66.

[7] J.F. Ormes et al., *A Large Isotope Spectrometer for Astromag*, NASA GSFC, Nov.1988.

[8] R.L. Golden et al., *WiZard: a proposal to measure the Cosmic Rays including Antiprotons, Positrons, Nuclei and to conduct a search for Primordial Antimatter*, College of Engineering, Editor NMSU, 1988. – P. Spillantini et al., Il Nuovo Cimento, 103B (1989) 625.

[9] T.A. Parnell et al., *Spectra, Composition and Interactions of Nuclei above 10 TeV*, NASA MSFC, Nov.1988.

[10] J.W. Mitchell et al., XXVI Int. Cosmic Ray Conf., 3 (1999) 113, Salt Lake City - M. Hof et al., Nucl. Instrum. and Meth., A454 (2000) 180 - T. Hams et al., XXVII Int. Cosmic Ray Conf. (2001) 1655, Hamburg.

[11] O. Adriani et al., XXIV Int. Cosmic Ray Conf., 3 (1995) 591, Rome – O. Adriani et al., Nucl. Instrum. And Meth., A478 (2002) 114.

[12] R. Battiston for the AMS collab., XXVII Int. Cosmic Ray Conf. (2001) 2192, Hamburg.

[13] A. Yamamoto et al., Adv. Space Res., 14 (1994) 75. - S.Orito et al., Phys. Rev. Lett., 84 (2000) 1078.

[14] E.S. Seo et al., XXVI Int. Cosmic Ray Conf., 3 (1999) 207, Salt Lake City - O. Ganel et al., XXVII Int. Cosmic Ray Conf. (2001) 2163, Hamburg.

[15] T. Guzik et al., XXVI Int. Cosmic Ray Conf. 5 (1999) 9, Salt Lake City - J.P. Wefel et al., XXVII Int. Cosmic Ray Conf. (2001) 2111, Hamburg.

[16] D. Podorozhnyi et al., XXVII Int. Cosmic Ray Conf. (2001) 2188, Hamburg.

[17] INCA collaboration, XXVI Int. Cosmic Ray Conf., Salt Lake City (1999) 1,219 - 3,203 - 4,215 - R.A. Mukhamedzhin et al., Nucl. Phys. B (Proc. Suppl.) 97 (2001) 189.

[18] D. Podorozhnyi et al., XXVII Int. Cosmic Ray Conf. (2001) 2188, Hamburg.

[19] J.P. Wefel et al., XXVI Int. Cosmic Ray Conf., 5 (1999) 84, Salt Lake City.

[20] W.R. Binns et al., XXVII Int. Cosmic Ray Conf. (2001) 2181, Hamburg.

[21] M. Tavani, this conference.

[22] P. Michelson, this conference.

[23] J.F. Krizmanic et al., AIP Conf. Proc. (1998) 433.

[24] L. Scarsi et al., *Extreme Universe Space Observatory (EUSO) proposal for ESA F2/F3 Missions*, 2000 – EUSO Design Report, ESA/MSM-GU/2000.462/RDA, Dec. 2000. - A.Petrolini, this conference.

[25] V.V. Alexandrov et al., XXVII Int. Cosmic Ray Conf. (2001) 831, Hamburg.

[26] B.A. Khrenov et al., Int. Workshop on Observing UHECR from Space and Earth, Mepetec, August 2000, AIP 2001.

[27] Pierre Auger Project Design Report, 1997, Auger coll., FNAL.

[28] J. Adams and D. Eichler, *Very High Energy Gamma Ray Spectroscopy*, Astrop. J. 317 (1987) 551.

[29] D. Kniffen, this conference.

[30] G. Palumbo, this conference.

[31] P. Giommi, this conference.

[32] A.J. Westphal et al., XXVI Int. Cosmic Ray Conf., 4 (1999) 160, Salt Lake City.

[33] M.H. Israel et el., XXVII Int. Cosmic Ray Conf. (2001) 2231, Hamburg.

[34] Kalashek, Kuzmin, Semokov, Sigl, *Ultra-High Energy Neutrino Fluxes and Their Constraints*, arXiv:hep-ph/0205050 v3 13 Dec 2002.

[35] P. Mazzinghi, this conference.

List of Participants

Altamura Francesco	University of Roma "Tor Vergata" and INFN
	altamura@roma2.infn.it
Antonelli Lucio Angelo	INAF-Osservatorio Astronomico di Roma
	a.antonelli@mporzio.astro.it
Aversa Massimo	Hamamatsu photonics Italia
	aversa@hamamatsu.it
Balbi Amedeo	University of Roma "Tor Vergata"
	Amedeo.Balbi@roma2.infn.it
Baldini Luca	INFN Pisa
	luca.baldini@pi.infn.it
Baret Bruny	L.P.S.C/IN2P3
	baret@lpsc.in2p3.fr
Basili Alessandro	INFN Roma2
	alessandro.basili@roma2.infn.it
Bassan Massimo	University of Roma "Tor Vergata" and INFN
	Massimo.Bassan@roma2.infn.it
Beilicke Matthias	Institut fuer Experimentalphysik, Uni Hamburg
	matthias.beilicke@desy.de
Belli Francesco	INFN Roma2
	francesco.belli@roma2.infn.it
Bencardino Raffaele	University of Roma "Tor Vergata" and INFN
	Raffaele.Bencardino@roma2.infn.it
Benussi Luigi	INFN-LNF
	luigi.benussi@lnf.infn.it
Berezinsky Veniamin	INFN-LNGS
	Venya.Berezinsky@lngs.infn.it
Bernabei Rita	University of Roma "Tor Vergata" and INFN Roma2
	rita.bernabei@roma2.infn.it
Bernardini Paolo	University of Lecce and INFN
	paolo.bernardini@le.infn.it
Bertani Monica	INFN-LNF
	monica.bertani@lnf.infn.it
Bertolucci Sergio	INFN-LNF
	sergio.bertolucci@lnf.infn.it
Bertone Gianfranco	NASA/FERMILAB
	bertone@fnal.gov
Bianco Stefano	INFN-LNF
	stefano.bianco@lnf.infn.it
Blasi Pasquale	INAF/Osservatorio Astrofisico di Arcetri
	blasi@arcetri.astro.it
Boezio Mirko	INFN Trieste
	Mirko.Boezio@ts.infn.it

Bongiorno Lavinia	INFN-LNF	
	lavinia.bongiorno@lnf.infn.it	
Bosnjak Zeljka Marija	SISSA/ISAS	
	bosnjak@sissa.it	
Bottino Alessandro	University of Torino and INFN	
	bottino@to.infn.it	
Bruel Philippe	Laboratoire Leprince-Ringuet	
	Philippe.Bruel@poly.in2p3.fr	
Buckley James	Washington University	
	buckley@wuphys.wustl.edu	
Buttaro Vincenzo	University of Roma "Tor Vergata"	
	vincenzo.buttaro@roma2.infn.it	
Caliandro Giuseppe Andrea	University of Bari	
	andrea.caliandro@ba.infn.it	
Cappella Fabio	University of Roma "Tor Vergata"	
	Fabio.Cappella@roma2.infn.it	
Casolino Marco	INFN Roma2	
	marco.casolino@roma2.infn.it	
Cecchi Claudia	University of Perugia and INFN	
	claudia.cecchi@pg.infn.it	
Censier Benjamin	CSNSM/CNRS	
	Censier@csnsm.in2p3.fr	
Cerulli Riccardo	INFN-LNGS	
	Riccardo.Cerulli@roma2.infn.it	
Chiosso Michela	University of Torino and INFN	
	chiosso@to.infn.it	
Chita Sabina-Madalina	Max-Planck Institut fur Radioastronomie	
	schita@mpifr-bonn.mpg.de	
Ciarcelluti Paolo	University of L'Aquila	
	ciarcelluti@lngs.infn.it	
Ciufolini Ignazio	University of Lecce	
	ignazio.ciufolini@unile.it	
Coccia Eugenio	University of Roma "Tor Vergata"	
	eugenio.coccia@roma2.infn.it	
Colafrancesco Sergio	INAF - Osservatorio Astronomico di Roma	
	cola@mporzio.astro.it	
Colaiuda Antonella	University of Roma "La Sapienza" and INFN	
	antonella2883@yahoo.it	
Currie Donald	Maryland University	
	currie@umd.edu	
Datta Anindya	University of Roma "La Sapienza" and INFN	
	Anindya.Datta@roma1.infn.it	
De Bernardis Paolo	University of Roma "La Sapienza"	
	Paolo.DeBernardis@roma1.infn.it	

De Sanctis Massimo	University of Roma "La Sapienza" and INFN	massimo.desanctis@roma1.infn.it
Dell' Agnello Simone	INFN-LNF	Simone.DellAgnello@lnf.infn.it
Demirkoz Bilge	MIT	bilge@mit.edu
de Sangro Riccardo	INFN-LNF	riccardo.desangro@lnf.infn.it
Di Pippo Simonetta	Italian Space Agency - ASi	simonetta.dipippo@asi.it
Donato Fiorenza	University of Torino and INFN	donato@to.infn.it
Fabbri Franco Luigi	INFN-LNF	franco.fabbri@lnf.infn.it
Fafone Viviana	INFN-LNF	viviana.fafone@lnf.infn.it
Fargion Daniele	University of Roma "La Sapienza" and INFN	Daniele.Fargion@roma1.infn.it
Fiocchi Maria Teresa	University of Roma "La Sapienza"	mariateresa.fiocchi@asdc.asi.it
Fleury Patrick	LLR- Ecole Polytechnique - IN2P3	patrick.fleury@in2p3.fr
Frieman Joshua	Fermilab	frieman@fnal.gov
Fusco-Femiano Roberto	IASF-INAF	dario@rm.iasf.cnr.it
Gambicorti Lisa	University of Firenze	lisag@arcetri.astro.it
Gentile Simonetta	University of Roma "La Sapienza"	Simonetta.Gentile@cern.ch
Gherardi Alessandro	University of Firenze	gherardi@arcetri.astro.it
Giovannini Massimo	CERN	Massimo.Giovannini@cern.ch
Giovenale Francesco	Hamamatsu Photonics Italia	giovenale@hamamastu.it
Giommi Paolo	ASI-ASDC	paolo.giommi@asdc.asi.it
Giuliani Andrea	IASF CNR	giuliani@mi.iasf.cnr.it
Grossi Marco	University of Roma "La Sapienza" and INFN	marco.grossi@roma1.infn.it

Haungs Andreas   Forschungszentrum Karlsruhe
Andreas.Haungs@ik.fzk.de

Hofmann Werner   Max-Planck-Institut fur Kernphysik
Werner.Hofmann@mpi-hd.mpg.de

Horns Dieter   Max-Planck-Institut f. Kernphysik
dieter.horns@mpi-hd.mpg.de

Jacholkowska Agnieszka   GAM/IN2P3/CNRS
Agnieszka.Jacholkowska@cern.ch

Kifune Tadashi   Faculty of Engineering, Shinshu University
tkifune@gipwc.shinshu-u.ac.jp

Kildea John   McGill University
kildea@physics.mcgill.ca

Kniffen Donald   NASA Headquarters
donald.a.kniffen@nasa.gov

Krennrich Frank   Iowa State University
krennrich@iastate.edu

Kron Richard   Fermilab
rich@oddjob.uchicago.edu

Giuseppe Lesci   Alenia
lesci.g@laben.it

Ligi Carlo   INFN-LNF
carlo.ligi@lnf.infn.it

Lionetto Andrea   INFN Roma2 and University of Roma "Tor Vergata"
Andrea.Lionetto@roma2.infn.it

Longo Francesco   University and INFN Trieste
francesco.longo@trieste.infn.it

Piergiorgio Lucentini   University of Roma "La Sapienza" and INFN
lucentin@roma1.infn.it

M'Bany Francis   G&A Engineering

Maerna Novo umberto   Hamamatsu Photonics Italia
maerna@hamamatsu.it

Marcucci Francesca   University of Perugia
francesca.marcucci@pg.infn.it

Mazzinghi Piero   Istituto Nazionale di Ottica Applicata
mazzinghi@ino.it

Mele Barbara   INFN Roma1
barbara.mele@roma1.infn.it

Michelson Peter   Stanford University
peterm@stanford.edu

Minenkov Yury   University of Roma "Tor Vergata"
yuri.minenkov@roma2.infn.it

Minori Mauro   INFN Roma2
mauro.minori@roma2.infn.it

Morselli Aldo   INFN Roma2 and University of Roma "Tor Vergata"
                     aldo.morselli@roma2.infn.it

Moscato Federica   University of Roma "La Sapienza"
                     famargar@inwind.it

Moskalenko Igor   NASA/Goddard Space Flight Center
                     imos@milkyway.gsfc.nasa.gov

Nagni Maurizio   INFN Roma2
                     nagni@roma2.infn.it

Narici Livio   INFN Roma2
                     livio.narici@roma2.infn.it

Navarra Gianni   University of Torino
                     navarra@to.infn.it

Nozzoli Francesco   University of Roma "Tor Vergata"
                     Francesco.Nozzoli@roma2.infn.it

Odman Carolina   University of Roma "La Sapienza"
                     Carolina.Odman@roma1.infn.it

Omodei Nicola   INFN Pisa
                     nicola.omodei@pi.infn.it

Pace Emanuele   INFN Firenze
                     pace@arcetri.astro.it

Pacini Franco   Osservatorio Astrofisico di Arcetri (Firenze)
                     pacini@arcetri.astro.it

Paganoni Marco   University of Milano Bicocca and INFN
                     marco.paganoni@mib.infn.it

Palumbo Giorgio   University of Bologna
                     ggcpalumbo@bo.astro.it

Paniccia Mercedes   University of Geneva
                     Mercedes.Paniccia@physics.unige.ch

Paoletti Riccardo   University of Siena
                     riccardo.paoletti@pi.infn.it

Paolozzi Antonio   University of Roma "La Sapienza"
                     antonio.paolozzi@uniroma1.it

Pearce Mark   KTH Fysik
                     pearce@particle.kth.se

Pellizzoni Alberto   IASF -Milano
                     alberto@mi.iasf.cnr.it

Pepe Monica   INFN Perugia
                     monica.pepe@pg.infn.it

Peron Roberto   University of Lecce
                     peron@ifsi.rm.cnr.it

Petrascu Catalina   INFN-LNF
                     Catalina.Petrascu@lnf.infn.it

Petrera Sergio	University of L'Aquila	sergio.petrera@aquila.infn.it
Petrolini Alessandro	INFN Genova	alessandro.petrolini@ge.infn.it
Picozza Piergiorgio	University of Roma "Tor Vergata"	picozza@roma2.infn.it
Pieri Lidia	University of Torino	pieri@to.infn.it
Pittori Carlotta	University of Roma "Tor Vergata"	carlotta.pittori@roma2.infn.it
Pradier Thierry	University Louis-Pasteur + IReS	Thierry.Pradier@IReS.in2p3.fr
Profumo Stefano	SISSA	profumo@sissa.it
Puehlhofer Gerd	Landessternwarte Heidelberg	Gerd.Puehlhofer@lsw.uni-heidelberg.de
Pullia Antonino	INFN Milano	Antonino.Pullia@mib.infn.it
Punch Michael	PCC/APC College de France	punch@in2p3.fr
Rathke Andreas	ESA Advanced Concepts Team	andreas.rathke@esa.int
Ratti Sergio P.	University of Pavia and INFN	sergio.ratti@pv.infn.it
Ricci Marco	INFN-LNF	marco.ricci@lnf.infn.it
Ronga Francesco	INFN-LNF	francesco.ronga@lnf.infn.it
Russo Stefano	INFN Napoli	stefano.russo@na.infn.it
Russo Stefano	INFN Roma2	stefano.russo@roma2.infn.it
Sathyaprakash Bangalore	Cardiff University	B.Sathyaprakash@astro.cf.ac.uk
Sbarra Cristina	INFN Bologna	Cristina.Sbarra@bo.infn.it
Sparvoli Roberta	University of Roma "Tor Vergata"	roberta.sparvoli@roma2.infn.it
Spillantini Piero	University of Firenze	piero.spillantini@fi.infn.it
Tavani Marco	IASF - CNR Rome	tavani@rm.iasf.cnr.it
Teshima Masahiro	Max-Planck-Institute for Physics	mteshima@mppmu.mpg.de

Ullio Piero   SISSA
          ullio@sissa.it
Vacchi Andrea   INFN Trieste
          andrea.vacchi@ts.infn.it
Vercellone Stefano IASF Milano
          stefano@mi.iasf.cnr.it
Vitale Stefano   University of Trento
          vitale@science.unitn.it
Volontè Sergio   ESA
          sergio.volonte@esa.int
Volpe Francesca   University of Bari
          francesca.volpe@ba.infn.it
Watson Alan A.   University of Leeds
          a.a.watson@leeds.ac.uk
Zdravkovic Vladimir University of Roma "Tor Vergata"
          zdrav@roma2.infn.it
Zuccon Paolo   INFN Perugia
          paolo.zuccon@pg.infn.it

AUTHOR INDEX

FRASCATI PHYSICS SERIES VOLUMES

Volume I
Heavy Quarks at Fixed Target
Eds. S. Bianco and F.L. Fabbri
Frascati, May 31–June 2, 1993
ISBN—88–86409–00–1

Volume II – Special Issue
Les Rencontres de Physique de la Vallée d'Aoste –
Results and Perspectives in Particle Physics
Ed. M. Greco
La Thuile, Aosta Valley, March 5 –11, 1995
ISBN—88–86409–03–6

Volume III
Heavy Quarks at Fixed Target
Ed. B. Cox
University of Virginia, Charlottesville
October 7–10, 1994, 11
ISBN—88–86409–04–4

Volume IV
Workshop on Physics and Detectors for DAΦNE
Eds. R. Baldini, F. Bossi, G. Capon, G. Pancheri
Frascati, April 4–7, 1995
ISBN—88–86409–05–2

Volume V – Special Issue
Les Rencontres de Physique de la Vallée d'Aoste –
Results and Perspectives in Particle Physics
Ed. M. Greco
La Thuile, Aosta Valley, March 3–9, 1996
ISBN—88–86409–07–9

Volume VI
Calorimetry in High Energy Physics
Eds. A. Antonelli, S. Bianco, A. Calcaterra, F.L. Fabbri
Frascati, June 8–14, 1996
ISBN—88–86409–10–9

Volume VII
Heavy Quarks at Fixed Target
Ed. L. Kőpke
Rhinefels Castle, St. Goar, October 3–6, 1996
ISBN—88–86409–11–7

Volume VIII
ADONE a milestone on the particle way
Ed. V. Valente 1997
ISBN—88–86409–12–5

Volume IX – Special Issue
Les Rencontres de Physique de la Vallée d'Aoste –
Results and Perspectives in Particle Physics
Ed. M. Greco
La Thuile, Aosta Valley, March 2–8, 1997
ISBN–88–86409–13–3

Volume X
Advanced ICFA Beam Dynamics
Workshop on Beam Dynamics Issue for e^+e^- Factories
Eds. L. Palumbo, G. Vignola
Frascati, October 20–25, 1997
ISBN—88–86409–14–1

Volume XI
Proceedings of the XVIII International Conference on
Physics in Collision
Eds. S. Bianco, A. Calcaterra, P. De Simone, F. L. Fabbri
Frascati, June 17–19, 1998
ISBN—88–86409–15–X

Volume XII – Special Issue
Les Rencontres de Physique de la Vallée d'Aoste –
Results and Perspectives in Particle Physics
Ed. M. Greco
La Thuile, Aosta Valley, March 1–7, 1998
ISBN—88–86409–16–8

Volume XIX
XX Physics in Collision
Ed. G. Barreira
Lisbon June 29–July1st. 2000
ISBN—88–86409–25–7

Volume XX
Heavy Quarks at Fixed Target
Eds. I. Bediaga, J. Miranda, A. Reis
Rio de Janeiro, Brasil, October 9–12, 2000
ISBN—88–86409–26–5

Volume XXI
IX International Conference on Calorimetry in
High Energy Physics
Eds. B. Aubert, J. Colas, P. Nédélec, L. Poggioli
Annecy Le Vieux Cedex, France, October 9–14, 2000
ISBN—88–86409–27–3

Volume XXII – Special Issue
Les Rencontres de Physique de la Vallée d'Aoste –
Results and Perspectives in Particle Physics
Ed. M. Greco
La Thuile, Aosta Valley, March 4–10, 2001
ISBN—88–86409–28–1

Volume XXIII
XXI Physics in Collision
Ed. Soo–Bong Kim
Seoul, Korea, June 28 30, 2001
ISBN—88–86409–30–3

Volume XXIV
International School of Space Science – 2001 Course on:
Astroparticle and Gamma–ray Physics in Space
Eds. A. Morselli, P. Picozza
L'Aquila, Italy, August 30 September 7, 2000
ISBN—88–86409–31–1